Calculation of $e^- - H$ Scattering Processes using Hyperspherical Coordinates

Thesis by

Diane Marie Hood

In Partial Fulfillment of the Requirements

for the Degree

Doctor of Philosophy

California Institute of Technology

Pasadena, California

1986

Submitted Jan. 7, 1986

ACKNOWLEDGMENTS

It pleases me to take this opportunity to thank all those who have contributed to my scientific endeavors at Caltech, as well as those who have enriched my life in other ways. Special thanks go to my advisor, Prof. Aron Kuppermann. Prof. Kuppermann has provided encouragement and expert advice throughout my years here.

Fellow Kuppermann group theorists Jack A. Kaye, Paul Hipes, Steve Cuccaro, Joseph Wong, and Tim Mattson have provided hours of invaluable stimulating scientific discussions as well as kaffee-klatches. The experimental members of the group — Kerry Walzl, Charles Koerting, Jim Garvey, Jerry Winniczek, Dave Moll, Garth R. Parker, Jr. and Jin Qiu and others — have each added to the Caltech experience.

I would also like to thank the following people for their friendship: Daniel Zirin, who as The Great Zar, system manager of the Chemistry Computer Centre, indefatigably kept the computer up and running; my former roommates, Maile Smith and Linda Halle; assorted Bobcats and Wm. R. Lambert Memorial Table members Pete "Bud" Felker, Wyman "Biff" Williams, and Capt. Bob Scheid; and Drs. Harold and Mary Zirin, who have shown a continuing interest in my work. Finally I wish to thank my parents, sisters and brothers for their love and support.

D.M.H.

Abstract

A method is presented for accurately solving the Schrödinger equation for the scattering of an electron from a hydrogen atom in three dimensions, which uses hyperspherical coordinates. Our motivation for using this new technique is that previous methods — coupled channel expansions using target atom eigenfunctions,[1] polarization functions and pseudostates,[2] and variational methods[3] — have all proven unsatisfactory. The coupled channel calculations tend to have difficulty obtaining convergence with respect to basis set size, and the variational method interjects spurious resonances. Previous applications of hyperspherical coordinates[4] have used methods that, while adequate for computing the energy level of the bound state of H^-, are not appropriate to full scattering calculations.

We have obtained converged surface functions at a set of discrete values of the hyperradius, which acts as a parameter. The surface functions are further expanded in a basis set that involves 1-dimensional functions of the hyperspherical angle, which are obtained by a finite difference method.

The surface functions have been used to expand the scattering functions. The resulting coupled equations are solved numerically. The wavefunctions are obtained separately at each energy and are converged with respect to the number of basis functions used. Calculations performed so far give converged results for $J = 0$ through $J = 5$ up to the $n = 4$ threshold. The method is both accurate and efficient, and has been implemented on a VAX 11/780 with an FPS164 attached processor.

Both the magnitude and phase of elements of the scattering matrix have converged. Integral cross sections have been obtained for energies up to the $n = 4$ threshold of hydrogen. Feshbach resonances have been detected below each threshold, and they have been characterized and classified.

[1]P. G. Burke, S. Ormonde, and W. Whitaker, *Proc. Phys. Soc.* **92**, 319, (1967).

[2]S. Geltman and P. G. Burke, *J. Phys. B* **3**, 1062, (1970).

[3]J. Callaway, *Phys. Rev. A* **26**, 199, (1982).

[4]C. D. Lin, *Phys. Rev. A* **23**, 1585, (1981).

TABLE OF CONTENTS

CHAPTER 1

BACKGROUND

The electron-hydrogen atom system has been extensively studied, both theoretically and experimentally, for the past two decades,[1] and displays a very rich behavior, in terms of resonance structure. It is important to the field of scattering because it is the simplest electron-atom system, yet its solutions are not known very accurately, due to the strong correlation between the two electrons. Definitive, converged calculations have remained beyond the means of previous methods, and the dynamics of two-electron systems is still not completely understood. The purpose of this research is to solve the $e^- - H$ scattering problem accurately, with the use of hyperspherical coordinates, at energies below the ionization level.

1.1 Jacobi-coordinate Calculations

In the independent electron model, each electron is assumed to move in the combined field of the nucleus and the average distribution of the other electron(s). The natural coordinates for describing this are r_1 and r_2, the respective distances of the electrons e_1 and e_2 to the proton. The close-coupling method used by Burke *et al.* uses target atom eigenfunctions to expand the full wavefunction.[2] Integro-differential scattering equations are obtained, which are solved by an iterative method of numerical integration.[3] The basis set is thus entirely independent of the presence of the second electron, except that it is antisymmetrized due to the

identicity of the electrons. It is not entirely surprising therefore that this basis set is slowly convergent when used to describe a system where the second electron plays an all-important role. Furthermore, the integral equation aspect of the formalism makes the use of large basis sets numerically cumbersome. The close-coupling method can be modified to include correlation functions[4] and pseudostate functions[5] in the expansion. The largest close-coupling calculations included six H-atom states; fairly converged results were obtained for energies below the $n = 3$ threshold, but there was disagreement with the magnitude, but not the shape of the experimental $1s \rightarrow 2s$ cross section.[6]

In the variational method,[7] the coupled scattering equations are formulated using a pseudostate expansion. The pseudostate basis contains all of the open channel exact target atom eigenstates, while the higher bound and continuum states are represented by pseudostates chosen to be orthogonal, each of which has an associated effective energy level. The inclusion of pseudostates is preferred to having atomic eigenfunctions because of the difficulty in describing dipole polarization correctly with atomic eigenfunctions. The coefficients of the pseudostates are determined by diagonalizing the hamiltonian in the specified basis, and the Kohn variational procedure, or one of several other procedures[8,9] (inverse Kohn, optimized minimum norm-OMN, optimized anomaly free-OAF), is used for the solutions of the integro-differential equations. A major drawback of variational calculations is that there is no way to judge which set of variational results is best if the different methods give significantly different results. Another problem is the existence of non-physical resonances below the pseudostate effective energies.

Fairly accurate values of the elastic scattering phaseshifts below the inelastic threshold for partial waves $J \leq 3$ have been obtained with the variational method, beginning with the work on S-states by Schwartz.[10] and carried on to higher partial waves by Armstead,[11] Shimamura,[12] Register and Poe,[13] and Callaway.[14]

For energies between $n = 2$ and $n = 3$, the best calculations, using 14 basis functions $(6s - 5p - 2d - 1f)$, were performed by Morgan, McDowell and Callaway, and by Callaway.[15] These calculations achieved accuracy of about 1–2% in the total cross section for elastic scattering, and of about 5–10% in the total cross section for excitation of the $n = 2$ states. Excitation cross sections between the $n = 1, 2$ and 3 levels of hydrogen at energies up to the $n = 4$ threshold were performed by Hata, Morgan and McDowell[16] using 14 to 18 basis functions. These are the only calculations of cross sections in this energy range so far.

1.2 The Hyperspherical Coordinate Method

The use of hyperspherical coordinates and local surface functions in electron-atom scattering problems[17] and in 3D reactive scattering problems[18] has been suggested for over a decade, but so far converged calculations of differential or integral cross sections of inelastic or reactive processes using this methodology have not been published. The formalism is conceptually simple and in principle very powerful, affording a united treatment of non-reactive and reactive processes for molecule-molecule collisions, and of direct and exchange processes for electron-molecule collisions. It has by now been extensively tested for collinear atom-diatom reactive scattering.[19,20]

One of the difficulties in applying this approach is the accurate and efficient calculation of local hyperspherical surface functions, especially for reactive scattering processes. In the case of the electron-hydrogen atom system, these difficulties are alleviated by the symmetry of the system, the large proton to electron mass ratio, and the simple, analytically known form of the potential energy function. As a result, this is a very convenient system for the application and testing of this methodology. It is also, in some senses, an extreme prototype of light-heavy-light

triatomic reactive systems in which the light-light arrangement is either not bound, or disallowed for energetic reasons.

1.3 The Physical Basis for the Hyperspherical Coordinate Approach

The two electrons in the $e^- - H$ system do not move independently; indeed they each exert influence on the other. This is called correlation, and correlation is the reason hyperspherical coordinates are so useful for describing two electron systems. Correlation is ignored in the simplest versions of the independent electron model,[2] but more sophisticated methods attempt to add in short range correlation effects.[4]

The utility of hyperspherical coordinates becomes clear by contrast, because a large part of the electron correlation is contained in the corresponding surface function basis set. The hyperradius ρ, defined approximately by

$$\rho = (r_1^2 + r_2^2)^{\frac{1}{2}} \tag{1.1}$$

simultaneously depends on the distances of both electrons to the proton, and is a measure of the "size" of the system. The surface functions are defined as eigenfunctions of the system's hamiltonian with frozen hyperradius. The use of this variable injects some radial correlation in these functions. The non-physical hyperspherical angle ω, defined by

$$\omega = 2 \arctan \frac{r_1}{r_2} \tag{1.2}$$

is a function of the relative distances. In converting from coordinates r_1, r_2 to the hyperspherical coordinates ρ, ω one exchanges two infinite range variables for one bound and one infinite range variable. This then leads to the quasi-separability of the scattering wavefunction. Furthermore, the surface functions also depend on γ, the angle between the position vectors $\mathbf{r_1}$ and $\mathbf{r_2}$ of the two electrons with respect to the proton, and its use leads to the inclusion of angular correlation. When the latter

is expanded in hyperspherical surface functions, this expansion converges rapidly because of this quasi-separability and of the large amount of electron correlation built into those functions.

The surface function basis is considered as a family of "channels." In the surface function expansion these channels are only weakly coupled to each other and this coupling is completely neglected in the adiabatic approximation.[21] Physically this approximate decoupling implies a separation of time scales for motion in the hyperradial coordinate from motion in all the other angular coordinates, analogous to electron motion being much faster than the nuclear motion in polyatomic molecules. The angular motion is bounded, by definition, as opposed to the infinite range of the hyperradial coordinate. This separation of motion means that in slow $e^- - \mathrm{H}(1s)$ collisions certain properties of the whole system (mathematically expressed through quantum numbers) are nearly conserved. Resonance energy levels can be computed from potential curves corresponding to each channel. In this study, we solve the fully coupled channel scattering problem, and make no approximations. Since we have only differential equations to solve, not integro-differential equations, the method is computationally efficient making it possible to include a larger number of states than for other methods. The largest calculation described here included 49 surface functions, and was done on a relatively small system, a VAX 11/780 with an attached FPS164 processor. This largest calculation took 95 minutes to calculate the full surface functions, and 9 minutes for a scattering calculation.

The hyperspherical approach was used by Macek in 1968 to study the properties of Rydberg series of autoionizing levels of He.[17] Subsequent studies on the correlations of two excited electrons have been performed by Lin[21] and by Fano.[22] The hyperspherical calculations that have been performed so far have been limited due to inaccuracies in the evaluation of matrix elements $P_{\mu\nu}$ (the first derivative coupling matrix in the adiabatic representation), and most of the

calculations either ignore the coupling or severely restrict the number of states included in the expansion (up to four). In the formulation we will present, this matrix is not needed, because we use the diabatic representation in which the surface functions calculated at discrete rather than continuous values of the hyperradius.

1.4 The Interpretation of Resonances using Hyperspherical Coordinates

Hyperspherical coordinates have been found to be useful in analyzing doubly excited states, such as the Rydberg series of states of helium observed experimentally by Madden and Codling.[23] which had been unexpected, and were not explained by the close-coupling theory. The theory at the time of the discovery was incomplete because, even though levels of states could be calculated, there was no interpretation for the similarities and series found. Then Macek used hyperspherical coordinates and was able to explain the observed behavior.[17]

The cross sections we have calculated contain features that are attributed to resonances. One explanation for the resonances is the presence of autoionizing states of H^-. To understand what we mean by "autoionizing states" and "doubly-excited" states it is useful to refer to the independent electron model as applied to H^-. In the independent electron model, each electron is separately given a set of quantum numbers, $n_1 l_1$ and $n_2 l_2$, leading to a system configuration $n_1 l_1 n_2 l_2$. (The m_l and m_s quantum states for each electron are combined to form total angular momentum states J, M_J, S and M_S.)

The ground state of H^- has the configuration ^1S ($1s^2$), because both electrons are in the lowest orbital. Its energy is -0.52775 hartree.[24] If one electron is excited to a continuum level, the configuration is $1s\epsilon s$. The total energy for such a system is greater than -0.5 hartree. As it turns out, there are no singly-excited states (configuration $1s2s$, $1s3s$, etc.) of H^-, though such states do exist for the helium atom. When the total energy of the H^- system is higher than the second threshold,

at -0.125 hartree, there are two possible detached configurations — we are limiting this discussion to s orbitals — namely $1s\epsilon s$, as before, and $2s\epsilon s$, where one electron is excited to a $2s$ orbital and the other is free. But what about doubly-excited states? Configurations such as $2s^2$, $2s3s$, etc., will exist at certain energies below the $n = 2$ threshold — they must be lower, because the second electron does not have enough energy to reach the continuum. The coupling between the doubly excited state and the continuum configuration $1s\epsilon s$ allows the former to decay away. Such states are called "autodetaching" (in the case of helium, autoionizing), have a finite lifetime, and lead to the resonances observed in scattering.

However, in addition to the bound ^{1}S ($1s^2$) state of H^- there is a second (barely) bound (i. e., quadratically integrable) state of this system designated $^3P^{even}$, with the configuration $2p^2$ and energy -0.12538 hartree.[25,26] There is no $^3P^{even}$ channel that asymptotically correlates with the $1s$ state of hydrogen, because the parity of $^3P^{even}$ is $(-1)^{J+1}$. If LS-coupling is a good approximation, there is no lower state to which the $2p^2$ level may couple, thus the $2p^2$ state does not decay to the ground state nor does it autoionize. There are no other bound excited states of H^-.

Recently a new classification scheme for states of 2-electron atoms, based on the set of internal correlation quantum numbers K, T, and A has been introduced[27] Supermultiplet structure observed for intrashell states[28] may be interpreted, as well as predicted, by this scheme.

1.5 Hydrogen Atom Excitation Energies

For convenience in reading the rest of this thesis, we list in Table $1-1$ the hydrogen atom threshold energies in hartree, measured from ionization of the atom, and in rydbergs, measured from the ground state of the hydrogen atom. Furthermore, in order to make a comparison of our scattering calculations with

experimental results we must make the appropriate conversion from atomic units to the experimental units (usually eV). The conversion factors used depend on the type of experiment.[29] When comparing to a scattering experiment, the infinite-mass rydberg (13.605826 eV) is used. This is due to an effective cancellation of reduced-mass and center-of-mass effects.[29] When comparing to a photodetachment spectrum, one computes the photon energy using the hydrogen reduced-mass rydberg (13.598420 eV), and then adds in the electron affinity for hydrogen, which is 0.75422 eV. The energies in electron volts consistent with the two types of experiments are also listed in Table 1.1.

1.6 Overview

The method of hyperspherical coordinates is presented in this thesis, and the results from its application to hydrogen atom electron scattering are reported. In Chapter 2 we present the formalism used in the hyperspherical coordinate method, and in Chapter 3 we present the asymptotic analysis. Convergence studies and computational features are presented in Chapter 4. We study the basis functions, the surface functions, and the eigenvalues in Chapter 5. In Chapter 6 we present our scattering results, including discussion and analysis. In Appendix A we discuss an alternate method of expanding the surface functions in hyperspherical harmonics, and an alternative coordinate system, cylindrical coordinates. In Appendix B we give perturbation theory derivation of the asymptotic behavior of the surface functions.

Table 1-1: Energy levels of hydrogen atom.

n	E_n			
	hartree	Rydberg[b]	eV[c]	eV[d]
1	−0.50000	0.0	0.0	0.75422
2	−0.12500	0.75000	10.204	10.95859
3	−0.05556	0.88889	12.093	12.84829
4	−0.03125	0.93750	12.755	13.502
5	−0.02000	0.96000	13.061	13.81581
6	−0.01333	0.97333	13.242	13.98211
7	−0.01020	0.97959	13.327	14.08238

[a]Energy, in hartree, with respect to the ionized atom.

[b]Energy, in Rydberg, with respect to the H($1s$) state.

[c]Energy, in eV, with respect to the H($1s$) state, using the infinite mass Rydberg for conversion to eV (1 Ryd=13.605826 eV).

[d]Energy, in eV, with respect to the H^- ground ^1S state, (H atom electron affinity equals 0.75422 eV) and the reduced mass Rydberg for conversion to eV (1 Ryd=13.59842 eV).

1.7 References

1. For a review see U. Fano, *Rep. Prog. Phys.*, **46**, 97 (1983).
2. P. G. Burke, S. Ormonde, and W. Whitaker, *Proc. Phys. Soc.*, **92**, 319 (1967).
3. P. Burke and H. Schey, *Phys. Rev.*, **126**, 147 (1962).
4. P. G. Burke and A. J. Taylor, *Proc. Phys. Soc.*, **88**, 549 (1966).
5. S. Geltman and P. G. Burke, *J. Phys. B*, **3**, 1062 (1970).
6. J. F. Williams, *J. Phys. B*, **9**, 1519 (1976).
7. J. Callaway, *Phys. Rep.*, **45**, 89 (1978).
8. R. K. Nesbet, *Phys. Rev.*, **179**, 60 (1969).
9. R. K. Nesbet and R. S. Oberoi, *Phys. Rev. A*, **6**, 855 (1972).
10. C. Schwartz, *Phys. Rev.*, **124**, 1468 (1961).
11. R. L. Armstead, *Phys. Rev.*, **171**, 91 (1968).
12. I. Shimamura, *J. Phys. Soc. Jpn.*, **31**, 852 (1971).
13. D. Register and R. T. Poe, *Phys. Lett.*, **51A**, 431 (1975).
14. J. Callaway, *Phys. Lett.*, **65A**, 199 (1978).
15. L. A. Morgan, M. R. C. McDowell, and J. Callaway, *J. Phys. B*, **10**, 3297 (1977).
16. J. Hata, L. A. Morgan, and M. R. C. McDowell, *J. Phys. B*, **13**, 4453 (1980; **13**, L347, 1980).
17. J. Macek, *J. Phys. B*, **1**, 831 (1968).
18. a) A. Kuppermann, *Chem. Phys. Lett.*, **32**, 374 (1975); b) R. T. Ling and A. Kuppermann, in: *Electronic and Atomic Collisions, Abstracts of Papers of the 9th International Conference on the Physics of Electronic and Atomic Collisions*, Seattle, Washington, 24-30 July 1975, eds. J. S. Risley and R. Geballe (University of Washington Press, Seattle, 1975) pp. 353,354.

19. a) A. Kuppermann, J. A. Kaye, and J. P. Dwyer, *Chem. Phys. Lett.*, **74**, 257 (1980); b) J. A. Kaye and A. Kuppermann, *Chem. Phys. Lett.*, **77**, 573 (1981); c) J. A. Kaye and A. Kuppermann, *Chem. Phys. Lett.*, **78**, 546 (1981).

20. a) G. Hauke, J. Manz, and J. Römelt, *J. Chem. Phys.*, **73**, 5040 (1980);b) J. Römelt, *Chem. Phys. Lett.*, **74**, 263 (1980); c) J. Manz and J. Römelt, *Chem. Phys. Lett.*, **76**, 337 (1980); d) J. Manz and J. Römelt, *Chem. Phys. Lett.*, **77**, 172 (1981); e) J. Manz and J. Römelt, *Chem. Phys. Lett.*, **81**, 179 (1981).

21. a) C. D. Lin, *Phys. Rev. A*, **10**, 1986 (1974); b) C. D. Lin, *Phys. Rev. Lett.*, **35**, 1150 (1975); c) C. D. Lin, *Phys. Rev. A*, **14**, 30 (1976); d) C. D. Lin, *Phys. Rev. A*, **23**, 1585 (1981).

22. U. Fano, *Phys. Rev. A*, **24**, 2402 (1981).

23. R. P. Madden and K. Codling, *Phys. Rev. Lett.*, **10**, 516 (1963).

24. C. L. Pekeris, *Phys. Rev.*, **115**, 1216 (1959).

25. G. W. F. Drake, *Phys. Rev. Lett.*, **24**, 126 (1970).

26. A. Bhatia, *Phys. Rev. A*, **2**, 1667 (1970).

27. C. D. Lin, *Phys. Rev. Lett.*, **51**, 1348 (1983); *Phys. Rev. A*,**29**, 1019, (1984).

28. a) D. R. Herrick and M. E. Kellman, *Phys. Rev. A*, **21**, 418 (1980)b) D. R. Herrick, M. E. Kellman, and R. D. Poliak, *Phys. Rev. A*, **22**, 1517 (1980).

29. A. K. Bhatia and A. Temkin, *Phys. Rev. A*, **11**, 2018 (1975).

CHAPTER 2

FORMULATION OF THE SCATTERING PROBLEM

For electron-hydrogen atom scattering at low energies (below the ionization threshold) there are two arrangement channels, e_1+H (channel 1), and e_2+H (channel 2), where e_1 and e_2 are the two electrons. A third arrangement, in which the electrons are close to each other but distant from the proton, does not need to be considered, since it is not a stable one.

In this chapter we will set up the general Schrödinger equation for a three particle system, remove the center of mass motion, and transform to Delves' coordinates. Then we will transform to symmetrized hyperspherical coordinates and discuss features of the potential energy surface. We will describe the method used for solution of the Schrödinger equation, including the surface function expansion, calculation of potential matrix elements, and solution of the coupled radial equation.

2.1 General Three Body Problem

In this section we present the general theory for treating three body systems $A+BC$ in three dimensions. The Hamiltonian for such a system, with nine degrees of freedom, is written

$$H^{9D} = -\frac{\hbar^2}{2m_A}\nabla^2_{\mathbf{p}_A} - \frac{\hbar^2}{2m_B}\nabla^2_{\mathbf{p}_B} - \frac{\hbar^2}{2m_C}\nabla^2_{\mathbf{p}_C} + V \tag{2.1}$$

where m_A, m_B, and m_C are the masses, $\mathbf{p}_A$, $\mathbf{p}_B$, and $\mathbf{p}_C$ are position vectors from the origin of a space-fixed set of cartesian axes, $\nabla^2_{\mathbf{p}_i}$ is the Laplacian for particle i, and V is the potential energy of the system. The relative coordinates $\mathbf{r}'_A, \mathbf{R}'_A$, and $\mathbf{R}_G$ are defined by the relations

$$\begin{aligned} \mathbf{r}'_A &= \mathbf{p}_C - \mathbf{p}_B \\ \mathbf{R}'_A &= \mathbf{p}_A - \mathbf{p}_{G_{BC}} = \mathbf{p}_A - \frac{m_B\mathbf{p}_B + m_C\mathbf{p}_C}{m_B + m_C} \\ \mathbf{R}_G &= \frac{m_A\mathbf{p}_A + m_B\mathbf{p}_B + m_C\mathbf{p}_C}{M} \end{aligned} \tag{2.2}$$

where M is the total mass, G_{BC} is the center of mass of BC, and G is the center of mass of ABC. Transformation to these relative coordinates gives

$$H^{9D} = -\frac{\hbar^2}{2\mu_{A,BC}}\nabla^2_{\mathbf{R}'_A} - \frac{\hbar^2}{2\mu_{BC}}\nabla^2_{\mathbf{r}'_A} + V(R'_A, r'_A, \gamma_A) - \frac{\hbar^2}{2M}\nabla^2_{\mathbf{R}_G} \tag{2.3}$$

where the reduced masses μ_{BC} and $\mu_{A,BC}$ are defined as

$$\begin{aligned} \mu_{BC} &= \frac{m_B m_C}{m_B + m_C} \\ \mu_{A,BC} &= \frac{m_A(m_B + m_C)}{M} \end{aligned} \tag{2.4}$$

and γ_A is the angle between the vectors $\mathbf{r}'_A$ and $\mathbf{R}'_A$:

$$\cos\gamma_A = \frac{\mathbf{r}'_A \cdot \mathbf{R}'_A}{|\mathbf{r}'_A|\,|\mathbf{R}'_A|}, \qquad 0 \le \gamma_A \le \pi \tag{2.5}$$

The kinetic energy operator for the center of mass is now dropped, because the overall translation of the system is not of interest; therefore one is left with a six-dimensional problem whose Hamiltonian H is given by the first three terms in the right hand side of Eq. 2.3.

One may write the corresponding six dimensional Schrödinger equation in terms

of one mass, μ, which is independent of channel A, by transforming to Delves mass-scaled coordinates:[1]

$$\begin{aligned} \mathbf{R}_A &= \left(\frac{\mu_{A,BC}}{\mu}\right)^{1/2} \mathbf{R}'_A \\ \mathbf{r}_A &= \left(\frac{\mu_{BC}}{\mu}\right)^{1/2} \mathbf{r}'_A \\ \mu &= \left(\frac{m_A m_B m_C}{m_A + m_B + m_C}\right)^{1/2} \end{aligned} \tag{2.6}$$

The Hamiltonian H in Delves' coordinates is

$$H = -\frac{\hbar^2}{2\mu}(\nabla^2_{\mathbf{R}_A} + \nabla^2_{\mathbf{r}_A}) + V_A(R_A, r_A, \gamma_A) \tag{2.7}$$

where

$$\nabla^2_{\mathbf{R}_A} = \left(\frac{\partial^2}{\partial R_A^2}\right) + \frac{2}{R_A}\left(\frac{\partial}{\partial R_A}\right) - \frac{\hat{L}_A^2}{\hbar^2 R_A^2} \tag{2.8}$$

and

$$\nabla^2_{\mathbf{r}_A} = \left(\frac{\partial^2}{\partial r_A^2}\right) + \frac{2}{r_A}\left(\frac{\partial}{\partial r_A}\right) - \frac{\hat{L}_{r_A}^2}{\hbar^2 r_A^2} \tag{2.9}$$

If one uses laboratory-fixed coordinates,[2] by which we mean a system $Oxyz$ whose origin O is the center of mass and whose axes are parallel to a system of laboratory-fixed axes,[3] $\mathbf{r}_A$ is represented by distance r_A, azimuth θ_{r_A}, and polar angle φ_{r_A}, while $\mathbf{R}_A$ is represented by R_A, θ_{R_A}, and φ_{R_A}. The orbital angular momentum terms $\hat{L}_A^2$ and $\hat{L}_{r_A}^2$ are expressible in terms of the angles θ_{R_A}, φ_{R_A}, and θ_{r_A}, φ_{r_A}, respectively. More generally, one may rewrite the Hamiltonian using (λ, ν, κ) to represent a cyclic permutation of (ABC).

Let us consider the particular case of two electrons and one nucleus of charge Ze. The center of mass of the system will be assumed to lie on the nucleus. The error introduced by this assumption is negligible compared with the desired scattering calculation accuracy, and can be corrected for if desired by an appropriate perturbation expansion. The configuration in arrangement channel λ

is described by two mass-scaled relative separation vectors, $\mathbf{r}_\lambda = (r_\lambda, \theta_{r_\lambda}, \varphi_{r_\lambda})$ and $\mathbf{R}_\lambda = (R_\lambda, \theta_{R_\lambda}, \varphi_{R_\lambda})$.

One may also formulate the theory in terms of the "body-fixed" coordinate representation.[4,5] This representation has advantages over the laboratory-fixed representation, when certain approximations are made.[6] We will not be making these approximations, however, and will use the laboratory-fixed representation[2] throughout, except when considering the potential energy function. In the body-fixed coordinate representation the angles θ_{r_λ} and φ_{r_λ} are replaced by γ_λ, the angle between the two vectors $\mathbf{r}_\lambda$ and $\mathbf{R}_\lambda$, and ψ_λ, the "tumbling" angle. By definition ψ_λ is the angle between π_1 and π_2, where π_1 is the half-plane defined by $\mathbf{R}_\lambda$ and the space-fixed Oz-axis, and π_2 is the half-plane defined by $\mathbf{R}_\lambda$ and $\mathbf{r}_\lambda$. This so-called "tumbling" angle ranges from 0 to 2π, and is one of the three Euler angles $(\varphi_\lambda, \theta_\lambda, \psi_\lambda)$.[7]

When considering atom-diatom reactive scattering, there is an essential difference between $\hat{L}_\lambda$ and $\hat{L}_{r_\lambda}$, because L_{r_λ} refers to the rotation of the diatom, while L_λ describes the rotation of the atom with respect to the diatom. In the present application the two angular momentum operators describe the same thing, but for different electrons; therefore it makes sense to relabel them. We will use $\hat{l}_1$ for $\hat{L}_{r_\lambda}$,and $\hat{l}_2$ for $\hat{L}_\lambda$.

2.2 Hyperspherical Coordinates

We will next change to a system of coordinates in which there is only one unbounded coordinate and the rest are angular. This procedure is analogous to transformation from cartesian to polar coordinates in the collinear (1-dimensional) representation, and, in fact, may be generalized to an n-particle $(3n-3)$-dimensional system.

2.2.1 Coordinate transformation

It is advantageous to define the hyperspherical coordinates[8] ρ, ω_λ for arrangement channel $\lambda = 1, 2$ by:

$$\begin{aligned} \rho^2 &= R_\lambda^2 + r_\lambda^2 \\ \tan\frac{\omega_\lambda}{2} &= \frac{r_\lambda}{R_\lambda} \end{aligned} \tag{2.10}$$

The four angular degrees of freedom remain the same. Thus the whole system is described with six coordinates, $\rho, \omega_\lambda, \theta_{r_\lambda}, \varphi_{r_\lambda}, \theta_{R_\lambda}, \varphi_{R_\lambda}$. For simplicity, and without loss of generality, we set $\lambda = 1$ and designate these coordinates as $\rho, \omega, \theta_1, \varphi_1, \theta_2$, and φ_2, where by convention $\omega = \omega_1$. The quantity ρ is the hyperradius and the five angles are the hyperangles in the six dimensional configuration space of the system.

The coordinates in one channel are related very simply to the coordinates in the other channel, due to the symmetry inherent in the system; r_1 is the same as R_2; R_1 equals r_2; ρ_1 equals ρ_2 and thus is channel independent, and $\omega = \pi - \omega_2$. The relationships between the four angles are $\theta_{R_1} = \theta_{r_2}$, $\varphi_{R_1} = \varphi_{r_2}$, and conversely, $\theta_{r_1} = \theta_{R_2}$, $\varphi_{r_1} = \varphi_2$. The angle γ is the angle between $\mathbf{r_1}$ and $\mathbf{R_1}$ or $\mathbf{r_2}$ and $\mathbf{R_2}$ and is independent of λ. From now on, we will for simplicity replace $\mathbf{r_1}$ and $\mathbf{R_1}$ by $\mathbf{r}$ and $\mathbf{R}$, respectively, unless otherwise stated.

An important property of these coordinates is that the map of $V(\rho, \omega, \gamma)$ is not distorted when one changes from coordinates $\lambda = 1$ to $\lambda = 2$; it is only rotated.[8] The rotation is by 180° in the current problem. It is to insure this property that we have introduced the seemingly superfluous factor of $\frac{1}{2}$ in Eq. 2.10. These coordinates, without that factor of $\frac{1}{2}$, were first used by Macek[9] in studying properties of autoionizing states of He. The simplicity of the transformation from $\lambda = 1$ coordinates to $\lambda = 2$ coordinates implies that the same coordinate system may be used for both channels. There is no need for separate solutions in each

channel region, and hence no need to match the solutions[10] at the boundary of the region.

2.2.2 Hamiltonian

The Schrödinger equation we will proceed to solve is

$$H\Psi(\mathbf{r},\mathbf{R}) = E\Psi(\mathbf{r},\mathbf{R}) \tag{2.11}$$

where E is the total energy and $\Psi(\mathbf{r},\mathbf{R})$ is the six-dimensional wave function. We intend to apply standard partial wave analysis. The total angular momentum operator $\hat{J}$ is the vector sum of $\hat{l_1}$ and $\hat{l_2}$

$$\hat{J} = \hat{l_1} + \hat{l_2} \tag{2.12}$$

and is independent of channel λ. Since $\hat{J}^2$, $\hat{J}_z$, and H all commute, we expand Ψ in terms of their simultaneous eigenfunctions Ψ^{JM}:

$$\Psi = \sum_{J=0}^{\infty} \sum_{M=-J}^{+J} C_{JM}\Psi^{\mathrm{JM}} \tag{2.13}$$

The wavefunctions Ψ^{JM} therefore satisfy the equations

$$\begin{aligned} H\Psi^{\mathrm{JM}} &= E\Psi^{\mathrm{JM}} \\ \hat{J}^2\Psi^{\mathrm{JM}} &= J(J+1)\hbar^2\Psi^{\mathrm{JM}} \\ \hat{J}_z^2\Psi^{\mathrm{JM}} &= M\hbar\Psi^{\mathrm{JM}} \end{aligned} \tag{2.14}$$

The Hamiltonian H in hyperspherical coordinates is given by

$$H = -\frac{\hbar^2}{2\mu}\left(\frac{\partial^2}{\partial\rho^2} + \frac{5}{\rho}\frac{\partial}{\partial\rho}\right) + \frac{\hat{\Lambda}^2}{2\mu\rho^2} + V(\rho,\omega,\gamma) \tag{2.15}$$

where the Grand Canonical angular momentum operator $\hat{\Lambda}^2$ (also known as Casimir's operator for the O_6 group)[9] is

$$\hat{\Lambda}^2 = \hat{L}_\omega^2 + \frac{\hat{l_1}^2}{\sin^2\frac{\omega}{2}} + \frac{\hat{l_2}^2}{\cos^2\frac{\omega}{2}} \tag{2.16}$$

and the hyperspherical pseudo-angular momentum operator $\hat{L}_\omega^2$ is

$$\begin{aligned}\hat{L}_\omega^2 &= -4\hbar^2\Big(\frac{\partial^2}{\partial\omega^2} + 2\cot\omega\frac{\partial}{\partial\omega}\Big) \\ &= -4\hbar^2\frac{1}{\sin\omega}\Big(\frac{\partial^2}{\partial\omega^2} + 1\Big)\sin\omega\end{aligned} \tag{2.17}$$

The eigenfunctions Φ_η of $\hat{\Lambda}^2$ are the analytically known hyperspherical harmonics, with eigenvalues $\eta(\eta+4)$, where η is an integer.[11] However, the potential V does not commute with $\hat{\Lambda}^2$, so the wavefunction is not factorizable into an angular part (involving the five hyperangles) and a $\rho-$dependent part. The eigenfunctions of $\hat{\Lambda}^2$ may be used to expand the wavefunction, however, which we consider in Appendix A.

2.2.3 Potential energy function

The potential energy function for the system of two electrons and a nucleus of charge Z is the sum of the Coulomb interactions of the three particles:

$$V(\mathbf{r}',\mathbf{R}') = -\frac{Ze^2}{|\mathbf{r}'|} - \frac{Ze^2}{|\mathbf{R}'|} + \frac{e^2}{|\mathbf{r}'-\mathbf{R}'|} \tag{2.18}$$

Here the zero of energy is taken to be the energy of the configuration for which the three particles are infinitely separated. Since the mass scaling factors are very close to unity, we may set $\mathbf{r}=\mathbf{r}'$ and $\mathbf{R}=\mathbf{R}'$ without loss of accuracy. In hyperspherical coordinates the potential becomes

$$V(\rho,\omega,\gamma) = -\frac{e^2}{\rho}\Big(\frac{Z}{\cos\frac{\omega}{2}} + \frac{Z}{\sin\frac{\omega}{2}} - \frac{1}{\sqrt{1-\sin\omega\cos\gamma}}\Big) \tag{2.19}$$

Note that this potential has a simple $1/\rho$ dependence. We might expect that the forces involved will be long range and die off slowly.

In order to better visualize the properties of the electron-hydrogen atom system, we obtained contour plots of V for energies both above and below the ionization

potential. This was done by establishing a correspondence between the three-dimensional internal configuration space spanned by coordinates ρ, ω, and γ and points P in space $OXYZ$.[8] This correspondence is given by the relations

$$\begin{aligned} Z &= \rho \cos\omega \\ X &= \rho \sin\omega \cos\gamma \\ Y &= \rho \sin\omega \sin\gamma \end{aligned} \tag{2.20}$$

by which we see that the internal coordinates are being treated as spherical polar coordinates in this mapping. The range of γ is 0 to π, and there is a one-to-one correspondence between points in the $Y \geq 0$ half-space of the $OXYZ$ space and configurations of the system. For display purposes, we will extend the range of γ to 0 to 2π and make all of our plots of the potential energy symmetric about the OXZ ($\gamma = 0, \pi$) plane.

The potential of the system with the energy origin shifted to the ground state of an isolated hydrogen atom will be labeled V_0. Plots of the equipotential for $V_0 = 10.5$ eV ($V = -3.1$ eV) were obtained at constant values of Z ranging from 0 to 24 bohr, at 2 bohr intervals. These were used to construct a wooden model of the surface, which has been helpful in visualizing the scattering processes. We found that this equipotential surface resembled a cylindrical pipe with a sharp dimple, or puncture, reaching to the cylinder's axis. A photograph of that model is given in Figure 2.1.

The most interesting feature of the potential surface is the part near the origin, the dimple. Consider what happens when $Z = 0$, that is, $\omega = \frac{\pi}{2}$:

$$\begin{aligned} r &= \rho \sin\frac{\omega}{2} = \rho/\sqrt{2} \\ R &= \rho \cos\frac{\omega}{2} = \rho/\sqrt{2} \end{aligned} \tag{2.21}$$

These configurations correspond to the two electrons being equidistant from the proton. The angle between the vectors **r** and **R** is γ, as usual. The contour at $Z = 0$ is given by the equation

$$\rho V = C_1 + \frac{C_2}{\sqrt{1 - \cos\gamma}} \tag{2.22}$$

where C_1 and C_2 are constants easily obtained from Eq. 2.19. This is approximately the equation of a cardioid, provided V (not V_0) is negative. In Figure 2.2 we show several contours, from which we see that a cusp forms around $\gamma = 0$, which corresponds to $Y = 0$, $X > 0$. This is due to the high repulsion between the two electrons, which are very close to one another in this region. On the other side, for $\gamma = \pi$ (and X negative), the electrons are separated by the proton and the energy of the system is finite. The contours (for $Z = 0$) extend further and further out as one considers higher energies. The limit is reached at $V_0 = 13.6$ eV, which corresponds to ionization of the hydrogen atom. The equation of the corresponding contour is now

$$\cos\gamma = C_3 \tag{2.23}$$

The bottom of the heart shape has retreated to infinity, and the top (in three dimensions) becomes a cone-shaped potential surface. The points along the axis of the cone correspond to $\gamma = 0$ and $\omega = \frac{\pi}{2}$. The potential is infinitely positive along this positive X axis, corresponding to the two electrons on top of one another and the proton elsewhere.

We show the contours obtained at higher values at Z =constant in Figures 2.3– 5. One can see from the series of curves that as Z increases, the contours become increasing circular. Besides this lack of dependence on γ, the contours asymptotically become independent of Z. The potential on the Z azis (for $\rho \neq 0$) is negative infinity, and the corresponding configuration is one electron on top of the proton and the other electron elsewhere.

By plotting contours obtained at constant $Y = 0$ in Figure 2.6 we get a view of the equipotential surface on a cut perpendicular to that in Figure 2.2. In these plots γ equals 0 in the right half of the plane and π in the left half. One can see that the three-dimensional internal configuration space is divided into two symmetric arrangement channels by the $Z = 0$ ($\omega = \frac{\pi}{2}$) plane.

A scattering experiment can be visualized as follows. One end of the tube corresponds to $e_1 + pe_2$. As e_1 approaches the atom, the system can either "bounce" off the cone, resulting in non-exchange, or the system can undergo exchange, that is, it passes through to the other end of the cone, which represents $e_2 + pe_1$. If the energy is larger than the ionization potential I of hydrogen, the walls of the vertical tube no longer bind the system. Instead the system can penetrate into the $V = I$ cone and a larger region of configuration space is energetically accessible.

2.3 Symmetry Properties

The Hamiltonian of the system is invariant with respect to exchange of the electrons and to inversion of the electrons through the proton (in the infinite mass approximation for the proton being adopted in these calculations). As a result, solutions to the Schrödinger equation can be found which are simultaneously eigenfunctions of the exchange operator $\hat{P}_{12}$ and the inversion operator $\hat{\Im}$. This leads to quantum numbers $p = \pm 1$ for exchange and $(-1)^{\Pi}$, where $\Pi = 0, 1$ for inversion for the orbital part of the wavefunction.

$$\begin{aligned} \hat{P}_{12}\Psi^{JMS\Pi}(1) &= \Psi^{JMS\Pi}(2) = p\Psi^{JMS\Pi}(1) \\ \hat{\Im}\Psi^{JMS\Pi} &= (-1)^{\Pi}\Psi^{JMS\Pi} \end{aligned} \tag{2.24}$$

The Pauli principle requires that the total wavefunction change sign when the coordinates of the two identical fermion particles are exchanged. The total wavefunction is the product of the orbital part with the spin part; therefore a

function that is anti-symmetric in the spin function, indicating a singlet ($S = 0$) spin state must be spatially symmetric with respect to exchange. Likewise the Pauli principle dictates that the triplet ($S = 1$) spin state, which is symmetric with respect to exchange, must go with an anti-symmetric spatial wavefunction. Thus we make the following correspondence between exchange and spin quantum numbers:

$$p = (-1)^S \tag{2.25}$$

There is no similar connection between Π and S. In the physical wavefunction S will still be a good quantum number, but it is necessary to take linear combinations of the even and odd parity states.

2.4 Surface Function Expansion

Motion in the ρ coordinate is almost decoupled from the hyperangular coordinates. To the extent that this is true, it makes sense to try to separate the $\rho-$dependence from the angular dependence in the wave function. This being the case, we construct basis functions (analogous to vibrational functions) that have only parametrical dependence on ρ.

The pseudoangle ω is a function of the ratio of the distances of the two electrons to the proton. The kinetic energy associated with pseudoangular motion is greater than that due to radial motion, because the pseudoangular variable is bounded whereas the radius is not.[12] This suggests the use of a Born-Oppenheimer type expansion,[13] analogous to the expansion of the wavefunction of a atom-diatom $A + BC$ system in the vibrational states of BC. In the first approximation, this expansion is then truncated to only one term.[9]

The surface functions $\Phi^{JMS\Pi}$ (so called because they are defined on the *surface* of the hypersphere) are defined as the eigenfunctions of the surface Hamiltonian $\overline{H}$

which is obtained by omitting in the Hamiltonian H the hyperradial kinetic energy operator:[9]

$$\overline{H}(\rho) = \frac{\hat{\Lambda}^2}{2\mu\rho^2} + V(\rho,\omega,\gamma) \tag{2.26}$$

Therefore

$$\overline{H}(\rho)\ \Phi_i^{JMS\Pi}(\omega, 4 \text{ angles}; \rho) = \varepsilon_i^{JS\Pi}(\rho)\ \Phi_i^{JMS\Pi} \tag{2.27}$$

where i is an index here introduced to label these surface functions. We expand $\Psi_i^{JMS\Pi}$ in the surface functions with coefficients $b^{JS\Pi}{}_i^{i'}$ and put in the $\rho^{-5/2}$ factor to simplify the resulting equations:[9]

$$\Psi_{i'}^{JMS\Pi} = \rho^{-\frac{5}{2}} \sum_i b^{JS\Pi}{}_i^{i'}\ \Phi_i^{JMS\Pi}(\omega, 4 \text{ angles}; \rho) \tag{2.28}$$

The index i' is introduced to permit consideration of a set of many linearly independent solutions of the Schrödinger equation which are needed to obtain the appropriate scattering matrices.

2.4.1 Expansion of surface functions in non-symmetric basis

The eigenfunctions of $\hat{l}_j^2$ are spherical harmonics, $Y_{l_j m_j}(\theta_j, \varphi_j)$. Following Arthurs and Dalgarno,[2] we couple the $Y_{l_1 m_1}$ and $Y_{l_2 m_2}$ to form orthonormal eigenfunctions of the total angular momentum operator J^2 and its projection J_z, as well as $\hat{l_1}^2$ and $\hat{l_2}^2$:

$$\mathcal{Y}_{l_2 l_1}^{JM}(\theta_2, \varphi_2, \theta_1, \varphi_1) = \sum_{m_1 m_2} C(l_1 l_2 J; m_1 m_2 M) Y_{l_2 m_2}(\theta_2, \varphi_2) Y_{l_1 m_1}(\theta_1, \varphi_1) \tag{2.29}$$

where the C's are Clebsch-Gordan coefficients in the notation of Rose.[14]

Let us expand the surface functions $\Phi_i^{JMS\Pi}$ in these coupled spherical harmonics. The expansion coefficients $f^{JS\Pi}{}_{l_2 l_1}^{i}(\omega;\rho)$ will be called the one-dimensional surface functions.

$$\Phi_i^{JMS\Pi} = \sum_{l_2 l_1} \mathcal{Y}_{l_2 l_1}^{JM}(\theta_2, \varphi_2, \theta_1, \varphi_1) f^{JS\Pi}{}_{l_2 l_1}^{i}(\omega;\rho) \tag{2.30}$$

This expansion is substituted into the Schrödinger equation for $\Phi^{JMS\Pi}$, using the known relationships satisfied by the $\mathcal{Y}^{JM}_{l_2 l_1}$. We multiply both sides of the resulting equation by $\mathcal{Y}^{JM}_{l_2' l_1'}(\theta_2, \varphi_2, \theta_1, \varphi_1)$ and integrate over the four angles, taking advantage of the orthonormality of these functions. The following equation results:

$$\frac{1}{2\mu\rho^2}\left(\hat{L}^2_\omega + \frac{l_1'(l_1'+1)\hbar^2}{\sin^2\frac{\omega}{2}} + \frac{l_2'(l_2'+1)\hbar^2}{\cos^2\frac{\omega}{2}}\right) f^{JS\Pi i}_{l_2' l_1'}(\omega;\rho) + \sum_{l_2 l_1} V^{J\Pi l_2 l_1}_{l_2' l_1'} f^{JS\Pi i}_{l_2 l_1}(\omega;\rho) = \varepsilon_i^{JS\Pi}(\rho) f^{JS\Pi i}_{l_2' l_1'} \tag{2.31}$$

where the $V^{J\Pi l_2 l_1}_{l_2' l_1'}$ are the surface potential matrix elements

$$V^{J\Pi l_2 l_1}_{l_2' l_1'}(\omega;\rho) = \langle \mathcal{Y}^{JM}_{l_2 l_1} \mid V(\rho,\omega,\gamma) \mid \mathcal{Y}^{JM}_{l_2' l_1'} \rangle \tag{2.32}$$

It is simple to show that $V^{J\Pi l_2 l_1}_{l_2' l_1'}(\omega;\rho) = V^{J\Pi l_1 l_2}_{l_1' l_2'}(\omega;\rho)$ and that it is a symmetric function of ω:

$$V^{J\Pi l_2 l_1}_{l_2' l_1'}(\omega;\rho) = V^{J\Pi l_2 l_1}_{l_2' l_1'}(\pi-\omega;\rho).$$

Now we expand $f^{JS\Pi i}_{l_2 l_1}$ in functions $t_p^{Jl_2 l_1}(\omega;\rho)$. We have not yet specified what form these functions will take; that is discussed below.

$$f^{JS\Pi i}_{l_2 l_1} = \sum_p c^{JS\Pi i}_{l_2 l_1 p} t_p^{Jl_2 l_1}(\omega;\rho) \tag{2.33}$$

The functions $t_p^{Jl_2 l_1}(\omega;\rho)$ appearing in Eq. 2.33 form a complete set which can be arbitrarily chosen. The criteria for their choice are that they be easy to compute and give fast convergence of the expansion in Eq. 2.33, permitting it to be truncated after just a few terms.

A simple choice for $t_p^{Jl_2 l_1}(\omega;\rho)$ would be to solve the equation which results from Eq. 2.31 if one neglects V entirely.[13] This approach has some good points. The solutions[11] then are analytically known functions, the Jacobi polynomials, which when multiplied by $\mathcal{Y}^{JM}_{l_2 l_1}$, are eigenfunctions of $\hat{\Lambda}^2$. Also, that equation is solved

independent of ρ, so the same basis functions can be used to expand the surface functions at every value of ρ, which is a computational advantage. However, this basis works well only for a small range of ρ and converges very slowly for larger values of ρ.[15,16] We consider this method separately in Appendix A.

We decided to use solutions to the following differential equation, in which we neglect the off-diagonal terms of the potential matrix, such that

$$\left[\frac{1}{2\mu\rho^2}\left(\hat{L}_\omega^2+\frac{l_1(l_1+1)}{\sin^2\frac{\omega}{2}}+\frac{l_2(l_2+1)}{\cos^2\frac{\omega}{2}}\right)+V^{J\Pi\,l_2l_1}_{\;\;l_2l_1}(\omega;\rho)\right]t_p^{Jl_2l_1}(\omega;\rho) = \nu_p^{J\Pi l_2l_1}(\rho)\,t_p^{Jl_2l_1}(\omega;\rho) \tag{2.34}$$

where $\nu_p^{J\Pi l_2l_1}(\rho)$ are the eigenvalues of the equation. In Eq. 2.34 the only variable (upon which the differential operator $\hat{L}_\omega^2$ operates) is ω. The quantity ρ acts as a parametric variable. If one makes the change of variable from ω to $\pi-\omega$, one gets the same equation, but with l_1 interchanged with l_2. This means that

$$t_p^{Jl_2l_1}(\pi-\omega;\rho)=t_p^{Jl_1l_2}(\omega;\rho), \tag{2.35}$$

except in the special case where $l_1=l_2$, where both symmetric and antisymmetric solutions are possible, as is discussed below in greater detail.

This equation is solved numerically using finite difference methods to obtain the eigenvalues and eigenfunctions. Section 5.1 is devoted to studying these functions in detail and contains figures of them. To make the numerical solution simpler, we divide out $\sin\omega$ to remove the first derivative:

$$T_p^{Jl_2l_1}(\omega;\rho)=\sin\omega\,t_p^{Jl_2l_1}(\omega;\rho) \tag{2.36}$$

This forces the boundary condition $T_p^{Jl_2l_1}(\omega=0;\rho)=0$, $T_p^{Jl_2l_1}(\omega=\pi;\rho)=0$ in order for $t_p^{Jl_2l_1}(\omega;\rho)$ to be finite at those values of ω. Then the coupled differential equation becomes

$$-\frac{2\hbar^2}{\mu\rho^2}\frac{d^2}{d\omega^2}T_p^{Jl_2l_1}(\omega;\rho)+V_{\text{eff}}^{Jl_2l_1}\,T_p^{Jl_2l_1}(\omega;\rho)=\nu_p^{J\Pi l_2l_1}(\rho)\;T_p^{Jl_2l_1}(\omega;\rho) \tag{2.37}$$

where the effective potential is

$$V_{\rm eff}^{Jl_2l_1} = -\frac{\hbar^2}{2\mu\rho^2}\left(4 - \frac{l_2(l_2+1)}{\cos^2\frac{\omega}{2}} - \frac{l_1(l_1+1)}{\sin^2\frac{\omega}{2}}\right) + V^{J\Pi\,l_2l_1}_{l_2l_1}(\omega;\rho) \qquad (2.38)$$

The ρ dependence in $V^{J\Pi\,l_2l_1}_{l_2l_1}(\omega;\rho)$ can be factored out according to Eq. 2.19. However, since that is a ρ^{-1} dependence while the kinetic energy operators have a ρ^{-2} dependence, ρ cannot be removed entirely from the equations, and the eigenfunctions $T_p^{Jl_2l_1}(\omega;\rho)$ must be computed separately for each value of ρ. One approach is to compute the $T_p^{Jl_2l_1}(\omega;\rho)$ at a discrete set of values $\bar{\rho}_i$ of ρ such that for each $\bar{\rho}_i$, that set is appropriate for a range of values of ρ (see section 2.6).

The basis functions $T_p^{Jl_2l_1}(\omega;\rho)$ (which we will call "primitives" to distinguish them from the surface functions, which also are basis functions, after all) are determined separately for each $[l_2l_1]$ combination. Basis functions with the same $[l_1l_2]$ are orthogonal. These functions are normalized according to

$$\int_0^\pi T_p^{Jl_2l_1}(\omega;\rho)\; T_{p'}^{Jl_2l_1}(\omega;\rho)\; d\omega = \delta^p_{p'} \qquad (2.39)$$

If l_1 equals l_2 then the effective potential $V_{\rm eff}^{Jl_2l_1}$ is symmetric with respect to $\omega = \frac{\pi}{2}$ (i. e., with respect to exchange between r_1 and r_2). The T_p^{Jll} functions are therefore either symmetric or antisymmetric, and are obtained in separate calculations. A function that is symmetric in ω does not always correspond to a 5-dimensional basis function that is symmetric overall (i. e., with respect to exchange of the two electrons), however. The symmetry of $\mathcal{Y}_{ll}^{JM}$ is determined by the evenness or oddness of J because the parity Π is always even when l_1 equals l_2. Thus if J is even, the singlet basis functions will be symmetric with respect to $\omega = \frac{\pi}{2}$, but if J is odd, then it is the triplet basis functions that have this symmetry. If J is odd, the singlet 5-dimensional basis functions, which are even overall, are antisymmetric

with respect to $\omega = \frac{\pi}{2}$. We will therefore use the notation T^{Jll}_{pJ+s} and a similar notation for t^{Jll}_{pJ+s}.

Using the primitives defined by Eq. 2.37 and Eq. 2.39, we can transform Eq. 2.31 into an algebraic eigenvalue-eigenvector equation in the $\varepsilon_i^{JS\Pi}(\rho)$ and $c^{JS\Pi i}_{l_2 l_1 p}$. Indeed we get, replacing Eq. 2.33 into Eq. 2.31,

$$\sum_p \Big[\nu_p^{J\Pi l_2 l_1}(\rho) - \varepsilon_i^{JS\Pi}(\rho) - V^{J\Pi}{}^{l_2 l_1}_{l_2 l_1}(\omega;\rho)\Big] c^{JS\Pi i}_{l_2 l_1 p}\, t_p^{Jl_2 l_1}(\omega;\rho) + \sum_{l_2' l_1' p} c^{JS\Pi i}_{l_2' l_1' p}(\rho) V^{J\Pi}{}^{l_2 l_1}_{l_2' l_1'}\, t_p^{Jl_2' l_1'}(\omega;\rho) = 0 \tag{2.40}$$

The above equation is multiplied by $\sin^2\omega\ t_{p'}^{Jl_2 l_1}(\omega;\rho)$ and integrated over $d\omega$, which results in the following equation after p' and p are interchanged:

$$\sum_{p'} \Big\{ \big[\nu_p^{J\Pi l_2 l_1}(\rho) - \varepsilon_i^{JS\Pi}(\rho)\big]\delta^p_{p'} - V^{J\Pi}{}^{l_2 l_1 p}_{l_2 l_1 p'} \Big\} c^{JS\Pi i}_{l_2 l_1 p} + \sum_{l_2' l_1' p'} c^{JS\Pi i}_{l_2' l_1' p'}(\rho) V^{J\Pi}{}^{l_2 l_1 p}_{l_2' l_1' p'} = 0 \tag{2.41}$$

where

$$V^{J\Pi}{}^{l_2 l_1 p}_{l_2' l_1' p'} = \left\langle t_p^{Jl_2 l_1}(\omega;\rho) \,\middle|\, V^{J\Pi}{}^{l_2 l_1}_{l_2' l_1'} \,\middle|\, t_{p'}^{Jl_2' l_1'} \right\rangle \tag{2.42}$$

This is the desired algebraic eigenvalue-eigenvector problem. We define the diagonal matrices

$$(\mathbf{u}^{J\Pi})^{l_2 l_1 p}_{l_2' l_1' p'} = \delta^{l_2 l_1 p}_{l_2' l_1' p'}\, \nu_p^{J\Pi l_2 l_1}(\rho) \tag{2.43}$$

$$(\mathbf{e}^{J\Pi})^{Si}_{S'i'} = \delta^{Si}_{S'i'} \varepsilon_i^{JS\Pi}(\rho) \tag{2.44}$$

the interaction matrix $\mathbf{V_0}^{J\Pi}$,

$$(\mathbf{V_0}^{J\Pi})^{l_2 l_1 p}_{l_2' l_1' p'}(\rho) = (1 - \delta^{l_2 l_1}_{l_2' l_1'}) V^{J\Pi}{}^{l_2 l_1 p}_{l_2' l_1' p'} \tag{2.45}$$

which is symmetric and only has elements in off-diagonal blocks, and the eigenvector matrix $\mathbf{c}^{J\Pi}$

$$(\mathbf{c}^{J\Pi})^{Si}_{l_2 l_1 p} = c^{JS\Pi i}_{l_2 l_1 p}(\rho) \tag{2.46}$$

Stating the eigenvector problem in matrix notation we have

$$(\mathbf{V_0}^{J\Pi} + \mathbf{u}^{J\Pi})\ \mathbf{c}^{J\Pi} = \mathbf{c}^{J\Pi}\ \mathbf{e}^{J\Pi} \tag{2.47}$$

Thus we have obtained an equation that is decoupled in both J and Π, but not according to spin, which is included as a column index in $\mathbf{c}^{J\Pi}$ as well as the index i. In the next section we will obtain a transformed equation which has been decoupled in S as well.

2.4.2 Symmetrized basis

If the basis functions in which we expand the surface functions $\Phi_i^{JMS\Pi}$ have the same property regarding exchange and therefore spin as $\Psi^{JMS\Pi}$ in Eq. 2.24, then the matrix equations decouple and much effort is saved. Therefore we require that our new primitive basis functions $\Theta^{JMS\Pi}$ behave as follows:[17]

$$\Theta^{JMS\Pi}_{l_2 l_1 p}(\omega, \theta_1, \varphi_1, \theta_2, \varphi_2; \rho) = (-1)^{\mathrm{S}} \Theta^{JMS\Pi}_{l_2 l_1 p}(\pi - \omega, \theta_2, \varphi_2, \theta_1, \varphi_1; \rho) \tag{2.48}$$

The basis functions in which we have expanded $\Phi_i^{JMS\Pi}$ so far are decoupled with respect to parity, but not exchange. This can be shown as follows.

To invert the coordinates through the origin, one replaces θ_j, φ_j by $\pi - \theta_j, \pi + \varphi_j$ (ω is unchanged by inversion). From the definition of $\mathcal{Y}^{JM}_{l_2 l_1}$ (Eq. 2.29) and the properties of spherical harmonics one obtains

$$\hat{\Im} \mathcal{Y}^{JM}_{l_2 l_1}(\theta_2, \varphi_2, \theta_1, \varphi_1) = (-1)^{l_1 + l_2} \mathcal{Y}^{JM}_{l_2 l_1}(\theta_2, \varphi_2, \theta_1, \varphi_1) \tag{2.49}$$

from which we can link the parity quantum number to $l_1 + l_2$,

$$\Pi = (l_1 + l_2) \bmod 2 = \frac{1 - (-1)^{l_1 + l_2}}{2} \tag{2.50}$$

We have already seen the effect of exchanging coordinates (1) for (2) on

$t_p^{Jl_2l_1}(\omega;\rho)$ (see Eq. 2.35), but not on $\mathcal{Y}_{l_2l_1}^{JM}$. The relationship between $\mathcal{Y}_{l_2l_1}^{JM}$ and $\mathcal{Y}_{l_1l_2}^{JM}$ is easily obtained:[10]

$$\begin{aligned}\mathcal{Y}_{l_2l_1}^{JM}(\theta_2,\varphi_2,\theta_1,\varphi_1) &= (-1)^{J-l_2-l_1}\mathcal{Y}_{l_1l_2}^{JM}(\theta_1,\varphi_1,\theta_2,\varphi_2) \\ &= (-1)^{J-\Pi}\ \mathcal{Y}_{l_1l_2}^{JM}(\theta_1,\varphi_1,\theta_2,\varphi_2)\end{aligned} \tag{2.51}$$

Thus we see that changing the coordinate system from $\lambda = 1$ to $\lambda = 2$ has the effect of switching l_1 and l_2 as well as a possible change of sign in $\mathcal{Y}_{l_2l_1}^{JM}$. The effect of $\hat{P}_{12}$ on the entire primitive basis function is

$$\begin{aligned}&\hat{P}_{12}\left[\mathcal{Y}_{l_2l_1}^{JM}(\theta_2,\varphi_2,\theta_1,\varphi_1)\, t_p^{Jl_2l_1}(\omega;\rho)\right] = \\ &\qquad (-1)^{J-\Pi}\mathcal{Y}_{l_1l_2}^{JM}(\theta_2,\varphi_2,\theta_1,\varphi_1)\, t_p^{Jl_2l_1}(\pi-\omega;\rho)\end{aligned} \tag{2.52}$$

It is clear that the simple product function $\mathcal{Y}_{l_2l_1}^{JM}(\theta_2,\varphi_2,\theta_1,\varphi_1)\, t_p^{Jl_2l_1}(\omega;\rho)$ does not possess exchange symmetry.

To obtain such a property we take linear combinations of two such products according to

$$\begin{aligned}\Theta_{l_2l_1p}^{JMS\Pi} = N_{l_2l_1}\big[&\mathcal{Y}_{l_2l_1}^{JM}(\theta_2,\varphi_2,\theta_1,\varphi_1)\, t_p^{Jl_2l_1}(\omega;\rho) \\ &+ (-1)^{\Lambda}\mathcal{Y}_{l_1l_2}^{JM}(\theta_2,\varphi_2,\theta_1,\varphi_1)\, t_p^{Jl_2l_1}(\pi-\omega;\rho)\big]\end{aligned} \tag{2.53}$$

where

$$\Lambda = S + J - \Pi \tag{2.54}$$

and $N_{l_2l_1}$ is a normalization coefficient. Note that only the 5-dimensional function has been symmetrized. We do not form symmetric and antisymmetric functions of ω, nor do we symmetrize the $\mathcal{Y}_{l_2l_1}^{JM}$ functions, because to do so results in more work.[18] However, when $l_1 = l_2$ only one term is needed:

$$\Theta_{llp}^{JMS\Pi} = \mathcal{Y}_{ll}^{JM}(\theta_2,\varphi_2,\theta_1,\varphi_1)\ t_{p_{J+S}}^{Jll}(\omega;\rho) \tag{2.55}$$

The basis functions must be linearly independent, of course, and this leads to a restriction on the values assumed by l_1 and l_2, because $\Theta_{l_1l_2n}^{JMS\Pi}$ differs from $\Theta_{l_2l_1p}^{JMS\Pi}$

by, at most, a sign change. We therefore expand over pairs $[l_1 l_2]$, for which, by definition, $l_1 \leq l_2$.

$$\Phi_i^{JMS\Pi} = \sum_{[l_1 l_2]p} a_{l_2 l_1 p}^{JS\Pi i}(\rho)\ \Theta_{l_2 l_1 p}^{JMS\Pi}(\omega, 4 \text{ angles}; \rho) \tag{2.56}$$

The new coefficients $a_{l_2 l_1 p}^{JS\Pi i}(\rho)$ are obtained from $c_{l_2 l_1 p}^{JS\Pi i}$ by a linear transformation.

$$\begin{aligned} c_{l_2 l_1 p}^{JS\Pi i} &= \frac{1}{\sqrt{2}}\, a_{l_2 l_1 p}^{JS\Pi i}(\rho) \\ c_{l_1 l_2 p}^{JS\Pi i} &= \frac{1}{\sqrt{2}}(-1)^{\Lambda} a_{l_2 l_1 p}^{JS\Pi i}(\rho) \end{aligned} \tag{2.57}$$

where $l_1 < l_2$. This leads to

$$a_{l_2 l_1 p}^{JS\Pi i}(\rho) = \frac{1}{\sqrt{2}}\left(c_{l_2 l_1 p}^{JS\Pi i} + (-1)^{\Lambda} c_{l_1 l_2 p}^{JS\Pi i}\right) \tag{2.58}$$

We define the unitary matrix $\mathbf{T}$ such that we have

$$\mathbf{c}^{J\Pi} = \mathbf{T} \times \begin{bmatrix} \mathbf{a}^{J\Pi, S=0} & \mathbf{0} \\ \mathbf{0} & \mathbf{a}^{J\Pi, S=1} \end{bmatrix} \tag{2.59}$$

The new uncoupled eigenvector-eigenvalue equation is

$$(\mathbf{V_0}^{JS\Pi} + \mathbf{u}^{JS\Pi})\ \mathbf{a}^{JS\Pi} = \mathbf{a}^{JS\Pi}\ \mathbf{e}^{JS\Pi} \tag{2.60}$$

where we define the diagonal matrices

$$\begin{aligned} (\mathbf{u}^{JS\Pi})_{l_2' l_1' p'}^{l_2 l_1 p} &= \delta_{l_2' l_1' p'}^{l_2 l_1 p}\, \nu_p^{J\Pi l_2 l_1}(\rho) \\ (\mathbf{e}^{JS\Pi})_{i'}^{i} &= \delta_{i'}^{i} \varepsilon_i^{JS\Pi}(\rho) \end{aligned} \tag{2.61}$$

and the interaction matrices $\mathbf{V_0}^{JS\Pi}$ are obtained by a unitary transformation from $\mathbf{V_0}^{J\Pi}$:

$$\begin{bmatrix} \mathbf{V_0}^{J\Pi, S=0} & \mathbf{0} \\ \mathbf{0} & \mathbf{V_0}^{J\Pi, S=1} \end{bmatrix} = \tilde{\mathbf{T}} \mathbf{V_0}^{J\Pi} \mathbf{T} \tag{2.62}$$

The elements of $\mathbf{V_0}^{JS\Pi}$ are found to be, using Eq. 2.45,

$$(\mathbf{V_0}^{JS\Pi})_{l_2' l_1' p'}^{l_2 l_1 p}(\rho) = (1 - \delta_{l_2' l_1'}^{l_2 l_1}) V^{J\Pi\, l_2 l_1 p}_{\quad l_2' l_1' p'} + (-1)^{\Lambda} V^{J\Pi\, l_2 l_1 p}_{\quad l_1' l_2' p'} \tag{2.63}$$

which is also symmetric. It should be remembered that Λ has been defined by Eq. 2.54, and the values of l_1, l_2 and l_1', l_2' are restricted by the value of Π according to Eq. 2.50.

If one is considering a case where only $l_1 = l_2$ states are allowed (as is the case for $J = 0$ and for $J = 1$ with even Π), then the elements of $\mathbf{u}^{JS\Pi}$ depend on S since, in their determination from Eq. 2.34 they are calculated separately, as discussed after Eq. 2.39. In this case the elements of $\mathbf{u}^{JS\Pi}$ may be rewritten as

$$(\mathbf{u}^{JS\Pi})^{l_1 l_1 p}_{l_1' l_1' p'} = \delta^{l_1 p}_{l_1' p'} \nu^{J l_1 l_1}_{n_{J+S}}(\rho) \tag{2.64}$$

The eigenvector matrix $\mathbf{a}^{JS\Pi}$ is orthogonal since it is the eigenvector matrix of the real symmetric matrix $\mathbf{V_0}^{JS\Pi} + \mathbf{u}^{JS\Pi}$. We describe the method used to numerically calculate the potential functions $V^{J\Pi}{}^{l_2 l_1}_{l_2' l_1'}(\omega;\rho)$ and potential matrix elements $V^{J\Pi}{}^{l_2 l_1 p}_{l_2' l_1' p'}$ in the following section.

2.5. Calculation of Potential Matrix Elements

In this section we will show how the potential functions $V^{J\Pi}{}^{l_2 l_1}_{l_2' l_1'}(\omega;\rho)$ are calculated[19] as well as the matrix elements $V^{J\Pi}{}^{l_2 l_1 p}_{l_2' l_1' p'}(\rho)$. These numbers are needed in order to calculate the surface functions. The potential matrix is a function of ω at a fixed value of ρ, and was defined as follows in the previous section:

$$V^{J\Pi}{}^{l_2 l_1}_{l_2' l_1'}(\omega;\rho) = \langle \mathcal{Y}^{JM}_{l_2 l_1}(\theta_2,\varphi_2,\theta_1,\varphi_1) \mid V(\rho,\omega,\gamma) \mid \mathcal{Y}^{JM}_{l_2' l_1'}(\theta_2,\varphi_2,\theta_1,\varphi_1) \rangle \tag{2.65}$$

where the brackets indicate integration over the full range of the variables $\theta_1, \varphi_1, \theta_2$, and φ_2 (and therefore of γ).

The potential energy function is most easily expressed using the body-fixed angular coordinate γ, as well as the hyperspherical coordinates, ρ and ω.

$$V(\rho,\omega,\gamma) = -\frac{Ze^2}{\rho}\left(\frac{1}{\cos\frac{\omega}{2}} + \frac{1}{\sin\frac{\omega}{2}}\right) + \frac{e^2}{\rho}\frac{1}{\sqrt{1-\sin\omega\cos\gamma}} \tag{2.66}$$

The first two terms in the potential, representing electron-nucleus attraction, are independent of the integration variables of Eq. 2.65, and lead to diagonal terms in the potential matrix. The off-diagonal elements in those matrices results from the third (electron repulsion) term.

It is convenient, for the evaluation off the potential energy matrix elements, to make a change of variables from space-fixed angles to body-fixed angles, and to use the orthonormalized functions $\mathcal{D}^{JM}_{\Omega l_1}(\theta,\varphi,\gamma,\psi)$:

$$\mathcal{D}^{JM}_{\Omega l_1}(\theta,\varphi,\gamma,\psi) = \sqrt{\frac{2J+1}{8\pi^2}}\, D^{J}_{M\Omega}(\varphi,\theta,\psi) P^{\Omega}_{l_1}(\gamma) \tag{2.67}$$

These functions are products of Wigner rotation functions[14] $D^{J}_{M\Omega}$ and renormalized Legendre polynomials[10] $P^{\Omega}_{l_1}(\gamma)$,

$$P^{\Omega}_{l_1}(\gamma) = P^{|\Omega|}_{l_1}(\cos\gamma)\left(\frac{(l_1-|\Omega|)!}{(l_1+|\Omega|)!}\frac{2l_1+1}{2}\right)^{1/2} \times \begin{cases} (-1)^{|\Omega|} & \Omega > 0, \\ 1 & \Omega \leq 0 \end{cases} \tag{2.68}$$

The spherical harmonic $Y^{\Omega}_{l_1}$ is related to $P^{\Omega}_{l_1}(\gamma)$ by

$$Y^{\Omega}_{l_1}(\gamma,\phi) = P^{\Omega}_{l_1}(\gamma) \times \frac{e^{i\Omega\phi}}{\sqrt{2\pi}} \tag{2.69}$$

The functions $\mathcal{D}^{JM}_{\Omega l_1}$ are simultaneous eigenfunctions of the total angular momentum operator $\hat{J}^2$, its projection along the laboratory-fixed z-axis $\hat{J}_z$, as well as its projections along a body-fixed axis $\hat{J}_{z'}$ and of the square of the orbital angular momentum $\hat{l}_1^2$:

$$\begin{aligned} \hat{J}^2 \mathcal{D}^{JM}_{\Omega l_1} &= J(J+1)\hbar^2 \mathcal{D}^{JM}_{\Omega l_1} \\ \hat{J}_z^2 \mathcal{D}^{JM}_{\Omega l_1} &= M\hbar \mathcal{D}^{JM}_{\Omega l_1} \\ \hat{J}_{z'}^2 \mathcal{D}^{JM}_{\Omega l_1} &= \Omega\hbar \mathcal{D}^{JM}_{\Omega l_1} \\ \hat{l_1}^2 \mathcal{D}^{JM}_{\Omega l_1} &= l_1(l_1+1)\hbar^2 \mathcal{D}^{JM}_{\Omega l_1} \end{aligned} \tag{2.70}$$

The $\mathcal{Y}^{JM}_{l_2 l_1}$ and the $\mathcal{D}^{JM}_{\Omega l_1}$ are inter-related by the expression[10]

$$\mathcal{Y}^{JM}_{l_2 l_1}(\theta_2,\varphi_2,\theta_1,\varphi_1) = \sum_{\Omega=-J}^{J} (-1)^{l_1-\Omega} C(Jl_1l_2;\Omega\ -\Omega 0)\mathcal{D}^{JM}_{\Omega l_1}(\theta,\varphi,\gamma,\psi) \qquad (2.71)$$

where $\theta_2 = \theta$ and $\varphi_2 = \varphi$. Substituting for $\mathcal{Y}^{JM}_{l_2 l_1}$ in the potential matrix element expression Eq. 2.65, and taking advantage of the orthonormality of $\mathcal{D}^{JM}_{\Omega l_1}$ gives the following:

$$\begin{aligned} V^{J\Pi}{}^{l_2 l_1}_{l_2' l_1'} =& (-1)^{l_1+l_1'} \sum_{\Omega} C(Jl_1'l_2';\Omega\ -\Omega 0)C(Jl_1l_2;\Omega\ -\Omega 0)V^{\Omega}_{l_1 l_1'}(\omega;\rho) \\ & - \frac{1}{\rho}\,\delta^{l_1' l_2'}_{l_1 l_2}\left(\frac{1}{\cos\frac{\omega}{2}} + \frac{1}{\sin\frac{\omega}{2}}\right) \end{aligned} \qquad (2.72)$$

where we have defined a new quantity, $V^{\Omega}_{l_1 l_1'}(\omega;\rho)$, by

$$V^{\Omega}_{l_1 l_1'}(\omega;\rho) = \frac{1}{\rho}\int_0^{\pi} P^{\Omega *}_{l_1'}(\gamma)(1-\sin\omega\cos\gamma)^{-\frac{1}{2}} P^{\Omega}_{l_1}(\gamma)\sin\gamma d\gamma \qquad (2.73)$$

In order to compute this integral, we expand the repulsion energy term in a series of Legendre polynomials of $\cos\gamma$.[6] A different expansion results for $\omega < \frac{\pi}{2}$ than for $\omega > \frac{\pi}{2}$:

$$(1-\sin\omega\cos\gamma)^{-\frac{1}{2}} = \begin{cases} \dfrac{1}{\cos\frac{\omega}{2}} \displaystyle\sum_{k=0}^{\infty} P_k(\cos\gamma)\tan^k\frac{\omega}{2} & \text{for } 0 \le \omega \le \frac{\pi}{2} \\ \dfrac{1}{\sin\frac{\omega}{2}} \displaystyle\sum_{k=0}^{\infty} P_k(\cos\gamma)\cot^k\frac{\omega}{2} & \text{for } \frac{\pi}{2} \le \omega \le \pi \end{cases} \qquad (2.74)$$

Using this expansion leads to integrals over products of three associated Legendre functions, which can be evaluated analytically. The result[14] involves the product of two Clebsch-Gordan coefficients:

$$\int_0^{\pi} P^{\Omega *}_{l_1'}(\gamma)P_k(\cos\gamma)P^{\Omega}_{l_1}(\gamma)\sin\gamma d\gamma = \sqrt{\frac{2l_1+1}{2l_1'+1}}C(l_1kl_1';000)Cl_1kl_1';\Omega 0\Omega) \qquad (2.75)$$

The above expression vanishes in certain cases. First of all, the Clebsch-Gordan coefficient $C(l_1kl_1';000)$ is non-zero only if the sum l_1+k+l_1' is an even number.[14]

Secondly, there must be a triangular relation[14] among the integers l_1, k, l_1' which means that the infinite expansions in k of the repulsion are effectively truncated without approximation. The final exact expression for $V^{\Omega}_{l_1 l_1'}(\omega;\rho)$ is thus found to be the following:

$$V^{\Omega}_{l_1 l_1'}(\omega;\rho) = \frac{1}{\rho}\sqrt{\frac{2l_1+1}{2l_1'+1}}\sum_i C(l_1 k l_1';000)\, C(l_1 k l_1';\Omega 0\Omega)\frac{\tan^k \frac{\omega'}{2}}{\cos\frac{\omega'}{2}} \tag{2.76}$$

where ω' is an angle in the 0 to $\frac{\pi}{2}$ range defined by

$$\omega' = \begin{cases} \omega, & \text{for } 0 \le \omega \le \frac{\pi}{2} \\ \pi - \omega, & \text{for } \frac{\pi}{2} \le \omega \le \pi \end{cases} \tag{2.77}$$

Replacement of Eq. 2.76 into Eq. 2.72 gives finally

$$\begin{aligned} V^{J\Pi}{}^{l_2 l_1}_{l_2' l_1'} = (-1)^{l_1+l_1'}\frac{1}{\rho}\sqrt{\frac{2l_1+1}{2l_1'+1}}\sum_m \frac{\tan^m\frac{\omega'}{2}}{\cos\frac{\omega'}{2}}\, C(l_1 m l_1';000) \\ \times \sum_\Omega C(J l_1' l_2';\Omega\ -\Omega 0)\, C(J l_1 l_2;\Omega\ -\Omega 0)\, C(l_1 m l_1';\Omega 0\Omega) \\ -\frac{1}{\rho}\,\delta^{l_2' l_1'}_{l_2 l_1}\left(\frac{1}{\cos\frac{\omega}{2}}+\frac{1}{\sin\frac{\omega}{2}}\right). \end{aligned} \tag{2.78}$$

The matrix elements $V^{J\Pi}{}^{l_2 l_1 p}_{l_2' l_1' p'}(\rho)$ are obtained from Eq. 2.42 by trapezoidal rule integration over ω. This rule is used because the $t_p^{J l_2 l_1}(\omega;\rho)$ functions were obtained by a first order finite difference method as described in section 2.4.1.

2.6 Solution of the Coupled Equations

Once the surface functions $\Phi^{JMS\Pi}$ defined by Eq. 2.27 are obtained, the next step is to determine the radial function expansion coefficients $b^{JS\Pi}$ introduced in Eq. 2.28:

$$\Psi^{JMS\Pi}_{i'} = \rho^{-\frac{5}{2}}\sum_i b^{JS\Pi}{}^{i'}_{i}\ \Phi^{JMS\Pi}_i(\omega, 4 \text{ angles};\rho) \tag{2.32}$$

In section 2.2 we stated that the Hamiltonian in hyperspherical coordinates was H:

$$H = -\frac{\hbar^2}{2\mu}\left(\frac{\partial^2}{\partial\rho^2}+\frac{5}{\rho}\frac{\partial}{\partial\rho}\right)+\frac{\hat{\Lambda}^2}{2\mu\rho^2}+V(\rho,\omega,\gamma) \tag{2.79}$$

We find it convenient to define a new Hamiltonian here, $\widetilde{H}$:

$$\widetilde{H} = \rho^{\frac{5}{2}}\ H\ \rho^{-\frac{5}{2}} = -\frac{\hbar^2}{2\mu}\frac{\partial^2}{\partial\rho^2} + \frac{15\hbar^2}{8\mu\rho^2} + \frac{\hat{\Lambda}^2}{2\mu\rho^2} + V \tag{2.80}$$

such that

$$\widetilde{H}\ (\rho^{\frac{5}{2}}\ \Psi^{JMS\Pi}) = E(\rho^{\frac{5}{2}}\ \Psi^{JMS\Pi}). \tag{2.81}$$

There are two useful ways to treat the surface functions: one is to let them be continuously variable in ρ, the other is to let ρ take on only discrete values from the set $\{\bar{\rho}_j\}$.

We used the second option, which is to say we have a diabatic representation. This is in contrast to the work of C. D. Lin,[13,15] and of Klar[20] in hyperspherical coordinates, who both used the adiabatic representation. In the latter one needs to evaluate the derivatives of the surface functions with respect to ρ. In the diabatic representation all these derivatives are automatically equal to zero, because the surface functions (as opposed to the scattering wave function) do not depend on ρ. However it also means that each coefficient $b^{JS\Pi}$ depends on $\bar{\rho}_j$ as well as on ρ, and that there will be potential coupling in the scattering equations, in lieu of the coupling which derives from the ρ dependence of the surface functions in the adiabatic representation, as will be seen in Sections 2.6.1 and 2.6.2.

2.6.1. Diabatic representation

The equation coupling the expansion coefficients $b^{JS\Pi}$ is obtained by substituting the expansion in Eq. 2.28 into the Schrödinger equation (2.81), multiplying by an arbitrary surface function, and integrating over the five angles. The surface functions satisfy Eq. 2.27 with $\rho = \bar{\rho}$ and are orthonormal. The Hamiltonian $\widetilde{H}$ of Eq. 2.80 is re-expressed in terms of the surface function Hamiltonian $\overline{H}$ of Eq. 2.26 as

$$\widetilde{H} = -\frac{\hbar^2}{2\mu}\frac{\partial^2}{\partial\rho^2} + \frac{15\hbar^2}{8\mu\rho^2} + \left(\frac{\bar{\rho}}{\rho}\right)^2\overline{H}(\bar{\rho}) + V(\rho,\omega,\gamma) - \left(\frac{\bar{\rho}}{\rho}\right)^2 V(\bar{\rho},\omega,\gamma) \tag{2.82}$$

The substitution just mentioned gives

$$\sum_i \Bigg\{ \left[-\frac{\hbar^2}{2\mu}\frac{d^2}{d\rho^2} + \frac{15\hbar^2}{8\mu\rho^2} + \left(\frac{\bar{\rho}}{\rho}\right)^2 \varepsilon_i^{JS\Pi}(\bar{\rho}) - E \right] b^{JS\Pi}{}_i^{i'} \; \Phi_i^{JMS\Pi} + \left[V(\rho,\omega,\gamma) - \left(\frac{\bar{\rho}}{\rho}\right)^2 V(\bar{\rho},\omega,\gamma) \right] b^{JS\Pi}{}_i^{i'} \; \Phi_i^{JMS\Pi} \Bigg\} = 0 \tag{2.83}$$

One now multiplies by $\Phi_{i''}^{JMS\Pi *}$ and integrates over the five angles with the volume element $\sin^2\omega d\omega \sin\theta_1 d\theta_1 d\varphi_1 \sin\theta_2 d\theta_2 d\varphi_2$ appropriate for space-fixed hyperspherical coordinates leading to the following coupled equation:

$$-\frac{\hbar^2}{2\mu}\frac{d^2}{d\rho^2} b^{JS\Pi}{}_i^{i'} + \left[\frac{15\hbar^2}{8\mu\rho^2} + \left(\frac{\bar{\rho}}{\rho}\right)^2 \varepsilon_i^{JS\Pi}(\bar{\rho}) - E \right] b^{JS\Pi}{}_i^{i'}(\rho;\bar{\rho}) + \sum_{i''} \left\langle \Phi_i^{JMS\Pi} \,\middle|\, V(\rho,\omega,\gamma) - \left(\frac{\bar{\rho}}{\rho}\right)^2 V(\bar{\rho},\omega,\gamma) \,\middle|\, \Phi_{i''}^{JMS\Pi} \right\rangle b^{JS\Pi}{}_{i''}^{i'} = 0 \tag{2.84}$$

There are no $d\Phi_i^{JMS\Pi}/d\rho$ terms in the equation above because, by definition, $\Phi_i^{JMS\Pi}$ is independent of ρ. If we define

$$\left[\mathbf{\Delta V}^{JS\Pi}(\rho;\bar{\rho}) \right]_{i''}^{i} = \left\langle \Phi_i^{JMS\Pi} \,\middle|\, V(\rho,\omega,\gamma) - \left(\frac{\bar{\rho}}{\rho}\right)^2 V(\bar{\rho},\omega,\gamma) \,\middle|\, \Phi_{i''}^{JMS\Pi} \right\rangle \tag{2.85}$$

we get the following matrix equation:

$$-\frac{\hbar^2}{2\mu}\frac{d^2\mathbf{b}^{JS\Pi}}{d\rho^2} + \mathbf{\Delta V}^{JS\Pi}\mathbf{b}^{JS\Pi} + \left[\left(\frac{\bar{\rho}}{\rho}\right)^2 \mathbf{e}^{JS\Pi} + \left(\frac{15\hbar^2}{8\mu\rho^2} - E\right)\mathbf{I} \right] \mathbf{b}^{JS\Pi} = \mathbf{0} \tag{2.86}$$

All the matrices appearing in this equation are square and their dimension equals the number of surface functions used in Eq. 2.28. To put this equation in more general form we define $\mathbf{U}^{JS\Pi}$:

$$\mathbf{U}^{JS\Pi} = -\frac{2\mu}{\hbar^2}\left(\mathbf{\Delta V}^{JS\Pi} + \left(\frac{\bar{\rho}}{\rho}\right)^2 \mathbf{e}^{JS\Pi} + \left(\frac{15\hbar^2}{8\mu\rho^2} - E\right)\mathbf{I} \right) \tag{2.87}$$

which gives

$$\frac{d^2\mathbf{b}^{JS\Pi}}{d\rho^2} + \mathbf{U}^{JS\Pi}\mathbf{b}^{JS\Pi} = \mathbf{0}. \tag{2.88}$$

This is the coupled differential equation for the radial coefficients $b^{JS\Pi}$ using the diabatic representation. The rest of this section is devoted to solving this equation and to calculating the coupling matrix $\mathbf{\Delta V}^{JS\Pi}$, which is symmetric, as can be seen from Eq. 2.85.

The ρ dependence factors out of the matrix elements of $\mathbf{\Delta V}^{JS\Pi}(\rho;\bar{\rho})$. Indeed, we may write Eq. 2.19 in the form

$$V(\rho,\omega,\gamma) = \frac{1}{\rho}\, C(\omega,\gamma) \tag{2.89}$$

where

$$C(\omega,\gamma) = -e^2\left[\frac{\mathrm{Z}}{\cos^2\frac{\omega}{2}} + \frac{\mathrm{Z}}{\sin^2\frac{\omega}{2}} - \frac{1}{\sqrt{1-\sin\omega\cos\gamma}}\right] \tag{2.90}$$

As a result we can write

$$V(\rho,\omega,\gamma) - \left(\frac{\bar{\rho}}{\rho}\right)^2 V(\bar{\rho},\omega,\gamma) = \frac{1}{\rho}\left[1-\left(\frac{\bar{\rho}}{\rho}\right)\right] C(\omega,\gamma) \tag{2.91}$$

We then substitute the expansion of the surface functions into the integral expression to obtain

$$\mathbf{\Delta V}^{JS\Pi}(\rho;\bar{\rho}) = \frac{1}{\rho}\left[1-\left(\frac{\bar{\rho}}{\rho}\right)\right]\, \tilde{\mathbf{a}}^{JS\Pi}(\bar{\rho})\, \mathbf{C}^{JS\Pi}(\bar{\rho})\, \mathbf{a}^{JS\Pi}(\bar{\rho}) \tag{2.92}$$

where we have defined $\mathbf{C}^{JS\Pi}(\bar{\rho})$ as the matrix with elements

$$\begin{aligned} C^{JS\Pi}(\bar{\rho})^{l_2' l_1' p'}_{l_2 l_1 p} &= \left\langle \Theta^{JMS\Pi}_{l_2' l_1' p'} \,\middle|\, C(\omega,\gamma) \,\middle|\, \Theta^{JMS\Pi}_{l_2 l_1 p} \right\rangle \\ &= \bar{\rho}\, \left(V^{J\Pi}{}^{l_2 l_1 p}_{l_2' l_1' p'} + (-1)^{\Lambda} V^{J\Pi}{}^{l_2 l_1 p}_{l_1' l_2' p'} \right) \end{aligned} \tag{2.93}$$

which are independent of ρ and only have to be evaluated once for each surface function. Actually, these coupling matrix elements are very closely related to the potential matrix elements needed for diagonalization in the surface function basis set. Only the elements in diagonal $(l_1 l_2)$ subblocks need to be calculated, for the others have been obtained already.

It should be noted that the $\mathbf{a}^{JS\Pi}$ matrix, whose rows are labeled by $l_2 l_1 p$, and whose columns are labeled by k (see Eq. 2.34), is not necessarily square. Nevertheless, the left hand side of Eq. 2.92 is appropriately square and has the dimensions specified after Eq. 2.86. This permits the number of surface functions used in Eq. 2.28 to be much smaller than the number of primitive functions used in Eq. 2.56 in the determination of these surface functions. This is a very important consideration leading to a major saving in computation time. Without such a truncation of basis size, one might as well have expanded the wavefunction Ψ^{JM} in the primitive functions directly.

If one integrates using Gordon's method,[21] the first and second derivative of $\mathbf{U}^{JS\Pi}$ with respect to ρ are also needed. The nice thing about Eq. 2.87 is that all the ρ dependence is in analytical form, so we get the derivatives analytically:

$$\begin{aligned} -\frac{\hbar^2}{2\mu}\frac{d}{d\rho}\mathbf{U}^{JS\Pi} &= -\frac{15\hbar^2}{4\mu\rho^3}\mathbf{I} - \frac{2\bar{\rho}^2}{\rho^3}\mathbf{e}^{J\Pi} - \frac{1}{\rho^2}\left[1-2\left(\frac{\bar{\rho}}{\rho}\right)\right]\overline{\mathbf{C}}^{JS\Pi}(\bar{\rho}) \\ -\frac{\hbar^2}{2\mu}\frac{d^2}{d\rho^2}\mathbf{U}^{JS\Pi} &= \frac{45\hbar^2}{4\mu\rho^4}\mathbf{I} + \frac{6\bar{\rho}^2}{\rho^4}\mathbf{e}^{J\Pi} + \frac{2}{\rho^3}\left[1-3\left(\frac{\bar{\rho}}{\rho}\right)\right]\overline{\mathbf{C}}^{JS\Pi}(\bar{\rho}) \end{aligned} \tag{2.94}$$

where

$$\overline{\mathbf{C}}^{JS\Pi}(\bar{\rho}) = \tilde{\mathbf{a}}^{JS\Pi}(\bar{\rho})\mathbf{C}^{JS\Pi}(\bar{\rho})\mathbf{a}^{JS\Pi}(\bar{\rho}).$$

2.6.1.1. Logarithmic derivative integration

Instead of solving the matrix differential equation (2.88), one can instead change the unknown function $\mathbf{b}^{JS\Pi}(\rho;\bar{\rho})$ to its logarithmic derivative, defined to be (dropping the omnipresent $JS\Pi$ superscript)

$$\mathbf{y}(\rho;\bar{\rho}) = \mathbf{b}'(\rho;\bar{\rho})\mathbf{b}^{-1}(\rho;\bar{\rho}) \tag{2.95}$$

The second order differential equation for $\mathbf{b}$ is thus transformed into the first order non-linear Ricatti differential equation for $\mathbf{y}$.[22]

$$\mathbf{y}'(\rho;\bar{\rho}) + \mathbf{y}^2(\rho;\bar{\rho}) + \mathbf{U}(\rho;\bar{\rho}) = 0 \tag{2.96}$$

We use an efficient procedure developed by Johnson[23] to numerically integrate this equation, using the initial condition $\mathbf{y} = 10^{36}\ \mathbf{I}$, that is, essentially infinite. This corresponds to the initial conditions of $\mathbf{b} = \mathbf{0}$, $\mathbf{b}' = \mathbf{I}$ at $\rho = \rho_0$, where ρ_0 is a value close to zero. These initial conditions are justified by the fact that the final results converge with respect to the particular choice of ρ_0.

The calculational method consists in integrating $\mathbf{b}$ or $\mathbf{y}$ out to a large enough ρ for the electron-hydrogen atom interaction to have become negligible. One then "projects" the resulting scattering wavefunction Ψ on the asymptotic hydrogen atom wavefunctions. The Johnson integration scheme is used to propagate the wavefunction from ρ_0 until the projection distance is reached. Then, if projecting at constant $R = R_{\text{proj}}$ (as explained in Chapter 3), one changes over to the Gordon method of integrating, which is described, briefly, below. One then continues integrating until ρ reaches a value large enough to have furnished the wavefunction at each projection point ($r_{\text{min}} \leq r \leq r_{\text{max}}$ at fixed R_{proj}). If one is instead projecting at constant ρ, the radial integration is complete at this stage and one moves directly into the projection phase.

2.6.1.2. Gordon Integration

The Gordon integrator,[21] which obtains both $\mathbf{b}(\rho;\bar{\rho})$ and $\mathbf{b}'(\rho;\bar{\rho})$, approximates the potential by a piecewise linear function and solves the equation analytically in each linear region using Airy functions. The solutions in each section are joined together continuously, and the step size is regulated by an internal check on the size of the error, based on the size of the first order perturbation term relative to the wavefunction itself. One begins the integration in an area where the wavefunction can be presumed to be null, because the potential energy is much greater than the total energy. However, in our application, the starting point is the beginning of the projection region, and one takes unity for $\mathbf{b}$ and the log-derivative $\mathbf{y}(\rho;\bar{\rho})$ for

$\mathbf{b}'$. Compared to the Johnson method, much more work is required per integration step, although much larger steps may be taken with Gordon's method, especially in regions where the potential flattens out. A good deal of the effort required in Gordon's method is energy-independent, which means the calculation for the first energy is long, but the calculations at subsequent energies are much faster by comparison. No such relative improvement is obtained using the Johnson method.

2.6.2 Adiabatic representation

In the adiabatic representation the surface functions are considered to change continuously as functions of ρ. Thus we can define and calculate derivatives of the surface functions with respect to ρ. There is no difference, when substituting into the full Schrödinger equation, between the value of ρ at which the surface functions are evaluated and the ρ in the equation. This means that the potential matrix term drops out, unlike the diabatic representation, because the surface functions are chosen to diagonalize $\overline{H}$. The coupling is therefore due to the first derivative term, not the potential energy. The corresponding matrix differential equation in this representation differs from that of the diabatic one.

Let us define $\mathbf{W^{(1)}}(\rho)$, the first derivative matrix, and $\mathbf{W^{(2)}}(\rho)$, the second derivative:

$$\mathbf{W^{(1)}}_{ij}(\rho) = \left\langle \Phi_i(\rho) \,\middle|\, \frac{\partial}{\partial \rho} \,\middle|\, \Phi_j(\rho) \right\rangle \tag{2.97}$$

$$\mathbf{W^{(2)}}_{ij}(\rho) = \left\langle \Phi_i \,\middle|\, \frac{\partial^2}{\partial \rho^2} \,\middle|\, \Phi_j \right\rangle \tag{2.98}$$

where the hyperspherical coordinate integration volume element in the integrals is the one given after Eq. 2.83. The second order equation obtained from Eq. 2.28 is now

$$\frac{d^2\mathbf{b}^{JS\Pi}}{d\rho^2} - 2\mathbf{W^{(1)}}\frac{d\mathbf{b}^{JS\Pi}}{d\rho} - \left(\mathbf{W^{(2)}} + E\mathbf{I} - \mathbf{e}(\rho)\right)\mathbf{b}^{JS\Pi} = \mathbf{0} \tag{2.99}$$

All the coupling in this equation comes from the off-diagonal elements of $\mathbf{W^{(1)}}$ and $\mathbf{W^{(2)}}$, whereas the coupling in the diabatic representation Eq. 2.88 comes from the off-diagonal terms in the potential matrix Eq. 2.87. The appearance of a $d\mathbf{b}^{JS\Pi}/d\rho$ term in Eq. 2.99 is a disadvantage of the adiabatic representation.

It is easy to show that the first derivative matrix is non-Hermitian, but that $i\mathbf{W^{(1)}}$ is Hermitian,[24] as a simple consequence of the orthogonality of the Φ_j basis functions, as we now show.[25] The orthonormality of the functions is stated mathematically as

$$\left\langle \Phi_i \middle| \Phi_j \right\rangle = \delta_{ij} \tag{2.100}$$

where the integration volumen element is, as usual, the one indicated after Eqs. 2.83 and 2.98. Both sides of this equation are differentiated with respect to ρ, which leaves

$$\left\langle \frac{\partial \Phi_i}{\partial \rho} \middle| \Phi_j \right\rangle + \left\langle \Phi_i \middle| \frac{\partial \Phi_j}{\partial \rho} \right\rangle = 0 \tag{2.101}$$

which directly gives

$$\mathbf{W^{(1)}}^*_{ji} = -\mathbf{W^{(1)}}_{ij} \tag{2.102}$$

from which it follows that $i\mathbf{W^{(1)}}$ is Hermitian. The basis functions Φ_i have complex components due to the $\mathcal{Y}^{JM}_{l_2 l_1}$ functions, but one can see that $\mathbf{W^{(1)}}$ is real by substituting expansion (2.56) into the integrals. Then one obtains

$$\mathbf{W^{(1)}} = \tilde{\mathbf{a}}^{JS\Pi} \, \frac{d\mathbf{a}^{JS\Pi}}{d\rho} + \tilde{\mathbf{a}}^{JS\Pi} \, \mathbf{T^{(1)}} \, \mathbf{a}^{JS\Pi} \tag{2.103}$$

where $\mathbf{T^{(1)}}$ is a matrix diagonal in l_1 and l_2, and skew symmetric, defined by

$$\left[\mathbf{T^{(1)}}\right]^{l_2 l_1 p}_{l_2' l_1' p'} = \left\langle t_p^{J l_2 l_1}(\omega;\rho) \middle| \frac{\partial}{\partial \rho} \middle| t_{p'}^{J l_2' l_1'} \right\rangle \delta^{l_2' l_1'}_{l_2 l_1} \tag{2.104}$$

and $\mathbf{a}^{JS\Pi}$ is the eigenvector matrix obtained by diagonalizing the real symmetric matrix $\mathbf{V_0}^{JS\Pi} + \mathbf{u}^{JS\Pi}$. Since we have shown that $\mathbf{W^{(1)}}$ is real it follows from

Eq. 2.102 that $\mathbf{W^{(1)}}$ is skew-symmetric. We use an analogous procedure to determine that the second derivative matrix can be written as

$$\mathbf{W^{(2)}} = \tilde{\mathbf{a}}^{JS\Pi}\left[\mathbf{I}\frac{d^2}{d\rho^2} + \mathbf{T^{(2)}} + 2\mathbf{T^{(1)}}\frac{d}{d\rho}\right]\mathbf{a}^{JS\Pi} \tag{2.105}$$

where $\mathbf{T^{(2)}}$ is defined just like $\mathbf{T^{(1)}}$ but with the second derivative operator replacing the first derivative one. We will now investigate the properties of $\mathbf{W^{(2)}}$. For reasons that will become clear later, we differentiate the equation for $\mathbf{W^{(1)}}$, obtaining

$$\frac{d}{d\rho}\mathbf{W^{(1)}}_{ij} = \left\langle \frac{\partial\Phi_i}{\partial\rho}\middle|\ \frac{\partial\Phi_j}{\partial\rho}\right\rangle + \left\langle \Phi_i\middle|\ \frac{\partial^2\Phi_j}{\partial\rho^2}\right\rangle \tag{2.106}$$

$$= \left\langle \frac{\partial\Phi_i}{\partial\rho}\middle|\ \frac{\partial\Phi_j}{\partial\rho}\right\rangle + \mathbf{W^{(2)}}_{ij} \tag{2.107}$$

The skew-symmetry of $\mathbf{W^{(1)}}$ thus leads to

$$\mathbf{W^{(2)}}_{ij} + \mathbf{W^{(2)}}_{ji} = -2\left\langle \frac{\partial\Phi_i}{\partial\rho}\middle|\ \frac{\partial\Phi_j}{\partial\rho}\right\rangle \tag{2.108}$$

For the diagonal elements of $\mathbf{W^{(2)}}$ one obtains

$$\mathbf{W^{(2)}}_{jj} = -\left\langle \frac{\partial\Phi_j}{\partial\rho}\middle|\ \frac{\partial\Phi_j}{\partial\rho}\right\rangle \tag{2.109}$$

from which it is apparent that $\mathbf{W^{(2)}}$ is not skew symmetric. This could also have been ascertained from Eq. 2.105. $\mathbf{T^{(2)}}$ is also not skew symmetric. Let us now calculate the matrix elements of $\mathbf{W^{(1)}}^2$. By definition,

$$(\mathbf{W^{(1)}})^2_{ij} = \sum_k \left\langle \Phi_i\middle|\ \frac{\partial\Phi_k}{\partial\rho}\right\rangle\left\langle \Phi_k\middle|\ \frac{\partial\Phi_j}{\partial\rho}\right\rangle \tag{2.110}$$

We use the fact that $\mathbf{W^{(1)}}$ is skew symmetric and real to obtain

$$(\mathbf{W^{(1)}})^2_{ij} = -\sum_k \left\langle \frac{\partial\Phi_i}{\partial\rho}\middle|\ \Phi_k\right\rangle\left\langle \Phi_k\middle|\ \frac{\partial\Phi_j}{\partial\rho}\right\rangle \tag{2.111}$$

Since the Φ_j form a complete orthonormal set, one uses the completeness relation

$$\sum_k \left|\ \Phi_k\right\rangle\left\langle \Phi_k\ \right| = 1 \tag{2.112}$$

to obtain for $\mathbf{W}^{(1)^2}$ the following result.

$$(\mathbf{W}^{(1)})^2_{ij} = -\left\langle \frac{\partial \Phi_i}{\partial \rho} \middle| \frac{\partial \Phi_j}{\partial \rho} \right\rangle \tag{2.113}$$

Therefore we can express $\mathbf{W}^{(2)}$ in terms of $\mathbf{W}^{(1)}$ as follows:

$$\mathbf{W}^{(2)}{}_{ij} = \frac{d}{d\rho}\mathbf{W}^{(1)}{}_{ij} + (\mathbf{W}^{(1)})^2_{ij} \tag{2.114}$$

Thus one notices that $\mathbf{W}^{(2)}$ has no special symmetry, as it has been decomposed into the sum of a skew-symmetric matrix, $\mathbf{W}^{(1)'}$, and a symmetric matrix, $\mathbf{W}^{(1)^2}$, both of which are non-trivial.

We decided to proceed using the "diabatic" method, because of the ready availability of programs to solve differential equations of the type $g'' + Ug = 0$, or equivalently of the Ricatti type, $y' + y^2 + U = 0$.

2.7 Continuity and Overlap of Surface Functions

When we change from one set of surface functions calculated at a value of $\bar{\rho} = \bar{\rho}_j$ to the next set calculated at $\bar{\rho} = \bar{\rho}_{j+1}$, the scattering wavefunction and its derivative with respect to ρ should themselves not change. Therefore, the wavefunctions in both representations are set equal to one another, multiplied by a new surface function, and integrated, in order to find the new coefficients $\mathbf{b}^{JS\Pi}$. The integral generates the "overlap" of the new functions with the old:

$$b_i^{JS\Pi}(\rho;\bar{\rho}_{j+1}) = \sum_k b_k^{JS\Pi}(\rho;\bar{\rho}_j)\langle \Phi_i^{JMS\Pi}(\bar{\rho}_{j+1})|\Phi_k^{JMS\Pi}(\bar{\rho}_j)\rangle \tag{2.115}$$

In matrix notation this is

$$\mathbf{b}^{JS\Pi}(\rho;\bar{\rho}_{j+1}) = \mathbf{O}^{JS\Pi}(\bar{\rho}_{j+1},\bar{\rho}_j)\mathbf{b}^{JS\Pi}(\rho;\bar{\rho}_j) \tag{2.116}$$

The derivative is transformed exactly the same way:

$$\mathbf{b}^{JS\Pi'}(\rho;\bar{\rho}_{j+1}) = \mathbf{O}^{JS\Pi}(\bar{\rho}_{j+1},\bar{\rho}_j)\mathbf{b}^{JS\Pi'}(\rho;\bar{\rho}_j) \tag{2.117}$$

The transformation for the logarithmic derivative is just

$$\mathbf{y}(\rho;\bar{\rho}_2) = \mathbf{O}^{JS\Pi}(\bar{\rho}_2,\bar{\rho}_1)\mathbf{y}(\rho;\bar{\rho}_1)\widetilde{\mathbf{O}}^{JS\Pi}(\bar{\rho}_2,\bar{\rho}_1) \tag{2.118}$$

where we have used the unitarity of $\mathbf{O}^{JS\Pi}$ to replace the inverse of the overlap matrix with the transpose. Strictly, the transpose is only equal to the inverse in the limit of an infinite set; however we have found that this is a reasonable approximation and a large time saver.

Symmetry is preserved in the Johnson algorithm (as opposed to the computer code). But the code is formulated to force retention of symmetry. Using the transpose of the overlap matrix instead of the inverse guarantees the preservation of this symmetry upon a change of basis set.

Another way of enforcing symmetry in the wavefunction is to invert the overlap matrix and then replace each set of off-diagonal elements in the logarithmic derivative with its respective arithmetic mean. There is no reason to prefer this approximation, so we have used the one that saves the most computer time.

The overlap matrix for 5-dimensional surface functions is obtained by plugging in the expansion in Eq. 2.56 into the integral form. One finds that $\mathbf{O}^{JS\Pi}$ is related by a simple transformation to $\mathbf{o}^{JS\Pi}$ as follows:

$$\mathbf{O}^{JS\Pi} = \tilde{\mathbf{a}}^{JS\Pi}\ \mathbf{o}^{J\Pi}\ \mathbf{a}^{JS\Pi} \tag{2.119}$$

where $\mathbf{o}^{J\Pi}$ is block diagonal and each block $\mathbf{O}^{\mathbf{J}}_{\mathbf{l_2 l_1}}$ has matrix elements found by calculating the overlap of 1-dimensional primitives, $t_p^{Jl_2l_1}(\omega;\rho)$.

$$[\mathbf{O}^{\mathbf{J}}_{\mathbf{l_2 l_1}}]_p^{p'} = \left\langle t_p^{Jl_2l_1}(\omega;\bar{\rho}_{j+1}) \,\middle|\, t_{p'}^{Jl_2l_1}(\omega;\bar{\rho}_j)\right\rangle \tag{2.120}$$

2.8 References

1. L. M. Delves, *Nucl. Phys.*, **9**, 3091 (1959); **20**, 275 (1960).
2. A. M. Arthurs and A. Dalgarno, *Proc. R. Soc. London A*, **256**, 540 (1960).
3. A. Kuppermann, in: Theoretical Chemistry: Advances and Perspectives, Vol. 6A, ed. D. Henderson (Academic Press, New York, 1981), pp. 79-164.
4. D. Jepson and J. O. Hirschfelder, *Proc. Nat. Acad. Sci.*, **45**, 249 (1959).
5. C. F. Curtiss, J. O. Hirschfelder, and F. T.'Adler, *J. Chem. Phys.*, **18**, 1638 (1950).
6. R. T. Pack, *J. Chem. Phys.*, **60**, 633 (1974).
7. A. S. Davydov, Quantum Mechanics, (Pergamon, Oxford, 1976) , 2nd ed., p. 167.
8. A. Kuppermann, *Chem. Phys. Lett.*, **32**, 374 (1975).
9. J. Macek, *J. Phys. B*, **1**, 831 (1968).
10. G. C. Schatz and A. Kuppermann, *J. Chem. Phys.*, **65**, 4642 (1976).
11. F. T. Smith, *J. Math. Phys.*, **3**, 735 (1962).
12. U. Fano and C. D. Lin, in: Atomic Physics, Vol. 4, ed. G. Zu. Putlitz, E. W. Weber, and A. Winnacker (Plenum, New York, 1975), p. 47.
13. C. D. Lin, *Phys. Rev. A*, **10**, 1986 (1974).
14. M. E. Rose, Elementary Theory of Angular Momentum, (Wiley, New York, 1957) , Chap. 2.
15. C. D. Lin, *Phys. Rev. A*, **14**, 30 (1976).
16. H. Klar and M. Klar, *Phys. Rev. A*, **17**, 1007 (1978).
17. A. K. Bhatia and A. Temkin, *Rev. Mod. Phys.*, **36**, 1050 (1964).
18. B. Christensen-Dalsgaard, *J. Chem. Phys.*, **29**, 470 (1984).
19. U. Fano and G. Racah, Irreducible Tensorial Sets, (Academic Press, New York, 1959) .
20. H. Klar, *J. Phys. B*, **7**, L436 (1974).

21. R. Gordon, *J. Chem. Phys.*, **51**, 14 (1969).

22. Handbook of Mathematical Functions, edited by M. Abramowitz and I. A. Stegun (National Bureau of Standards, Washington, D. C., 1964).

23. B. R. Johnson, *J. Comp. Phys.*, **13**, 445 (1973); **67**, 4086 (1977).

24. U. Fano, *Rep. Prog. Phys.*, **46**, 97 (1983).

25. J. A. Kaye, Ph. D. Thesis, California Institute of Technology, 1982.

2.9 Figure Captions

FIG. 2.1: Photograph of the potential contour at 10.5 eV.

FIG. 2.2: Potential contours for the e^-−H reaction in the $OXYZ$ space having spherical coordinates $\rho = (r^2 + R^2)^{\frac{1}{2}}$, $\omega = 2 \arctan r/R$ and γ for $\gamma = 0$ and 180 deg for $Z = 0$ bohr.

FIG. 2.3: Potential contours as in Figure 2.2 for $Z = 1$ bohr.

FIG. 2.4: Potential contours as in Figure 2.2 for $Z = 2$ bohr.

FIG. 2.5: Potential contours as in Figure 2.2 for $Z = 10$ bohr.

FIG. 2.6: Potential contours for the e^-−H reaction for $\gamma = 0$ degrees.

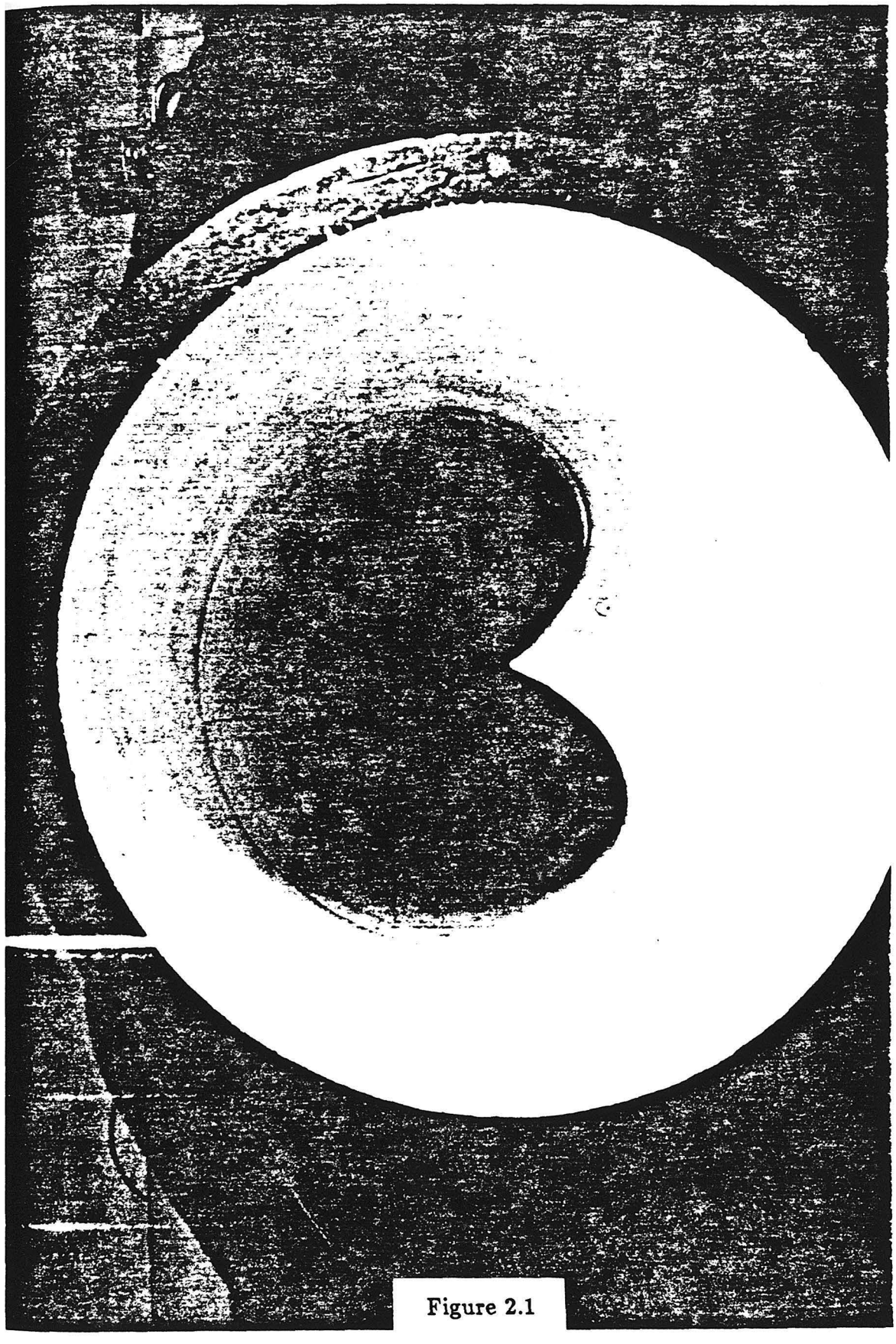

Figure 2.1

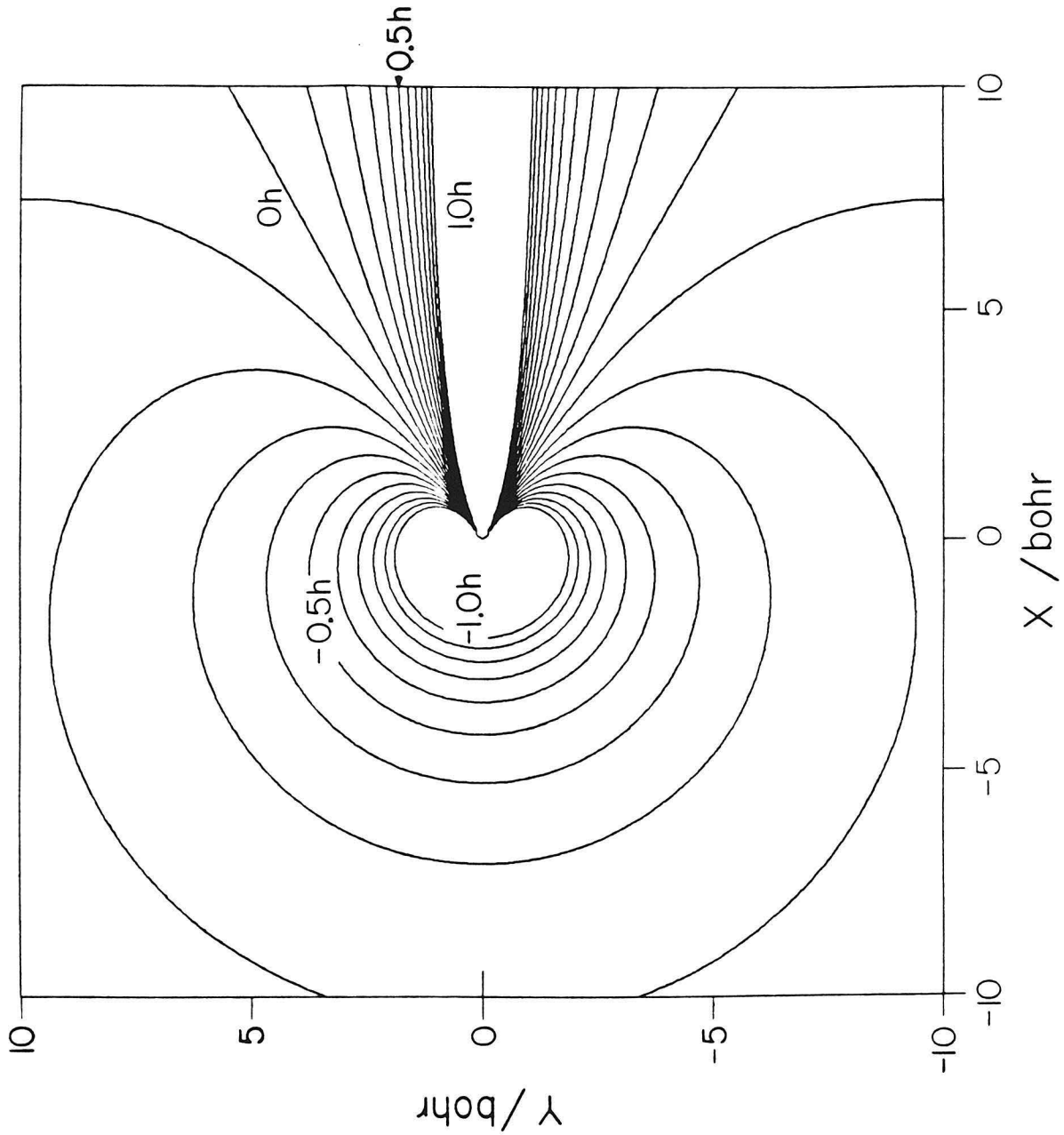

Figure 2.2

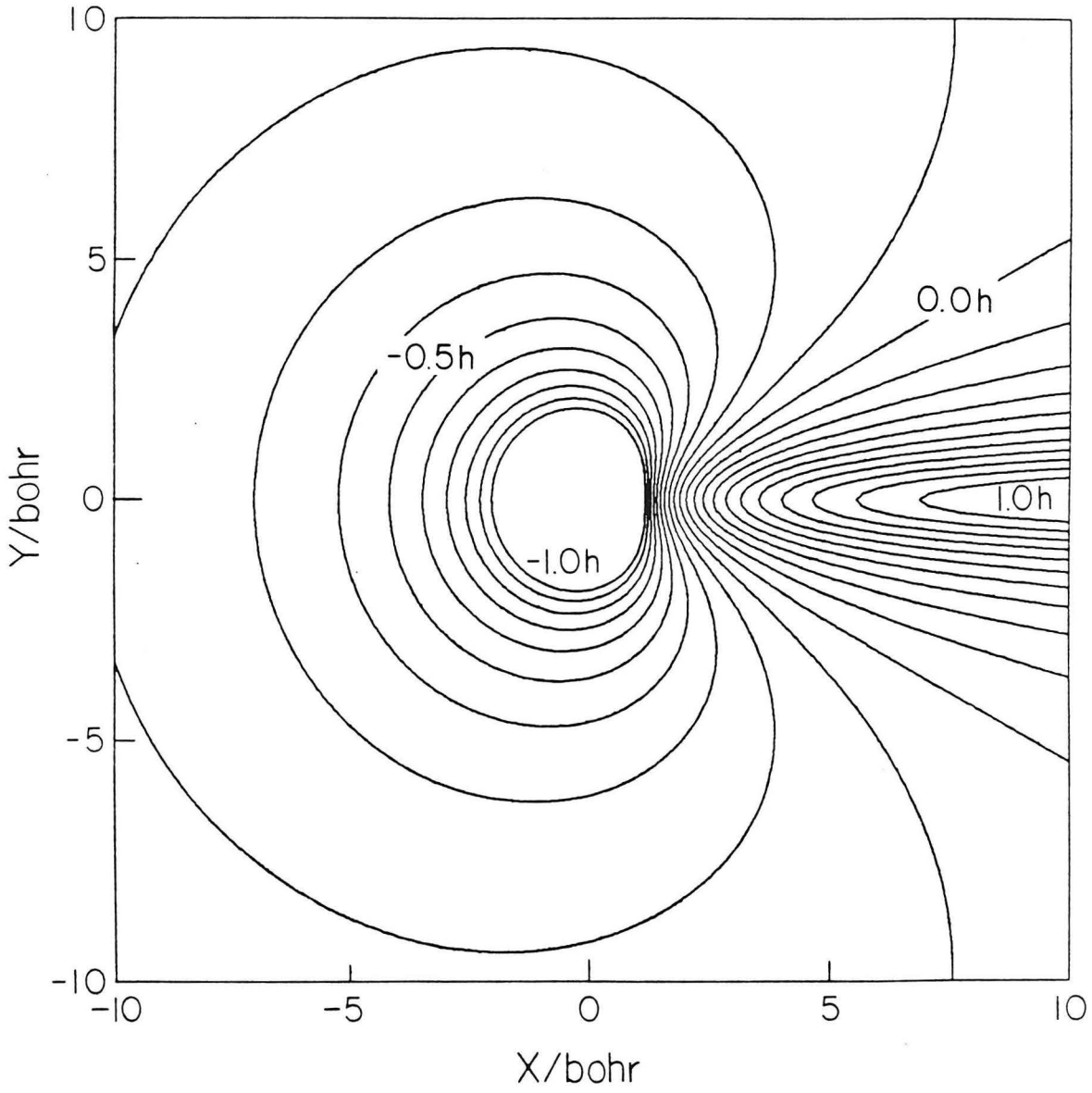

Figure 2.3

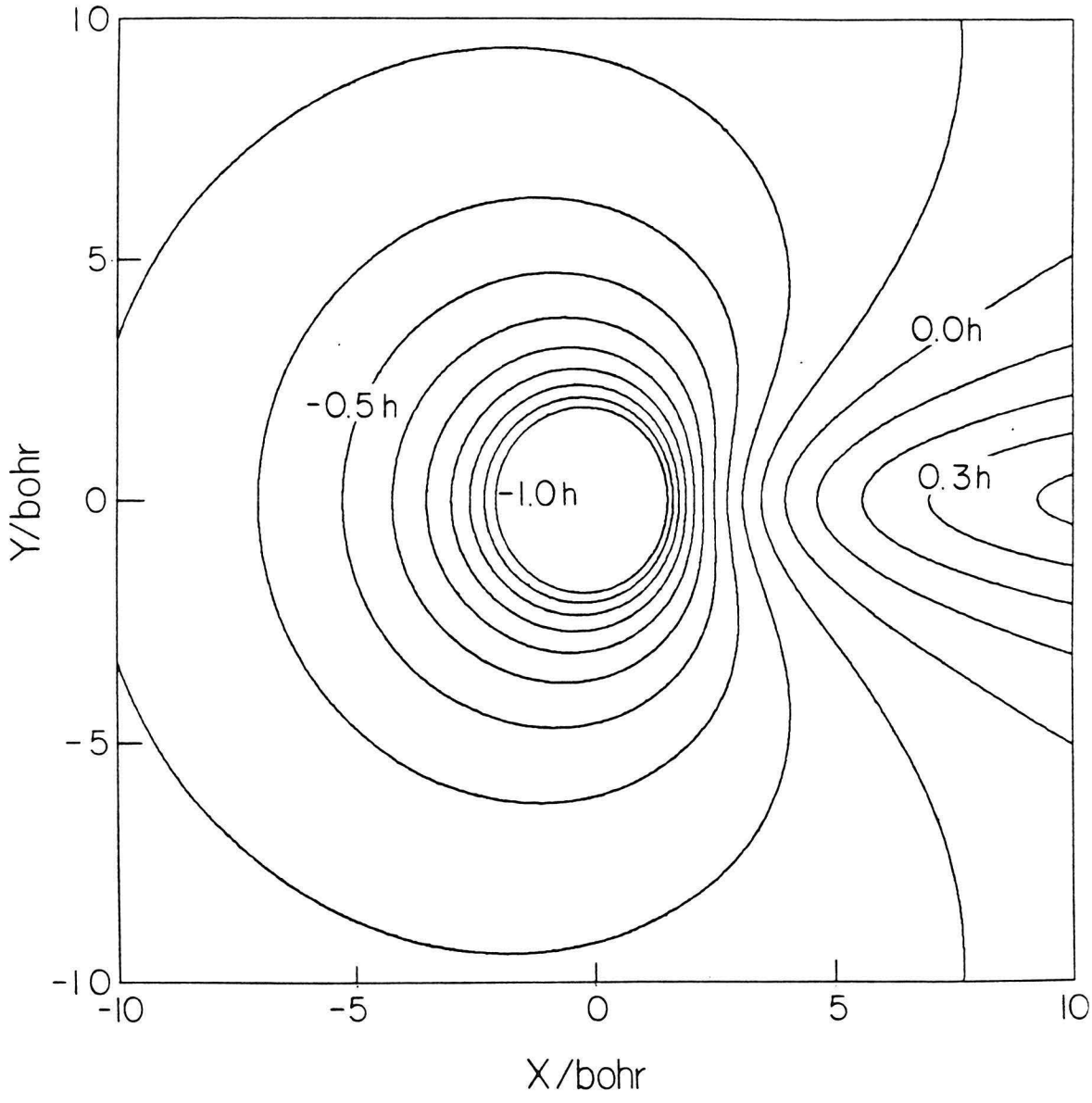

Figure 2.4

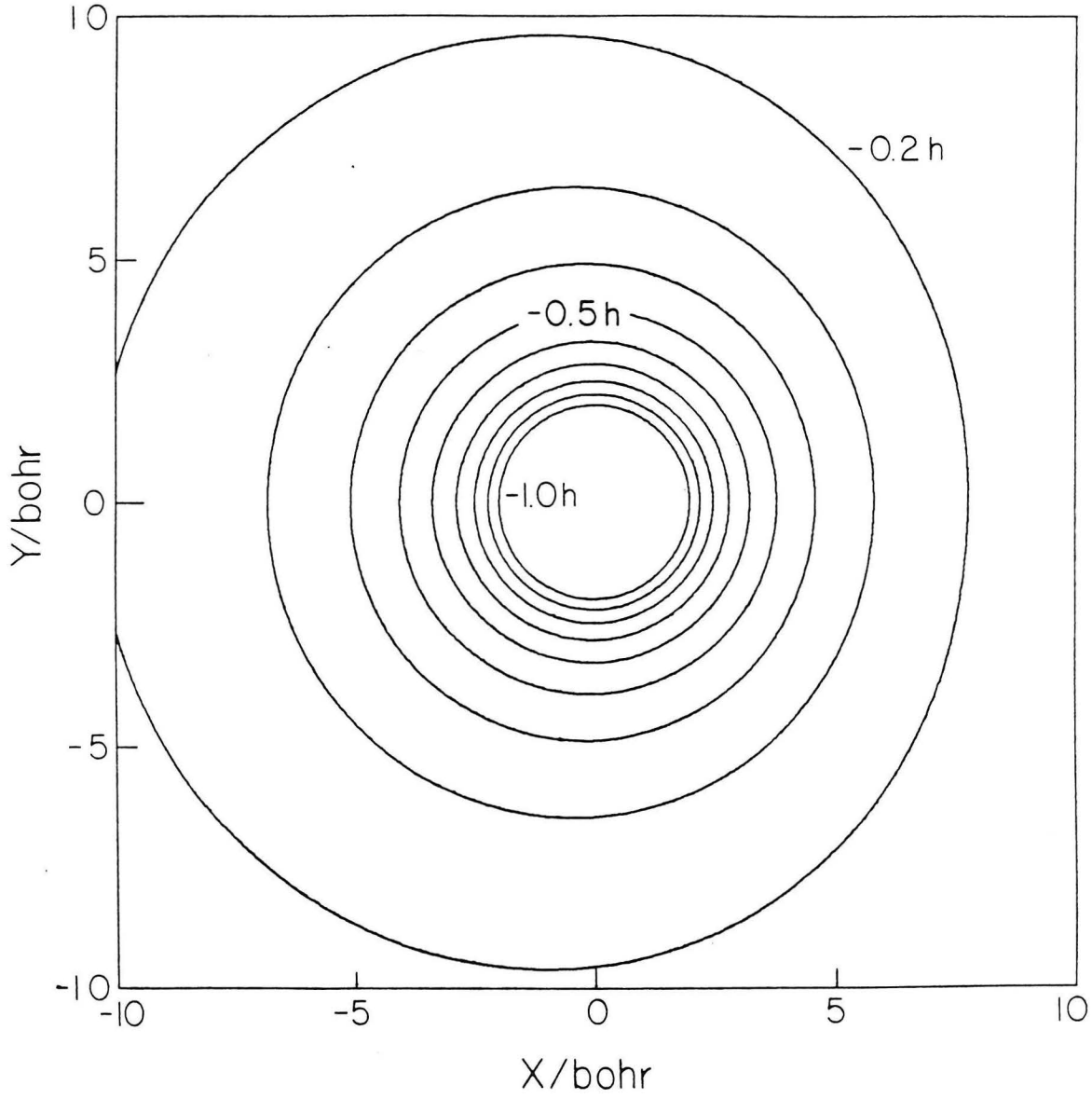

Figure 2.5

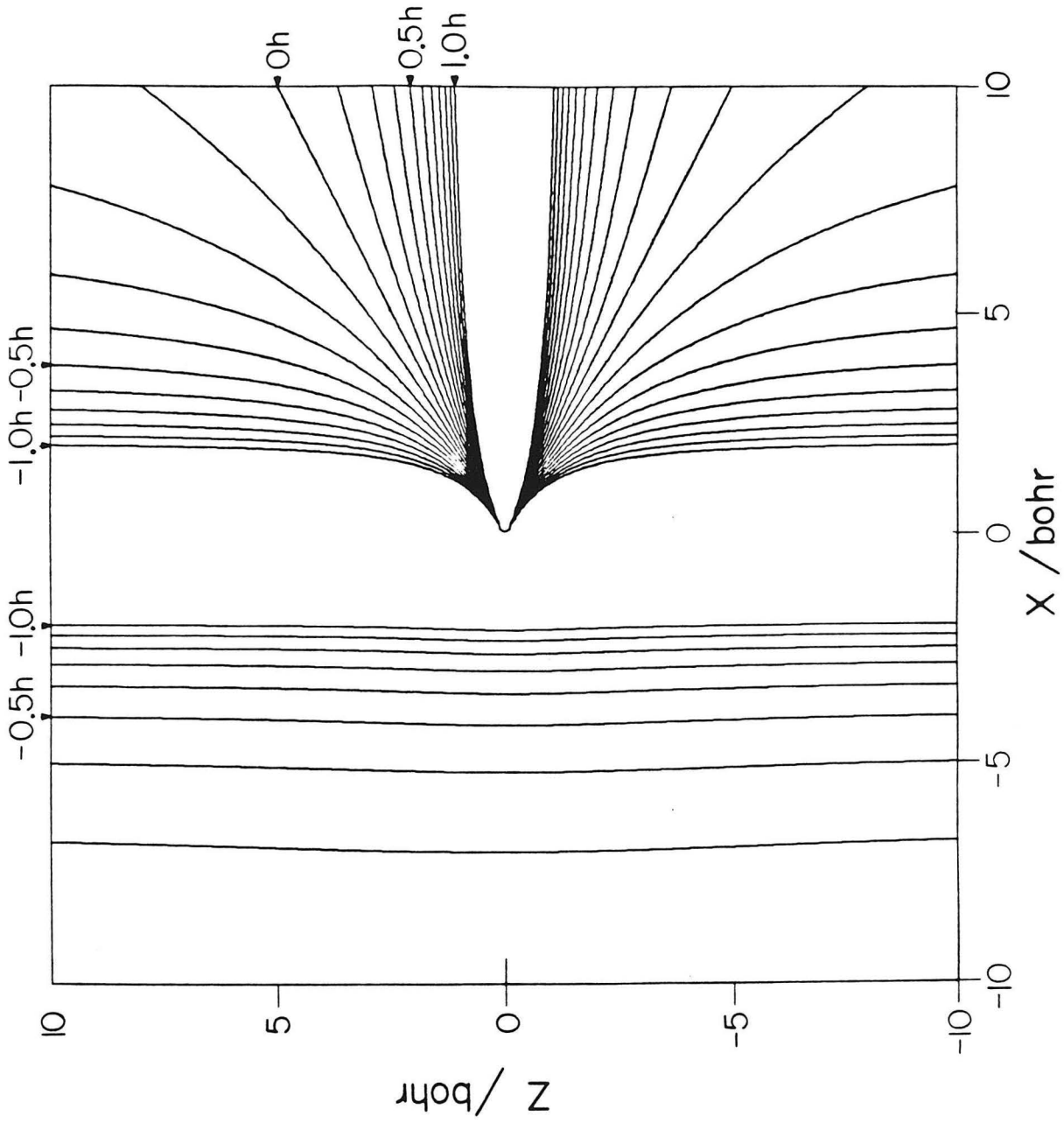

Figure 2.6

CHAPTER 3

PROJECTION AND ASYMPTOTIC ANALYSIS

In this chapter we obtain the asymptotic form of arbitrary solutions of the Schrödinger equation. We then obtain expressions for the reactance matrix $\mathbf{R}^{JS\Pi}$ and scattering matrix $\mathbf{S}^{JS\Pi}$. These matrices are designated by symmetry type $(S,\ \Pi)$ and not by arrangement channel. We then define reactance and scattering solutions and relate them to the physical solution, from which we obtain expressions for the scattering amplitudes and cross sections.[1]

3.1 Asymptotic Analysis

Asymptotically as $R \to \infty$ arbitrary solutions of the 6-dimensional Schrödinger equation $\Psi_{i'}^{JMS\Pi}$ have the form

$$\Psi_{i'}^{JMS\Pi} \widetilde{_{R\to\infty}} \sum_{nl_1l_2} \frac{1}{R} U_{nl_1l_2}^{JS\Pi i'}(R) \Phi_{nl_1l_2}^{JM\Pi}(r,\mathbf{\Omega}) \tag{3.1}$$

where $\Phi_{nl_1l_2}^{JM\Pi}(r,\mathbf{\Omega})$ is the product of $\mathcal{Y}_{l_2l_1}^{JM}(\theta_2,\varphi_2,\theta_1,\varphi_1)$ and the hydrogen radial function $R_{Nl_1}(r)$. The general radial functions $U^{JS\Pi}(R)$ behave asymptotically as

$$U_{nl_1l_2}^{JS\Pi i'}(R) \widetilde{_{R\to\infty}} v_n^{-1/2} \left[\mathcal{I}_{nl_1l_2}(R) A_{nl_1l_2}^{JS\Pi i'} - \mathcal{O}_{nl_1l_2}(R) B_{nl_1l_2}^{JS\Pi i'} \right] \tag{3.2}$$

In this equation $\mathbf{A}^{JS\Pi}$ and $\mathbf{B}^{JS\Pi}$ are square matrices of integration constants, whose rows are spanned by the indices nl_1l_2, and whose columns are spanned

by the general index $i' = n'l_1'l_2'$. $\mathcal{I}$ and $\mathcal{O}$ are diagonal matrices (for which the subscripts indicate both row and column indices) representing the incoming and outgoing waves and are given by

$$\mathcal{I}_{nl_1l_2}(R) = \begin{cases} \exp[-i(k_nR - l_2\pi/2)] & \text{for open channels} \\ \exp(|k_n|R) & \text{for closed channels, and} \end{cases} \tag{3.3}$$

$$\mathcal{O}_{nl_1l_2}(R) = \begin{cases} \exp[+i(k_nR - l_2\pi/2)] & \text{for open channels} \\ \exp(-|k_n|R) & \text{for closed channels.} \end{cases} \tag{3.4}$$

Additionally, v_n is the velocity $\hbar|k_n|/\mu$, and k_n is the wave number given by

$$k_n = \hbar^{-1}\sqrt{2\mu(E - E_n)} \tag{3.5}$$

where E_n is the energy of a hydrogen atom with principal quantum number n. We can rewrite Eq. 3.2 in matrix form as

$$\mathbf{U}^{JS\Pi}(R) \widetilde{_{R\to\infty}} \mathbf{v}^{-1/2}[\mathcal{I}(R)\mathbf{A}^{JS\Pi} - \mathcal{O}(R)\mathbf{B}^{JS\Pi}] \tag{3.6}$$

The scattering matrix for partial wave J, spin S, and parity Π is then defined by

$$\mathbf{B}^{JS\Pi} = \mathbf{S}^{JS\Pi}\mathbf{A}^{JS\Pi} \tag{3.7}$$

An alternative way of expressing Eq. 3.1 is in terms of the reactance matrix, such that the exponential terms representing waves are replaced by their non-imaginary counterparts, the sine and cosine functions. We may write

$$\mathbf{U}^{JS\Pi}(R) \widetilde{_{R\to\infty}} \mathbf{v}^{-1/2}[\mathcal{S}(R)\mathbf{C}^{JS\Pi} + \mathcal{C}(R)\mathbf{D}^{JS\Pi}] \tag{3.8}$$

where $\mathbf{C}^{JS\Pi}$ and $\mathbf{D}^{JS\Pi}$ are new integration constant matrices and $\mathcal{S}$ and $\mathcal{C}$ are diagonal matrices given by

$$\mathcal{S}_{nl_1l_2}(R) = \begin{cases} \sin(k_nR - l_2\pi/2) & \text{for open channels} \\ \exp(|k_n|R) & \text{for closed channels, and} \end{cases} \tag{3.9}$$

$$C_{nl_1l_2}(R) = \begin{cases} \cos(k_nR - l_2\pi/2) & \text{for open channels} \\ \exp(-|k_n|R) & \text{for closed channels.} \end{cases} \tag{3.10}$$

The reactance matrix is defined by

$$\mathbf{D}^{JS\Pi} = \mathbf{R}^{JS\Pi}\mathbf{C}^{JS\Pi} \tag{3.11}$$

Expressing the wavefunction in terms of sines and cosines, as in Eq. 3.8, is good in the far asymptotic region. In the closer asymptotic region $\mathbf{U}^{JS\Pi}$ behaves as a combination of Riccati-Bessel functions,

$$U^{JS\Pi i'}_{nl_1l_2}(R) \widetilde{_{R\to\infty}} \sum_{\bar{n}\bar{l_1}\bar{l_2}} \left[J^{\bar{n}\bar{l_1}\bar{l_2}}_{nl_1l_2}(R) - \sum_{\hat{n}\hat{l_1}\hat{l_2}} N^{\hat{n}\hat{l_1}\hat{l_2}}_{nl_1l_2}(R) R^{JS\Pi\,\bar{n}\bar{l_1}\bar{l_2}}_{\hat{n}\hat{l_1}\hat{l_2}} \right] C^{JS\Pi i'}_{\bar{n}\bar{l_1}\bar{l_2}} \tag{3.12}$$

where the $C^{JS\Pi}$ coefficents are integration constants as defined before, and $\mathbf{R}^{JS\Pi}$ is the reactance matrix for this partial wave and symmetry type. In matrix form we have

$$\mathbf{U}^{JS\Pi}{}_{R\to\infty} \left[\mathbf{J}(R) - \mathbf{N}(R)\mathbf{R}^{JS\Pi} \right] \mathbf{C}^{JS\Pi} \tag{3.13}$$

where $\mathbf{J}$ and $\mathbf{N}$ are diagonal matrices. We will find it convenient to use a "stacked" notation in which two equations are written in one line, such that the first equation corresponds to using the top element within each set of square brackets, and similarly the second equation uses the bottom elements. The open channel elements of $\mathbf{J}$ and $\mathbf{N}$ are given by

$$\begin{bmatrix} \mathbf{J}(R) \\ \mathbf{N}(R) \end{bmatrix}^{\bar{n}\bar{l_1}\bar{l_2}}_{nl_1l_2} = \delta^{\bar{n}\bar{l_1}\bar{l_2}}_{nl_1l_2}\, v_n{}^{-\frac{1}{2}}(k_nR) \begin{bmatrix} j_{l_2}(k_nR) \\ y_{l_2}(k_nR) \end{bmatrix} \tag{3.14}$$

where j_{l_2} and y_{l_2} are spherical Bessel functions,[2] v_n is the velocity $\hbar|k_n|/\mu$, and k_n is the wave number as specified previously. It can be shown, using the asymptotic forms of these functions[2] that Eq. 3.13 reduces to Eq. 3.8 in the far asymptotic limit. The closed channel elements of $\mathbf{J}$ and $\mathbf{N}$ are given by

$$\begin{bmatrix} \mathbf{J}(R) \\ \mathbf{N}(R) \end{bmatrix}^{\bar{n}\bar{l_1}\bar{l_2}}_{nl_1l_2} = \delta^{\bar{n}\bar{l_1}\bar{l_2}}_{nl_1l_2}\, v_n{}^{-\frac{1}{2}}(\kappa_nR) \begin{bmatrix} i_{l_2}(\kappa_nR) \\ k_{l_2}(\kappa_nR) \end{bmatrix} \tag{3.15}$$

where $i_{l_2}(z)$ and $k_{l_2}(z)$ are modified spherical Bessel functions[3] of the first and third kinds, and $\kappa_n = |k_n|$.

We only obtain the open-open sub-block of the reactance matrix — the symbol $\mathbf{R}_{\mathbf{o}}^{JS\Pi}$ will refer to the subblock obtained by keeping only the open columns, but all of the rows, and $\mathbf{R}_{oo}^{JS\Pi}$ will refer to the open-open subblock. The open-open reactance matrix $\mathbf{R}_{oo}^{JS\Pi}$ is real and symmetric in an exact calculation. We can consider the amount of asymmetry in the actual open-open reactance matrices obtained to be a measure of the error in the calculation. However, in our calculation we have forced the logarithmic derivative to be symmetric throughout the propagation, which increases the computational efficiency but eliminates the use of the symmetry of $\mathbf{R}_{oo}^{JS\Pi}$ as an accuracy test. The open-open part of the scattering matrix $\mathbf{S}_{oo}^{JS\Pi}$ is obtained from the reactance matrix using the relationship[4]

$$\mathbf{S}_{oo}^{JS\Pi} = \frac{\mathbf{I} + i\mathbf{R}_{oo}^{JS\Pi}}{\mathbf{I} - i\mathbf{R}_{oo}^{JS\Pi}} \tag{3.16}$$

The open-open part of the scattering matrix is both symmetric and unitary, for exact solutions of the Schrödinger equation, due to time reversal invariance of the Schrödinger equation.[5]

The asymptotic solutions have been defined in terms of distance vectors $\mathbf{r}$ and $\mathbf{R}$ — not in hyperspherical coordinates. We now show how to project from a hyperspherical basis set to an asymptotic basis.

3.2 Projection

The "projection" is a change of basis from surface functions to asymptotic solutions. After we obtain the wavefunction at a large value of ρ, we assume that the interaction between the two electrons is small and that the asymptotic functions will form a good basis.

The asymptotic wavefunctions are functions of $\mathbf{r}_\lambda$, depending on the channel λ, and on $\widehat{\mathbf{R}}_\lambda$, but independent of R_λ. They are related to the radial part of the bound states of the hydrogen atom, (as defined after Eq. 3.1) and which are independent of the distance of the second electron to the proton. In contrast, the surface functions depend on the distances of both electrons to the proton, constrained in such a way that ρ is constant, with the angle ω being a variable.

One could project the hyperspherical surface functions onto the asymptotic functions at constant R_λ; alternatively, one could project the asymptotic solutions in $\mathbf{r}_\lambda, \mathbf{R}_\lambda$ coordinates onto the surface functions at constant ρ. We studied both of these methods and present the resulting equations in the next sections.

The transformation between (ρ, ω) and (r, R) is (Eq. 2.10)

$$\begin{aligned} r &= \rho \sin \frac{\omega}{2} \\ R &= \rho \cos \frac{\omega}{2} \end{aligned} \tag{3.17}$$

Let us look at how this relationship behaves in the asymptotic channels. Asymptotically in channel 1, where ρ is large and $\omega \approx 0$, one has $R \approx \rho$ and $r \approx \frac{1}{2}\rho\omega$. In channel 2 ρ is again large but ω approaches π. There $r \approx \rho$ and $R \approx \frac{1}{2}\rho(\pi - \omega)$. For surface functions whose energy is negative, the larger ρ is, the smaller the range of ω in which those functions have amplitudes significantly greater than zero.

The general scattering wavefunction $\Psi_{i'}^{JMS\Pi}$ (where i' stands for a set of indices of the nl_1l_2 type) is expanded in surface functions of hyperspherical coordinates as

$$\Psi_{i'}^{JMS\Pi}(\rho, \omega, \theta_1, \varphi_1, \theta_2, \varphi_2) = \rho^{-\frac{5}{2}} \sum_i b^{JS\Pi}{}_i^{i'}(\rho; \bar{\rho}) \Phi_i^{JMS\Pi}(\omega, \mathbf{\Omega}; \rho) \tag{3.18}$$

The surface functions in turn are expanded as (see Eq. 2.28)

$$\begin{aligned} \Phi_i^{JMS\Pi} = \sum_{[l_1 l_2]} \sum_p a_{l_2 l_1 p}^{JS\Pi i}(\rho) N_{l_2 l_1} \times \\ \left[\mathcal{Y}_{l_2 l_1}^{JM}(\mathbf{\Omega})\, t_p^{Jl_2 l_1}(\omega; \rho) + (-1)^\Lambda \mathcal{Y}_{l_1 l_2}^{JM}(\mathbf{\Omega})\, t_p^{Jl_2 l_1}(\pi - \omega; \rho) \right] \end{aligned} \tag{3.19}$$

where $\mathbf{\Omega}$ is the ordered set of angles $(\theta_2, \varphi_2, \theta_1, \varphi_1)$ and the pairs $[l_1 l_2]$ imply that $l_1 \leq l_2$ (see Eq. 2.56). In the asymptotic region of arrangement channel 1, where R is very large, this same general scattering wavefunction can be written in terms of hydrogen radial wavefunctions $R_{nl_1}(r)$ as

$$\Psi_{i'}^{JMS\Pi} = \sum_{nl_1l_2} \mathcal{Y}_{l_2l_1}^{JM}(\theta_2, \varphi_2, \theta_1, \varphi_1)\, G_{nl_1l_2}^{JS\Pi i'}(R)\, R_{nl_1}(r) \tag{3.20}$$

where $G_{nl_1l_2}^{JS\Pi i'}(R)$ is the $U_{nl_1l_2}^{JS\Pi i'}/R$ of Eq. 3.1. The angular part of the hydrogen wavefunction, $Y_{l_1m_1}(\theta_1, \varphi_1)$, is included in the coupled spherical harmonic, $\mathcal{Y}_{l_2l_1}^{JM}$. The sum over l_1 and l_2 in the asymptotic expansion is not limited to the $l_1 \leq l_2$ pairs $[l_1 l_2]$ as in the surface function expansion Eq. 3.19. This is because the surface functions have been symmetrized, as explained in Section 2.4.

We need to set the two expressions for $\Psi_{i'}^{JMS\Pi}$ equal to each other in order to determine the relationship between $b^{JS\Pi}{}_{i}^{i'}(\rho)$ and $G_{nl_1l_2}^{JS\Pi i'}(R)$. Multiplying Eq. 3.18 and Eq. 3.20 by $\mathcal{Y}_{l_2'l_1'}^{JM*}$, integrating over $(\theta_1, \varphi_1, \theta_2, \varphi_2)$, using Eq. 3.19 and identifying the results gives the following:

$$\rho^{-\frac{5}{2}} \sum_{i} b^{JS\Pi}{}_{i}^{i'} \sum_{[l_1l_2]p} a_{l_2l_1p}^{JS\Pi i}(\rho) N_{l_2l_1} \Big[\delta_{l_2l_1}^{l_2'l_1'}\, t_p^{Jl_2l_1}(\omega;\rho) + (-1)^{\Lambda} \delta_{l_1l_2}^{l_2'l_1'}\, t_p^{Jl_2l_1}(\pi-\omega;\rho) \Big] = \sum_{nl_1l_2} \delta_{l_2l_1}^{l_2'l_1'} G_{nl_1l_2}^{JS\Pi i'}(R) R_{nl_1}(r) \tag{3.21}$$

There are two ways to proceed from here. One is to find an expression for $G_{nl_1l_2}^{JS\Pi i'}(R)$ in terms of $b^{JS\Pi}{}_{i}^{i'}(\rho;\bar{\rho})$, in which case the projection is done at a constant value of R. The other process is just the reverse: express the $b^{JS\Pi}{}_{i}^{i'}(\rho;\bar{\rho})$ in terms of the $G_{nl_1l_2}^{JS\Pi i'}(R)$. This will be called the constant ρ projection.

3.2.1 Constant R projection

In this section we will describe the projection of hyperspherical surface functions onto cartesian coordinate (r, R) asymptotic functions. Besides the four angles

included in $\hat{\mathbf{r}}$ and $\widehat{\mathbf{R}}$, the only independent variable in the asymptotic functions is the distance r, which is the distance of the bound electron from the proton. The fixed distance of the other electron to the proton during the projection will be designated $R_{\rm p}$. The hyperspherical coordinates ρ and ω need to be expressed as functions of r and the parameter $R_{\rm p}$:

$$\begin{aligned} \rho &= \rho(r; R_{\rm p}) \\ \omega &= \omega(r; R_{\rm p}) \end{aligned} \tag{3.22}$$

We multiply Eq. 3.21 on both sides by $r^2 R_{n'l'_1}(r)$ and integrate over r from zero to infinity. The radial functions are orthonormal in the n index, resulting in the expression:

$$\begin{aligned} G^{JS\Pi i'}_{n'l'_1 l'_2}(R_{\rm p}) = \sum_{[l_1 l_2]p} \int \Big[\delta^{l'_2 l'_1}_{l_2 l_1}\, t_p^{Jl_2 l_1}(\omega;\rho) + (-1)^{\Lambda} \delta^{l'_2 l'_1}_{l_1 l_2}\, t_p^{Jl_2 l_1}(\pi-\omega;\rho) \Big] N_{l_2 l_1} \\ \times \sum_i a^{JS\Pi i}_{l_2 l_1 p}(\rho)\; b^{JS\Pi i'}_{\;\;i}(\rho;\bar{\rho})\; R_{n'l'_1}(r) \rho^{-\frac{5}{2}} r^2 dr \end{aligned} \tag{3.23}$$

The above expression can be written in matrix form as the integral of $\mathbf{g}^{JS\Pi}(r; R_{\rm p})$,

$$\mathbf{G}^{JS\Pi}(R_{\rm p}) = \int \mathbf{g}^{JS\Pi}(r; R_{\rm p})\, dr \tag{3.24}$$

where we have defined $\mathbf{g}^{JS\Pi}(r; R_{\rm p})$ as the matrix product

$$\mathbf{g}^{JS\Pi}(r; R_{\rm p}) = \mathbf{F}^{JS\Pi}(r; R_{\rm p})\, \mathbf{a}^{JS\Pi}(\bar{\rho})\, \mathbf{b}^{JS\Pi}[\rho(r); \bar{\rho}]\, r^2 \rho^{-\frac{5}{2}} \tag{3.25}$$

$\mathbf{F}^{JS\Pi}(r; R_{\rm p})$ being a new matrix which is the product of radial hydrogen functions and one-dimensional hyperspherical basis functions:

$$(\mathbf{F}^{JS\Pi})^{l_2 l_1 p}_{n'l'_1 l'_2} = R_{n'l'_1}(r) \big(\delta^{l'_2 l'_1}_{l_2 l_1}\, t_p^{Jl_2 l_1}(\omega;\rho) + (-1)^{\Lambda} \delta^{l'_2 l'_1}_{l_1 l_2}\, t_p^{Jl_2 l_1}(\pi-\omega;\rho) \big) \tag{3.26}$$

In order to compute the reactance matrix we also need the derivative of $\mathbf{G}^{JS\Pi}$

with respect to R (where, in Eq. 3.24, R_p is replaced by R). First we find an expression for the partial derivative with respect to R in hyperspherical coordinates:

$$\begin{aligned}\left(\frac{\partial}{\partial R}\right) &= \left(\frac{\partial \rho}{\partial R}\right)_r \left(\frac{\partial}{\partial \rho}\right) + \left(\frac{\partial \omega}{\partial R}\right)_r \left(\frac{\partial}{\partial \omega}\right) \\ &= \left(\frac{R}{\rho}\right)\left(\frac{\partial}{\partial \rho}\right) - \left(\frac{2r}{\rho^2}\right)\left(\frac{\partial}{\partial \omega}\right)\end{aligned} \tag{3.27}$$

Taking the derivative of Eq. 3.25 one obtains, after simplifying,

$$\begin{aligned}\frac{d\mathbf{g}^{JS\Pi}}{dR}(r;R_p) = &\left(\frac{r^2 R_p}{\rho^{7/2}}\right)\mathbf{F}^{JS\Pi}(r;R_p)\ \mathbf{a}^{JS\Pi}(\bar{\rho})\frac{d\mathbf{b}^{JS\Pi}}{d\rho}(\rho;\bar{\rho}) \\ &- \frac{5}{2}\left(\frac{r^2 R_p}{\rho^{9/2}}\right)\mathbf{F}^{JS\Pi}(r;R_p)\mathbf{a}^{JS\Pi}(\bar{\rho})\mathbf{b}^{JS\Pi}(\rho;\bar{\rho}) \\ &- \left(\frac{2r^3}{\rho^{9/2}}\right)\mathbf{f}^{JS\Pi}(r;R_p)\mathbf{a}^{JS\Pi}(\bar{\rho})\mathbf{b}^{JS\Pi}(\rho;\bar{\rho})\end{aligned} \tag{3.28}$$

where we have defined $\mathbf{f}^{JS\Pi}(r;R_p)$, similarly to $\mathbf{F}^{JS\Pi}$, as

$$(\mathbf{f}^{JS\Pi})^{l_2 l_1 p}_{n' l_1' l_2'} = R_{n' l_1'}(r)\left(\delta^{l_2' l_1'}_{l_2 l_1}\frac{\partial\, t_p^{J l_2 l_1}(\omega;\rho)}{\partial \omega} + (-1)^{\Lambda}\delta^{l_2' l_1'}_{l_1 l_2}\frac{\partial\, t_p^{J l_2 l_1}(\pi-\omega;\rho)}{\partial \omega}\right) \tag{3.29}$$

One doesn't really calculate the derivative of $t_p^{J l_2 l_1}(\omega;\rho)$ with respect to ω, however. The surface functions are obtained at the points ω_i corresponding to projection points r_i via spline-fitting. Because the projection points r_i are evenly spaced, whereas the angular points which correspond are not, it is easier to do the spline fit using r_i rather than ω_i. This means that the derivative obtained in the spline fitting routine is with respect to r, not ω. We obtain the ω derivative using the relation

$$\left(\frac{\partial \omega}{\partial r}\right)_R \left(\frac{\partial}{\partial \omega}\right)_\rho t_p^{J l_2 l_1}(\omega;\rho) = \left(\frac{\partial}{\partial r}\right)_R t_p^{J l_2 l_1}(\omega;\rho) \tag{3.30}$$

Substituting this into Eq. 3.29 gives the following expression for $\mathbf{f}^{JS\Pi}$:

$$\begin{aligned}(\mathbf{f}^{JS\Pi})^{l_2 l_1 p}_{n' l_1' l_2'} = \frac{\rho^2}{R}R_{n' l_1'}(r)\Bigg[&\delta^{l_2' l_1'}_{l_2 l_1}\left(\frac{\partial}{\partial r}\right)_R t_p^{J l_2 l_1}(\omega;\rho) \\ &+ (-1)^{\Lambda}\delta^{l_2' l_1'}_{l_1 l_2}\left(\frac{\partial}{\partial r}\right)_R t_p^{J l_2 l_1}(\pi-\omega;\rho)\Bigg]\end{aligned} \tag{3.31}$$

When we replace Eq. 3.28 and Eq. 3.31 in the analog of Eq. 3.24 in which the derivative $d\mathbf{g}^{JS\Pi}(r;R_{\rm p})/dR$ appears in the integrand instead of $\mathbf{g}^{JS\Pi}(r;R_{\rm p})$, we get $d\mathbf{G}^{JS\Pi}/dR$.

We have thus shown how we calculate the integral matrices $\mathbf{G}^{JS\Pi}$ and $d\mathbf{G}^{JS\Pi}/dR$. We use them to construct $\mathbf{Z}^{JS\Pi}$, the logarithmic derivative of $\mathbf{U}^{JS\Pi}$ as follows: From the remark after Eq. 3.20 we have

$$\mathbf{U}^{JS\Pi}(R) = R\mathbf{G}^{JS\Pi}(R) \tag{3.32}$$

and therefore

$$\mathbf{U}'^{JS\Pi}(R) = \mathbf{G}^{JS\Pi}(R) + R\mathbf{G}'^{JS\Pi} \tag{3.33}$$

This gives

$$\mathbf{Z}^{JS\Pi}(R) = \mathbf{U}'^{JS\Pi}\mathbf{U}^{JS\Pi\,-1} = \frac{1}{R}\mathbf{I} + \mathbf{G}'^{JS\Pi}\mathbf{G}^{JS\Pi\,-1} \tag{3.34}$$

Thus we have shown how to obtain the logarithmic derivative after projection, which is all that is needed to obtain the R-matrix. However, to get $\mathbf{Z}^{JS\Pi}$, we needed to have both $\mathbf{b}^{JS\Pi}$ and $\mathbf{b}^{JS\Pi'}$ before the projection at constant R. The method used to obtain the R-matrix is presented in the next section.

3.2.2 Reactance matrix using constant R projection

There are two equations relating $\mathbf{U}^{JS\Pi}$ to the reactance matrix and the constants $\mathbf{C}^{JS\Pi}$ of Eq. 3.8. Eq. 3.13 and its derivative with respect to R can be considered as a system of two linear matrix equations in the two unknowns $\mathbf{C}^{JS\Pi}$ and $\mathbf{R}^{JS\Pi}$:

$$\mathbf{U}^{JS\Pi} = (\mathbf{J} - \mathbf{N}\mathbf{R}^{JS\Pi})\mathbf{C}^{JS\Pi} \tag{3.35}$$

$$\mathbf{U}'^{JS\Pi} = (\mathbf{J}' - \mathbf{N}'\mathbf{R}^{JS\Pi})\mathbf{C}^{JS\Pi} \tag{3.36}$$

Right multiplying Eq. 3.36 by the inverse of Eq. 3.35 $\mathbf{C}^{JS\Pi}$ cancels out and we obtain the logarithmic derivative:

$$\mathbf{Z}^{JS\Pi} = \left[\mathbf{J}' - \mathbf{N}'\mathbf{R}^{JS\Pi}\right] \times \left[\mathbf{J} - \mathbf{N}\mathbf{R}^{JS\Pi}\right]^{-1} \tag{3.37}$$

This equation is rearranged to obtain the R-matrix.

$$\mathbf{R}^{JS\Pi} = \left[\mathbf{Z}^{JS\Pi}\mathbf{N} - \mathbf{N}'\right]^{-1} \times \left[\mathbf{Z}^{JS\Pi}\mathbf{J} - \mathbf{J}'\right] \tag{3.38}$$

The full reactance matrix may be written out in block form, with the open rows and columns displayed separately:

$$\mathbf{R}^{JS\Pi} = \begin{bmatrix} \mathbf{R}_{oo}^{JS\Pi} & \mathbf{R}_{oc}^{JS\Pi} \\ \mathbf{R}_{co}^{JS\Pi} & \mathbf{R}_{cc}^{JS\Pi} \end{bmatrix}. \tag{3.39}$$

Then if we write $\mathbf{R}^{JS\Pi} = \mathbf{A}^{-1}\mathbf{B}$, and $\mathbf{a} = \mathbf{A}^{-1}$, and write Eq. 3.38 in similar fashion, we have

$$\begin{bmatrix} \mathbf{R}_{oo}^{JS\Pi} & \mathbf{R}_{oc}^{JS\Pi} \\ \mathbf{R}_{co}^{JS\Pi} & \mathbf{R}_{cc}^{JS\Pi} \end{bmatrix} = \begin{bmatrix} \mathbf{a}_{oo} & \mathbf{a}_{oc} \\ \mathbf{a}_{co} & \mathbf{a}_{cc} \end{bmatrix} \begin{bmatrix} \mathbf{B}_{oo} & \mathbf{B}_{oc} \\ \mathbf{B}_{co} & \mathbf{B}_{cc} \end{bmatrix} \tag{3.40}$$

where

$$\mathbf{a} = \left[\mathbf{Z}^{JS\Pi}\mathbf{N} - \mathbf{N}'\right]^{-1} \tag{3.41}$$

and

$$\mathbf{B} = \left[\mathbf{Z}^{JS\Pi}\mathbf{J} - \mathbf{J}'\right] \tag{3.42}$$

The open-open part $\mathbf{R}_{oo}^{JS\Pi}$ of $\mathbf{R}^{JS\Pi}$ is given by

$$\mathbf{R}_{oo}^{JS\Pi} = \mathbf{a}_{oo}\mathbf{B}_{oo} + \mathbf{a}_{oc}\mathbf{B}_{co} \tag{3.43}$$

From this equation it is obvious that $\mathbf{B}_{oc}$ and $\mathbf{B}_{cc}$ are not needed for our purposes. These are the matrices that contain the closed parts of $\mathbf{J}$ and $\mathbf{J}'$, as seen from the definition of $\mathbf{B}$:

$$\begin{bmatrix} \mathbf{B}_{oo} & \mathbf{B}_{oc} \\ \mathbf{B}_{co} & \mathbf{B}_{cc} \end{bmatrix} = \begin{bmatrix} \mathbf{Z}_{oo}^{JS\Pi}\mathbf{J}_o - \mathbf{J}'_o & \mathbf{Z}_{oc}^{JS\Pi}\mathbf{J}_c \\ \mathbf{Z}_{co}^{JS\Pi}\mathbf{J}_o & \mathbf{Z}_{cc}^{JS\Pi}\mathbf{J}_c - \mathbf{J}'_c \end{bmatrix} \tag{3.44}$$

The closed channel elements of $\mathbf{N}$ are needed, however, because all of $\mathbf{A}$ must be calculated in order to take the inverse and get $\mathbf{a}_{oo}$ and $\mathbf{a}_{oc}$. When the spherical

Bessel function expressions are put in for $\mathbf{J}$ and $\mathbf{N}$ one obtains the following expression for the open columns of the R-matrix:

$$\mathbf{R}_{\mathbf{o}}^{JS\Pi} = \mathbf{k}^{-\frac{1}{2}}\left[(R\mathbf{Z}^{JS\Pi} - \mathbf{I})\mathbf{y} - R\mathbf{k}\mathbf{y}'\right]^{-1} \times \left[(R\mathbf{Z}^{JS\Pi} - \mathbf{I})\mathbf{j} - R\mathbf{k}\mathbf{j}'\right]\mathbf{k}_{\mathbf{o}}{}^{\frac{1}{2}} \quad (3.45)$$

where $\mathbf{j}$ and $\mathbf{j}'$ are open channel diagonal matrices whose elements are $j_{l_2}(k_n R)$ (defined in Eq. 3.14), and the derivative with respect to the argument, respectively, and $\mathbf{y}$ is a full diagonal matrix whose open channel elements are the $y_{l_2}(k_n R)$ (defined in Eq. 3.14), and whose closed channel elements are the $k_{l_2}(\kappa_n R)$ (defined in Eq. 3.15) while $\mathbf{y}'$ is the derivative of $\mathbf{y}$ with respect to the argument, and $\mathbf{k}$ is a diagonal matrix with elements $k_n \delta_{nl_1l_2}^{n'l_1'l_2'}$ for the open states and $\kappa_n \delta_{nl_1l_2}^{n'l_1'l_2'}$ for closed states. $\mathbf{k_o}$ is the open-open part of $\mathbf{k}$. Thus we have found the expression which relates the logarithmic derivative $\mathbf{Z}^{JS\Pi}(R)$ to the reactance matrix $\mathbf{R}_{\mathbf{o}}^{JS\Pi}$.

We have shown above that in order to obtain the logarithmic derivative after projection one needs to calculate two matrices, $\mathbf{G}^{JS\Pi}$ and $d\mathbf{G}^{JS\Pi}/dR$, the elements of which are found by computing integrals over the variable r, from $r = 0$ to ∞. In actual practice one chooses a value of $r_{\mathbf{max}}$ as the upper limit of the integrals, which are computed using the trapezoidal rule. Truncation of the integral at finite $r_{\mathbf{max}}$ is justified because the hydrogen atom functions die out exponentially with r. In order to compute $\mathbf{G}^{JS\Pi}$ and $d\mathbf{G}^{JS\Pi}/dr$, one must have $\mathbf{b}^{JS\Pi}[\rho(r;R_{\mathrm{p}});\bar{\rho}]$ and $\mathbf{b}^{JS\Pi'}[\rho(r;R_{\mathrm{p}});\bar{\rho}]$ at each value of $\rho(r_i)$, where r_i are evenly spaced. These are found using the Gordon integrator.

The range of ρ from $\rho(r_1;R_{\mathrm{p}})$ to $\rho(r_{\mathbf{max}};R_{\mathrm{p}})$ is called the "projection region." It is possible for there to be one or several values of $\bar{\rho}_j$ in this region (that is, changes of surface functions) and one must know for each r_i, the value of $\bar{\rho}$ as well as the range of values of ω that correspond to each $\bar{\rho}$. One must also decide the value of R_{p} at which to do the projection. R_{p} must be large enough for the system no longer

to be strongly interacting. In the next section we show how we project at constant ρ, which turns out to be computationally a much simpler procedure.

3.2.3 Constant ρ projection

In this section we describe the alternate method to the one described above, that is, we project the hydrogenic radial functions onto the hyperspherical surface functions. One reason for projecting this way is that the resulting expression for the reactance matrix requires only the logarithmic derivative of the wavefunction, as opposed to both the wavefunction and its derivative separately, making the simple and efficient Johnson integrator usable throughout. This is particularly appropriate for implementation on the hypercube architecture concurrent processor being developed at the California Institute of Technology.[6] Also, since the projection is done at one value of ρ, there is no need for a "projection region" as in section 3.2.1. This method of matching hyperspherical functions to asymptotic cartesian coordinate functions is in the same spirit of that used by Christensen-Dalsgaard.[7]

As for the constant R projection, we write two expressions for the complete scattering wavefunction. First the wavefunction is expanded in hyperspherical surface functions with hyperradial coefficients $b^{JS\Pi}{}_{i}^{i'}(\rho;\bar{\rho})$ according to Eq. 3.18.

$$\Psi_{i'}^{JMS\Pi}(\rho,\omega,\theta_1,\varphi_1,\theta_2,\varphi_2) = \rho^{-\frac{5}{2}} \sum_{i} b^{JS\Pi}{}_{i}^{i'}(\rho;\bar{\rho})\ \Phi_{i}^{JMS\Pi}(\omega,\mathbf{\Omega};\rho)$$

The surface functions $\Phi_i^{JMS\Pi}$ contain all the symmetry properties of the full wavefunction. Secondly the scattering wavefunction is also expanded in asymptotic hydrogen atom functions in one channel, according to Eq. 3.1. The wavefunction is only being considered in the asymptotic region,

$$\Psi_{i'}^{JMS\Pi} \widetilde{_{R\to\infty}} \sum_{nl_1l_2} \frac{U_{nl_1l_2}^{JS\Pi i'}(R)}{R} \Phi_{nl_1l_2}^{JM\Pi}(r,\mathbf{\Omega})$$

where $\Phi^{JM\Pi}_{nl_1l_2}(r,\mathbf{\Omega})$ is the product of $\mathcal{Y}^{JM}_{l_2l_1}(\theta_2,\varphi_2,\theta_1,\varphi_1)$ and the hydrogen radial function $R_{nl_1}(r)$, as before.

The surface functions are orthonormal in the space defined by the five angles. They are also orthogonal, due to their symmetry properties (but not normalized) over only half the space, that is, if one restricts the range of ω to be from 0 to $\pi/2$. Therefore we set the two expressions for $\Psi_{i'}$ equal to each other, multiply by $\Phi^{JMS\Pi}_{k}{}^{*}\sin\theta_1\,d\theta_1\,d\varphi_1\sin\theta_2\,d\theta_2\,d\varphi_2\sin^2\omega\,d\omega$ and integrate over the full range of the four angles $(\theta_1,\varphi_1,\theta_2,\varphi_2)$, but over ω from 0 to $\pi/2$ only.

It is important that this integration not be carried over the whole range of ω. The reason is that the hydrogen atom bound states, $R_{nl_1}(r)$ are defined in one channel only, which can be considered to be separated from the other channel by the $\omega=\pi/2$ boundary.

The resulting expression for $b^{JS\Pi}{}^{i'}_{i}(\rho;\bar{\rho})$ is:

$$\rho^{-\frac{5}{2}}b^{JS\Pi}{}^{i'}_{i}=2\sum_{nl_1l_2}\int d\mathbf{\Omega}\sin^2\omega\,d\omega\Phi^{JMS\Pi}_{i}(\omega,\mathbf{\Omega})\Phi^{JM\Pi}_{nl_1l_2}(r,\mathbf{\Omega})\frac{U^{JS\Pi i'}_{nl_1l_2}(R)}{R} \tag{3.46}$$

The surface functions are further expanded in primitive basis functions $\Theta^{JMS\Pi}_{l_2'l_1'p'}(\omega,\mathbf{\Omega};\bar{\rho})$ with the coefficients $a^{JS\Pi i}_{l_2'l_1'p'}(\bar{\rho})$ as described in Chapter 2:

$$\Phi^{JMS\Pi}_{i}=\sum_{l_2'l_1'p'}a^{JS\Pi i}_{l_2'l_1'p'}(\bar{\rho})\Theta^{JMS\Pi}_{l_2'l_1'p'}(\omega,\mathbf{\Omega};\bar{\rho}) \tag{3.47}$$

The coefficients $a^{JS\Pi i}_{l_2'l_1'p'}(\bar{\rho})$ are independent of the angular coordinates. Therefore when the above equation is substituted into Eq. 3.46, they may be removed from the integral, yielding:

$$\rho^{-\frac{5}{2}}b^{JS\Pi}{}^{i'}_{i}=2\sum_{l_2'l_1'p'}a^{JS\Pi i}_{l_2'l_1'p'}\sum_{nl_1l_2}\int d\mathbf{\Omega}\sin^2\omega\,d\omega\,\Theta^{JMS\Pi}_{l_2'l_1'p'}\Phi^{JM\Pi}_{nl_1l_2}\frac{U^{JS\Pi i'}_{nl_1l_2}(R)}{R} \tag{3.48}$$

The only functions that depend on the angular variables $(\theta_2,\varphi_2,\theta_1,\varphi_1)$, called $\mathbf{\Omega}$ collectively (as an ordered set), are $\Theta^{JMS\Pi}_{l_2'l_1'p'}$ and $\Phi^{JM\Pi}_{nl_1l_2}$, because the distance R

is expressed as a function only of ρ and ω. Let us then define a new term which will contain the entire integral over $\mathbf{\Omega}$, $F^{JS\Pi}{}^{nl_1l_2}_{l_2'l_1'p'}(r,\omega;\bar{\rho})$:

$$F^{JS\Pi}{}^{nl_1l_2}_{l_2'l_1'p'} = 2\int \Theta^{JMS\Pi}_{l_2'l_1'p'}(\omega,\mathbf{\Omega};\bar{\rho})\bar{\Phi}^{JM\Pi}_{nl_1l_2}(r,\mathbf{\Omega})\,d\mathbf{\Omega} \tag{3.49}$$

When this is substituted in we get the following:

$$\rho^{-\frac{5}{2}}b^{JS\Pi}{}^{i'}_{i} = \sum_{l_2'l_1'p'} a^{JS\Pi i}_{l_2'l_1'p'} \sum_{nl_1l_2}\int F^{JS\Pi}{}^{nl_1l_2}_{l_2'l_1'p'}\frac{U^{JS\Pi i'}_{nl_1l_2}(R)}{R}\sin^2\omega\,d\omega \tag{3.50}$$

From Eq. 3.12 we have that the asymptotic behavior of $U^{JS\Pi}(R)$ is

$$U^{JS\Pi i'}_{nl_1l_2}(R)\widetilde{_{R\to\infty}} \sum_{\bar{n}\bar{l}_1\bar{l}_2}\Big[J^{\bar{n}\bar{l}_1\bar{l}_2}_{nl_1l_2}(R) - \sum_{\hat{n}\hat{l}_1\hat{l}_2} N^{\hat{n}\hat{l}_1\hat{l}_2}_{nl_1l_2}(R)R^{JS\Pi}{}^{\bar{n}\bar{l}_1\bar{l}_2}_{\hat{n}\hat{l}_1\hat{l}_2}\Big]C^{JS\Pi i'}_{\bar{n}\bar{l}_1\bar{l}_2}$$

which is substituted into Eq. 3.50. The matrix $\mathbf{C}^{JS\Pi}$ is constant, so it too can be removed from under the integral sign, yielding

$$\begin{aligned}\rho^{-\frac{5}{2}}b^{JS\Pi}{}^{i'}_{i} = \sum_{l_2'l_1'p'} a^{JS\Pi i}_{l_2'l_1'p'} \sum_{nl_1l_2}\sum_{\bar{n}\bar{l}_1\bar{l}_2}\int F^{JS\Pi}{}^{nl_1l_2}_{l_2'l_1'p'}(\omega,r;\bar{\rho})\frac{1}{R}\Big[J^{\bar{n}\bar{l}_1\bar{l}_2}_{nl_1l_2}(R)\\ - \sum_{\hat{n}\hat{l}_1\hat{l}_2} N^{\hat{n}\hat{l}_1\hat{l}_2}_{nl_1l_2}(R)R^{JS\Pi}{}^{\bar{n}\bar{l}_1\bar{l}_2}_{\hat{n}\hat{l}_1\hat{l}_2}\Big]\sin^2\omega\,d\omega \times C^{JS\Pi i'}_{\bar{n}\bar{l}_1\bar{l}_2}\end{aligned} \tag{3.51}$$

In matrix notation, the above equation becomes

$$\rho^{-\frac{5}{2}}\mathbf{b}^{JS\Pi} = \tilde{\mathbf{a}}^{JS\Pi}\int \mathbf{F}^{JS\Pi}\big[\mathbf{J}(R) - \mathbf{N}(R)\mathbf{R}^{JS\Pi}\big]\frac{\sin^2\omega}{\rho\cos\frac{\omega}{2}}d\omega\mathbf{C}^{JS\Pi} \tag{3.52}$$

where we have substituted $\rho\cos\frac{\omega}{2}$ for R.

The corresponding expression for the derivative of $\mathbf{b}^{JS\Pi}$ with respect to ρ is:

$$\begin{aligned}\frac{d\mathbf{b}^{JS\Pi}}{d\rho} =& \frac{3}{2\rho}\mathbf{b}^{JS\Pi} + \rho^{\frac{5}{2}}\tilde{\mathbf{a}}^{JS\Pi}\int\frac{\partial\mathbf{F}^{JS\Pi}}{\partial\rho}(\mathbf{J}-\mathbf{N}\mathbf{R}^{JS\Pi})\frac{\sin^2\omega}{\cos\frac{\omega}{2}}\,d\omega\mathbf{C}^{JS\Pi}\\ &+\rho^{\frac{5}{2}}\tilde{\mathbf{a}}^{JS\Pi}\int\mathbf{F}^{JS\Pi}\Big(\frac{\partial\mathbf{J}}{\partial\rho}-\frac{\partial\mathbf{N}}{\partial\rho}\mathbf{R}^{JS\Pi}\Big)\frac{\sin^2\omega}{\cos\frac{\omega}{2}}\,d\omega\mathbf{C}^{JS\Pi}\end{aligned} \tag{3.53}$$

The R-matrix is not a function of ω, and so doesn't have to be included in the integral. Let us define the following matrices, $\mathbf{A_1}^{JS\Pi}$, $\mathbf{B_1}^{JS\Pi}$, $\mathbf{A_2}^{JS\Pi}$, and $\mathbf{B_2}^{JS\Pi}$:

$$\begin{bmatrix} \mathbf{A_1}^{JS\Pi} \\ \mathbf{B_1}^{JS\Pi} \end{bmatrix} = \int \mathbf{F}^{JS\Pi}(\omega, r) \begin{bmatrix} \mathbf{J}(R) \\ \mathbf{N}(R) \end{bmatrix} \frac{\sin^2 \omega}{\cos \frac{\omega}{2}} \, d\omega \tag{3.54}$$

$$\begin{aligned} \begin{bmatrix} \mathbf{A_2}^{JS\Pi} \\ \mathbf{B_2}^{JS\Pi} \end{bmatrix} = \int \Bigg\{ & \left(\frac{\partial \mathbf{F}^{JS\Pi}(\omega, r)}{\partial \rho} \right)_{\omega} \begin{bmatrix} \mathbf{J}(R) \\ \mathbf{N}(R) \end{bmatrix} \\ & + \mathbf{F}^{JS\Pi}(\omega, r) \begin{bmatrix} \partial \mathbf{J}(R)/\partial \rho \\ \partial \mathbf{N}(R)/\partial \rho \end{bmatrix} \Bigg\} \frac{\sin^2 \omega}{\cos \frac{\omega}{2}} d\omega \end{aligned} \tag{3.55}$$

where R and r are considered to be functions of ρ and ω according to Eq. 3.17, the matrix $\mathbf{F}^{JS\Pi}$ is defined by Eq. 3.49, and the matrices $\mathbf{J}$ and $\mathbf{N}$ have been jointly defined by Eq. 3.14 and Eq. 3.15. Using this nomenclature, the expressions for $\mathbf{b}^{JS\Pi}$ and $\mathbf{b}^{JS\Pi'}$ are

$$\begin{aligned} \mathbf{b}^{JS\Pi} &= \rho^{\frac{s}{2}} \tilde{\mathbf{a}}^{JS\Pi} (\mathbf{A_1}^{JS\Pi} - \mathbf{B_1}^{JS\Pi} \mathbf{R}^{JS\Pi}) \mathbf{C}^{JS\Pi} \\ \frac{d\mathbf{b}^{JS\Pi}}{d\rho} &= \frac{3}{2\rho} \mathbf{b}^{JS\Pi} + \rho^{\frac{s}{2}} \tilde{\mathbf{a}}^{JS\Pi} (\mathbf{A_2}^{JS\Pi} - \mathbf{B_2}^{JS\Pi} \mathbf{R}^{JS\Pi}) \mathbf{C}^{JS\Pi} \end{aligned} \tag{3.56}$$

3.2.4 Reactance matrix using constant ρ projection

We now do a little algebra to extract an expression for the reactance matrix from Eq. 3.56. First, we obtain the logarithmic derivative of $\mathbf{b}^{JS\Pi}$. This is the quantity one obtains computationally from the coupled channel numerical solution of the Schrödinger equation. Part of the reason for doing the projection at constant ρ is that the wavefunction is only needed in the form of its logarithmic derivative, and so we can propagate the coupled channel equation using the very efficient Johnson logarithmic derivative integrator.[8] It will be convenient if we define a new matrix, $\mathbf{X}^{JS\Pi}$, which will contain the logarithmic derivative as well as the constant term that arises from the way we have defined the radial matrix $\mathbf{b}^{JS\Pi}$:

$$\mathbf{X}^{JS\Pi} = \frac{d\mathbf{b}^{JS\Pi}}{d\rho} \mathbf{b}^{JS\Pi^{-1}} - \frac{3}{2\rho} \mathbf{I} \tag{3.57}$$

Forming the logarithmic derivative from Eq. 3.56 we eliminate $\mathbf{C}^{JS\Pi}$ and solve for the R-matrix, using Eq. 3.57 to simplify:

$$\begin{aligned}\mathbf{R}^{JS\Pi} = &\left[\mathbf{X}^{JS\Pi}\tilde{\mathbf{a}}^{JS\Pi}\mathbf{B}_{\mathbf{1}}^{JS\Pi} - \tilde{\mathbf{a}}^{JS\Pi}\mathbf{B}_{\mathbf{2}}^{JS\Pi}\right]^{-1} \\ &\times\left[\mathbf{X}^{JS\Pi}\tilde{\mathbf{a}}^{JS\Pi}\mathbf{A}_{\mathbf{1}}^{JS\Pi} - \tilde{\mathbf{a}}^{JS\Pi}\mathbf{A}_{\mathbf{2}}^{JS\Pi}\right]\end{aligned} \tag{3.58}$$

Let us summarize what the various terms mean, and how we get them. First, the log-derivative of $\mathbf{b}^{JS\Pi}$ is obtained from the Johnson integrator. The transpose of the coefficient matrix $\tilde{\mathbf{a}}^{JS\Pi}$ is obtained in the surface function calculation. $\mathbf{A}_{\mathbf{1}}^{JS\Pi}$, $\mathbf{B}_{\mathbf{1}}^{JS\Pi}$, $\mathbf{A}_{\mathbf{2}}^{JS\Pi}$, and $\mathbf{B}_{\mathbf{2}}^{JS\Pi}$ have been defined in Eq. 3.54 and Eq. 3.55 above, and must be calculated after the radial equation propagation. The matrices $\mathbf{F}^{JS\Pi}$ and $\partial\mathbf{F}^{JS\Pi}/\partial\rho$ are needed for their computation. From Eq. 3.49, Eq. 2.53 and the remark after Eq. 3.1 we have

$$\begin{aligned}F^{JS\Pi}{}^{nl_1l_2}_{l_2'l_1'p'} = 2\int &\left[\mathcal{Y}^{JM}_{l_2'l_1'}(\Omega)t^{Jl_2'l_1'}_{p'}(\omega;\rho) + (-1)^{\Lambda}\mathcal{Y}^{JM}_{l_1'l_2'}(\Omega)t^{Jl_1'l_2'}_{p'}(\omega;\rho)\right] \\ &\times N_{l_2'l_1'}R_{nl_1}(r)\mathcal{Y}^{JM}_{l_2l_1}d\Omega\end{aligned} \tag{3.59}$$

The integral over the four angles is easily done, due to the orthogonality of the $\mathcal{Y}^{JM}_{l_2l_1}$ functions, which leaves the expression

$$F^{JS\Pi}{}^{nl_1l_2}_{l_2'l_1'p'}\left[r(\omega;\rho),\omega;\rho\right] = N_{l_2'l_1'}R_{nl_1}(r)\,t^{Jl_2l_1}_{p'}(\omega;\rho)\left[\delta^{l_2l_1}_{l_2'l_1'} + (-1)^{\Lambda}\delta^{l_2l_1}_{l_1'l_2'}\right] \tag{3.60}$$

where $N_{l_2'l_1'}$ is a normalization factor. Now let's look at the derivative terms. To take the partial derivative one uses

$$\left(\frac{\partial}{\partial\rho}\right)_{\omega} = \cos\frac{\omega}{2}\left(\frac{\partial}{\partial R}\right)_{r} + \sin\frac{\omega}{2}\left(\frac{\partial}{\partial r}\right)_{R} \tag{3.61}$$

Taking the partial derivative of F we obtain

$$\begin{aligned}\frac{\partial}{\partial\rho}F^{JS\Pi}{}^{nl_1l_2}_{l_2'l_1'p'}\left[r,\omega\right] &= \left[\frac{\partial}{\partial\rho}R_{nl_1}(r)\right]_{\omega}N_{l_2'l_1'}\,t^{Jl_2l_1}_{p'}(\omega;\rho)\left[\delta^{l_2l_1}_{l_2'l_1'} + (-1)^{\Lambda}\delta^{l_2l_1}_{l_1'l_2'}\right] \\ &= \sin\frac{\omega}{2}R'_{nl_1}(r)N_{l_2'l_1'}\,t^{Jl_2l_1}_{p'}(\omega;\rho)\left[\delta^{l_2l_1}_{l_2'l_1'} + (-1)^{\Lambda}\delta^{l_2l_1}_{l_1'l_2'}\right]\end{aligned} \tag{3.62}$$

We can define a new matrix $\mathbf{f}^{JS\Pi}$ as follows:

$$\mathbf{f}^{JS\Pi}{}^{nl_1l_2}_{l_2'l_1'p'} = R'_{nl_1}(r)N_{l_2'l_1'}\,t^{Jl_2l_1}_{p'}(\omega;\rho)\left[\delta^{l_2l_1}_{l_2'l_1'} + (-1)^{\Lambda}\delta^{l_2l_1}_{l_1'l_2'}\right] \tag{3.63}$$

If one writes the expressions for $\mathbf{A}_2^{JS\Pi}$ and $\mathbf{B}_2^{JS\Pi}$ using this, one gets

$$\begin{aligned}\begin{bmatrix}\mathbf{A}_2^{JS\Pi}\\ \mathbf{B}_2^{JS\Pi}\end{bmatrix} = \int_0^{\pi/2}\mathbf{f}^{JS\Pi}\begin{bmatrix}\mathbf{J}(R)\\ \mathbf{N}(R)\end{bmatrix}\sin^3\frac{\omega}{2}\cos\frac{\omega}{2}\,d\omega \\ + \int_0^{\pi/2}\mathbf{F}^{JS\Pi}\frac{d}{dR}\begin{bmatrix}\mathbf{J}(R)\\ \mathbf{N}(R)\end{bmatrix}\sin^2\omega\,d\omega\end{aligned} \tag{3.64}$$

The derivatives of the Bessel function terms are found to be

$$\frac{d}{dR}\begin{bmatrix}\mathbf{J}(R)\\ \mathbf{N}(R)\end{bmatrix}^{\bar{n}\bar{l}_1\bar{l}_2}_{nl_1l_2} = \delta^{\bar{n}\bar{l}_1\bar{l}_2}_{nl_1l_2}k_nv_n^{-\frac{1}{2}}\left((k_nR)\begin{bmatrix}j'_{l_2}(k_nR)\\ y'_{l_2}(k_nR)\end{bmatrix} + \begin{bmatrix}j_{l_2}(k_nR)\\ y_{l_2}(k_nR)\end{bmatrix}\right) \tag{3.65}$$

for open states. For closed states we replace $y_{l_2}(k_nR)$ with $k_{l_2}(\kappa_nR)$. We define the following matrices that will ultimately be what we calculate:

$$\begin{aligned}\begin{bmatrix}\Xi_1\\ \Upsilon_1\end{bmatrix}^{nl_1l_2}_{l_2'l_1'p'} &= \int_0^{\pi/2}F^{JS\Pi}{}^{nl_1l_2}_{l_2'l_1'p'}\begin{bmatrix}j_{l_2}(k_nR)\\ y_{l_2}(k_nR)\end{bmatrix}\sin^2\omega\,d\omega \\ \begin{bmatrix}\Xi_2\\ \Upsilon_2\end{bmatrix}^{nl_1l_2}_{l_2'l_1'p'} &= \int_0^{\pi/2}f^{JS\Pi}{}^{nl_1l_2}_{l_2'l_1'p'}\begin{bmatrix}j_{l_2}(k_nR)\\ y_{l_2}(k_nR)\end{bmatrix}\sin\frac{\omega}{2}\sin^2\omega\,d\omega \\ \begin{bmatrix}\Xi_3\\ \Upsilon_3\end{bmatrix}^{nl_1l_2}_{l_2'l_1'p'} &= \int_0^{\pi/2}F^{JS\Pi}{}^{nl_1l_2}_{l_2'l_1'p'}\begin{bmatrix}j'_{l_2}(k_nR)\\ y'_{l_2}(k_nR)\end{bmatrix}k_n\cos\frac{\omega}{2}\sin^2\omega\,d\omega\end{aligned} \tag{3.66}$$

Let it be understood in all cases that the closed channel elements are obtained by substituting κ_n for k_n, and k_{l_2} for y_{l_2}. From Eq. 3.54, Eq. 3.55, and Eq. 3.62 through Eq. 3.66 we obtain, after some algebraic effort,

$$\begin{aligned}\mathbf{A}_1^{JS\Pi} &= \rho\Xi_1\mathbf{k}^{\frac{1}{2}} \\ \mathbf{B}_1^{JS\Pi} &= \rho\Upsilon_1\mathbf{k}^{\frac{1}{2}} \\ \mathbf{A}_2^{JS\Pi} &= \left[\Xi_1 + \rho(\Xi_2 + \Xi_3)\right]\mathbf{k}^{\frac{1}{2}} \\ \mathbf{B}_2^{JS\Pi} &= \left[\Upsilon_1 + \rho(\Upsilon_2 + \Upsilon_3)\right]\mathbf{k}^{\frac{1}{2}}\end{aligned} \tag{3.67}$$

where $\mathbf{k}$ was defined in Eq. 3.45.

Using these matrices we can rewrite the expression for the reactance matrix as

$$\begin{aligned}\mathbf{R}_{o}^{JS\Pi} = \mathbf{k}^{-\frac{1}{2}}\left[(\rho\mathbf{X}^{JS\Pi} - \mathbf{I})\tilde{\mathbf{a}}^{JS\Pi}\boldsymbol{\Upsilon}_{\mathbf{1}} - \rho\tilde{\mathbf{a}}^{JS\Pi}(\boldsymbol{\Upsilon}_{\mathbf{2}} + \boldsymbol{\Upsilon}_{\mathbf{3}})\right]^{-1} \\ \times \left[(\rho\mathbf{X}^{JS\Pi} - \mathbf{I})\tilde{\mathbf{a}}^{JS\Pi}\boldsymbol{\Xi}_{\mathbf{1}} - \rho\tilde{\mathbf{a}}^{JS\Pi}(\boldsymbol{\Xi}_{\mathbf{2}} + \boldsymbol{\Xi}_{\mathbf{3}})\right]\mathbf{k}^{\frac{1}{2}}\end{aligned} \tag{3.68}$$

This final expression is used for the calculation of $\mathbf{R}_{oo}^{JS\Pi}$.

3.3 Reactance and Scattering Matrix Solutions

In this section we define the reactance matrix and scattering matrix solutions[9] and relate them to the general wavefunction obtained in section 3.1. These solutions are defined to have the asymptotic forms

$$\Psi_{n'l_1'l_2'}^{JMS\Pi}[R \text{ or } S]\widetilde{_{R\to\infty}} \sum_{nl_1l_2} \frac{1}{R} U^{JS\Pi}{}_{nl_1l_2}^{n'l_1'l_2'}[R \text{ or } S](R)\Phi_{nl_1l_2}^{JM\Pi}(r,\boldsymbol{\Omega}) \tag{3.69}$$

where $\Phi_{nl_1l_2}^{JM\Pi}(r,\boldsymbol{\Omega})$ is the product of $\mathcal{Y}_{l_2l_1}^{JM}(\theta_2,\varphi_2,\theta_1,\varphi_1)$ and the hydrogen radial function $R_{nl_1}(r)$, as previously. By definition, the scattering matrix radial functions $U^{JS\Pi}[S]$ behave asymptotically as

$$U^{JS\Pi}{}_{nl_1l_2}^{n'l_1'l_2'}[S]\widetilde{_{R\to\infty}} v_n^{-1/2}\left[\mathcal{I}_{nl_1l_2}(R)\delta_{nl_1l_2}^{n'l_1'l_2'} - \mathcal{O}_{nl_1l_2}(R)(S^{JS\Pi})_{nl_1l_2}^{n'l_1'l_2'}\right] \tag{3.70}$$

and the reactance matrix functions as

$$U^{JS\Pi}{}_{nl_1l_2}^{n'l_1'l_2'}[R]\widetilde{_{R\to\infty}} v_n^{-1/2}\left[\mathcal{S}_{nl_1l_2}(R)\delta_{nl_1l_2}^{n'l_1'l_2'} - \mathcal{C}_{nl_1l_2}(R)(R^{JS\Pi})_{nl_1l_2}^{n'l_1'l_2'}\right] \tag{3.71}$$

where the $\mathcal{I}$, $\mathcal{O}$, $\mathcal{S}$, and $\mathcal{C}$ have been defined in Equations 3.3, 3.4, 3.9, and 3.10. The reactance function is obtained from the general function by setting the matrix $\mathbf{C}^{JS\Pi}$ in Eq. 3.8 equal to the unit matrix. In similar fashion the scattering function is obtained by setting the matrix $\mathbf{A}^{JS\Pi}$ in Eq. 3.6 to unity.

3.4 Scattering Amplitudes and Integral Cross Sections

We wish to find particular solutions of the space-fixed Schrödinger equation that satisfy the *physical* asymptotic condition for large R and are eigenfunctions of

$\hat{S}^2$. The axis of quantization for m_1' is the direction of the initial wave-numbervector $\mathbf{k}_n$ which has been chosen to lie along the space-fixed Oz axis. The component of $\mathbf{R}_\lambda$ along that axis is z_λ. The asymptotic form of the spatial part of the physical wavefunction in each channel consists of an incoming plane wave multiplied by an open channel hydrogen atom wavefunction, $\phi_{n'l_1'm_1'}(\mathbf{r})$, and a sum over all hydrogen atom wavefunctions, both those in open and closed channels, each multiplied by an outgoing spherical wave and by the scattering amplitude.

$$\begin{aligned}\Psi^{(1)n'l_1'm_1'}[P]\widetilde{_{R\to\infty}} & e^{ik_{n'}^{(1)}z_1}\phi_{n'l_1'm_1'}(\mathbf{r}) + \sum_{nl_1m_1} f^{(1)n'l_1'm_1'}_{(1)nl_1m_1}(\hat{\mathbf{R}})\frac{e^{ik_nR}}{R}\phi_{nl_1m_1}(\mathbf{r}) \\ & \widetilde{r\to\infty} \sum_{nl_1m_1} f^{(1)n'l_1'm_1'}_{(2)nl_1m_1}(\hat{\mathbf{r}})\frac{e^{ik_nr}}{r}\phi_{nl_1m_1}(\mathbf{R})\end{aligned} \tag{3.72}$$

for $\lambda = 1$ and

$$\begin{aligned}\Psi^{(2)n'l_1'm_1'}[P]\widetilde{_{r\to\infty}} & e^{ik_{n'}^{(2)}z_2}\phi_{n'l_1'm_1'}(\mathbf{R}) + \sum_{nl_1m_1} f^{(2)n'l_1'm_1'}_{(2)nl_1m_1}(\hat{\mathbf{r}})\frac{e^{ik_nr}}{r}\phi_{nl_1m_1}(\mathbf{R}) \\ & \widetilde{R\to\infty} \sum_{nl_1m_1} f^{(2)n'l_1'm_1'}_{(1)nl_1m_1}(\hat{\mathbf{R}})\frac{e^{ik_nR}}{R}\phi_{nl_1m_1}(\mathbf{r})\end{aligned} \tag{3.73}$$

for $\lambda = 2$. We take the sum and difference of $\Psi^{(1)}$ and $\Psi^{(2)}$ as R goes to infinity to form spatial wavefunctions that satisfy the Pauli principle, which introduces the quantum number S.

$$\Psi^{Sn'l_1'm_1'}[P]\widetilde{_{R\to\infty}} e^{ik_{n'}z}\phi_{n'l_1'm_1'}(\mathbf{r}) + \sum_{nl_1m_1} f^{Sn'l_1'm_1'}_{nl_1m_1}(\hat{\mathbf{R}})\frac{e^{ik_nR}}{R}\phi_{nl_1m_1}(\mathbf{r}) \tag{3.74}$$

where we have defined the symmetrized scattering amplitudes, $f^{Sn'l_1'm_1'}_{nl_1m_1}(\hat{\mathbf{R}})$, as

$$f^{Sn'l_1'm_1'}_{nl_1m_1}(\hat{\mathbf{R}}) = f^{(1)n'l_1'm_1'}_{(1)nl_1m_1}(\hat{\mathbf{R}}) + (-1)^S f^{(2)n'l_1'm_1'}_{(1)nl_1m_1} \tag{3.75}$$

We treat the incoming plane wave separately from the outgoing scattered wave.

$$\Psi^{Sn'l_1'm_1'}[P]\widetilde{_{R\to\infty}} \Psi^{Sn'l_1'm_1'}_{\text{inc}} + \Psi^{Sn'l_1'm_1'}_{\text{scatt}} \tag{3.76}$$

The spin part which multiplies this spatial wavefunction is an eigenfunction of $\hat{S}^2$ and $\hat{S}_z$.

The spatial physical wavefunction $\Psi^{Sn'l_1'm_1'}[P]$ can be expressed as a linear combination of reactance or scattering matrix solutions $\Psi^{JMS\Pi}_{n'l_1'l_2'}[R \text{ or } S]$ which are simultaneous eigenfunctions of the total orbital angular momentum operator and its laboratory-fixed z-axis projection.

$$\Psi^{Sn'l_1'm_1'}[P] = \sum_{JMl_2'} c^{Sn'l_1'm_1'}_{JMl_2'}[R \text{ or } S]\Psi^{JMS\Pi}_{n'l_1'l_2'}[R \text{ or } S] \tag{3.77}$$

We need to expand Ψ_{inc} and Ψ_{scatt}, first in spherical harmonics $Y_{l_2m_2}(\hat{\mathbf{R}})$, and secondly in partial waves, to be able to relate the *physical* solution to the scattering solution already determined. It will be useful to know the asymptotic forms of the spherical Bessel functions. These are[2]

$$\begin{aligned} j_l(x) &\widetilde{\underset{x\to\infty}{}} \frac{1}{x}\sin(x - \frac{l\pi}{2}) \\ y_l(x) &\widetilde{\underset{x\to\infty}{}} -\frac{1}{x}\cos(x - \frac{l\pi}{2}) \end{aligned} \tag{3.78}$$

Using the above equations, expansion of the plane wave gives

$$\begin{aligned} \exp(ik_{n'}z) &= \exp(ik_{n'}R\cos\theta) \\ &= \sum_{l_2=0}^{\infty}(2l_2+1)i^{l_2}\, j_{l_2}(k_{n'}R)P_{l_2}(\cos\theta) \\ &= \sum_{l_2m_2}\delta^0_{m_2}\frac{\sqrt{(2l_2+1)\pi}}{ik_{n'}R}(e^{ik_{n'}R} - e^{-ik_{n'}R}i^{2l_2})Y_{l_2m_2}(\hat{\mathbf{R}}) \end{aligned} \tag{3.79}$$

The scattering amplitude is also expanded in spherical harmonics.

$$f^{Sn'l_1'm_1'}_{nl_1m_1}(\hat{\mathbf{R}}) = \sum_{\Pi l_2m_2} Y_{l_2m_2}(\hat{\mathbf{R}})b^{Sn'l_1'm_1'}_{\Pi nl_1m_1l_2m_2} \tag{3.80}$$

The sum in Eq. 3.80 is over all values of l_2, and thus is in effect a sum over states with different parity Π, too, which is why the sum over the index Π is indicated

explicitly. Substitution of the last two expansions into the wavefunction expression Eq. 3.74 leads to

$$\Psi_{\rm inc}^{Sn'l_1'm_1'} = \sum_{l_2 m_2} \delta_{m_2}^0 \frac{\sqrt{(2l_2+1)\pi}}{ik_{n'}R}(e^{ik_{n'}R} - e^{-ik_{n'}R} i^{2l_2}) Y_{l_2 m_2}(\hat{\mathbf{R}}) \phi_{n'l_1'm_1'}(\mathbf{r}) \quad (3.81)$$

for the incoming plane wave and

$$\Psi_{\rm sph}^{Sn'l_1'm_1'} = \sum_{\Pi l_2 m_2} \sum_{n l_1 m_1} b_{\Pi n l_1 m_1 l_2 m_2}^{Sn'l_1'm_1'} Y_{l_2 m_2}(\hat{\mathbf{R}}) \frac{e^{ik_n R}}{R} \phi_{nl_1m_1}(\mathbf{r}) \quad (3.82)$$

for the outgoing spherical wave. We recall the asymptotic form of the spatial scattering matrix wavefunction from Eq. 3.69 and Eq. 3.71:

$$\begin{aligned}\Psi_{n'l_1'l_2'}^{JMS\Pi}[S] &\widetilde{R\to\infty} \sum_{nl_1l_2} \mathcal{Y}_{l_2l_1}^{JM}(\hat{\mathbf{R}};\hat{\mathbf{r}}) \frac{1}{R} U^{JS\Pi}{}_{nl_1l_2}^{n'l_1'l_2'}[S](R)\, R_{nl_1}(r) \\ &\widetilde{R\to\infty} \sum_{nl_1l_2} \frac{i^{l_2}}{R\sqrt{v_n}} \left(e^{-ik_nR}\delta_{nl_1l_2}^{n'l_1'l_2'} - e^{ik_nR} i^{-2l_2} S_{nl_1l_2}^{JS\Pi n'l_1'l_2'} \right) \\ &\qquad \times \Phi_{nl_1l_2}^{JM\Pi}(r,\Omega)\end{aligned} \quad (3.83)$$

where we have substituted Eqs. 3.3 and 3.4 for I and O, respectively. Identifying the coefficients of the open channel incoming waves $e^{-ik_{n'}R}$ in $\Psi^{Sn'l_1'm_1'}$ and the wavefunction in Eq. 3.77 one obtains:

$$\begin{aligned}\sum_{JMl_2'} c_{JMl_2'}^{Sn'l_1'm_1'} \frac{i^{l_2'}}{\sqrt{v_{n'}}} \quad &\Phi_{n'l_1'l_2'}^{JM\Pi}(\mathbf{r},\hat{\mathbf{R}}) \\ &= \sum_{l_2'm_2'} \delta_0^{m_2'} \sqrt{(2l_2'+1)\pi}\, \frac{i^{2l_2'+1}}{k_{n'}} Y_{l_2'm_2'}\, \phi_{n'l_1'm_1'}(\mathbf{r})\end{aligned} \quad (3.84)$$

If we re-express $\Phi_{n'l_1'l_2'}^{JM\Pi}$ in terms of a sum over products of hydrogen atom functions and spherical harmonics we obtain

$$\Phi_{n'l_1'l_2'}^{JM\Pi}(\mathbf{r},\hat{\mathbf{R}}) = \sum_{m_1''m_2'} C(l_1'l_2'J; m_1''m_2'M)\, Y_{l_2'm_2'}\, \phi_{n'l_1'm_1''}(\mathbf{r}) \quad (3.85)$$

The expression above is substituted into Eq. 3.84; one multiplies both sides of the resulting equation by $\phi_{nl_1m_1}$ and integrates over $d\mathbf{r}$, obtaining the following:

$$\sum_{JMl_2'} c_{JMl_2'}^{Sn'l_1'm_1'} \frac{i^{l_2'}}{\sqrt{v_{n'}}} \sum_{m_2'} C(l_1'l_2'J;m_1m_2'M) Y_{l_2'm_2'}(\hat{\mathbf{R}}) = \sum_{l_2'm_2'} \delta_0^{m_2'} \sqrt{(2l_2'+1)\pi}\, \frac{i^{2l_2'+1}}{k_{n'}} Y_{l_2'm_2'} \tag{3.86}$$

We then multiply by $Y_{l_2''m_2''}(\hat{\mathbf{R}})$ and integrate over $d\hat{\mathbf{R}}$, interchanging $l_2'm_2'$ for l_2'', m_2'', which yields

$$\sum_{JM} c_{JMl_2'}^{Sn'l_1'm_1'} C(l_1'l_2'J;m_1m_2'M) = \delta_0^{m_2'} \sqrt{(2l_2'+1)\pi}\, \frac{i^{l_2'+1}\sqrt{v_{n'}}}{k_{n'}} \tag{3.87}$$

We multiply Eq. 3.87 by $C(l_1'l_2'J';m_1m_2'M')$ and sum over m_1 and m_2'. The Clebsh-Gordan completeness relation

$$\delta_{JM}^{J'M'} = \sum_{m_1m_2} C(l_1l_2J;m_1m_2M) C(l_1l_2J';m_1m_2M') \tag{3.88}$$

is then used to remove all the sums on the left hand side, such that we obtain the simple expression

$$c_{JMl_2'}^{Sn'l_1'm_1'} = C(l_1'l_2'J;m_1'0m_1') \sqrt{(2l_2'+1)\pi}\, i^{l_2'+1} \left(\frac{\sqrt{v_{n'}}}{k_{n'}}\right) \delta_M^{m_1'} \tag{3.89}$$

Next we set equal the outgoing waves (e^{+ik_nR}/R). This will give a relationship between the scattering matrix and the scattering amplitudes f^S:

$$\begin{aligned} &\sum_{l_2m_2} \delta_0^{m_2} \frac{\sqrt{(2l_2+1)\pi}}{ik_{n'}R} e^{ik_{n'}R} Y_{l_2m_2}(\hat{\mathbf{R}}) \phi_{n'l_1'm_1'}(\mathbf{r}) \\ &\quad + \sum_{\Pi l_2m_2} \sum_{nl_1m_1} b_{\Pi nl_1m_1l_2m_2}^{Sn'l_1'm_1'} \frac{e^{ik_nR}}{R} Y_{l_2m_2}(\hat{\mathbf{R}}) \phi_{nl_1m_1}(\mathbf{r}) \\ &\quad = -\sum_{JMl_2'} c_{JMl_2'}^{Sn'l_1'm_1'} \sum_{nl_1l_2} \frac{i^{-l_2}}{R\sqrt{v_n}} S_{nl_1l_2}^{JS\Pi n'l_1'l_2'} e^{ik_nR} \Phi_{nl_1l_2}^{JM\Pi}(r,\mathbf{\Omega}) \end{aligned} \tag{3.90}$$

The spherical harmonics form a complete orthonormal set as do the hydrogen basis functions. Therefore one removes the sums over $nl_1m_1l_2m_2$ by multiplying by an arbitrary spherical harmonic and hydrogen basis function, and then integrating over the variables $\mathbf{r}, \widehat{\mathbf{R}}$. The equation that results is

$$\begin{aligned} \delta_0^{m_2}\delta_{nl_1m_1}^{n'l_1'm_1'}\frac{\sqrt{(2l_2+1)\pi}}{ik_n} \quad &+ \quad b_{\Pi nl_1m_1l_2m_2}^{Sn'l_1'm_1'} \\ &= -\sum_{JMl_2'} c_{JMl_2'}^{Sn'l_1'm_1'}\frac{i^{-l_2}}{\sqrt{v_n}} S_{nl_1l_2}^{JS\Pi n'l_1'l_2'} C(l_1l_2J;m_1m_2M) \end{aligned} \tag{3.91}$$

If we replace $c_{JMl_2'}^{Sn'l_1'm_1'}$ with the value calculated in Eq. 3.89, use

$$\delta_{m_2}^0\delta_{m_1}^{m_1'} = \sum_{JM} C(l_1l_2J;m_1m_2M)C(l_1l_2J;m_1'0M) \tag{3.92}$$

to introduce a sum over J and M in the first term of Eq. 3.91, and simplify, we obtain the expression for $b_{\Pi nl_1m_1l_2m_2}^{Sn'l_1'm_1'}$ in terms of the scattering matrix:

$$\begin{aligned} b_{\Pi nl_1m_1l_2m_2}^{Sn'l_1'm_1'} = \sum_{JMl_2'} &\left(\delta_{nl_1l_2}^{n'l_1'l_2'} - S_{nl_1l_2}^{JS\Pi n'l_1'l_2'}\right)\sqrt{(2l_2'+1)\pi}\left(\frac{i^{1+l_2'-l_2}}{k_{n'}}\right) \\ &\times C(l_1l_2J;m_1m_2M)C(l_1'l_2'J;m_1'0M)\left(\frac{v_{n'}}{v_n}\right)^{\frac{1}{2}} \end{aligned} \tag{3.93}$$

The form of this expression leads us to define the transition matrix from the open-open sub-block of the scattering matrix.

$$\mathbf{T}^{JS\Pi} = \mathbf{I} - \mathbf{S}_{oo}^{JS\Pi} \tag{3.94}$$

With this new definition the scattering amplitude expansion coefficients are written

$$\begin{aligned} b_{\Pi nl_1m_1l_2m_2}^{Sn'l_1'm_1'} = \sum_{l_2'} &\sqrt{(2l_2'+1)\pi}\, i^{l_2'-l_2}\left(\frac{v_{n'}}{v_n}\right)^{\frac{1}{2}}\left(\frac{i}{k_{n'}}\right) \\ &\sum_{JM} C(l_1'l_2'J;m_1'0M)\, C(l_1l_2J;m_1m_2M)\, T_{nl_1l_2}^{JS\Pi n'l_1'l_2'} \end{aligned} \tag{3.95}$$

We may define a new T-matrix, labeled $\mathbf{T}^{S\Pi}$ (without a J), which is still square, but has extra rows and columns spanned by the indices $l_2 m_2$ and $l_2' m_2'$ respectively, as

$$T^{S\Pi\, n' l_1' m_1' l_2' m_2'}_{\quad n l_1 m_1 l_2 m_2} = \delta^0_{m_2'} \sum_{JM} C(l_1' l_2' J; m_1' 0 M) C(l_1 l_2 J; m_1 m_2 M) T^{J S\Pi\, n' l_1' l_2'}_{\quad n l_1 l_2} \tag{3.96}$$

The sum over M may be performed, and the simplified form is

$$T^{S\Pi\, n' l_1' m_1' l_2' m_2'}_{\quad n l_1 m_1 l_2 m_2} = \delta^0_{m_2'} \sum_{J} C(l_1' l_2' J; m_1' 0 m_1') C(l_1 l_2 J; m_1 m_2 m_1') T^{J S\Pi\, n' l_1' l_2'}_{\quad n l_1 l_2} \tag{3.97}$$

where the Clebsch-Gordan coefficients imply that $m_2 = m_1' - m_1$ or else the corresponding $\mathbf{T}^{S\Pi}$ matrix element is zero. We obtain for the scattering amplitude the following:

$$\begin{aligned} f^{S n' l_1' m_1'}_{n l_1 m_1} = \sum_{\Pi l_2 l_2'} \left(\frac{v_{n'}}{v_n}\right)^{\frac{1}{2}} \left(\frac{i^{1+l_2'-l_2}}{k_{n'}}\right) e^{i(m_1'-m_1)\varphi} \sqrt{\frac{2l_2'+1}{2}}\, P_{l_2}^{m_1'-m_1}(\theta) \\ \sum_J T^{J S\Pi\, n' l_1' l_2'}_{\quad n l_1 l_2} C(l_1' l_2' J; m_1' 0 m_1') C(l_1 l_2 J; m_1\ m_1'-m_1\ m_1') \end{aligned} \tag{3.98}$$

where the P_j^m were defined in Eq. 2.68.[10]

The differential cross section σ^S (with the Pauli principle already having been satisfied in Eq. 3.74) is found from the scattering amplitude, and is independent of the angle φ:

$$\begin{aligned} \sigma^{S n' l_1' m_1'}_{n l_1 m_1} &= \frac{v_n}{v_{n'}} \left| f^{S n' l_1' m_1'}_{n l_1 m_1}(\hat{\mathbf{R}}) \right|^2 \\ &= \frac{1}{2k_{n'}^2} \left| \sum_{\Pi l_2 l_2'} i^{l_2'-l_2} P_{l_2}^{m_1'-m_1}(\theta)(2l_2'+1)^{\frac{1}{2}} T^{S\Pi\, n' l_1' m_1' l_2' 0}_{\quad n l_1 m_1 l_2 m_2} \right|^2 \end{aligned} \tag{3.99}$$

Examining the properties of the renormalized associated Legendre functions P_j^m at $\theta = 0$ and $\theta = \pi$ leads to interesting results for forward and backwards scattering. These functions are zero for $\theta = 0, \pi$ except if $m = 0$, which leads to the selection rule $m_1' = m_1$ for non-zero scattering in those directions.

To obtain the integral cross section we integrate over $d\widehat{\mathbf{R}}$:

$$
\begin{aligned}
Q^{Sn'l_1'm_1'}_{nl_1m_1} &= \int \sigma^{Sn'l_1'm_1'}_{nl_1m_1}(\widehat{\mathbf{R}})d\widehat{\mathbf{R}} \;=\; \frac{v_n}{v_{n'}} \sum_{\Pi l_2 m_2} \left| b^{Sn'l_1'm_1'}_{\Pi nl_1m_1l_2m_2} \right|^2 \\
&= \frac{\pi}{k^2_{n'}} \sum_{\Pi l_2' l_2''} \sqrt{(2l_2'+1)(2l_2''+1)}\; i^{l_2'-l_2''} \\
&\quad \times \sum_{l_2 m_2} T^{S\Pi\, n'l_1'm_1'l_2'0}_{\quad\; nl_1m_1l_2m_2} T^{S\Pi\, n'l_1'm_1'l_2''0\;\,*}_{\quad\; nl_1m_1l_2m_2}
\end{aligned}
\tag{3.100}
$$

where the integration over θ was performed explicitly using the orthogonality relation obeyed by the P^m_j. The sums over l_2' and l_2'' lead to the mixing of states of different parity. The integral cross section can also be written

$$
\begin{aligned}
Q^{Sn'l_1'm_1'}_{nl_1m_1} &= \frac{\pi}{k^2_{n'}} \sum_{\Pi l_2' l_2''} \sqrt{(2l_2'+1)(2l_2''+1)}\, i^{l_2'-l_2''} \\
&\quad \times \left[\left(\mathbf{T}^{S\Pi\, n'l_1'm_1'}_{\quad\; nl_1m_1} \right)^{\dagger} \left(\mathbf{T}^{S\Pi\, n'l_1'm_1'}_{\quad\; nl_1m_1} \right) \right]^{l_2'0}_{l_2''0}
\end{aligned}
\tag{3.101}
$$

where we have indicated in square brackets the multiplication of a sub-block of the T-matrix with its adjoint. Now we sum over final projection quantum numbers m_1 and average over initial states m_1'.

$$
Q^{Sn'l_1'}_{nl_1} = \frac{1}{(2l_1'+1)} \sum_{m_1} \sum_{m_1'} Q^{Sn'l_1'm_1'}_{nl_1m_1} \tag{3.102}
$$

The quantity $Q^{Sn'l_1'}_{nl_1}$ is called the summed and averaged cross section (with respect to the magnetic quantum numbers m_1 and m_1').

The total cross section can be expanded in partial wave contributions

$$
Q^{Sn'l_1'}_{\quad nl_1} = \sum_J Q^{SJn'l_1'}_{\quad\; nl_1} \tag{3.103}
$$

where the $Q^{SJn'l_1'}_{\quad\; nl_1}$ are the partial cross sections obtained as follows. If the total

state-to-state cross section expression is written out in full and rearranged, one obtains

$$\begin{aligned} Q_{nl_1}^{Sn'l_1'} =& \frac{1}{(2l_1'+1)} \sum_{m_1'} \sum_{l_2 l_2'} \sum_{\substack{JM \\ J'M'}} C(l_1' l_2' J; m_1' 0 M) T^{JS\Pi\, n'l_1'l_2'}_{\quad nl_1 l_2} \sqrt{(2l_2'+1)\pi} \\ & \times \sum_{l_2''} \sqrt{(2l_2''+1)\pi} \left(\frac{i^{l_2'-l_2''}}{k_{n'}^2} \right) C(l_1' l_2'' J'; m_1' 0 M') T^{J'S\Pi\, n'l_1'l_2''*}_{\quad nl_1 l_2} \\ & \times \sum_{m_1 m_2} C(l_1 l_2 J; m_1 m_2 M) C(l_1 l_2 J'; m_1 m_2 M') \end{aligned} \tag{3.104}$$

Using the completeness of the Clebsch-Gordan coefficients, we can perform the sum over m_1, m_2 which gives a $\delta_{JM}^{J'M'}$, which leaves the following:

$$\begin{aligned} Q_{nl_1}^{Sn'l_1'} =& \frac{1}{(2l_1'+1)} \left(\frac{\pi}{k_{n'}^2} \right) \sum_{m_1'} \sum_{l_2} \sum_{l_2' l_2''} \sum_{JM} \sqrt{(2l_2'+1)(2l_2''+1)}\, i^{l_2'-l_2''} \\ & \times C(l_1' l_2' J; m_1' 0 M)\, T^{JS\Pi\, n'l_1'l_2'}_{\quad nl_1 l_2}\, C(l_1' l_2'' J; m_1' 0 M)\, T^{JS\Pi\, n'l_1'l_2''*}_{\quad nl_1 l_2} \end{aligned} \tag{3.105}$$

The sum over m_1' can be performed because the Clebsch-Gordan coefficients are zero unless $m_1' = M$. Then there is another Clebsch-Gordan simplification due to the relation

$$\sum_M C(l_1' l_2' J; M 0 M)\, C(l_1' l_2'' J; M 0 M) = \delta_{l_2''}^{l_2'} \frac{(2J+1)}{\sqrt{(2l_2'+1)(2l_2''+1)}} \tag{3.106}$$

Using this relation, we are left with a simple expression for the integral cross section for scattering from state $(n'l_1')$ to state (nl_1):

$$Q_{nl_1}^{Sn'l_1'} = \frac{\pi}{k_{n'}^2} \sum_J (2J+1) P^{JS\, n'l_1'}_{\quad nl_1} \tag{3.107}$$

where we have defined the opacity $P^{JS\, n'l_1'}_{\quad nl_1}$ by the following:

$$P^{JS\, n'l_1'}_{\quad nl_1} = \frac{1}{(2l_1'+1)} \sum_{\Pi l_2 l_2'} \left| T^{JS\Pi\, n'l_1'l_2'}_{\quad nl_1 l_2} \right|^2 \tag{3.108}$$

The above expression leads us to define the partial wave contribution as follows:

$$Q_{nl_1}^{JSn'l_1'} = \frac{(2J+1)\pi}{k_{n'}^2} P_{nl_1}^{JSn'l_1'} \tag{3.109}$$

From this we can also define a cross section[11] that is directly related to the scattering matrix obtained in the space-fixed representation $\{Jnl_1l_2\}$:

$$Q_{nl_1l_2}^{JS\Pi n'l_1'l_2'} \equiv \frac{(2J+1)\pi}{(2l_1'+1)k_{n'}^2} |T_{nl_1l_2}^{JS\Pi n'l_1'l_2'}|^2 \tag{3.110}$$

in terms of which

$$Q_{nl_1}^{Sn'l_1'} = \sum_{J\Pi l_2 l_2'} Q_{nl_1l_2}^{JS\Pi n'l_1'l_2'} \tag{3.111}$$

The spin weighting has not been included in the above derivation. To do so one just averages the $S = 0, 1$ contributions with weights $(2S+1)/4$ in any of the expressions (3.99), (3.101), (3.102), (3.103), (3.104), and (3.109) through (3.111).

$$Q = \frac{1}{4}Q^{S=0} + \frac{3}{4}Q^{S=1} \tag{3.112}$$

3.5 Distinguishable-electron Scattering Amplitudes

The cross sections we have obtained above have antisymmetrization built right in. Now we will obtain expressions for the scattering amplitudes for when we can distinguish between the electrons,[12] for example when a polarized beam of electrons with spin α are scattered off polarized H-atoms. This procedure is analogous to that used by Schatz for $H + H_2$,[13] but simpler because there are only two identical particles.

Let us then consider the spin wavefunctions of the separated electron plus hydrogen atom system in arrangement channel 1. There are four such wavefunctions

$$\begin{aligned} v_1(1,2) &= \alpha(1)\alpha(2) \\ v_2(1,2) &= \beta(1)\alpha(2) \\ v_3(1,2) &= \alpha(1)\beta(2) \\ v_4(1,2) &= \beta(1)\beta(2) \end{aligned} \tag{3.113}$$

They are orthonormal eigenfunctions of S_z but v_2 and v_3 are not eigenfunctions of S^2; however they are related by the symmetry property

$$v_2(1,2) = v_3(2,1) \tag{3.114}$$

Let $\Psi_{\text{phy}}^{\lambda n' l_1' m_1'}$ be a "physical" solution to the Schrödinger equation, which behaves asymptotically at large R_λ and R_ν as

$$\begin{aligned}\Psi_{\text{phy}}^{\lambda n' l_1' m_1'} &\underset{R_\lambda \to \infty}{\sim} e^{ik_{n'}^{\lambda} z_\lambda} \phi_{n' l_1' m_1'}(\mathbf{r}_\lambda) \\ &\quad + \sum_{n l_1 m_1} \frac{e^{ik_n^\lambda R_\lambda}}{R_\lambda} f_{\lambda n l_1 m_1}^{\lambda n' l_1' m_1'}(\theta_{R_\lambda}, \varphi_{R_\lambda}) \phi_{n l_1 m_1}(\mathbf{r}_\lambda) \\ &\underset{R_\nu \to \infty}{\sim} \sum_{n l_1 m_1} \frac{e^{ik_n^\nu R_\nu}}{R_\nu} f_{\nu n l_1 m_1}^{\lambda n' l_1' m_1'}(\theta_{R_\nu}, \varphi_{R_\nu}) \phi_{n l_1 m_1}(\mathbf{r}_\nu)\end{aligned} \tag{3.115}$$

Rewriting this expression with the choice $\lambda = 1$, such that $R_\lambda = r_\nu = R$, and likewise $r_\lambda = R_\nu = r$, we have

$$\begin{aligned}\Psi_{\text{phy}}^{1 n' l_1' m_1'}(1,2) &\underset{R \to \infty}{\sim} e^{ik_{n'} z} \phi_{n' l_1' m_1'}(\mathbf{r}) \\ &\quad + \sum_{n l_1 m_1} \frac{e^{i(k_n R)}}{R} f_{1 n l_1 m_1}^{1 n' l_1' m_1'}(\theta_R, \varphi_R) \phi_{n l_1 m_1}(\mathbf{r}) \\ &\underset{r \to \infty}{\sim} \sum_{n l_1 m_1} \frac{e^{ik_n r}}{r} f_{2 n l_1 m_1}^{1 n' l_1' m_1'}(\theta_r, \varphi_r) \phi_{n l_1 m_1}(\mathbf{R})\end{aligned} \tag{3.116}$$

We now form the completely antisymmetric wavefunction, including spin, noting that $\Psi^2(1,2) = \Psi^1(2,1)$:

$$\Psi^{A n' l_1' m_1'(i)} = \Psi_{\text{phy}}^{1 n' l_1' m_1'}(1,2) v_i(1,2) - \Psi_{\text{phy}}^{1 n' l_1' m_1'}(2,1) v_i(2,1) \tag{3.117}$$

The asymptotic behavior of this wavefunction is

$$\begin{aligned}\Psi^{A n' l_1' m_1'(i)} &\underset{R \to \infty}{\sim} e^{ik_{n'} z} \phi_{n' l_1' m_1'}(\mathbf{r}) v_i(1,2) \\ &\quad + \sum_{n l_1 m_1} \frac{e^{i(k_n R)}}{R} \phi_{n l_1 m_1}(\mathbf{r}) \left[f_{1 n l_1 m_1}^{1 n' l_1' m_1'} v_i(1,2) - f_{1 n l_1 m_1}^{2 n' l_1' m_1'} v_i(2,1) \right]\end{aligned} \tag{3.118}$$

This has the form of a physical scattering solution. Now we re-express it in terms of the $v_i(1,2)$ spin functions of the separated electron-atom ($i = 1,4$). Thus we have

$$f^{1n'l_1'm_1'}_{1nl_1m_1} v_i(1,2) - f^{2n'l_1'm_1'}_{1nl_1m_1} v_i(2,1) = \sum_{k=1}^{4} f^{(k)n'l_1'm_1'}_{(i)nl_1m_1} v_k(1,2) \tag{3.119}$$

where $f^{(k)n'l_1'm_1'}_{(i)nl_1m_1}$ is the antisymmetrized scattering amplitude for scattering from initial state $(i)nl_1m_1$ to final state $(k)n'l_1'm_1'$. We can solve for $f^{(k)n'l_1'm_1'}_{(i)nl_1m_1}$ by inspection, or by using the completeness of the orthonormal set of functions. The resulting expressions for the scattering amplitudes are found in Table 3–1. The state-to-state differential cross sections are

$$\sigma^{(k)n'l_1'm_1'}_{(i)nl_1m_1} = \frac{1}{k_{n'}} \left| f^{(k)n'l_1'm_1'}_{(i)nl_1m_1} \right|^2 \tag{3.120}$$

There are six non-vanishing space-spin cross sections:

$$\begin{aligned}
\sigma^{(\alpha\alpha)n'l_1'm_1'}_{(\alpha\alpha)nl_1m_1} &= \sigma^{(\beta\beta)n'l_1'm_1'}_{(\beta\beta)nl_1m_1} = \frac{1}{k_{n'}} \left| f^{1n'l_1'm_1'}_{1nl_1m_1} - f^{2n'l_1'm_1'}_{1nl_1m_1} \right|^2 \\
\sigma^{(\alpha\beta)n'l_1'm_1'}_{(\alpha\beta)nl_1m_1} &= \sigma^{(\beta\alpha)n'l_1'm_1'}_{(\beta\alpha)nl_1m_1} = \frac{1}{k_{n'}} \left| f^{1n'l_1'm_1'}_{1nl_1m_1} \right|^2 \\
\sigma^{(\alpha\beta)n'l_1'm_1'}_{(\beta\alpha)nl_1m_1} &= \sigma^{(\beta\alpha)n'l_1'm_1'}_{(\alpha\beta)nl_1m_1} = \frac{1}{k_{n'}} \left| -f^{2n'l_1'm_1'}_{1nl_1m_1} \right|^2
\end{aligned} \tag{3.121}$$

If we sum over the final spin states, we can find the cross section for each initial spin state.

$$\begin{aligned}
\sigma^{(\alpha\alpha)n'l_1'm_1'}_{nl_1m_1} &= \sigma^{(\beta\beta)n'l_1'm_1'}_{nl_1m_1} = \frac{1}{k_{n'}} \left| f^{1n'l_1'm_1'}_{1nl_1m_1} - f^{2n'l_1'm_1'}_{1nl_1m_1} \right|^2 \\
\sigma^{(\alpha\beta)n'l_1'm_1'}_{nl_1m_1} &= \sigma^{(\beta\alpha)n'l_1'm_1'}_{nl_1m_1} = \frac{1}{k_{n'}} \left(\left| f^{1n'l_1'm_1'}_{1nl_1m_1} \right|^2 + \left| f^{2n'l_1'm_1'}_{1nl_1m_1} \right|^2 \right)
\end{aligned} \tag{3.122}$$

Averaging over initial spin states one obtains

$$\begin{aligned}
\sigma^{n'l_1'm_1'}_{nl_1m_1} &= \frac{1}{k_n} \left[\tfrac{1}{2} \left| f^{1n'l_1'm_1'}_{1nl_1m_1} - f^{2n'l_1'm_1'}_{1nl_1m_1} \right|^2 + \tfrac{1}{2} \left| f^{1n'l_1'm_1'}_{1nl_1m_1} \right|^2 + \tfrac{1}{2} \left| f^{2n'l_1'm_1'}_{1nl_1m_1} \right|^2 \right] \\
&= \frac{1}{k_n} \left[\tfrac{1}{4} \left| f^{1n'l_1'm_1'}_{1nl_1m_1} + f^{2n'l_1'm_1'}_{1nl_1m_1} \right|^2 + \tfrac{3}{4} \left| f^{1n'l_1'm_1'}_{1nl_1m_1} - f^{2n'l_1'm_1'}_{1nl_1m_1} \right|^2 \right]
\end{aligned} \tag{3.123}$$

From Eq. 3.74 this can be rewritten as

$$\sigma_{nl_1m_1}^{n'l_1'm_1'} = \frac{1}{k_n}\left[\tfrac{1}{4}\left|f_{nl_1m_1}^{S=0,n'l_1'm_1'}\right|^2 + \tfrac{3}{4}\left|f_{nl_1m_1}^{S=1,n'l_1'm_1'}\right|^2\right] \tag{3.124}$$

From the above equation we express $\sigma_{nl_1m_1}^{n'l_1'm_1'}$ in terms of the singlet and triplet differential cross section as

$$\sigma_{nl_1m_1}^{n'l_1'm_1'} = \frac{1}{4}\sigma_{nl_1m_1}^{S=0,n'l_1'm_1'} + \frac{3}{4}\sigma_{nl_1m_1}^{S=1,n'l_1'm_1'}. \tag{3.125}$$

Table 3-1: Antisymmetrized scattering amplitudes $f_{(i)nl_1m_1}^{(k)n'l_1'm_1'}$ and their relation to the distinguishable particle amplitudes $f_{1nl_1m_1}^{1n'l_1'm_1'}$ and $f_{1nl_1m_1}^{2n'l_1'm_1'}$.[a]

$i\backslash k$	$\alpha\alpha$	$\beta\alpha$	$\alpha\beta$	$\beta\beta$
$\alpha\alpha$	$f_1^1 - f_2^1$	0	0	0
$\beta\alpha$	0	f_1^1	$-f_2^1$	0
$\alpha\beta$	0	$-f_2^1$	f_1^1	0
$\beta\beta$	0	0	0	$f_1^1 - f_2^1$

[a] The indices nl_1m_1 and $n'l_1'm_1'$ are omitted.

3.6 References

1. J. M. Blatt and L. C. Biedenharn, *Rev. Mod. Phys.*, **24**, 258 (1952); R. Huby, *Proc. Phys. Soc.*, **A67**, 1103 (1954).
2. Handbook of Mathematical Functions, edited by M. Abramowitz and I. A. Stegun (National Bureau of Standards, Washington, D. C., 1964).
3. $k_n(x) = (\pi/2x)^{1/2} K_{n+1/2}(x)$, where K_m is the modified cylindrical Bessel function of the third kind.[2].
4. N. S. F. Mott and H. S. W. Massey, The Theory of Atomic Collisions (Clarendon, Oxford, 1965), 3rd ed., Ch. 14, 15.
5. A. M. Lane and R. G. Thomas, *Rev. Mod. Phys.*, **30**, 257 (1958).
6. G. Fox and S. Otto, *Physics Today*, 50, (May 1984).
7. B. Christensen-Dalsgaard, *Phys. Rev. A*, **29**, 2242 (1984).
8. B. R. Johnson, *J. Comp. Phys.*, **13**, 445 (1973).
9. A. Kuppermann, in *Proceedings of the Summer School on Chemical Photophysics*, "Dynamique Réactionelle des Etas Excités", Les Houches, France, 18-30 June 1979, eds. P. Glorieux, D. Lecher and R. Vetter (Centre de la Recherche Scientifique, Paris, 1979) pp. 293-384.
10. G. C. Schatz and A. Kuppermann, *J. Chem. Phys.*, **65**, 4642 (1976).
11. I. C. Percival and M. J. Seaton, *Proc. Cambridge Phil. Soc.*, **53**, 654 (1957).
12. L. I. Schiff, Quantum Mechanics (McGraw-Hill, New York, 1968), 3rd ed., pp. 384-395.
13. A. Kuppermann, G. C. Schatz, and M. Baer, *J. Chem. Phys.*, **65**, 4596 (1976).

CHAPTER 4

CONVERGENCE STUDIES

Although the method we have described in Chapters 2 and 3 contains no outright approximations, the calculation still depends on many computational parameters which must be carefully chosen to achieve convergence. In this chapter we describe how we tested the computation with regards to several of these parameters.

4.1 Step Sizes in the Johnson Integrator

The Johnson integrator[1] has no error estimation, and therefore has no criteria for choosing the next integration step size, two features the Gordon integrator does have.[2] Johnson's method also differs from Gordon's in that it is a "function-following," as opposed to "potential-following"[3] routine. In classically "allowed" regions the potential is a much more slowly varying function of the independent variable than the wavefunction is. Because of this, one might expect that the step sizes needed to achieve the same relative accuracy in such regions would have to be smaller in the Johnson integrator. Nevertheless, we used it because it is both faster and simpler than the Gordon method.

We needed to specify the step sizes for the hyperradius ρ as input parameters. Increasingly larger step sizes were used as the integration progressed. Experience

gained from using the Gordon integrator on this problem was used as a guide for choosing the step sizes. We tested for convergence by making calculations with more closely spaced points. For example, we tested the $^1F^{odd}$ and $^3F^{odd}$ states at the energies 0.76 Ryd and 0.90 Ryd, projecting at 30 bohr, and found five decimal digit agreement in the scattering matrices obtained using the set of step sizes given in Table 4–1, and using steps of 0.05 bohr uniform length. We therefore decided upon the step sizes given in Table 4–1 for energies up to 0.96 Ryd (the threshold for $n = 5$ H atom states).

These steps are only slightly smaller than those that would have been used by the Gordon integrator. The Johnson integrator is a fourth order method which uses a two-step algorithm; the potential is evaluated at the half-way point and at the end of each step. This amount of numerical work per step in the Johnson integrator is significantly less than that in the Gordon, which accounts for the larger efficiency of the former.

4.2 Initial Value of ρ

The solution to the coupled differential equation in ρ is found by choosing a value of the wave function and its derivative at the origin and propagating outward from the origin. The $\mathbf{b}^{JS\Pi}(\rho;\bar{\rho})$ matrix (Eq. 2.28) must vanish at the origin to keep the wavefunction from diverging. We choose $\frac{d}{d\rho}\mathbf{b}^{JS\Pi}(0) = \mathbf{I}$ because the scattering matrix is unique and independent of the choice of initial derivative matrix. Since we cannot actually compute the potential matrix defined by Eq. 2.87 at $\rho = 0$, we must choose an initial value of ρ, $\rho_0 > 0$. The choice of ρ_0 should be close enough to zero for the initial conditions to remain essentially valid. Numerically, this means that the scattering calculation should be independent of slight variations in the choice of ρ_0, provided ρ_0 is small enough.

The results of the first of our tests for convergence with respect to ρ_0 have been listed in Table 4–2. Here we have compared the integral cross sections (Eq. 3.108) and phase associated with the $S^{JS\Pi}{}^{n'l_1'l_2'}_{nl_1l_2}$ matrix element for $J = 0$, $S = 0$, $\Pi = 0$, $l_2 = l_1$, and $l_2' = l_1'$ for total energies 0.76 and 0.78 Ryd (with respect to the ground state of H). From this it was determined that ρ_0=0.1 a_0 was acceptably close to zero. (Convergence with respect to the other computational parameters may not have been yet achieved in these calculations. We assume that convergence with respect to the initial value of ρ is independent of these other parameters. For this reason the cross sections and phases reported in this section should not be assumed to be accurate, and may not agree exactly with our accurate cross sections reported in Chapter 6.) The projection was done at $R_p = 30$ bohr, with 6 surface functions and 15 primitives. In Table 4–3 we list the same quantities for a total energy of 0.76 Ryd and 0.90 Ryd, with the calculation using the "constant-ρ" projection method. The similarity of the results at 0.76 Ryd using these two different projection methods suggests that convergence with respect to computational parameters other than ρ_0 has also been achieved.[4]

The ^{3}S state cross sections (at the energies tested) were not sensitive to the value of ρ_0. This is most likely because of the strong repulsive nature of the potential term ($\mathbf{e}^{JS\Pi} + \frac{15\hbar^2}{8\mu\rho^2}\mathbf{I}$ in Eq. 2.87) in the triplet state, as will be seen in Chapter 5.

For higher angular momentum states, there is a large centrifugal repulsion that makes the small ρ region hard to penetrate. One expects that for higher J the minimum values of ρ and $\bar{\rho}$ will be larger than those for S-states. This indeed is the case. We did subsequent convergence tests on $J = 2$ even parity and $J = 3$ odd parity states and found that at 0.76 and 0.90 Ryd ρ_0 could be increased from 0.1 bohr to 0.5 bohr without any significant change in the final scattering matrices. Similarly the first set of surface functions may be calculated at 2.5 bohr instead of at 0.1 bohr for $J \geq 2$.

4.3 Convergence with respect to projection parameters

Both projection methods, at constant R and at constant ρ, are exact for an infinite surface function basis set. We must, however, use a truncated basis, which will introduce some error. If the calculation is converged with respect to the number of surface basis functions required, the two methods should give the same results.

4.3.1 Projection at Constant R

In the constant-R projection, the projection variable is r and the projection integral is computed using the trapezoidal rule over the region from 0 to r_{max}. This trapezoidal rule is consistent with the fact that the primitive basis functions of Eq. 2.34 were obtained using a first order finite difference method. It is possible to truncate the integral at r_{max} because the H-atom radial functions decay exponentially with r. At constant R, ω becomes a function of r, the value of ω_{max} corresponding to r_{max} decreases as R_p increases, and the primitives approach zero at ω_{max}.

The integrals must be converged with respect to r_{max} and to the r-integration step size Δr, which is determined by the number of steps into which the r-integration region is divided. Convergence with respect to these parameters must be tested.

One can estimate r_{max} by considering the average radius of the hydrogen atom in its various bound states. After the value of r_{max} is chosen, the value of each asymptotic hydrogen atom function at r_{max} is compared with its peak value and a warning is issued by the computer code if the function has not declined to 1% of peak. We used a value of $r_{max} = 50$ bohr for the calculations done for energies below the $n = 3$ threshold, with a value of R_p for the projection of 50 bohr. Reducing r_{max} to 40 bohr made no significant difference when surface functions through $n = 3$ were included.

We also used 70 points equally spaced in r along the projection cut, which makes step size Δr approximately equal to 0.7 bohr. For these choices of $r_{\max}$ and Δr the **R**-matrix is converged to about five decimal digits.

4.3.2 Projection at constant ρ

For the constant ρ projection method the projection variable is ω and the projection points are the same values of ω_i at which the 1-dimensional surface functions are calculated. That one doesn't need a different set of "projection points" is one of the advantages of this method.

Careful consideration must be given to the range of ω over which the integrals in Eq. 3.46 should be performed. First, the points $r(\omega;\rho_{\text{proj}})$, which appear in the hydrogen atom functions, do not extend out to infinity, because ω reaches a maximum. These H-atom functions still are peaked near $\omega = 0$. However the Riccati-Bessel functions appearing in the integrals Eq. 3.66 have an exponential dependence on $R(\omega;\rho_{\text{proj}})$, requiring the use of large values of ω. As mentioned in Chapter 3, it is very important that one compute the projection integral only up to $\omega = \frac{\pi}{2}$. The reason one must limit the integration to the $0 \leq \omega \leq \frac{\pi}{2}$ range is that one is projecting on asymptotic functions in one arrangement channel only. It is interesting to note that if we were by mistake to extend this integration range to $0 \leq \omega \leq \pi$, there are terms in the integrand of Eq. 3.46 that increase exponentially with $R(\omega;\rho)$, making the integrals unphysically large.

Upon implementation of the code, we found that it was not possible to truncate the integrals before $\omega = \frac{\pi}{2}$ because of the opposing ω dependence of the various factors in the integrand.

4.3.3 Comparison of Projection Methods

In Figure 4.1 we compare the ^{1}S contribution to the $1s \rightarrow 2s$ cross section calculated with the two different projection methods, constant R and constant ρ.

Using 15 primitives and six surface functions we projected at 40 bohr. As is evident from the figure, the two methods give very close results. The two projection methods are therefore indeed equivalent. In most of the calculations presented in this research we used the constant ρ method because, as pointed out in Section 3.2.3, it is the most convenient one to use in conjuction with the logarithmic derivative method and the Concurrent Processor being developed at Caltech.[5]

4.4 Frequency of Evaluation of Surface Functions

The scattering results (e.g., scattering matrices, cross sections) are very sensitive to the basis set used, and to the frequency of change of surface functions. One would expect that an increase of that frequency would increase the accuracy of a calculation of this sort. However it is also possible that an excessive frequency of changing surface functions could worsen the accuracy because of the numerical errors inherent in their calculation.

As one would expect, it is necessary to have surface functions closer together at small values of $\bar{\rho}$ where they change rapidly with this variable. At larger values of $\bar{\rho}$, one can use the same surface functions over larger ranges of ρ.

In an exact calculation, the overlap matrix $\mathbf{O}^{JS\Pi}$ between surface functions at different $\bar{\rho}$ is real and of infinite order and is orthogonal. In practice, of course, that matrix is truncated to finite order. The difference from orthogonality, measured by the matrix gives a first indication of $\mathbf{I} - \tilde{\mathbf{O}}^{JS\Pi}\mathbf{O}^{JS\Pi}$, how converged the scattering calculation for a given surface function basis set is. If the elements of this matrix are close to zero, at least for the lower channels, there is little flux being lost due to lack of completeness of the basis.

We have chosen the values of $\bar{\rho}$ at which to calculate surface functions such that the overlap matrix between neighboring $\bar{\rho}$ is close to a *unit* matrix, with most diagonal elements greater than 0.9995, most off-diagonal elements less than 0.001

and the largest off-diagonal elements of each row or column usually of order 0.01. The exception is in the area of an avoided crossing between two $\varepsilon_i^{JS\Pi}(\bar{\rho})$ vs. $\bar{\rho}$ curves (see Eq. 2.61), where the two states that mix have smaller diagonal elements, and the off-diagonal element between the two is relatively large. One must be careful to truncate the surface function set properly, so as not to have avoided crossings between included and excluded states, at least not when a crossing state is expected to be important. If such a crossing happened, it would lead to a very small diagonal element of the overlap matrix, but the compensating off-diagonal element would have been excluded, thus leading to loss of flux. For our choice of the $\bar{\rho}$, the elements of $\mathbf{I} - \tilde{\mathbf{O}}^{JS\Pi}\mathbf{O}^{JS\Pi}$ for successive $\bar{\rho}$ are usually of the order of 10^{-4} or smaller, and the scattering calculations were converged as described below.

The ranges we found to be adequate were

ρ(bohr)	$\Delta\bar{\rho}$(bohr)
0.1 – 5.0	0.1
5.0 – 20.	0.2
20. – 40.	0.5
40. – 60.	1.0
60. – 100.	2.0
over 100.	5.0

For these ranges it was found that the scattering matrix for $J = 0$ was converged to about ± 0.003, the ^{1}S elastic cross section $Q(1s \rightarrow 1s)$ was converged to 0.3%, and all other ^{1}S and ^{3}S cross sections were converged to better than 0.1%, in the test calculations done at energies below the $n = 3$ threshold.

As was mentioned in Section 4.2, the small ρ region for larger J is strongly forbidden. We are able to use the first set of surface functions at $\bar{\rho} = 0.5$ bohr without any noticeable change in the scattering matrices over using 0.1 bohr instead for $J > 1$, and moving all the way to $\bar{\rho} = 2.0$ bohr only made slight changes (about the fifth decimal place of the scattering matrix elements).

4.5 Projection Distance

After we have propagated the hyperradial part of the wavefunction out to a suitable distance, we project from the hyperspherical surface functions onto the hydrogen atom functions. This section discusses how one determines that distance. If one projects too soon, one expects convergence problems, because it is only in the asymptotic region that the hyperspherical surface functions become similar to the bound states. In principle once the asymptotic region is reached the results should be independent of the projection distance. However in practice we discovered divergent results if the projection is done at too large a distance, and that the correct distance is energy dependent. The full nature of this problem is not understood.

The projection distances used in our calculations were determined by comparing the results obtained from different projection distances. Often we had much less trouble converging inelastic partial cross sections than the elastic ones, which implies that it is the phase of the scattering matrix which is more sensitive to projection distance, since the former cross sections are phase-independent whereas the latter are not.

The low energy phaseshifts of the ^{1}S partial wave were tested for convergence with respect to both projection distance and number of surface functions and were found to be very sensitive. The very low energy ($k^2 = 0.01$, 0.04 Ryd) phaseshifts obtained by projecting anywhere between 6 bohr and 10 bohr agreed to about 0.01 rad, and also gave good agreement with the Schwartz calculation.[6] However extending the projection distance to 15 or 20 bohr or beyond produced a sharp rise in the phase shift.

In Figure 4.2 we give an example of how the phaseshift depends on the projection distance. The figure contains data from the ^{1}S lowest energy range, where there is only one open channel. The calculations were performed using 15

primitive basis functions and three surface functions. Figure 4.2 shows the phase vs. energy for projection distances 8, 10, 12, 15, and 20 bohr, as well as the benchmark values obtained by Schwartz.[6] The agreement over most of the energy with Schwartz is quite good.

It is evident from Figure 4.2 that the position of the resonance is shifted to lower energy as the projection distance is increased. Since the position of the lowest ^{1}S resonance has been calculated fairly accurately, we can use this value as a test for the present calculations. The resonance energy is taken as the energy for which the corresponding collision lifetime eigenvalue has a maximum (see Chapter 6) which, for the present single open channel case, is the same as the energy for which the partial phase shift versus energy curve has an inflection point.

Figure 4.3 shows, for $k = 0.1$ through 0.8 bohr^{-1}, how the phase varies with projection distance and number of surface functions, and how our calculations compare with Schwartz's, which are given at the left axis. The agreement at 8 bohr with 3 surface functions (the triangles in the figure) is good. At the lowest energy the results of the $\rho_{\text{proj}} = 20$ bohr calculation differ from Schwartz's by 0.45 rad, or 25 deg. At the highest energy tabulated by Schwartz, our calculations all agree to 0.02 rad. Looking at the $k = 0.1$ bohr^{-1} points, one sees that there is basis set convergence at $\rho = 8$ bohr. As ρ is increased, the phaseshift undergoes periods of rapid increase and then stability, repeatedly. Although not included in the figure, we have found that this happens all the way out to projecting at 100 bohr. The effect of adding surface functions is to usually decrease the phase. The phases at higher energies ($k = 0.4 - 0.8$ bohr^{-1}) are much more converged with respect to projection distance. The 1-surface function values for the phase at $k = 0.7$ and 0.8 bohr^{-1} have been omitted from the figure because they are 10 to 20 degrees too low. This shows that coupling to closed channels becomes important even at energies as low as 0.49 Ryd (6.8 eV).

Above 0.65 Ryd closed channels become important, and the inclusion of higher states must usually be accompanied by projecting at a larger distance. We found, for instance, that the position of the first ^{1}S resonance is converged using basis 3/5 and projecting at 30 bohr. The differences due to basis set are larger than those due to projection distance for this resonance. The second ^{1}S resonance is much closer to threshold and requires projection at a distance larger than 30 bohr to even be seen. The position of this resonance converges within 0.0005 Ryd. We have also calculated the position of the ^{3}S resonance, which is ten times narrower than the second ^{1}S resonance. The convergence of these low energy resonances with basis size and projection distance is discussed in further detail in Section 6.2.

At energies above the inelastic threshold, one uses the unitarity of the scattering matrix as a test of convergence. (At energies lower than this the scattering matrix always has modulus one.) We decided that if a calculation at a particular projection distance had poor unitarity of the S-matrix (worse than 1.15, say) then that distance was too close and a larger projection distance should be tried. If the unitarity improves, this is taken as an indication that the new projection distance is more appropriate. The distances we finally chose are 20 bohr for energies up to $k^2 = 0.65$ Ryd, 40 bohr for energies larger than this but less than the $n = 2$ threshold, 60 bohr for energies between the $n = 2$ and $n = 3$ thresholds, 80 bohr for energies between $n = 3$ and $n = 4$, and 110 bohr for energies above $n = 4$.

According to Callaway,[7] the region just above threshold is a difficult one for calculations, because one must go to rather largevalues of ρ before the channel wave functions assume simple asymptotic forms. Our experience was much the same — the region just above threshold was very sensitive to the projection distance, whereas the resonance region slightly below the opening of a new channel was converged in this respect, in most instances. In our calculations, the same projection distance is used throughout an energy region (from threshold to threshold). It remains to be

seen what would happen if instead one projected farther out for energies just above threshold than for higher energies. Perhaps doing this would have an effect on the many "shape" resonances we have detected (see Chapter 6).

In Figure 4.4 the phase and squared modulus of the $1s - 2s$ element of the ^1S scattering matrix at projection distances of 50 and 60 bohr are plotted for energies between the $n = 2$ and $n = 3$ thresholds. We used 10 surface functions and 15 primitives to obtain these points. The agreement is to about 0.07 rad for the phase and to within plotting accuracy for the square of the modulus, except at 0.78 Ryd, which is close to the $n = 2$ threshold and the agreement is to about 0.01.

4.6 Number of Surface Functions

The convergence of the scattering calculations with respect to the number of surface functions and of primitive basis functions is discussed in Section 5.4.

Table 4-1: Step sizes for Johnson integrator.

range of ρ (bohr)	step size (bohr)	number of steps
0.05–15.0	0.05	299
15.0–45.0	0.10	300
45.0–105.	0.20	300

Table 4-2: ^{1}S cross sections (in πa_0^2) and phases (in radians) for varying values of starting point ρ_0, projecting at $R_p = 30$ bohr.

ρ_0 (bohr)	0.20	0.15	0.10	0.05	0.01
			E = 0.76 Ryd		
Q^{1S} (1s→1s)	0.663	0.670	0.673	0.673	0.674
Q^{1S} (1s→2s)	0.0317	0.0317	0.0316	0.0317	0.0316
Q^{1S} (1s→2p)	0.0204	0.0204	0.0204	0.0204	0.0204
$\phi^{1S}(1s0 \rightarrow 1s0)$	1.664	1.674	1.679	1.680	1.681
$\phi^{1S}(1s0 \rightarrow 2s0)$	−0.771	−0.765	−0.764	−0.763	−0.763
$\phi^{1S}(1s0 \rightarrow 2p1)$	−2.584	−2.581	−2.576	−2.578	−2.575
			E = 0.78 Ryd		
Q^{1S} (1s→1s)	0.628	0.634	0.637	0.637	0.638
Q^{1S} (1s→2s)	0.0492	0.0492	0.0490	0.0491	0.0490
Q^{1S} (1s→2p)	0.0237	0.0237	0.0236	0.0236	0.0236
$\phi^{1S}(1s0 \rightarrow 1s0)$	1.683	1.693	1.698	1.699	1.700
$\phi^{1S}(1s0 \rightarrow 2s0)$	−1.827	−1.823	−1.821	−1.820	−1.820
$\phi^{1S}(1s0 \rightarrow 2p1)$	2.903	2.908	2.912	2.911	2.913

Table 4-3: ^{1}S cross sections (in πa_0^2) and phases (in radians) for varying values of starting point ρ_0, projecting at $\rho_{\rm proj}$ = 30 bohr.

ρ_0(bohr)	0.20	0.15	0.10	0.05
		E = 0.76 Ryd		
$Q^{^1S}$ (1s→1s)	0.661	0.667	0.670	0.671
$Q^{^1S}$ (1s→2s)	0.0325	0.0324	0.0324	0.0324
$Q^{^1S}$ (1s→2p)	0.0194	0.0194	0.0194	0.0194
$\phi^{^1S}(1s0 \rightarrow 1s0)$	1.662	1.672	1.677	1.678
$\phi^{^1S}(1s0 \rightarrow 2s0)$	−0.737	−0.732	−0.730	−0.729
$\phi^{^1S}(1s0 \rightarrow 2p1)$	−2.649	−2.644	−2.642	−2.641
		E = 0.90 Ryd		
$Q^{^1S}$ (1s→1s)	0.484	0.490	0.492	0.493
$Q^{^1S}$ (1s→2s)	0.0383	0.0383	0.0383	0.0383
$Q^{^1S}$ (1s→2p)	0.0196	0.0194	0.0194	0.0194
$\phi^{^1S}(1s0 \rightarrow 1s0)$	1.583	1.595	1.600	1.601
$\phi^{^1S}(1s0 \rightarrow 2s0)$	−3.001	−2.995	−2.992	−2.992
$\phi^{^1S}(1s0 \rightarrow 2p1)$	1.494	1.499	1.501	1.501

4.7 References

1. B. R. Johnson, *J. Comp. Phys.*, **13**, 445 (1973).
2. R. Gordon, *J. Chem. Phys.*, **51**, 14 (1969).
3. D. Secrest, *Proceedings of the NRCC Workshop on Algorithms and Computer Codes in Atomic and Molecular Quantum Scattering Theory* (Lawrence Berkeley Laboratory Report LBL-9501, 1979), Vol. I.
4. From the way our code has been written, it becomes very important that one change the number of steps taken by the Johnson integrator to make sure that the integration is stopped exactly at ρ_{proj}. Otherwise the results appear not to converge at all. On the other hand, when one projects at constant R, it does not matter, for our code, where the Johnson integration is stopped, so long as we do so before the beginning of the projection region.
5. G. Fox and S. Otto, *Physics Today*, 50, (May 1984).
6. C. Schwartz, *Phys. Rev.*, **124**, 1468 (1961).
7. J. Callaway, *Phys. Lett.*, **81A**, 495 (1981).

4.8 Figure Captions

FIG. 4.1: Comparison of projection methods. The dots are the values of the ^{1}S ($1s \rightarrow 2s$) cross section obtained projecting at $\rho = 40$ bohr. The crosses are the values obtained projecting at a constant value of $R = 40$ bohr.

FIG. 4.2: ^{1}S phaseshift vs. energy for various projection distances: 8 bohr (- - -), 10 bohr (— - —), 12 bohr (– – –), 15 bohr (— — —), and 20 bohr (– - - –). Values calculated by Schwartz[6] are indicated by $\triangle$.

FIG. 4.3: ^{1}S phase (twice the phaseshift) vs. projection distance. The results of Schwartz[5] are given by the lines on the inner side of the ordinate axis. The + points were calculated using only one surface function at k=0.1, 0.2, 0.3, 0.4, 0.5, and 0.6 bohr^{-1}. The other basis sets — $\triangle$ for 3 surface functions, $\square$ for 6 surface functions, and $\times$ for 10 surface functions — were used at k=0.7 and 0.8 bohr^{-1} in addition.

FIG. 4.4: $1s0 - 2s0$ element of ^{1}S scattering matrix, for two different projection distances, vs. energy, at energies between the $n = 2$ and $n = 3$ thresholds. The $\triangle$'s represent projection at 50 bohr, the $\square$'s 60 bohr. Top: phase (in rad). Bottom: square of modulus. The basis set used was 10 surface functions out of 15 primitives.

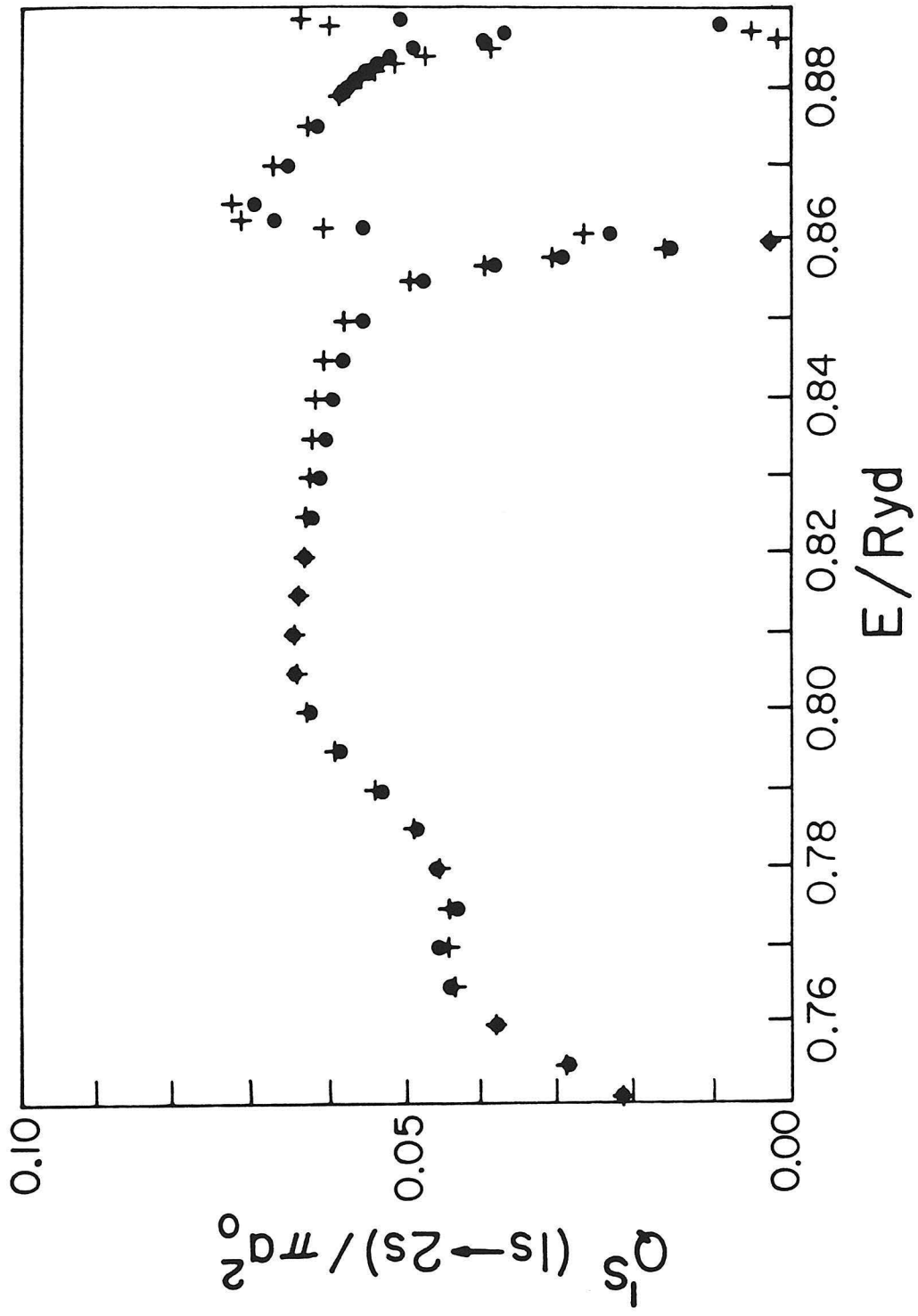

Figure 4.1

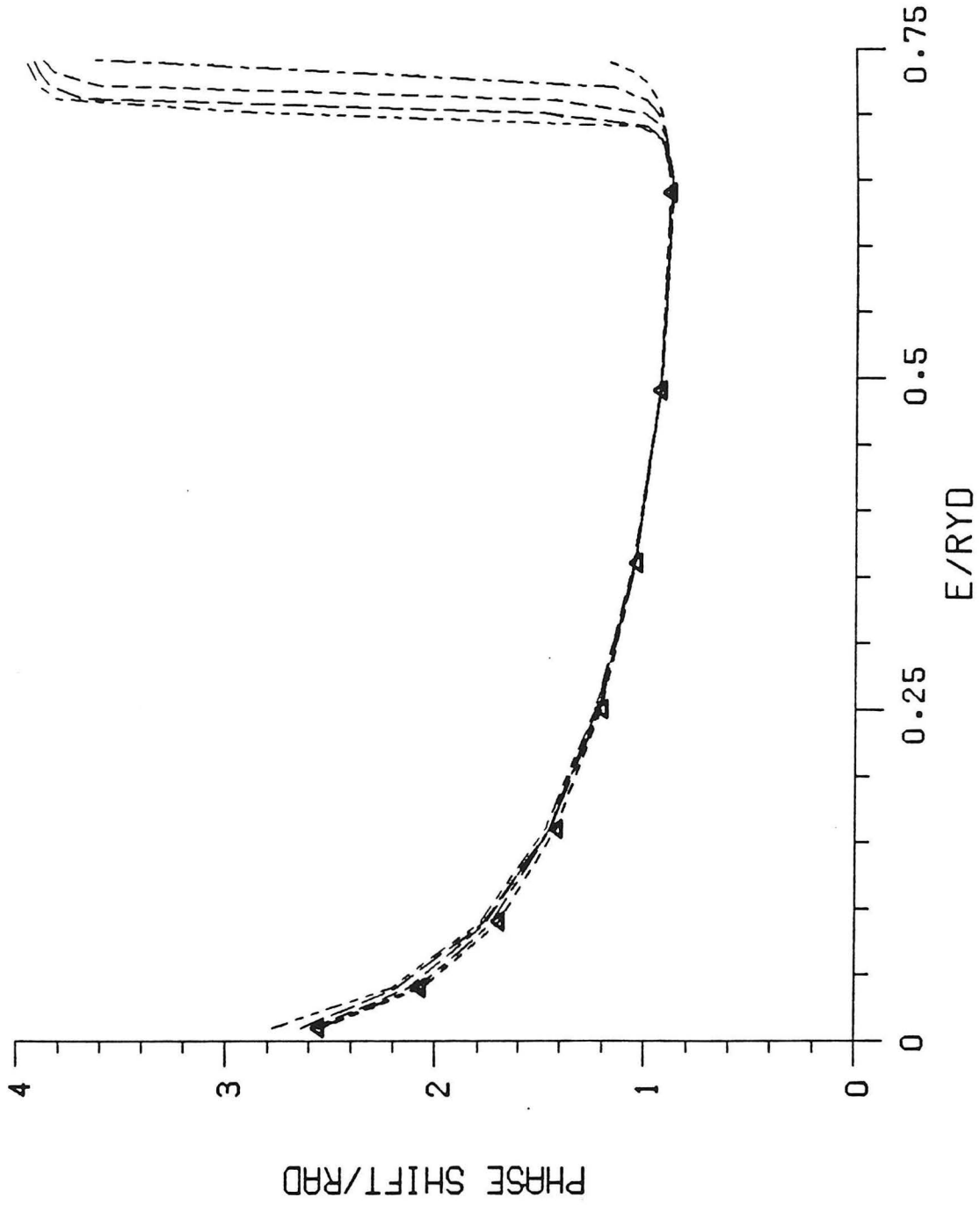

Figure 4.2

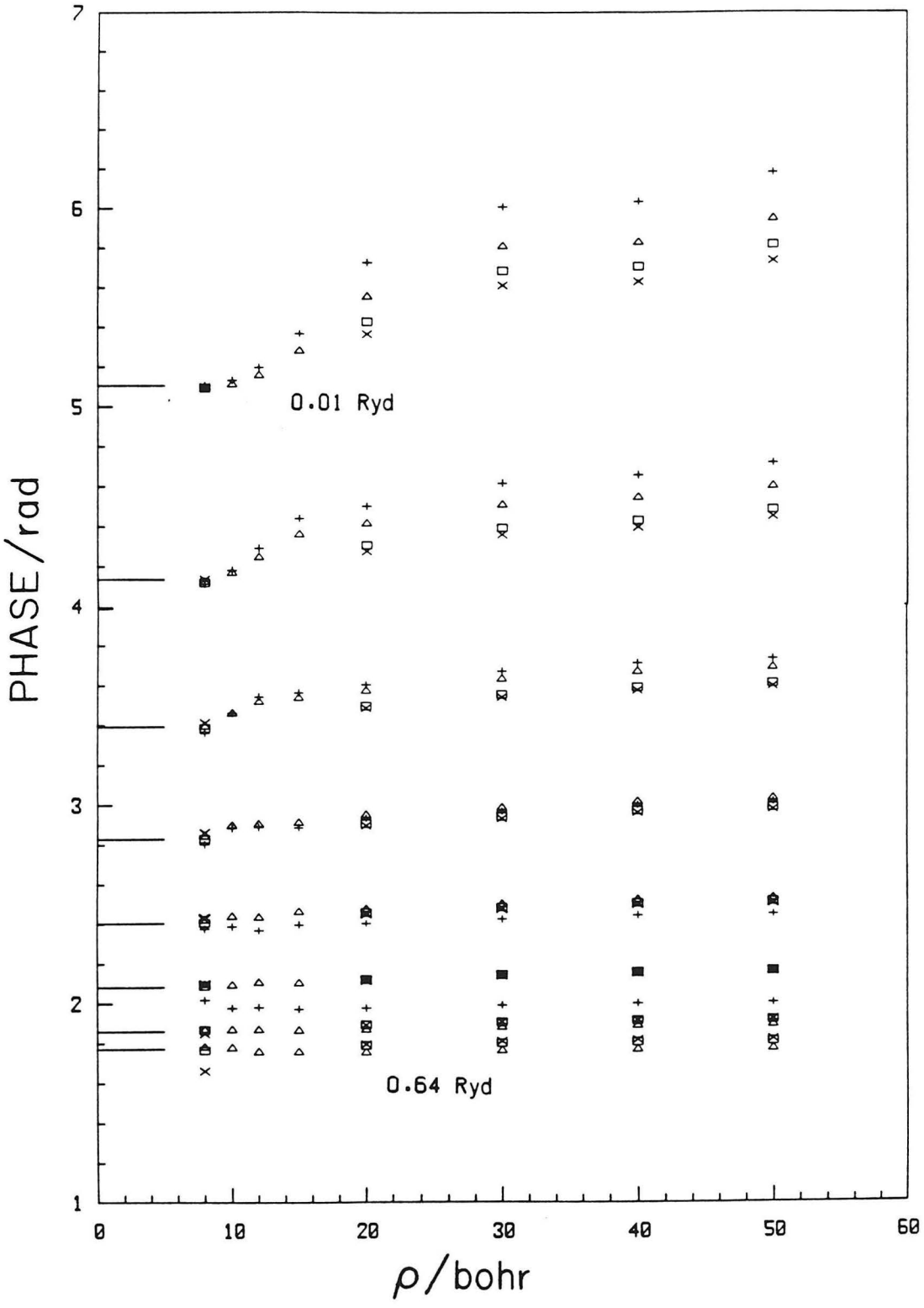

Figure 4.3

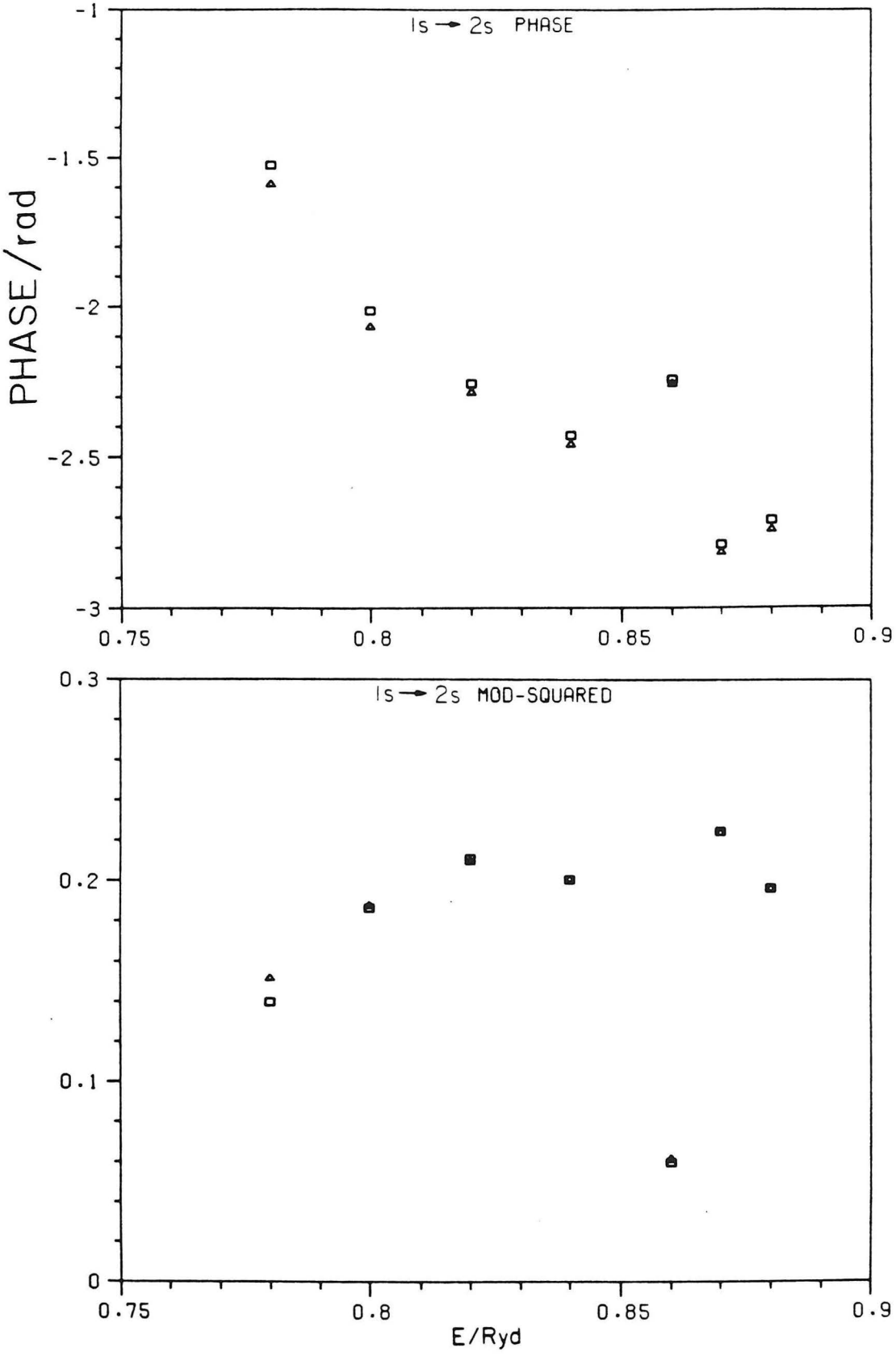
1s → 2s PHASE
PHASE/rad
-1
-1.5
-2
-2.5
-3
0.75
0.8
0.85
0.9
1s → 2s MOD-SQUARED
0.3
0.2
0.1
0
0.75
0.8
0.85
0.9
E/Ryd

Figure 4.4

CHAPTER 5

SURFACE FUNCTION STUDIES

In this chapter we will analyze the surface functions used to expand the full wavefunction in more detail. We will discuss and provide plots of the primitive basis functions, and the potentials of which they are the eigenfunctions. The surface eigenvalues will be studied, as well as the nodal structure of the surface functions themselves. Finally we will discuss the convergence behavior of several sets of surface functions bases.

5.1 Primitive Basis Set

As explained in Chapter 2, the wavefunction $\Psi^{JMS\Pi}$ is expanded in surface functions $\Phi^{JMS\Pi}$ which are then expanded in primitive basis functions which are appropriately symmetrized or antisymmetrized sums of terms of the form

$$\mathcal{Y}^{JM}_{l_2 l_1}(\theta_2, \varphi_2, \theta_1, \varphi_1)\, T_p^{Jl_2l_1}(\omega;\rho)/\sin\omega.$$

Since the $\mathcal{Y}^{JM}_{l_2l_1}$'s are analytically known functions and the $T_p^{Jl_2l_1}(\omega;\rho)$'s are obtained numerically, we will concern ourselves with the latter 1-dimensional primitive basis functions. These functions are the numerically determined solutions to the differential equation

$$\left[-\frac{\hbar^2}{2\mu\rho^2}4\left(\frac{d^2}{d\omega^2}+1\right)+V_{\text{eff}}^{Jl_2l_1}\right]T_p^{Jl_2l_1}(\omega;\rho) = \nu_p^{J\Pi l_2 l_1}(\rho)\;\; T_p^{Jl_2l_1}(\omega;\rho) \tag{5.1}$$

where $V_{\text{eff}}^{J l_2 l_1}$ is given by Eq. 2.38.

Each basis function has a corresponding energy eigenvalue $\nu_p^{J\Pi l_2 l_1}(\rho)$, which approaches a hydrogen bound state level $-1/2n^2$ hartrees asymptotically. The principal quantum number n is related to the index p, but not in a simple way, and the two should not be confused. We label the lowest (l_1, l_2) eigenfunction with $p = 1$, regardless of whether the lowest eigenvalue correlates asymptotically with the $n = 1$ H atom level. In general the number of basis functions exceeds the number of surface functions actually used in the expansion of the scattering wave function. This feature is one of the reasons we do a double expansion (i. e., the surface function is expanded in primitive basis functions and the scattering function is separately expanded in surface functions). Whereas any number of functions $T_p^{J l_2 l_1}(\omega; \rho)$, $p = 1, 2, \ldots, p_{\max}$ could be included in the primitive basis set, for any number of l_1, l_2 combinations, we have found that it is most appropriate to include those basis functions which correlate asymptotically to an isolated atom bound state that has a principal quantum number less than or equal to some given $n_{\max}$. The corresponding number of primitive basis functions depends not only on $n_{\max}$, but also on the total orbital angular momentum J and on the parity Π, to which $(-1)^{l_1+l_2}$ is related according to Eq. 2.50.

A list of the possible basis functions is presented in Table $5-1$. For each asymptotic energy level given by n we have listed the additional (i. e., those in addition to the values for $0, 1, \ldots, n-1$) asymptotic l_1, l_2 values that are allowed for each J and Π. For instance, for $n = 3$ and $J = 0$ we have the following $(l_1, l_2), p$ values: (0,0), $p = 1$ for $n = 1$; (0,0), $p = 2$ and (1,1), $p = 1$ for $n = 2$; (0,0), $p = 3$, (1,1), $p = 2$, and (2,2), $p = 1$ for $n = 3$. The total number of primitive basis functions for each J and parity are given in Table $5-2$. There are both singlet and triplet surface functions for each primitive basis function listed in Table $5-1$ and counted in Table $5-2$. Asymptotically we may have both $l_1 > l_2$ and $l_1 < l_2$ states,

which correspond to two separate primitive $T_p^{Jl_2l_1}(\omega;\rho)$ eigenfunctions of the same $[l_1l_2]$ potential (see Eq. 2.37).

When $l_1 = l_2$, as is always the case for $J = 0$ and $J = 1$, even parity (due to the triangle inequality between l_1, l_2 and J), two separate basis functions exist, namely $T_{p+}^{Jll}(\omega;\rho)$, which is symmetric with respect to $\omega = \frac{\pi}{2}$, and $T_{p-}^{Jll}(\omega;\rho)$, which is antisymmetric. The $(+)$ or $(-)$ distinction depends on the sign of $(-1)^{J+S}$, which is why we designate these basis functions $T_{p_{J+S}}^{Jll}$.

When $l_2 \neq l_1$, as in the odd $J = 1$ case, symmetrized surface functions are obtained by combining $T_p^{Jl_2l_1}(\omega;\bar{\rho})$ and $T_p^{Jl_1l_2}(\omega;\bar{\rho})$ appropriately as described in Section 2.4. Actually, $T_p^{Jl_1l_2}(\omega;\bar{\rho})$ is equal to $T_p^{Jl_2l_1}(\pi-\omega;\rho)$, so we only calculate $T_p^{Jl_2l_1}(\omega;\bar{\rho})$, over the entire range of ω, using the two boundary conditions, one at $\omega = 0$ and one at $\omega = \pi$. This is in contrast to the $l_2 = l_1$ case, where one boundary condition is at $\omega = 0$, and the other condition is on either the function or its derivative at $\omega = \frac{\pi}{2}$; these functions are only calculated over the range $0 \leq \omega \leq \frac{\pi}{2}$ and the rest is inferred by symmetry. (See Section 2.4.2.)

The principal quantum number of the ground state is $n = 1$. Since l_1 can take values from 0 to $n - 1$, we must have $l_1 = 0$. That means the parity of a primitive basis function which correlates asymptotically with the $1s$ H-atom state is $(-1)^{l_2}$, and the triangle relationship between J, l_1 and l_2 leads to $l_2 = J$ as the only possible value for l_2. Thus the parity of the $n = 1$ state is $(-1)^J$. As a result, and as indicated in the $n \geq 1$ row of Table $5 - 1$, there is one, and only one, state that asymptotically approaches the $1s$ H state for each J and S. This affords us a significant saving in computer time if we are only interested in transitions from the ground $(1s)$ state, because we need include only the states with the same parity as

the $1s$ state in the calculation,[1] and can omit the other parity.*

For $J = 0$ there are no odd parity states allowed. For $J = 1$ (P states) the P^{odd} states contribute to transitions from the ground state, but the P^{even} ones do not. However, as one can see from the Table $5-2$, there are fewer P^{even} functions than P^{odd}, so the time saving is small, but not insignificant. In a similar manner the D^{even} states are needed for transitions from the ground state, but the D^{odd} states are not.

If we look at the P^{odd} entries for $n \geq 1$ and $n \geq 2$ in Table $5-2$, we see that for $n_{max} = 2$ (0,1), (1,0), and (1,2) states are permitted. Why are both (0,1) and (1,0) allowed but only (1,2) and not (2,1)? The reason is that l_1 is restricted to values $0, \ldots, n-1$, because l_1 is the asymptotic orbital quantum number. On the other hand l_2 is only restricted to be between $|J - l_1|$ and $|J + l_1|$, and so is allowed to be greater than n.

If the number of surface functions equals the number of basis functions, one might as well have expanded the total scattering wavefunction in the primitive basis set directly. However, one can use a large number of primitive functions in order to get a much better, but small number of surface functions. Since the computation time for solving the scattering (i. e., propagation) equations increases with the cube of the number of surface functions used in the scattering function expansion (regardless of the number of primitive functions used in the expansion of the surface functions), the use of larger primitive basis sets for a fixed number of surface functions permits us to improve the accuracy of the calculation without significantly affecting the propagation time.

---

* Some authors[2] denote states with parity different from the $1s$ state as being "odd," which may lead to some confusion. These states are alternately labeled "parity-disfavored."

5.1.1 Choice of grid points for finite difference calculation

The primitive basis eigenfunction-eigenvalue equation (Eq. 5.1) is solved using a first order finite difference method. The potential function which appears in it (see Eq. 2.32) has an infinitely deep well at both ends (i. e., $\omega = 0$ and $\omega = \pi$). When the centrifugal terms are added in we obtain the effective potential V_{eff},

$$V_{\text{eff}}^{J l_2 l_1} = V^{J\Pi}{}_{l_2 l_1}^{l_2 l_1}(\omega;\rho) - \frac{\hbar^2}{2\mu\rho^2}\left[4 - \frac{l_2(l_2+1)}{\cos^2\frac{\omega}{2}} - \frac{l_1(l_1+1)}{\sin^2\frac{\omega}{2}}\right] + \frac{15\hbar^2}{8\mu\rho^2} \qquad (5.2)$$

This differs from Eq. 2.38 by the inclusion of the $\frac{15\hbar^2}{8\mu\rho^2}$ term which appears in Eqs. 2.80 and 2.86. This is done for subsequent convenience. The potential of Eq. 5.2 diverges to $+\infty$ at $\omega = 0$ and π for $l_1 \neq 0$ and $l_2 \neq 0$. If either $l_1 = 0$ or $l_2 = 0$, the corresponding centrifugal term vanishes and the effective potential has an infinitely deep well at the respective end(s) ($\omega = 0$ or π). To illustrate, the effective potential for $J = 0$, $l_1 = l_2 = 0$ has been plotted in Figure 5.1 for several values of ρ, and the counterpart for $l_1 = l_2 = 1$ has been plotted in Figure 5.2. In Figure 5.3 we show an example of a non-symmetric effective potential that has one repulsive wall and one infinitely deep well, obtained with $J = 1$, $l_1 = 0$, and $l_2 = 1$, and in Figure 5.4 is displayed the $J = 1$, $l_1 = 1$, $l_2 = 2$ effective potential, which consists of two finite wells of different depths. A noticeable feature of these potential curves is that there is a discontinuity in their derivatives at $\omega = \pi/2$. The potential itself is, however, continuous everywhere, except at $\omega = 0$ and π.

The finite difference method approximates the eigenfunction with straight line segments for the evaluation of first derivatives and this is not a very good approximation for classically allowed regions of space in which the potential changes rapidly, as is the case for infinitely deep attractive wells. We determined that near $\omega = 0$ for $l_1 = 0$ the finite difference grid points need to be spaced 1-2 orders of magnitude closer together than in the central region ($\omega \sim \frac{\pi}{2}$) where the potential flattens out.

When $l_1 \neq 0$ (or $l_2 \neq 0$), this extra dense grid is not needed, as the wavefunction is very small near $\omega = 0$ (or $\omega = \pi$). Therefore we used two different sets of values of ω to calculate the 1-dimensional basis functions. When $l_1 = 0$, we set up five regions of equally spaced grid points in the range 0 to $\frac{\pi}{2}$. The points for $\omega > \frac{\pi}{2}$ were arranged symmetrically. When $l_1 > 0$, we collapsed the first region into one point, so there were only four regions. Up to a certain ρ-cutoff, the regions were defined by an angular range, independent of ρ. These regions and grid point positions are listed in Table 5 – 3. After this cutoff (usually 106 bohr) we chose the points according to the method described next.

We found that in the asymptotic region of large ρ the 1-dimensional wavefunction $T_p^{Jl_2l_1}(\omega;\rho)$ was independent of ρ if the variable ω was scaled by ρ, i. e., that

$$T(\omega;\rho_2) \approx T(\frac{\rho_2}{\rho_1}\omega;\rho_1) \tag{5.3}$$

Thus it was appropriate in this large ρ regime to define the ω regions by a length of arc, instead of by an angle. This injects an added complication in the computation of overlap integrals, because the primitive functions for different ρ (in this range) are obtained at different ω grid points. This factor was taken care of by appropriate cubic spline fits to the eigenfunctions.[3]

The even-parity primitive basis functions with $J > 1$ have a feature that is not present in odd ones or in lower J functions. The basis functions with $l_2 = l_1$ will have the normalization constant $N_{l_2l_1} = 1$, but the $l_2 > l_1$ functions have $N_{l_2l_1} = 1/\sqrt{2}$ because the symmetrized function is the sum or difference of two separately normalized non-symmetrized functions of the form given at the beginning of Section 5.1. The normalization factors must be taken into account when calculating potential matrix elements and projection integrals. The normalization factors $N_{l_2l_1}$ cannot be collected, via the distributive property, into one overall

normalization factor N for the total wavefunction, as they would be for ^{1,3}S or ^{1,3}P^{odd} states, for example. But it is not necessary that the total wavefunction be normalized, because any normalization factors will not affect the final scattering matrix.

5.1.2 Basis function plots

In this section we will describe the primitive eigenfunctions that were obtained from the potential functions graphed in Figures 5.1-3. In Figure 5.5 we have plotted the lowest three ^{3}S (i. e., antisymmetric) eigenfunctions corresponding to $l_1 = l_2 = 0$ at the same values of ρ as in Fig. 5.1. The ^{3}S eigenfunctions corresponding to $l_1 = l_2 = 1$ are plotted in Figure 5.6.

The effective potential is symmetric — giving rise to symmetric and antisymmetric eigensolutions — only if $l_1 = l_2$, as stated before. If $l_1 \neq l_2$, then the potential has the form of a double well, with one well deeper than the other and a relative maximum at $\omega = \frac{\pi}{2}$. (If l_1 or $l_2 = 0$, one well is infinitely deep.) The P^{odd} primitive eigenfunctions with $l_1 = 0$ and $l_2 = 1$ are plotted in Figure 5.7. Note that no spin state is indicated for the odd $J = 1$ primitives, because spin, which is used to label surface functions, is not a good quantum number for primitive basis functions which are neither symmetric nor antisymmetric around $\omega = \frac{\pi}{2}$.

For $l_1 \neq 0$ and $l_2 \neq 0$, and for small values of ρ, the effective potential looks like a single well and its eigenvalues are significantly larger than the well minima. The corresponding eigenfunctions are similar to sine waves, spanning the entire range of ω. As ρ is increased, the potential wells become narrower and the eigenvalues drop to lower energies. When the eigenvalue drops below the maximum in the potential at $\omega = \frac{\pi}{2}$, the shape of the eigenfunction is dramatically affected. The function must tunnel through the barrier to get from the $\omega = 0$ to the $\omega = \pi$ side of the barrier. For sufficiently large ρ the barrier is so wide that each eigenfunction is

concentrated in either one well or the other or both if the potential is symmetric. Their values are very small in the wide classically forbidden region. This behavior is clearly seen in Figure 5.7. This kind of behavior is also displayed by the lowest eigenfunctions in Figures 5.5 and 5.6 also even though $l_1 = 0$ for these potentials. The reason is that in this case also the width of the barrier becomes large and for eigenvalues below the top of the central barrier the eigenfunctions become localized in one or the other (or both for $l_1 = l_2 = 0$) of the narrow well regions.

For $l_1 = l_2$, and eigenvalues below the top of the barrier, asymptotically the symmetric functions look just like the antisymmetric functions in the 0 to $\frac{\pi}{2}$ range and at the same time, the corresponding eigenvalues become degenerate.

We have observed numerically that the eigenvalues of a non-symmetric potential, except for the lower eigenvalues, come in pairs, which become degenerate as ρ approaches infinity. This is to be expected because the eigenvalues should be approaching the hydrogen spectrum in each well separately. The number of non-degenerate levels is equal to $|l_2 - l_1|$, and these will correspond to the lowest eigenvalues in the deeper well.

5.2 Surface Function Eigenvalues

In this section we examine the behavior of the surface eigenvalues $\epsilon_i^{JS\Pi}(\rho)$ as functions of ρ. These eigenvalues are the major contribution to the diagonal elements of the interaction potential $\mathbf{U}^{JS\Pi}$ in the radial equation (see Eqs. 2.84 and 2.87) and are obtained by diagonalizing the potential matrix $\mathbf{V_0}^{JS\Pi} + \mathbf{u}^{JS\Pi}$ which appears in Eq. 2.60. Others have made model calculations of the resonance energies and the bound state level of H^- from such curves.[4,5] It will be useful to examine how features of these eigenvalue adiabatic curves correlate with the scattering behavior. As a general rule we find that the adiabatic potentials formed by the ^1S and $^3P^{odd}$ eigenvalues are much more attractive than those of the ^3S and

$^1P^{odd}$ curves, respectively. We also find, as expected, that these eigenvalue curves become more repulsive as J increases.

As ρ goes to zero, the surface functions and primitive basis set become the hyperspherical harmonics $X^{JM}_{l_2 l_1 \lambda}$, which are given by the analytically known Jacobi polynomials $y^{l_2 l_1}_{\lambda}(\omega)$ multiplied by $\mathcal{Y}^{JM}_{l_2 l_1}$ and the corresponding eigenvalues are given by $\lambda(\lambda+4)/2\rho^2$, where λ is a non-negative integer.[6] These eigenvalues are degenerate in l_1 and l_2. The ordering of states at $\rho \sim 0$ is different from the asymptotic ordering (at $\rho \sim \infty$), which is that of the principal quantum number n, and states which are nearly degenerate at small ρ will not necessarily be degenerate at large ρ. Most of the adiabatic curves will cross at small values of ρ, where the eigenvalues are still large, and the surface function coefficient matrix $a^{JS\Pi i}_{l_2 l_1 p}$ (see Eq. 2.56) is close to diagonal. This kind of crossing is different from the "avoided crossing" which usually occurs at larger values of ρ, near or beyond the minimum of the eigenvalue. In Table 5 – 4 we have indicated the correlation between the states for small (0.1 bohr) and large values of ρ for the ^1S functions. We will not go into detail here as to how these λ, l_1, and l_2 combinations are determined,[6] but let us mention that for even parity states such as ^1S, λ is only allowed positive even values. (We should also notice that the asymptotic states are not eigenstates of $\hat{l_{1z}}$, the z component of angular momentum of the isolated H atom, but are linear combinations of such states having the same n and l_1 quantum numbers.)

Looking at the first entry in the table we see that the lowest eigenvalue corresponds to $\lambda = 0$, $(l_1, l_2) = (0,0)$, the second lowest state has $\lambda = 2$, $(l_1, l_2) = (1,1)$, and for $\lambda = 4$ we have two degenerate states, $(l_1, l_2) = (0,0)$ and (2,2). The reason there is no ^1S (0,0) state corresponding to $\lambda = 2$ is that the second lowest (0,0) Jacobi polynomial is antisymmetric, and corresponds to ^3S. Corresponding to $\lambda = 6$ we have both (1,1) and (3,3), and for $\lambda = 8$ we have three degenerate states, with (l_1, l_2) equal to (0,0), (2,2), and (4,4). It is fairly easy to

assign the $\rho \sim 0$ functions to their counterpart asymptotic functions. If we do so, we see that the small ρ energy ordering of states is as follows: $1s$; $2p$; $2s$ and $3d$; $3p$ and $4f$; $3s$, $4d$, and $5g$, etc. We will return to this when we make plots of the surface functions and examine their nodal structure, in Section 5.3.

One of the most interesting features exhibited by the surface eigenvalues is the presence of "avoided crossings," at which two states become almost degenerate, and "repel" each other. In our calculation we have kept all off-diagonal terms in the radial equation coupling matrix, but certain approximate methods, in which such coupling are omitted, assume that the surface functions vary slowly with ρ (i. e., display adiabatic behavior) and have to treat these avoided crossing regions in a special way, so as to preserve the character of the surface functions across these regions. The first such example of an avoided crossing we encountered occurs in the $^1P^{odd}$ partial wave, between the second and third lowest states. This avoided crossing will be discussed in more detail in Section 5.2.2.2.

We have labeled the surface functions by the general index k, along with total angular momentum J, spin S, and parity Π. The index k simply orders the eigenvectors according to their eigenvalues, the eigenvector with the lowest eigenvalue being labeled $k = 1$. The index k stands for a **set** of quantum numbers yet to be determined. Each surface function eigenvalue asymptotically approaches an H atom energy level n, but l_1 and l_2 are not good quantum numbers for labeling surface functions.

A scheme has recently been developed which assigns quantum numbers (K, T) and A to the surface functions. The values of (K, T) and A are assigned phenomenologically after the surface functions and energies have been obtained as a function of ρ. These assignments are based upon features of the angular and radial correlations evident from the surface functions[7,8] and result in the eigenvalue curves

with similar (K,T) and A, but different J, S and Π, having similar features. The quantum numbers which replace l_1 and l_2 are K and T. The (K,T) classification scheme is more suited to the adiabatic decoupling approximation because it assumes surface functions whose character does not change with ρ.

The potential curves we obtain fall into three broad classes, which have been assigned values of $A = \pm 1, 0$ by Lin.[8] The $A = +1$ curves have deep attractive wells, at relatively small values of ρ. The $A = -1$ curves are also attractive, but the wells are much shallower, broader and therefore reach their minimum value at larger values of ρ. The $A = 0$ curves are generally repulsive. In Lin's classification scheme $A = +1$ and $A = -1$ curves can cross, but the $A = 0$ curves, which are usually much higher than the other curves, aren't allowed to cross. For Lin's adiabatic surface functions the quantum numbers $(K,T)^A$ are independent of ρ. Our non-adiabatic surface functions, to be classified similarly, would have to be analyzed on the basis of the adiabatic characteristics, which would make $(K,T)^A$ change across an avoided crossing. Lin has shown, for states of the He atom, that as J increases, fewer of the states have $A = +1$ and more of the states correspond to $A = 0$. This agrees with our general observation that the eigenvalue curves become more repulsive with higher angular momentum.

5.2.1 n=1 eigenvalues

The next series of figures show how the surface function eigenvalues vary with ρ, and how their eigenvalues converge at large ρ to the hydrogen atom eigenvalues. (The energies plotted have had the term $\frac{15\hbar^2}{8\mu\rho^2}$ added to the eigenvalue $\varepsilon_i^{JS\Pi}(\rho)$. This term comes from replacing Ψ with $\rho^{-\frac{5}{2}}\Psi$ to remove the first derivative in ρ term, as indicated in Eqs. 2.81 and 2.82.) The lowest ^{1,3}S, ^{1,3}P$^{\text{odd}}$, ^{1,3}D$^{\text{even}}$ and ^{1,3}F$^{\text{odd}}$ eigenvalue curves that converge to the ground state of H at large ρ are shown in Figure 5.8. Each corresponds to an effective potential seen in the

elastic scattering for that particular J, S, and Π in the adiabatic decoupling approximation. Summarizing the main features we note that only the ^{1}S curve has a significantly deep attractive well (having a depth of 0.26 h with the minimum occurring at 1.7 a_0). The ^{3}S curve has a very shallow well, only 0.007 h deep, with a minimum at 6.8 a_0. Purely repulsive potentials are obtained in the $^1\mathrm{P}^{\mathrm{odd}}$, $^3\mathrm{P}^{\mathrm{odd}}$, and all higher J states. At large values of ρ, the eigenvalue curves for J and $J-1$ are separated from each other by J/ρ^2, which corresponds to the difference in the centrifugal potential given by $J(J+1)/2\rho^2$. The lowest potential curves obtained by Lin[4] match ours very well. For $J \geq 2$, the splitting between the singlet and triplet curves is very small, making those curves coincide with the plotting accuracy of Fig. 5.8. The reason for this behavior is that the centrifugal term dominates.

5.2.2 n=2 eigenvalues

There are two $n = 2$ eigenvalues each for the ^{1}S and ^{3}S surface functions ($2s0$ and $2p1$), three such states for all higher J states with parity $(-1)^J$ ($2sJ$, $2pJ-1$, and $2pJ+1$), and just one for states with parity $(-1)^{J-1}$ (which is $2pJ$). These surface functions form a one-to-one correspondence with the same number of $n = 2$ level asymptotic states (quantum numbers $JS\Pi nl_1l_2$). There are three distinct types of eigenvalue potential, as can be seen in Figs. 5.9 through 5.13: deep well, shallow well, and repulsive wall. We have found that the deeper wells, for all J, have minima at around 7.5 bohr, whereas for the shallower wells these minima occur at about 15 bohr, which is consistent with the observations of Lin.[8] Considering that the second Bohr radius is 4 bohr, and that the average distances $\langle r \rangle$ from the nucleus of the $2s$ and $2p$ electrons are $6a_0$ and $5a_0$, respectively, the well minima are all larger than these measures of the size of an atom. However, that should not come as a surprise, since the hyperradius ρ depends on the radial coordinate of both electrons, $\rho = \sqrt{r_1^2 + r_2^2}$. The shorter well distance, 7.5 bohr, is roughly

equivalent to the square root of the sum of $\langle r_{2s} \rangle^2$ and $\langle r_{2p} \rangle^2$, and the larger distance is commensurate with the square root of the sum of $\langle r_{2l_1} \rangle^2$ and $\langle r_{3l_1'} \rangle^2$.

It has been mentioned that the ^{1}S, ^{3}S and ^{3}P^{odd}, ^{1}P^{odd} eigenvalue curves resemble those of the H_2 molecule for bonding and anti-bonding states.[4] In H_2^+, the repulsive $^2\Sigma_u^+$ curve results from the antisymmetric character of the electronic wavefunction, with a node midway between the nuclei. Likewise, the ^{3}S state has an extra node, compared to the singlet state, at $\omega = \frac{\pi}{2}$.

There exists a one-to-one correspondence between parity-disfavored states ($\Pi = (-1)^{J+1}$) with quantum numbers J, K, T, and another set of parity-favored states which are one energy level lower, characterized by quantum numbers $J-1$, $K-1$, $T-1$ and have different spin quantum numbers (singlet $\leftrightarrow$ triplet).[8] This can partially be seen from Table 5 – 2, where only the total number of states for each J and parity are listed. Thus, for example, the behavior of ^{1}P^{even} and ^{3}P^{even} $n = 2$ eigenvalues is expected to mimic the ^{3}S and ^{1}S $n = 1$ eigenvalues, respectively. Indeed this is exactly what we have found, which will be discussed below.

5.2.2.1 ^{1}S and ^{3}S eigenvalues

The two curves of ^{1}S eigenvalues that converge to the $n = 2$ H level at large ρ are shown in Figure 5.9, along with the three that converge to $n = 3$ and the four that converge to $n = 4$ levels. Considering just the $n = 2$ eigenvalue curves, the lowest one has a well of 0.068 h, the bottom being placed at 7.6 a_0. The other curve is repulsive and has an interesting plateau from 11 a_0 to 16 a_0 at −0.115 h, which is not an avoided crossing. The $n = 2$ eigenvalue curves for the ^{3}S states are the lowest two curves plotted in Figure 5.10. The well in the lowest is much shallower than that for the corresponding singlet, being only 0.012 h deep with a minimum at 15.0 a_0. Once again, the other one is repulsive. Both the singlet and the triplet $J = 0$ $n = 2$ eigenvalue curves become nearly degenerate by 25 a_0. According to

the $(K,T)^A$ nomenclature, all ^{1}S states have a value of$A$ equal to $+1$. Conversely, all ^{3}S states are assigned an A value of -1.

It is apparent from Figs. 5.8 and 5.9 that the attractive ^{1}S eigenvalue curves are much more attractive than the corresponding ^{3}S ones. The repulsive behavior of the ^{3}S curve comes from the extra node in the ^{3}S surface functions at $\omega = \frac{\pi}{2}$.

5.2.2.2 ^{1,3}P^{odd} and ^{1,3}P^{even} eigenvalues

The eigenvalues of the three ^{1}P^{odd} states and one ^{3}P^{even} state that asymptotically have principal quantum number $n = 2$ are plotted in Figure 5.11. The lowest ^{1}P^{odd} state has a well depth of 0.0217 h at 8.0 bohr; there is also an avoided crossing between the two lowest ^{1}P^{odd} curves which gives rise to a maximum at 14.0 bohr and another minimum at 15.2 bohr in the lowest of these curves. This avoided crossing also causes the second eigenvalue curve to have a well of 0.0071 h at 13.6 bohr and a small barrier, 0.0001 h above the $n = 2$ hydrogen level, at $\rho = 35$ bohr. The third ^{1}P^{odd} state is repulsive. It is the barrier in the second eigenvalue curve which leads to the ^{1}P^{odd} shape resonance at 0.7511 Ryd (see Section 6.3). The single ^{3}P^{even} eigenvalue curve has a well 0.0234 h deep at 8.0 bohr, which has been shown to be deep enough to support a true bound state.[4] For values of ρ smaller than 13 bohr the ^{3}P^{even} eigenvalue curve is close to the lowest ^{1}P^{odd} one, but then crosses over to become very close to the second curve. At small values of ρ, the difference is due to the different dominant value of l_2, ($l_2 = 1$ in the ^{3}P^{even} state, but the lowest $n = 2$ ^{1}P^{odd} surface function contains mixtures of $l_2 = 0$ and $l_2 = 1$ primitives, primarily) which determines the centrifugal potential. Apparently the difference between the two potentials (and the fact that for the ^{1}P^{odd} partial wave there is a lower, 1s level with which it may couple), is enough to change a bound state into a shape resonance.

Of the three ^{1}P^{odd} eigenvalue curves that asymptotically approach $n = 2$ level,

the lowest is usually labeled $2sp+$, meaning that the independent-electron model quantum numbers (l_1, l_2) are primarily $(0,1)$ and $(1,0)$, and that the dependence of the surface function on ω is nearly symmetric about $\frac{\pi}{2}$.[9] Similarly the second is given the label $2sp-$. This means that there is an extra node in the wavefunction of the $2sp-$ state around $\omega = \frac{\pi}{2}$ which prevents both electrons from being close to the nucleus at the same time. The pronounced avoided crossing at 13.5 bohr causes the lower curve and corresponding eigenfunction to change in character from + to −, and vice-versa for the second curve. The higher, repulsive curve is given the label pd, meaning $(l_1, l_2) = (1,2)$. The pd state is not very important in the discussion of the $^1\mathrm{P}^{\mathrm{odd}}$ shape resonance.

It is interesting to compare how these simple labels correlate with the surface function expansion coefficients for the appropriate primitive functions, which are the second and third eigenfunctions $T_p^{J=1,l_1=0,l_2=1}(\omega)$ and the lowest $T_p^{112}(\omega)$ one. From the plots of $\mathrm{P}^{\mathrm{odd}}$ primitives in Fig. 5.7 it is seen that $T_{p=2}^{101}(\omega)$ has one node, and at large values of ρ the density is concentrated at the $\omega = \pi$ end, and the node becomes negligible. (By saying a node "becomes negligible" we mean that the node exists between where the function is vanishingly small but positive, and where it is vanishingly small but negative.) This primitive function correlates with the $2p$ function at large ρ. The next primitive has two nodes, one of which becomes negligible for large ρ, and correlates asymptotically with the $2s$ function.

The actual coefficients of the $^1\mathrm{P}^{\mathrm{odd}}$ $n = 2$ surface functions, at $\rho = 20$ bohr are

$$\begin{array}{c} \\ \Phi_2 \\ \Phi_3 \\ \Phi_4 \end{array} \begin{array}{c} \begin{array}{ccc} T_2^{101} & T_3^{101} & T_1^{112} \end{array} \\ \begin{pmatrix} .47 & -.83 & .30 \\ .82 & .28 & -.49 \\ -.32 & -.48 & -.81 \end{pmatrix} \end{array}$$

From this matrix it is evident that the labels $2sp+$, $2sp-$, and pd are somewhat misleading. It is true that the relative sign of the coefficients of the two 'sp' primitive

functions is reversed in going from Φ_2 to Φ_3, and that the '*pd*' primitive function is the major contributor to Φ_4. But in Φ_3 the '*pd*' primitive contributes more than the second '*sp*' primitive, so its contribution is non-trivial. Each of the surface functions has a coefficient greater than 0.8 for one contributing primitive, instead of the expected $2sp \pm 2ps$ structure. The coefficients are not much different just before the avoided crossing, at $\rho = 12$ bohr, but the characters of Φ_2 and Φ_3 are interchanged:

$$\begin{array}{c} \\ \Phi_2 \\ \Phi_3 \\ \Phi_4 \end{array} \begin{array}{c} \begin{array}{ccc} T_2^{101} & T_3^{101} & T_1^{112} \end{array} \\ \begin{pmatrix} .85 & .12 & -.47 \\ .24 & -.94 & .22 \\ .40 & .31 & .83 \end{pmatrix} \end{array}$$

The only place where Φ_2 and Φ_3 have approximately equal contributions (with opposite signs) from the two *sp* primitives is when they are undergoing the transformation, in the region of the avoided crossing (the ρ range 13.4 to 13.6 bohr).

Comparing these eigenvalues to those reported by Klar and Klar,[10] we find that these authors obtain an avoided crossing at about $\rho = 14$ bohr, but our eigenvalues are about 0.01 hartrees lower. Lin also gave the results for $^1P^{odd}$ states, but he used an adiabatic representation which leads to true crossings between the corresponding eigenvalue curves.[4a] When the curves are allowed to cross, Lin obtains for the + state a well 0.019 h deep, located approximately at 8.5 bohr, a barrier 0.0024 h high (measured from the asymptotic value of the energy) and an asymptotic potential that varies as $+2/\rho^2$. The − state gives a shallower well (0.006 h, minimum at about 15 bohr) which behaves as $-3.71/\rho^2$ asymptotically. Lin's calculation only included $[l_1, l_2] = [0,1]$ and $[1,2]$ states, and the diagonal term of the second derivative coupling matrix (see Eq. 2.98) has been added to the eigenvalue term. Our calculation uses 25 primitive functions as listed in Table 5 − 2, and because we have diabatically changing surface functions, there is no second derivative coupling term. Using this much larger basis, the potential

curves obtained are lower in energy, but the barrier is still present. The shape resonance is still clearly seen in our $^1P^{odd}$ scattering results. This resonance has also been seen by Callaway,[11] and verified experimentally by Hamm, *et al.*[12]

The $^3P^{odd}$ eigenvalue curves correlating asymptotically to $n = 2$ H atom level are displayed as the three solid curves in Figure 5.12. The lowest of them is attractive, having a well 0.055 h deep at about 7 bohr, and the other two are repulsive states. The attractive well is much deeper than the corresponding $^1P^{odd}$ well in Fig. 5.11, but not quite as deep as that for the corresponding ^1S state of Fig. 5.9. There is no crossing between these $^3P^{odd}$ $n = 2$ states, which leads Lin to conclude that an $n = 2$ shape resonance in $^3P^{odd}$ is impossible.[4] This is in direct contradiction to the prediction of such a shape resonance on group theoretical grounds by Herrick.[13] In our calculation we find evidence of a short-lived shape resonance in the $^3P^{odd}$ partial wave. We have found similarly short-lived resonances in other partial waves as well, using a collision lifetime matrix eigenvalues analysis. The $^1P^{even}$ eigenvalue curve is almost repulsive, having a very shallow well, much like the ^3S $n = 1$ eigenvalue curve. This occurs for the same reason; the extra node about $\omega = \frac{\pi}{2}$ in the $^1P^{even}$ primitive functions which is not present in the $^3P^{even}$ primitives.

5.2.2.3 Higher J states

From Figure 5.13 it is seen that the $^1D^{even}$ $n = 2$ lowest eigenvalue curve has a well 0.027 h deep at 8.4 a_0 and the two other ones are repulsive. The $^3D^{even}$ $n = 2$ eigenvalue curves are shown in Figure 5.14: the well in the lowest occurs at 15 a_0 and is 0.004 h deep, while the two others are repulsive. The lowest eigenvalue curves for the $n = 2$ $^1D^{odd}$ and $^3D^{odd}$ surface functions (not displayed) are both repulsive. All of the $n = 2$ eigenvalue curves of the $J = 3$ surface functions are repulsive; however one of them has a shallow well if the $\frac{15\hbar^2}{8\mu\rho^2}$ term is not added in.

For all higher values of J we expect purely repulsive eigenvalue curves, because of the large centrifugal potential.

5.2.3 n=3 eigenvalues

The eigenvalue curves for higher energy states ($n = 3, 4$) display a larger number of avoided crossings and barriers. The two lowest ^{1}S $n = 3$ curves each have a well, 0.030 h deep at 18.6 bohr, and 0.010 h deep at 19.4 bohr, respectively (see Fig. 5.9). The two lowest ^{3}S $n = 3$ curves (see Fig. 5.10) also have wells which are not as deep, just as for the corresponding $n = 2$ curves. These wells are 0.009 h deep at 28.5 bohr, and 0.0007 h deep at 34 bohr, respectively. The third state, both for the singlet and triplet spin states, is repulsive.

There are five $J = 1$ states of odd parity for $n = 3$ for each spin. The corresponding eigenvalue curves are plotted, along with those for $n = 4$, in Figure 5.15 for $^1P^{odd}$ and Figure 5.16 for $^3P^{odd}$. The five $^1P^{odd}$ curves which asymptotically correlate with the $n = 3$ H atom levels have the following characteristics. The lowest curve has a well 0.0200 h deep at 18.8 bohr and an avoided crossing with the second curve around 30 bohr. This second curve, which has a well 0.0085 h deep at 28.5 bohr, also avoids crossing the third one, at around 20 bohr. The third eigenvalue curve has a barrier less than 0.0001 h high, due to the aforementioned avoided crossing with the second curve. The fourth and fifth curves are purely repulsive. The fifth one also exhibits an avoided crossing with an $n = 4$ higher state.

The lowest $^3P^{odd}$ eigenvalue curve has a well at 18.4 bohr which is 0.0281 h deep. The second one, due to an avoided crossing, has a double well, the minima of which are at 19.8 bohr (0.0071 h deep) and 29.5 bohr (0.0047 h deep), with a relative maximum 0.0027 h high, measured from the bottom of the deeper well. The third curve also has a well (0.0035 h deep at 26 bohr), and the fourth one

is repulsive. The highest curve exhibits an avoided crossing with an $n = 4$ curve, which gives a barrier 0.0004 h high with respect to the bottom of the adjacent well.

There are six surface functions that asymptotically approach linear combinations of $n = 3$ H atom states for $J > 1$. As seen in Fig. 5.13, the three lowest $^1D^{even}$ eigenvalue curves are attractive, with minima at 18.2, 18.8, and 28.0 bohr respectively, and corresponding depths of 0.024, 0.008, and 0.003 h. The minimum in the third curve is due to an avoided crossing with the second one. The fourth curve, due to an avoided crossing with the third, has a minimum at 25.5 bohr and a barrier to its right which is 0.0008 h high, measured from that minimum. The fifth curve is repulsive, and the sixth one has an avoided crossing with an $n = 4$ curve. The lowest three $^3D^{even}$ $n = 3$ eigenvalue curves (see Fig. 5.14) are attractive with minima at 18.6, 29.5, and 32.5 bohr, with corresponding well depths of 0.018, 0.003, and 0.0014 h. The fourth and fifth curves are repulsive, and the sixth and highest curve has a ledge at about 35.5 bohr caused by an avoided crossing with an $n = 4$ curve.

The two lowest $n = 3$ $^1F^{odd}$ eigenvalue curves, as seen in Figure 5.17, have an avoided crossing, as a result of which the lowest has a barrier (in addition to a well), and the second a well. The next three curves are repulsive, and the last one has a sharp avoided crossing with an $n = 4$ curve at 39 bohr which produces a barrier, though the curve is still repulsive. As seen in Figure 5.18the lowest $n = 3$ $^3F^{odd}$ eigenvalue curve has a relatively deep well, followed by three repulsive curves which interact relatively little, and two more which have a sharp avoided crossing with each other. In addition, the highest curve has a sharp avoided crossing with the lowest $n = 4$ curve.

5.2.4 n $\geq$ 4 eigenvalues

The number of surface functions which correlate asymptotically to $n = 4$ and

$n = 5$ H atom levels increases dramatically, especially for large J. The asymptotic energies also become closer as n increases, so the $n = 4$ curves don't separate from $n = 5$ and $n = 6$ ones until large values of ρ, of about 100 bohr are reached. The proximity of these eigenvalue curves, out to large ρ, produces multitudinous avoided crossings. As a result, to obtain converged $n = 4$ level eigenvalues in the interaction region (i. e., relatively small ρ) one needs to include primitive basis functions up to $n = 6$.

5.3 Surface Function Plots

In this section we describe a method for making contour plots of the amplitudes of surface functions. The nature of electron correlations between two excited electrons can be examined in terms of these contour plots. The surface functions are actually five-dimensional, but if we use the body-fixed, instead of space-fixed, representation, the functions can be expanded in the analytically known Wigner rotation functions, $D^{JM}_{\Omega}(\varphi,\theta,\psi)$.[14] The expansion is

$$\Phi_i^{JMS\Pi} = \sum_{\Omega}(-1)^{\Omega}\Big(\frac{2J+1}{8\pi^2}\Big) D^{JM}_{\Omega}(\varphi,\theta,\psi)\, F_{i\Omega}^{JS\Pi}(\omega,\gamma;\rho) \tag{5.4}$$

where the range of Ω is from $-J$ to J. The angles φ, θ, and ψ have been defined at the end of Section 2.1. For $J = 0$ this summation reduces to a single term and $\Phi_i^{00S\Pi}$ and $F_{i0}^{0S\Pi}$ become proportional to one another since D_0^{00} is a constant. The two dimensional functions, $F_{i\Omega}^{JS\Pi}(\omega,\gamma;\rho)$, are found by equating the expansion for $\Phi_i^{JMS\Pi}$ above with that made in Chapter 2 in space-fixed coordinates, namely Eq. 2.56. Doing so one obtains

$$\begin{aligned} F_{i\Omega}^{JS\Pi}(\omega,\gamma;\rho) = \sum_{l_2 l_1 p} a_{l_2 l_1 p}^{JS\Pi i}(\rho)\Big[&(-1)^{l_1} C(Jl_1l_2;\Omega,-\Omega,0)\, P_{l_1}^{\Omega}(\gamma)\, t_p^{Jl_2l_1}(\omega;\rho) \\ &+(-1)^{J+S-\Pi+l_2} C(Jl_2l_1;\Omega,-\Omega,0)\, P_{l_2}^{\Omega}(\gamma)\, t_p^{Jl_2l_1}(\pi-\omega;\rho)\Big] \end{aligned} \tag{5.5}$$

where $t_p^{Jl_2l_1}(\omega;\rho)$ are the 1-dimensional primitive basis functions defined by Eq. 2.34, $a_{l_2l_1p}^{JS\Pi i}(\rho)$ are elements of the surface function coefficient matrix obtained by solving Eq. 2.60, and $P_{l_2}^{\Omega}(\gamma)$ is the renormalized Legendre polynomial defined by Eq. 2.68. It is easily shown that $\left|F_{i\Omega}^{JS\Pi}(\omega,\gamma;\rho)\right|$ is independent of the sign of Ω. From the definition of the renormalized Legendre polynomial one has

$$P_{l_1}^{-\Omega}(\gamma) = (-1)^{\Omega} P_{l_1}^{\Omega}(\gamma) \tag{5.6}$$

and from elementary properties of Clebsch-Gordan coefficients one has

$$C(Jl_1l_2;\Omega,-\Omega,0) = (-1)^{J+l_1-l_2} C(Jl_1l_2;-\Omega,\Omega,0) \tag{5.7}$$

Combining Eqs. 5.5, 5.6, and 5.7 one obtains for $F_{i,-\Omega}^{JS\Pi}$ the following result:

$$\begin{aligned} F_{i,-\Omega}^{JS\Pi} = (-1)^{\Omega+J} \sum_{l_2l_1p} a_{l_2l_1p}^{JS\Pi i}(\rho) \Big[& (-1)^{-l_2} C(Jl_1l_2;\Omega,-\Omega,0) P_{l_1}^{\Omega}(\gamma)\, t_p^{Jl_2l_1}(\omega;\rho) \\ & + (-1)^{J+S-\Pi-l_1} C(Jl_2l_1;\Omega,-\Omega,0) P_{l_2}^{\Omega}(\gamma)\, t_p^{Jl_2l_1}(\pi-\omega;\rho) \Big] \end{aligned} \tag{5.8}$$

The right hand side of this expressions differs from Eq. 5.5 only by the presence of the factor $(-1)^{\Omega+J}$, and by factors $(-1)^{l_1-l_2}$ contained within the summation. However, since the sum is over states all having the same parity, one has

$$(-1)^{\Pi} = (-1)^{l_1-l_2} \tag{5.9}$$

and these terms can be factored outside the sum over l_1 and l_2. Therefore there are $J+1$ subfunctions $F_{i|\Omega|}^{JS\Pi}$ for each set of quantum numbers $JS\Pi i$ which must be calculated. The hyperspherical coordinates ρ, ω, and γ are related to the 3-dimensional mathematical space $OXYZ$ (described in Section 2.2.3) which was used to obtain a physical model of the potential energy function, and the angles ω and γ are defined as spherical polar angles in this space.

In order to represent the functions $F_{i\Omega}^{JS\Pi}(\omega,\gamma;\rho)$ it is convenient to map the hemisphere in $OXYZ$ space defined by $\rho = constant$, $0 \leq \gamma \leq \pi$, $0 \leq \omega \leq \pi$ onto a plane. Such a mapping may be achieved for $0 \leq \omega \leq \frac{\pi}{2}$, corresponding to the northern (i. e., top) half of that hemisphere by defining a plane Π_N tangent to it at the point N for which $\omega = 0$ (i. e., the north pole, as displayed in Figure 5.19). We define axes NX_N and NY_N on that tangent plane which are parallel to OX and OY, respectively. To a point $P(\omega,\gamma;\rho)$ $(0 \leq \omega \leq \frac{\pi}{2})$ on the northern "quartersphere" we associate a point Q on the intersection with the plane defined by OZ and P and for which the N to Q distance is equal to $\rho\omega$, i. e., the length of the NP arc of circle. For points on the southern quartersphere, we adopt a similar mapping onto the plane Π_S tangent to that quartersphere at the south pole S. We can now display the functions $F_{i\Omega}^{JS\Pi}(\omega,\gamma;\rho)$ by contour diagrams on the OX_NY_N $(Y_N \geq 0)$ or OX_SY_S $(Y_S \geq 0)$ half planes.

The cartesian coordinates of the point $Q(X_N, Y_N)$ are related to the hyperspherical coordinates of the point P by the following realtions:

$$\begin{aligned} X_N &= \rho\omega\cos\gamma \\ Y_N &= \rho\omega\sin\gamma \end{aligned} \tag{5.10}$$

Lines passing through the origin have equations of the form $\gamma = constant$ and circles centered on N have equations of the form $\omega = constant$, corresponding respectively to meridian lines and parallel lines on the hemispherical surface in $OXYZ$ space.

The $J > 0$ surface function coefficients $F_{i\Omega}^{JS\Pi}(\omega,\gamma;\rho)$ do not have symmetry with respect to $\omega = \frac{\pi}{2}$, so for them it is necessary to make plots for both quarterspheres. Sometimes it is more useful to map onto a plane tangent to the hemisphere at the point $\gamma = 0$, $\omega = \frac{\pi}{2}$ situated on the OX axis or at the point $\gamma = \frac{\pi}{2}$, $\omega = \frac{\pi}{2}$ situated on the OY axis. The best display involves mapping onto all three of these planes.

The boundary conditions satisfied by $F_{i\Omega}^{JS\Pi}(\omega,\gamma;\rho)$ for $\gamma = 0$ and $\gamma = \pi$ depend on the value of Ω; for $\Omega = 0$ the first derivative of this function with respect to γ vanishes at the boundaries, whereas for odd values of Ω the function itself vanishes, and for non-zero even values of Ω both the function and its derivative vanishes. These conditions, which are proved below, arise naturally out of the surface function expansion Eq. 2.30, which contained spherical harmonics in space-fixed angles, and are necessary to insure single valuedness of the $\Phi_i^{JMS\Pi}$.

The tumbling angle ψ is undefined when $\gamma = 0$ or π, because the two vectors $\mathbf{r_1}$ and $\mathbf{r_2}$ are in alignment. The Wigner rotation functions have the form

$$D_{\Omega}^{JM}(\varphi,\theta,\psi) = \mathrm{e}^{iM\phi} d_{M\Omega}^{J}(\theta) \mathrm{e}^{i\Omega\psi}$$

In order for the surface function (Eq. 5.4) to be single-valued, one of two conditions must hold. Either $D_{\Omega}^{JM}(\varphi,\theta,\psi)$ is independent of ψ, or the coefficient $F_{i\Omega}^{JS\Pi}(\omega,\gamma;\rho)$ vanishes. If $\Omega = 0$, the first condition is true, which allows $F_{i,0}^{JS\Pi}$ to be non-vanishing along the $\gamma = 0$ border. If $\Omega \neq 0$, the coefficient $F_{i\Omega}^{JS\Pi}(\omega,\gamma;\rho)$ of the Wigner function must vanish at $\gamma = 0$ and π:

$$F_{i\Omega}^{JS\Pi}(\omega,\gamma;\rho)\Big|_{\gamma=0,\pi} = 0 \quad \text{for } \Omega \neq 0 \tag{5.11}$$

To obtain the boundary condition on the derivative of $F_{i\Omega}^{JS\Pi}(\omega,\gamma;\rho)$ at $\gamma = 0$ and π we examine the values of the Lengendre polynomials and their derivatives with respect to γ, since $F_{i\Omega}^{JS\Pi}(\omega,\gamma;\rho)$ has been expanded in them. An examination of these functions reveals that for all j, if Ω is an even integer the value of the derivative at $\gamma = 0$ is zero. The derivative is non-zero when Ω is an odd integer.

The hyperradius ρ is not directly involved with describing the correlation between the electrons. Excitation in ρ corresponds to an increase in the size of the system and singly excited states. Lin has used a different scheme[15] to plot the

"surface charge density" of the surface functions. For values of J greater than 0 he averages over the Euler angles, as opposed to our method where we obtain separate plots for each value of $|\Omega|$. Although it would be nice to compare our surface functions with those obtained by Lin, the differences in representation make this somewhat difficult. We have chosen to plot the amplitude functions $F_{i\Omega}^{JS\Pi}(\omega,\gamma;\rho)$, using the polar coordinates (ω,γ), whereas Lin has converted $\omega/2$ and γ into cartesian coordinates for his plots, and plots the square of the wavefunction times the volume element. This difference makes it difficult to comment on the points discussed by Lin, though there are some features, namely the nodes, which are similar. He has shown that all singly excited states of H^- have nodal lines along ρ = *constant*, and no radial nodal structure in the ω coordinate, while doubly excited states have nodes in ω.

The plots of $F_{i\Omega}^{JS\Pi}(\omega,\gamma;\rho)$ are useful in analyzing the nodal structure of the surface functions, for demonstrating the quasiadiabatic evolution of the functions with ρ, and for comparing them to hydrogenic functions. We know that hydrogen bound states can have both radial $(R_{nl_1}(r)=0)$ and angular $(Y_{l_2m_2}(\hat{\mathbf{r}})=0)$ nodes. We define the dependence of the $F_{i\Omega}^{JS\Pi}(\omega,\gamma;\rho)$ on ω as "radial" correlation and on γ as "angular" correlation. In the limit of no Coulombic interaction potential the surface functions for $J=0$ are products of Jacobi polynomials in $\sin\omega$ and Legendre polynomials in $\cos\gamma$.[6] The corresponding nodal lines are in this case obtainable from the zeroes of these polynomials. The electron-electron interaction term at finite values of ρ makes the Schrödinger equation non-separable and causes the nodes to no longer be purely of the "ω"-type or of the "γ"-type. At small values of ρ the interaction term is relatively unimportant compared to the kinetic energy terms, which have a $1/\rho^2$ dependence.

5.3.1 J=0 surface functions

The S states are actually independent of the Euler angles, since they have zero total orbital angular momentum. The surface functions in the $J = 0$ case depend only on ω and γ (and parametrically on ρ). The ^{1}S surface functions are symmetric about $\omega = \frac{\pi}{2}$, and the ^{3}S surface functions have a nodal line there and are anti-symmetric. Therefore we need only plot the upper quartersphere for S states because the lower part is determined by symmetry. The functions have been evaluated at some points that correspond to the lower quartersphere (but which show up in our rectangular representation) anyway (by extending the rule NQ=length of NP arc to those points), which serves to emphasize the presence of a node or antinode along the equator. The points on the $\omega = \frac{\pi}{2}$ plane in $OXYZ$ space lie along a half-circle of radius $\frac{\pi}{2}\rho$ on the OX_NY_N, $Y_N \geq 0$ half-plane.

The first six $\rho = 1.0$ bohr ^{1}S surface functions (in order of increasing eigenenergy) are displayed in Figure 5.20, projected onto the plane Π_N (see Fig. 5.19) and are labeled $\Phi_i^{^1S}$ (i=1 through 6). They are normalized according to Eq. 2.100, using, however, the integration volume element $\sin^2\omega d\omega \sin\gamma d\gamma \sin\theta d\theta d\phi d\psi$ appropriate for body-fixed hyperspherical coordinates. $\Phi_1^{^1S}$ has no nodes, and is fairly large everywhere, including along the $\omega = \frac{\pi}{2}$ boundary. The contours for small values of ω are roughly circular. The nodal lines in $\Phi_2^{^1S}$ and $\Phi_3^{^1S}$ give an interesting example of different types of nodal lines. At $\rho = 1$ bohr, $\Phi_2^{^1S}$ has a nodal line characterized by $X_N = \rho\omega\cos\gamma = constant \approx 0$, i. e., $\gamma \approx \frac{\pi}{2}$ which we call an "angular" node. On the hemispherical $\rho = 1$ bohr surface this is a meridian (constant longitude) line. One the other hand, $\Phi_3^{^1S}$ has a nodal line which is a half circle of constant radius $\rho\omega$ and therefore has an equation of the type $\omega \approx constant$. We call this a "radial" node. On the hemisphere this is a parallel (i. e., constant latitude) line. In this respect it is similar to the contours of the lowest surface function.

We saw in the previous section that at very small ρ the ^{1}S surface functions corresponded to the following ordering: $1s$; $2p$; $2s$ and $3d$; $3p$ and $4f$; $3s$, $4d$, and $5g$, etc. At $\rho = 1.0$ bohr we have seen that the first and third functions are very similar, except for an added "radial" node in the higher state. This is, indeed, the hyperspherical coordinate analog to the nodal pattern found in hydrogen bound states, where the $1s$ function has no nodes, the $2s$ function has the same angular part as the $1s$, but has an added node in the radial part (radial node), and the $2p$ function has an angular node and no radial nodes.

The fourth ^{1}S surface function $\Phi_4^{^1S}$ for $\rho = 1.0$ bohr has two nodal lines, which can be classified approximately as "angular," because they tend to be straight with γ approximately constant and meet at the origin N, where $\omega = 0$. This function is large at the top and bottom of the figure (viewed with N at the top), and appears symmetric across the $\gamma = \frac{\pi}{2}$ (i. e., $X_N = 0$) lines. The fifth surface function $\Phi_5^{^1S}$ has an interesting contour pattern that is caused by the near crossing of two nodal lines, one purely "radial," the other purely "angular." Asymptotically we would expect the sixth function $\Phi_6^{^1S}$ to have only two nodal lines, but since the small ρ ordering places the $4f$ function below the $3s$ in energy, it is not surprising that it has instead three "angular" nodes. As ρ increases these nodes will become obscured and lose their simple designations "radial" or "angular."

Figure 5.21 shows the $\Phi_2^{^1S}$ surface function at $\rho = 4$, 5, and $\rho = 10$ bohr, and Figure 5.22 is similar for $\Phi_3^{^1S}$. From these graphs it is apparent that as one goes out to higher ρ, the straight line node in $\Phi_2^{^1S}$ bends around, until it forms a semi-circle (for $\rho = 15$, which is not shown). The circle is however not centered around N and is therefore not truly an $\omega = \textit{constant}$ line. Likewise the radial node in $\Phi_3^{^1S}$ becomes less curved as ρ increases, but the line is not quite straight and not quite of the $\gamma = \textit{constant}$ form. As an approximate classification we nevertheless designate the nodal line in $\Phi_2^{^1S}$ at large ρ as radial, because it spans the entire range of γ

but only a small range of ω, and the nodal line in Φ_3^{1S} at large ρ as angular, since it spans a small range of γ. The Φ_2^{1S} and Φ_3^{1S} surface functions for $\rho \geq 20$ bohr are not pure $2l_1$ hydrogenic states; rather Φ_2^{1S} is approximately a 60-40 mixture of $2s$ and $2p$, and Φ_3^{1S} a 40-60 mixture of those two states. The reason is that the region of configuarion space for which $0 \leq r_1 \leq r_{1max}$ (for which the isolated H atom wavefunction is non-negligible) and $\rho >> r_{1max}$ corresponds to an electron at a large distance form an H atom, which as a result splits the l_1 degeneracy and mixes the $2s$ and $2p$ states.

The surface functions Φ_4^{1S}, Φ_5^{1S}, and Φ_6^{1S} mix and cross with higher functions at larger values of ρ. We display these functions in Figure 5.23, Figure 5.24, and Figure 5.25, respectively, for $\rho = 5$, 10, 15, and 20 bohr. As the surface functions cross, the nodal patterns change. As mentioned above Φ_6^{1S} has three angular nodes at $\rho = 1.0$, whereas Φ_7^{1S} has two radial nodes. This must mean that a surface function correlating with the $n = 4$ asymptotic state is lower in energy than the highest $n = 3$ state at $\rho = 1.0$, even though it has more nodal lines. Since the ^{1}S surface functions are symmetric across the $\omega = \frac{\pi}{2}$ line, each surface function with n_{rc} radial nodes in the quartersphere plotted has additional n_{rc} radial nodes in the lower quartersphere; therefore each radial node in the plotted surface function counts twice in the figuring of total number of nodes. Each angular node, on the other hand, is continuous across the $\omega = \frac{\pi}{2}$ division, and so counts as only one node. Asymptotically the surface functions are ordered according to number, and type, of nodal lines. Radial nodes generally produce lower energy states than angular nodes for large values of ρ which are not quite asymptotic, i. e., values of ρ for which eigenvalues corresponding to the same n have not become degenerate. The state Φ_6^{1S} with three nodal lines crosses with and becomes Φ_7^{1S} somewhere between 5 and 10 bohr. The two-radial node state eventually crosses all of these, becoming the fourth lowest state.

The ^{1}S surface functions are displayed in their asymptotic form in Figure 5.26, for which $\rho = 50$ bohr. We find that $\Phi_1^{^1S}$ is concentrated about N, and is independent of γ, with no nodes. (The zero value contour (the unlabeled one, around the perimeter) is not a real node, but merely a numerical artifact. The function is so small in this region that a small error changes the sign.) $\Phi_2^{^1S}$ and $\Phi_3^{^1S}$ each have one nodal line, as discussed above. We find that $\Phi_4^{^1S}$ has two radial nodes, $\Phi_5^{^1S}$ has the interesting pattern that occurs when one radial and one angular node cross, and $\Phi_6^{^1S}$ has two angular nodes.

The ^{3}S surface functions have one extra nodal line, compared to the singlet state, located at $\omega = \frac{\pi}{2}$. We have seen (see Fig. 5.8, for example) that the singlet eigenvalues become degenerate with the triplet at large values of ρ; the surface functions also become identical except for the added node and a change of sign for $\frac{\pi}{2} \leq \omega \leq \pi$. This is possible because the node is in a region of negligible density. Consideration of the potential energy function explains why the surface functions tend to concentrate at smaller values of ω as ρ increases. The potential takes on a cylindrical shape asymptotically, which implies that the region which is classically allowed has constant linear dimensions as ρ is increased, but the angle subtended by this region (ω) decreases as $1/\rho$.

5.3.2 J=1 surface functions

The much discussed "avoided crossing" between the second and third ^{1}P^{odd} eigenvalues (see Section 5.2.2.2 and Fig. 5.11) leads to a subsequent change in the corresponding surface functions. We demonstrate this by plotting contours of Φ_2 (^{1}P^{odd}) and Φ_3 (^{1}P^{odd}) on a plane tangent to the $OXYZ$ space $\rho = constant$ hemisphere at a point A on the OX axis (i. e., a plane perpendicular to that axis). The axes on that plane are AZ_A and AY_A which are respectively parallel to OZ and OY and we are limited to the half plane $Y_A \geq 0$ (corresponding to $0 \leq \gamma \leq \pi$).

This plane is shown in Figure 5.27. In Figure 5.28 the surface functions have been computed at $\rho = 12$ bohr, and in Figure 5.29 they have been computed at 14 bohr, while the crossing occurs at about 13.5 bohr. It is apparent from the two sets of figures that the states have crossed, albeit "avoidedly."

5.4 Basis Size

It will be useful, in this section, to refer back to Table $1-1$, which lists the hydrogen atom thresholds and the number of nl_1 states that are open within each energy range. We will refer to energies between the $n = 1$ and $n = 2$ thresholds as being in the "first" energy range, where there is one open state. The "second" energy range is between the $n = 2$ and $n = 3$ thresholds, where there are three open nl_1 states, $1s$, $2s$, and $2p$, although there are four nl_1l_2 states of the same parity of J for $J > 0$, as can be seen from Table $5-2$. Similarly we will refer to the third energy range between the $n = 3$ and $n = 4$ threshold, and the term "6-state" refers to the asymptotic open nl_1 states $1s-2s-2p-3s-3p-3d$. There are ten nl_1l_2 states in this range of the same parity as J for $J > 1$. The generalization to the higher energy ranges is evident.

5.4.1 J=0 basis

In the second and third energy ranges, we compared the $J = 0$ partial wave scattering matrix elements obtained using three different surface function sets, as shown in Table $5-5$. The $(1s \rightarrow 1s)$ probabilities and phases are converged to 1% of their value using only 6 surface functions, out of a primitive basis set of 15 functions. The off-diagonal elements are smaller, and so the relative convergence is not as good. Most of the probabilities are converged to 5% of their value with six surface functions. Using ten surface functions out of 15 primitives gives better than 1% convergence in the probabilities and 0.01 rad in the phases, at energies below the $n = 3$ threshold. At the energies above that threshold the smaller basis is

sometimes very good, but at points the probabilities can differ by 10% from the 15-state calculation. The only troublesome spots are those energies close to resonances, like 0.86 Ryd and 0.93 Ryd (see Section 6.2). One can detect the presence of the resonance at 0.86 Ryd by the 6-state calculation, but the results are not nearly as accurate as with 10 or 15 states. One doesn't expect to get good results with only six surface functions (which includes all states up to $n = 3$) at 0.93 Ryd because there is a resonance involving the $n = 4$ states at this energy and also because the cross section is changing so quickly with energy.

5.4.2 Basis for higher J

We have studied the convergence of the scattering matrix element phases with surface function basis size for $J = 2$, even parity, singlet spin, and present the results in Table $5-6$ for energies in the range 0.76 to 0.93 Ryd. The $n = 3$, 4, and 5 eigenvalues are not well separated (see Figs. 5.13 and 5.14) and crossings in the eigenvalues *vs.* ρ curves are frequent, due to the large number of states contained in the primitive basis. Therefore we did not use a subset of surface functions as a basis — each entry has the same number of surface functions as primitive functions. The bases used to test convergence were 10 functions ($n_{\max} = 3$), 19 functions ($n_{\max} = 4$) and 31 functions ($n_{\max} = 5$). Convergence to about 0.01-0.04 rad (i. e., $\sim 0.6 - 2°$) has been achieved in most cases. Naturally, the convergence is not as good at the highest energies listed in the table. Relative convergence of the diagonal element phases is about 2.5%.

The corresponding elastic cross sections, tabulated in the first and fourth colmns of Table $5-7$, are very sensitive to the phase values and are converged to about 5%. This is because, according to Eq. 3.110, the relative error in the phase is doubled in the elastic cross section, since the T-matrix is squared. Our values show that the elastic cross sections found by Burke *et al.*,[16] using six target-atom

eigenfunctions, are not converged due to too small a basis set. The 6-state close-coupling values fall somewhere in between our minimum basis (entry 'a,' 4 surface functions) and our basis 'b,' which is also a 6-state basis ($1s-2s-2p-3s-3p-3d$) involving 10 surface functions, and have been listed as entry (e). We see that the results obtained using the 6-state basis with the hyperspherical method are closer to the converged result than those obtained with a comparable number of target atom (or close-coupling) eigenfunctions.

Our $J = 2$ inelastic cross sections are well converged even with only ten surface functions, since the integral (as opposed to differential) cross section does not depend on the phase for inelastic transitions. The $^1D^{even}$ inelastic $1s \rightarrow 2s$ and $1s \rightarrow 2p$ cross sections are also tabulated in Table $5-7$ in the second and third columns. These results will be compared with other calculations in Section 6.3.

The inelastic partial cross sections we obtained for J=3, 4, and 5, which are not listed here, agree very well with the close-coupling (6-state) results published by Burke *et al.*[16] These cross sections are all very small. We found that most of our results agreed with the 6-state results of Burke *et al.* to within 0.0002 πa_0^2. In those cases where the difference was larger than 0.0002, the change was always in the same direction as and of smaller magnitude than the difference between the 3-state and 6-state close-coupling calculations.

The results for elastic cross sections present a different picture. We have tabulated these cross sections for the $^1F^{odd}$ and $^3F^{odd}$ partial waves in Table $5-8$. Our cross sections are roughly four times larger than the corresponding quantities reported by Burke *et al.*[16] for $J = 3$. The explanation for this behavior is probably that the Burke results are not converged. Those results definitely show a large change (50 to 100%) in going from the 3-state calculation to the 6-state, so convergence has not been demonstrated by those authors. Furthermore, we have

seen that with the hyperspherical basis the elastic cross sections are not converged very well by including only states up to $n = 2$, nor up to $n = 3$. However, even our minimum basis (3 nl_1 states, 4 nl_1l_2 surface functions) is "better," in the sense that it is closer to the converged-basis result, than the 6-state results of Burke *et al.*[16] It is also possible that the aforementioned (Section 4.5) projection distance problem has influenced our results.

5.4.3 Summary

The final calculations reported in this thesis (see Chapter 6) were performed using all the surface functions up to and including those with $n = 5$ for total energies below the the $n = 4$ threshold. At energies above this threshold, we usually added another level of surface functions, up to $n = 6$. Exceptions will be noted. We did not experience any serious difficulty with these basis set sizes. Representative times on a VAX 11/780–FPS164 system are given in Table $5 - 9$.

Table 5-1: Allowed l_1, l_2 values for basis functions $T_p^{Jl_2l_1}(\omega;\rho)$, for $J = 0,1,2,3$ (S,P,D,F), $\Pi = 0,1$ (even, odd).

	S^{even}	P^{even}	P^{odd}	D^{even}	D^{odd}	F^{even}	F^{odd}
$n \geq 1$	(0,0)	–	(0,1)	(0,2)	–	–	(0,3)
$n \geq 2$	(1,1)	(1,1)	(1,0)	(1,1)	(1,2)	(1,3)	(1,2)
			(1,2)	(1,3)			(1,4)
$n \geq 3$	(2,2)	(2,2)	(2,1)	(2,0)	(2,1)	(2,2)	(2,1)
			(2,3)	(2,2)	(2,3)	(2,4)	(2,3)
				(2,4)			(2,5)
$n \geq 4$	(3,3)	(3,3)	(3,2)	(3,1)	(3,2)	(3,1)	(3,0)
		(3,3)	(3,4)	(3,3)	(3,4)	(3,3)	(3,2)
				(3,5)		(3,5)	(3,4)
							(3,6)
$n \geq 5$	(4,4)	(4,4)	(4,3)	(4,2)	(4,3)	(4,2)	(4,1)
			(4,5)	(4,4)	(4,5)	(4,4)	(4,3)
				(4,6)		(4,6)	(4,5)
							(4,7)
$n \geq 6$	(5,5)	(5,5)	(5,4)	(5,3)	(5,4)	(5,3)	(5,2)
			(5,6)	(5,5)	(5,6)	(5,5)	(5,4)
				(5,7)		(5,7)	(5,6)
							(5,8)

Table 5-2: Total number of primitive basis functions for each spin by symmetry type and corresponding naximum number of surface functions.[a]

		S	P	D	F	G	H	J	Highest nl_1	Total
n_{max}=1	even	1	0	1	0	1	0	1	$1s$	1
	odd	0	1	0	1	0	1	0		
n_{max}=2	even	3	1	4	1	4	1	4	$2p$	3
	odd	0	4	1	4	1	4	1		
n_{max}=3	even	6	3	10	4	10	4	10	$3d$	6
	odd	0	9	4	10	4	10	4		
n_{max}=4	even	10	6	19	10	20	10	20	$4f$	10
	odd	0	16	9	20	10	20	10		
n_{max}=5	even	15	10	31	19	35	20	35	$5g$	15
	odd	0	25	16	34	20	35	20		
n_{max}=6	even	21	15	46	31	55	35	56	$6h$	21
	odd	0	36	25	52	34	56	35		
n_{max}=7	even	28	21	64	46	80	55	84	$7i$	28
	odd	0	49	36	74	52	83	56		

[a] A scattering calculation using the maximum number of surface functions given in this table is called an i−state calculation where i is the number given in the last column.

Table 5-3: Grid points used to obtain primitive one-dimensional basis functions.

When $l_1 = 0$:

Region	Point number	from ω_{min} (rad)	to ω_{max} (rad)	Spacing $\Delta\omega$ (rad)	Extent of region (rad)
1	1 - 50	0.000200	0.010000	2.00E-4	0.0098
2	50 - 80	0.010000	0.028974	6.32E-4	0.0190
3	80 - 110	0.028974	0.128974	3.33E-3	0.100
4	110- 140	0.128974	0.580796	1.51E-2	0.452
5	140- 170	0.580796	1.570796	3.24E-2	0.990

When $l_1 \neq 0$:

Region	Point number	from ω_{min} (rad)	to ω_{max} (rad)	Spacing $\Delta\omega$ (rad)	Extent of region (rad)
1	1 - 31	0.000954	0.029554	9.54E-4	0.0286
2	31 - 61	0.029554	0.129554	3.33E-3	0.100
3	61 - 91	0.129554	0.581376	1.51E-2	0.452
4	91 - 120	0.581376	1.570796	3.36E-2	0.990

Table 5-4: ^{1}S Jacobi polynomial eigenvalues and the asymptotic states to which they correlate.

λ	$\lambda(\lambda+4)$	$2\rho^2\epsilon + \frac{15\hbar^2}{8\mu\rho^2}$	(l_1, l_2)	nl_1
		$\rho = 0.1$		
0	0	3.3	(0,0)	$1s$
2	12	15.4	(1,1)	$2p$
4	32	35.0	(0,0)	$2s$
		35.5	(2,2)	$3d$
6	60	63.2	(1,1)	$3p$
		63.5	(3,3)	$4f$
8	96	98.7	(0,0)	$3s$
		99.2	(2,2)	$4d$
		99.5	(3,3)	$5g$
10	140	142.8	(1,1)	$4p$
		143.2	(3,3)	$5f$
12	192	194.3	(0,0)	$4s$
		194.8	(2,2)	$5d$
14	252	254.2	(1,1)	$5p$
16	320	321.0	(0,0)	$5s$

Table 5-5: Convergence of ^{1}S scattering matrix *vs.* number of surface functions.[a]

E/Ryd	$\lvert S_{11}^b\rvert^2$	ϕ_{11}(rad)	$\lvert S_{21}\rvert^2$	ϕ_{21}(rad)	$\lvert S_{31}\rvert^2$	ϕ_{31}(rad)
0.76	0.79438	1.6946	0.12391	−0.4395	0.08200	−2.1357
	0.78660	1.7132	0.12759	−0.4972	0.08586	−2.2081
	0.78690	1.7213	0.12640	−0.5122	0.08769	−2.2216
0.78	0.75952	1.6960	0.15335	−1.5815	0.08667	−3.0749
	0.75725	1.7086	0.15142	−1.5889	0.09233	−3.0867
	0.75684	1.7177	0.15053	−1.5981	0.09242	−3.0948
0.81	0.72116	1.6621	0.20904	−2.1947	0.07058	2.5241
	0.72134	1.6774	0.20747	−2.1921	0.07240	2.5262
	0.72197	1.6873	0.20788	−2.1910	0.07086	2.5250
0.83	0.71690	1.6339	0.20478	−2.3958	0.07804	2.5241
	0.71637	1.6500	0.20530	−2.3797	0.07930	2.2088
	0.71635	1.6598	0.20460	−2.3767	0.07881	2.2150
0.86	0.97546	1.7275	0.00959	−3.0617	0.01468	−0.8591
	0.92064	1.6423	0.06224	−2.2640	0.01491	3.1386
	0.91313	1.6487	0.06880	−2.2557	0.01747	3.0400
0.90	0.72296	1.6012	0.13780	−2.9926	0.07000	1.5008
	0.70491	1.6311	0.15032	−2.9634	0.06334	1.4216
	0.70075	1.6375	0.15052	−2.9670	0.07156	1.4610
0.93	0.66242	1.5614	0.15262	3.0329	0.09831	1.3004
	0.66216	1.6107	0.16222	3.1054	0.08232	1.1280
	0.63749	1.6201	0.15802	3.1128	0.09248	1.3782

[a] Projection was done at ρ=50 bohr. For each energy, the first entry has 6 surface functions, the second 10, and the third 15; all calculations used the same 15 primitive basis functions.

[b] The first index refers to the initial state, the second to the final state. 1, 2, and 3 refer to 1*s*, 2*s*, and 2*p*, respectively.

Table 5-6: Convergence of $^1D^{even}$ scattering matrix phases *vs.* number of surface functions.[a]

E/Ryd	ϕ^b_{11}(rad)	ϕ_{21}(rad)	ϕ_{31}(rad)	ϕ_{41}(rad)
0.76	0.203	2.869	1.502	0.908
	0.216	2.832	1.474	0.868
	0.222	2.813	1.462	0.846
0.78	0.213	2.536	0.836	0.978
	0.227	2.517	0.826	0.951
	0.233	2.509	0.823	0.943
0.81	0.222	2.237	0.360	1.000
	0.237	2.240	0.366	1.002
	0.244	2.240	0.368	1.002
0.83	0.223	2.162	0.182	1.076
	0.239	2.176	0.196	1.087
	0.246	2.179	0.200	1.092
0.86	0.210	2.249	0.119	1.404
	0.225	2.321	0.171	1.473
	0.232	2.249	0.178	1.482
0.90	0.210	2.070	−0.125	1.433
	0.226	2.176	−0.063	1.615
	0.210	2.186	−0.054	1.622
0.93	0.210	1.959	−0.267	1.435
	0.231	1.976	−0.235	1.498
	0.239	2.017	−0.216	1.525

[a] Projection was done at ρ=50 bohr. For each energy, the first entry has 10 surface functions/10 primitive functions, the second 19/19, and the third 31/31.

[b] The first index refers to the initial state, the second to the final state. 1, 2, 3, and 4 refer to the sets of quantum numbers nl_1l_2= 1*s*2, 2*s*2, 2*p*1, and 2*p*3, respectively.

Table 5-7: $^1D^{even}$ and $^3D^{even}$ contributions to total cross section (units of πa_0^2).

E		$Q^{^1D^e}_{1s\rightarrow 1s}$	$Q^{^1D^e}_{1s\rightarrow 2s}$	$Q^{^1D^e}_{1s\rightarrow 2p}$	$Q^{^3D^e}_{1s\rightarrow 1s}$
0.76 Ryd	(*a*)	0.0468	0.0501	0.0863	0.1047
	(*b*)	0.0676	0.0484	0.0894	0.1714
	(*c*)	0.0762	0.0457	0.0870	0.1964
	(*d*)	0.0803	0.0451	0.0866	0.2081
	(*e*)	0.042	0.0540	0.0914	0.097
0.78 Ryd	(*a*)	0.0457	0.0507	0.1008	0.0992
	(*b*)	0.0722	0.0491	0.0930	0.1687
	(*c*)	0.0818	0.0484	0.0934	0.1945
	(*d*)	0.0863	0.0482	0.0934	0.2066
	(*e*)	0.050	0.0555	0.0937	0.101
0.83 Ryd	(*a*)	0.0439	0.0508	0.1396	0.0882
	(*b*)	0.0766	0.0608	0.1362	0.1646
	(*c*)	0.0869	0.0599	0.1361	0.1924
	(*d*)	0.0916	0.0597	0.1359	0.2054
	(*e*)	0.058	0.0624	0.1430	0.106
0.86 Ryd	(*a*)	0.0415	0.0484	0.1553	0.0830
	(*b*)	0.0693	0.0697	0.1704	0.1623
	(*c*)	0.0777	0.0702	0.1725	0.1910
	(*d*)	0.0822	0.0700	0.1721	0.2045
	(*e*)	0.052	0.0810	0.1679	0.106
0.90 Ryd	(*b*)	0.0660	0.0474	0.1485	0.1569
	(*c*)	0.0739	0.0395	0.1318	0.1868
	(*d*)	0.0787	0.0402	0.1330	0.2008
	(*e*)	0.053	0.0510	0.1481	0.109
0.93 Ryd	(*b*)	0.0651	0.0415	0.1508	0.1542
	(*c*)	0.0751	0.0295	0.1203	0.1844
	(*d*)	0.0793	0.0286	0.1153	0.1994
	(*e*)	0.051	0.0352	0.1332	0.112

(*a*) 4 surface- (and primitive) functions, (*b*) 10 functions, (*c*) 19 functions, (*d*) 31 functions. Projection done at same distance (50 bohr) for all calculations. (e) 6-state results from reference no. 16.

Table 5-8: $^1F^{odd}$ and $^3F^{odd}$ contributions to total $1s \rightarrow 1s$ cross section.

	$Q^{^1F^\circ}_{1s\rightarrow 1s}$		$Q^{^3F^\circ}_{1s\rightarrow 1s}$
		E = 0.76 Ryd	
(*a*)	0.0115		0.0339
(*b*)	0.0188		0.0579
(*c*)	0.0244		0.0753
(*d*)	0.0274		0.0844
(*e*)	0.007		0.022
		E = 0.81 Ryd	
(*a*)	0.0098		0.0287
(*b*)	0.0179		0.0546
(*c*)	0.0243		0.0742
(*d*)	0.0276		0.0842
(*e*)	0.008		0.024
		E = 0.83 Ryd	
(*a*)	0.0090		0.0260
(*b*)	0.0173		0.0517
(*c*)	0.0239		0.0718
(*d*)	0.0273		0.0820
(*e*)	0.008		0.025
		E = 0.85 Ryd	
(*a*)	0.0083		0.0235
(*b*)	0.0168		0.0490
(*c*)	0.0236		0.0696
(*d*)	0.0272		0.0800
(*e*)	0.009		0.025

(*a*) 3-state calculation (4 surface functions), (*b*) 6-state calculation (10 functions), (*c*) 10-state calculation (20 functions), (*d*) 15-state calculation (34 functions). Number of primitive functions equals number of surface functions. Projection done at $\rho = 50$ bohr.

(*e*) 6-state close-coupling calculation, ref. 16.

Table 5-9: Times for different J.

	# states	each E (sec)	surf. func. (min)
^1S, ^3S	15	20	18
P^{odd}	25	90	19
$^1D^{even}$, $^3D^{even}$	31	130	47
F^{odd}	34	190	32

The odd parity states combine one set of spinless basis functions to obtain both singlet and triplet, which shortens the amount of time needed to obtain surface functions.

5.5 References

1. P. G. Burke and K. Smith, *Rev. Mod. Phys.*, **34**, 458 (1962).
2. J. Hata, L. A. Morgan and M. R. C. McDowell, *J. Phys. B*, **13**, L347 (1980).
3. A. Ralston and P. Rabinowitz, A First Course in Numerical Analysis (McGraw-Hill, New York, 1978), 2nd ed., pp. 73-78.
4. a) C. D. Lin, *Phys. Rev. A*, **12**, 493 (1975); b) C. D. Lin, *Phys. Rev. Lett.*, **35**, 1150 (1975); c) C. D. Lin, *Phys. Rev. A*, **14**, 30 (1976).
5. H. Klar and M. Klar, *Phys. Rev. A*, **17**, 1007 (1978).
6. a) Yu. A. Simonov, *Yad. Fiz.*, **3**, 630 (1966); b) P. M. Morse and H. Feshbach, Methods of Theoretical Physics (McGraw-Hill, New York, 1953), p. 1730; c) F. T. Smith, *Phys. Rev.*, **120**, 1058 (1960).
7. a) D. R. Herrick, *Phys. Rev. A*, **17**, 1 (1978); b) D. R. Herrick and M. E. Kellman, *Phys. Rev. A*, **21**, 418 (1980); c) M. E. Kellman and D. R. Herrick, *Phys. Rev. A*, **22**, 1536 (1980).
8. C. D. Lin, *Phys. Rev. A*, **29**, 1019 (1984).
9. J. W. Cooper, U. Fano, and F. Prats, *Phys. Rev. Lett.*, **10**, 518 (1963).
10. H. Klar and M. Klar, *J. Phys. B*, **13**, 1057 (1980).
11. J. Callaway, *Phys. Lett.*, **81A**, 495 (1981).
12. M. E. Hamm, R. W. Hamm, J. Donahue, P. A. M. Gram, J. C. Pratt, M. A. Yates, R. D. Bolton, D. A. Clark, H. C. Bryant, C. A. Frost, and W. W. Smith, *Phys. Rev. Lett.*, **43**, 1715 (1979).
13. a) D. Herrick and O. Sinanoğlu, *Phys. Rev. A*, **11**, 97 (1975); b) D. M. Herrick, *Phys. Rev. A*, **12**, 413 (1975).
14. R. T. Pack, *J. Chem. Phys.*, **60**, 633 (1974).
15. C. D. Lin, *Phys. Rev. A*, **25**, 76 (1982).
16. P. G. Burke, S. Ormonde and W. Whitaker, *Proc. Phys. Soc.*, **92**, 319 (1967).

5.6 Figures and Captions

FIG. 5.1: Effective potential $V_{\rm eff}^{Jl_2l_1}$ vs. ω, for ρ=1 (solid line), 5 (dotted line), 10 (dot-dash line), and 20 bohr (dash line), where $J = 0$, and $l_1 = l_2 = 0$.

FIG. 5.2: Effective potential $V_{\rm eff}^{Jl_2l_1}$ vs. ω, for same values of ρ as in Figure 5.1, with $J = 0$, and $l_1 = l_2 = 1$.

FIG. 5.3: Effective potential $V_{\rm eff}^{Jl_2l_1}$ vs. ω, for ρ=5 (dotted line), 10 (dot-dash line), 20 (dash line), and 40 bohr (dash-dot-dot line), with $J = 1$, and $l_1 = 0$, and $l_2 = 1$.

FIG. 5.4: Effective potential as in Figure 5.3, for $J = 1$, and $l_1 = 1$, and $l_2 = 2$.

FIG. 5.5: The three lowest antisymmetric ^{3}S 1-dimensional eigenfunctions $T_p^{Jl_2l_1}(\omega;\rho)$ corresponding to the potential in Figure 5.1. The line types are the same as in Figure 5.1. Only half the range of ω is shown.

FIG. 5.6: The three lowest antisymmetric ^{1}S 1-dimensional eigenfunctions $T_p^{Jl_2l_1}(\omega;\rho)$ corresponding to the potential in Figure 5.2. The line types are the same as in Figure 5.2. Only half the range of ω is shown.

FIG. 5.7: The 1-dimensional $\mathrm{P^{odd}}$ eigenfunctions $T_p^{Jl_2l_1}(\omega;\rho)$ corresponding to the lowest three eigenvalues of the potential in Figure 5.3. The line types are the same as in Figure 5.3, with the addition of the solid line for $\bar{\rho} = 1$ bohr.

FIG. 5.8: Lowest eigenvalue $\epsilon_i^{JS\Pi}(\rho) + \frac{15\hbar^2}{8\mu\rho^2}$ converging to $n = 1$ level for total orbital angular momentum $J = 0, 1, 2$ and 3 and singlet and triplet spins as a function of hyperradius ρ. The singlet and triplet become undistinguishable for $J \geq 2$, within plotting accuracy.

FIG. 5.9: ^{1}S surface eigenvalues converging to n=2, 3, and 4 levels versus ρ, obtained with a basis set of 15 primitive functions.

FIG. 5.10: ^{3}S surface eigenvalues converging to n=2, 3, and 4 levels versus ρ obtained with a basis set of 15 primitive functions.

FIG. 5.11: $^1P^{odd}$ and $^3P^{even}$ eigenvalue curves converging to the $n = 2$ levels asymptotically, obtained with a basis set of 25 and 15 primitive functions, respectively. The full curves correspond to $^1P^{odd}$ and the dashed to $^3P^{even}$.

FIG. 5.12: $^3P^{odd}$ and $^1P^{even}$ eigenvalue curves converging to the $n = 2$ levels asymptotically, obtained with a basis set of 25 and 15 primitive functions, respectively. The full curves correspond to $^3P^{odd}$ and the dashed to $^1P^{even}$.

FIG. 5.13: $^1D^{even}$ eigenvalue curves converging to the $n = 2$ and $n = 3$ levels asymptotically, obtained with a basis set of 31 primitive functions.

FIG. 5.14: $^3D^{even}$ eigenvalue curves converging to the $n = 2$ and $n = 3$ levels asymptotically, obtained with a basis set of 31 primitive functions.

FIG. 5.15: $^1P^{odd}$ eigenvalue curves converging to the $n = 3$ and $n = 4$ levels asymptotically, obtained with a basis set of 25 primitive functions.

FIG. 5.16: $^3P^{odd}$ eigenvalue curves converging to the $n = 3$ and $n = 4$ levels asymptotically, obtained with a basis set of 25 primitive functions.

FIG. 5.17: $^1F^{odd}$ eigenvalue curves converging to the $n = 3$ and $n = 4$ levels asymptotically, obtained with a basis set of 34 primitive functions.

FIG. 5.18: $^3F^{odd}$ eigenvalue curves converging to the $n = 3$ and $n = 4$ levels asymptotically, obtained with a basis set of 34 primitive functions.

FIG. 5.19: Projection plane tangent at north pole.

FIG. 5.20: Contours of the lowest six ^{1}S surface functions at $\rho = 1$ bohr projected onto a plane tangent to the northern quartersphere at a point on the Z-axis. (a) Φ_1^{1S}, Φ_2^{1S}, and Φ_3^{1S}. (b) Φ_4^{1S}, Φ_5^{1S}, and Φ_6^{1S}.

FIG. 5.21: Contours of the second lowest ^{1}S surface function, $\Phi_2^{^1S}$, at ρ=4, 5, and 10 bohr on a plane tangent at N.

FIG. 5.22: Contours of the third lowest ^{1}S surface function, $\Phi_3^{^1S}$, at ρ=4, 5, and 10 bohr on a plane tangent at N.

FIG. 5.23: Contours of the fourth lowest ^{1}S surface function, $\Phi_4^{^1S}$, at ρ=5, 10, 15 and 20 bohr on a plane tangent at N.

FIG. 5.24: Contours of the second lowest ^{1}S surface function, $\Phi_5^{^1S}$, at ρ=5, 10, 15 and 20 bohr on a plane tangent at N.

FIG. 5.25: Contours of the second lowest ^{1}S surface function, $\Phi_6^{^1S}$, at ρ=5, 10, 15 and 20 bohr on a plane tangent at N.

FIG. 5.26: Contours of the lowest six ^{1}S surface functions projected onto a at $\rho = 50$ bohr on a plane tangent at N.

FIG. 5.27: Projection plane perpendicular to OX axis.

FIG. 5.28: Contours $F_{i\Omega}^{JS\Pi}(\omega,\gamma;\rho)$ of $^1\mathrm{P}^{\mathrm{odd}}$ surface functions on the AY_AZ_A plane of Fig. 5.27 at $\rho = 12$ bohr, for $i = 2,3$ and $\Omega = 0,1$: (a) $F_{2\Omega}^{^1\mathrm{P}^{\mathrm{odd}}}$; (b) $F_{3\Omega}^{^1\mathrm{P}^{\mathrm{odd}}}$.

FIG. 5.29: Contours $F_{i\Omega}^{JS\Pi}(\omega,\gamma;\rho)$ of $^1\mathrm{P}^{\mathrm{odd}}$ surface functions on the AY_AZ_A plane of Fig. 5.27 at $\rho = 14$ bohr, for $i = 2,3$ and $\Omega = 0,1$: (a) $F_{2\Omega}^{^1\mathrm{P}^{\mathrm{odd}}}$; (b) $F_{3\Omega}^{^1\mathrm{P}^{\mathrm{odd}}}$.

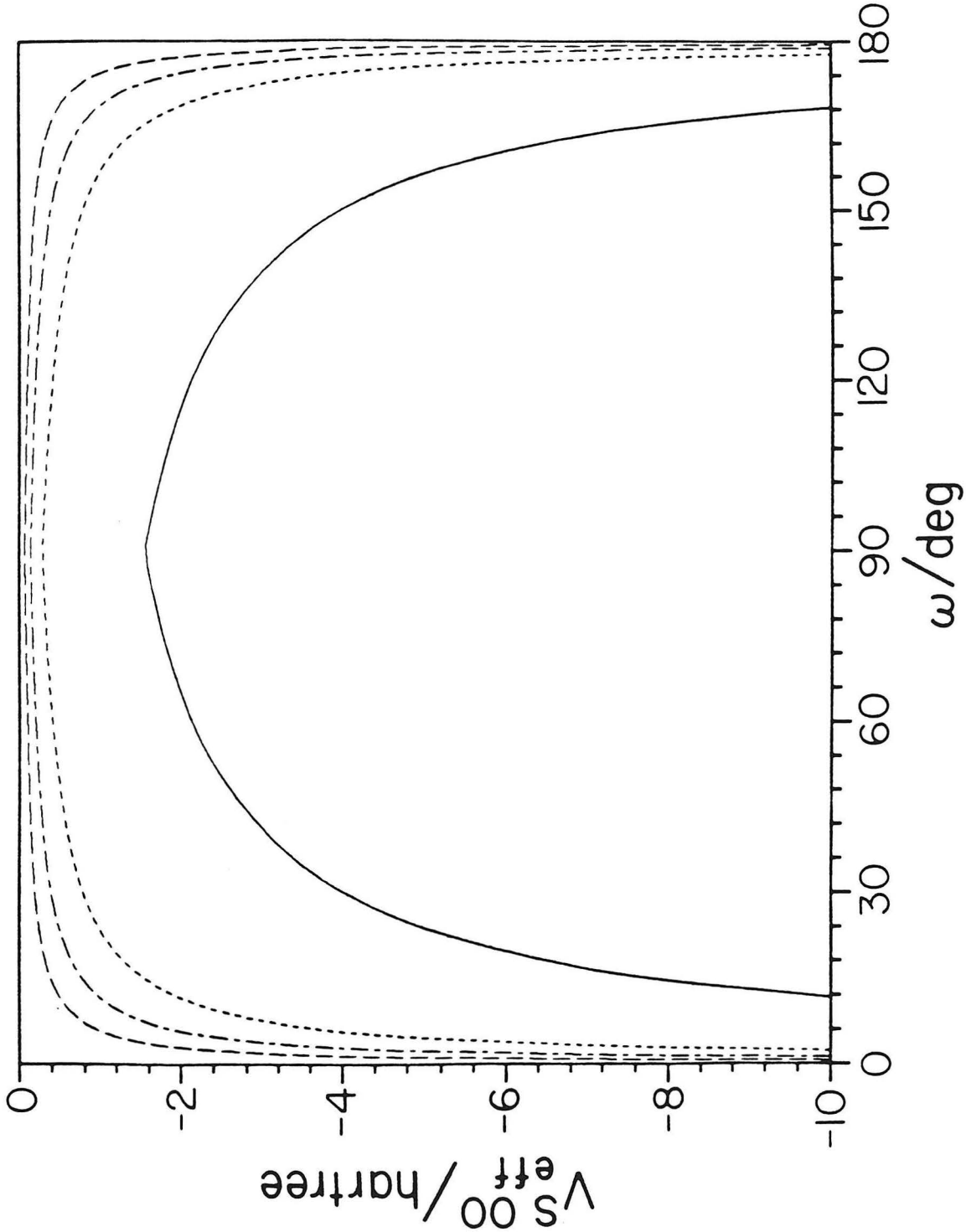

Figure 5.1

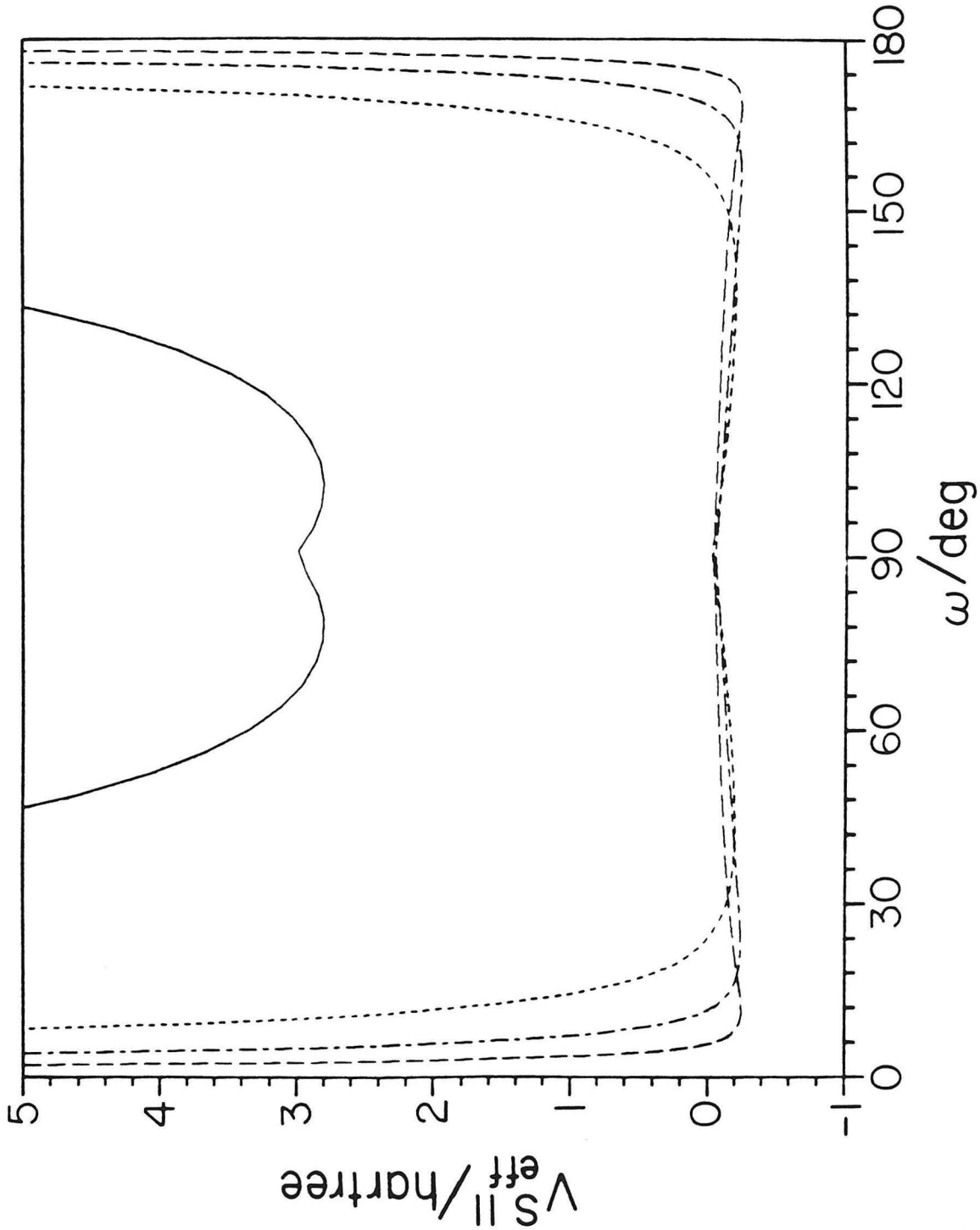

Figure 5.2

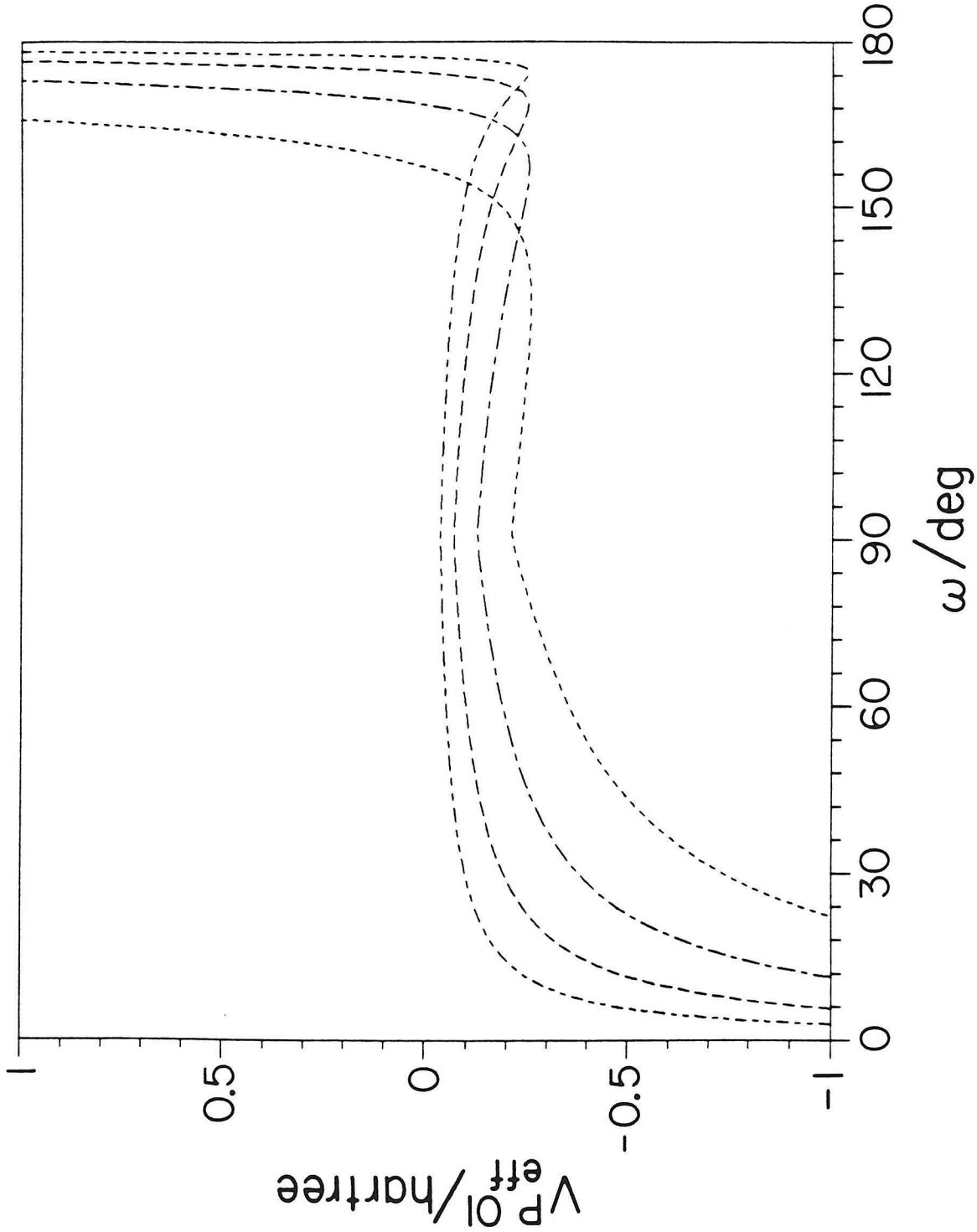

Figure 5.3

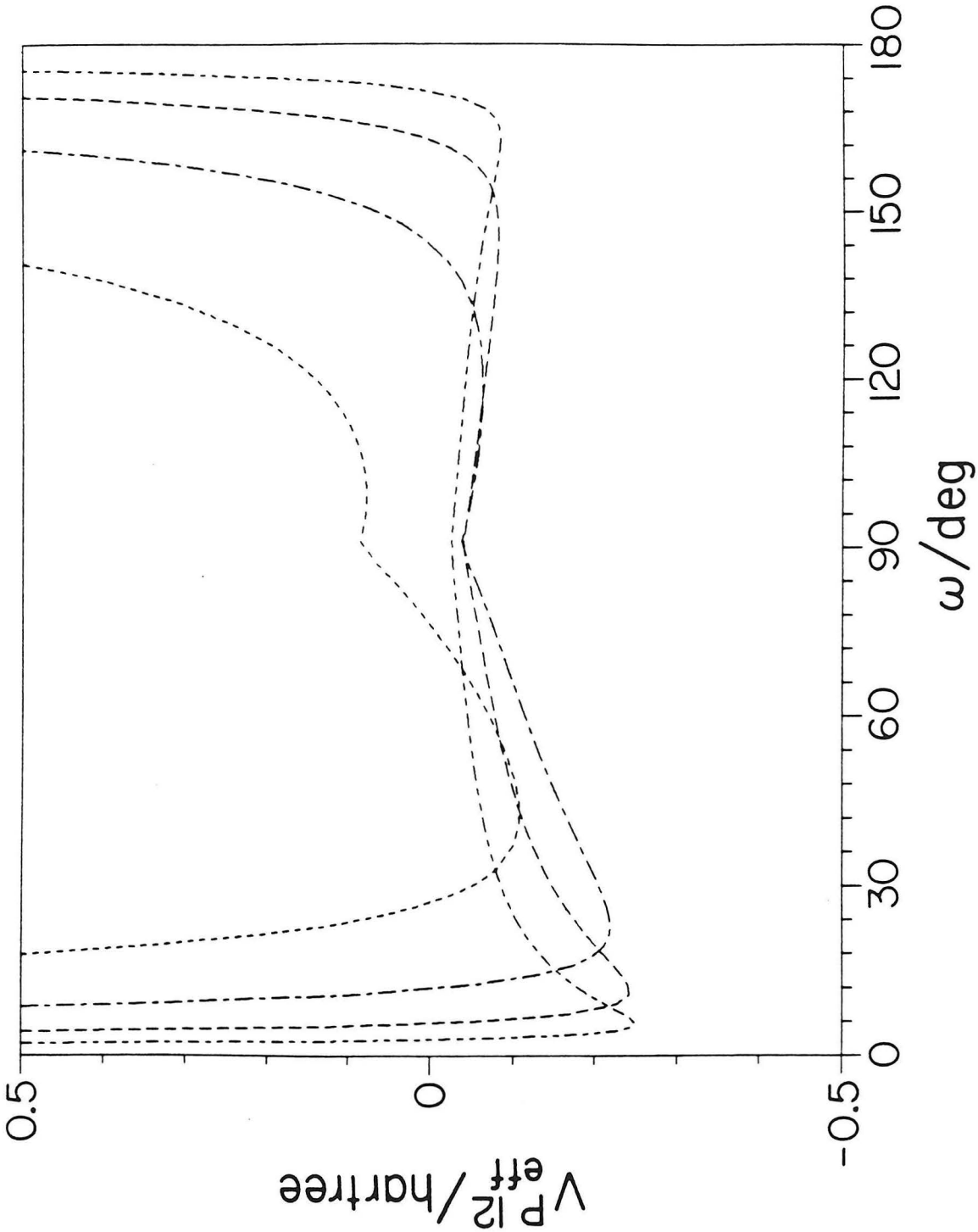

Figure 5.4

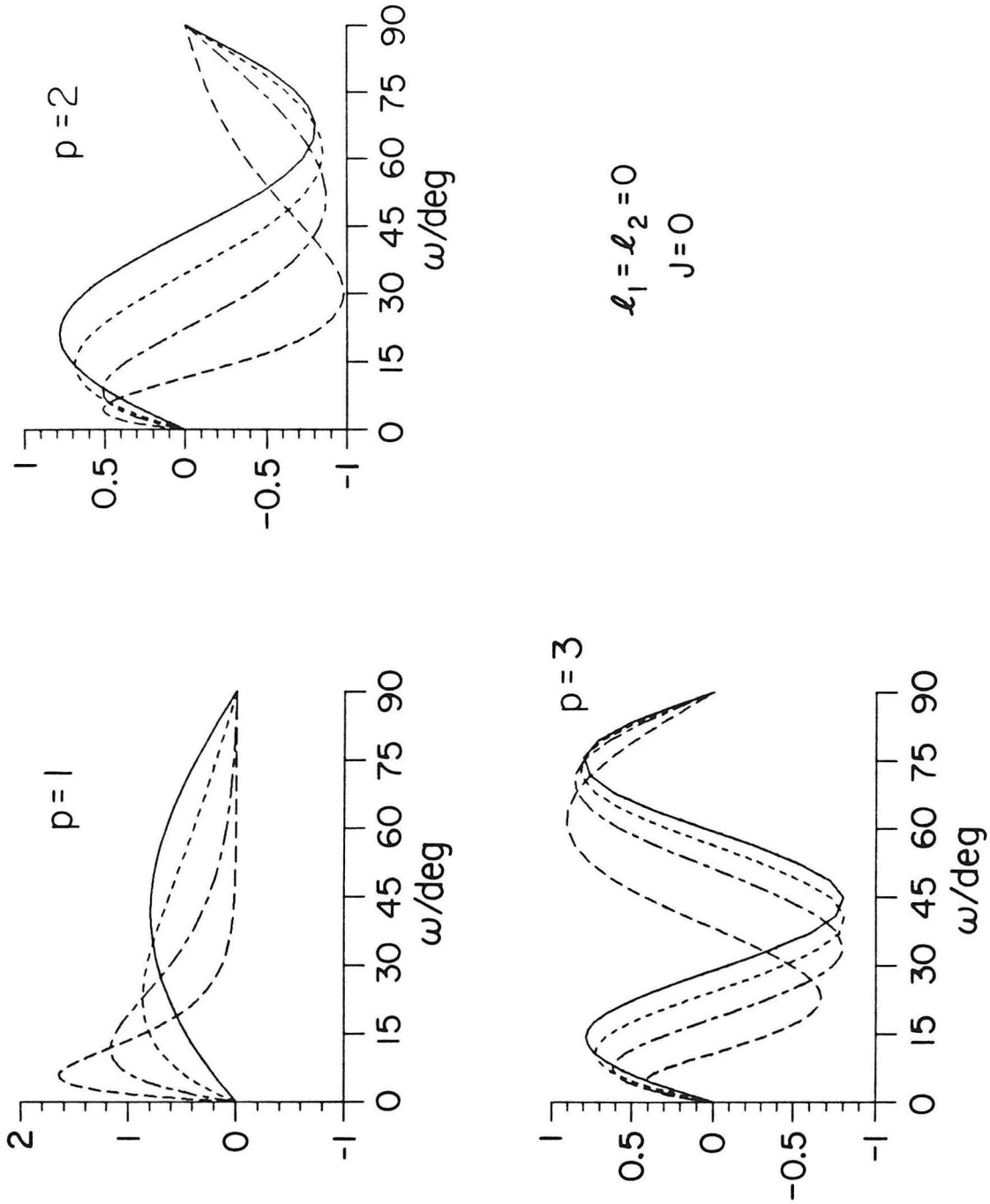

Figure 5.5

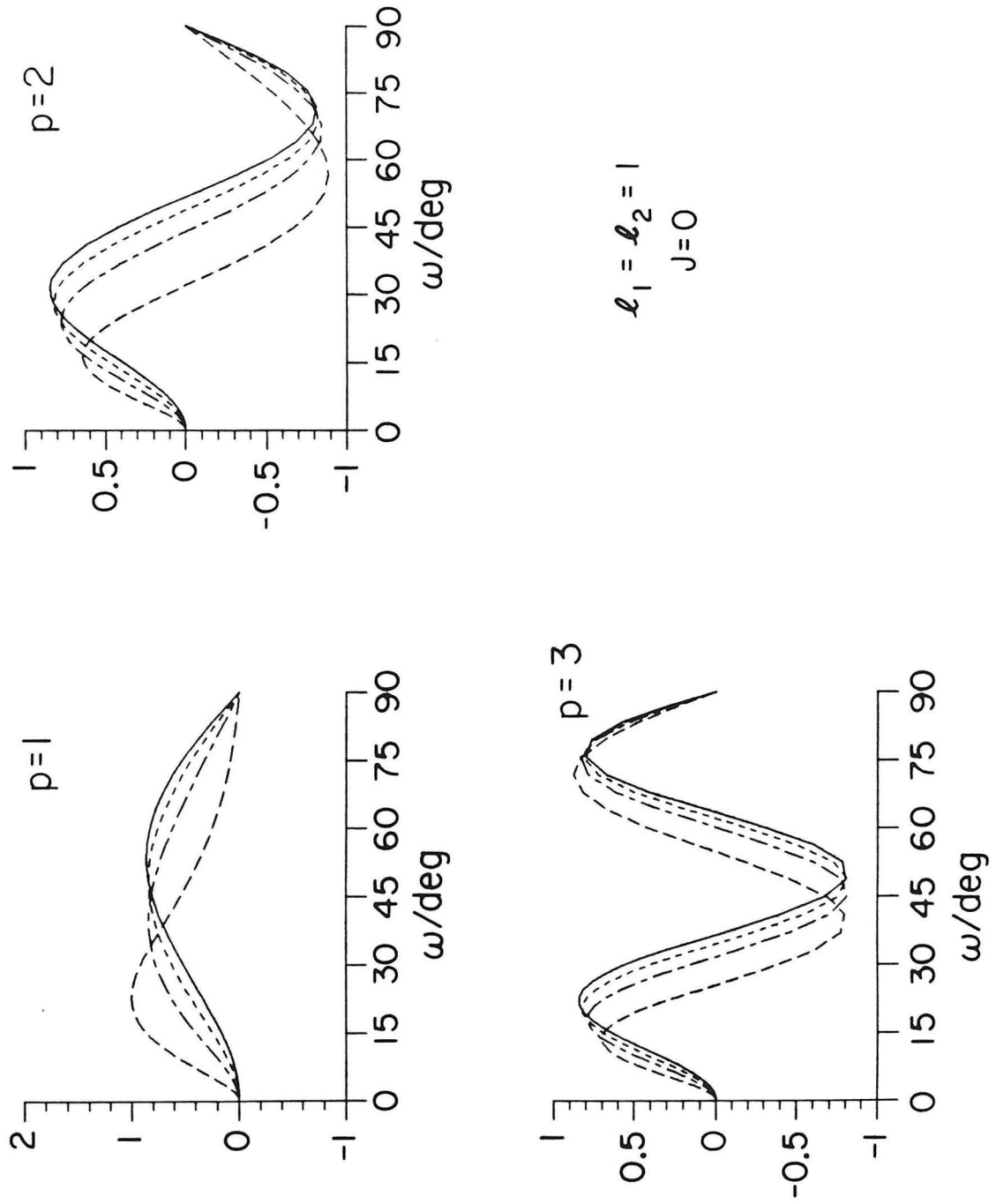
p=2
p=1
p=3
$\ell_1 = \ell_2 = 1$
J=0
ω/deg
ω/deg
ω/deg
2
1
0.5
0
-0.5
-1
0
15
30
45
60
75
90

Figure 5.6

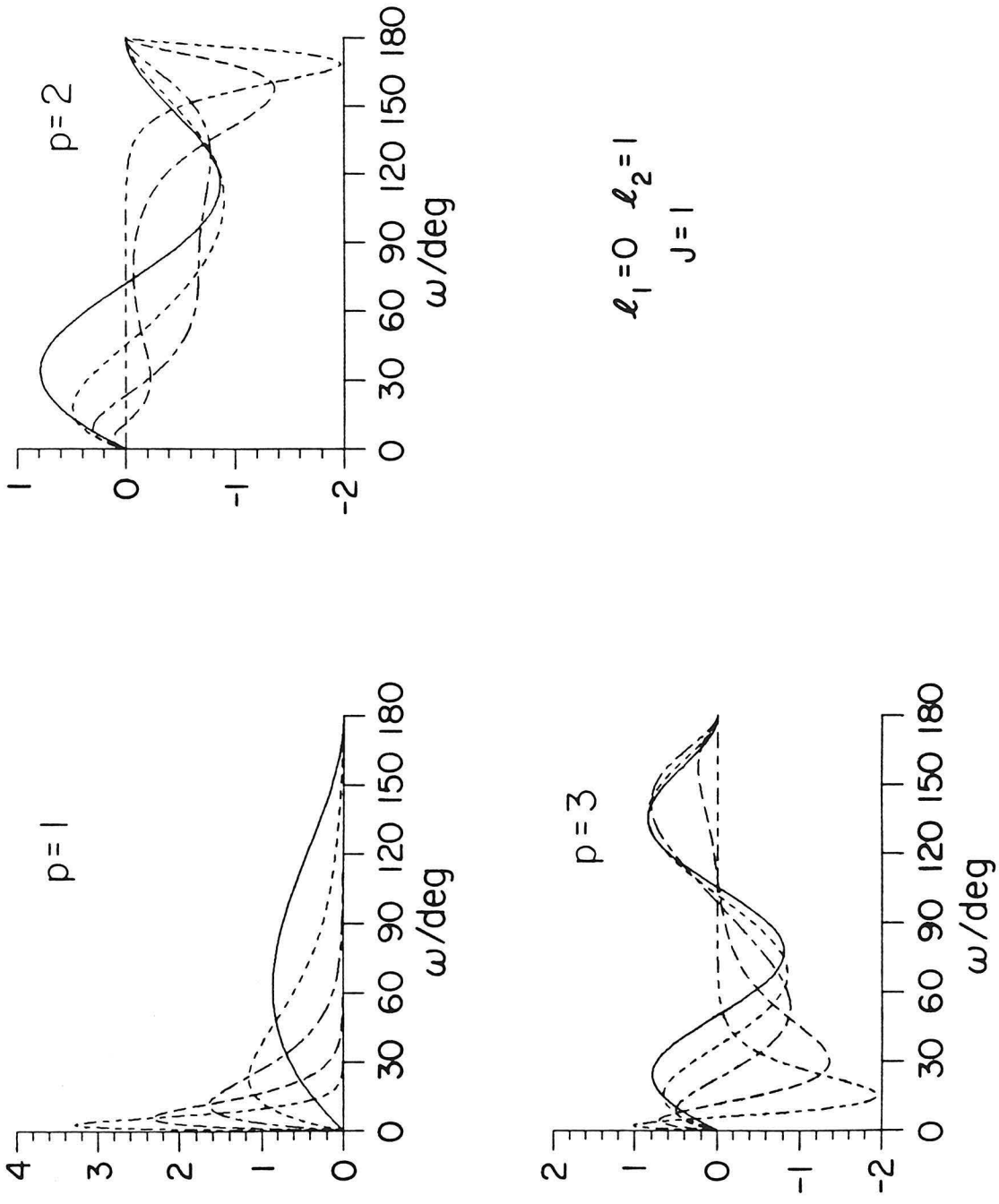
p=2
p=1
p=3
$\ell_1=0$ $\ell_2=1$
J=1
ω/deg
0 30 60 90 120 150 180
1
0
-1
-2
4
3
2
1
0
2
1
0
-1
-2

Figure 5.7

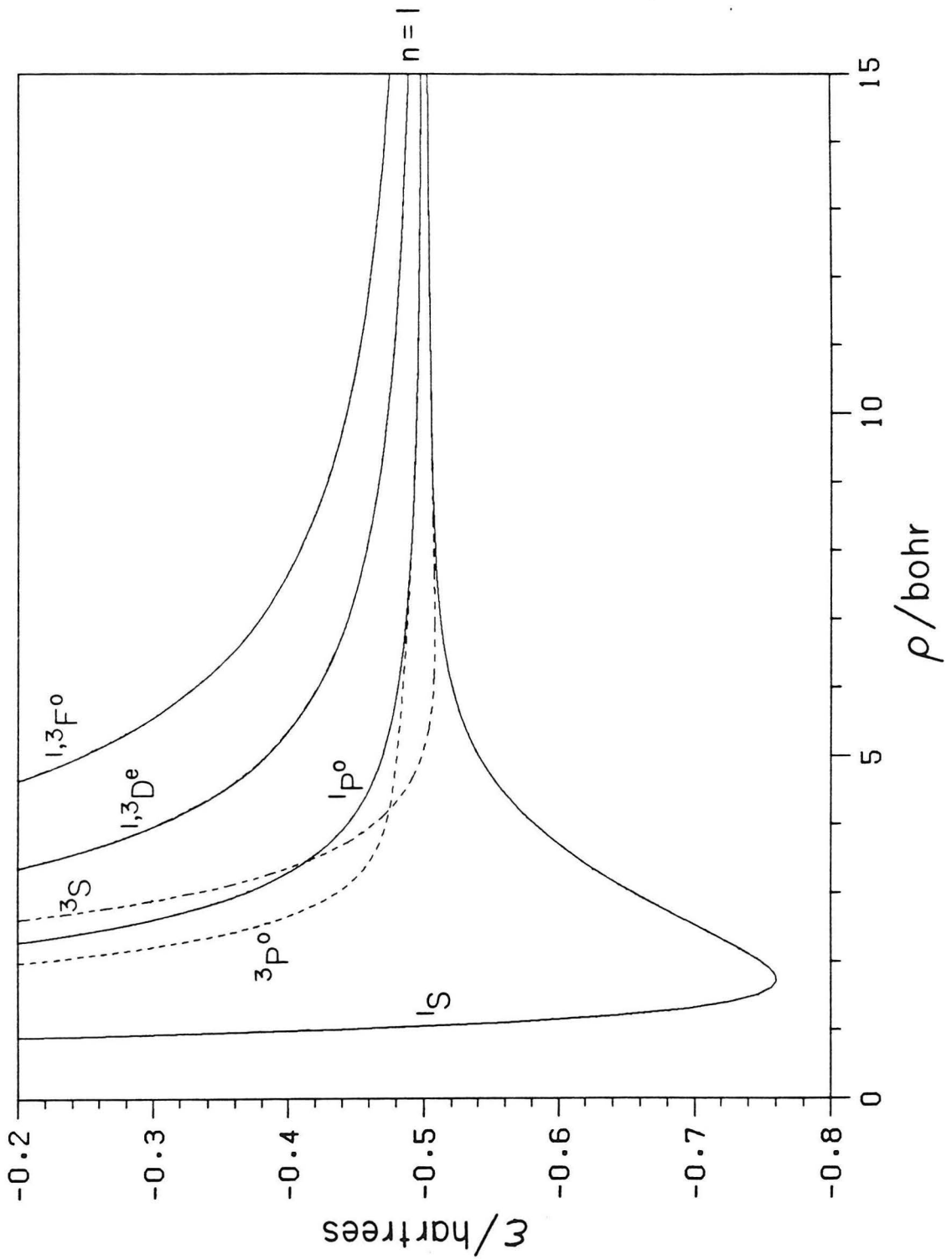
n = 1
$^{1,3}F^o$
$^{1,3}D^e$
$^1P^o$
^3S
$^3P^o$
^1S
-0.2
-0.3
-0.4
-0.5
-0.6
-0.7
-0.8
ε/hartrees
0
5
10
15
ρ/bohr

Figure 5.8

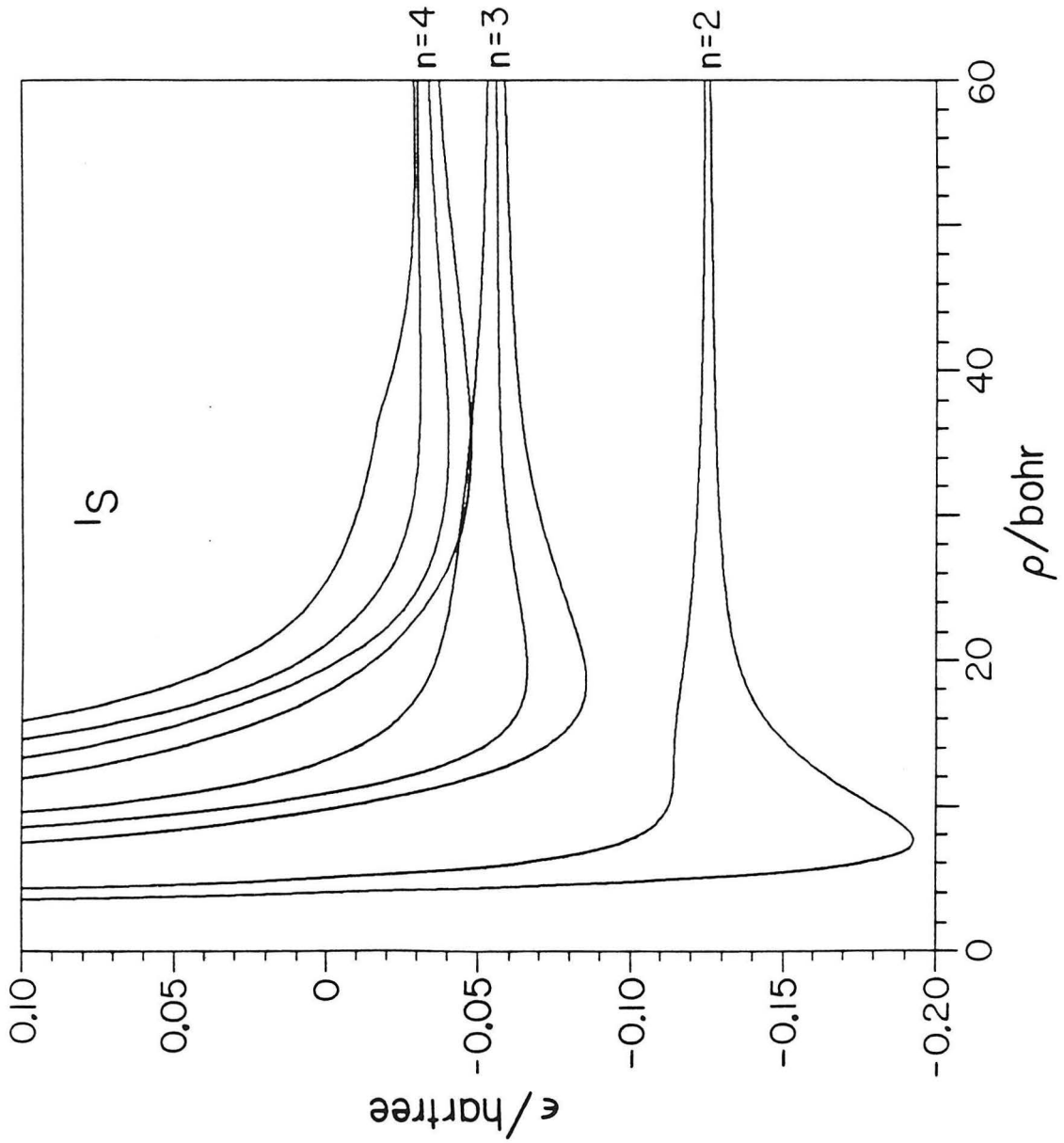

Figure 5.9

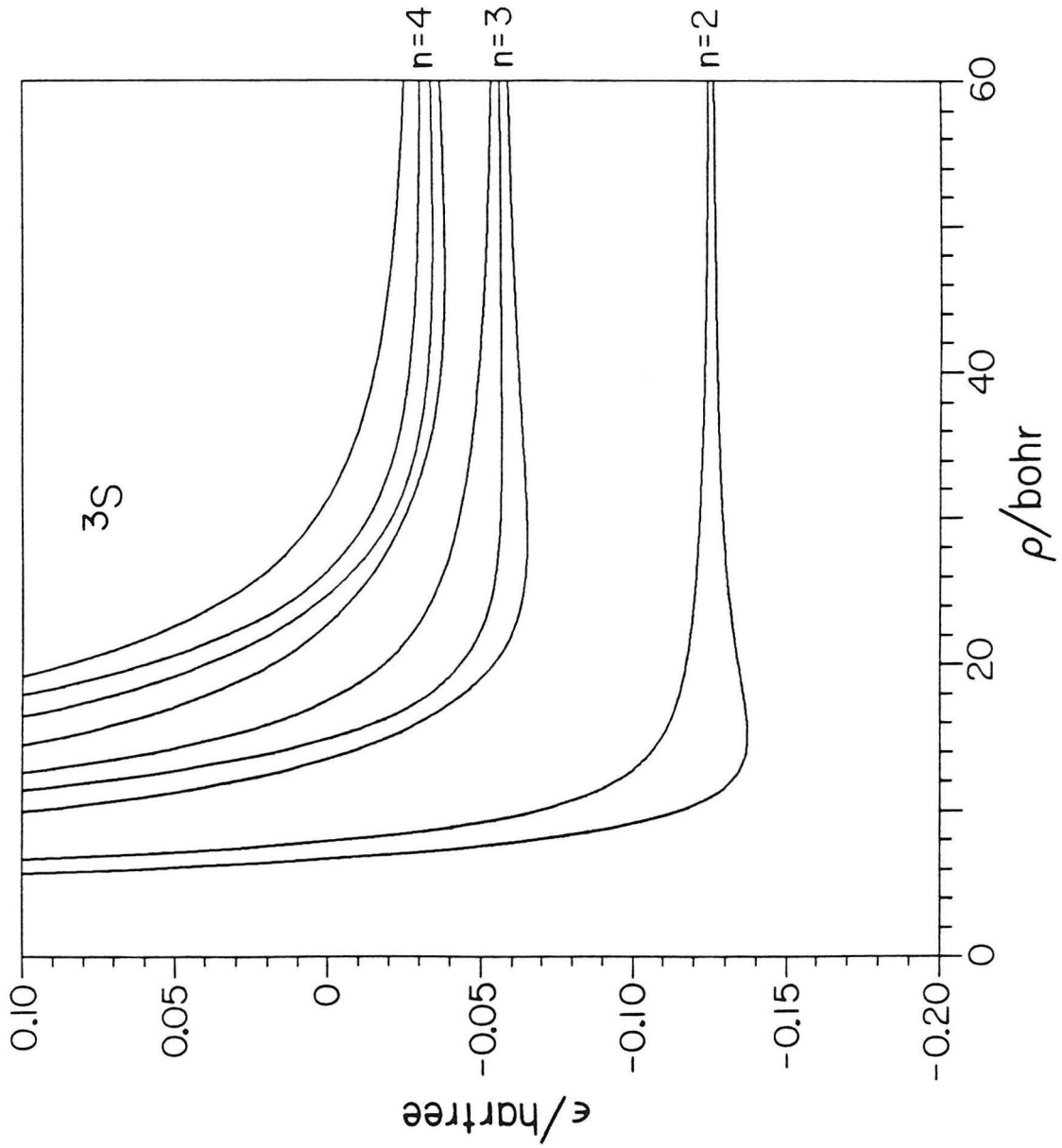

Figure 5.10

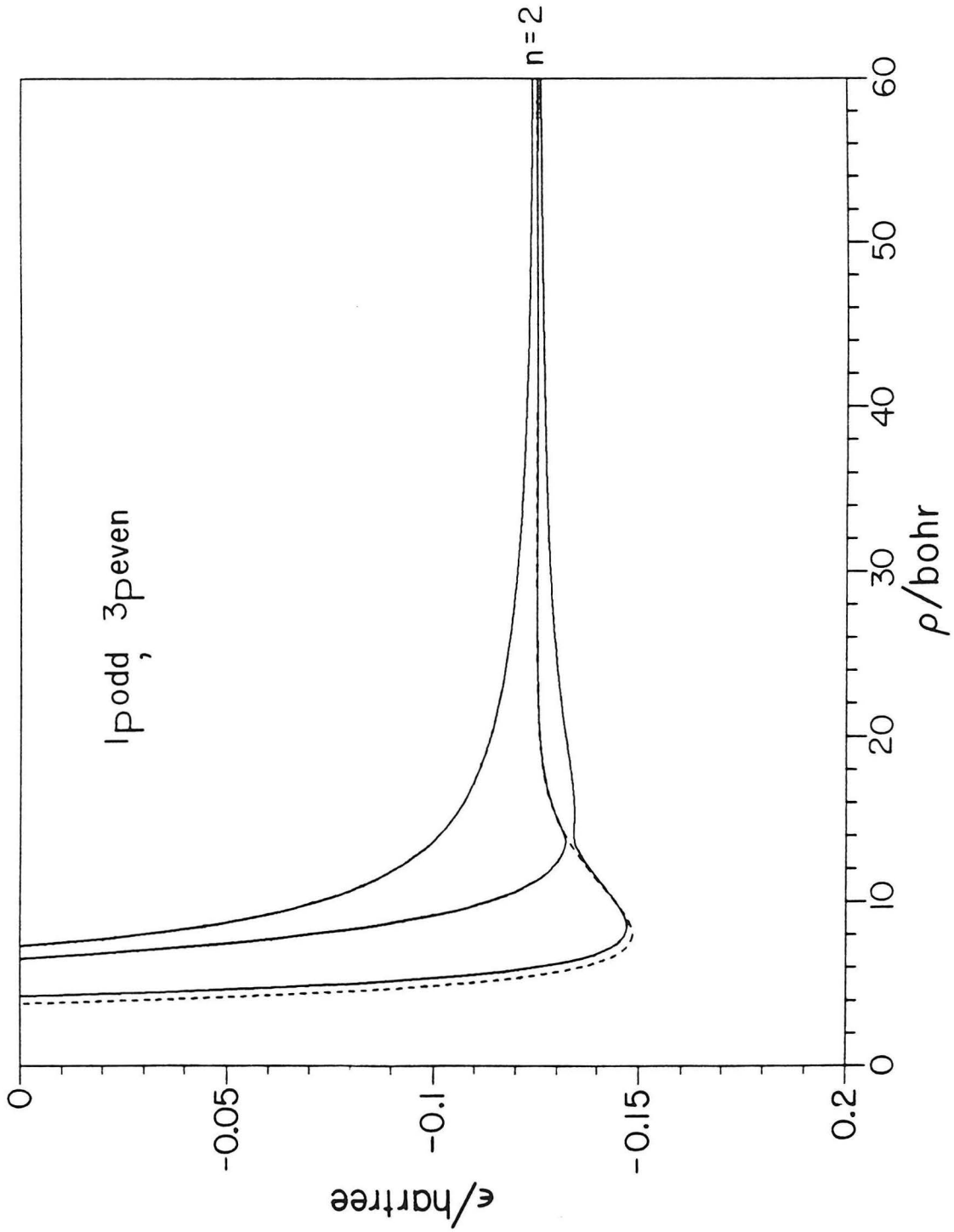
n=2
$^1p_{odd}$, $^3p_{even}$
0
-0.05
-0.1
-0.15
0.2
ε/hartree
0
10
20
30
40
50
60
ρ/bohr

Figure 5.11

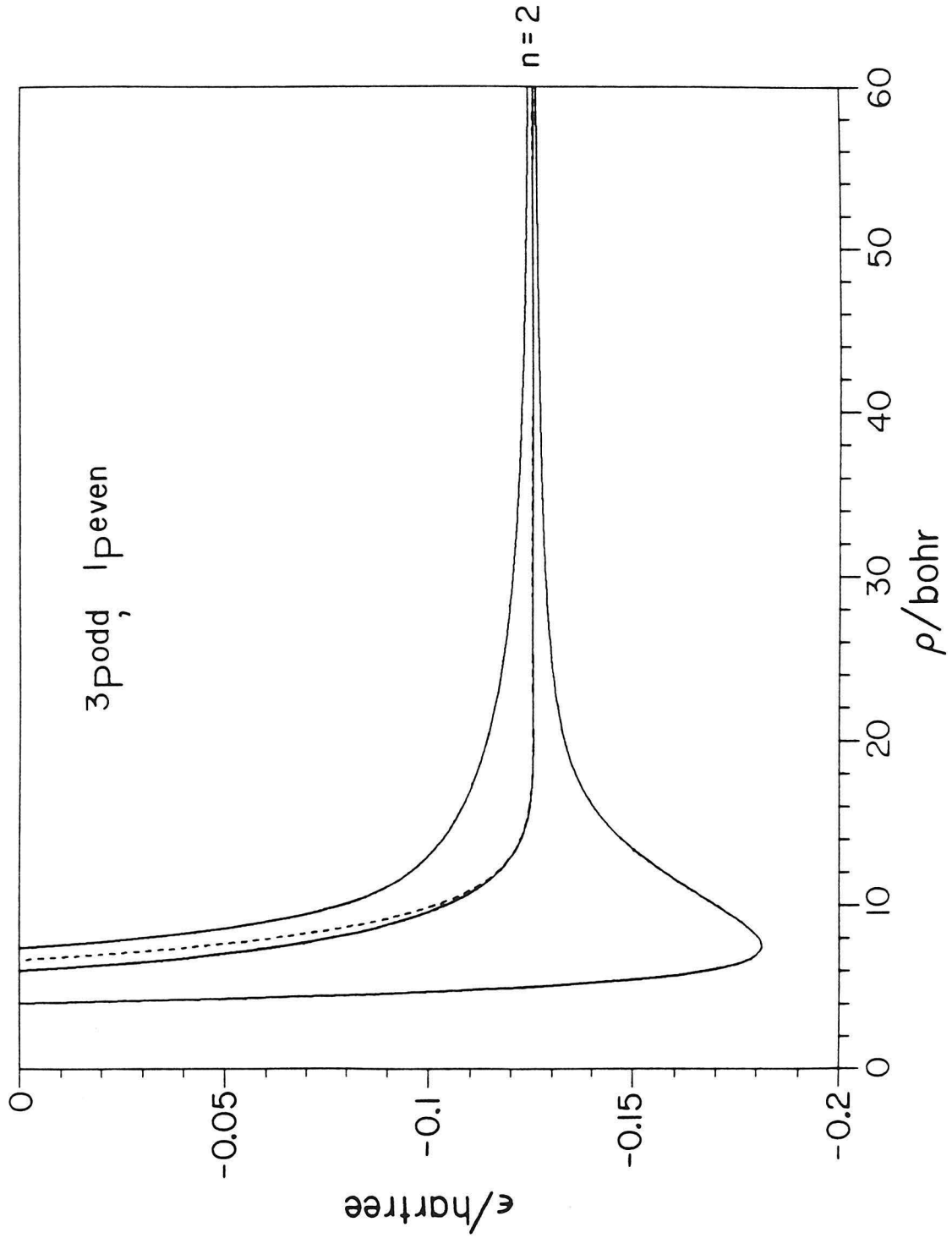
n = 2
$^3P_{odd}$, $^1P_{even}$
0
-0.05
-0.1
-0.15
-0.2
ε/hartree
0
10
20
30
40
50
60
ρ/bohr

Figure 5.12

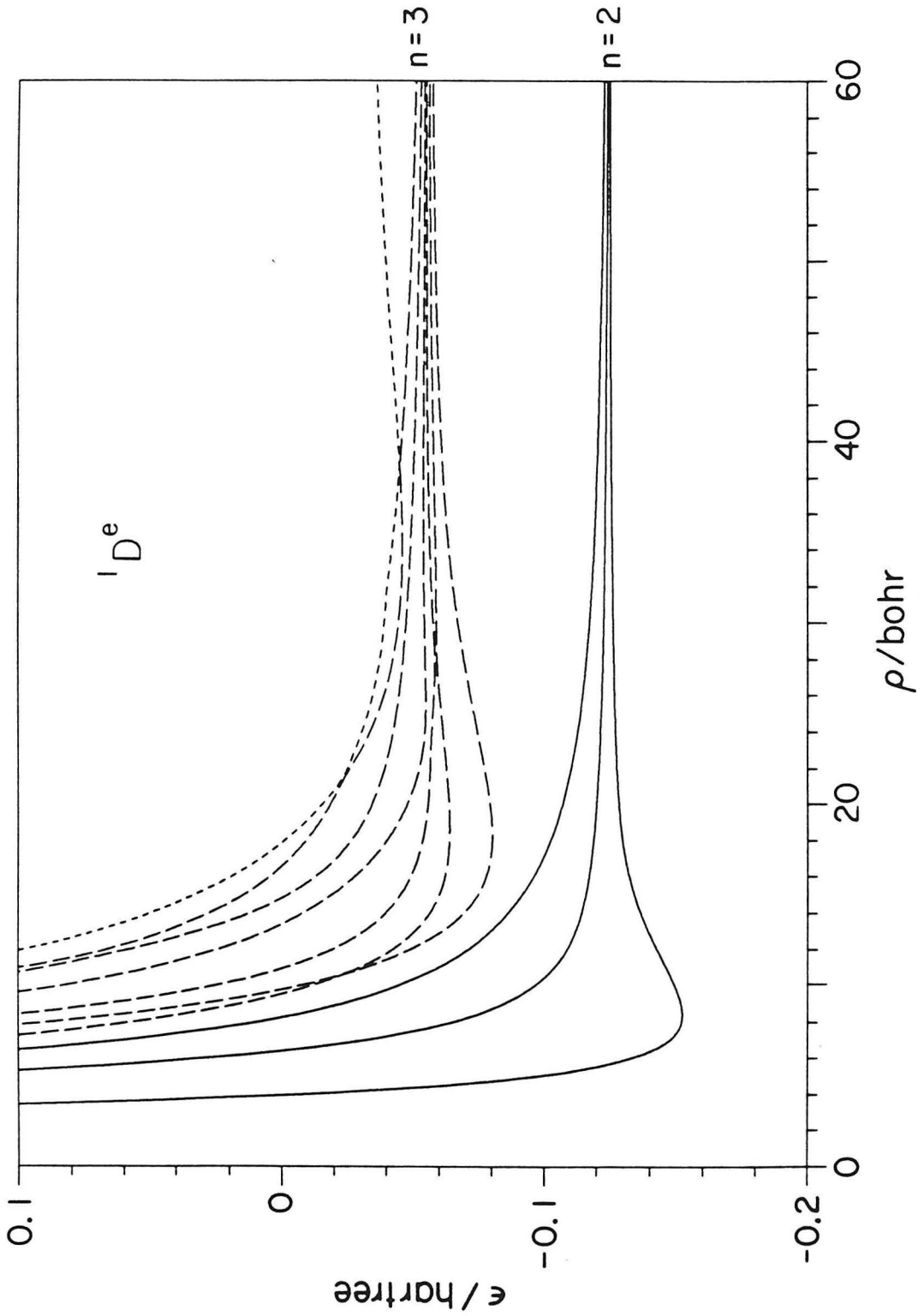

Figure 5.13

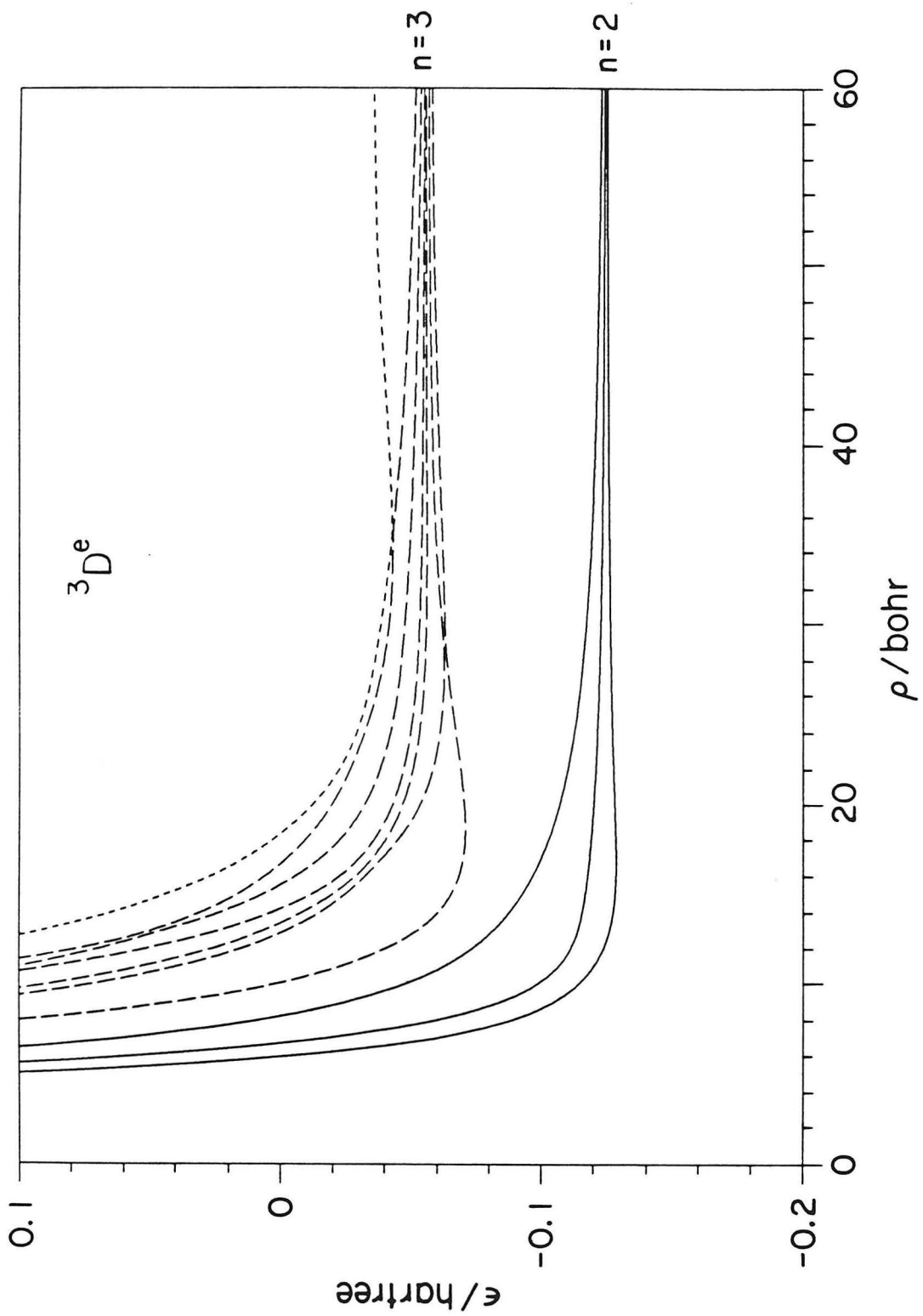

Figure 5.14

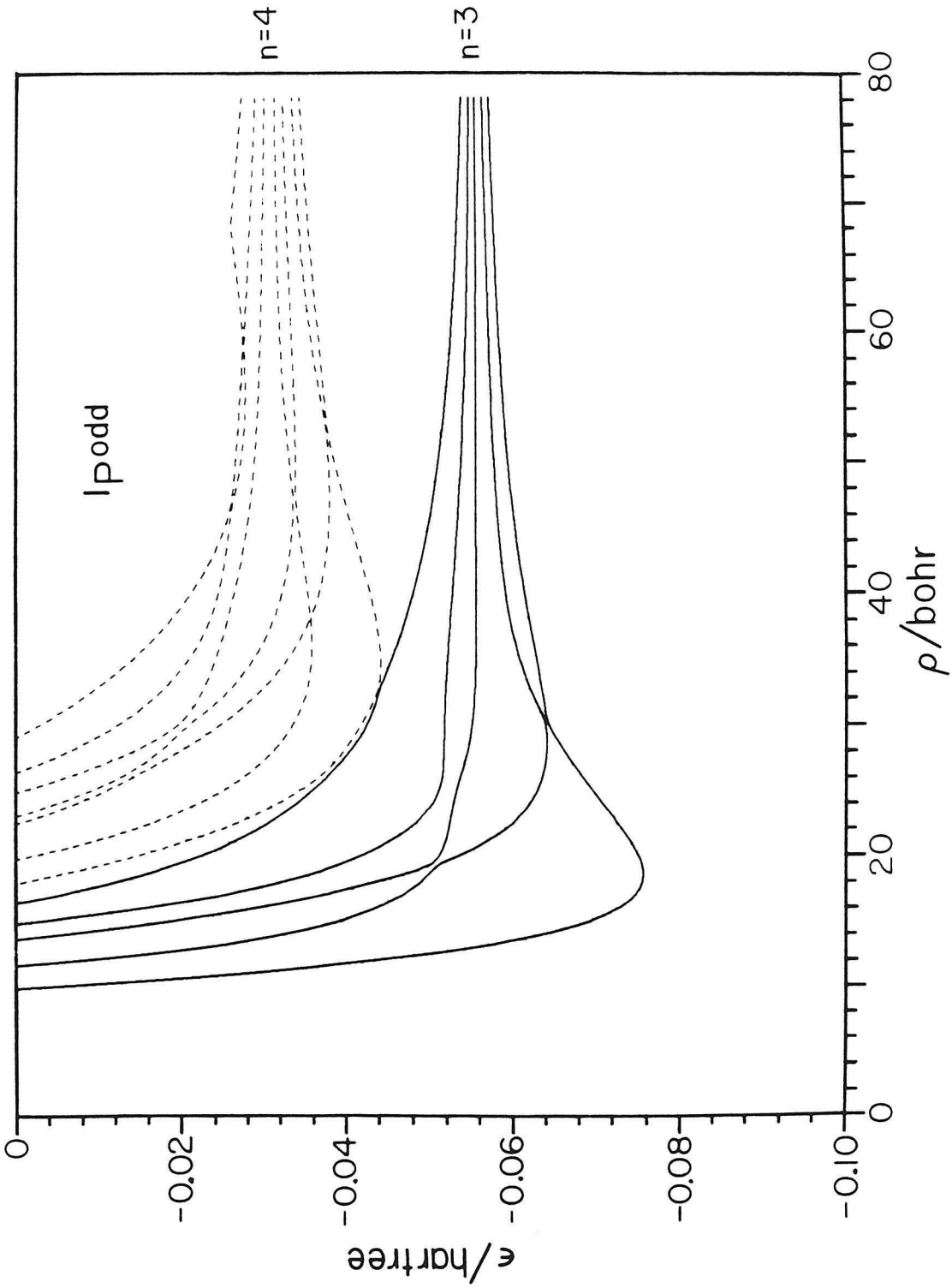

Figure 5.15

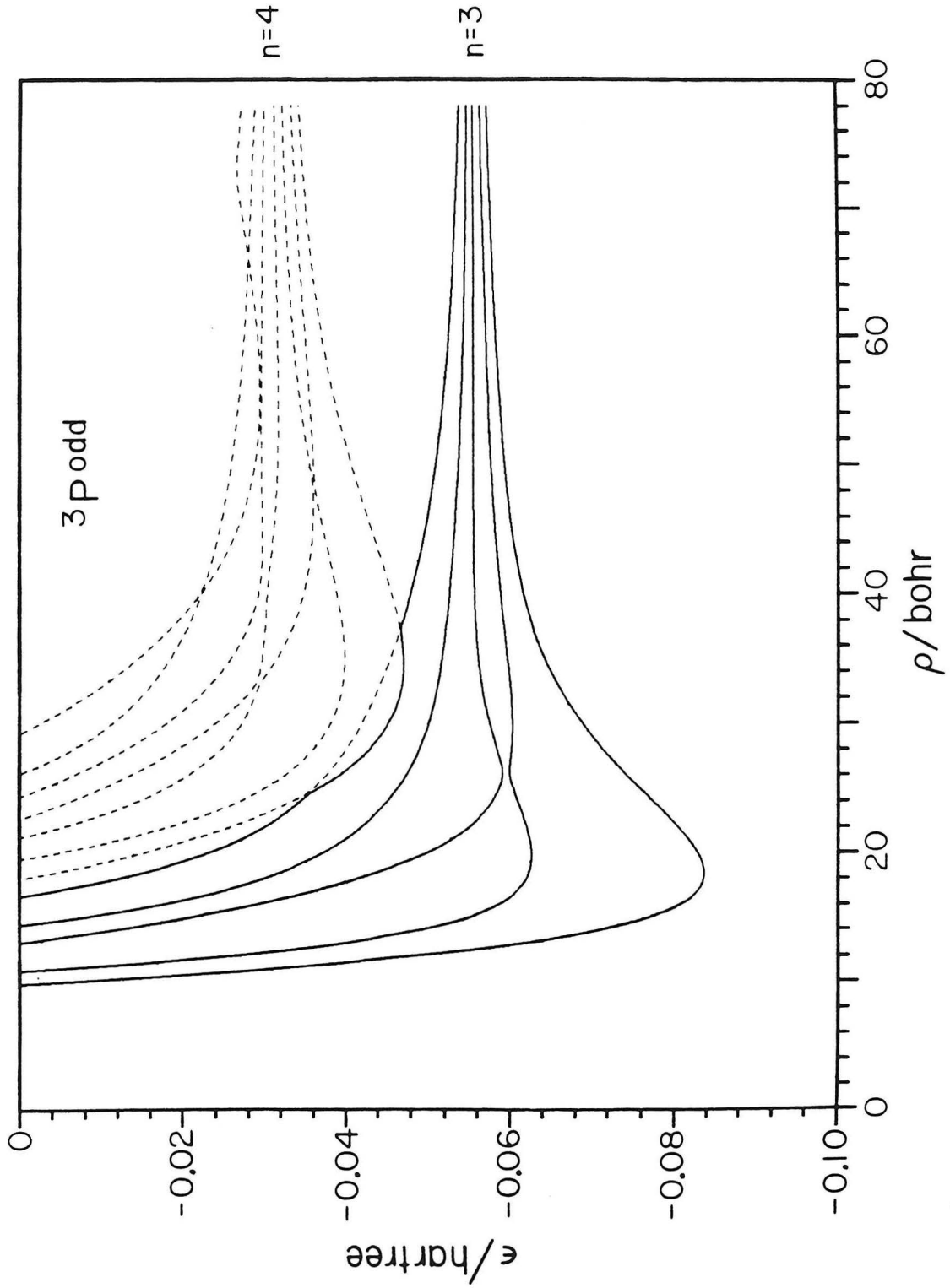

Figure 5.16

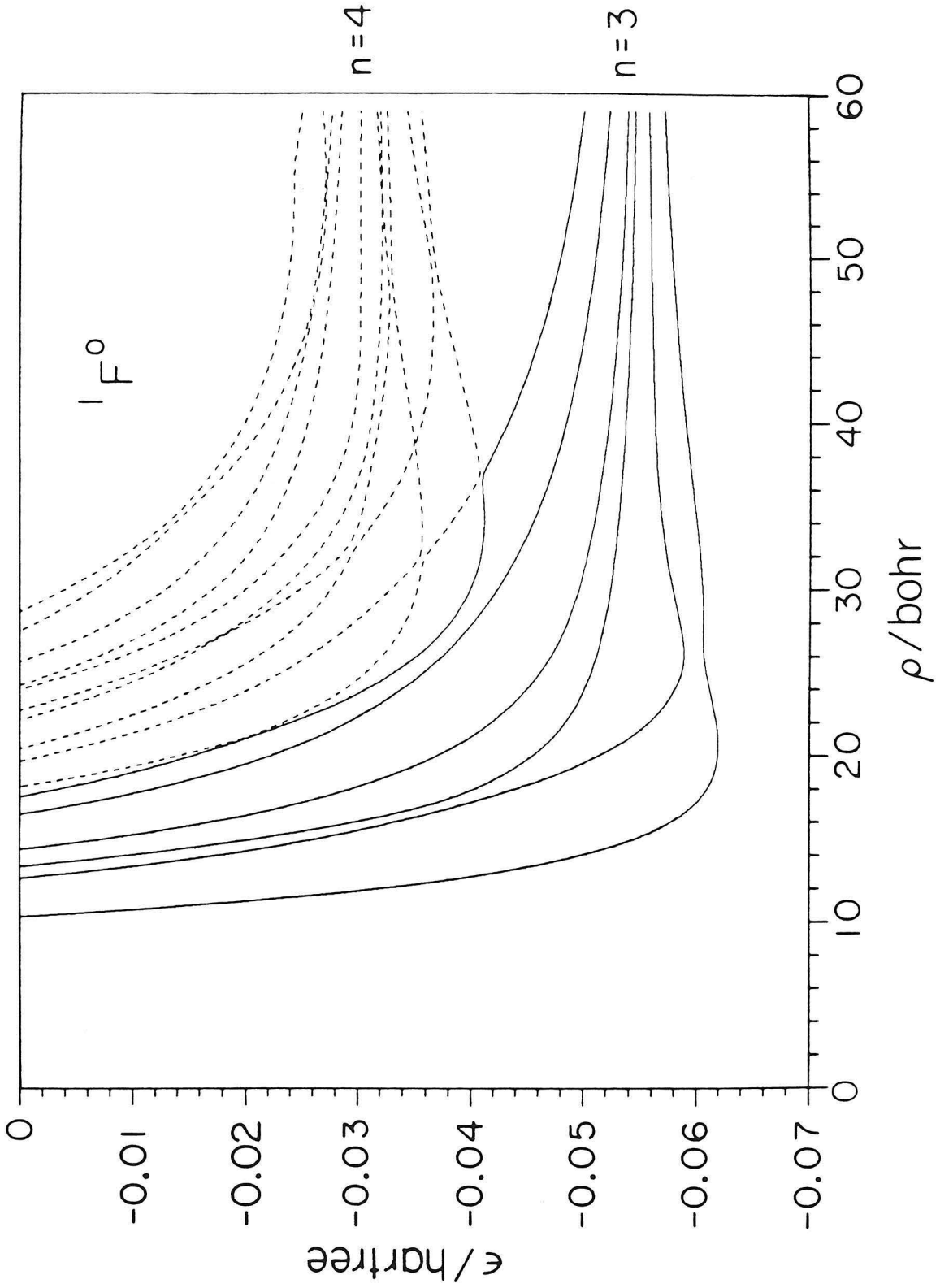
n=4
n=3
$^1F^o$
0
-0.01
-0.02
-0.03
-0.04
-0.05
-0.06
-0.07
ε / hartree
0
10
20
30
40
50
60
ρ / bohr

Figure 5.17

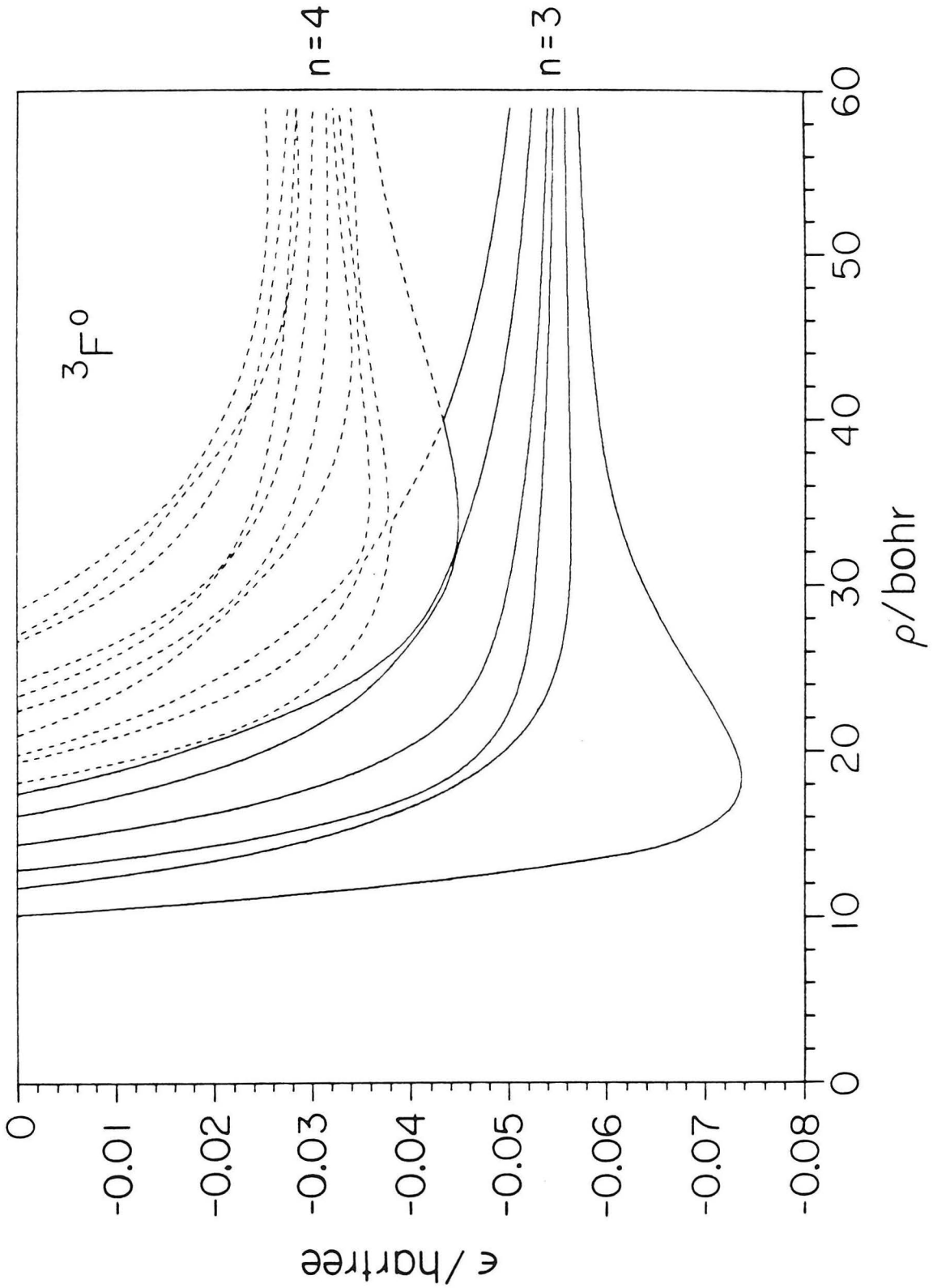
n=4
n=3
$^3F^o$
0
-0.01
-0.02
-0.03
-0.04
-0.05
-0.06
-0.07
-0.08
ε /hartree
0
10
20
30
40
50
60
ρ/bohr

Figure 5.18

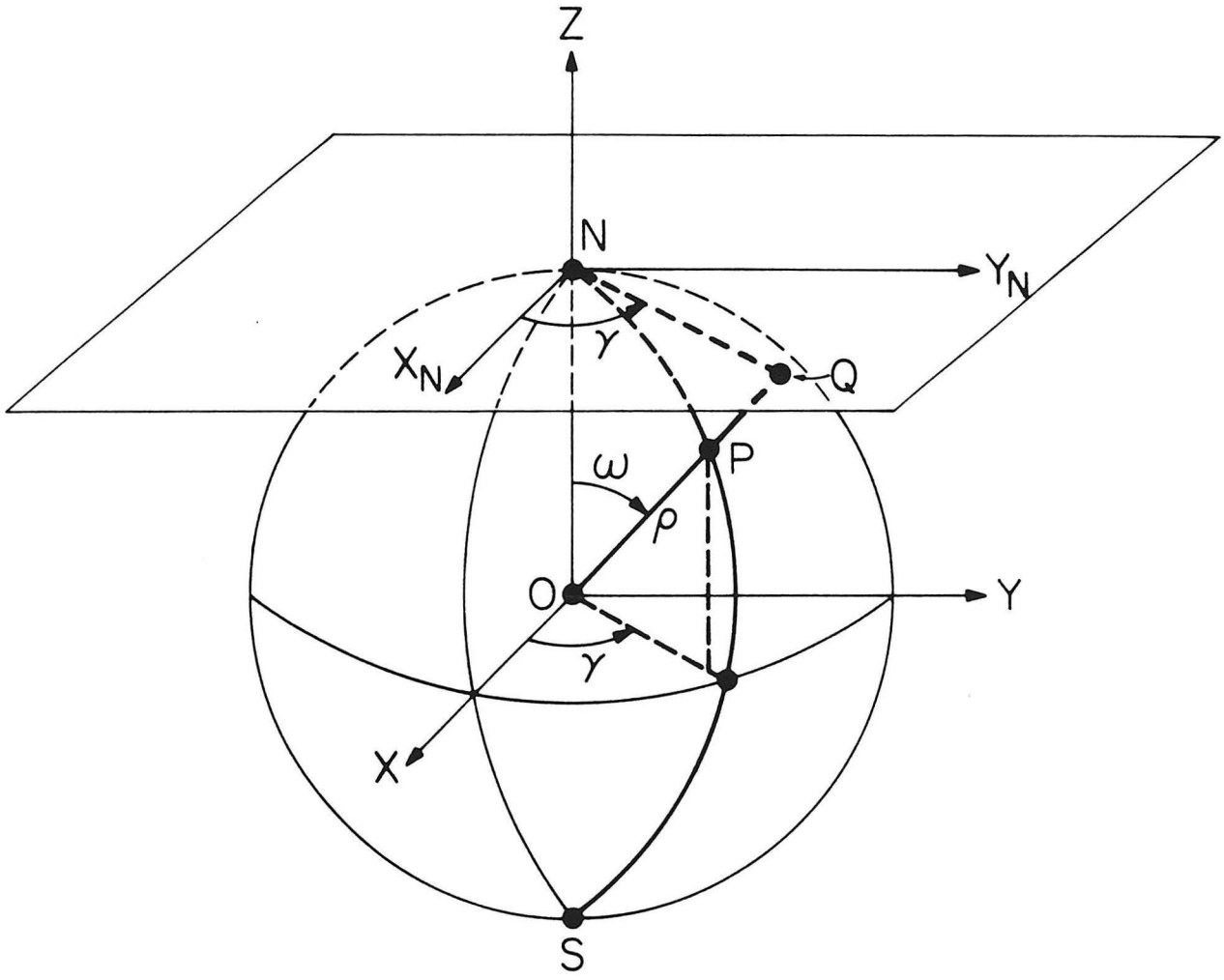

Figure 5.19

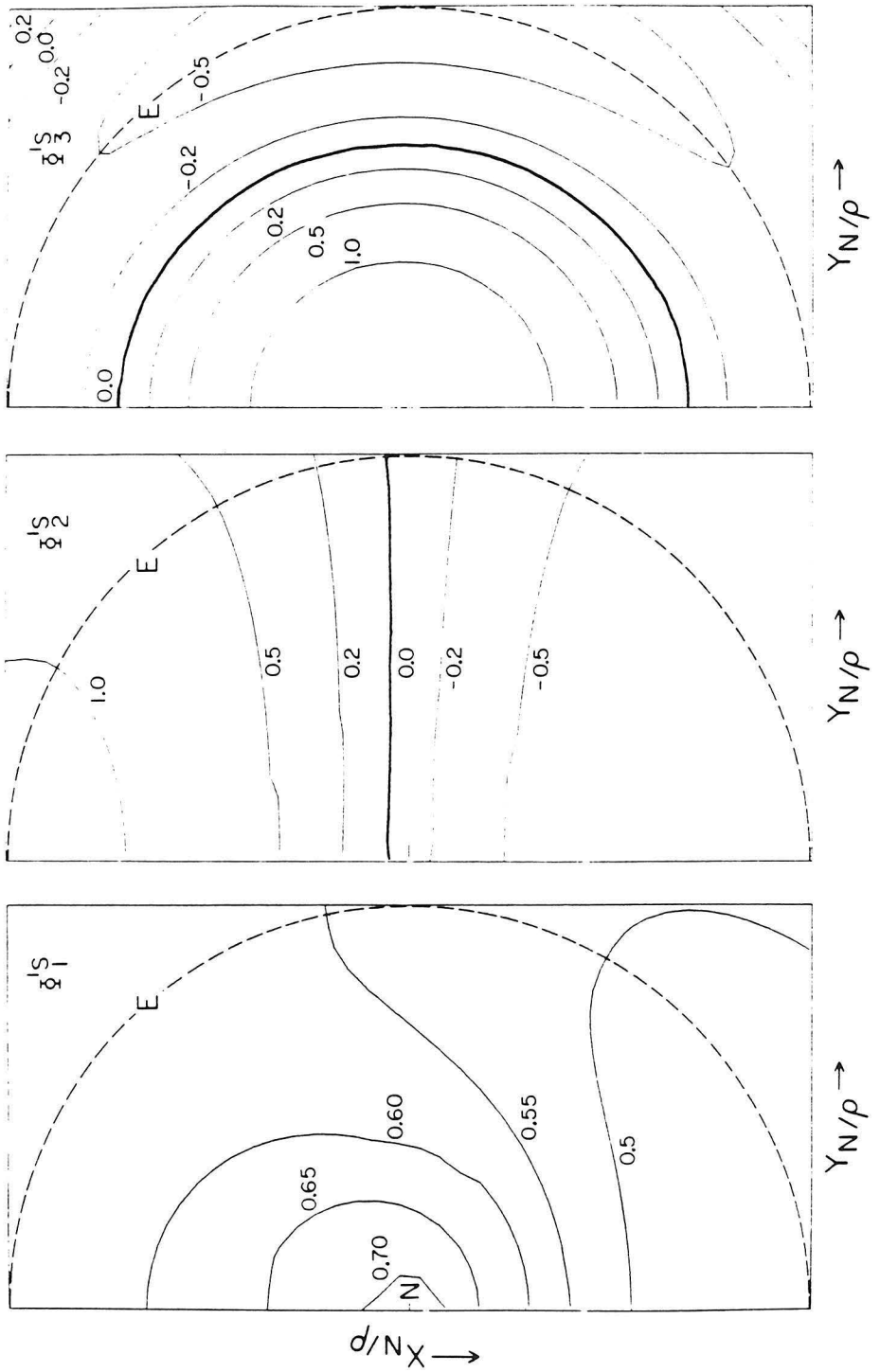
$^1S_3$
E
0.2
0.0
-0.2
-0.5
-0.2
0.2
0.5
1.0
0.0
$Y_N/\rho \rightarrow$
$^1S_2$
E
1.0
0.5
0.2
0.0
-0.2
-0.5
$Y_N/\rho \rightarrow$
$^1S_1$
E
0.60
0.55
0.5
0.65
0.70
N
$Y_N/\rho \rightarrow$
$d/N_X \longrightarrow$

Figure 5.20a

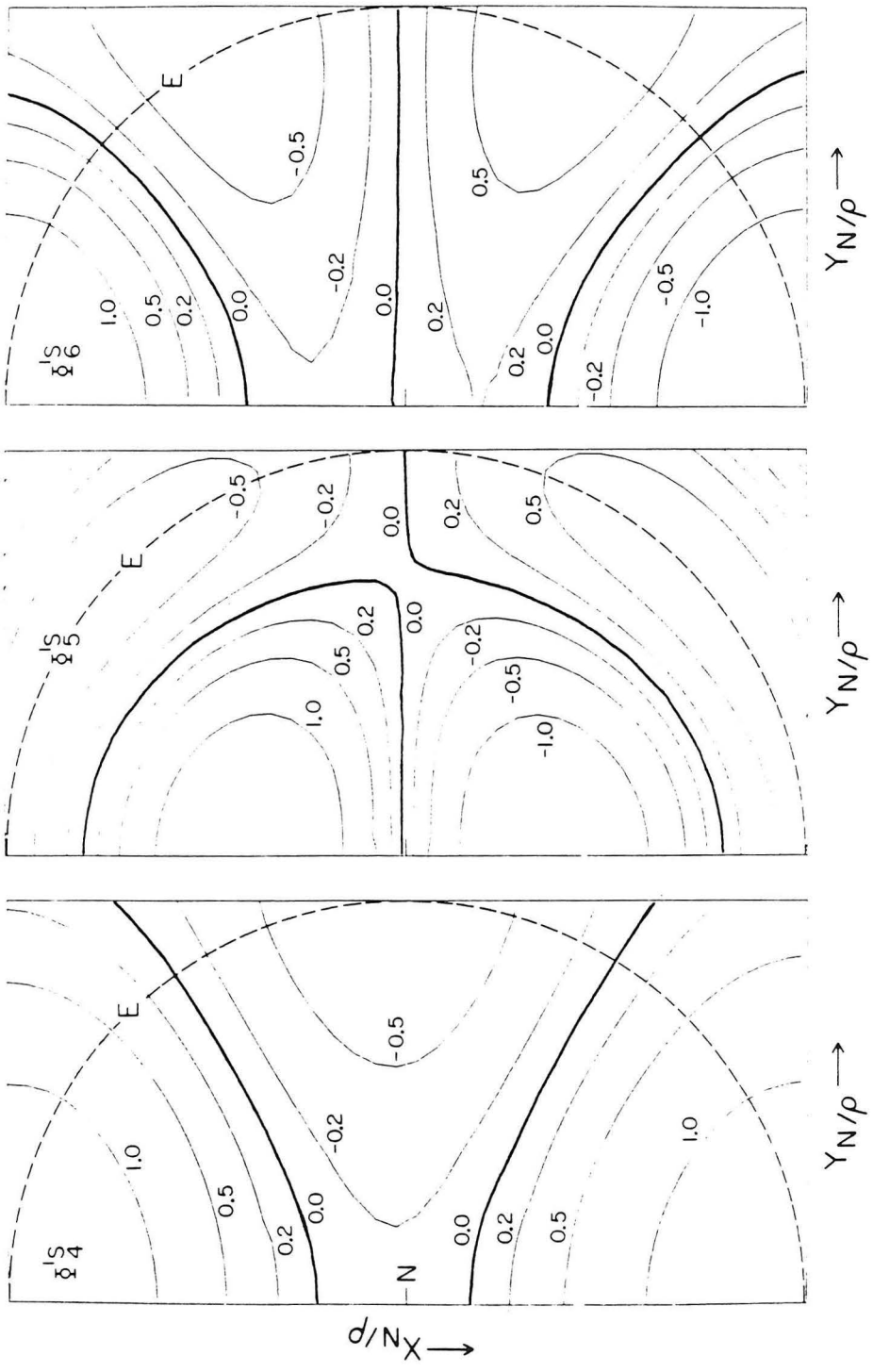

Figure 5.20b

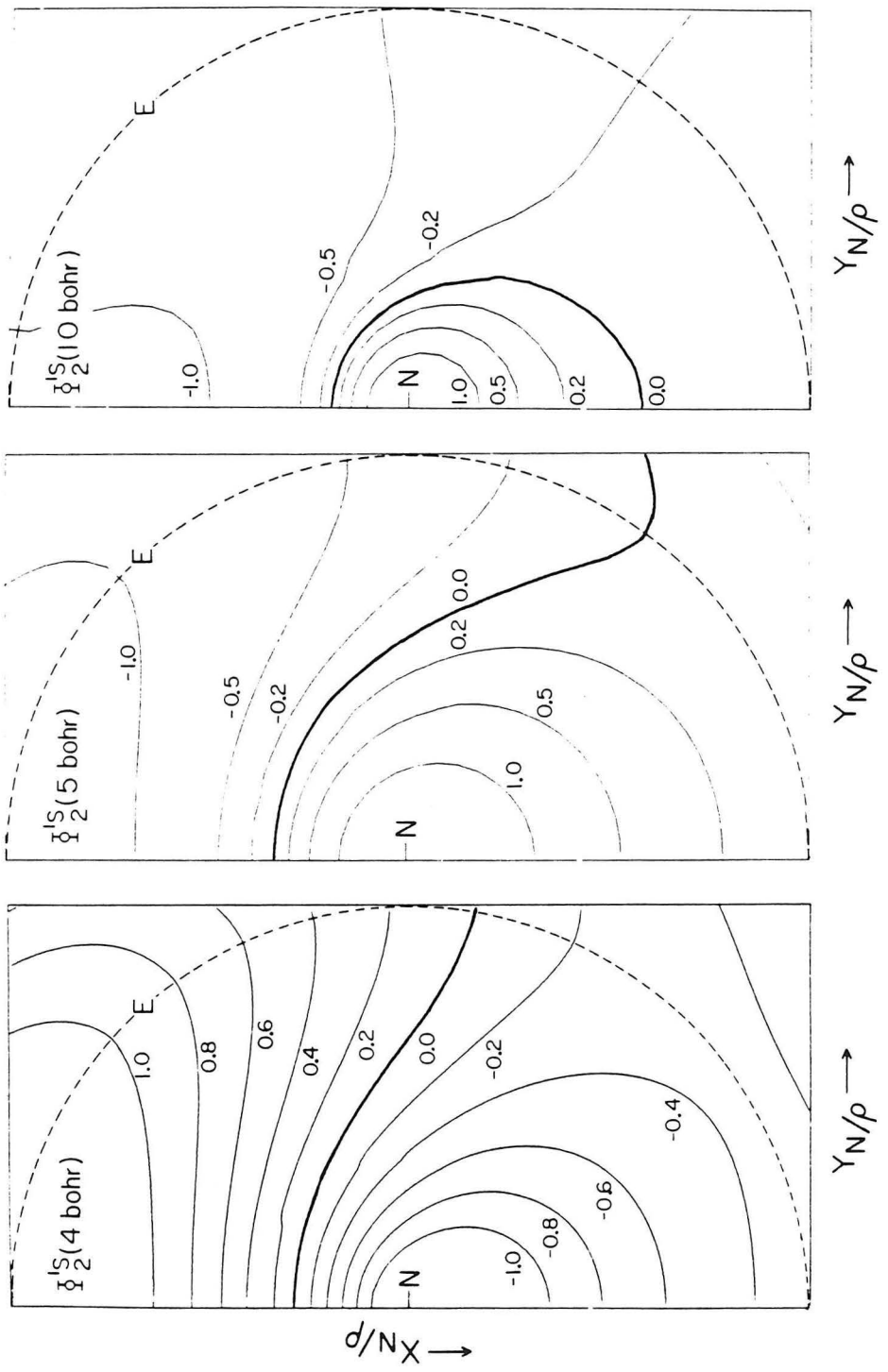
$^1\Sigma_2^+$(4 bohr)
$^1\Sigma_2^+$(5 bohr)
$^1\Sigma_2^+$(10 bohr)
E
N
1.0
0.8
0.6
0.4
0.2
0.0
-0.2
-0.4
-0.6
-0.8
-1.0
0.5
-0.5
$X_{N/\rho}$ ⟶
$Y_{N/\rho}$ ⟶

Figure 5.21

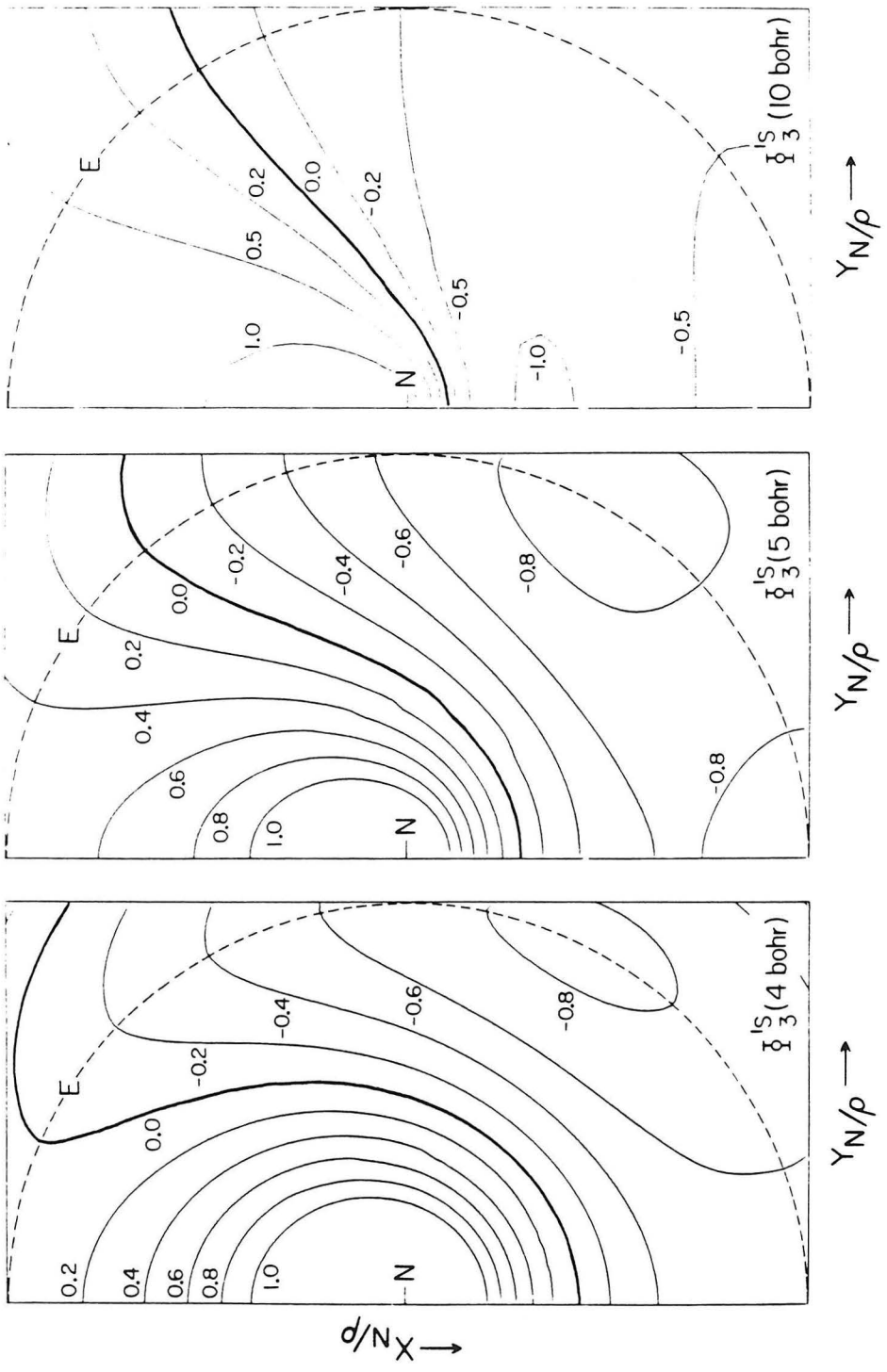
$^1S_3$ (10 bohr)
$^1S_3$(5 bohr)
$^1S_3$(4 bohr)
E
N
1.0
0.5
0.2
0.0
-0.2
-0.5
-1.0
0.4
0.6
0.8
-0.4
-0.6
-0.8
$Y_{N/\rho}$ ⟶
$X_{N/\rho}$ ⟶

Figure 5.22

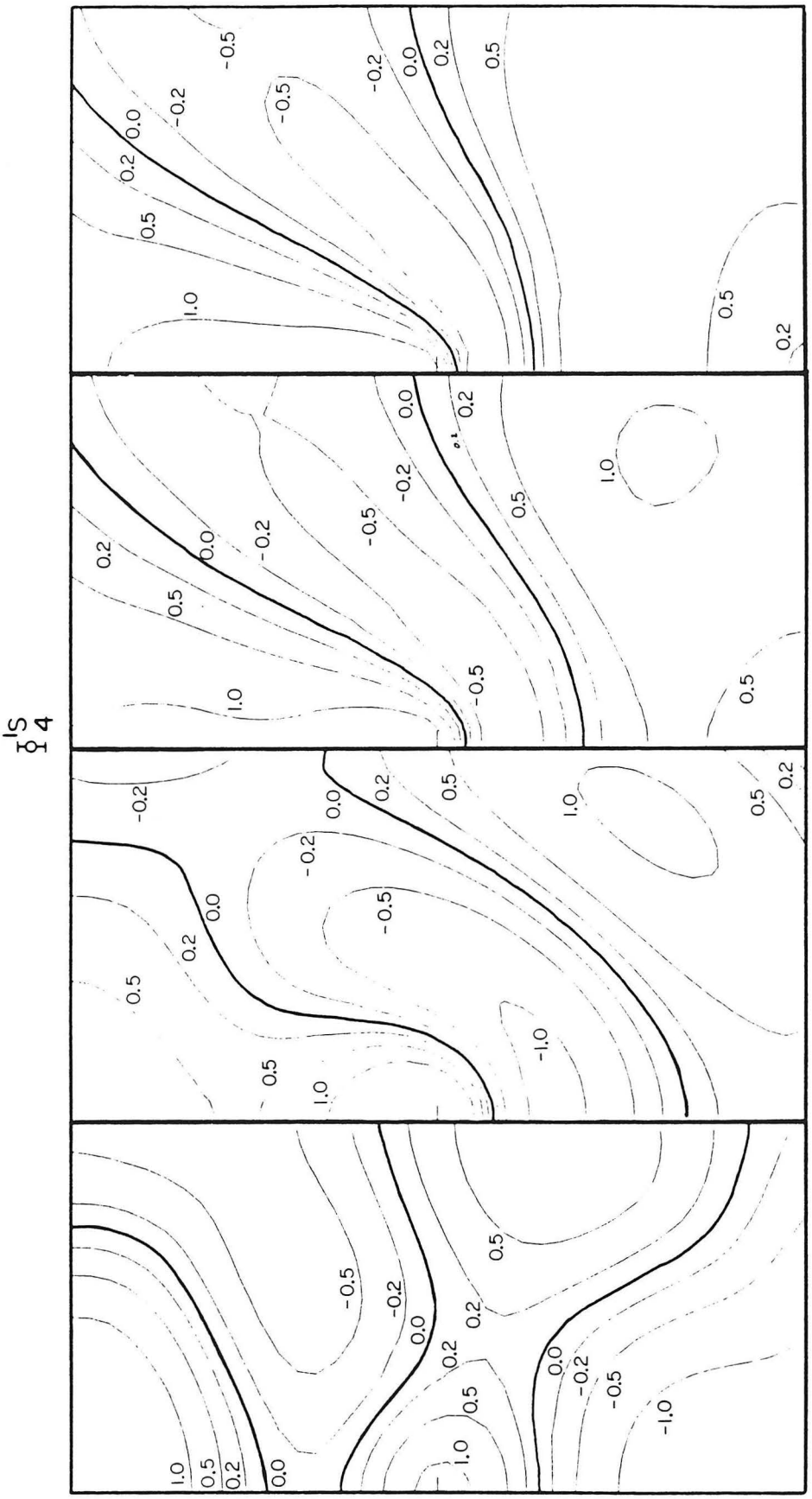

Figure 5.23

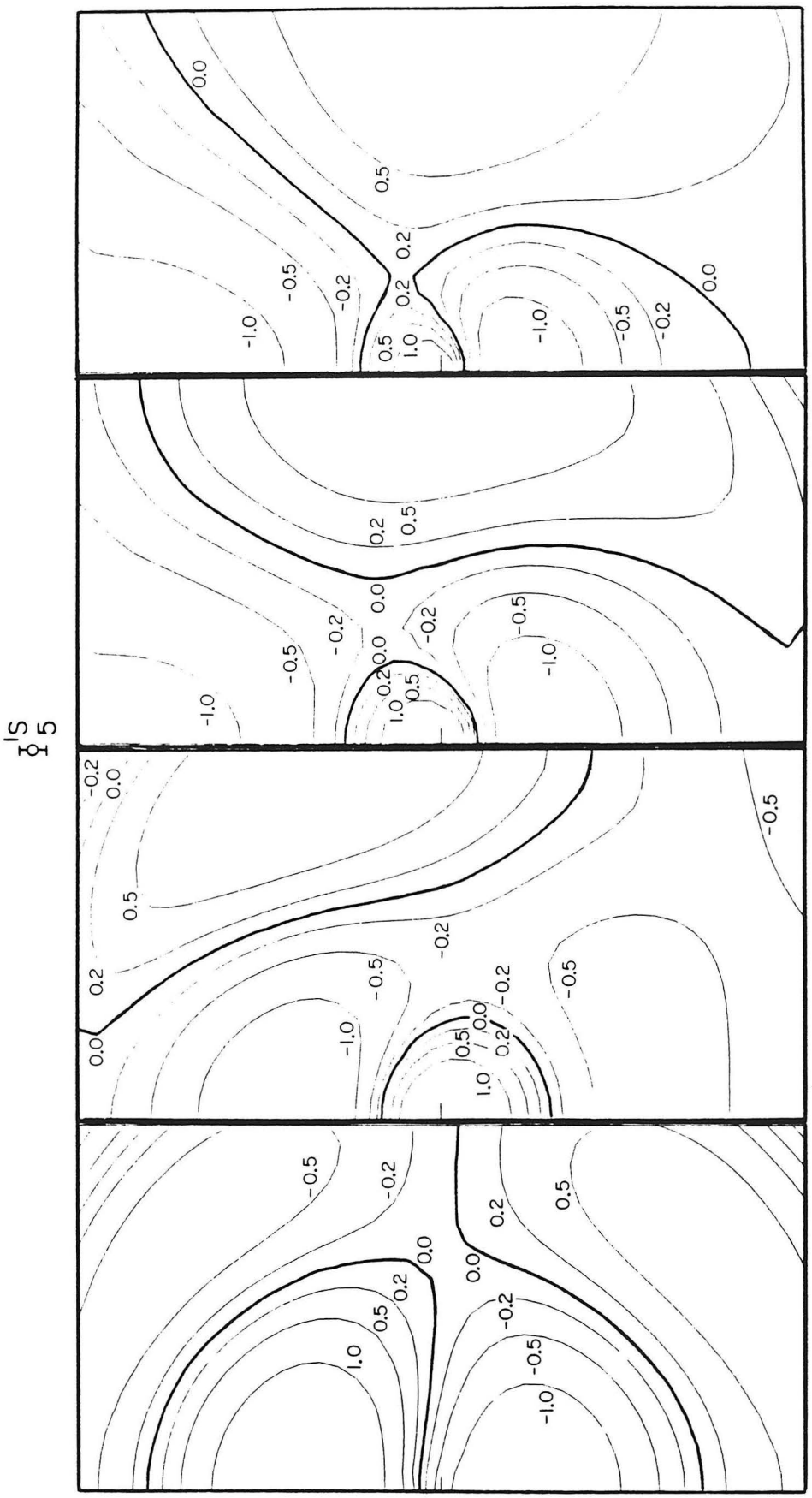

Figure 5.24

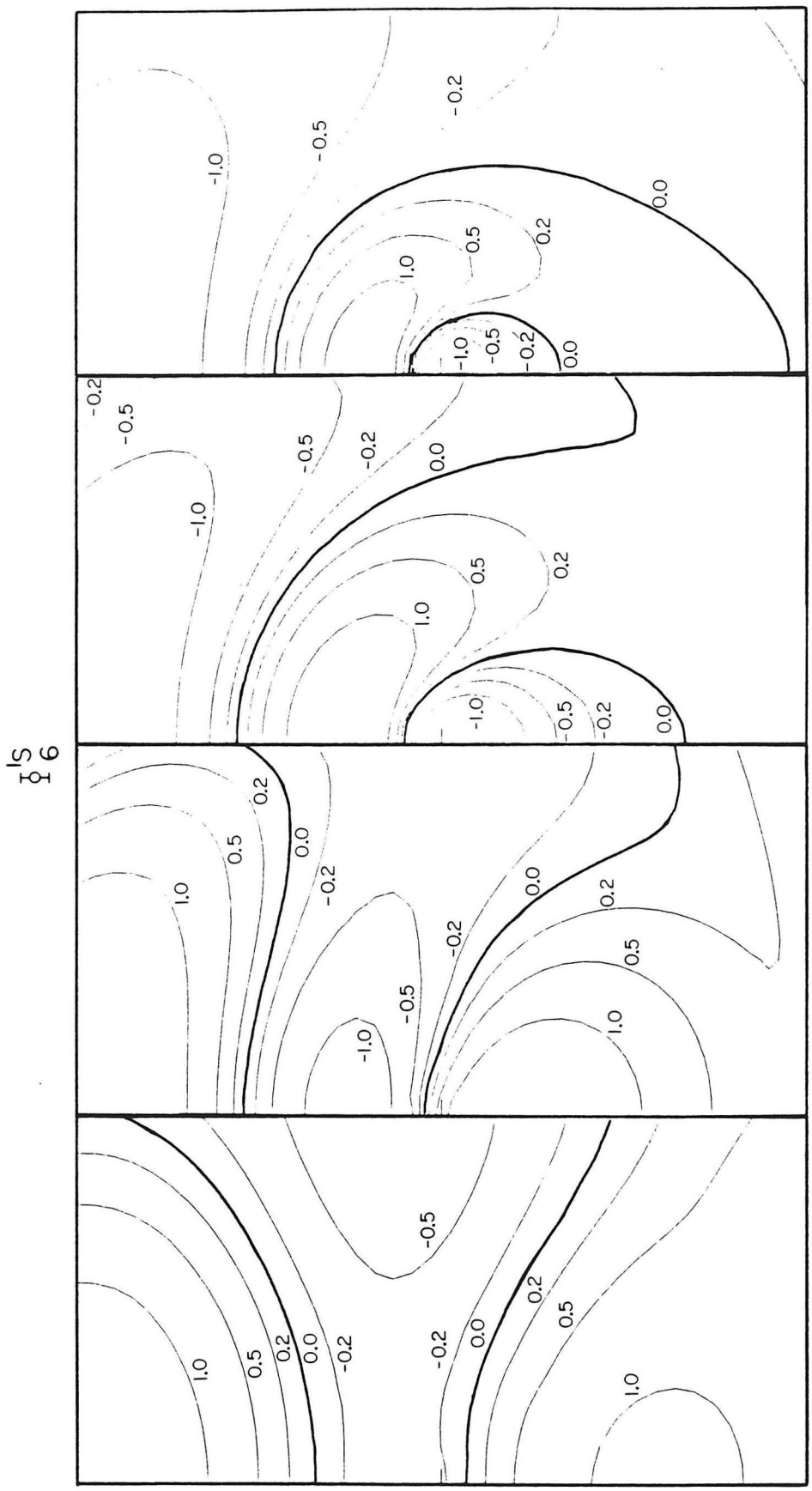

Figure 5.25

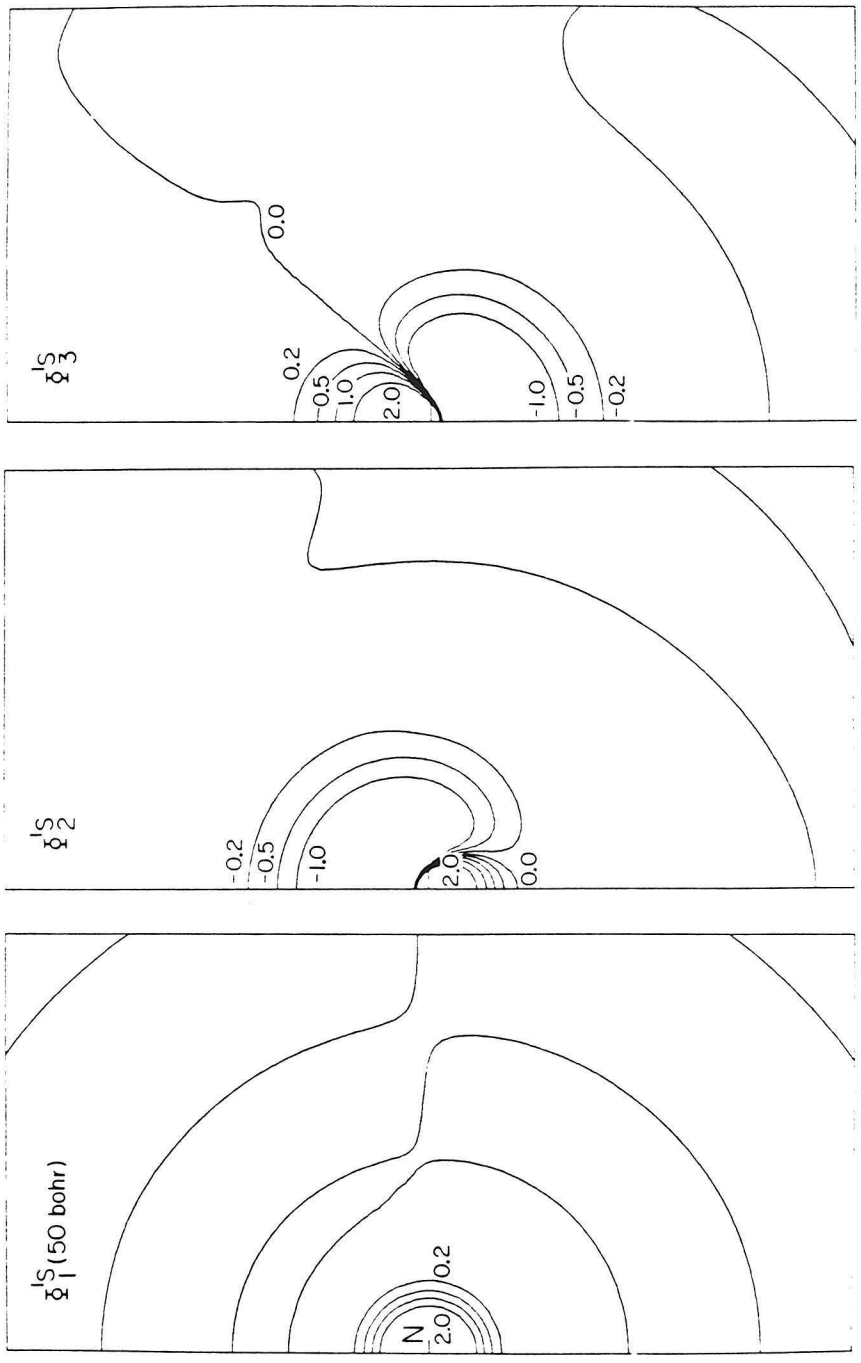
$\delta^{1}S_{3}$
0.0
0.2
0.5
1.0
2.0
1.0
0.5
0.2
$\delta^{1}S_{2}$
0.2
0.5
1.0
2.0
0.0
$\delta^{1}S_{1}$ (50 bohr)
0.2
N
2.0

Figure 5.26a

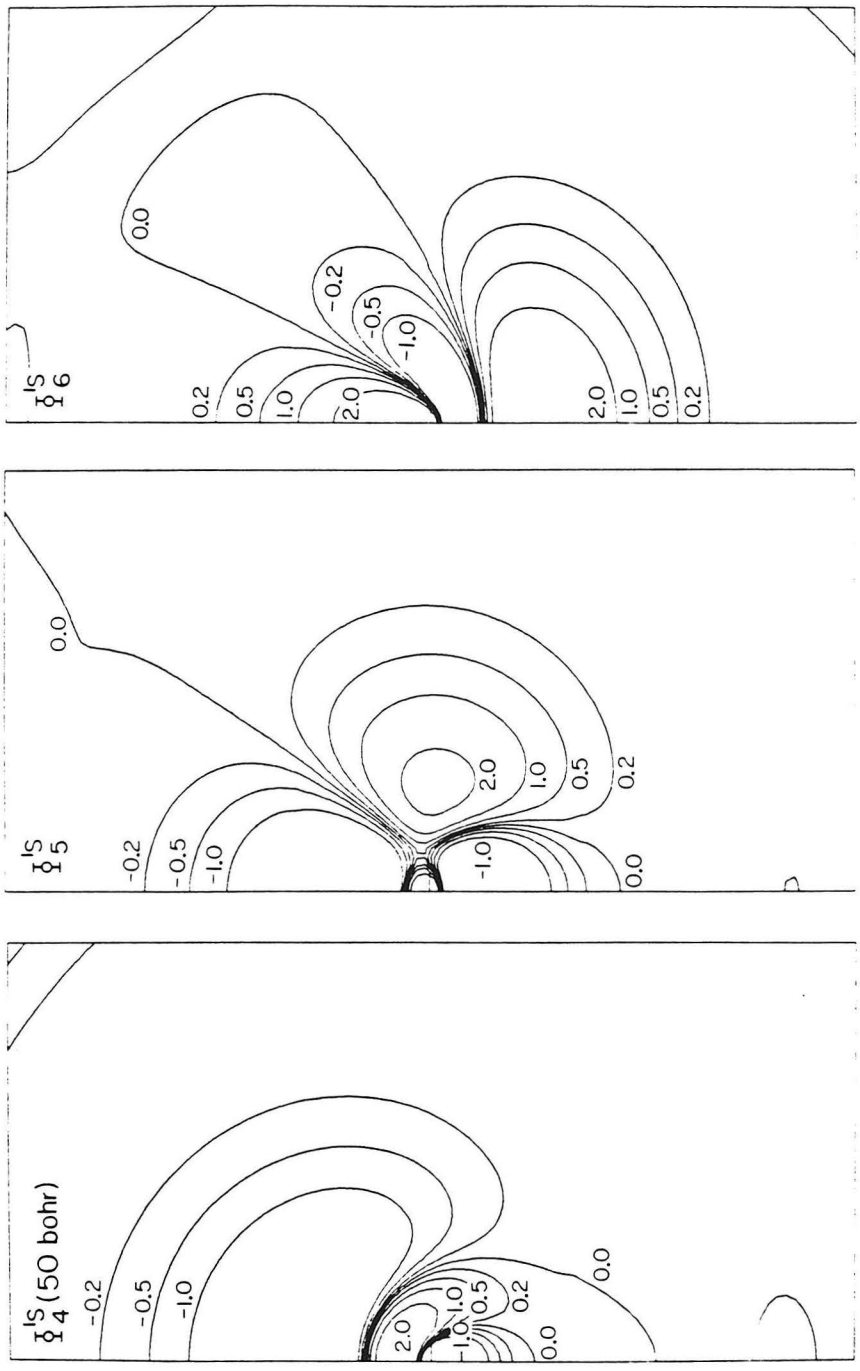
ϕ^{1S}_6
0.0
-0.2
-0.5
-1.0
0.2
0.5
1.0
2.0
2.0
1.0
0.5
0.2
ϕ^{1S}_5
0.0
-0.2
-0.5
-1.0
2.0
1.0
0.5
0.2
-1.0
0.0
ϕ^{1S}_4 (50 bohr)
-0.2
-0.5
-1.0
0.0
2.0
-1.0
1.0
0.5
0.2
0.0

Figure 5.26b

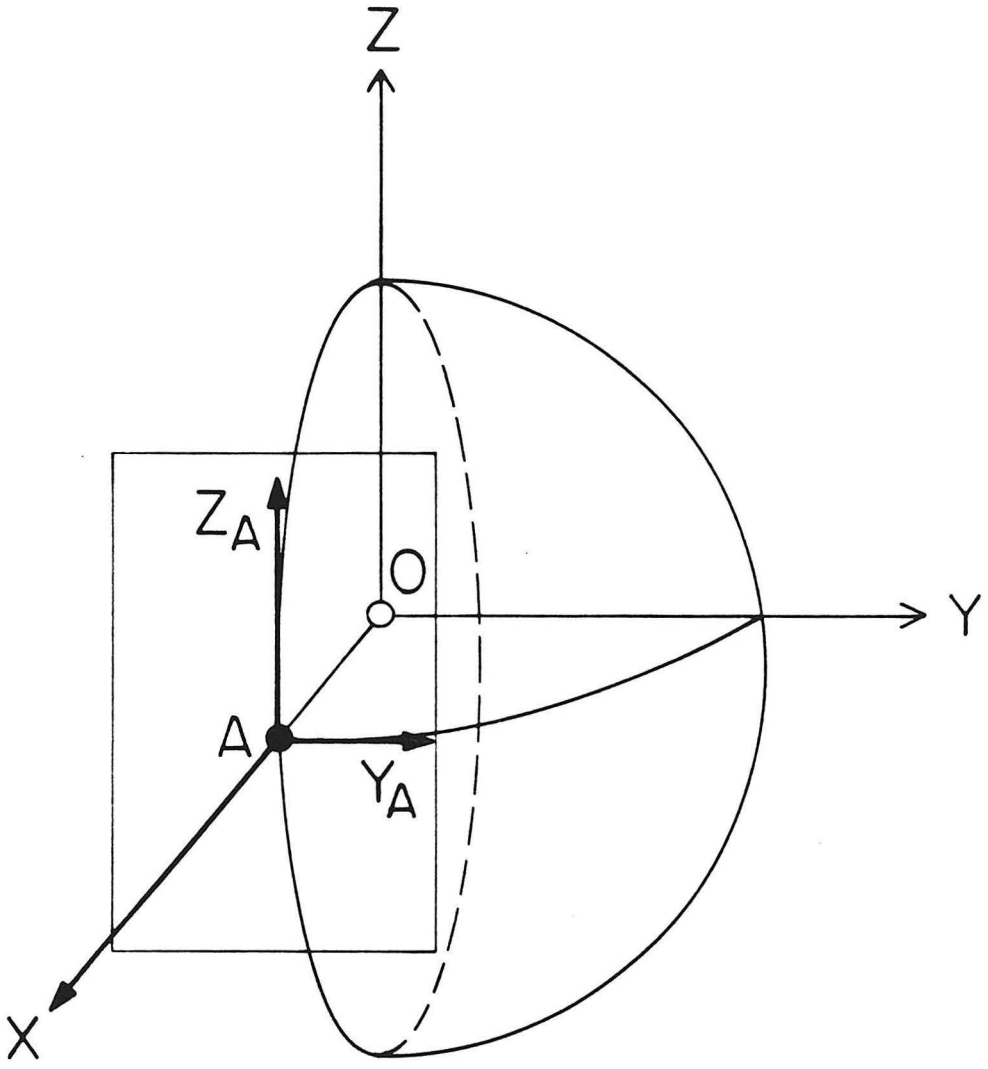

Figure 5.27

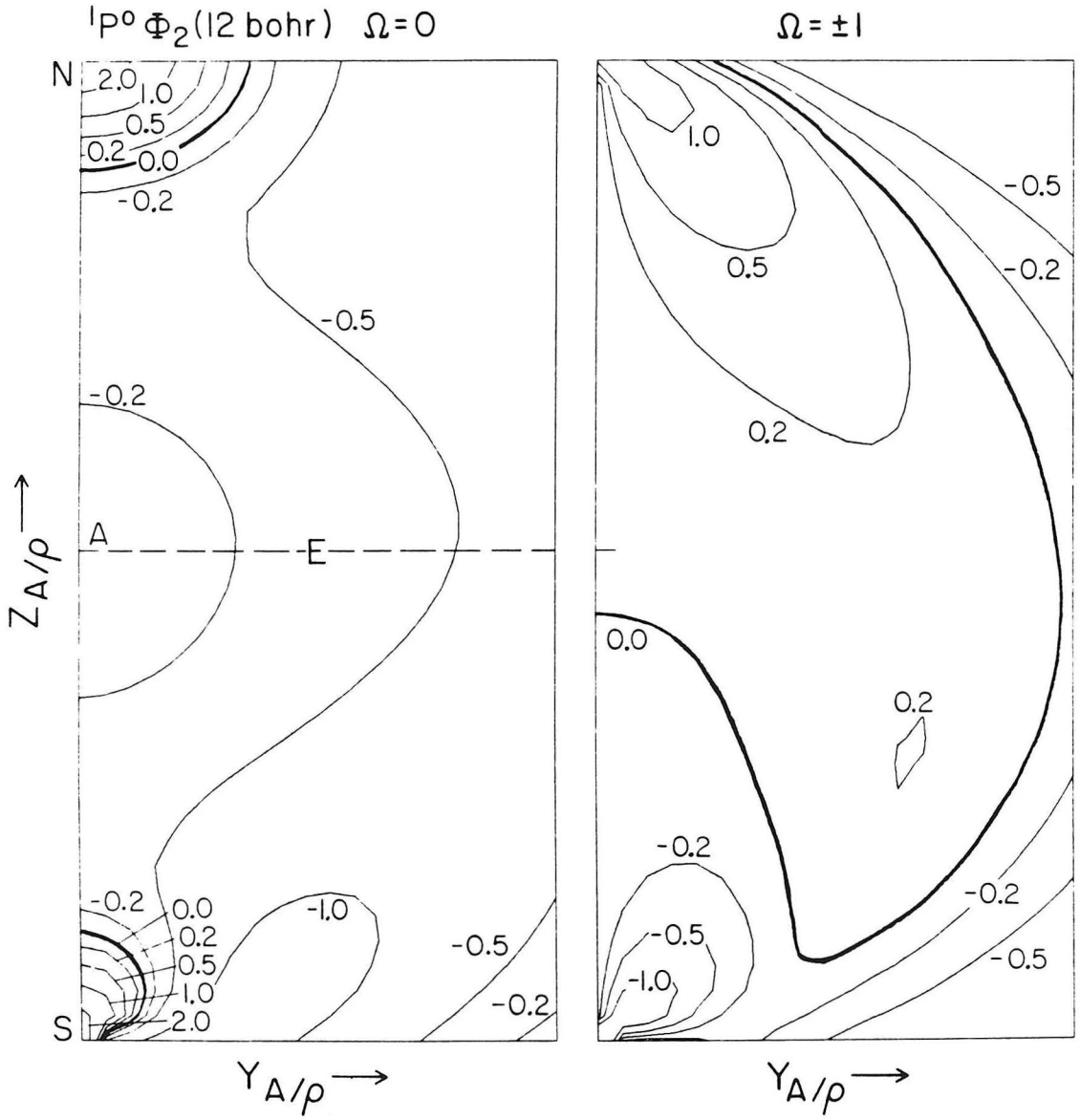
$^1P^o\,\Phi_2$(12 bohr) Ω = 0
Ω = ±1
N
S
A
E
2.0
1.0
0.5
0.2
0.0
-0.2
-0.5
-1.0
$Z_{A/\rho}$
$Y_{A/\rho}$
$Y_{A/\rho}$

Figure 5.28a

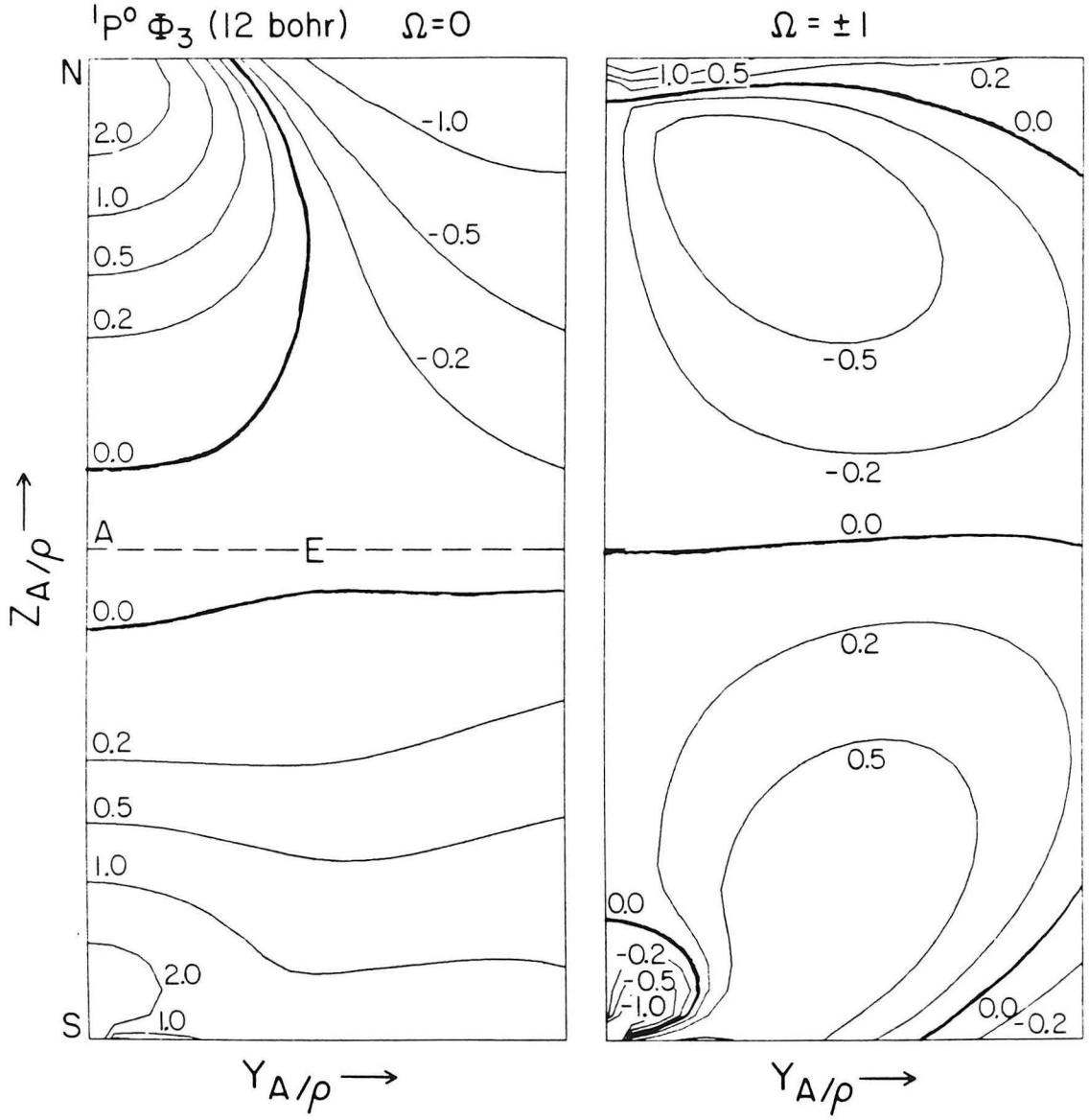
$^1P^o\ \Phi_3$ (12 bohr) Ω=0
Ω = ±1
N
S
A
E
2.0
1.0
0.5
0.2
0.0
-0.2
-0.5
-1.0
$Z_{A/\rho}$ ⟶
$Y_{A/\rho}$ ⟶
$Y_{A/\rho}$ ⟶

Figure 5.28b

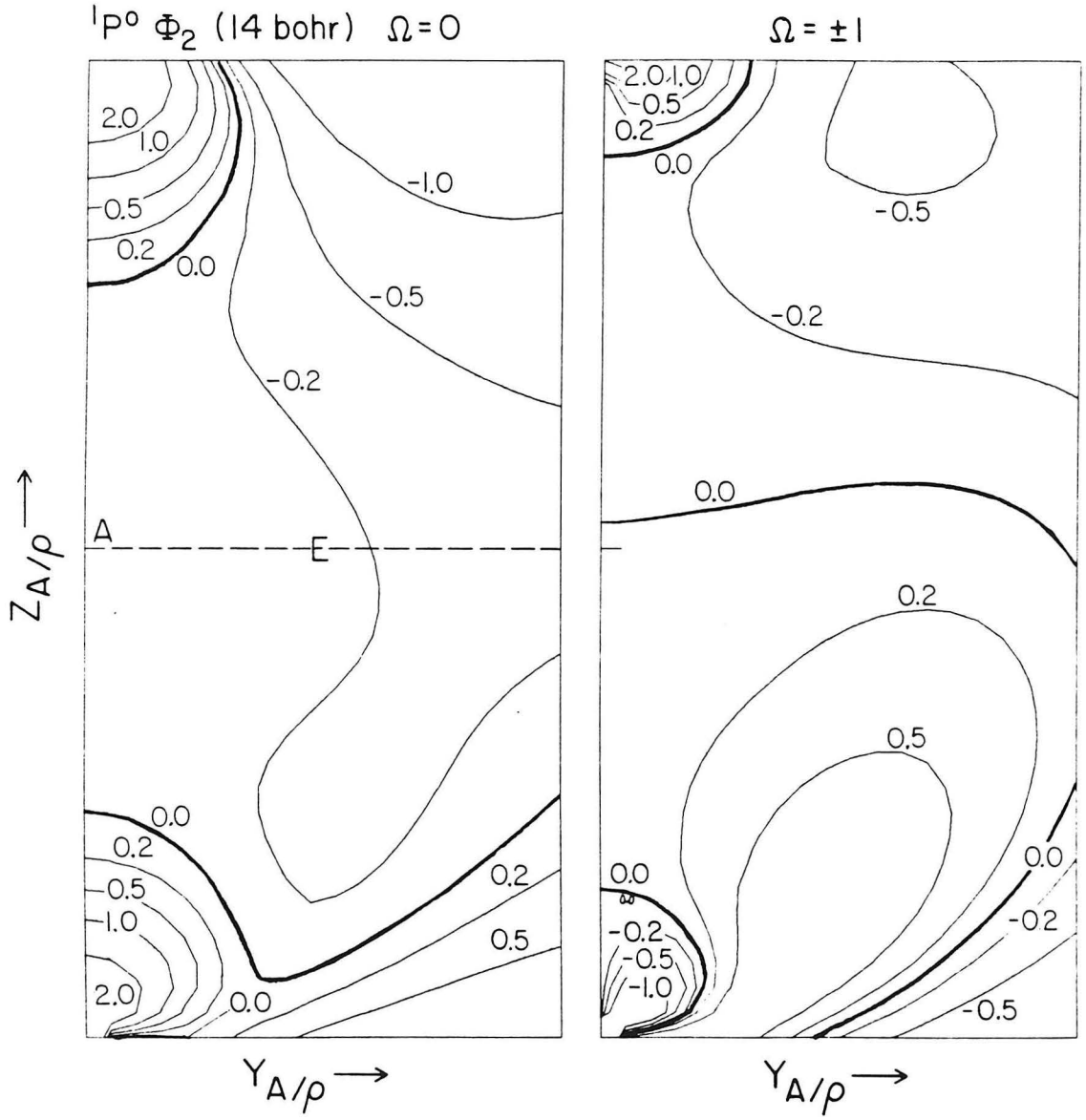
$^1P^o$ Φ_2 (14 bohr) $\Omega = 0$
$\Omega = \pm 1$
$Z_{A/\rho}$ ⟶
$Y_{A/\rho}$ ⟶
$Y_{A/\rho}$ ⟶
A
E
2.0
1.0
0.5
0.2
0.0
-0.2
-0.5
-1.0

Figure 5.29a

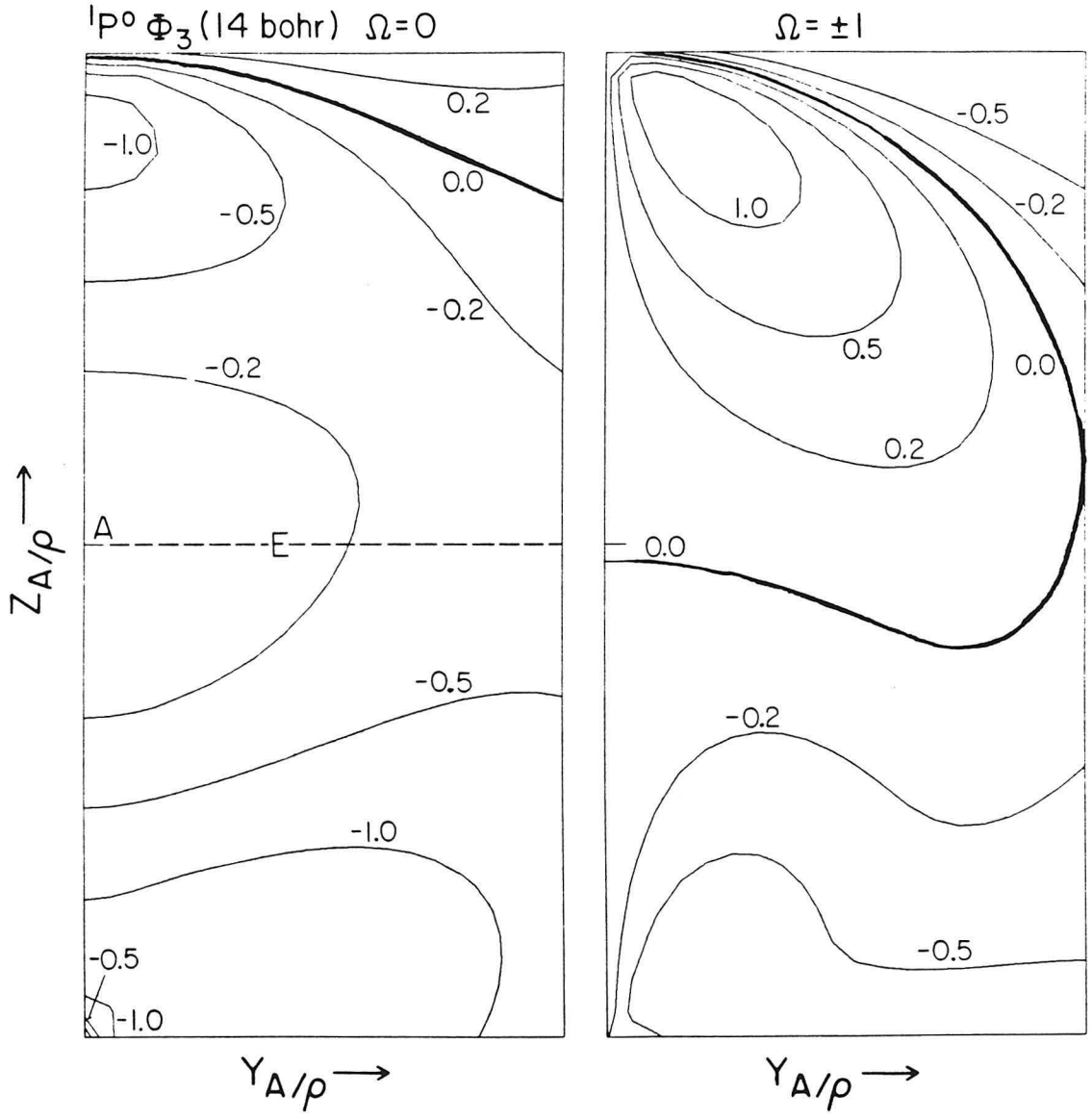
$^1P^o\ \Phi_3$ (14 bohr) $\Omega=0$
$\Omega=\pm1$
0.2
-1.0
0.0
-0.5
-0.2
-0.2
A
E
-0.5
-1.0
-0.5
-1.0
1.0
-0.5
-0.2
0.5
0.0
0.2
0.0
-0.2
-0.5
$Z_{A/\rho}$
$Y_{A/\rho}$
$Y_{A/\rho}$

Figure 5.29b

CHAPTER 6

SCATTERING RESULTS

In this chapter we present the results of our calculation of electron scattering off hydrogen atoms using hyperspherical coordinates. The chapter is organized as follows: First we discuss the various means of analyzing the scattering data obtained. Then we present results for purely elastic scattering, at energies below the $n = 2$ H atom level threshold, and compare our results with those in the literature. Next we present results for energies between the $n = 2$ and $n = 3$ thresholds. The elastic and inelastic cross sections are both presented. The cross sections obtained for energies in higher energy ranges are presented subsequently, including some preliminary results at energies above the $n = 4$ threshold. The resonances found are discussed separately in each section.

6.1 Analysis of Resonances

Resonances have been observed in a wide variety of scattering processes and are known to be associated with the existence of long-lived metastable states.[1] The effect of a strong resonance is to drastically alter the value of the cross section for some transitions across a relatively narrow range of energies. A similarly rapid change in the phase and magnitude of elements of the scattering matrix accompanies a resonance.

It has been known for some time that infinite sequences of resonances occur below the inelastic threshold of electron-hydrogen scattering when the hydrogen levels are assumed to be exactly degenerate in l_1.[2] In reality, this number is finite because of fine structure effects.[3] We will concentrate on the lower energy resonances which are wide enough to be detected with an energy grid of 10^{-4} Ryd, and analyzed by a density to 10^{-6} Ryd where needed. There are various means of determining the position of resonances in the e^-−H system. Some researchers fit their scattering data (such as the eigenphase sum) to a formula, such as the Breit-Wigner formula or Fano lineshape,[4] to determine the positions and widths. Others compute the approximate position of resonances without doing the scattering calculation, by finding the eigenvalues of the potential in the radial equation. This method assumes that the coupling between channels is small and can be neglected. Physically, this means that the motion of the system in one coordinate, the hyperradius ρ, occurs on a different time scale than the motion in the other (hyperangular) coordinates, and so can be treated separately. We have found the collision lifetime matrix[5] useful to determine the position of the resonances and the lifetimes of the metastable states. Argand diagrams have been used to study the results of reactive scattering calculations,[6] and we have found them to be useful in electron scattering.

We can classify resonances as two basic types: closed channel and open channel. The closed channel resonances were first obtained with the Feshbach operator formalism,[7] and are usually called "Feshbach" resonances. The Feshbach resonance corresponds to the physical process of the particle accessing a level of the system that is closed asymptotically, but may be open for low values of ρ. Therefore one would expect to see Feshbach resonances at some energy below the n-th threshold whenever the eigenvalue potentials corresponding asymptotically to that same n-th level consist of one or more sufficiently deep wells. The Feshbach resonances are caused by long-range dipole interaction.[2]

The second type of resonance is the open-channel, or "shape", resonance. A shape resonance may occur as the result of a barrier in the potential (i. e., the eigenvalue) which the particle feels, such that the particle remains for a period of time within the region of the well, before finally leaking out. Thus shape resonances are expected at energies just above threshold. The first encountered example of this observed in the $e^- - H$ system is in the $^1P^{odd}$ state at 0.751 Ryd. This is a very strong resonance, and dominates the cross section at this energy. We find that this shape resonance is caused by the barrier in the potential curves of $^1P^{odd}$, which in turn is caused by the short-range attraction and long-range dipole repulsion.

The $(K,T)^A$ nomenclature (see Section 5.2) is especially useful in categorizing resonances.[8] Certain features of the resonance structure can be predicted using this classification of states. For example, the near degeneracy of resonances in $^1P^{even}$ and $^3P^{odd}$ states, $^1D^{odd}$ and $^3D^{even}$ states, etc., is predicted by this theory. The similarity in parity-disfavored states, given by quantum numbers (J, S, $\Pi = (-1)^{J+1}$, and n), where n indicates the energy level, to the lower energy, lower J state, given by quantum numbers ($J-1$, alternate spin, same parity, and $n-1$) is also predicted. The $^1D^{odd}$ collision lifetime eigenvalues at energies between the $n = 3$ and $n = 4$ threshold are a perfect example of this behavior, because qualitatively these collision lifetimes behave similarly to the $^3P^{odd}$ state lifetimes in the $n = 2$ to 3 region.

6.1.1 Argand diagrams

The use of "Argand diagrams" has been shown to be a useful tool for analyzing the results of scattering calculations.[9-11] An Argand diagram is a cartesian plot in which the real and imaginary parts of an element of the scattering matrix are the coordinates of a point, whose position depends on the energy as a parameter. This representation allows one to examine both the phase and the modulus of

the scattering matrix elements. The direct (i. e., non-resonant) contribution to the phase is expected to decrease with increasing energy, whereas the resonant contribution increases by 2π across a strong resonance, and the modulus is expected to be slowly varying with energy except in the region of a resonance.

These two factors lead to the following general statement about Argand diagrams: in the non-resonant region the representative points approximately traverse circles clockwise around the origin of the system of coordinates as the energy increases due to the continually decreasing phase. In the region of a pure strong resonance (one with no direct contribution), the phase goes through a very fast increase (with energy) of 2π, leading to a counter-clockwise circle whose initial point is the origin and whose center is away from that point, the modulus changing therefore very rapidly with energy. In the presence of a direct background, the initial point on this circle shifts from the origin to the point representing the direct contribution to the scattering matrix element. The distance of the point from the center of the resonant circle is proportional to the relative decay width of the resonance into that channel.[12] Thus in comparing Argand plots of different S-matrix elements (i. e., channels) for the same angular momentum J and spin S, a single resonance may exhibit a large circle for the first element, and yet form a very small circle in the next. Furthermore, it is only in the case of strong, isolated resonances that the full circle is completed. We have found instances of both isolated and interfering resonances in our calculations.

6.1.2 Collision Lifetime Matrix

In this section we describe the formalism of the collision-lifetime matrix developed by Smith.[5] The results of our collision lifetime matrix analysis will be presented in the sections that follow. That matrix, defined by

$$\mathbf{Q} = i\hbar \mathbf{S} \frac{d\mathbf{S}^\dagger}{dE} \tag{6.1}$$

where **S** is the open part of the scattering matrix, has been used by Kuppermann and Kaye[13] for collinear chemical reactions. After computing **Q**, we obtain its eigenvalues q_n, which, when large and positive, indicate a resonance whose lifetime is equal to that eigenvalue. It has turned out that each resonance is associated with only one collision lifetime eigenchannel, although not all resonances need be in the same eigenchannel. Furthermore, each resonance belongs to a series of resonances of a specific eigenchannel that converges on the threshold.

It is convenient to express the eigenvalues q_n in atomic units of time, $t_0 = \hbar/$ 1 hartree, which is equal to 2.42×10^{-17} sec, and is the time required for an electron in the first Bohr orbit of a hydrogen atom to traverse one radian.[14]

Since **S** is unitary, **Q** is hermitian. The energy derivative of the **S** matrix is obtained using a three-point Lagrangian interpolation formula. The resulting **Q** matrix was averaged with its hermitian conjugate to correct for small numerical inaccuracies in this differentiation procedure and thereby ensure real eigenvalues. Plots of the eigenvalues q_n vs. the energy of the system are presented in later sections of this chapter.

6.1.3 Eigenphaseshifts

Eigenphaseshifts are defined as the arctangents of the eigenvalues of the open part of the reactance matrix, or, equivalently, as one half of the phases of the eigenvalues of the open part of the scattering matrix. It should be noted that these eigenphaseshifts are determined modulo π. Furthermore, there is no *a priori* connection between the sets of such eigenphaseshifts calculated at different energies. By requiring the corresponding eigenvectors to be continuous functions of the energy, and by adding π or $-\pi$ to the corresponding eigenphaseshifts, it is possible to obtain curves of eigenphaseshifts vs. energy which are continuous, thereby establishing the missing relationship.

The rationale for calculating the eigenphaseshifts is that resonances tend to cause a large shift in some, but not all, of them.[9] However this simple picture is often complicated by crossings or avoided crossings of eigenphaseshift curves. When there are many resonances in a small energy region, we get both avoided crossings and straight crossings. This is determined by observing how the elements of each eigenvector change with energy, requiring the change to be smooth. At an avoided crossing of two eigenvalues, the two eigenvectors will change slowly, first into vectors which are mixtures of the original ones, and then into vectors with switched characteristics. In a straight crossing the eigenvectors retain the same character throughout — there is no mixing of eigenvectors. Crossings such as these are usually found at energies near a strong narrow resonance. The eigenphase corresponding to the resonant channel experiences a large increase over a short range of energy, but the other channels are unaffected if the crossing is not avoided.

One must have a sufficiently dense grid of energy points in order to determine whether or not the eigenvectors mix. If the grid is too sparse, then the avoided crossing may take place at energies in between the calculated points, and one would not be able to detect the "avoidedness" of the crossing. Because of this problem, and the fact that the phases are only found modulo π, we found that the eigenphaseshifts were not as useful for analyzing the resonances in e^-–H as the other methods, especially at higher energies where there are many open channels.

Another use of the eigenphaseshifts is to calculate their sum. When all of the open states are included in the basis set, this eigenphase sum obeys an upper limit principle[15] which permits us to compare two different approximate calculations, and choose the one with the largest sum as the one giving the better approximation.

6.2 Low Energy Scattering

For energies below the $n = 2$ threshold at 0.75 Ryd with respect to e^-–H $(1s)$,

there is only one open asymptotic state, so there can be no transitions from the $1s$ state to higher states. The only process allowed is "elastic scattering" from that state, including the possibility of exchange. The cross sections we report are not for the direct process solely, i. e., they include both singlet and triplet contributions as indicated by Eq. 3.111. We showed in Chapter 3 that the direct and exchange scattering amplitudes can be obtained from the sum and difference of the singlet and triplet scattering amplitudes, as indicated by the remarks after Eq. 3.118 and the formulæ of Table 3.1.

The behavior of the elastic cross section below the $n = 2$ threshold has been accurately calculated for partial waves $J \leq 3$.[16–20] Schwartz used Kohn's variational principle to calculate the S-wave phaseshifts,[16] which were found to higher precision by Ho, Bhatia, and Temkin,[17] and are generally accepted as exact to the number of figures quoted. This method was applied to $J = 1$ partial waves by by Armstead.[18] Register and Poe[19] calculated the phaseshifts for D-waves using an algebraic variational method. Finally, Callaway[20] calculated phaseshifts for $J = 3$.

The first close-coupling calculation on e^-–H was by Burke and Schey[21] who used a three state approximation ($1s - 2s - 2p$) to calculate phase shifts for states with J=0, 1, or 2. These calculations were followed by a six-state close-coupling calculation,[12] in which higher energies were also considered, and by Burke and Taylor's work,[22] in which correlation functions were added to the 3-state close-coupling basis.

Lin used hyperspherical coordinates to calculate channel potentials[23] such as the ε vs. ρ functions shown in Chapter 5 (Fig. 5.8–15). Assuming that the coupling between channels is so weak that it can be ignored (adiabatic approximation), he modeled the ground state of H^- as an eigenvalue of the lowest channel potential. He also calculated the elastic ^1S phase shift by scattering from this potential. The

phase calculated in this manner behaves correctly at threshold, and is closer than the 3-state close-coupling phase[21] to the exact results, but it becomes rapidly too small with increasing energy. That relatively poor results were obtained even at fairly low energies indicates the weakness of the adiabatic approximation, even when potential crossings (or avoided crossings) are not a factor, as is the case here.

Improved hyperspherical channels may be obtained by using the post-adiabatic approximation,[24] which involves calculating potentials dependent on the collision energy. This was done by Klar and Klar,[25] using up to four "Born-Oppenheimer" channels (in which even the diagonal elements of the coupling matrix P are ignored), which are subsequently linearly combined. Their four-channel calculation gave excellent agreement with Schwartz over the entire range of energy considered (k = 0.1 to 0.7). Their three-channel results are better than the three-state calculation of Burke and Schey; since we intend to include all of the coupling terms we expect our results to be even better than this. Recently a combined hyperspherical and Jacobi coordinate description has been used[26] by Christensen-Dalsgaard to obtain the elastic ^{1}S phase shift.

6.2.1 Elastic phase shifts

Using the lowest three or six surface functions and a projection hyperradius of 8 bohr (see Section 4.5), we obtained the phase shift for S-wave scattering at energies where there is only one open channel. The phase shifts obtained agreed with previous results, as shown in Table 6 – 1. The agreement between our 3-state calculation and Schwartz's is within 0.007 rad and is much better than that of the other calculations presented.

We compare the phase shifts obtained using hyperspherical coordinates for partial waves other than ^{1}S with previous results in Table 6 – 2. The ^{3}S phaseshifts

obtained by our method agree with Schwartz to 0.01 rad ($\sim 6°$). The phaseshifts for $J > 0$ are very small except in the region of resonance. The agreement is in the 0.005–0.025 rad range.

6.2.2 Low energy resonances

The cross section $Q(1s \rightarrow 1s)$ will be affected by resonances lying just below the $n = 2$ threshold of hydrogen.[27] In the dipole representation,[28] the asymptotic form of the radial equation is given by

$$\left(\frac{\partial^2}{\partial r^2} + \frac{l_2(l_2+1) + \alpha_{ij}}{r^2} - k^2\right) F(r) = 0 \tag{6.2}$$

where α_{ij} represents the coupling between the various states. These matrix elements are given by $\langle nl_1l_2JM|rP_l(\cos\gamma)|n'l_1'l_2'JM\rangle$. In the first approximation, only the degenerate levels ($n = n'$) are coupled. The matrix given by $l_2(l_2+1) + \alpha_{ij}$ is diagonalized, giving eigenvalues $\lambda(\lambda+1)$. An infinite series of resonances convergent on the threshold results for each eigenvalue less than $-\frac{1}{4}$. There is such an eigenvalue for $J = 0, 1$ and 2 only below the $n = 2$ threshold. These resonances are due to the long range r^{-2} interaction arising from the degeneracy the target atom states, namely the $2s$ and $2p$ states of hydrogen atom.[15,2]

Gailitis and Damburg[2] showed that the long-range dipole interaction causes resonances below the $n = 2$ threshold for partial waves with $J = 0, 1$, and 2. The dipole interaction is too weak to produce resonances in the higher partial waves, and we saw in Section 5.2 (in particular, Fig. 5.16–17) that the $n = 2$ eigenvalue curves were all repulsive for $J > 2$. We have calculated resonance positions in the ^{1}S, ^{3}S, ^{1}P^{odd}, ^{3}P^{odd}, and ^{1}D^{even} partial waves. The positions, lifetimes and widths obtained are summarized in Table 6 – 3, where we also compare with other theoretical predictions and some experimental observations of resonances.

to about 20% accuracy. The position of the lowest ^{1}S resonance is converged using 10 surface functions by 50 bohr, and has been calculated as 0.70217 Ryd (9.5536 eV). Our lifetime for the ^{1}S resonance is 2300 t_0, and the full width at half-maximum is 3.5 mRyd (0.0476 eV). There have been many other calculations which have determined the position of this resonance. For example, Shimamura calculated its position as 0.702452 Ryd and its width as 3.47 mRyd.[29] Electron transmission spectroscopy experiments by Sanche and Burrow[30] have indicated a resonance at 9.558 ± 0.010 eV, which agrees with our result within their experimental error.

There is a second resonance which is narrower and closer to threshold. We have found that in order to observe the narrower resonances, one must integrate further out. We have calculated the position of this ^{1}S(2) resonance as 0.74787 Ryd (10.175 eV), its width as 0.24 mRyd (0.0033 eV), and its lifetime as 3.3×10^4 t_0 (using 10 surface functions and projecting at 50 bohr). This resonance has not been observed experimentally.

Shimamura also has found a very narrow resonance in the ^{3}S state at 10.1489 eV.[29] Klar and Klar[31] predict its position at 10.169 eV, Schulz[32] observed 10.150 eV experimentally. Our calculation did not detect a ^{3}S resonance when the integration was stopped at 20 bohr. However integrating out to 40 bohr with six surface functions produces an extremely long-lived (2×10^6 t_0) narrow resonance at 0.745389 Ryd (10.1416 eV), with a width of less than 4×10^{-3} mRyd (0.0005 eV). If ten surface functions are used (15 primitives) the resonance position is calculated at 0.745473 Ryd (10.1428 eV), obtained with a projection distance of 50 bohr. Temkin and Sullivan[33] also found that resonances very close to the $n = 2$ threshold level do not show up in calculations in which the integration does not extend past 30 bohr.

A very narrow (width 2×10^{-3} mRyd) ^{1}P Feshbach resonance, separated from the shape resonance above the $n = 2$ threshold by about 0.003 Ryd (0.0450 eV) is

A very narrow (width 2×10^{-3} mRyd) ^{1}P Feshbach resonance, separated from the shape resonance above the $n = 2$ threshold by about 0.003 Ryd (0.0450 eV) is known to exist from photodetachment experiments[34] and has also been predicted theoretically[35] to exist at 0.747901 Ryd. By calculating the eigenvalues of the '$-$' eigenvalue curve (see discussion in Section 5.2), Lin has calculated the positions of the first two members of the Feshbach series as 0.74810 Ryd (10.173 eV) and 0.74994 Ryd (10.198 eV), using the hyperspherical coordinate adiabatic approximation.[23]

We have calculated the position of this $^1P^{odd}$ resonance and the results are shown in Table 6$-$3. If the projection is done at 20 bohr, we were not able to detect a $^1P^{odd}$ resonance with basis '3/5' (surface functions up to $n = 3$, primitives up to $n = 5$). However if one projects farther out, the resonance is obtained. Projecting at 40 bohr with the same basis set, the resonance position is calculated at 0.747790 Ryd (10.1743 eV), with a lifetime of at least 1.9×10^6 t_0, and width of 4×10^{-3} mRyd. The calculated position is moved somewhat lower, to 0.747329 Ryd (lifetime 1.2×10^6 t_0), with width 5×10^{-3}mRyd if the projection is done at ρ=60 bohr. Whereas Callaway calculates the ^{1}S(2) state as lying 0.6 meV lower than the $^1P^{odd}$ resonance state, the data of Bryant *et al.*(1983) indicate that the ^{1}S resonance lies above the $^1P^{odd}$ one. Our result supports the experimental finding, as the $^1P^{odd}$ resonance, which is 2 orders of magnitude narrower than the ^{1}S(2), is found to be 2.2 mev lower.

The calculated positions of the two lowest $^3P^{odd}$ resonances below the $n = 2$ are tabulated, for different basis sets and different projection distances, in Table 6 $-$ 3. The largest calculation gave the position of the first as 0.71559 Ryd (9.7362 eV) and the width as 0.43 mRyd (0.0059 eV), which is in relatively good agreement with the experimental observation of 9.738 ± 0.010 eV and 0.0056 ± 0.0005 eV, respectively. The lifetime is found to be 18,600 t_0. The position and width of this resonance were determined by Das and Rudge[36] to be 0.715735 Ryd and 0.430 mRyd respectively.

Our calculated width is in excellent agreement, though our position is 0.00014 Ryd lower. Other calculated positions are also listed in the table. The second $^3P^{odd}$ resonance is just below threshold, at 0.74951 Ryd (10.198 eV) with a lifetime of 190,000 t_0.

We have determined the position of the $^1D^{even}$ resonance as 0.74395 Ry (10.122 eV), with lifetime 12,500 t_0, and width 0.65 mRyd, as compared to Callaway, who obtained E=0.744152 Ryd, width=0.64 mRyd, and Register and Poe,[19] who obtained E=0.743924 Ryd, width=0.66 mRyd using a Hylleraas type basis containing up to 84 terms. Sanche and Burrow[30] detected the $^1D^{even}$ resonance at 10.128 ± 0.010eV and determined the width to be 0.0073 ± 0.002 eV. The presence of this state has been observed[34b] in the photodetachment spectrum of H^- in intense (greater than 400 kV/cm) electric fields. The single-photon transition from the ground state of H^- (^1S) to $^1D^{even}$ is forbidden, but the electric field allows mixing between the $^1P^{even}$ and $^1D^{even}$ states. We did not find any $^3D^{even}$ resonance, which is not surprising due to the fact that the eigenvalue potential curve is only 0.004 h deep. No other calculations have yielded a $^3D^{even}$ resonance, either.

The relatively wide Feshbach resonances calculated in ^1S, $^3P^{odd}$, and $^1D^{even}$ correlate with the fact that these partial waves all have a deep well channel potential at the $n = 2$ level (see Fig. 5–9, 5–12, and 5–13). The corresponding curves of the alternate spin (^3S, $^1P^{odd}$, $^3D^{even}$) are all much less attractive, and as such are either not deep enough to produce a Feshbach resonance, or the resonance is extremely narrow.

6.2.3 Total elastic cross section

The total elastic cross section, obtained from the $J = 0$, 1, and 2 partial waves using ten functions and projecting at 50 bohr, is plotted in Figure 6.1, for energies 0.69 to 0.75 Ryd (the resonance region). It is estimated that higher partial waves

will add about 2% to the cross section. Also plotted in this figure are the total singlet and triplet contributions. The grid of energy points that was used was not fine enough to show the ^{3}S resonance, but we used a finer grid in the region of the $^1P^{odd}$ resonance, which is just as narrow, to distinguish it from the ^{1}S(2) resonance, which is accidentally degenerate. It may be difficult to see that the structure at 0.748 Ryd is due to two resonances from this energy scale.

6.3 Energies above n=2 Threshold and below n=3 Threshold

We now consider the second energy range, from the opening up of the $n = 2$ channels at 0.75 Ryd to the $n = 3$ threshold at 0.8889 Ryd. There are three open nl_1 channels in this region: $1s$, $2s$, and $2p$. There are four open channels with quantum numbers nl_1l_2 for $J > 0$ (parity-favored states), but only three for $J = 0$. In parity-disfavored states, i. e., where $\Pi = (-1)^{J+1}$, there is only one open state, that is, $2p$ ($l_2 = J$).

The cross sections $Q(1s \rightarrow 2s)$ and $Q(1s \rightarrow 2p)$ will be affected by resonances lying just below the $n = 3$ threshold of hydrogen.[37] An infinite series of resonances convergent on the threshold results for each eigenvalue of Eq. 6.2 less than $-\frac{1}{4}$. There are two such eigenvalues for $J = 1$ and 2 for the $n = 3$ threshold, and just one for $J = 0$, 3, and 4. These resonances are due to the long range r^{-2} interaction arising from the degeneracy the target atom states.[10,2] We did in fact find resonances in the ^{1,3}S, $^{1,3}P^{odd}$, $^{1,3}D^{even}$, $^{1,3}F^{odd}$ and $^1G^{even}$ partial waves, as expected, but no resonances were seen for $^3G^{even}$ and none for $J = 5$. In general, resonances will not be present below the n^{th} threshold in partial waves $J > 2(n-1)$. Consideration of the allowed intrashell doubly excited states partially explains why. For example, for $n = 3$, the doubly excited state with the highest total angular momentum is $2d^2$, which is an allowed $^1G^{even}$ configuration (in the independent particle model), but which is not allowed (by the Pauli principle) for $^3G^{even}$. One

needn't, however, always have to be able to construct an intrashell doubly excited state to see resonances. The ^{3}S resonances are necessarily related to intershell states; in the $(K,T)^A$ nomenclature these states all have $A = -1$. The intrashell resonances, on the other hand, all have $A = +1$, and are much wider.

Besides the presence of resonances below threshold, Gailitis and Damburg also predict that those partial waves which have Feshbach resonances below the $n = 2$ threshold ($J < 3$) will have non-vanishing inelastic cross sections just above that threshold.[2] In Section 6.2 we described how resonances are found below the $n = 2$ threshold for $J = 0, 1$ and 2. The inelastic cross sections for these partial waves are indeed large at energies close to the $n = 2$ threshold. The behavior of the higher partial wave cross sections ($J \geq 3$) is markedly different in that the inelastic cross section increases slowly with energy, from being negligible at threshold, to sizeable in the resonance region.

Calculated resonance positions are listed for all the partial waves through $J = 4$ in Table $6-4$. We have also listed the computed resonance lifetime and full-width of the lifetime at half-maximum, and some resonance positions calculated by other authors. The first calculation which was able to observe resonant behavior was the 6-state close-coupling calculation of Burke.[12] Inclusion of the $3s$, $3p$, and $3d$ states in the basis gave rise naturally to resonances of the Feshbach type,[7] that were impossible to obtain with only a 3-state basis.[21,38] Ho has used complex rotation to predict resonance positions with much success.[8,39] We also compare to the resonance positions calculated using Callaway's variational procedures.[35,40]

In Figure 6.2 we have organized the $n = 3$ Feshbach resonances according to the $(K,T)^A$ configurations in order to show the supermultiplet structure. The resonances obtained have been assigned quantum numbers K, T, and A as described by Lin,[71] taking into account the width of each resonance. A striking pattern can

be seen for states with different J, S and Π but the same (K,T) and A, if $A = \pm 1$. There is a series of relatively wide, lower energy resonances starting with the ^{1}S $(2,0)^+$ state, that continues through $^3P^{odd}$, $^1D^{even}$, $^3F^{odd}$, and $^1G^{even}$. There is a similar series of extremely narrow resonances, beginning with the ^{3}S $(2,0)^-$ state, and continuing through $^1P^{odd}$, $^3D^{even}$, and $^1F^{odd}$.

In the tables that follow (Tables 6−5 through 6−14) we will compare our results obtained using the $n_{max} = 5$ basis set and projecting at 60 bohr to those obtained by the following authors: Burke, Ormonde and Whitaker[12] (BOW), who performed 6-state close-coupling calculations; Taylor and Burke[38] (TB), who supplemented a 3-state close-coupling basis with 20 correlation functions; Geltman and Burke[41] (GB), who used three pseudo-states along with the $(1s, 2s, 2p)$ functions; and Callaway,[42] who used an algebraic variational approach with 14 basis functions: 6 atomic states and 8 pseudostates. In some of these tables we have also listed our (unconverged) 6-state cross sections, in order to compare methods using the same size basis set.

6.3.1 S-wave scattering

The ^{1}S partial cross sections ($1s \rightarrow 1s$, $1s \rightarrow 2s$, and $1s \rightarrow 2p$) are shown in Figure 6.3 and listed for a few energies between $n = 2$ at 0.75 Ryd and $n = 3$ at 0.889 Ryd in Table 6 − 5, where our results are compared with some other calculations. The agreement is satisfactory. Our cross section vs. energy curves are generally of the same shape as others and resonances are found at about the same energies as others (see Table 6 − 3). Our results are closest to the 3-state plus correlation calculation.[38] Comparison with our 6-state and 15-state values shows that the 6-state close-coupling[12] and 3-state-plus-3-pseudostates[41] calculations are not fully converged. It also is a demonstration of how correlation is included in the hyperspherical surface function basis set. From the table we can see some trends: as more correlation is included in the wavefunction, the elastic cross section

increases and the inelastic cross sections decrease. Our calculations, which have the most correlation, continue the trend. The agreement with Callaway, who used a variational approach, is very good.[42]

The ^{1}S scattering cross section shows three Feshbach resonances just below the $n = 3$ threshold, at 0.8619, 0.8846, and 0.88775 Ryd as listed in Table 6 – 4. The positions of these resonances were determined by finding the maxima in the largest collision lifetime eigenvalue, as discussed in Section 6.1. These collision lifetime eigenvalues are displayed in Figure 6.4. To compare with scattering experiments we have converted into electron volts using the infinite mass Rydberg (1 Ryd = 13.605 eV, see Section 1.5). Our lowest resonance energy (11.73 eV) agrees satisfactorily with the position of dips in the total inelastic cross sections found experimentally by Williams,[43] who used an electron energy resolution of 12 to 30 meV to study resonances. Williams found dips in the $1s \rightarrow 2s$ and $1s \rightarrow 2p$ cross sections at 11.73 ± 0.06 eV and 11.75 ± 0.06 eV respectively. Earlier experiments by McGowan *et al.*[44] place the ^{1}S resonance at 11.65 ± 0.03 eV, which is too low.

The scattering in the ^{3}S partial wave is almost all due to elastic scattering. The cross sections for inelastic scattering are very small, but at the same time they are very sensitive to resonances which are almost undetectable in the ^{3}S elastic cross section. These are plotted in Figure 6.5, and compared with other calculations in Table 6 – 6. We found one very narrow resonance in this partial wave, at 0.88201 Ryd, compared with Callaway's 0.88203.[35] He also obtains a second even narrower resonance at 0.88752 Ryd, which we did not detect. The narrowness of our ^{3}S resonance is due to the weak coupling among channels,[2] and is the reason it has not been detected experimentally.

6.3.2 P-wave scattering

Our results for elastic scattering in $J = 1$ partial waves are given in Table 6 – 7.

The inelastic results, cross sections for transition to the $2s$ and $2p$ states are given in Table 6 – 8 and Table 6 – 9, respectively. The $^1P^{odd}$ partial cross sections are plotted in Figure 6.6, and the $^3P^{odd}$ cross sections are plotted in Figure 6.7.

The most dramatic result is the shape resonance found in the $^1P^{odd}$ channel just above the opening of the n=2 level. We compute the position of this resonance at 0.75108 Ryd† and its lifetime as 6200 t_0 (when using the full $n_{max} = 5$ set of 25 surface functions and projecting at 60 bohr). The full width of the collision lifetime at half its peak is 1.0 mRyd (0.014 eV). The $n = 2$ Feshbach resonance is only 0.00337 Ryd lower in energy, by our calculation. Using an 11 state basis, Callaway[35] determined the position of the resonance to be 0.75121 Ryd and the width to be 1.47 Ryd by fitting the eigenphase sum to the formula

$$\delta_T(E) + \frac{a}{E - E_{th}} + b + c(E - E_{th}) + \tan^{-1}\frac{\Gamma}{2(E - E_{th})} \qquad (6.3)$$

This resonance was also seen by Taylor and Burke,[38] discussed by Macek and Burke,[45] and by Lin.[46]

Higher resolution than that used by Koschmieder *et al.*[47] and Oed[48] (150 meV) is required to resolve resonances in the experimental cross section. Presence of the $^1P^{odd}$ resonance was first observed in the $1s \rightarrow 2p$ cross section by McGowan *et al.*[44] The measurements of Williams and Willis[49] showed the energy of the $^1P^{odd}$ resonance to be 10.210 ± 0.005 eV, and obtained no other oscillations in the $1s \rightarrow 2p$ cross section between 10.200 and 11.000 eV, in contrast to the earlier result,[44] where a second unexplained maximum had been obtained at 10.45 ± 0.03 eV. The width we have obtained is somewhat narrower than that calculated by Callaway; the experimentalists had suggested that the previously calculated width of the resonance was too wide.[49]

† 10.219 eV, converted with infinite Rydberg, with respect to ground state of H atom, 10.968 eV with respect to ground state of H^-, using reduced Ryd.

The shape resonance, as well as the $^1P^{odd}$ Feshbach resonance below the $n = 2$ threshold, has been detected experimentally in the H^- photodetachment cross section.[34] The estimated width of the shape resonance from these experiments is 23 ± 6 meV. Gram *et al.*[50] studied the effect of an electric field on the photodetachment cross section and obtained a shape resonance at a photon energy of 10.98 eV, while aligning their observed Feshbach resonance to agree with the theoretical resonance energy of Broad and Reinhardt[51] (10.930 eV). The theory of the photoionization (photodetachment) of H^- has also been treated by Macek,[52] and by Hyman *et al.*[53] and by Wendoloski and Reinhardt[54] who used the method of complex coordinates to obtain $E_R = 0.75130$ Ryd, $\Gamma = 1.04$ mRyd for the resonance position and width.

As was discussed in Chapter 5, two of the three eigenvalue potentials converging to the $n = 2$ threshold exhibit an avoided crossing at about 13.5 bohr (see Fig. 5.11). One of these curves forms a shallow well which can support an infinite number of resonant states (the number is actually less than infinite due to the fine-structure effects).[3] The other eigenvalue potential forms a barrier, caused by the long range polarization effects between the degenerate $2s$ and $2p$ states. This barrier potential is the reason for the shape resonance.

The eigenphaseshifts and eigenphase sum for $^1P^{odd}$ partial wave in the vicinity of the shape resonance are plotted as functions of the energy in Figure 6.8. The eigenphase sum has been used by others to compute the position of the resonance, and also as a relative measure of the correctness of a calculation.[35] The non-resonant contribution to the eigenphase sum near the shape resonance is a rapidly decreasing function of energy, which complicates the analysis. A comparison of the partial cross sections for elastic and excitation processes with those obtained by Callaway[35] is presented in Figure 6.9. It can be seen that for the $1s \rightarrow 1s$, $1s \rightarrow 2s$, and $1s \rightarrow 2p$ processes, our cross sections have maxima at 0.7510, 0.7513, and 0.7513 Ryd

respectivley, whereas Callaway's occur at 0.7513, 0.7515, and 0.7515 Ryd. These are to be compared with the energy of 0.7511 Ryd we determined from the maxima in the collision lifetime eigenvalue curve. The collision lifetime method is more reliable and less ambiguous for determining the position of the resonance than choosing the extrema in the cross section curves.

We also get shape resonance behavior in partial waves other than $^1P^{odd}$. No other calculation has found a shape resonance above the $n = 2$ threshold other than in the $^1P^{odd}$ partial wave, and experiments have also been interpreted as having only the $^1P^{odd}$ shape resonance.[49] We have found that $^3P^{odd}$ partial wave has a resonance ten times shorter lived than that $^1P^{odd}$. We have also found that the longest lived $n = 2$ shape resonance occurs in the $^3D^{even}$ partial wave, with lifetime $14,500\ t_0$. The lifetimes steadily decrease with J for $J > 2$: for $^{1,3}F^{odd}$ the lifetime is $1200\ t_0$, for $^{1,3}G^{even}$ it is only $450\ t_0$, and for $^{1,3}H^{odd}$ it is only about $50\ t_0$. The positions of these resonances move out further from threshold as J is increased (for $J > 2$). Only in the $J = 0$ partial wave (where there is one less state) is there definitely no shape resonance, because all three collision lifetime eigenvalues are negative right above threshold.

Full calculations were not performed on the parity-disfavored partial waves ($^{1,3}F^{even}$, $^{1,3}D^{odd}$, etc.) in the $n = 2$ to $n = 3$ energy range because the only cross section at energies below the $n = 3$ threshold to which these partial waves contribute is the $2p \rightarrow 2p$ elastic cross section, in which we were not particularly interested. However we have calculated resonance energy positions for some of these partial waves. A few calculations at energies close to the $n = 2$ threshold were performed on the $J = 1$ partial wave of even parity. These have shown a positive peak in the collision lifetime eigenvalue for $^1P^{even}$ ($720\ t_0$ at 0.7506 Ryd), but none in $^3P^{even}$. Analyzing the eigenvalue potentials (see Figs. 5.11 and 5.12) we can identify the cause. The triplet curve is very attractive, with a well 0.0234 h deep, which results

in a bound state.[55,56] The curve for $^1P^{even}$, on the other hand, has a very shallow well and barrier. The barrier height is 0.00024 h from the bottom of the well, which is only 0.0001 h less than the asymptotic $n = 2$ energy level.

Resonances are sometimes classified as belonging either to '+' or '−' series,[57] just as we discussed '+' and '−' surface functions in Chapter 5. Of the four $^1P^{odd}$ resonances seen converging to the $n = 3$ threshold, the first and fourth are classified as '+,' and the second and third resonances, which are an order of magnitude narrower, are classified as '−.'[58] The classification is based on a labelling of surface function eigenvalue curves, and obtaining the resonance levels by computing the bound states supported by those curves. The '+' curves are more attractive at small ρ, and two-electron excitations to such a level is expected to be 1 to 2 orders of magnitude more likely than excitation to the less attractive '−' state.[58]

We compare our resonance positions with other authors in Table 6 − 4. We have detected only two $^1P^{odd}$ Feshbach resonances, at 0.8745 Ryd† and 0.882862 Ryd‡ in our standard calculation, projection at 60 bohr. Other calculations have seen higher members of the series, but projecting at 60 bohr we have not detected them. In particular, Callaway[35] calculated the positions of four $^1P^{odd}$ resonances, at 0.87457, 0.88286, 0.88777, and 0.88820 Ryd. Our positions and widths agree well with the first two of these. The width of Callaway's 4th resonance at 0.88820 Ryd is $\sim$ 10 times that calculated for his resonance at 0.88286 Ryd. The conclusion drawn from this statement is that lack of energy resolution is not the reason resonance #4 goes undetected in our calculation. (Resonance #3 is extremely narrow, according to Callaway.) Based on our experience with the

† 11.90 eV with respect to ground state of H atom, 12.646 eV photon energy with respect to ground state of H^-.

‡ 12.0121 eV with respect to ground state of H atom, 12.7597 eV with respect to ground state of H^-.

$n = 2$ resonances and observing that the largest $^1P^{odd}$ collision lifetime eigenvalue is monotonically increasing above 0.884 Ryd, we suggest that a larger projection distance (80 bohr) may be necessary to observe some of the resonances less than 0.001 Ryd below the $n = 3$ threshold.[59]

The two relatively broad $^1P^{odd}$ resonances have been seen in measurements of the photodetachment of the H^- ion, by Hamm *et al.*[60] who obtain resonance energies of 12.650 ± 0.004 (width 0.0275 ± 0.0008 eV) and 12.837 ± 0.004 eV (width 0.0016 ± 0.0003 eV). They interpreted these as the first two members of a Feshbach resonance series of the '+' type. The first resonance agrees within their experimental error with our result, and the second is the missing one we discussed above. These authors also have seen some weak structure near 12.78 eV, which they think may be a resonance of the '−' class, and which agrees within 0.02 eV with our second resonance position. The lowest energy $^1P^{odd}$ Feshbach resonance has also been detected in electron scattering experiments,[43] causing dips in the $1s \rightarrow 2s$ and $1s \rightarrow 2p$ cross sections at 11.91 ± 0.06 and 11.97 ± 0.06 eV, respectively.

We have computed the positions of three $^3P^{odd}$ Feshbach resonances, at 0.8641 Ryd (11.76 eV), 0.8855 Ryd (12.05 eV), and 0.88747 Ryd (12.075 eV). Experimentally, the $^3P^{odd}$ resonance is not clearly defined, because the energy resolution of the experiments is usually greater than the energy separation of the various resonances. Theoretically, the lowest $^3P^{odd}$ $n = 3$ Feshbach resonance lies only 0.03 eV above the ^1S resonance. The relative error in energy determination in Williams experiment is 0.02 eV.[43] Williams has tentatively assigned a minimum in the $1s \rightarrow 2p$ excitation cross section at 11.75 ± 0.06 eV to the $^3P^{odd}$ resonance. It is clear from Fig. 6.5 that the $^3P^{odd}$ resonance at 0.8641 Ryd does indeed cause a large dip in the $1s \rightarrow 2p$ cross section, which is significant in the total cross section too (see Figure 6.15).

6.3.3 D-wave scattering

The elastic scattering cross sections for $J = 2$ are compared with the literature in Table 6 – 10. The inelastic scattering cross sections for excitation to the $2s$ and $2p$ states for $J = 2$ are given in Table 6 – 11 and Table 6 – 12, respectively. Our results for the inelastic cross sections give only fair agreement with previous calculations, and the elastic cross sections are about twice those obtained by Burke *et al.*[12]. We believe that the latter are not converged with respect to basis size. (See Table 4–5 in Chapter 4 for convergence tests.)

We have plotted the collision eigenvalues for $^1D^{even}$ in Figure 6.10. $^1D^{even}$ resonances are obtained at 0.8680 (11.81 eV) and 0.8868 Ryd (12.07 eV), whereas Burke *et al.*[12] obtained only one resonance at 0.8687 Ryd (11.82 eV), with width 3.62 mRyd (0.049 eV). Callaway also predicts a resonance position of 0.8681 Ryd (11.81 eV).[35] Williams' detected a resonance attributed to the $^1D^{even}$ partial wave at 11.85 ± 0.080 eV in the $1s \rightarrow 2p$ cross section, agreeing with theory within experimental error.

It has been shown that the position of the experimentally observed $^1D^{even}$ resonance[61] below the $n = 2$ threshold is not given correctly by the 3-state close coupling calculation.[62] The position predicted by the 6-state close-coupling calculation is shifted down 0.07 eV compared with the McGowan *et al.* experimental result of 11.89 eV.[44] McGowan *et al.* have suggested that the 6-state calculation was unconverged and that the resonance position would shift further in a larger calculation; however our result is 0.0007 Ryd lower than Burke's and agrees with the experiment by Williams.[43] The conclusion is that McGowan *et al.*'s suggestion is probably incorrect.

We have obtained a series of maxima in the collision lifetime eigenvalue curves just above the $n = 2$ threshold. (See Table 6 – 4.) The largest of these is in the

$^3D^{even}$ partial wave, located at 0.75040 Ryd (lifetime 14,500 and width 0.45mRyd). The lowest $^3D^{even}$ $n = 2$ eigenvalue curve, as seen in Fig. 5.14, is attractive but not enough so to support a Feshbach resonance below threshold. The result apparently is a shape resonance just above the $n = 2$ threshold, which nevertheless is surprising, because the eigenvalue potential does not have any barrier. Subsequent peaks are located at 0.754 Ryd (10.26 eV) and 0.763 (10.38 eV) with corresponding lifetimes of 400 t_0 and about 60 t_0. McGowan *et al.*[44] also report a second small maxima in the cross section at 10.45 ± 0.03 eV (0.768 Ryd) just after the inelastic threshold. It was suggested that this structure may be part of the oscillatory structure predicted by Damburg and Gailitis.[2]

6.3.4 Higher partial wave scattering

According to Gailitis and Damburg[2] the inelastic partial cross sections for transition $1s \rightarrow 2s$ and $1s \rightarrow 2p$ will tend toward zero at the $n = 2$ threshold for $J \geq 3$. The contribution of $J = 3$ partial waves to the total cross section is much smaller than the lower J ones, but not sufficiently small to conclude that the total cross section has converged once the F-wave contributions are included. These cross sections are presented in Table 6 – 13 (elastic), Table 6 – 14 ($1s \rightarrow 2s$), and Table 6 – 15 ($1s \rightarrow 2p$). $^1F^{odd}$ cross sections are displayed in Figure 6.11, $^3F^{odd}$ cross sections in Figure 6.12. They are particularly influenced by the presence of two sharp resonances, at 0.8872 Ryd (12.07 eV) for the $^1F^{odd}$ and at 0.8769 Ryd (11.93 eV) for the $^3F^{odd}$ partial wave. The collision lifetime eigenvalues for $^1F^{odd}$ and $^3F^{odd}$ are graphed in Figure 6.13. The $^3F^{odd}$ resonance produces a sharp increase in the ($1s \rightarrow 2s$) and ($1s \rightarrow 2p$) total cross sections, as seen in Fig. 6.12. We suspect that there is a second $^3F^{odd}$ resonance that is very narrow and even closer to the $n = 3$ threshold; Callaway predicted its position as 0.8880 Ryd.[35] We were not able to detect this resonance, projecting at 60 bohr and using an energy

grid of 10^{-6} Ryd in the neighborhood of 0.888 Ryd. A higher energy resolution was not attempted.

The collision lifetime analysis also indicates a series of shorter-lived resonances just above the $n = 2$ threshold at 0.7545, 0.763, and 0.78 Ryd (10.266, 10.38 and 10.6 eV, respectively) with lifetimes of 1200, 200, and 80 t_0, respectively. These lifetimes are so small compared to those occurring slightly below the $n = 3$ threshold that one might wonder whether they are not simply numerical artifacts, but these resonances produce a noticeable effect on the probablity of transitions for which the initial state is not the ground state. All three resonances are seen in the $^3F^{odd}$ partial elastic $2p \rightarrow 2p$ scattering cross section, as seen in Figure 6.14.

Some of the Argand diagrams corresponding to the $^3F^{odd}$ resonances (Figure 6.15) are remarkable in that the curves are drawn counter-clockwise throughout much of the energy range. The resonance at 0.877 produces a large counter-clockwise circle, as expected, in the plot of each matrix element, but the resonances at lower energy give rise to circular arcs not passing through the origin, which are most evident in the Argand diagram of the $2p2 \rightarrow 2p2$ and $2p4 \rightarrow 2p4$ elements of the scattering matrix, indicating weaker resonances superimposed on the direct contribution to these elastic processes. Some of these resonances are very wide and short-lived. The largest collision lifetime eigenvalue is however never negative, confirming the resonance nature of the features slightly above the $n = 2$ threshold.

The $^1F^{odd}$ and $^3F^{odd}$ partial waves have similar behavior at energies close to this threshold. The partial cross sections for the $1s \rightarrow 2s$ and $1s \rightarrow 2p$ processes from the ground state increase steadily and slowly with energy, starting at negligible values near the $n = 2$ threshold and increasing to values of the order of 0.01 and $0.05\pi a_0^2$, respectively, as the $n = 3$ threshold approaches. There is not much change in phase over this energy range, as seen from the Argand diagrams for

the $(1s3 \rightarrow 2s3)$, $(1s3 \rightarrow 2p2)$, and $(1s3 \rightarrow 2p4)$ matrix elements. By contrast, the $J = 3$ cross sections for transitions from excited states, of which Figure 6.12 is an example, are peaked at energies close to the $n = 2$ threshold, after which they decrease by 1 to 2 orders of magnitude.

6.3.5 Total cross sections

Comparison of theory and experiment is this energy range is straightforward and not complicated by processes that may be present at higher energies, such as cascade processes and ionization; however theoretical results have to be "folded" with the experimental energy distribution to make a meaningful comparison.

The major difficulty in electron-hydrogen atom scattering experiments is in producing an intense beam of atomic hydrogen. The first high-resolution experiment (electron-bream resolution 0.07 eV) of an excitation cross section in H was made by McGowan, Williams, and Curley,[44] and confirmed the theoretical prediction of resonances occurring slightly below the $n = 3$ threshold. There have been several experimental measurements of the total cross sections for impact excitation to the $2s$ state.[63] Resonances in the $2s$ channel were measured by Oed,[48] and subsequently by Koschmieder *et al.*[47] The latter achieved an energy resolution of 110 meV. The experimental results have indicated that 6-state close coupling calculations overestimate the cross section by 10% to 15% above 11 eV. More recent experimental data are available for the total cross section for the excitation of the $2s$ and $2p$ states,[49,43] which does not rely on any theoretical calculation for normalization. The energy resolution in these experiments was 0.07 eV (0.005 Ryd). Still better resolution is required to identify separate resonances that occur close in energy.

The total elastic cross section of electrons with H($1s$) atoms in the energy range from the $n = 2$ threshold to the $n = 3$ threshold is shown in Figure 6.16. We have listed the partial wave contributions to the elastic and inelastic cross sections

from the ground state and the total cross sections in Table 6 – 16 for a selection of energies between the $n = 2$ and $n = 3$ thresholds, where we have also compared with the theoretical results of Callaway.[35] The total cross section for excitation to the $2s$ state is shown in Figure 6.17a, and the total cross section for excitation to the $2p$ state is shown in Fig. 6.15b. The major structural features are due to the $^1P^{odd}$ shape resonance at 0.7511 Ryd at the low energy end, and to the several wide Feshbach resonances below the $n = 3$ threshold. The $^3F^{odd}$ resonance at 0.877 Ryd produces a sharp peak in both excitation cross sections. The higher lying resonances are very narrow and closely spaced. The agreement with experiment,[43] though not shown, is very good, given the resolution.

6.4 Energies between the n=3 and n=4 Thresholds

In this section we examine the scattering processes accessible at energies between the $n = 3$ and $n = 4$ thresholds. We will consider excitation both from the ground state to the upper states and from the $2s$ and $2p$ states to the $n = 3$ states, as well as elastic scattering of the ground state. Both parities need to be considered when calculating transitions from the $2p$ state.

The only previous scattering calculations in the $n = 3$ to $n = 4$ energy range have been those obtained by Hata *et al.* using variational methods;[64] although Burke *et al.*[12] did some 6-state close coupling calculations at a few select higher energies, those calculations did not include the $n = 4$ states in the basis set, which has been shown to be important for convergence.[65]

6.4.1 Resonances

We have computed the positions of over 80 resonances between the $n = 3$ and $n = 4$ thresholds using the collision lifetime matrix eigenvalues. These generally agree with, but are more complete than, the resonance positions and widths computed by complex rotation.[8] All the resonances found for $J = 0$ through 5

are listed in Table 6 – 17. The lifetimes are given by the peak values of the collision lifetime matrix eigenvalues, taken as functions of the energy, and the widths are defined as the full-width at half-maximum of the collision lifetime eigenvalue vs. energy curve. The widths are approximately inversely proportional to the lifetime, as is expected from the uncertainty principle. We list the widths even though they aren't as accurately determined as the lifetimes, in order to make comparisons with other calculations in which the width of the resonance, but not the lifetime, was computed.

The resonance energies for states with parity $(-1)^{J+1}$ are closely associated with resonances of the other parity, if one switches spin. This is called "T-doubling." For example, in the $^1P^{even}$ partial wave there is one resonance at 0.93403 Ryd, whose position and lifetime is comparable to the resonance at 0.93408 Ryd in the $^3P^{odd}$ state. And for $^3P^{even}$ we find three resonances, at 0.9255, 0.9358, and 0.93707 Ryd, of which the latter two have energies just slightly below those of the corresponding $^1P^{odd}$ resonances at 0.9359 and 0.93713 Ryd. This phenomenon is seen in the higher partial waves as well. Recently a new classification scheme based on the set of internal correlation quantum numbers K, T, and A has been introduced, and the "T-doubling" feature is predicted by the scheme.[66,67] Resonant states with the same values of K, T, and A are obtained as quasi-bound states of eigenvalue potential curves (see Chapter 5) which are similar in shape, and hence the resonance energies are close together, even though the J, Π and S quantum numbers may be different. Another consequence is that supermultiplet structure observed for intrashell states[68] may be interpreted, as well as predicted, by this scheme. Approximate selection rules for e^-–H scattering have been proposed based on this model.

In Figure 6.18 we have organized the $n = 4$ Feshbach resonances according to the $(K,T)^A$ configurations in order to show the I-type supermultiplet structure.[68]

The resonances obtained have been assigned quantum numbers K, T, and A as described by Lin,[71] taking into account the width of each resonance. We find many instances of "T-doubling," two nearly degenerate resonances with the same J, but different S and Π. A striking pattern can be seen for states with different J, S and Π but the same (K,T) and A, if $A = \pm 1$. There is a series of relatively wide, lower energy resonances starting with the ^{1}S $(3,0)^+$ state, that continues through $^3P^{odd}$, $^1D^{even}$, $^3F^{odd}$, $^1G^{even}$ and $^3H^{odd}$. If we had done $J = 6$ calculations, there would be an $^1I^{even}$ resonance of this type as well. There is a similar series of extremely narrow resonances, beginning with the ^{3}S $(3,0)^-$ state, and continuing through $^1P^{odd}$, $^3D^{even}$, $^1F^{odd}$, $^3G^{even}$, and $^1H^{odd}$. This structure is similar to what was seen in Figure 6.2.

6.4.2 S-wave scattering

Cross sections for $J = 0$ partial waves were obtained using 15 surface functions ($n_{max} = 5$) and projecting at 80 bohr. The cross sections are presented graphically in Figure 6.19. The ^{3}S contributions to the $1s \rightarrow 3l_1$ cross sections are found to be exceedingly small, all less than $10^{-4}\pi$ a_0^2, which is neglible compared to the ^{1}S contribution. The same situation held for the energy region between the $n = 2$ and $n = 3$ threshold where most of the scattering from the ground state in the ^{3}S partial wave is elastic in nature, and where the resonances are few, very long-lived and narrow.

Comparison of the $J = 0$ cross sections of Hata *et al.*[64] using the full basis $1s \rightarrow 3l_1$ (6 states plus 8 pseudostates) at E=0.90 Ryd, summed over spins, with our own results, and with the 6-state close-coupling results,[12] is made in Table 6−18. Our total $J = 0$ $1 \rightarrow 3$ cross section agrees with Hata *et al.* to about 5%. The individual cross sections are small, and the percent difference between them is large, except for the $1s \rightarrow 3p$ contribution, where agreement is quite good.

The ^{1}S partial wave may perhaps have a resonance right above the $n = 3$ threshold; we found the largest lifetime eigenvalue increases to over 10^4 t_0 as the energy decreases to the $n = 3$ threshold, but no maxima is achieved. However there appears to be a shoulder in that eigenvalue at a slightly higher energy. Whether this shoulder indicates a weak shape resonance we were not able to determine. The ^{1}S partial wave contribution to the $1s \rightarrow 3s$ cross section definitely indicates the presence of a resonance, as a very sharp peak exists just above threshold. The resonance is not nearly as pronounced in the other ^{1}S channels, however. Pilot hyperspherical calculations by Lin[23] predicted a shape resonance in the ^{1}S partial wave above the $n = 3$ limit, based on the potential curves obtained. Our ^{1}S potential curves do have crossing, whereas the ^{3}S ones do not (see Fig. 5.9 and 5.10) and we have seen in the $^1P^{odd}$ partial wave (at the $n = 2$ threshold) that barriers formed by states that cross can lead to shape resonances. Lin calculates a barrier of 12.13 eV, which is fairly consistent with the experimental resonance energy of 12.16 eV.[69]

The Argand diagrams are equally difficult to interpret. Whereas the Argand plot gives a clockwise motion from E=0.8889 to 0.895 Ryd for most of the scattering matrix elements , there are a few which may be interpreted as giving slightly counter-clockwise moving curves. The Argand diagram for the $2s \rightarrow 3d$ ^{1}S matrix element is shown in Figure 6.20, and has the most curvature near the $n = 3$ threshold. The curve bends back in the opposite direction at about 0.895 Ryd, forms half of a small circle between 0.920 and 0.925 Ryd, which indicates the resonance at 0.921 Ryd, and then loops into a much larger oblong shape between 0.930 and 0.935 Ryd, the result of two close resonances at 0.93125 and 0.93325 Ryd.

On the other hand, a shape resonance *is* indicated by the collision lifetime analysis in the ^{3}S partial wave above the $n = 3$ threshold, as seen in Figure 6.21. We calculate its position at 0.8898 Ryd with lifetime 2200 t_0 and width 1.2 mRyd, which is fairly short-lived. This is compared to Hata *et al.*'s result of 0.8907 Ryd

with width 4.3 mRyd.[70] The effect of this resonance on the cross sections, however, is hard to see. Only in the $2p \rightarrow 3s, 3d$ and $2s \rightarrow 3s$ ^{3}S partial cross sections is any kind of structure seen at the resonance energy (see Fig. 6.19). Hata *et al.* have found a maximum in the ^{3}S $1s - 3d$ cross section, where we find only a small bump, not a major peak. They further state that the resonance is due to the angular momentum barrier in the $3p$ and $3d$ channels, caused by short-range repulsive interaction, along with strong long-range dipole interaction between the degenerate $n = 3$ hydrogen atom states.

The Argand diagrams for most of the ^{3}S scattering matrix elements do not indicate a shape resonance, but we have plotted one that does, $(2p1 \rightarrow 3d2)$, in Figure 6.22. This diagram clearly indicates the two Feshbach resonances (see below) as well, and also has some complicated structure in the non-resonant energy region 0.91 to 0.93 Ryd.

The Feshbach resonances in the ^{3}S partial wave just below the $n = 4$ threshold are long-lived and narrow, just as was found below the $n = 3$ threshold. Both of them cause sharp variations in all of the state to state partial cross sections, except for the $1s \rightarrow 1s$ elastic process, which is the major contribution to the total elastic cross section and insensitive to the resonances.

6.4.2 P-wave scattering

Cross sections for $J = 1$ odd parity partial waves were obtained using 25 surface functions ($n_{\max} = 5$) and projecting at 80 bohr. The cross sections are presented graphically in Figure 6.23. We compare resonance positions and widths/lifetimes in Table 6 – 17. Our calculations have detected four ^{1}P$^{\text{odd}}$ Feshbach resonances below the $n = 4$ threshold of hydrogen, plus a shape resonance above the $n = 3$ threshold. After the opening of the $n = 3$ channel we have a small maxima in the largest collision lifetime eigenvalue ($\sim 1200\ t_0$) at 0.8906 Ryd, width 1.9 mRyd, which may

indicate a weak $^1P^{odd}$ shape resonance there. The widest two Feshbach resonances, located at 0.9257 (width=2.0 mRyd) and 0.9359 Ryd (width=0.9 mRyd), were also detected by Hata *et al.*[64] who obtained 0.9265 Ryd (width 3.3 mRyd) and 0.9359 Ryd (width 0.6 mRyd) and by Ho,[71] whose results are closer to our own. We have found, in addition, two long-lived narrow resonances in $^1P^{odd}$, at 0.93145 and 0.93713 Ryd, the second of which had not been previously reported. The narrower resonances go undetected in the partial elastic scattering cross section, and have only a miniscule effect on the $1s \rightarrow 2l_1$ partial cross sections. Their effect is much more pronounced in the transitions to $3l_1$ final states. Figure 6.24 displays an Argand diagram for the $(1s1) \rightarrow (2p2)$ element of the scattering matrix for the $^1P^{odd}$ partial wave in the energy region between the hydrogen $n = 3$ and $n = 4$ thresholds. The counter-clockwise circles indicate the presence of five resonances, two of which are very narrow. The corresponding lifetimes of these five resonances (4 Feshbach, 1 shape) are displayed in Figure 6.25.

We find a much longer lived shape resonance in the $^3P^{odd}$ partial wave at 0.8903 Ryd, just above the $n = 3$ threshold (lifetime 4900, width 1.3 mRyd). Hata *et al.*[64] were unable to resolve any $J = 1$ resonances in this energy region. The lowest Feshbach resonance in $^3P^{odd}$ is at 0.9213 Ryd. This value agrees will with Ho's results[0] (0.9214) but the Hata *et al.* calculation[64] gives 0.9220. At slightly higher energies we find three interfering resonances. The first two of these, at 0.9317 and 0.9335 Ryd are of comparable lifetime and width, but are so closely spaced that the effect of the resonance at 0.9317 Ryd on the partial cross section of the $1s \rightarrow 3s$, $2s \rightarrow 3p$, $2p \rightarrow 3s$ and $2p \rightarrow 3p$ processes is a shoulder to the large dip caused by the 0.9335 Ryd resonance. The $2s \rightarrow 3s$ cross section is an exception to this behavior, since it displays three deep dips corresponding to the three wide Feshbach resonances. The fourth resonance is very narrow, and exists within the width of the third resonance, as can be seen from the collision lifetimes

plotted in Figure 6.26. We calculate its position at 0.9341 Ryd, with a lifetime of 140,000 atomic units. It is in cases such as this that the collision lifetime matrix is very useful, because a narrow resonance in the region of a strong, wider resonance would be very hard to detect from the partial cross section data alone. The collision lifetime matrix eigenvalues, on the other hand, clearly show a major peak, once the energy grid is fine enough. Even with a coarser grid of points, there is indication of a resonance because the eigenvalues fluctutate dramatically, as demonstrated in Figure 6.27.

The Hata *et al.*[64] resonance positions and widths were obtained by fitting Fano profiles[71] to the eigenphase sum, assuming that the resonances are isolated. From diagonalizing the appropriate $J = 1$ version of Eq. 6.2, they obtained three negative eigenvalues $\lambda(\lambda + 1)$ less than $-\frac{1}{4}$, from which one expects to find three series of resonances. To determine if two resonances belong to the same series, one may examine the eigenvectors of the collision lifetime matrix which correspond to the largest eigenvalue at the resonant energy to see if they correlate with each other. We have shown that the three Feshbach resonances at 0.9317, 0.9335, and 0.9341 Ryd are isolated, but nevertheless there are three of them occurring within 0.003 Ryd. The other methods for locating resonances are much less precise and show the presence of only one.

There are fewer P^{even} than P^{odd} states (see Table $5-2$), and as a consequence there are fewer P^{even} resonances. As mentioned in Section 6.4.1, the P^{even} resonances occur at energies close to P^{odd} resonances, as seen in Figure 6.18 and Table $6-17$.

6.4.3 D-wave scattering

Cross sections for $J = 2$ even parity partial waves were obtained using 31 surface functions, ($n_{max} = 5$) and projecting at 80 bohr. The cross sections

are presented in graphical form in Figure 6.28.

The resonances obtained for $J = 2$ are listed in Table 6 – 17c, along with the computed lifetimes and widths. The shorter-lived resonances have the largest effect on the cross section, as can be seen from Figure 6.28. The elastic scattering cross sections from the ground state for the $^1D^{even}$ and $^3D^{even}$ partial waves are very different. The latter shows little variation with energy, while in the former the two strong, broad resonances are clearly shown. In the $^3D^{even}$ wave, the $1s \rightarrow nl_1$ cross sections for $n = 2$ and 3 are an order of magnitude smaller than their $^1D^{even}$ counterparts.

There are two very sharp peaks in several of the $^3D^{even}$ cross sections just above the $n = 3$ threshold, which are most pronounced in transitions to the $3d$ state. This is due to a shape resonance at 0.88918 Ryd which has a lifetime of 24,000 t_0.

The sharp $^1D^{even}$ resonance at 0.93382 Ryd lies very close to a wider resonance at 0.9341 Ryd. The collision lifetime eigenvalue curves corresponding to the $^1D^{even}$ partial wave at this energy are shown in Figure 6.29. We claim that there are two resonances here because two of the collision lifetime eigenvalues change rapidly as a function of energy in this region, but this point bears more discussion.

It has been proposed, but not proven, that each resonance causes a peak in just one lifetime eigenvalue vs. energy curve.[13] If two lifetime eigenvalues peak at the same energy, or at nearly the same energy, does this mean the there is accidental degeneracy between two different resonances, or is it possible for a resonance to involve two different eigenchannels? The pair of $^1D^{even}$ resonances is one such situation, but we have encountered it in the $^3P^{odd}$ partial wave below the $n = 5$ threshold and in $^1P^{odd}$ below $n = 6$. In both of these cases there was one narrow peak in the collision lifetimes nearly, but not quite, centered at the same energy as

the peak in a second eigenvalue, which was much broader and lower.

Let us consider what should happen to the collision lifetime eigenvalues associated with two resonances in different lifetime eigenchannels as the energy separation (between the resonances) is decreased. For large separations, the resonances are isolated and one obtains two separate peaks in the larger eigenvalue, with very small values in between. The smaller eigenvalue is negative (or at least very small) for the entire range, and we assume the two states cross at some non-resonant energy.

Now assume the energy separation is comparable to the average width of the resonances. The first eigenvalue will peak at the first resonance energy, and then decrease, as expected. Meanwhile, the second eigenvalue begins to increase, until it is almost degenerate with the first. At this point the two eigenchannels cross. The crossing is evident in the associated eigenvectors as well. The larger eigenvalue will refer to the second eigenchannel, and vice-versa, for energies above the crossing. We do not reorder the eigenvalues. The upper eigenvalue has a minima, and the lower eigenvalue a maxima, at the crossing point. The peak in the lower eigenvalue is construed as a crossing only, and is not interpreted as a resonance lifetime, as would a peak in the largest eigenvalue.

Let us suppose that the energy separation of the two resonances is even smaller. The two peaks in the eigenvalue will approach each other, until finally there is only one peak with a shoulder. The presence of the second resonance will be clear because of the peak in the lower curve. One may have to estimate the wider resonance position and corresponding collision lifetime if the peak assumedly falls beneath the curve for the sharper resonance.

The odd parity $J = 2$ $2p \rightarrow 3p$ and $2p \rightarrow 3d$ cross sections have been plotted in Figure 6.30. As expected we find the $^1D^{odd}$ resonances are very close to those in

$^3D^{even}$, and $^3D^{odd}$ positions correlate with $^1D^{even}$ energies.

6.4.4 F-wave scattering

The cross sections obtained for the $^1F^{odd}$ and $^3F^{odd}$ partial waves are presented in Figure 6.31. The odd parity basis set consisted of 34 surface functions, which includes all states up to $n_{max} = 5$, inclusive. The cross sections for transitions from the $^1F^{odd}$ ground state are relatively small, but not negligible. We have evidence of two shape resonances just above the $n = 3$ threshold, after which the cross sections smoothly increase with increasing energy until the Feshbach resonance region is reached. Similar behavior is seen in the $^3F^{odd}$ cross sections, but the strong resonances in this partial wave seem to be wider than those in $^1F^{odd}$.

The lowest $n = 4$ $^3F^{odd}$ Feshbach resonance energy is 0.9244 Ryd. The third resonance, at 0.9352 Ryd, belongs to the same series, given by $(3,0)^+$, because the same collision lifetime matrix eigenvalue is involved. The second resonance is close in energy, at 0.93475 Ryd, and the peaks formed by the two collision lifetime eigenvalues overlap a sizeable amount. We have found one $^3F^{odd}$ resonance of the '$-$' type, at 0.93606 Ryd. As we have found for other '$-$' type resonances, the resonance is very long-lived (on the order of 2×10^5 atomic units), and the collision lifetime eigenvalue corresponding to this resonance is lower than all the other eigenvalues outside the width of the resonance, so it crosses up, peaks, and then comes back down to negative values. Calculations were repeated using 90 bohr as the projection distance for energies very close to the $n = 4$ threshold. The second $(3,0)^+$ resonance position shifted with the new projection distance, but the $(1,2)^+$ resonance did not shift, such that the two became accidentally degenerate. The narrow resonance also shifted slightly to lower energy. Right below threshold we were able to discern one resonance which had not converged in the $\rho = 80$ bohr calculation.

We have plotted the $J = 3$ even parity $2p \rightarrow 3p$ and $2p \rightarrow 3d$ cross sections in Figure 6.32. As expected we find the $^1F^{even}$ resonances are very close to those in $^3F^{odd}$, and $^3F^{even}$ positions correlate with $^1F^{odd}$ energies.

6.4.6 Higher partial wave scattering

The cross sections obtained for the $^1G^{even}$ and $^3G^{even}$ partial waves are presented in Figure 6.33. The figure clearly shows the presence of two strong $^1G^{even}$ Feshbach resonances, listed in Table 6 – 17, and a shape resonance above the $n = 3$ threshold. The cross sections are very smooth in the energy region after the shape resonance and up to the Feshbach resonance region.

The longest-lived shape resonance above the $n = 3$ threshold was found in the $J = 4$, $^3G^{even}$ partial wave. The resonance position was calculated to be 0.88930 Ryd, its collision lifetime 90,000 t_0, and its width 0.09 mRyd. A second, smaller peak was found in the collision lifetime curve slightly above this resonance, 2300 t_0 high at 0.8922 Ryd. In addition, as tabulated, two closely-spaced, narrow Feshbach resonances are found at 0.93435 and 0.93468 Ryd with lifetimes of 25,000 and 127,000 t_0, and widths of 0.35 and 0.06 mRyd respectively.

For higher values of J, there isn't much difference between the partial cross sections for different spin states. That is, the ratio of triplet partial cross sections to the corresponding ones of the singlet is about 3 : 1, reflecting just the spin weighting factors. This was true for F-wave states just above the $n = 2$ threshold, and it is also true for H-wave states above the $n = 3$ threshold. The $J = 5$ cross sections for the energy region between the $n = 3$ and $n = 4$ thresholds of hydrogen are presented in Figure 6.34. For most of the cross sections, the triplet is about three times the corresponding singlet cross section, which is consistent with the spin weighting. Both $^1H^{odd}$ and $^3H^{odd}$ have a weak shape resonance at 0.8914 Ryd, according to the collision lifetime matrix. There is a single sharp Feshbach resonance present in

the $^3H^{odd}$ state.

6.4.7 Total elastic and inelastic cross sections from the ground state

The integral cross sections for transitions from the ground state are listed in Table 6 – 19 summed over spin and parity for each partial wave J from 0 through 5, for seven energies in this region, and the inelastic cross sections are plotted as a function of energy in Figure 6.35. These calculations were performed with a basis set that consisted of all surface functions up to the $n = 5$ level (a 15-state calculation). The total cross section is also given. The elastic cross section from the $1s$ state seems to be converging slowly with J, but the $1s \rightarrow 2s$, $2p$, $3s$, $3p$ and $3d$ cross sections seem to be already converged to better than 1%.

We also compare our $1s \rightarrow 3l_1$ cross sections, for $l_1 = 0$, 1 and 2, summed over J and spin, with the 14-state results of Hata *et al.*[64] and the 6-state calculation of Burke *et al.*[12] in Table 6 – 20. The agreement is generally better than 10% between our results and the 14-state calculation, but the 6-state calculation is much worse, as is to be expected. There are no published experimental results of either cross sections or resonances in this energy range.

6.4.8 Total inelastic cross sections from 2s and 2p excited states

At these energies one can obtain excitation cross sections from initial states other than the ground state. Transitions from $n = 2$ states to $n = 3$ states are used in the determination of the populations of excited states in plasmas, and can also be used to find collisional population and depopulation rates for individual atomic levels.[72,73] The same resonances are seen in the $2l_1 \rightarrow 3l_1'$ transitions as in those from the ground state. In fact, some of the resonances are more clearly seen in these cross sections from excited states. There are six different processes involved: $(2s \rightarrow 3s)$, $(2s \rightarrow 3p)$, $(2s \rightarrow 3d)$, $(2p \rightarrow 3s)$, $(2p \rightarrow 3p)$, and $(2p \rightarrow 3d)$. Parity

disfavored states (such as P^{even}) do have a $2p$ channel, therefore the $(2p \rightarrow 3p)$ and $(2p \rightarrow 3d)$ cross sections are summed over parity.

The partial wave contributions to the cross sections for processes where the initial state is in the first excited level ($2s$ or $2p$) are given in Table 6−21, where they are compared with previous calculations at one total energy, 0.90 Ryd (with respect to e^-−H ($1s$) as the zero of energy) corresponding to an initial translational energy of 0.15 Ryd. The cross sections are plotted as a function of energy in Figure 6.36 (for initial state $2s$) and Figure 6.37 (initial state $2p$). All of these results have been obtained with 15 nl_1 (parity-favored) states, which corresponds to 15 surface functions for $J = 0$, 25 for $J = 1$, 31 for $J = 2$, and 34 for $J = 3$ and 35 for all $J > 3$. The s-type states are not included in the parity-disfavored basis, which leads to 10 functions for $J = 1$, 16 for $J = 2$, 19 for $J = 3$, and 20 for $J > 3$. In all cases, all surface functions up to $n = 5$ are used in these calculations. Comparison is made with the 14-state (6 hydrogen atom states — all states up to $n = 3$ — plus 8 pseudostates) variational calculation of Hata *et al.*[64] and with the 6-state close-coupling results of Ormonde *et al.*[74]

Let us compare some of the partial wave results given in Table 6 − 21. The 6-state results for $J = 1$ in Table 6 − 21 agree with each other, except for the $2p \rightarrow 2p$ and $2p \rightarrow 3d$ cross sections, which have both parities contributing. Hata *et al.* have shown that neglect of exchange couplings between $n = 2$ and $n = 3$ states by Ormonde *et al.* has led to large disagreement in the parity-disfavored contributions between the two sets of 6-state results. Hata *et al.*'s full basis results are, in some cases, very different from their 6-state ones. There seems to be a discrepancy between our results and those obtained by Hata *et al.* The hyperspherical coordinates results are very different. Where the $J = 1$ $(2s - 3d)$ cross section was reduced by a factor of about 3 in going from 6-state to 14-state, it is now increased by a factor of 5 in going from 14-state to our 15-state hyperspherical

result. The $J = 1$ $(2p \rightarrow 3s)$ cross section had correspondingly increased by a factor of 3, and then increased again by a factor of 4. The disagreement in the $(2p \rightarrow 3p)$ cross sections is less pronounced.

The $J = 2$ cross sections evidently are equally hard to converge. In particular, our value for the $J = 2$ $(2s - 3s)$ cross section is about 7 times that calculated by Hata *et al.* in their best basis,[64] which itself was about one-third that calculated by them with the 6-state basis. The agreement for the other cross sections is better, but still not good, the differences between our results and the 14 states ones being of the order of 20%.

These excited state inelastic cross sections are summed over spin and final value of l_1 in Table $6 - 22$, where they are compared with the 6-state result of Ormonde *et al.* and the 14-state results of Hata *et al.* Our $2s \rightarrow 3l_1$ cross sections agree satisfactorily with 14-state results for most of the partial waves. The $J = 5$ results disagree, but Hata *et al.* have warned that these results are not as accurate. Our total $2p \rightarrow 3l_1$ results are, in most cases, larger than the 14-state results and smaller than the 6-state results. The percent agreement on average is only 30%.

Finally, in Table $6-23$ we have tabulated the total cross sections for transitions from the $2s$ and $2p$ states to each $n = 3$ level state. These calculations include all partial waves up to and including $J = 5$, and are summed over both parities and spin.

While there are no measurements of excited state cross sections, Burgess *et al.* have obtained collisional excitation and de-excitation rates for first excited states from observations on laser pumped atomic hydrogen plasmas.[73] A semi-empirical formula, due to Johnson,[75] is often used to obtain total $n \rightarrow n'$ cross sections. The total cross section form $n = 2$ to $n = 3$ obtained in this way agrees fairly well with the 6-state close-coupling calculation;[12] however, Burgess suggested that the

Johnson results must be five times too high.[73] Johnson's total cross sections results are generally 20-30 percent higher than ours but those of Hata *et al.* are lower than ours, ranging from 25 percent lower at 0.90 Ryd to 12 percent lower at 0.925 Ryd. The two calculations agree to 1% at 0.93 Ryd. Not all of the discrepancies reported by Burgess *et al.* are accounted for.

6.5 Energies between the n=4 and n=5 Thresholds

Recent photodetachment experiments have investigated the energy region up to the $n = 7$ hydrogen atom threshold.[76] We have determined to obtain results for the $^1P^{odd}$ partial wave at these higher energies in order to compare with the experiment. In this section we present our preliminary results for S and P waves at energies above the $n = 4$ threshold. The basis set used at lower energies contained all the states up to and including those which correspond asymptotically with $n = 5$ hydrogen atom functions. Use of that basis set in the $n = 4$ to $n = 5$ energy region would give only one level of closed functions, which is insufficient. Furthermore, inclusion of the $n = 6$ primitive functions will give better converged $n = 5$ (and to a lesser extent, $n = 4$) surface functions, which are very important in this energy range. For these reasons, calculations between the $n = 4$ and $n = 5$ thresholds were performed using all the surface functions obtained from a primitive basis with $n_{max} = 6$. For S-states, this meant using 21 surface functions; for P-states, there were 36 surface functions used. The projection was performed using the "constant-ρ" method, with ρ taken to be 110 bohr. There have been no scattering calculations reported in this energy range that have included all the open states in the calculation.[77]

This energy region is rich with resonance structure. Our resonance positions, lifetimes, and widths are given in Table 6 – 24, where they are compared with the resonance positions found by Ho and Callaway using complex rotation.[8] We

note that, for $J = 0$, only the two wider ^{1}S resonances were predicted by Ho and Callaway, but none of the three narrow ^{3}S ones. We also note the presence of some relatively short-lived shape resonances in both ^{1}S and ^{3}S.

In Table 6 – 25 we list the ^{1}S and ^{3}S contributions to the individual partial cross sections at four energies for transitions from the ground state. The $1s \rightarrow 4l_1$ cross sections are all very small. Individual cross sections for transitions from the excited $2s$ and $2p$ states are listed, for ^{1}S and ^{3}S, in Table 6 – 26.

The partial cross sections at four energies between the $n = 4$ and $n = 5$ thresholds for the ^{1}P^{odd} and ^{3}P^{odd} partial waves from the ground state are listed in Table 6 – 27. The partial inelastic cross sections from the $2s$ and $2p$ excited states are listed for the ^{1}P^{odd} and ^{3}P^{odd} partial waves in Table 6 – 28.

Resonances have been clearly seen in all channels. Collision lifetime analysis shows that there are six resonances below the $n = 5$ threshold in the ^{1}P^{odd} partial wave. There is apparently also a shape resonance just above the $n = 4$ threshold, at 0.9388 Ryd. The corresponding Argand diagrams for ^{1}P^{odd} in the energy region are quite complicated, as would be expected for a region with seven closely-spaced (and therefore possibly interfering) resonances. One representative Argand diagram for a first row element ($1s1 \rightarrow 4d3$) is presented in Figure 6.38. This one consists of several partial circles, and two sharp changes in direction, separating the shape resonance region from the non-resonant from the Feshbach resonances.

There is a peak in the ^{3}P^{odd} collision lifetime about 1 mRyd above the $n = 4$ threshold; but there is a second maxima at 0.945 Ryd. This peak is very wide compared to the others, and also relatively low, having a lifetime of 2000 t_0. We have seen, however, in other energy regions and for other partial waves, resonances with similar lifetimes that had quite noticeable effects in the cross section. If we consider this peak to designate a weak resonance, we find that the entire $n = 4$ to $n = 5$

energy region is affected by at least one of the several $^3P^{odd}$ resonances. There are $^3P^{odd}$ Feshbach resonances at 0.9487, 0.9540, 0.95630, 0.95945, and 0.959705 Ryd, and another one at 0.95629, which is hard to place exactly because of the sharper resonance right near by.

In the very low energy end of this region, just after the $n = 4$ threshold, the largest $^3P^{odd}$ collision lifetime eigenvalue decreases monotonically as the energy increases. Since there is no maximum in this lifetime, perhaps it is the tail of a resonance below threshold (see Fig. 6.27), or possibly there is a shape resonance even closer to threshold than our calculations. Our closest calculation was at 0.00001 Ryd above the 0.9375 Ryd threshold, and the lowest energy point for which the collision lifetime matrix was calculated (since we use a 3-point derivative formula) was at 0.93752 Ryd.

Because of the recent experimental measurements of resonances in the $^1P^{odd}$ partial wave at energies beyond the $n = 5$ threshold, we also performed some calculations at higher energies. The $J = 1$ basis used contained all the surface functions through the $n = 7$ level, which amounts to 49 functions. The projection was done at 110 bohr, just as for the $n = 4$ to 5 region. Based on experience at lower energies, this projection distance is probably adequate, but no tests at larger distances were performed. The resonance positions, lifetimes and widths are listed in Table 6 – 29. We found six wide $^1P^{odd}$ resonances at 0.9615 (lifetime 4800), 0.9633 (3300), 0.9661 (4700), 0.9692 (6200), 0.9701 (13000), and 0.9717 Ryd (17000 t_0) with widths 1.7, 2.4, 1.7, 1.3, 0.6, and 0.5 mRyd, respectively. We suspect that there are even more resonances that are very narrow. In particular, a very narrow resonance was obtained very close to a wider one.

We have not yet investigated this energy range for $J > 1$, but we expect to find much structure due to many resonances.

6.6 Summary

We have presented the results obtained using the hyperspherical coordinate formulation for $e + H$ elastic and inelastic scattering using local surface functions and have shown that they are accurate. We have calculated the state-to-state integral cross sections for all partial waves up to and including $J = 5$ for energies between the $n = 2$ and $n = 4$ threshold levels of the hydrogen atom, for the S and P partial waves for energies up to the $n = 5$ threshold, and for the $^1P^{odd}$ patial wave for energies up to the $n = 6$ threshold. This method can in principle be extended to energies above the range we have considered, indeed, even to energies above the ionization threshold by including hyperspherical harmonics in the surface function basis set. This approach is very promising and should lead to a very complete description of the $e + H$ scattering processes.

Table 6-1: ^{1}S elastic phase shift (in radians) for $e-\mathrm{H}(1s)$ scattering at energies below the $n = 2$ threshold of the H atom.

k(bohr^{-1})	Schwartz[a]	Lin[b]	PA3[c]	PA4[d]	Burke *et al.*[e]	Present[f]
0.1	2.553	2.513	2.636	2.585	2.491	2.548
0.2	2.067	1.983	2.119	2.093	1.974	2.062
0.3	1.696	1.568	1.740	1.735	1.596	1.696
0.4	1.415	1.242	1.423	1.433	1.302	1.420
0.5	1.202	0.989	1.221	1.209	1.092	1.209
0.6	1.041	0.784	1.067	1.059	0.93	1.046
0.7	0.930	0.618	0.927	0.931	0.82	0.933
0.8	0.887	–	–	–	0.77	0.889

a: Ref. 16 Schwartz.

b: Ref. 23 Lin.

c: Ref. 25 Klar and Klar, post-adiabatic approximation using 3 states.

d: Ref. 25, using 4 states.

e: Ref. 12 Burke *et al.*.

f: Present calculation, 3 surface functions, projection at 8 bohr. This distance was chosen in view of the convergence studies of Section 4.5 and Figures 4.2 and 4.3.

Table 6-2: Elastic phase shifts (in radians) for e^-−H $1s$ scattering[a] at energies below the $n = 2$ threshold of the H atom.

k(bohr^{-1})	^3S	^1P	^3P	^1D	^3D	^1F	^3F
0.1	2.9385	0.007	0.0114	0.0012	0.0013		
	2.9335	0.0028	0.0070	0.0001	0.0001	0.0000	0.0000
0.2	2.7174	0.0147	0.0450	0.0052	0.0052	0.0018	0.0019
	2.7234	0.0170	0.0488	0.0022	0.0022	0.0001	0.0001
0.2	2.4997	0.0170	0.1063	0.0108	0.0114	0.0038	0.0038
	2.5123	0.0340	0.1278	0.0121	0.0120	0.0009	0.0009
0.4	2.2941	0.0100	0.1872	0.0183	0.0198	0.0066	0.0067
	2.3057	0.0354	0.2138	0.0326	0.0328	0.0045	0.0045
0.5	2.1046	−0.0007	0.2705	0.0274	0.0304	0.0102	0.0103
	2.1113	0.0179	0.2861	0.0549	0.0562	0.0130	0.0133
0.6	1.9328	−0.009	0.3412	0.0383	0.0424	0.0145	0.0147
	1.9361	−0.0032	0.3476	0.0677	0.0704	0.0248	0.0260
0.7	1.7794	−0.013	0.3927	0.0523	0.0559	0.0194	0.0197
	1.7829	−0.0118	0.3992	0.0720	0.0739	0.0350	0.0365
0.8	1.6438	−0.004	0.427	0.0745	0.0697	0.0259	0.0263
	1.6499	−0.0008	0.435	0.0833	0.0752	0.0404	0.0401

[a]The numbers on the first line for each k value were obtained from Callaway, Physics Reports, **45**, Table 5, p. 134. The second line values are from this calculation, projecting at 8 bohr using all surface function which asymptotically go to $n = 1$ or $n = 2$ and primitive functions which go to $n = 1$ through $n = 5$. (See Table 5 − 2.)

Table 6-3a: ^{1}S (1) resonance.

Description		Lifetime	Pos.	Width	Pos.	Width
Basis	Proj/bohr	t_0	Ryd		eV	
3 sf/15 prim	20		0.699		9.51	
6 sf/15 prim	20	2304	0.70218	0.0035	9.5537	0.0476
3 sf/15 prim	40		0.699		9.51	
6 sf/15 prim	40	2341	0.70192		9.5502	
10 sf/15 prim	40	2339	0.70192	0.0034	9.5502	0.0463
3 sf/15 prim	50		0.699		9.51	
6 sf/15 prim	50	2302	0.70217	0.0034	9.5536	0.0463
10 sf/15 prim	50	2299	0.70217	0.0035	9.5536	0.0476
10 sf/15 prim	60	2300	0.70216	0.0035	9.5536	0.0476
Hylleraas correlation, Ho, Bhatia, and Temkin (Ref. 17)			0.702445	0.003466	9.55735 $\pm 5 \times 10^{-5}$	0.04717 $\pm 2 \times 10^{-5}$
Kohn variational, Shimamura (Ref. 29)			0.702452	0.00347	9.5574	0.0472
QHQ and polarized orbital, Bhatia and Temkin (Ref. 78)			0.70238	0.00350	9.556 ± 0.002	0.0476
Scattering, 6 cc (Ref. 12)			0.70254	0.00373	9.5586	0.0507
Scattering, 3 cc+16 corr, Burke and Taylor (Ref. 22)			0.70266	0.00349	9.5603	0.0475
Register and Poe (Ref. 19)			0.70223	0.00357	9.5544	0.0486
Experimental, Sanche and Burrow (Ref. 30)					9.558 ± 0.010	
Experimental, McGowan (Ref. 79)			0.7027 ± 0.0007	0.0032 ± 0.0004	9.561 ± 0.010	0.043 ± 0.006
Lin, adiabatic hyperspherical coord. (Ref. 56)			0.70302		9.565	

Table 6-3b: ^{1}S (2) resonance.

Description		Lifetime	Pos.	Width	Pos.	Width
Basis	Proj/bohr	t_0	Ryd		eV	
3 sf/15 prim	40		~0.748		10.2	
6 sf/15 prim	40	26000	0.74803	0.00030	10.178	0.0041
10 sf/15 prim	40	28500	0.74842	0.00028	10.183	0.0038
3 sf/15 prim	50		~0.746		10.1	
6 sf/15 prim	50	30000	0.74749	0.00027	10.170	0.0037
10 sf/15 prim	50	33000	0.74787	0.00024	10.175	0.0033
10 sf/15 prim	60	37000	0.74767	0.00022	10.173	0.0030
Scattering, 3 cc+16 corr, Burke and Taylor (Ref. 22)			0.748062	0.000161	10.1780	0.00219
Callaway (Ref. 20)			0.747856	0.000415	10.1752	0.00565
Lin, adiabatic hyperspherical coord. (Ref. 56)			0.74825		10.181	

Table 6-3c: ^{3}S resonance.

Description		Lifetime	Pos.	Width	Pos.	Width
Basis	Proj/bohr	t_0	Ryd		eV	
3 sf/15 prim	40		~0.743		10.1	
6 sf/15 prim	40	1.9×10^6	0.745389	4×10^{-6}	10.1416	0.0005
10 sf/15 prim	40	1.8×10^6	0.745717	5×10^{-6}	10.1461	0.0007
3 sf/15 prim	50		~0.743		10.1	
6 sf/15 prim	50	1.7×10^6	0.745145	4×10^{-6}	10.1383	0.0005
10 sf/15 prim	50	1.6×10^6	0.745473	5×10^{-6}	10.1428	0.0007
10 sf/15 prim	60	1.7×10^6	0.745412	4×10^{-6}	10.1419	0.0005
Shimamura (Ref. 29)			0.745923	2.59×10^{-6}	10.1489	3.52×10^{-5}
Klar and Klar (Ref. 31)			0.74740		10.169	
Experiment, Schultz (Ref. 32)			0.74600		10.150	
Scattering, 3 cc+16 corr, Burke and Taylor (Ref. 22)			0.745982	1.5×10^{-6}	10.1497	2.06×10^{-5}
Lin, adiabatic hyperspherical coord. (Ref. 56)			0.74604		10.151	

Table 6-3d: $^1P^{odd}$ resonance.

Description		Lifetime	Pos.	Width	Pos.	Width
Basis	Proj/bohr	t_0	Ryd		eV	
9 sf/25 prim	30		~0.7485			
9 sf/25 prim	40	1.9×10^6	0.747790	4×10^{-6}	10.1743	5×10^{-5}
9 sf/25 prim	50		~0.7475			
9 sf/25 prim	60	1.2×10^6	0.747329	5×10^{-6}	10.1680	7×10^{-5}
16 sf/25 prim	40	1.8×10^6	0.748046	4×10^{-6}	10.1778	5×10^{-5}
16 sf/25 prim	50	1.9×10^6	0.747706	4×10^{-6}	10.1732	5×10^{-5}
Pseudostate, 6-5-2-1 basis, Callaway (Ref. 20)			0.747901	2.73×10^{-6}	10.1758	3.73×10^{-5}
Lin, adiabatic hyperspherical coord. (Ref. 56)			0.74810		10.179	
Experimental, Bryant *et al.* (Ref. 34)			0.74810		10.173	

Table 6-3e: $^3P^{odd}$ (1) resonance.

Description		Lifetime	Pos.	Width	Pos.	Width
Basis	Proj/bohr	t_0	Ryd		eV	
9 sf/25 prim	20	17800	0.71572	0.00045	9.7380	0.0061
9 sf/25 prim	40	18500	0.71534	0.00043	9.7328	0.0059
9 sf/25 prim	50	18600	0.71534	0.00043	9.7328	0.0059
16 sf/25 prim	40	18600	0.71559	0.00043	9.7362	0.0059
16 sf/25 prim	50	18600	0.71559	0.00043	9.7362	0.0059
Das and Rudge (Ref. 36)			0.715735	0.000430	9.73817	0.00585
Register and Poe (Ref. 19)			0.71654	0.00049	9.7491	0.0067
Scattering, Burke (Ref. 80)			0.71599		9.7417	0.0059
Experimental, Sanche and Burrow (Ref. 30)					9.738 ± 0.010	0.0056 ± 0.0005
Experimental, McGowan *et al.* (Ref. 61)					9.71 ± 0.03	
Lin, adiabatic hyperspherical coord. (Ref. 56)			0.71472		9.724	

Table 6-3f: $^3P^{odd}$ (2) resonance.

Description		Lifetime	Pos.	Width	Pos.	Width
Basis	Proj/bohr	t_0	Ryd		eV	
16 sf/25 prim	50	190,000	0.74951	0.000045	10.198	0.0006
Lin, adiabatic hyperspherical coord. (Ref. 56)			0.74928		10.195	

Table 6-3g: $^1D^{even}$ resonance.

Description		Lifetime	Pos.	Width	Pos.	Width
Basis	Proj/bohr	t_0	Ryd		eV	
4 sf/31 prim	20	11200	0.74155	0.00071	10.089	0.0097
10 sf/31 prim	20	10800	0.74505	0.00074	10.137	0.0101
19 sf/31 prim	20	10600	0.74535	0.00076	10.141	0.0103
4 sf/31 prim	30	11600	0.7401	0.0007	10.07	0.01
10 sf/31 prim	30	12000	0.74385	0.00068	10.121	0.0093
10 sf/31 prim	40	12600	0.74365	0.00066	10.118	0.0090
19 sf/31 prim	40	12400	0.74395	0.00065	10.122	0.0088
10 sf/31 prim	50	12600	0.74365	0.00065	10.118	0.0088
19 sf/31 prim	50	12700	0.74395	0.00062	10.122	0.0084
Callaway (Ref. 20)			0.744152	0.00064	10.1248	0.0087
Register and Poe, Kohn, inverse Kohn (Ref. 19)			0.743924	0.00066	10.1217	0.0090
3-state, Ormonde *et al.* (Ref. 62)			0.74674	0.00057	10.160	0.0078
6-state, Ormonde *et al.* (Ref. 62)			0.74417	0.00065	10.125	0.0088
Experimental, Sanche and Burrow (Ref. 30)					10.128 ± 0.010	0.0073 ± 0.002
Experimental, McGowan *et al.* (Ref. 61)					10.13 ± 0.015	

Table 6-4a: Positions, lifetimes, and widths of resonances for partial waves $J = 0, 1$ at energies between the $n = 2$ and $n = 3$ thresholds of the H atom.

Energy/Ryd		Lifetime/a.u.	Width/mRyd
Present results[1,2]	Previous results		
	^{1}S		
0.8619 ± .0001	0.8624,[a] 0.8621,[b] 0.86199,[c] 0.86200[d]	2,800	2.8
0.8846 ± .0002	0.88474,[a] 0.88461,[b] 0.88445[c]	8,800	0.9
0.88775 ± .00005	0.88773[c]	38,000	0.22
	^{3}S		
0.882012 ± .000002	0.88212[b], 0.88203[c]	360,000	0.023
	^{1}podd		
0.75108 ± .00001	0.75121,[c] 0.751325,[y] 0.75130[x]	6,200	1.0
0.8745 ± .0001	0.8758,[a] 0.87495,[b] 0.87457,[c] 0.87458[d]	3,300	2.4
0.882862 ± .000002	0.88297,[b] 0.88286[c]	350,000	0.023
	^{3}podd		
0.7513		600	1.0
0.8641 ± .0001	0.8647,[a] 0.86428,[b] 0.86416,[c] 0.86420[d]	2,400	3.3
0.8855 ± .0001	0.88555,[a] 0.88526,[b] 0.88516[c]	8,900	0.9
0.887472 ± .000002	0.88724[c]	530,000	0.015

[1]Present results obtained using all surface functions up to $n_{max} = 5$, a 15-state calculation. The projection distance was 60 bohr.

[2]The uncertainty represents the precision in locating the position of the maximum in the collision lifetime eigenvalue, rather than the absolute accuracy of the calculation.

Table 6-4b: Continuation of Table 6 – 5a for the partial waves $^1D^{even}$, $^3D^{even}$, $^1F^{odd}$, $^3F^{odd}$, and $^1G^{even}$.

Energy/Ryd		Lifetime/a.u.	Width/mRyd
Present results[1,2]	Previous results		
	$^1D^{even}$		
0.7508 ± .0001		3,200	1.4
0.8680 ± .0005	0.8687,[a] 0.8682,[b] 0.86809[c], 0.8681[e]	2,200	3.7
0.8868 ± .0001	0.88647,[b] 0.88636[c]	9,600	0.84
	$^3D^{even}$		
0.75040 ± .00005		14,500	0.45
0.8820 ± .0001	0.88212,[b] 0.88207[c], 0.88204[e]	9,900	0.8
0.884600 ± .000005	0.88463,[b] 0.88453[c]	340,000	0.025
	$^1F^{odd}$		
0.7528 ± .0002		1,200	3.1
0.887195 ± .000005	0.88701,[b] 0.88689[c]	350,000	0.02
	$^3F^{odd}$		
0.7528 ± .0002		1,200	3.1
0.87694 ± .00001	0.8772,[b] 0.87697[c], 0.87698[e]	36,000	0.22
	$^1G^{even}$		
0.756 ± .001		450	
0.88755 ± .00005	None.	7,100	1.2

[a]Ref. 12. [b]Ref. 40. [c]Ref. 35.
[d]Ref. 39. [e]Ref. 8. [x]Ref. 54.
[y]Ref. 45.

Table 6-5a: ^{1}S contribution to $1s \rightarrow 1s$ cross section in πa_0^2 at energies between the $n = 2$ and $n = 3$ thresholds of the H atom.

Energy	15-state[a]	6-state[a]	BOW[b]	TB[c]	GB[d]	C[e]
0.76	0.69637	0.6627	0.536	0.650	0.555	0.6445
0.78	0.65454	0.6337	0.502	0.613	0.521	0.6073
0.81	0.59766	0.5790	0.455	0.560	0.473	0.5554
0.83	0.56502	0.5493	0.428	0.524	0.446	0.5266
0.85	0.54144			0.500		0.5036
0.86	0.60435	0.6638	0.448			

Table 6-5b: ^{1}S contribution to $1s \rightarrow 2s$ cross section in πa_0^2 at energies between the $n = 2$ and $n = 3$ thresholds of the H atom.

Energy	15-state[a]	6-state[a]	BOW[b]	TB[c]	GB[d]	C[e]
0.76	0.03624	0.0408	0.0402	0.0392	0.0395	0.0374
0.78	0.04456	0.0491	0.0449	0.0432	0.0436	0.0410
0.81	0.06255	0.0645	0.0625	0.0601	0.0619	0.0592
0.83	0.06198	0.0617	0.0632	0.0621	0.0638	0.0617
0.85	0.05414			0.0561		0.0553
0.86	0.01958	0.0028	0.0218			

[a]Projection at $\rho = 60$ bohr.

[b]Ref. no. 12.

[c]Ref. No. 38.

[d]Ref. no. 41.

[e]Ref. no. 42.

Table 6-5c: ^{1}S contribution to $1s \rightarrow 2p$ cross section in πa_0^2 at energies between the $n = 2$ and $n = 3$ thresholds of the H atom.

Energy	15-state[a]	6-state[a]	BOW[b]	TB[c]	GB[d]	C[e]
0.76	0.02378	0.0270	0.0306	0.0286	0.0297	0.0282
0.78	0.02866	0.0278	0.0373	0.0339	0.0364	0.0347
0.81	0.02199	0.0218	0.0285	0.0255	0.0277	0.0257
0.83	0.02385	0.0235	0.0298	0.0247	0.0278	0.0248
0.85	0.02461			0.0245		0.0248
0.86	0.00540	0.0044	0.0120			

[a]Projection at $\rho = 60$ bohr. [b]Ref. no. 12.

[c]Ref. No. 38. [d]Ref. no. 41.

[e]Ref. no. 42.

Table 6-6: ^{3}S contribution to $1s \rightarrow 1s$ cross section in πa_0^2 at energies between the $n = 2$ and $n = 3$ thresholds of the H atom.

Energy	15-state[a]	6-state[a]	BOW[b]	TB[c]	GB[d]	C[e]
0.76	3.9450	3.9457	3.944	3.944	3.944	3.9447
0.78	3.8436	3.8434	3.839	3.840	3.839	3.8406
0.81	3.6985	3.6967	3.690	3.693	3.690	3.6917
0.83	3.6062	3.6031	3.595	3.600	3.594	3.5972
0.85	3.5169			3.507		3.5060
0.86	3.4734	3.4687	3.459			

[a]Projection at $\rho = 60$ bohr. [b]Ref. no. 12.

[c]Ref. No. 38. [d]Ref. no. 41.

[e]Ref. no. 42.

Table 6-7a: $^1P^{odd}$ contribution to $1s \rightarrow 1s$ cross section in πa_0^2 at energies between the $n = 2$ and $n = 3$ thresholds of the H atom.

Energy	15-state[a]	6-state[a]	BOW[b]	TB[c]	GB[d]	C[e]
0.76	0.0044	0.0022	0.019	0.002	0.006	0.0016
0.78	0.0053	0.0024	0.009	0.001	0.003	0.0007
0.81	0.0067	0.0032	0.006	0.001	0.003	0.0010
0.83	0.0075	0.0038	0.005	0.001	0.002	0.0014
0.85	0.0081			0.001		0.0020
0.86	0.0084	0.0046	0.006			

Table 6-7b: $^3P^{odd}$ contribution to $1s \rightarrow 1s$ cross section in πa_0^2 at energies between the $n = 2$ and $n = 3$ thresholds of the H atom.

Energy	15-state[a]	6-state[a]	BOW[b]	TB[c]	GB[d]	C[e]
0.76	2.340	2.204	1.888	1.927	1.929	2.0865
0.78	2.288	2.155	1.848	1.884	1.888	2.0406
0.81	2.204	2.064	1.784	1.823	1.821	1.9691
0.83	2.138	1.999	1.737	1.780	1.774	1.9194
0.85	2.076			1.737		1.8676
0.86	2.049	1.912	1.663			

[a]Projection at $\rho = 60$ bohr.

[b]Ref. no. 12.

[c]Ref. No. 38.

[d]Ref. no. 41.

[e]Ref. no. 42.

Table 6-8a: $^1P^{odd}$ contribution to $1s \rightarrow 2s$ cross section in πa_0^2 at energies between the $n = 2$ and $n = 3$ thresholds of the H atom.

Energy	15-state[a]	6-state[a]	BOW[b]	TB[c]	GB[d]	C[e]
0.76	0.0077	0.0072	0.0194	0.0076	0.0086	0.0079
0.78	0.0046	0.0049	0.0048	0.0030	0.0035	0.0032
0.81	0.0049	0.0054	0.0050	0.0027	0.0036	0.0033
0.83	0.0064	0.0070	0.0061	0.0033	0.0046	0.0043
0.85	0.0085			0.0043		0.0059
0.86	0.0100	0.0108	0.0090			

Table 6-8b: $^3P^{odd}$ contribution to $1s \rightarrow 2s$ cross section in πa_0^2 at energies between the $n = 2$ and $n = 3$ thresholds of the H atom.

Energy	15-state[a]	6-state[a]	BOW[b]	TB[c]	GB[d]	C[e]
0.76	0.0382	0.0453	0.0461	0.0384	0.0429	0.0368
0.78	0.0442	0.0471	0.0567	0.0421	0.0521	0.0454
0.81	0.0541	0.0572	0.0672	0.0503	0.0614	0.0524
0.83	0.0579	0.0584	0.0735	0.0563	0.0668	0.0564
0.85	0.0568			0.0596		0.0563
0.86	0.0381	0.0315	0.0516			

[a]Projection at $\rho = 60$ bohr.

[b]Ref. no. 12.

[c]Ref. No. 38.

[d]Ref. no. 41.

[e]Ref. no. 42.

Table 6-9a: $^1P^{odd}$ contribution to $1s \rightarrow 2p$ cross section in πa_0^2 at energies between the $n = 2$ and $n = 3$ thresholds of the H atom.

Energy	15-state[a]	6-state[a]	BOW[b]	TB[c]	GB[d]	C[e]
0.76	0.0654	0.0655	0.0927	0.0660	0.0702	0.0657
0.78	0.0473	0.0472	0.0657	0.0458	0.0517	0.0485
0.81	0.0501	0.0492	0.0544	0.0463	0.0553	0.0519
0.83	0.0565	0.0560	0.0680	0.0514	0.0617	0.0581
0.85	0.0643			0.0585		0.0668
0.86	0.0700	0.0704	0.0872			

Table 6-9b: $^3P^{odd}$ contribution to $1s \rightarrow 2p$ cross section in πa_0^2 at energies between the $n = 2$ and $n = 3$ thresholds of the H atom.

Energy	15-state[a]	6-state[a]	BOW[b]	TB[c]	GB[d]	C[e]
0.76	0.0327	0.0403	0.0478	0.0406	0.0442	0.0377
0.78	0.0394	0.0413	0.0539	0.0456	0.0502	0.0413
0.81	0.0446	0.0453	0.0638	0.0498	0.0584	0.0474
0.83	0.0474	0.0470	0.0674	0.0495	0.0609	0.0488
0.85	0.0450			0.0491		0.0464
0.86	0.0311	0.0255	0.0496			

[a]Projection at $\rho = 60$ bohr.

[b]Ref. no. 12.

[c]Ref. No. 38.

[d]Ref. no. 41.

[e]Ref. no. 42.

Table 6-10a: $^1D^{even}$ contribution to $1s \rightarrow 1s$ cross section in πa_0^2 at energies between the $n = 2$ and $n = 3$ thresholds of the H atom.

Energy	15-state[a]	6-state[a]	BOW[b]	TB[c]	GB[d]	C[e]
0.76	0.0854	0.0676	0.042	0.040	0.042	0.0485
0.78	0.0914	0.0722	0.050	0.046	0.049	0.0560
0.81	0.0952	0.0762	0.056	0.050	0.055	0.0615
0.83	0.0965	0.0766	0.058	0.053	0.057	0.0635
0.85	0.0942	0.0747		0.054		0.0626
0.86	0.0864	0.0693	0.052			

Table 6-10b: $^3D^{even}$ contribution to $1s \rightarrow 1s$ cross section in πa_0^2 at energies between the $n = 2$ and $n = 3$ thresholds of the H atom.

Energy	15-state[a]	6-state[a]	BOW[b]	TB[c]	GB[d]	C[e]
0.76	0.2242	0.1714	0.097	0.091	0.100	0.1212
0.78	0.2230	0.1687	0.101	0.093	0.102	0.1235
0.81	0.2194	0.1657	0.104	0.095	0.105	0.1266
0.83	0.2186	0.1646	0.105	0.098	0.106	0.1280
0.85	0.2183	0.1633		0.100		0.1294
0.86	0.2176	0.1623	0.106			

[a]Projection at $\rho = 60$ bohr.

[b]Ref. no. 12.

[c]Ref. No. 38.

[d]Ref. no. 41.

[e]Ref. no. 42.

Table 6-11a: $^1D^{even}$ contribution to $1s \rightarrow 2s$ cross section in πa_0^2 at energies between the $n = 2$ and $n = 3$ thresholds of the H atom.

Energy	15-state[a]	6-state[a]	BOW[b]	TB[c]	GB[d]	C[e]
0.76	0.0557	0.0484	0.0540	0.0544	0.0540	0.0538
0.78	0.0518	0.0491	0.0555	0.0580	0.0556	0.0552
0.81	0.0546	0.0534	0.0553	0.0647	0.0602	0.0606
0.83	0.0607	0.0608	0.0624	0.0715	0.0657	0.0663
0.85	0.0658	0.0649		0.0797		0.0745
0.86	0.0709	0.0697	0.0810			

Table 6-11b: $^3D^{even}$ contribution to $1s \rightarrow 2s$ cross section in πa_0^2 at energies between the $n = 2$ and $n = 3$ thresholds of the H atom.

Energy	15-state[a]	6-state[a]	BOW[b]	TB[c]	GB[d]	C[e]
0.76	0.0000	0.0001	0.0000	0.0000	0.0000	0.0000
0.78	0.0009	0.0007	0.0006	0.0002	0.0006	0.0004
0.81	0.0035	0.0035	0.0036	0.0017	0.0030	0.0026
0.83	0.0056	0.0056	0.0061	0.0031	0.0049	0.0042
0.85	0.0077	0.0080		0.0044		0.0055
0.86	0.0082	0.0087	0.0080			

[a]Projection at $\rho = 60$ bohr.

[b]Ref. no. 12.

[c]Ref. No. 38.

[d]Ref. no. 41.

[e]Ref. no. 42.

Table 6-12a: $^1D^{even}$ contribution to $1s \rightarrow 2p$ cross section in πa_0^2 at energies between the $n = 2$ and $n = 3$ thresholds of the H atom.

Energy	15-state[a]	6-state[a]	BOW[b]	TB[c]	GB[d]	C[e]
0.76	0.0992	0.0894	0.0914	0.0917	0.0916	0.0900
0.78	0.0961	0.0930	0.0937	0.0933	0.0934	0.0914
0.81	0.1140	0.1151	0.1218	0.1090	0.1131	0.1112
0.83	0.1347	0.1362	0.1430	0.1256	0.1319	0.1298
0.85	0.1565	0.1571		0.1469		0.1522
0.86	0.1701	0.1704	0.1679			

Table 6-12b: $^3D^{even}$ contribution to $1s \rightarrow 2p$ cross section in πa_0^2 at energies between the $n = 2$ and $n = 3$ thresholds of the H atom.

Energy	15-state[a]	6-state[a]	BOW[b]	TB[c]	GB[d]	C[e]
0.78	0.0016	0.0016	0.0016	0.0012	0.0018	0.0017
0.81	0.0049	0.0049	0.0076	0.0055	0.0066	0.0061
0.83	0.0080	0.0077	0.0120	0.0088	0.0099	0.0093
0.85	0.0103	0.0101		0.0120		0.0119
0.86	0.0111	0.0110	0.0155			

[a]Projection at $\rho = 60$ bohr.

[b]Ref. no. 12.

[c]Ref. No. 38.

[d]Ref. no. 41.

[e]Ref. no. 42.

Table 6-13a: $^1F^{odd}$ contribution to $1s \rightarrow 1s$ cross section in πa_0^2 at energies between the $n = 2$ and $n = 3$ thresholds of the H atom.

Energy	15-state[a]	10-state[a]	BOW[b]	TB[c]	GB[d]	C[e]
0.76	0.0313	0.0280	0.007	0.006	0.007	0.0089
0.78	0.0311	0.0277	0.007	0.007	0.008	0.0093
0.81	0.0313	0.0277	0.008	0.008	0.008	0.0100
0.83	0.0310	0.0273	0.008	0.008	0.008	0.0104
0.85	0.0305	0.0267		0.007		0.0108
0.86	0.0304	0.0268	0.009			

Table 6-13b: $^3F^{odd}$ contribution to $1s \rightarrow 1s$ cross section in πa_0^2 at energies between the $n = 2$ and $n = 3$ thresholds of the H atom.

Energy	15-state[a]	10-state[a]	BOW[b]	TB[c]	GB[d]	C[e]
0.76	0.0961	0.0862	0.022	0.019	0.022	0.0279
0.78	0.0961	0.0857	0.023	0.022	0.024	0.0292
0.81	0.0954	0.0845	0.024	0.027	0.025	0.0308
0.83	0.0927	0.0816	0.025	0.023	0.025	0.0311
0.85	0.0900	0.0787		0.022		0.0315
0.86	0.0891		0.025			

[a]Projection at $\rho = 60$ bohr.

[b]Ref. no. 12.

[c]Ref. No. 38.

[d]Ref. no. 41.

[e]Ref. no. 42.

Table 6-14a: $^1F^{odd}$ contribution to $1s \rightarrow 2s$ cross section in πa_0^2 at energies between the $n = 2$ and $n = 3$ thresholds of the H atom.

Energy	15-state[a]	10-state[a]	BOW[b]	TB[c]	GB[d]	C[e]
0.76	0.0001	0.0001	0.0000	0.0000	0.0000	0.0000
0.78	0.0003	0.0003	0.0003	0.0003	0.0002	0.0003
0.81	0.0009	0.0009	0.0011	0.0009	0.0011	0.0009
0.83	0.0015	0.0016	0.0016	0.0015	0.0016	0.0016
0.85	0.0021	0.0021			0.0024	0.0020
0.86	0.0025	0.0025	0.0028			

Table 6-14b: $^3F^{odd}$ contribution to $1s \rightarrow 2s$ cross section in πa_0^2 at energies between the $n = 2$ and $n = 3$ thresholds of the H atom.

Energy	15-state[a]	10-state[a]	BOW[b]	TB[c]	GB[d]	C[e]
0.76	0.0006	0.0006	0.0004	0.0004	0.0004	0.0004
0.78	0.0031	0.0031	0.0037	0.0038	0.0041	0.0036
0.81	0.0091	0.0091	0.0127	0.0105	0.0131	0.0098
0.83	0.0091	0.0092	0.0148	0.0123	0.0122	0.0114
0.85	0.0085	0.0081			0.0124	0.0120
0.86	0.0082	0.0078	0.0142			

[a]Projection at $\rho = 60$ bohr.

[b]Ref. no. 12.

[c]Ref. No. 38.

[d]Ref. no. 41.

[e]Ref. no. 42.

Table 6-15a: $^1F^{odd}$ contribution to $1s \rightarrow 2p$ cross section in πa_0^2 at energies between the $n = 2$ and $n = 3$ thresholds of the H atom.

Energy	15-state[a]	10-state[a]	BOW[b]	TB[c]	GB[d]	C[e]
0.76	0.0001	0.0001	0.0002	0.0001	0.0002	0.0001
0.78	0.0010	0.0010	0.0010	0.0010	0.0008	0.0010
0.81	0.0031	0.0031	0.0035	0.0033	0.0035	0.0031
0.83	0.0050	0.0050	0.0054	0.0052	0.0058	0.0050
0.85	0.0073	0.0073			0.0079	0.0076
0.86	0.0086	0.0086	0.0090			

Table 6-15b: $^3F^{odd}$ contribution to $1s \rightarrow 2p$ cross section in πa_0^2 at energies between the $n = 2$ and $n = 3$ thresholds of the H atom.

Energy	15-state[a]	10-state[a]	BOW[b]	TB[c]	GB[d]	C[e]
0.76	0.0011	0.0011	0.0012	0.0012	0.0015	0.0011
0.78	0.0116	0.0115	0.0110	0.0114	0.0118	0.0105
0.81	0.0324	0.0324	0.0404	0.0342	0.0325	0.0322
0.83	0.0426	0.0427	0.0517	0.0446	0.0379	0.0417
0.85	0.0497	0.0502			0.0435	0.0468
0.86	0.0510	0.0515	0.0603			

[a]Projection at $\rho = 60$ bohr.

[b]Ref. no. 12.

[c]Ref. No. 38.

[d]Ref. no. 41.

[e]Ref. no. 42.

Table 6-16a: $Q(1s \rightarrow 1s)$, in πa_0^2, singlet and triplet contributions, for $J = 0$ through 4 and total cross section, in this calculation and from Callaway, Ref. 35, for energies between the $n = 2$ and $n = 3$ thresholds.

J	0		1		2		3		4		Total	Ref. 35
E/Ryd	S	T	S	T	S	T	S	T	S	T		
0.76	0.6964	3.9450	0.0044	2.3399	0.0854	0.2242	0.0313	0.0961	0.0206	0.0620	7.5051	6.909
0.78	0.6545	3.8436	0.0053	2.2881	0.0914	0.2230	0.0311	0.0961	0.0197	0.0593	7.3122	6.727
0.80	0.6127	3.7461	0.0062	2.2310	0.0949	0.2203	0.0313	0.0960	0.0187	0.0562	7.1135	6.552
0.82	0.5789	3.6519	0.0071	2.1707	0.0967	0.2188	0.0312	0.0942	0.0180	0.0543	6.9219	6.318
0.84	0.5530	3.5612	0.0078	2.1075	0.0957	0.2185	0.0307	0.0913	0.0178	0.0535	6.7370	6.216
0.86	0.6044	3.4734	0.0084	2.0492	0.0864	0.2176	0.0304	0.0891	0.0174	0.0525	6.6287	6.120
0.88	0.5029	3.3888	0.0097	2.0010	0.0958	0.2163	0.0304	0.0857	0.0167	0.0504	6.3977	5.912

Table 6-16b: $Q(1s \rightarrow 2s)$, in πa_0^2, singlet and triplet contributions, for $J = 0$ through 4 and total cross section, in this calculation and from Ref. 35, for energies between the $n = 2$ and $n = 3$ thresholds.

J	0		1		2		3		4		Total	Ref. 35
E/Ryd	S	T	S	T	S	T	S	T	S	T		
0.76	0.03624	.00054	0.00768	.03819	0.05569	0.00001	0.00009	0.00060	0.00004	0.00012	0.13921	0.136
0.78	0.04456	.00088	0.00456	.04419	0.05183	0.00095	0.00025	0.00309	0.00002	0.00007	0.15040	0.149
0.80	0.05795	.00111	0.00453	.05130	0.05579	0.00187	0.00060	0.00706	0.00006	0.00016	0.18044	0.176
0.82	0.06417	.00130	0.00542	.05783	0.05682	0.00464	0.00123	0.00992	0.00010	0.00030	0.20174	0.200
0.84	0.05959	.00136	0.00750	.05766	0.06226	0.00662	0.00182	0.00869	0.00018	0.00054	0.20624	0.212
0.86	0.01958	.00171	0.01004	.03808	0.07088	0.00824	0.00251	0.00824	0.00023	0.00074	0.16025	0.166
0.88	0.05648	.00194	0.00790	.05835	0.06786	0.00606	0.00364	0.01127	0.00027	0.00104	0.21481	0.222

Table 6-16c: $Q(1s \rightarrow 2p)$, in πa_0^2, singlet and triplet contributions, for $J = 0$ through 4 and total cross section, in this calculation and from Ref. 35, for energies between the $n = 2$ and $n = 3$ thresholds.

J	0		1		2		3		4		Total	Ref. 35
E/Ryd	S	T	S	T	S	T	S	T	S	T		
0.76	0.02378	.00030	0.06538	.03270	0.09919	0.00018	0.00014	0.00112	0.00002	0.00005	0.22285	0.224
0.78	0.02866	.00039	0.04734	.03936	0.09615	0.00156	0.00104	0.01156	0.00007	0.00020	0.22631	0.231
0.80	0.02407	.00053	0.04823	.04370	0.10677	0.00373	0.00234	0.02651	0.00020	0.00059	0.25665	0.261
0.82	0.02289	.00079	0.05303	.04719	0.12372	0.00656	0.00399	0.03839	0.00051	0.00147	0.29855	0.298
0.84	0.02485	.00102	0.05999	.04648	0.14469	0.00914	0.00605	0.04647	0.00111	0.00311	0.34293	0.341
0.86	0.00540	.00117	0.06995	.03115	0.17011	0.01111	0.00864	0.05105	0.00188	0.00512	0.35555	0.354
0.88	0.02762	.00144	0.06295	.04693	0.17918	0.00642	0.01085	0.06727	0.00281	0.00771	0.41317	0.411

Table 6-17a: ^{1,3}S resonance positions and widths at energies slightly below the $n = 4$ threshold of the hydrogen atom.[α]

Energy/Ryd	Lifetime/t_0	Width/mRyd	Previous results/Ryd
	^{1}S		
$0.9209 \pm .0001$	4,200	1.8	0.9218[a], 0.92075[b]
$0.93125 \pm .00005$	4,800	1.6	0.930[a], 0.93057[b]
$0.93325 \pm .00005$	8,500	0.9	0.934[a]
	^{3}S		
$0.8898 \pm .0001$	2,200	1.1	0.8907[a]
$0.931145 \pm .000005$	160,000	0.05	0.9320[a]
$0.936780 \pm .000005$	260,000	0.03	

[α]These calculations were done with a basis set that included all surface functions which asymptotically go to $n = 1$ through 5, and the same number of primitives.

[β]The uncertainty indicates the precision of location of the peak in the collision lifetime eigenvalue vs. energy curve, rather than an absolute accuracy of the calculation.

[a]Hata *et al.*, Ref. 64.

[b]Ho, Ref. 39.

[c]Ho and Callaway, Ref. 8.

Table 6-17b: $J = 1$ resonance positions and widths at energies between the $n = 3$ and $n = 4$ thresholds of the hydrogen atom.

Energy/Ryd	Lifetime/t_0	Width/mRyd	Previous results/Ryd
	$^1p^{even}$		
0.93403 ± .00001	140,000	0.06	
	$^3p^{even}$		
0.9255 ± .0001	3,800	2.0	0.92555[c]
0.9358 ± .0001	8,400	1.0	
0.93707 ± .00001	33,000	0.25	
	$^1p^{odd}$		
0.8906 ± .0001	1,200		
0.9257 ± .0001	3,900	2.0	0.9265,[a] 0.9256[b]
0.93145 ± .00001	134,000	0.065	
0.9359 ± .0001	8,800	0.9	0.9359[a]
0.937130 ± .000005	250,000	0.03	
	$^3p^{odd}$		
0.8903 ± .0001	4,900		
0.9213 ± .0001	3,900	1.9	0.9220,[a] 0.9214[b]
0.9317 ± .0001	6,600	1.2	0.9314[b]
0.9335 ± .0001	7,400	1.1	0.9343[a]
0.93408 ± .00001	140,000	0.1	

Table 6-17c: $J = 2$ resonance positions and widths at energies between the $n = 3$ and $n = 4$ thresholds of the hydrogen atom.

Energy/Ryd	Lifetime/t_0	Width/mRyd	Previous results/Ryd
	$^1D^{even}$		
0.8916 ± .0002	1,500		
0.9225 ± .0001	4,000	2.0	0.922525[c]
0.9310 ± .0001	5,100	1.5	0.93102[c]
0.93382 ± .00003	17,000	0.34	
0.9341 ± .0001	9,000	0.9	
0.93486 ± .00001	140,000	0.06	
	$^3D^{even}$		
0.88918 ± .00001	24,000		
0.9270 ± .0001	3,500	2.1	0.92685[c]
0.93212 ± .00001	130,000	0.055	
0.93650 ± .00005	8,400	1.0	
0.936928 ± .000002	268,000	0.03	
	$^1D^{odd}$		
0.88912 ± .00002	27,000	0.27	
0.9269 ± .0001	3,300	2.4	0.92696[c]
0.9365 ± .0001	7,500	1.1	
0.93691 ± .00001	200,000	0.04	
	$^3D^{odd}$		
0.88900 ± .00002	20,000	0.38	
0.9309 ± .0001	5,100	1.6	0.93095[c]
0.93479 ± .00001	150,000	0.05	

Table 6-17d: $J = 3$ resonance positions and widths at energies slightly below the $n = 4$ threshold of the hydrogen atom.[a]

Energy/Ryd	Lifetime/t_0	Width/mRyd	Previous results/Ryd
	$^1F^{even}$		
0.8901 ± .0001	7,000	0.85	
0.93475 ± .00005	13,600	0.6	0.93475[c]
0.93598 ± .00001	176,000	0.05	
	$^3F^{even}$		
0.88928 ± .00002	24,000	0.35	
0.9294 ± .0001	4,800	1.7	0.92946[c]
0.93707 ± .00001	11,400	0.7	
	$^1F^{odd}$		
0.88975 ± .00005	12,000	0.55	
0.9298 ± .0001	6100	1.3	0.92975[c]
0.93319 ± .00001	124,000	0.07	
0.9371 ± .0001	14,000	0.3	
	$^3F^{odd}$		
0.8902 ± .0001	4,300	1.0	
0.9244 ± .0001	2,800	2.8	0.9244[c]
0.93475 ± .00005	13,300	0.5	0.9347[c]
0.9352 ± .0001	5,500	1.6	
0.936056 ± .000002	240,000	0.034	

Table 6-17e: $J = 4$ and $J = 5$ resonances below the $n = 4$ threshold of the H atom.

Energy/Ryd	Lifetime/t_0	Width/mRyd	Previous results/Ryd
	$^1G^{even}$		
$0.8900 \pm .0001$	5,100	1.6	
$0.9273 \pm .0001$	5,400	1.5	0.92725[c]
$0.9364 \pm .0001$	10,000	0.8	
	$^3G^{even}$		
$0.88930 \pm .00001$	90,000	0.1	
$0.93435 \pm .00005$	25,000	0.3	0.9343[c]
$0.93468 \pm .00001$	127,000	0.06	
	$^1G^{odd}$		
$0.93376 \pm .00001$	46,000	0.2	0.93378[c]
	$^1H^{odd}$		
$0.8914 \pm .0002$	3,900	1.6	
$0.93659 \pm .00001$	200,000	0.04	
	$^3H^{odd}$		
$0.8914 \pm .0002$	4,000	1.5	
$0.93227 \pm .00001$	65,000	0.13	0.93219[c]

Table 6-18: Comparison of $1s \rightarrow 3l_1$ cross sections (in πa_0^2) from 3 calculations: (a) Hata *et al.* (ref. 64,65), (b)Burke *et al.* (ref. 12), and (c) present results.

J = 0	(a)	(b)	(c)
$1s - 3s$	0.0065	0.0074	0.0098
$1s - 3p$	0.0085	0.0099	0.0083
$1s - 3d$	0.0030	0.0034	0.0012
Total $n = 1 \rightarrow n = 3$	0.0180	0.0207	0.0193

Table 6-19a: $Q(1s \rightarrow 1s)$, in πa_0^2, summed over spin, for $J = 0$ through 5 and total cross section, for energies between the $n = 3$ and $n = 4$ thresholds.

E\J	0	1	2	3	4	5	Total
0.900	3.8215	2.0609	0.3427	0.1573	0.0960	0.0821	6.5614
0.905	3.7936	2.0447	0.3441	0.1566	0.0952	0.0811	6.5153
0.910	3.7702	2.0325	0.3427	0.1558	0.0946	0.0799	6.4758
0.915	3.7399	2.0169	0.3449	0.1546	0.0944	0.0785	6.4291
0.920	3.7044	1.9871	0.3477	0.1524	0.0943	0.0769	6.3628
0.925	3.6934	1.9987	0.3374	0.1522	0.0943	0.0753	6.3614
0.930	3.6796	1.9771	0.3448	0.1507	0.0942	0.0738	6.3103

Table 6-19b: $Q(1s \rightarrow 2s)$, in πa_0^2, summed over spin, for $J = 0$ through 5 and total cross section, for energies between the $n = 3$ and $n = 4$ thresholds.

E\J	0	1	2	3	4	5	Total
0.900	0.0473	0.0514	0.0505	0.0131	0.0022	0.0003	0.1650
0.905	0.0481	0.0534	0.0507	0.0134	0.0022	0.0004	0.1695
0.910	0.0467	0.0522	0.0499	0.0132	0.0023	0.0004	0.1646
0.915	0.0485	0.0559	0.0496	0.0129	0.0023	0.0004	0.1697
0.920	0.0534	0.0662	0.0613	0.0130	0.0024	0.0004	0.1966
0.925	0.0422	0.0508	0.0421	0.0121	0.0025	0.0004	0.1502
0.930	0.0463	0.0562	0.0489	0.0121	0.0026	0.0004	0.1665

Table 6-19c: $Q(1s \rightarrow 2p)$, in πa_0^2, summed over spin, for $J = 0$ through 5 and total cross section, for energies between the $n = 3$ and $n = 4$ thresholds.

E\J	0	1	2	3	4	5	Total
0.900	0.0232	0.0925	0.1427	0.0730	0.0135	0.0022	0.3471
0.905	0.0244	0.0917	0.1482	0.0754	0.0142	0.0024	0.3563
0.910	0.0244	0.0902	0.1455	0.0771	0.0151	0.0027	0.3550
0.915	0.0278	0.0899	0.1465	0.0789	0.0159	0.0030	0.3619
0.920	0.0316	0.0985	0.1725	0.0817	0.0167	0.0033	0.4041
0.925	0.0236	0.1078	0.1332	0.0818	0.0174	0.0036	0.3672
0.930	0.0291	0.0842	0.1418	0.0865	0.0192	0.0038	0.3647

Table 6-19d: $Q(1s \rightarrow 3s)$, in πa_0^2, summed over spin, for $J = 0$ through 5 and total cross section, for energies between the $n = 3$ and $n = 4$ thresholds.

E\J	0	1	2	3	4	5	Total	*a*	*b*
0.900	0.0098	0.0098	0.0145	0.0023	0.0001	0.0000	0.0365	.0321	.032
0.905	0.0097	0.0094	0.0139	0.0034	0.0001	0.0000	0.0365	.0383	
0.910	0.0110	0.0103	0.0155	0.0032	0.0001	0.0000	0.0401	.0413	
0.915	0.0105	0.0097	0.0161	0.0038	0.0001	0.0000	0.0403	.0377	
0.920	0.0024	0.0043	0.0118	0.0040	0.0001	0.0000	0.0226	.0240	
0.925	0.0149	0.0107	0.0197	0.0011	0.0002	0.0000	0.0465	.0506	
0.930	0.0124	0.0112	0.0175	0.0054	0.0002	0.0000	0.0467	.0495	.055

[a] 14-state calculation, Hata *et al.*, ref. 65.

[b] 6-state close-coupling calculation, Ref. 12.

Table 6-19e: $Q(1s \rightarrow 3p)$, in πa_0^2, summed over spin, for $J = 0$ through 5 and total cross section, for energies between the $n = 3$ and $n = 4$ thresholds.

E\J	0	1	2	3	4	5	Total	a	b
0.900	0.0083	0.0171	0.0227	0.0061	0.0002	0.0000	0.0545	.0575	.062
0.905	0.0077	0.0178	0.0227	0.0074	0.0002	0.0000	0.0560	.0625	
0.910	0.0087	0.0199	0.0247	0.0077	0.0003	0.0000	0.0613	.0644	
0.915	0.0078	0.0208	0.0255	0.0101	0.0004	0.0001	0.0647	.0686	
0.920	0.0007	0.0122	0.0188	0.0105	0.0005	0.0001	0.0439	.0474	
0.925	0.0103	0.0157	0.0322	0.0030	0.0006	0.0000	0.0619	.0726	
0.930	0.0078	0.0236	0.0302	0.0139	0.0005	0.0000	0.0760	.0856	.097

Table 6-19f: $Q(1s \rightarrow 3d)$, in πa_0^2, summed over spin, for $J = 0$ through 5 and total cross section, for energies between the $n = 3$ and $n = 4$ thresholds.

E\J	0	1	2	3	4	5	Total	a	b
0.900	0.0012	0.0072	0.0117	0.0044	0.0003	0.0000	0.0248	.0331	.034
0.905	0.0009	0.0079	0.0129	0.0053	0.0004	0.0000	0.0275	.0317	
0.910	0.0009	0.0081	0.0141	0.0052	0.0004	0.0001	0.0297	.0324	
0.915	0.0006	0.0087	0.0153	0.0072	0.0005	0.0001	0.0325	.0330	
0.920	0.0006	0.0076	0.0137	0.0081	0.0007	0.0001	0.0308	.0287	
0.925	0.0005	0.0059	0.0181	0.0023	0.0008	0.0001	0.0276	.0360	
0.930	0.0005	0.0104	0.0177	0.0083	0.0007	0.0001	0.0377	.0415	.056

Table 6-20: Total cross sections $Q_{1s\rightarrow 3l_1}$, $(l_1 = 0, 1, 2)$ in πa_0^2, summed over spin: (a) Hata *et al.*, ref. 65. (b) This work, $J = 0$ to 5. (c) Burke *et al.*, ref. 12.

	E/Ryd	(a)	(b)	(c)
$1s \rightarrow 3s$	0.900	0.0321	0.0365	0.032
	0.905	0.0383	0.0365	
	0.910	0.0413	0.0401	
	0.915	0.0377	0.0403	
	0.920	0.0240	0.0226	
	0.925	0.0506	0.0465	
	0.930	0.0495	0.0467	0.055
$1s \rightarrow 3p$	0.900	0.0575	0.0545	0.062
	0.905	0.0625	0.0560	
	0.910	0.0644	0.0613	
	0.915	0.0686	0.0647	
	0.920	0.0474	0.0439	
	0.925	0.0726	0.0618	
	0.930	0.0856	0.0760	0.097
$1s \rightarrow 3d$	0.900	0.0331	0.0248	0.034
	0.905	0.0317	0.0275	
	0.910	0.0324	0.0297	
	0.915	0.0330	0.0325	
	0.920	0.0287	0.0308	
	0.925	0.0360	0.0275	
	0.930	0.0415	0.0377	0.056

Table 6-21a: Partial wave contributions to $2s \rightarrow 3s$ cross section, in πa_0^2 at energies between $n = 3$ and $n = 4$ thresholds.

E/Ryd		^{1}S	^{3}S	^{1}P	^{3}P	^{1}D	^{3}D	^{1}F	^{3}F	^{1}G	^{3}G	^{1}H	^{3}H
.900	a)	0.2405	0.0201	0.0170	2.3815	0.8057	0.0154	0.1514	0.0932	0.2980	0.0040	0.0023	0.0528
	b)			← 3.97[e] →		← 0.116[e] →		← 0.289[e] →					
	c)			0.0424	4.937	0.3061	0.0079						
	d)			0.0287	4.851	← 0.878[e] →							
.905	a)	0.2166	0.0159	0.0127	1.5774	0.9954	0.0299	0.0973	0.1282	0.3714	0.0275	0.0049	0.1425
.910	a)	0.2260	0.0143	0.0055	1.3758	1.0305	0.0397	0.0692	0.1580	0.4595	0.0364	0.0087	0.2070
.915	a)	0.2235	0.0101	0.0087	1.2679	1.0066	0.0454	0.0337	0.2582	0.5004	0.0383	0.0182	0.3167
.920	a)	0.1357	0.0077	0.0147	0.8718	0.6960	0.0700	0.0152	0.2832	0.6349	0.0245	0.0253	0.3074
.925	a)	0.1860	0.0070	0.0456	0.6198	1.0627	0.1252	0.0041	0.0600	0.7754	0.0092	0.0281	0.3072
.930	a)	0.1328	0.0064	0.0107	0.3687	1.1855	0.0575	0.0989	0.2832	0.5666	0.0019	0.0351	0.3183

(a) This work.

(b) 14-state variational calculation, ref. 65.

(c) 6-state variational, ref. 65.

(d) 6-state close-coupling, ref.12.

(e) These results are the sum of the spin-weighted singlet and triplet contributions.

Table 6-21b: Partial wave contributions to $2s \rightarrow 3p$ cross section, in πa_0^2 at energies between $n = 3$ and $n = 4$ thresholds.

E/Ryd		^{1}S	^{3}S	^{1}P	^{3}P	^{1}D	^{3}D	^{1}F	^{3}F	^{1}G	^{3}G	^{1}H	^{3}H
.900	a)	0.0829	0.0198	0.2823	2.5835	1.5773	0.2745	0.1533	0.2254	1.1887	0.0218	0.0157	0.3370
	b)			$\leftarrow 2.19^e \rightarrow$		$\leftarrow 1.280^e \rightarrow$		$\leftarrow 0.366^e \rightarrow$					
	c)			0.161	1.787	1.0748	0.2999						
	d)			0.153	1.827	$\leftarrow 1.442^e \rightarrow$							
.905	a)	0.0778	0.0319	0.3838	2.5153	1.6131	0.2823	0.1392	0.2892	1.2384	0.0103	0.0269	0.7497
.910	a)	0.0839	0.0379	0.3312	2.6377	1.6979	0.3088	0.1393	0.3162	1.3526	0.0199	0.0401	0.9294
.915	a)	0.0679	0.0328	0.2511	2.3554	1.6510	0.3356	0.1383	0.3757	1.4354	0.0338	0.0493	1.0896
.920	a)	0.0018	0.0349	0.2004	0.9510	1.3048	0.3981	0.1302	0.4764	1.7259	0.0386	0.0579	1.0715
.925	a)	0.1254	0.0430	0.1542	2.7107	1.6778	0.5075	0.1318	0.4801	2.0238	0.0514	0.0727	1.1726
.930	a)	0.1517	0.0452	0.0891	2.4328	1.5665	0.5478	0.1422	0.4780	1.2531	0.0686	0.0871	1.1415

Table 6-21c: Partial wave contributions to $2s \rightarrow 3d$ cross section, in πa_0^2 at energies between $n = 3$ and $n = 4$ thresholds.

E/Ryd		^{1}S	^{3}S	^{1}P	^{3}P	^{1}D	^{3}D	^{1}F	^{3}F	^{1}G	^{3}G	^{1}H	^{3}H
.900	a)	0.0101	0.0126	0.0701	1.4598	0.7217	0.3475	0.2953	0.0711	0.8251	0.0517	0.0229	0.4632
	b)			$\leftarrow 0.317^e \rightarrow$		$\leftarrow 2.344^e \rightarrow$		$\leftarrow 0.312^e \rightarrow$					
	c)			0.0823	1.021	1.2760	0.2604						
	d)			0.0844	0.969	$\leftarrow 1.700^e \rightarrow$							
.905	a)	0.0218	0.0197	0.0892	1.6218	0.3800	0.3967	0.3488	0.0884	0.9010	0.1022	0.0395	0.9856
.910	a)	0.0315	0.0305	0.2420	1.8860	0.2925	0.4789	0.4468	0.1213	0.9164	0.1738	0.0622	1.1869
.915	a)	0.0385	0.0435	0.4004	1.8550	0.3024	0.5473	0.5307	0.1753	0.9560	0.2451	0.0913	1.3597
.920	a)	0.0712	0.0537	0.4542	0.9200	0.3456	0.5656	0.6446	0.2232	1.0077	0.2849	0.1358	1.3349
.925	a)	0.0900	0.0617	0.1750	3.0456	0.4964	0.4866	0.7795	0.1742	1.1309	0.2942	0.1723	1.2321
.930	a)	0.0914	0.0691	0.6206	3.2542	0.4274	0.5572	0.2992	0.3459	0.8804	0.2964	0.2209	1.1188

Table 6-21d: Partial wave contributions to $2p \rightarrow 3s$ cross section, in πa_0^2 at energies between $n = 3$ and $n = 4$ thresholds.

E/Ryd		^{1}S	^{3}S	^{1}P	^{3}P	^{1}D	^{3}D	^{1}F	^{3}F	^{1}G	^{3}G	^{1}H	^{3}H
.900	a)	0.0653	0.0100	0.0868	0.8590	0.3173	0.3197	0.2513	0.0617	0.1822	0.0364	0.0024	0.0376
	b)			$\leftarrow 0.213^e \rightarrow$		$\leftarrow 0.701^e \rightarrow$		$\leftarrow 0.347^e \rightarrow$					
	c)			0.0484	0.0238	0.3655	0.2840						
	d)			0.0474	0.0211	$\leftarrow 0.652^e \rightarrow$							
.905	a)	0.0566	0.0153	0.1167	0.9415	0.2260	0.3603	0.2012	0.0860	0.1738	0.0894	0.0046	0.0936
.910	a)	0.0594	0.0191	0.1273	1.0530	0.2309	0.3779	0.2186	0.1052	0.1932	0.1463	0.0066	0.0958
.915	a)	0.0523	0.0190	0.1192	0.9990	0.2296	0.3984	0.2088	0.1353	0.1952	0.2023	0.0108	0.1083
.920	a)	0.0048	0.0215	0.1061	0.4760	0.1676	0.4479	0.2354	0.1472	0.2351	0.2067	0.0154	0.0888
.925	a)	0.0805	0.0256	0.0334	1.3554	0.2709	0.5277	0.2706	0.1063	0.3048	0.2130	0.0213	0.0783
.930	a)	0.0700	0.0272	0.1145	1.4887	0.2286	0.3305	0.0248	0.1526	0.1607	0.2019	0.0310	0.0700

Table 6-21e: Partial wave contributions to $2p \rightarrow 3p$ cross section, in πa_0^2 summed over parities, at energies between $n = 3$ and $n = 4$ thresholds.

E/Ryd		^{1}S	^{3}S	^{1}P	^{3}P	^{1}D	^{3}D	^{1}F	^{3}F	^{1}G	^{3}G	^{1}H	^{3}H
.900	a)	0.0890	0.0075	0.3756	2.6354	0.8700	0.7381	0.1778	1.1070	0.7055	0.0311	0.0124	0.2415
	b)			$\leftarrow 1.821^e \rightarrow$		$\leftarrow 1.708^e \rightarrow$		$\leftarrow 0.837^e \rightarrow$		$\leftarrow even + .0267^e \rightarrow$			
	c)			$\leftarrow 1.969^e \rightarrow$		$\leftarrow 1.8779^e \rightarrow$							
	d)			$\leftarrow 3.047^e \rightarrow$									
.905	a)	0.0807	0.0082	0.4638	2.9741	0.7933	0.8142	0.1867	0.9871	0.7681	0.0733	0.0202	0.4923
.910	a)	0.0872	0.0097	0.5348	3.0318	0.7714	0.8918	0.2260	1.0042	0.8171	0.1254	0.0317	0.5946
.915	a)	0.0763	0.0105	0.5922	2.9765	0.7718	0.9845	0.2538	0.9526	0.8253	0.1839	0.0469	0.6955
.920	a)	0.0109	0.0117	0.5662	2.4220	0.6502	1.1373	0.2806	0.9946	0.9556	0.2187	0.0666	0.6296
.925	a)	0.0840	0.0130	0.1999	1.2367	0.8736	1.3009	0.3049	0.8526	1.0815	0.2452	0.0902	0.6123
.930	a)	0.0572	0.0134	0.6544	2.8248	0.8875	1.3905	0.1761	0.4753	0.7344	0.2679	0.1193	0.5531

Table 6-21f: Partial wave contributions to $2p \rightarrow 3d$ cross section, in πa_0^2 summed over parities, at energies between $n = 3$ and $n = 4$ thresholds.

E/Ryd		^{1}S	^{3}S	^{1}P	^{3}P	^{1}D	^{3}D	^{1}F	^{3}F	^{1}G	^{3}G	^{1}H	^{3}H
.900	a)	0.0219	0.0017	0.2817	1.4493	1.1483	2.2334	0.6534	2.1525	0.7544	0.1138	0.0251	0.3888
	b)			← 1.717^e →		← 2.187^e →		← 1.753^e →					
	c)			← 2.282^e →		← 3.0476^e →							
	d)			← 3.376^e →									
.905	a)	0.0237	0.0010	0.3009	1.1030	1.3599	2.3751	0.6781	2.2578	0.8457	0.2212	0.0321	0.7476
.910	a)	0.0260	0.0012	0.2700	1.0211	1.4694	2.5039	0.7366	2.5350	0.9477	0.3822	0.0511	0.9720
.915	a)	0.0235	0.0019	0.2758	1.2573	1.5529	2.7170	0.8149	2.8804	1.0799	0.5857	0.0749	1.1606
.920	a)	0.0047	0.0017	0.2864	1.5258	1.5530	2.9840	0.9237	3.3405	1.1926	0.7862	0.1114	1.2378
.925	a)	0.0299	0.0011	0.1517	0.3007	1.7202	3.1504	1.0726	3.8229	1.3474	0.9057	0.1476	1.3119
.930	a)	0.0264	0.0004	0.3193	1.5373	1.6115	3.0186	0.5369	1.3997	1.0779	1.0127	0.1869	1.3835

Table 6-22: Comparison of 6-state close-coupling,[a] 14-state variational,[b] and 15-state hyperspherical coordinate calculations. Cross sections for all J, summed over l_1, and summed over spin and parity, $(2s \rightarrow n = 3)$ and $(2p \rightarrow n = 3)$.

$$\sum_S \sum_{l_1} Q^{JS}_{2s \rightarrow 3l_1}$$

J	BOW[a]	HMM[b]	This work
0	0.520	0.388	0.3860
1	7.924	6.470	6.7943
2	4.002	3.740	3.7421
3	0.774	0.764	0.9896
4	3.367	2.554	2.3894
5	0.491	0.199	0.8939
Total	17.1	14.1	15.2

$$\sum_{S,\Pi} \sum_{l_1} Q^{JS}_{2p \rightarrow 3l_1}$$

J	BOW[a]	HMM[b]	This work
0	0.182	0.192	0.1955
1	6.499	3.782	5.6878
2	8.390	4.595	5.6268
3	6.247	2.370	4.4037
4	2.169	1.715	1.8234
5	0.326	0.165	0.7078
Total	23.8	12.8	18.4

[a]Ref. 12. [b]Ref. 65.

Table 6-23a: Total $2s \rightarrow nl_1$, $2p \rightarrow nl_1$ cross sections, $(l_1 = 0,1,2)$ in πa_0^2, summed over spin and parity.

E/Ryd		$Q_{2s\rightarrow 3s}$	$Q_{2s\rightarrow 3p}$	$Q_{2s\rightarrow 3d}$	$Q_{2p\rightarrow 3s}$	$Q_{2p\rightarrow 3p}$	$Q_{2p\rightarrow 3d}$
0.900	a)	4.0819	6.7624	4.3510	2.2299	6.9910	9.2243
	b)	5.009	5.309	3.840	1.516	5.215	6.089
	c)	6.93	5.69	4.47	1.48	8.86	13.30
0.905	a)	3.6197	7.3579	4.9947	2.3648	7.6620	9.9461
	b)	5.461	6.641	3.902	1.816	5.964	7.318
0.910	a)	3.6305	7.8951	5.8687	2.6334	8.1256	10.916
	b)	5.347	7.523	4.517	2.187	6.746	8.577
0.915	a)	3.7278	7.8158	6.5453	2.6783	8.3698	12.425
	b)	5.117	7.994	5.085	2.089	7.441	9.513
0.920	a)	3.0864	6.3915	6.0413	2.1525	7.9439	13.948
	b)	3.722	6.389	5.304	1.819	6.828	10.427
0.925	a)	3.2304	9.1509	8.1385	3.2878	6.8947	13.962
	b)	5.025	8.929	7.000	2.975	6.749	10.467
0.930	a)	3.0656	8.0035	8.1814	2.9005	8.1540	12.112
	b)	4.430	9.309	8.339	2.847	7.681	11.180
	c)	7.82	11.94	9.58	3.08	10.69	17.26

(a) This work.

(b) Hata *et al.* best basis. (Ref. 65)

(c) Burke, *et al.* (Ref. 12)

Table 6-23b: Total cross sections from $n = 2$ level to $n = 3$, $Q_{23} = \sum_{l_1}(\frac{1}{4}Q_{2s\to 3l_1} + \frac{3}{4}Q_{2p\to 3l_1})$, in πa_0^2.

E/Ryd	Present	Hata *et al.*	Johnson (1972)	Burke *et al.*
0.900	17.6	13.1	23.0	22.1
0.905	19.0	15.3	24.1	
0.910	20.6	17.5	25.2	
0.915	22.1	18.8	26.2	
0.920	21.9	18.2	27.2	
0.925	23.2	20.4	28.1	
0.930	22.2	22.4	29.0	30.6

Table 6-24: Positions and lifetimes of resonances below the $n = 5$ threshold.

E/Ryd	Lifetime/t_0	Width/mRyd	Comparison E[a]
	^1S		
0.9487 ± 0.00005	5,000	1.4	0.94845
0.9541 ± 0.00005	6,300	1.2	0.9530
0.95618 ± 0.00001	9,400	0.8	
0.95930 ± 0.00003	13,000	0.7	
	^3S		
0.9384 ± 0.00005	1,500		
0.95466 ± 0.00001	120,000	0.06	
0.95796 ± 0.00001	120,000	0.06	
0.95962 ± 0.00001	190,000	0.04	
	$^1p^{odd}$		
0.9388	3,000		
0.9510	4,800	1.7	0.95090
0.954765	120,000	0.06	
0.95675	7,800	1.0	0.95625
0.95775	9,000	0.9	
0.958125	120,000	0.07	
0.959685	200,000	0.04	
	$^3p^{odd}$		
0.9385	3,500	0.9	
0.945	1,000	5.5	
0.9487	5,000	1.5	0.94865
0.9540	5,500	1.5	0.95345
0.95629	8,800	0.7	
0.956295	110,000	0.06	
0.95945	12,000	0.8	
0.959703	220,000	0.04	

[a] Ho and Callaway, complex rotation.

Table 6-25a: ^{1}S contribution to $1s - nl_1$ cross section, $n = 1, 2, 3$ and 4, at $\rho = 110$, at energies between $n = 4$ and $n = 5$ thresholds.

Energy	$Q_{1s\to1s}$	$Q_{1s\to2s}$	$Q_{1s\to2p}$	$Q_{1s\to3s}$	$Q_{1s\to3p}$	$Q_{1s\to3d}$	$Q_{1s\to4s}$	$Q_{1s\to4p}$	$Q_{1s\to4d}$	$Q_{1s\to4f}$
0.940	0.4848	0.04185	0.02338	0.00885	0.00537	0.00008	0.00245	0.00291	0.00099	0.00021
0.945	0.4827	0.04049	0.02294	0.01087	0.00713	0.00031	0.00280	0.00286	0.00083	0.00013
0.950	0.4770	0.04088	0.02189	0.00707	0.00378	0.00004	0.00495	0.00476	0.00072	0.00001
0.955	0.4708	0.04000	0.02492	0.01210	0.00800	0.00048	0.00231	0.00223	0.00077	0.00026

Table 6-25b: ^{3}S contribution to $1s - nl_1$ cross section, $n = 1, 2, 3$ and 4, at $\rho = 110$, at energies between $n = 4$ and $n = 5$ thresholds.

Energy	$Q_{1s\to1s}$	$Q_{1s\to2s}$	$Q_{1s\to2p}$	$Q_{1s\to3s}$	$Q_{1s\to3p}$	$Q_{1s\to3d}$	$Q_{1s\to4s}$	$Q_{1s\to4p}$	$Q_{1s\to4d}$	$Q_{1s\to4f}$
0.940	3.1653	0.00253	0.00224	0.00003	0.00007	0.00001	0.00003	0.00000	0.00001	0.00000
0.945	3.1468	0.00263	0.00240	0.00001	0.00006	0.00001	0.00003	0.00000	0.00000	0.00000
0.950	3.1287	0.00266	0.00252	0.00011	0.00004	0.00000	0.00001	0.00001	0.00001	0.00000
0.955	3.1110	0.00265	0.00258	0.00010	0.00003	0.00000	0.00000	0.00000	0.00000	0.00000

Table 6-26a: ^{1}S contribution to $2s - nl_1$ cross section, $n = 2, 3$ and 4, at $\rho = 110$, at energies between $n = 4$ and $n = 5$ thresholds.

Energy	$Q_{2s\to 2s}$	$Q_{2s\to 2p}$	$Q_{2s\to 3s}$	$Q_{2s\to 3p}$	$Q_{2s\to 3d}$	$Q_{2s\to 4s}$	$Q_{2s\to 4p}$	$Q_{2s\to 4d}$	$Q_{2s\to 4f}$
0.940	2.8558	0.05258	0.08923	0.09009	0.07911	0.06310	0.02764	0.00468	0.01193
0.945	2.7200	0.06170	0.08462	0.09804	0.08483	0.08063	0.01604	0.00865	0.00660
0.950	2.6710	0.04354	0.05672	0.06955	0.08381	0.06994	0.03276	0.03329	0.00636
0.955	2.3840	0.06690	0.05665	0.10885	0.11708	0.07009	0.01653	0.01555	0.01084

Table 6-26b: ^{3}S contribution to $2s - nl_1$ cross section, $n = 2, 3$ and 4, at $\rho = 110$, at energies between $n = 4$ and $n = 5$ thresholds.

Energy	$Q_{2s\to 2s}$	$Q_{2s\to 2p}$	$Q_{2s\to 3s}$	$Q_{2s\to 3p}$	$Q_{2s\to 3d}$	$Q_{2s\to 4s}$	$Q_{2s\to 4p}$	$Q_{2s\to 4d}$	$Q_{2s\to 4f}$
0.940	6.1035	3.4082	0.00437	0.04891	0.08137	0.00088	0.00109	0.00074	0.00021
0.945	5.8861	3.3396	0.00306	0.05213	0.08728	0.00089	0.00108	0.00109	0.00014
0.950	5.6750	3.2760	0.00204	0.05030	0.09437	0.00113	0.00142	0.00178	0.00041
0.955	5.4590	3.2156	0.00135	0.04774	0.10107	0.00055	0.00207	0.00326	0.00084

Table 6-27a: $^1P^{odd}$ contribution to $1s - nl_1$ cross section, $n = 1, 2, 3$ and 4, at $\rho = 110$, at energies between $n = 4$ and $n = 5$ thresholds.

Energy	$Q_{1s\to1s}$	$Q_{1s\to2s}$	$Q_{1s\to2p}$	$Q_{1s\to3s}$	$Q_{1s\to3p}$	$Q_{1s\to3d}$	$Q_{1s\to4s}$	$Q_{1s\to4p}$	$Q_{1s\to4d}$	$Q_{1s\to4f}$
0.940	0.01885	0.00976	0.05767	0.00114	0.00948	0.00541	0.00042	0.00180	0.00199	0.00051
0.945	0.01899	0.01036	0.05948	0.00110	0.00866	0.00439	0.00031	0.00278	0.00267	0.00072
0.950	0.01902	0.00976	0.05357	0.00131	0.01080	0.00701	0.00036	0.00190	0.00187	0.00052
0.955	0.01905	0.01088	0.05890	0.00116	0.00850	0.00423	0.00072	0.00369	0.00355	0.00076

Table 6-27b: $^3P^{odd}$ contribution to $1s - nl_1$ cross section, $n = 1, 2, 3$ and 4, at $\rho = 110$, at energies between $n = 4$ and $n = 5$ thresholds.

Energy	$Q_{1s\to1s}$	$Q_{1s\to2s}$	$Q_{1s\to2p}$	$Q_{1s\to3s}$	$Q_{1s\to3p}$	$Q_{1s\to3d}$	$Q_{1s\to4s}$	$Q_{1s\to4p}$	$Q_{1s\to4d}$	$Q_{1s\to4f}$
0.940	2.0748	0.04145	0.03087	0.00620	0.00756	0.00107	0.00181	0.00312	0.00123	0.00014
0.945	2.0668	0.04003	0.02878	0.00777	0.00943	0.00191	0.00259	0.00313	0.00116	0.00014
0.950	2.0476	0.04168	0.03072	0.00476	0.00488	0.00077	0.00378	0.00501	0.00168	0.00017
0.955	2.0432	0.04083	0.02893	0.00887	0.01032	0.00240	0.00192	0.00285	0.00099	0.00015

Table 6-28a: $^1P^{odd}$ contribution to $2s - nl_1$ cross section, $n = 2, 3$ and 4, at $\rho = 110$, at energies between $n = 4$ and $n = 5$ thresholds.

Energy	$Q_{2s\to 2s}$	$Q_{2s\to 2p}$	$Q_{2s\to 3s}$	$Q_{2s\to 3p}$	$Q_{2s\to 3d}$	$Q_{2s\to 4s}$	$Q_{2s\to 4p}$	$Q_{2s\to 4d}$	$Q_{2s\to 4f}$
0.940	1.9216	2.6061	0.01706	0.06157	0.49301	0.01181	0.08438	0.02792	0.01186
0.945	1.9559	2.6006	0.02271	0.03840	0.47873	0.00973	0.08369	0.04580	0.02524
0.950	1.9214	2.5024	0.02165	0.02834	0.57862	0.01047	0.08076	0.02637	0.02842
0.955	1.9467	2.4816	0.02512	0.01498	0.48286	0.00950	0.06243	0.07682	0.10052

Table 6-28b: $^3P^{odd}$ contribution to $2s - nl_1$ cross section, $n = 2, 3$ and 4, at $\rho = 110$, at energies between $n = 4$ and $n = 5$ thresholds.

Energy	$Q_{2s\to 2s}$	$Q_{2s\to 2p}$	$Q_{2s\to 3s}$	$Q_{2s\to 3p}$	$Q_{2s\to 3d}$	$Q_{2s\to 4s}$	$Q_{2s\to 4p}$	$Q_{2s\to 4d}$	$Q_{2s\to 4f}$
0.940	21.261	4.9397	0.26099	1.5039	1.7574	0.57751	0.60249	0.18253	0.10130
0.945	20.934	4.3809	0.23358	1.6780	1.9760	0.53446	0.54844	0.25582	0.14247
0.950	20.233	5.0593	0.08948	1.0291	1.2161	0.25569	0.65706	0.79641	0.29411
0.955	20.740	3.6175	0.12701	1.7491	2.2397	0.48944	0.52014	0.23231	0.05194

Table 6-29: Positions and lifetimes of $^1P^{odd}$ resonances below the $n = 6$ threshold.

$^1p^{odd}$				
Present results			Ho and Callaway, 1983	
E/Ryd	Lifetime/t_0	Width/mRyd	E/Ryd	Width/mRyd
0.9615	4,800	1.7		
0.9633	3,300	2.4		
0.9661	4,700	1.7	0.96525	1.0
0.9692	6,200	1.3	0.96820	0.9
0.9701	13,000	0.6		
0.9717	17,000	0.5		

THIS PAGE INTENTIONALLY LEFT BLANK.

6.7 References

1. M. L. Goldberger and K. M. Watson, Collision Theory (Krieger, Huntington, NY, 1975), pp. 424-509.
2. M. Gailitis and R. Damburg, *Proc. Phys. Soc.A*, **82**, 192 (1963).
3. M. Gailitis, *J. Phys. B*, **13**, L479 (1980).
4. U. Fano, *Phys. Rev.*, **124**, 1866 (1961).
5. F. T. Smith, *Phys. Rev.*, **118**, 349 (1960).
6. a) G. C. Schatz and A. Kuppermann, *J. Chem. Phys.*, **59**, 964 (1973); b) J. A. Kaye and A. Kuppermann, *Chem. Phys. Lett.*, **77**, 573 (1981).
7. H. Feshbach, *Ann. Phys.*, **5**, 357 (1958); **19**, 287 (1962).
8. Y. K. Ho and J. Callaway, *Phys. Rev. A*, **27**, 1887 (1983).
9. A. Kuppermann, in: Potential Energy Surfaces and Dynamics Calculations, ed. D. G. Truhlar (Plenum Press, New York, 1981), pp. 375-420.
10. G. C. Schatz and A. Kuppermann, *J. Chem. Phys.*, **59**, 964 (1973).
11. R. K. Adair, *Phys. Rev.*, **113**, 338 (1959).
12. P. G. Burke, S. Ormonde, and W. Whitaker, *Proc. Phys. Soc.*, **92**, 319 (1967).
13. A. Kuppermann and J. A. Kaye, *J. Phys. Chem.*, **85**, 1969 (1981).
14. Michael A. Morrison, Thomas L. Estle, and Neal F. Lane, Quantum States of Atoms, Molecules and Solids, (Prentice-Hall, Englewood Cliffs, N. J., 1976) p. 555.
15. B. H. Bransden, Atomic Collision Theory (Benjamin, New York, 1970), pp. 213-221.
16. C. Schwartz, *Phys. Rev.*, **124**, 1468 (1961).
17. Y. Ho, A. Bhatia, and A. Temkin, *Phys. Rev. A*, **15**, 1423 (1977).
18. R. L. Armstead, *Phys. Rev.*, **171**, 91 (1968).
19. D. Register and R. T. Poe, *Phys. Lett.*, **51A**, 431 (1975).
20. J. Callaway, *Phys. Lett.*, **65A**, 199 (1978); **68A**, 315 (1978).

21. P. G. Burke and H. Schey, *Phys. Rev.*, **126**, 147 (1962).

22. P. Burke and A. J. Taylor, *Proc. Phys. Soc.*, **88**, 549 (1966).

23. C. D. Lin, *Phys. Rev. A*, **10**, 1986 (1974); **12**, 493 (1975).

24. H. Klar and U. Fano, *Phys. Rev. Lett.*, **37**, 1132 (1976).

25. H. Klar and M. Klar, *Phys. Rev. A*, **17**, 1007 (1978).

26. B. L. Christensen-Dalsgaard, *Phys. Rev. A*, **29**, 2242 (1984).

27. P. G. Burke, *Advanc. Phys.*, **14**, 521 (1965).

28. M. J. Seaton, *Proc. Phys. Soc.*, **77**, 174 (1961).

29. I. Shimamura, *J. Phys. Soc. (Japan)*, **30**, 1702 (1971); **31**, 852 (1971).

30. L. Sanche and P. D. Burrow, *Phys. Rev. Lett.*, **29**, 1639 (1972).

31. H. Klar and M. Klar, *J. Phys. B*, **13**, 1057 (1980).

32. G. Schulz, *Rev. Mod. Phys.*, **45**, 378 (1973).

33. A. Temkin and E. Sullivan, *Phys. Rev.*, **129**, 1250 (1963).

34. a) H. C. Bryant, B. D. Dieterle, J. Donahue, H. Sharifian, H. Tootoonchi, D. M. Wolfe, P. A. M. Gram, and M. A. Yates-Williams, *Phys. Rev. Lett.*, **38**, 228 (1977); b) H. C. Bryant, D. A. Clark, K. B. Butterfield, C. A. Frost, H. Sharifian, H. Tootoonchi, J. B. Donahue, P. A. M. Gram, M. E. Hamm, R. W. Hamm, J. C. Pratt, M. A. Yates, and W. W. Smith, *Phys. Rev. A*, **27**, 2889 (1983).

35. J. Callaway, *Phys. Rev. A*, **26**, 199 (1982); *Phys. Lett.*, **81A**, 495 (1981).

36. J. N. Das and M. R. H. Rudge, *J. Phys. B*, **9**, L131 (1976).

37. P. G. Burke, *Advanc. Phys.*, **14**, 521 (1965).

38. A. J. Taylor and P. G. Burke, *Proc. Phys. Soc.*, **92**, 336 (1967).

39. Y. K. Ho, *J. Phys. B*, **10**, L373 (1977); **12**, L543 (1979); *Phys. Lett.*, **77A**, 147 (1980).

40. L. A. Morgan, M. R. C. McDowell, and J. Callaway, *J. Phys. B*, **10**, 3297 (1977).

41. S. Geltman and P. G. Burke, *J. Phys. B*, **3**, 1062 (1970).

42. J. Callaway, *Phys. Rep.*, **45**, 89 (1978).

43. J. Williams, *J. Phys. B*, **9**, 1519 (1976).

44. J. W. McGowan, J. F. Williams, and E. K. Curley, *Phys. Rev.*, **180**, 132 (1969).

45. J. Macek and P. G. Burke, *Proc. Phys. Soc.*, **92**, 351 (1967).

46. C. D. Lin, *Phys. Rev. Lett.*, **35**, 1150 (1975).

47. H. Koschmieder, V. Raible, and H. Kleinpoppen, *Phys. Rev. A*, **8**, 1365 (1973).

48. A. Oed, *Phys. Lett.*, **34A**, 435 (1971).

49. J. Williams and J. Willis, *J. Phys. B*, **7**, L61 (1974).

50. P. A. M. Gram, J. C. Pratt, M. A. Yates-Williams, H. C. Bryant, J. Donahue, H. Sharifian, and H. Tootoonchi, *Phys. Rev. Lett.*, **40**, 107 (1978).

51. J. T. Broad and W. Reinhardt, *Phys. Rev. A*, **14**, 2159 (1976).

52. J. Macek, *Proc. Phys. Soc.*, **92**, 365 (1967).

53. H. A. Hyman, V. L. Jacobs, and P. G. Burke, *J. Phys. B*, **5**, 2282 (1972).

54. J. J. Wendoloski and W. Reinhardt, *Phys. Rev. A*, **17**, 195 (1976).

55. G. W. F. Drake, *Phys. Rev. Lett.*, **24**, 126 (1970).

56. C. D. Lin, *Phys. Rev. A*, **14**, 30 (1976).

57. J. W. Cooper, U. Fano, and F. Prats, *Phys. Rev. Lett.*, **10**, 518 (1963).

58. C. H. Greene, *J. Phys. B*, **13**, L39 (1980).

59. Subsequently we performed calculations with a 25 surface function basis set, projecting at 80 bohr, at a fine grid of energies above 0.88 Ryd on the $J = 1$ partial wave only. This calculation did indeed produce the two missing resonances, however in inverted energy order. The three highest $n = 3$ $^1P^{odd}$ resonance positions (lifetimes and widths) at 80 bohr are 0.882704 Ryd (450,000 t_0, 0.017 mRyd), 0.88824 Ryd (38,000 t_0, 0.20 mRyd), and 0.888433 Ryd (740,000 t_0, 0.011 mRyd).

60. M. E. Hamm, R. W. Hamm, J. Donahue, P. A. M. Gram, J, C, Pratt, M. A. Yates, R. D. Bolton, D. A. Clark, H. C. Bryant, C. A. Frost, and W. W. Smith, *Phys. Rev. Lett.*, **43**, 1715 (1979).

61. J. W. McGowan, E. M. Clarke, and E. K. Curley, *Phys. Rev. Lett.*, **15**, 917 (1965); **17E**, 66 (1966).

62. S. J. Ormonde, J. McEwen, and J. W. McGowan, *Phys. Rev. Lett.*, **22**, 1165 (1969).

63. a) W. R. Ott, W. E. Kauppila, and W. L. Fite, *Phys. Rev. A*, **1089**, 1 (1970); b) W. E. Kauppila, W. R. Ott, and W. L. Fite, *Phys. Rev. A*, **1**, 1099 (1970).

64. J. Hata, L. A. Morgan, and M. R. C. McDowell, *J. Phys. B*, **13**, 4453 (1980).

65. J. Hata, L. A. Morgan, and M. R. C. McDowell, *J. Phys. B*, **13**, L347 (1980).

66. C. D. Lin, *Phys. Rev. Lett.*, **51**, 1348 (1983); *Phys. Rev. A*,**29**, 1019 (1984).

67. D. R. Herrick and O. Sinanoğlu, *Phys. Rev. A*, **11**, 97 (1975).

68. a) D. R. Herrick and M. E. Kellman, *Phys. Rev. A*, **21**, 418 (1980); b) D. R. Herrick, M. E. Kellman, and R. D. Poliak, *Phys. Rev. A*, **22**, 1517 (1980).

69. G. Schultz, *Rev. Mod. Phys.*, **45**, 378 (1973).

70. There is some confusion about the spin of this resonance: Ref. 64 says triplet, but the same authors labeled it singlet in their previous letter, Ref. 65.

71. U. Fano, *Phys. Rev.*, **124**, 1866 (1961).

72. D. D. Burgess, G. Kolbe, and J. M. Ward, *J. Phys. B*, **11**, 2765 (1978).

73. D. D. Burgess, V. P. Myerscough, C. H. Skinner, and J. M. Ward, *J. Phys. B*, **13**, 1675 (1980).

74. S. Ormonde, W. Whitaker, W. Heubner, and P. G. Burke, *Technical Report* No. AFWL-TR-67-10, vol. 1, as referenced by Hata *et al.*

75. L. C. Johnson, *Astrophys. J.*, **174**, 227 (1972).

76. D. A. Clark, H. C. Bryant, K. B. Butterfield, C. A. Frost, R. Marchini, J. B. Donahue, P. A. Gram, and W. W. Smith, *Bull. Am. Phys. Soc.*, **26**, 1196 (1981).

77. There have been calculations extended to very high energies, but only $1s - 1s$, $1s - 2s$, and $1s - 2p$ cross sections were obtained.

78. A. K. Bhatia and A. Temkin, *Phys. Rev. A*, **11**, 2018 (1975).

79. J. W. McGowan, *Phys. Rev.*, **156**, 165 (1967).

80. P. G. Burke, in *Invited Papers of the Fifth International Conference on the Physics of Electronic and Atomic Collisions, 1967*, (University of Colorado Press, Boulder, CO, 1968), p. 128.

6.8 Figures and Captions

FIG. 6.1: Total elastic cross section from 0.69 Ryd to the $n = 2$ threshold, solid line. Total singlet and triplet contributions are given by the dashed and short-long dashed lines, respectively.

FIG. 6.2: Resonances below the $n = 3$ H atom threshold, plotted according to the I-supermultiplet classification of Herrick and Kellman,[72] for Top: intrashell states ($A = +1$). Middle: intershell states ($A = -1$). Bottom: Each resonance represents the second resonance of a particular $A = +1$ series.

FIG. 6.3: ^{1}S partial wave cross sections (in πa_0^2) between $n = 2$ and $n = 3$ thresholds. Solid line: $1s \rightarrow 1s$ elastic process. Dotted line: $1s \rightarrow 2s$. Dashed line: $1s \rightarrow 2p$.

FIG. 6.4: Collision lifetime eigenvalues of ^{1}S partial wave for energies below the $n = 3$ threshold, indicating three resonances.

FIG. 6.5: ^{3}S partial wave cross sections (in πa_0^2) between $n = 2$ and $n = 3$ thresholds. Line types are the same as for ^{1}S.

FIG. 6.6: $^1\mathrm{P}^{\mathrm{odd}}$ partial wave cross sections (in πa_0^2) between $n = 2$ and $n = 3$ thresholds. Top: $1s \rightarrow 1s$ elastic process. Middle: $1s \rightarrow 2s$. Bottom: $1s \rightarrow 2p$.

FIG. 6.7: $^3\mathrm{P}^{\mathrm{odd}}$ partial wave cross sections (in πa_0^2) between $n = 2$ and $n = 3$ thresholds. Top: $1s \rightarrow 1s$ elastic process. Middle: $1s \rightarrow 2s$. Bottom: $1s \rightarrow 2p$.

FIG. 6.8: Eigenphaseshifts and eigenphase sum (solid line) of the $^1\mathrm{P}^{\mathrm{odd}}$ partial wave of e^-–H *vs.* energy, at energies near the shape resonance at 0.751 Ryd.

FIG. 6.9: $^1\mathrm{P}^{\mathrm{odd}}$ partial wave cross sections at energies just above 0.75 Ryd ($n = 2$ threshold). The solid line is this calculation, the triangles are from the 11-state

variational calculation by Callaway, ref. 35. The cross sections are in units of πa_0^2. (a) $1s \rightarrow 1s$ and $1s \rightarrow 2s$ transitions. (b) $1s \rightarrow 2p$.

FIG. 6.10: Collision lifetime eigenvalues of $^1D^{even}$ partial wave for energies below the $n = 3$ threshold, indicating two resonances, at 0.8680 and 0.8868 Ryd.

FIG. 6.11: $^1F^{odd}$ cross sections. Top: $1s \rightarrow 1s$; middle: $1s \rightarrow 2s$; bottom: $1s \rightarrow 2p$.

FIG. 6.12: $^3F^{odd}$ cross sections. Top: $1s \rightarrow 1s$; middle: $1s \rightarrow 2s$; bottom: $1s \rightarrow 2p$.

FIG. 6.13: Collision lifetime eigenvalues for the $^1F^{odd}$ and $^3F^{odd}$ partial waves vs. energy, between the $n = 2$ and $n = 3$ thresholds. The $^1F^{odd}$ resonance at 0.8872 Ryd has a lifetime of 400,000 t_0, and the lifetime of the $^3F^{odd}$ resonance at 0.8769 Ryd is 36,000 t_0.

FIG. 6.14: $^3F^{odd}$ partial cross section for the $2p \rightarrow 2p$ elastic process in the energy region between the $n = 2$ and $n = 3$ thresholds.

FIG. 6.15: Argand diagrams of the $^3F^{odd}$ scattering matrix elements, indicating the Feshbach resonance at 0.8769 Ryd. The energy spanned is 0.75 Ryd to 0.889 Ryd. (a) Scattering matrix elements S_{12}, S_{13}, and S_{14}, where the initial state label '1' stands for $nl_1l_2 = (1s3)$, and final states 2, 3, and 4 have quantum numbers $(2s3)$, $(2p2)$, and $(2p4)$, respectively. The marked points are evenly spaced by 0.00005 Ryd from 0.8768 Ryd to 0.8772 Ryd. Each matrix element starts at the origin at 0.75 Ryd. (b) and (c) Diagonal elements of the scattering matrix, S_{33} and S_{44}, respectively. The points marked + are spaced by 0.02 Ryd, while the points marked by triangles are the same energies as marked in part (a).

FIG. 6.16: Total elastic cross section for e^-–H (1s) collisions, for energies between the $n = 2$ and $n = 3$ thresholds. The energy is given in Rydbergs, measured from

the ground state of the hydrogen atom. The cross section is given in πa_0^2.

FIG. 6.17: (a) Total cross section for the inelastic process from the ground state to the $2s$ state for energies from the $n = 2$ to the $n = 3$ hydrogen threshold. (b) Expanded energy scale for energies close to the $n = 3$ hydrogen threshold, with resonance positions indicated above. (c) Total cross section for the inelastic process from the ground state to the $2p$ state for energies from the $n = 2$ to the $n = 3$ hydrogen threshold. (d) Expanded energy scale for energies close to the $n = 3$ hydrogen threshold, with resonance positions indicated above.

FIG. 6.18: $n = 4$ resonances diagrammed according to $(K,T)^A$ formalism, to show I-supermultiplets, where $I = J - T$. (a) $A = +1$ type resonances, which are low in energy and relatively wide. (b) $A = -1$ type resonances, which are 1–2 orders of magnitude narrower. (c) The resonances shown here have the same indices as the lower resonance positions in (a). Each represents the second resonance of a particular series.

FIG. 6.19: $J = 0$ partial cross sections in πa_0^2 as functions of energy in the energy range between the $n = 3$ and $n = 4$ thresholds ^{1}S (left) and ^{3}S (right) partial waves. (a) $1s \rightarrow 1s$: solid line; $1s \rightarrow 2s$: dotted line; $1s \rightarrow 2p$: dashed line. (b) $1s \rightarrow 3l_1$, (c) $2s \rightarrow 3l_1$, (d) $2p \rightarrow 3l_1$: solid line: $l_1 = 3s$; dotted line: $l_1 = 3p$; dashed line: $l_1 = 3d$. The origin of energy is the isolated $1s$ H atom, the second electron being removed to infinity.

FIG. 6.20: Argand diagram for $2s0 - 3d2$ matrix element of ^{1}S scattering matrix, at energies between the $n = 3$ and $n = 4$ thresholds. The '+'s represent the points 0.890 to 0.935 Ryd, spaced every 0.005 Ryd. The blocks indicate the positions of Feshbach resonances.

FIG. 6.21: (a) Collision lifetime eigenvalues of ^{3}S partial wave between $n = 3$ and $n = 4$ thresholds as a function of energy. (b) Expanded energy scale. (The positive

and negative fluctuations seen at the resonance energy in some of the eigenvalues are due to numerical inaccuracies in taking the difference of close numbers.)

FIG. 6.22: (a) Argand diagram for $2p1 - 3d2$ matrix element of ^{3}S scattering matrix, at energies between the $n = 3$ and $n = 4$ thresholds. The triangles represent the points E=0.8889 to 0.8899 Ryd, spaced every 0.0001 Ryd. The '+'s represent the points 0.890 to 0.935 Ryd, spaced every 0.005 Ryd. The blocks indicate the positions of Feshbach resonances, as 0.931145 and 0.936780 Ryd. (b) Enlargement of region within the dotted lines in (a).

FIG. 6.23: $J = 1$ partial cross sections in πa_0^2 as functions of energy in the energy range between the $n = 3$ and $n = 4$ thresholds ^{1}P^{odd} (left) and ^{3}P^{odd} (right) partial waves. (a) $1s \rightarrow 1s$: solid line; $1s \rightarrow 2s$: dotted line; $1s \rightarrow 2p$: dashed line. (b) $1s \rightarrow 3l_1$, (c) $2s \rightarrow 3l_1$, (d) $2p \rightarrow 3l_1$: solid line: $l_1 = 3s$; dotted line: $l_1 = 3p$; dashed line: $l_1 = 3d$. The origin of energy is the isolated $1s$ H atom, the second electron being removed to infinity.

FIG. 6.24: Argand diagram for the ^{1}P^{odd} S-matrix element $(1s1) \rightarrow (2p2)$. The large arrows indicate the direction of increasing energy, from the $n = 3$ to $n = 4$ threshold. The '+'s correspond to energies every 0.010 Ryd, the triangles every 0.002 Ryd and the dots every 0.0004 Ryd. The origin of energy is the isolated $1s$ H atom, the second electron being removed to infinity.

FIG. 6.25: Collision lifetime eigenvalues of ^{1}P^{odd} partial wave vs. energy below the $n = 4$ threshold. Resonances (arrows) occur at 0.9257, 0.93145, 0.9359, and 0.93713 Ryd.

FIG. 6.26: Collision lifetime eigenvalues of ^{3}P^{odd} partial wave vs. energy between the $n = 3$ and $n = 4$ thresholds. Resonances occur at 0.8903, 0.9213, 0.9317, 0.9335, and 0.9341 Ryd.

FIG. 6.27: Collision lifetime eigenvalues of $^3P^{odd}$ partial wave just below the $n = 4$ threshold, using an insufficiently fine grid ($\Delta E = 0.2$ mRyd) of energy values. The heights of the peaks at 0.9317 and 0.9335 are nearly converged. The large negative peak bracketed by two small positive peaks is due to the narrow resonance at 0.93408 Ryd (width 0.1 mRyd).

FIG. 6.28: Parity favored $J = 2$ partial cross sections as functions of energy in the energy range between the $n = 3$ and $n = 4$ thresholds, for the $^1D^{even}$ (left) and $^3D^{even}$ (right) partial waves. (a) $1s \rightarrow 1s$: solid line; $1s \rightarrow 2s$: dotted line; $1s \rightarrow 2p$: dashed line. (b) $1s \rightarrow 3l_1$, (c) $2s \rightarrow 3l_1$, (d) $2p \rightarrow 3l_1$: solid line: $l_1 = 3s$; dotted line: $l_1 = 3p$; dashed line: $l_1 = 3d$. The origin of energy is the isolated $1s$ H atom, the second electron being removed to infinity.

FIG. 6.29: Collision lifetime eigenvalues of $^1D^{even}$ partial wave vs. energy between the $n = 3$ and $n = 4$ thresholds.

FIG. 6.30: $^1D^{odd}$ and $^3D^{odd}$ partial cross sections between $n = 3$ and $n = 4$ thresholds in πa_0^2.

FIG. 6.31: Parity favored $J = 3$ partial cross sections as functions of energy in the energy range between the $n = 3$ and $n = 4$ thresholds, for the $^1F^{odd}$ (left) and $^3F^{odd}$ (right) partial waves. (a) $1s \rightarrow 1s$: solid line; $1s \rightarrow 2s$: dotted line; $1s \rightarrow 2p$: dashed line. (b) $1s \rightarrow 3l_1$, (c) $2s \rightarrow 3l_1$, (d) $2p \rightarrow 3l_1$: solid line: $l_1 = 3s$; dotted line: $l_1 = 3p$; dashed line: $l_1 = 3d$. The origin of energy is the isolated $1s$ H atom, the second electron being removed to infinity.

FIG. 6.32: $^1F^{even}$ and $^3F^{even}$ partial cross sections between $n = 3$ and $n = 4$ thresholds in πa_0^2.

FIG. 6.33: Parity favored $J = 4$ partial cross sections as functions of energy in the energy range between the $n = 3$ and $n = 4$ thresholds, for the $^1G^{even}$ (left) and

$^3G^{even}$ (right) partial waves. (a) $1s \rightarrow 1s$: solid line; $1s \rightarrow 2s$: dotted line; $1s \rightarrow 2p$: dashed line. (b) $1s \rightarrow 3l_1$, (c) $2s \rightarrow 3l_1$, (d) $2p \rightarrow 3l_1$: solid line: $l_1 = 3s$; dotted line: $l_1 = 3p$; dashed line: $l_1 = 3d$. The origin of energy is the isolated $1s$ H atom, the second electron being removed to infinity.

FIG. 6.34: Parity favored $J = 5$ partial cross sections as functions of energy in the energy range between the $n = 3$ and $n = 4$ thresholds, for the $^1H^{odd}$ (left) and $^3H^{odd}$ (right) partial waves. (a) $1s \rightarrow 1s$: solid line; $1s \rightarrow 2s$: dotted line; $1s \rightarrow 2p$: dashed line. (b) $1s \rightarrow 3l_1$, (c) $2s \rightarrow 3l_1$, (d) $2p \rightarrow 3l_1$: solid line: $l_1 = 3s$; dotted line: $l_1 = 3p$; dashed line: $l_1 = 3d$. The origin of energy is the isolated $1s$ H atom, the second electron being removed to infinity.

FIG. 6.35: Total cross sections between $n = 3$ and $n = 4$ threshold from the $1s$ initial state to $n = 1, 2$ and 3 states. (a) $1s \rightarrow 1s$. (b) Solid line $1s \rightarrow 2s$; dashed line $1s \rightarrow 2p$. (c) $1s \rightarrow 3l_1$.

FIG. 6.36: Total cross sections between $n = 3$ and $n = 4$ threshold from the $2s$ initial state to $n = 3$ states. (a) $2s \rightarrow 3s$; (b) $2s \rightarrow 3p$; (c) $2s \rightarrow 3d$.

FIG. 6.37: Total cross sections between $n = 3$ and $n = 4$ threshold from the $2p$ initial state to $n = 3$ states. Solid line $2p \rightarrow 3s$; dashed line $2p \rightarrow 3p$; dotted line $2p \rightarrow 3d$.

FIG. 6.38: Argand diagram for $(1s1 - 4d3)$ matrix element of $^1P^{odd}$ scattering matrix, at energies between the $n = 4$ and $n = 5$ thresholds. The blocks represent the energies at which there is a resonance.

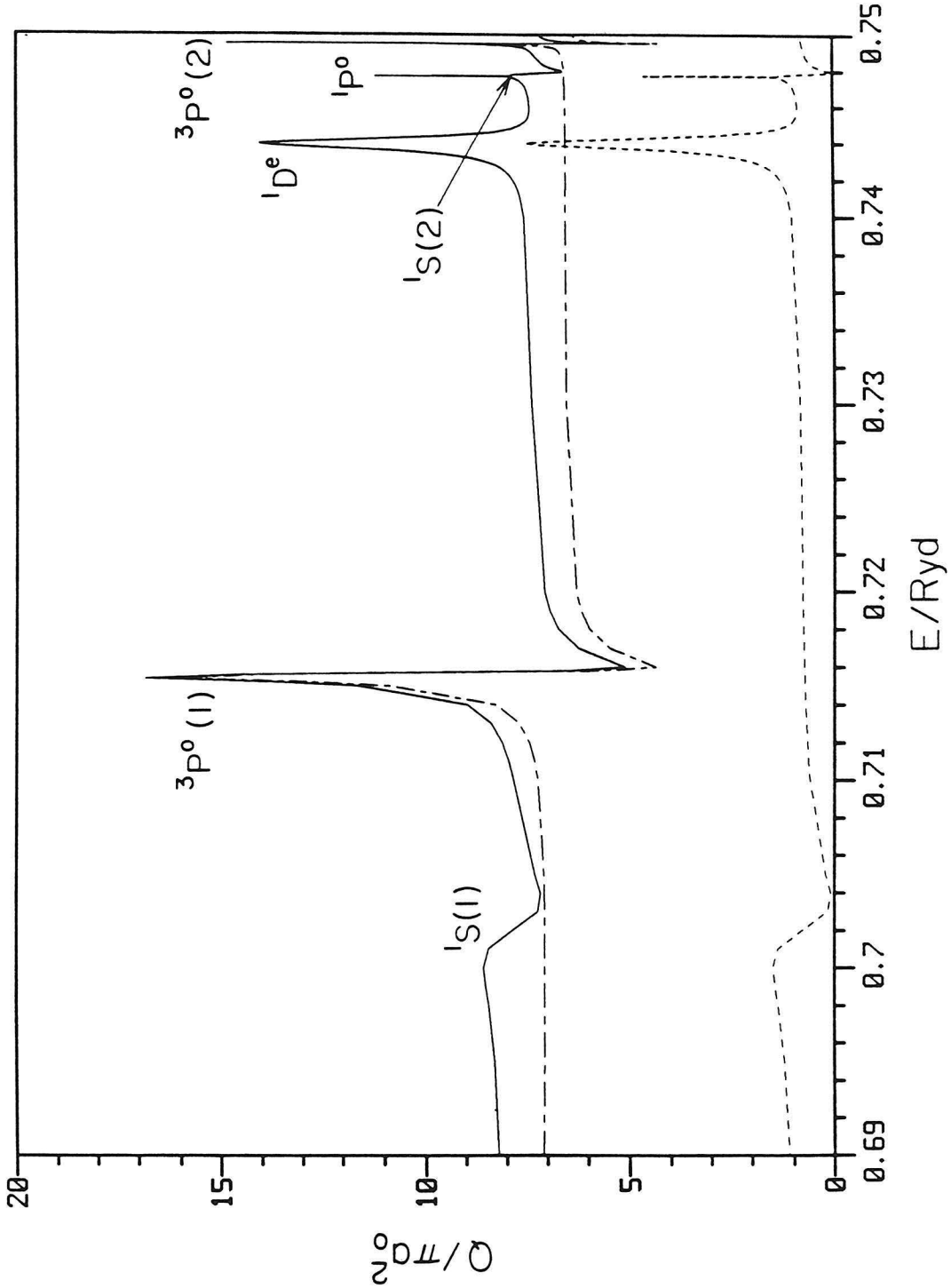
$^3P^o(2)$
$^1P^o$
$^1D^e$
$^1S(2)$
$^3P^o(1)$
$^1S(1)$
$Q/\pi a_o^2$
E/Ryd
0.69
0.7
0.71
0.72
0.73
0.74
0.75
0
5
10
15
20

Figure 6.1

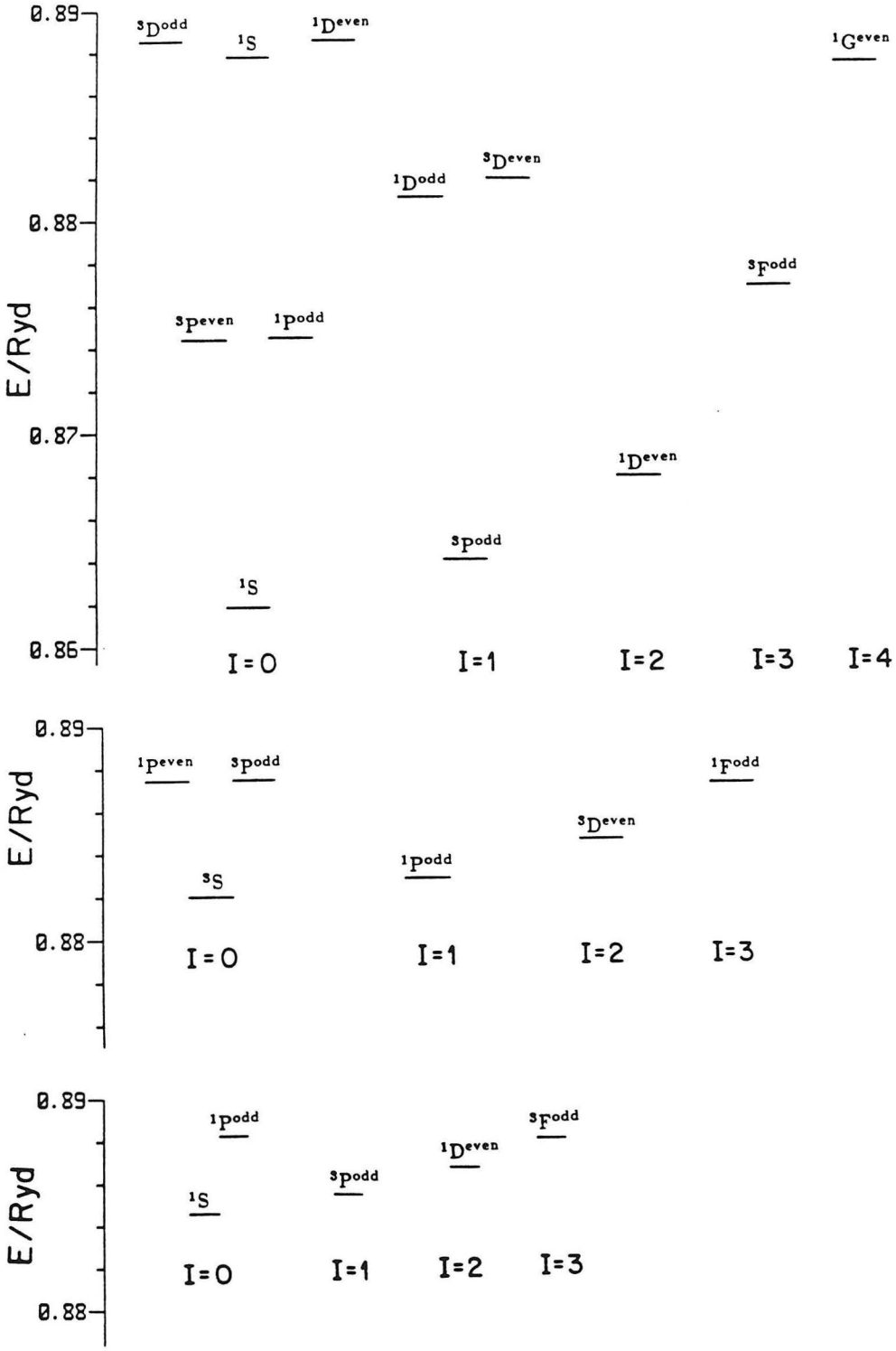
0.89
0.88
0.87
0.86
E/Ryd
$^3D^{odd}$
^1S
$^1D^{even}$
$^1G^{even}$
$^1D^{odd}$
$^3D^{even}$
$^3F^{odd}$
$^3P^{even}$
$^1P^{odd}$
$^1D^{even}$
$^3P^{odd}$
^1S
I=0
I=1
I=2
I=3
I=4
0.89
0.88
E/Ryd
$^1P^{even}$
$^3P^{odd}$
$^1F^{odd}$
$^3D^{even}$
$^1P^{odd}$
^3S
I=0
I=1
I=2
I=3
0.89
0.88
E/Ryd
$^1P^{odd}$
$^3F^{odd}$
$^1D^{even}$
$^3P^{odd}$
^1S
I=0
I=1
I=2
I=3

Figure 6.2

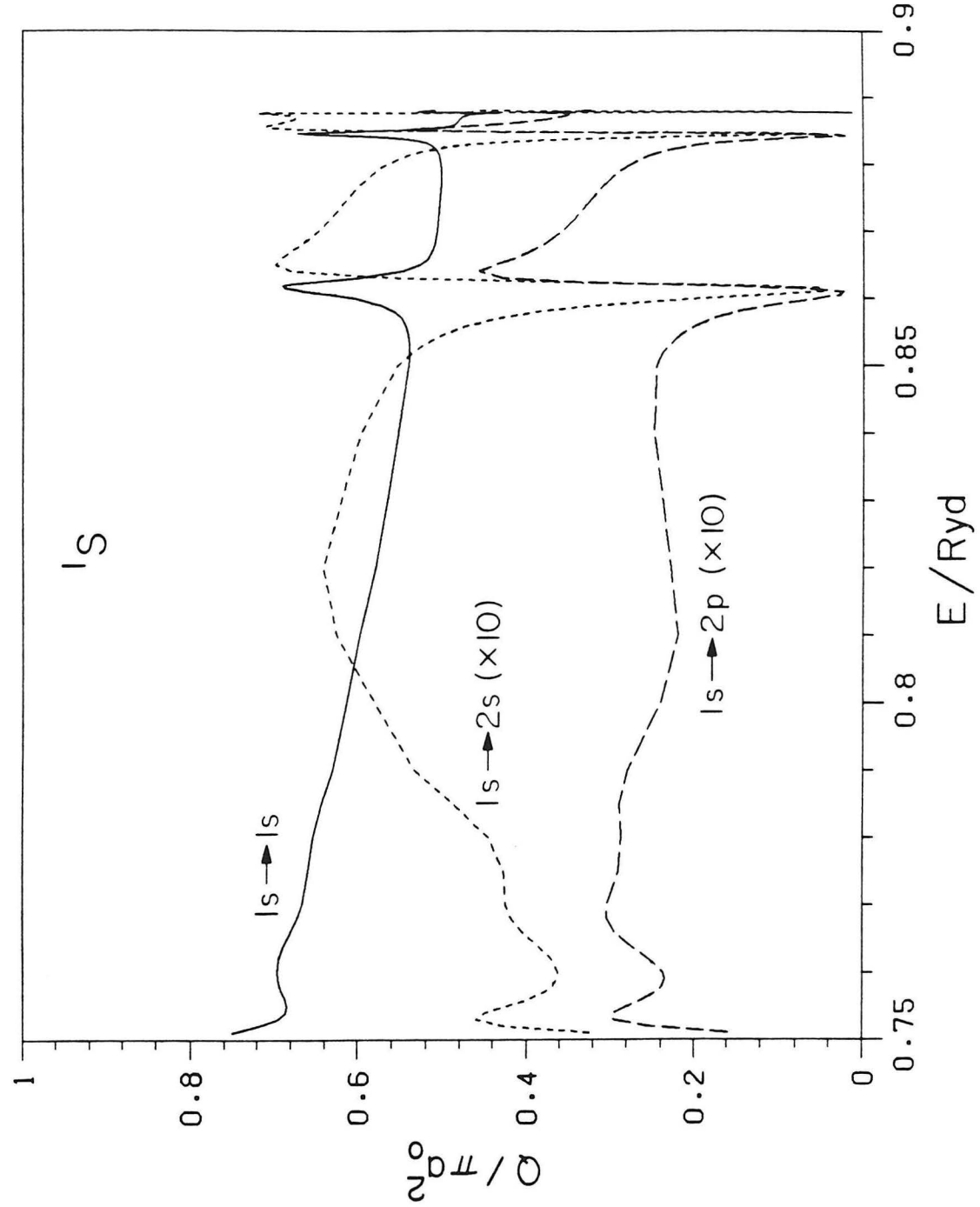
^1S
1s → 1s
1s → 2s (×10)
1s → 2p (×10)
$\Omega / \pi a_o^2$
E/Ryd
0
0.2
0.4
0.6
0.8
1
0.75
0.8
0.85
0.9

Figure 6.3

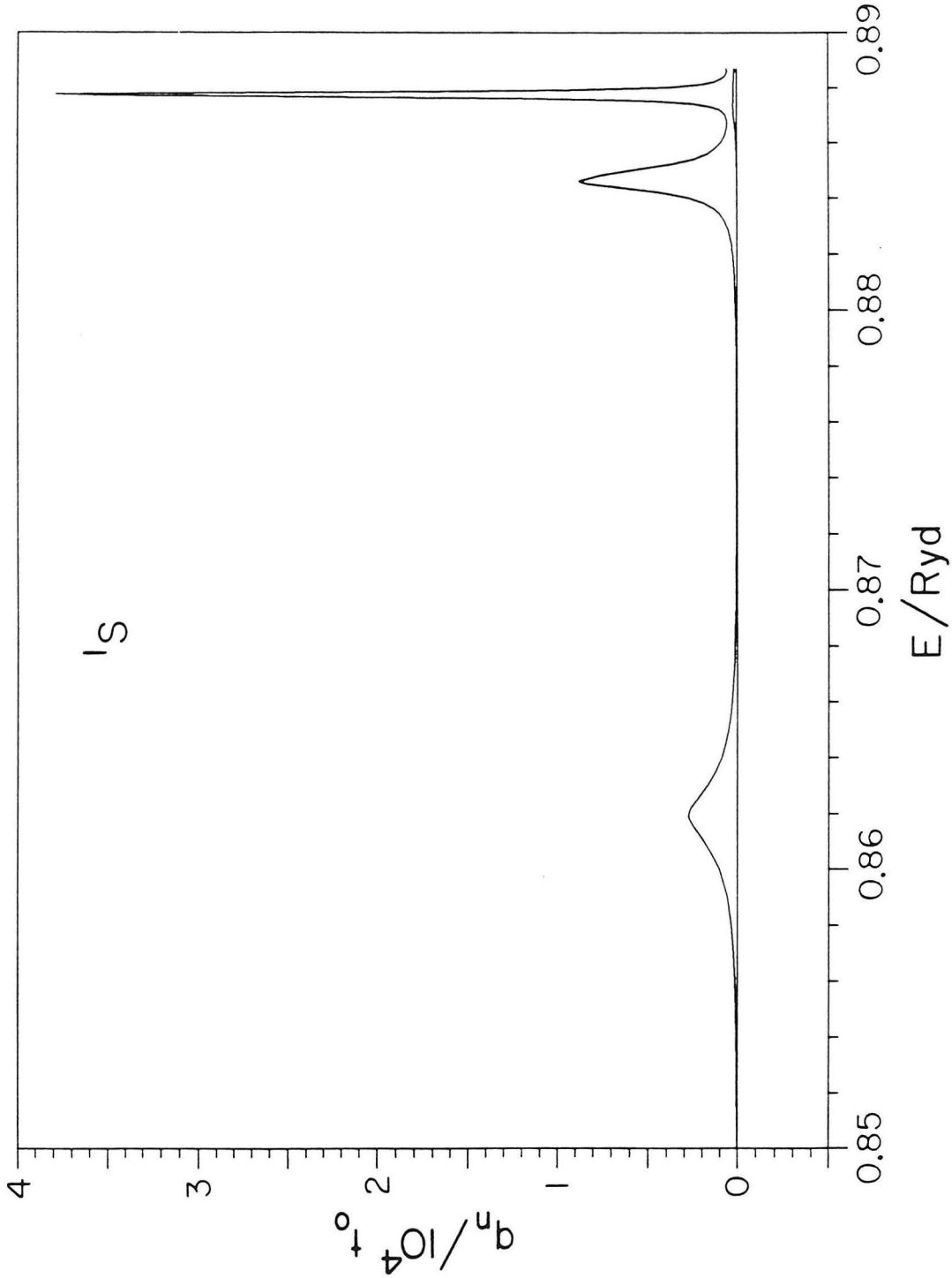

Figure 6.4

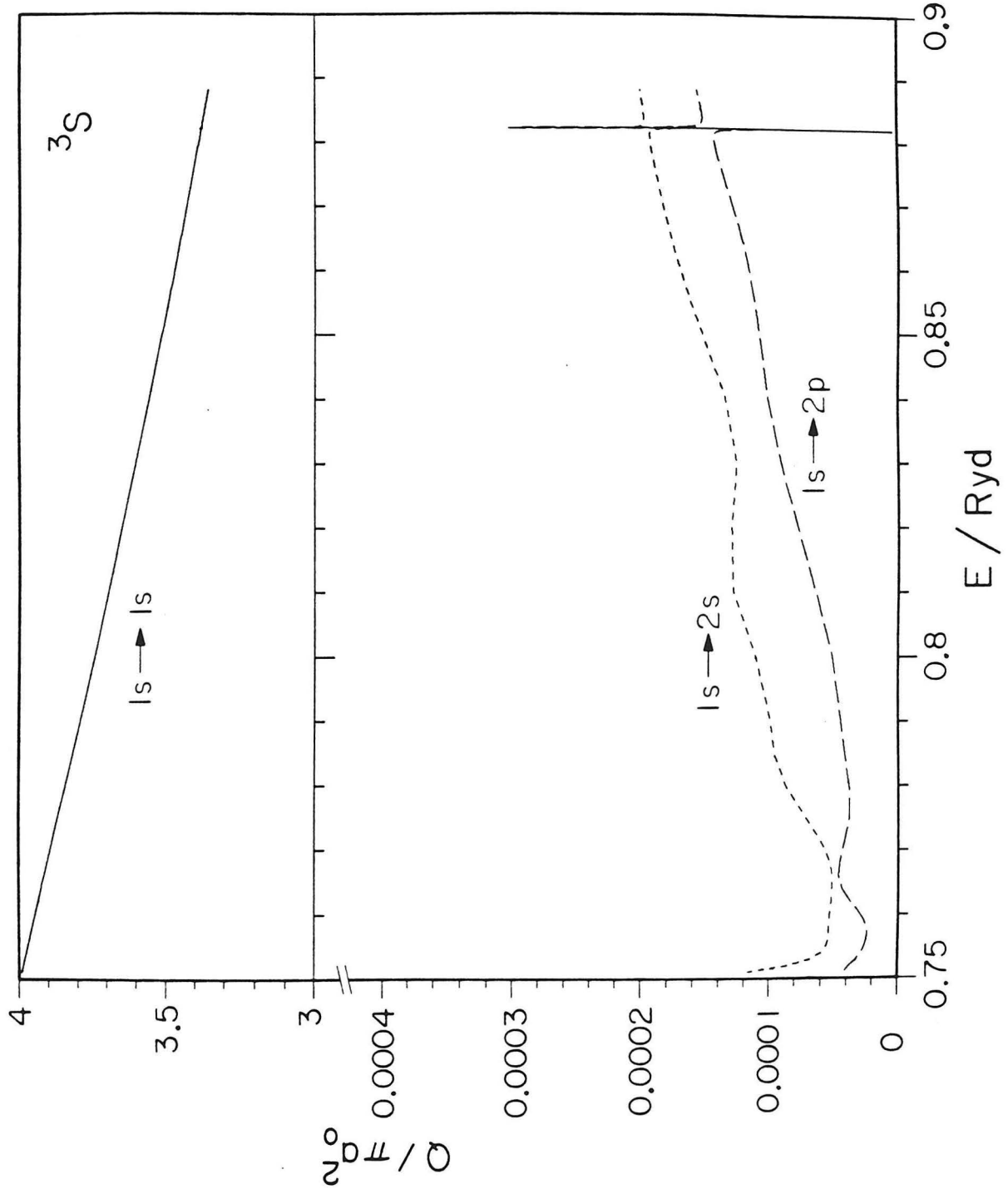
^3S
1s → 1s
1s → 2s
1s → 2p
$\Omega / \pi a_0^2$
E / Ryd
4
3.5
3
0.0004
0.0003
0.0002
0.0001
0
0.75
0.8
0.85
0.9

Figure 6.5

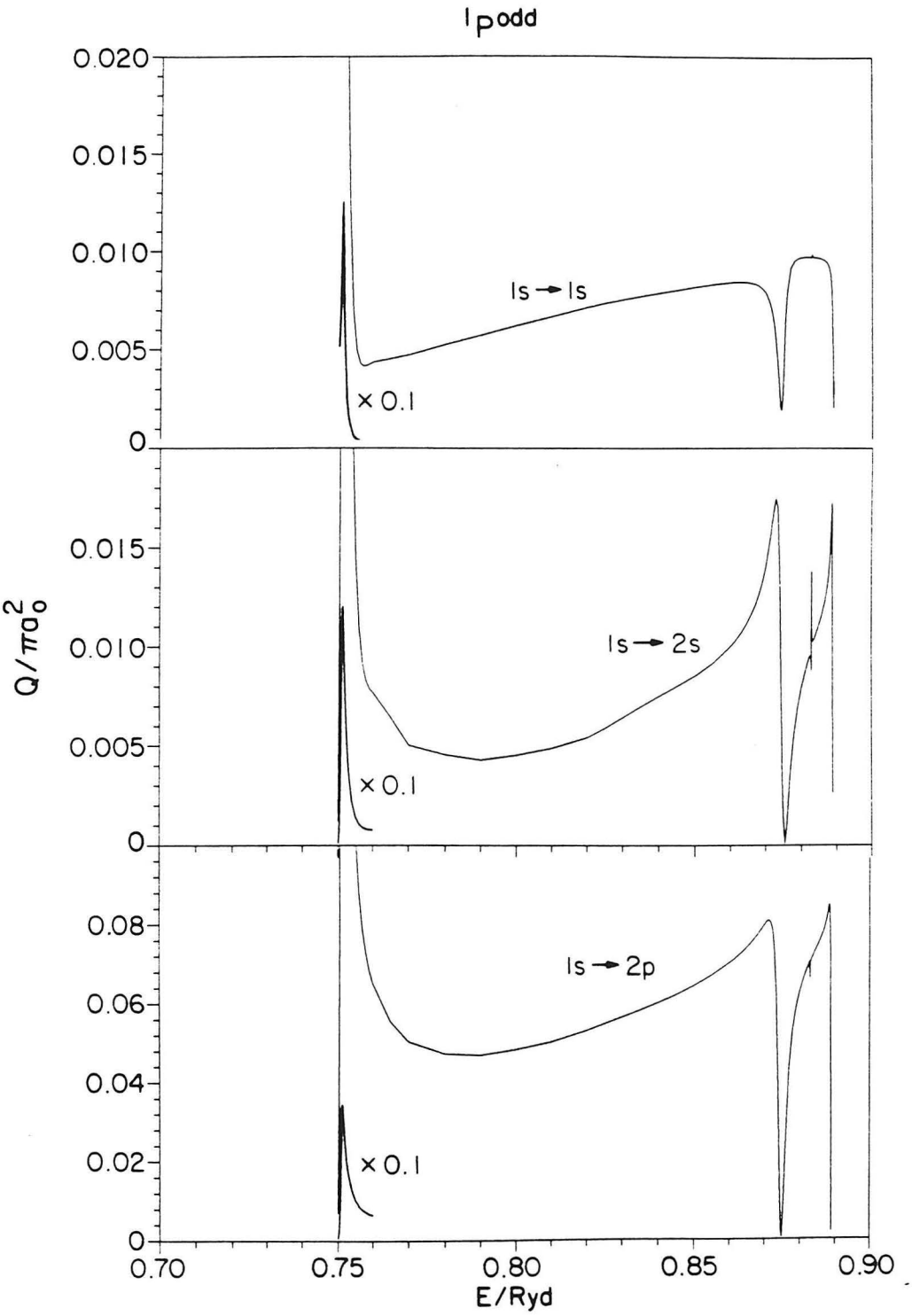
1p odd
0.020
0.015
0.010
0.005
0
1s → 1s
× 0.1
0.015
0.010
0.005
0
1s → 2s
× 0.1
0.08
0.06
0.04
0.02
0
1s → 2p
× 0.1
Q/πa₀²
0.70
0.75
0.80
0.85
0.90
E/Ryd

Figure 6.6

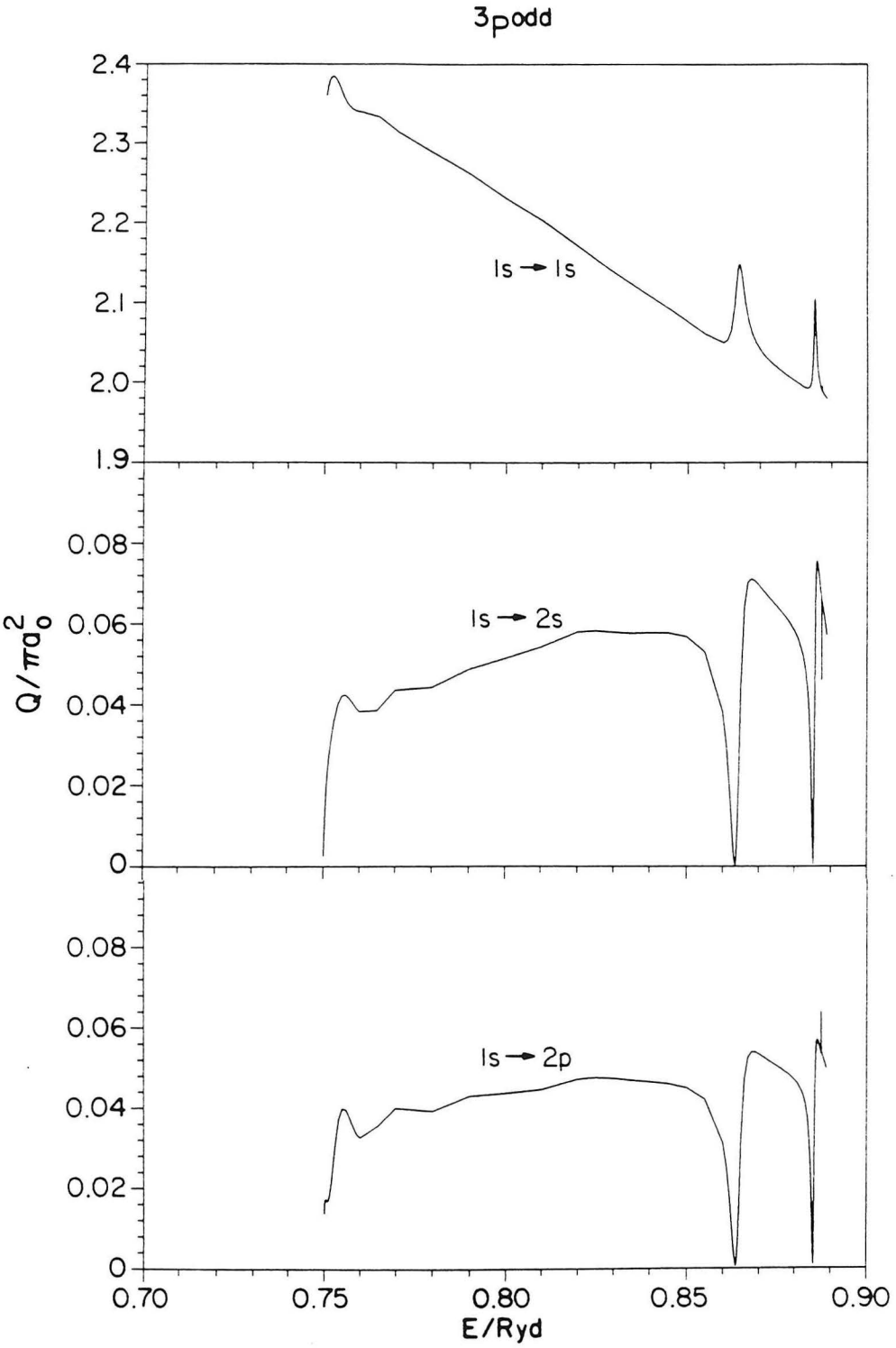
3podd
2.4
2.3
2.2
2.1
2.0
1.9
1s → 1s
0.08
0.06
0.04
0.02
0
1s → 2s
0.08
0.06
0.04
0.02
0
1s → 2p
0.70
0.75
0.80
0.85
0.90
E/Ryd
Q/πa₀²

Figure 6.7

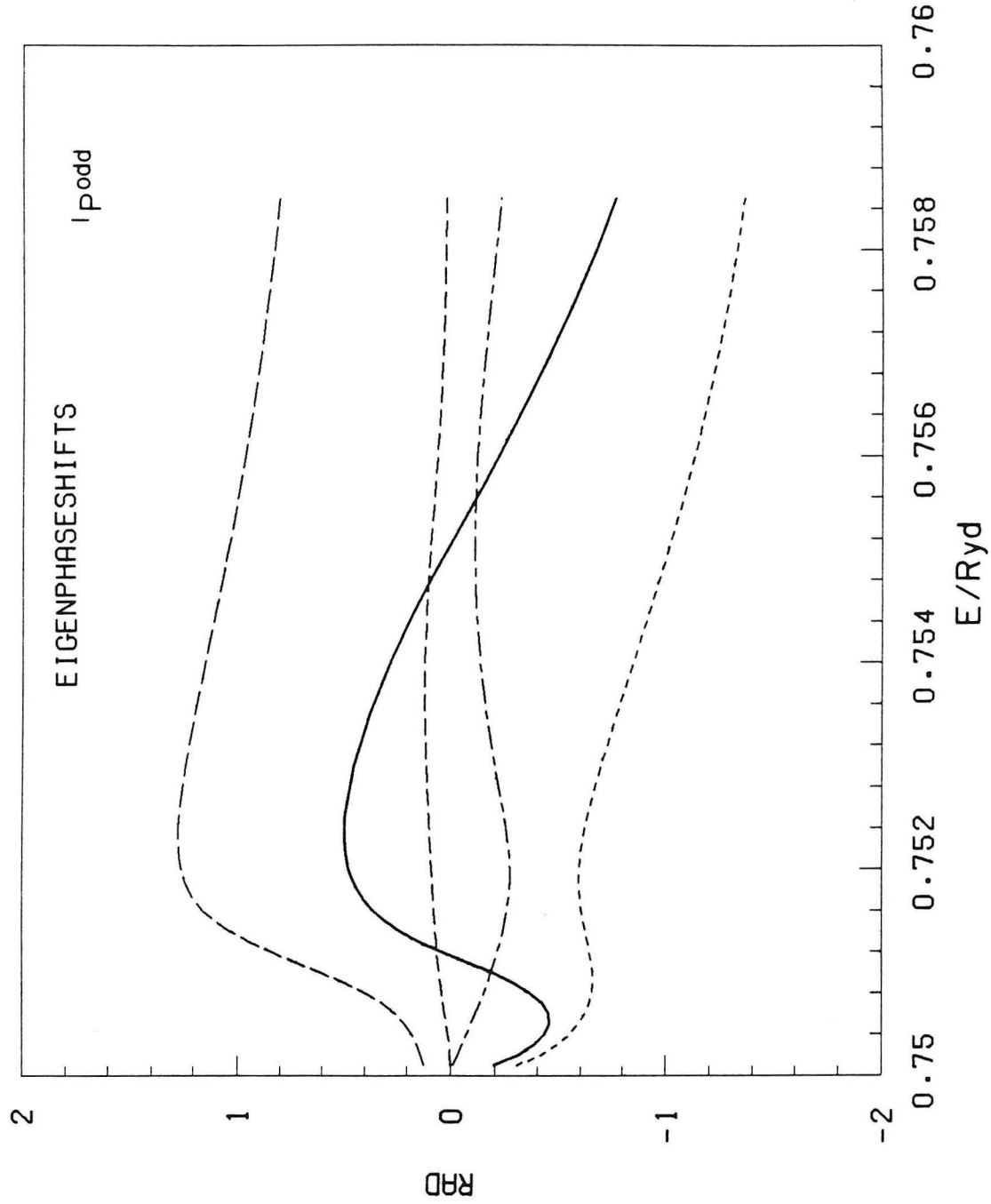
EIGENPHASESHIFTS
lpodd
RAD
2
1
0
-1
-2
0.75
0.752
0.754
0.756
0.758
0.76
E/Ryd

Figure 6.8

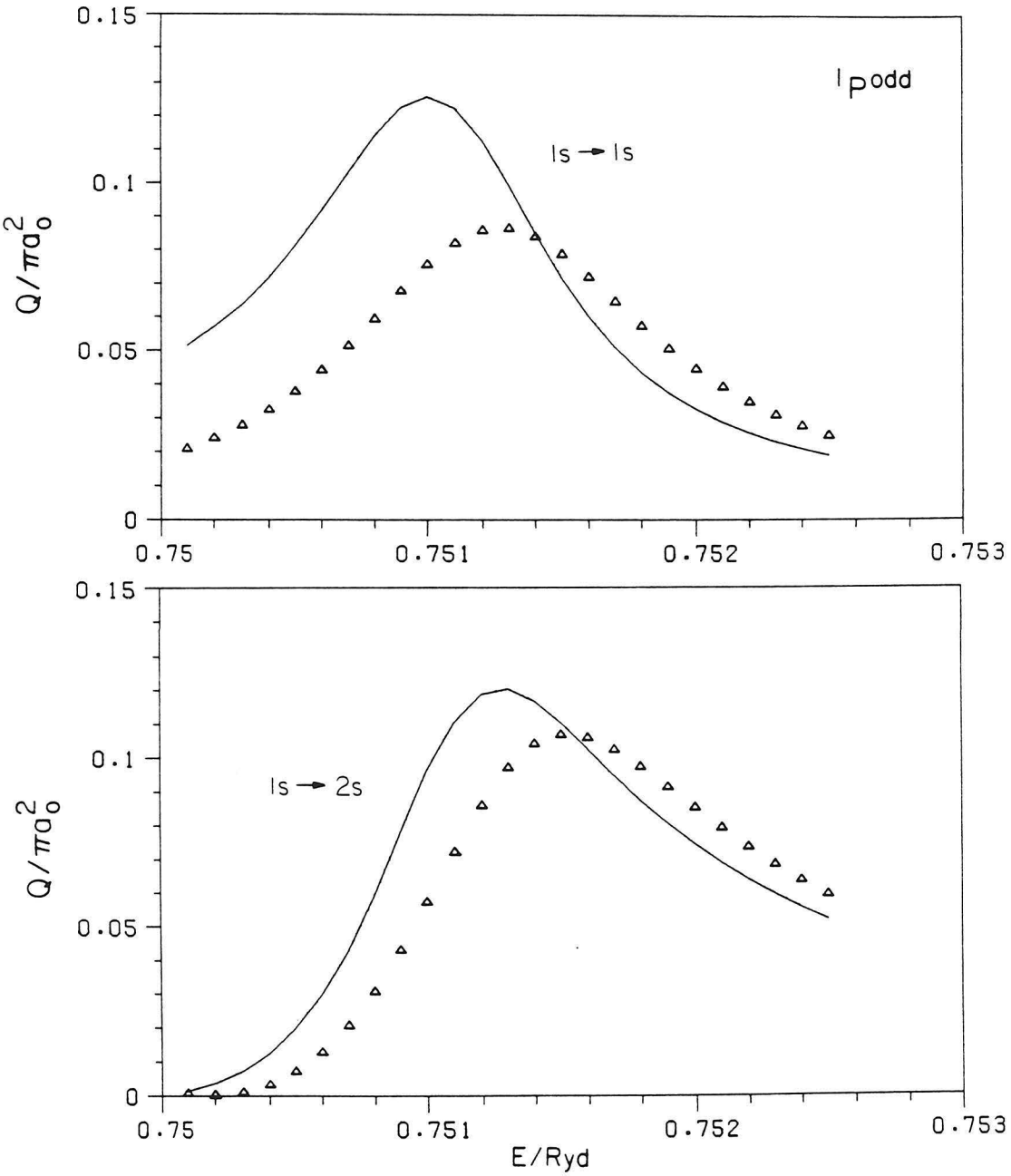
0.15
0.1
0.05
0
$Q/\pi a_o^2$
$^1P^{odd}$
$1s \rightarrow 1s$
0.75
0.751
0.752
0.753
0.15
0.1
0.05
0
$Q/\pi a_o^2$
$1s \rightarrow 2s$
0.75
0.751
0.752
0.753
E/Ryd

Figure 6.9a

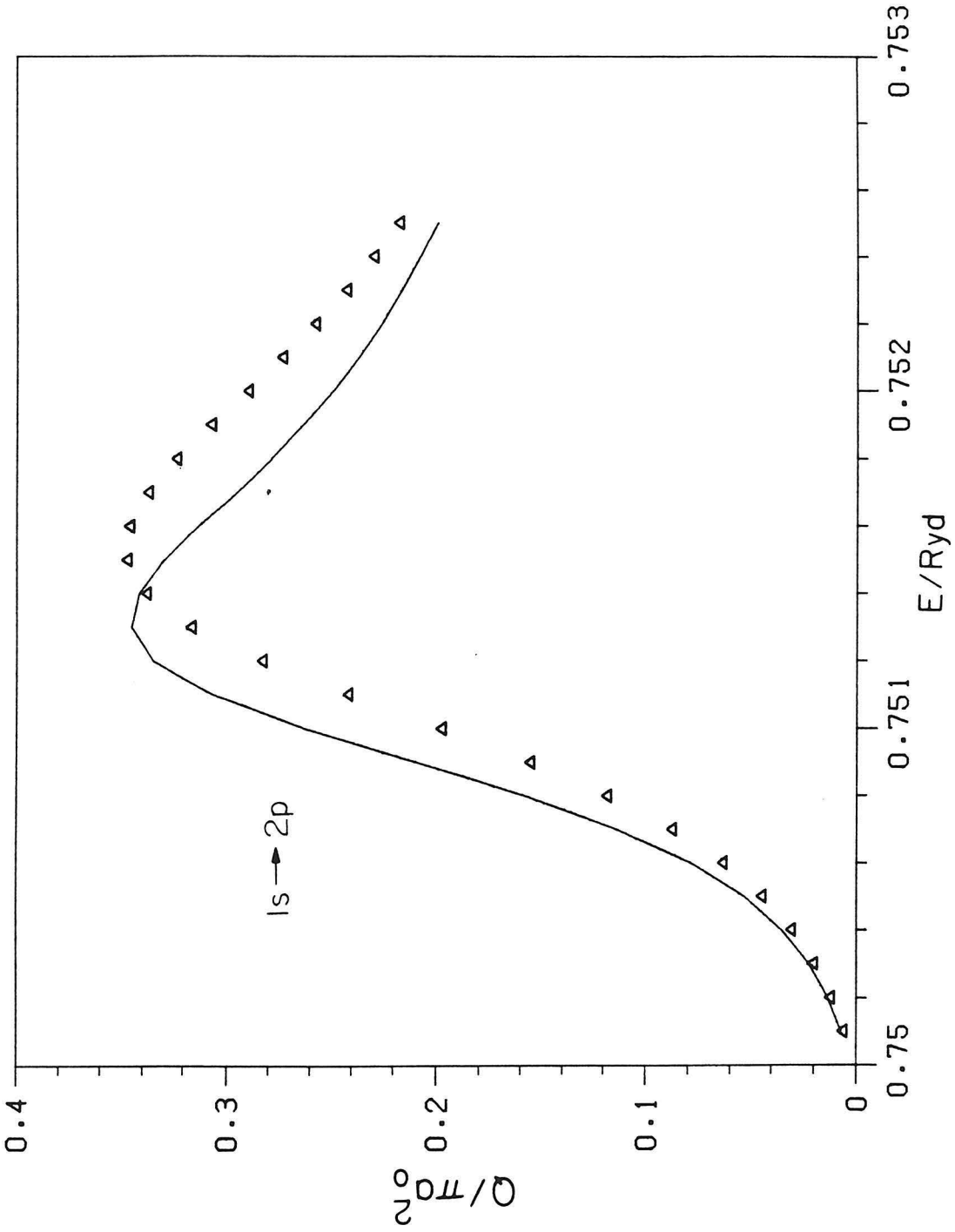

Figure 6.9b

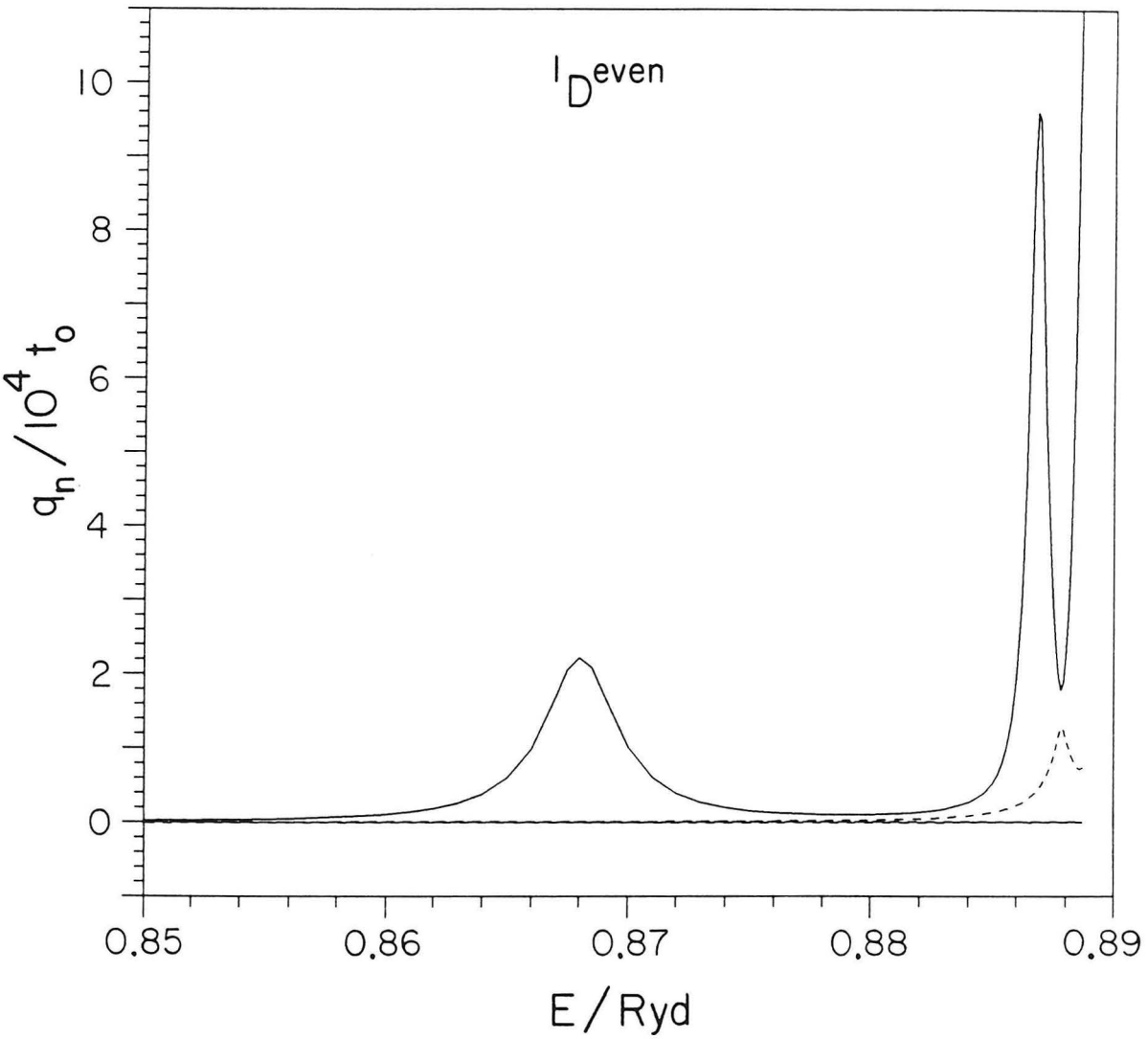

Figure 6.10

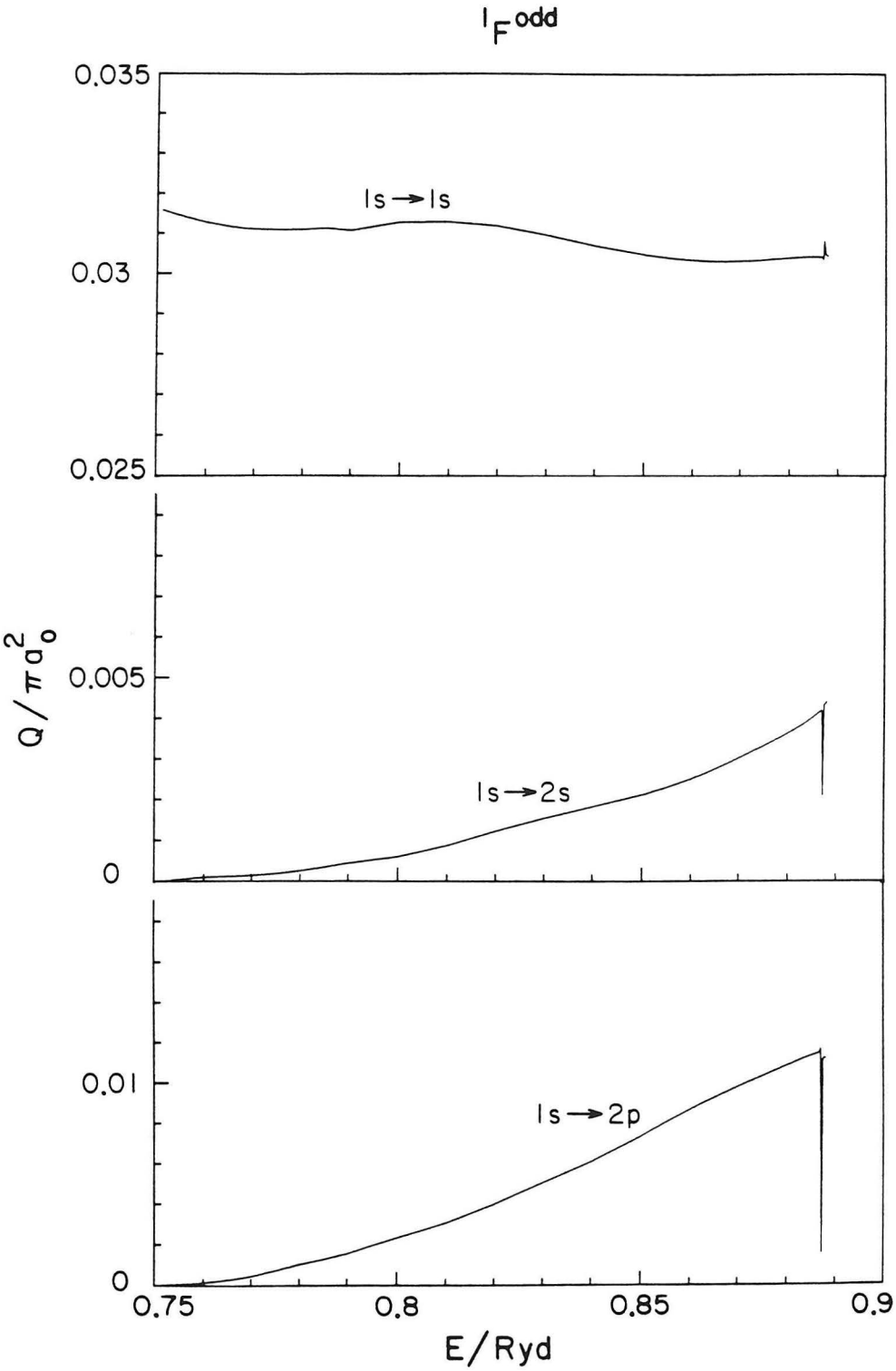
l_F^{odd}
0.035
0.03
0.025
1s → 1s
0.005
0
1s → 2s
0.01
0
1s → 2p
$Q/\pi a_o^2$
0.75
0.8
0.85
0.9
E/Ryd

Figure 6.11

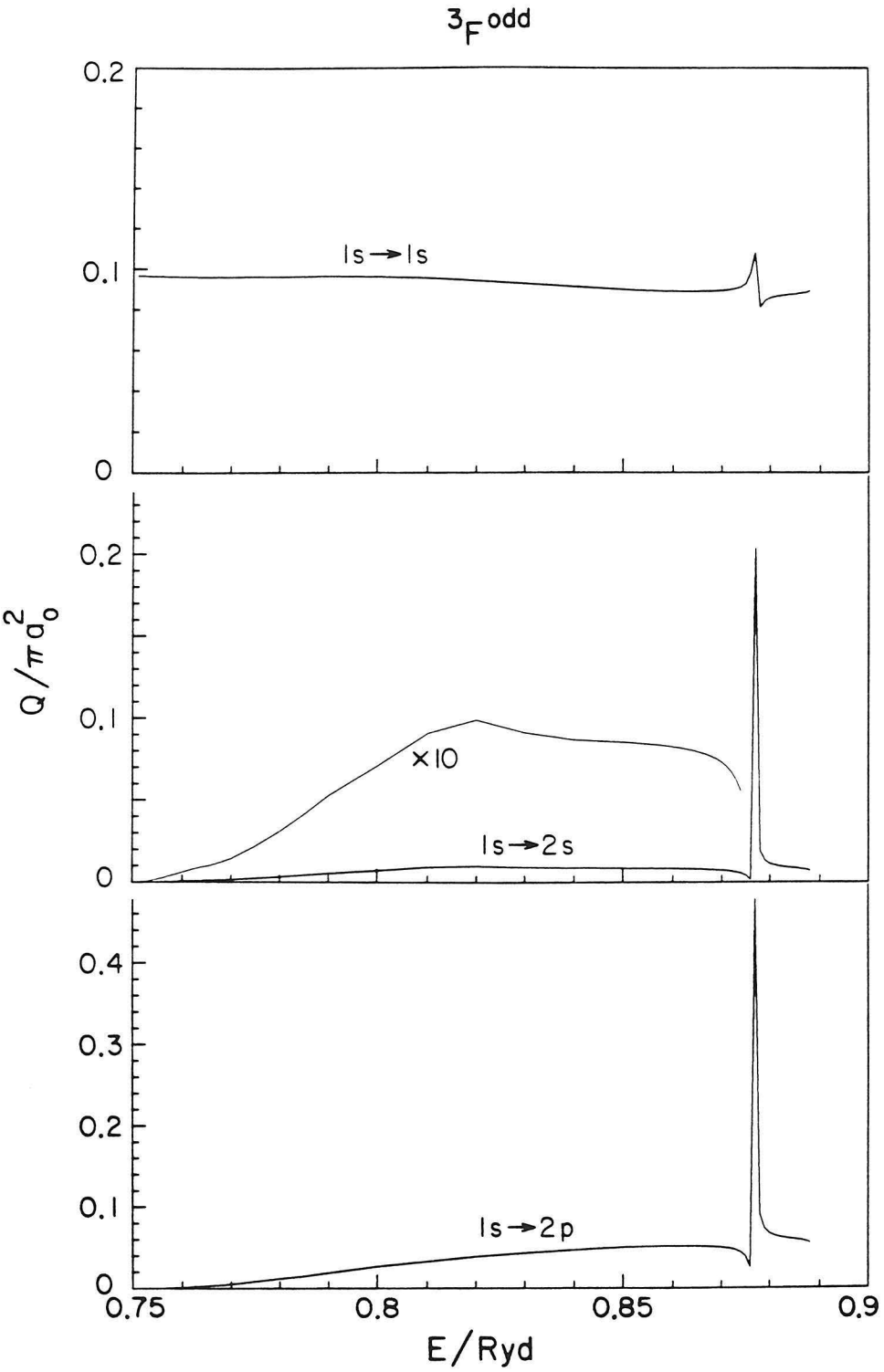
^3_Fodd
0.2
0.1
0
1s→1s
0.2
0.1
0
×10
1s→2s
$Q/\pi a_0^2$
0.4
0.3
0.2
0.1
0
1s→2p
0.75
0.8
0.85
0.9
E/Ryd

Figure 6.12

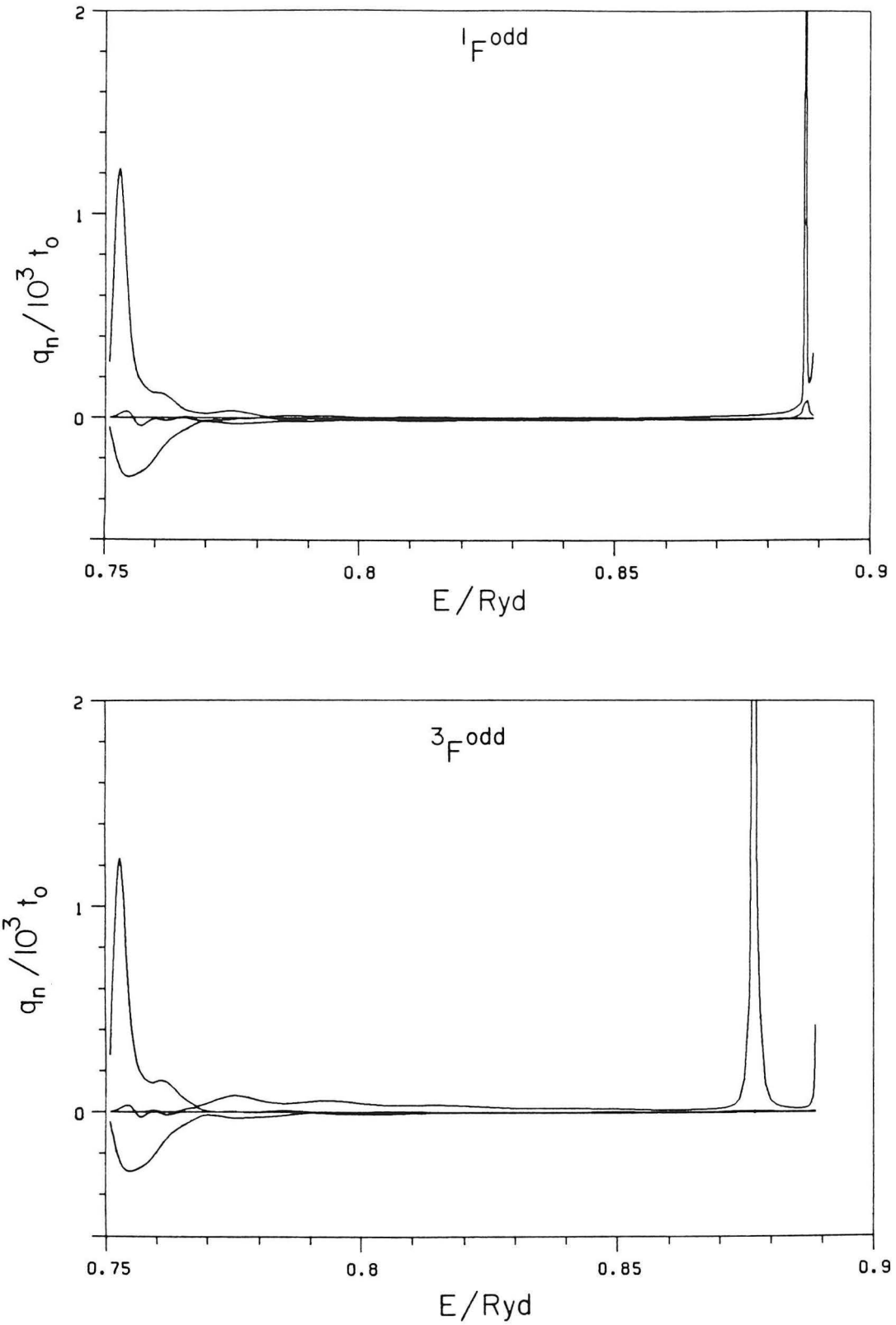
$^1F^{odd}$
$q_n / 10^3 t_o$
2
1
0
0.75
0.8
0.85
0.9
E / Ryd
$^3F^{odd}$
$q_n / 10^3 t_o$
2
1
0
0.75
0.8
0.85
0.9
E / Ryd

Figure 6.13

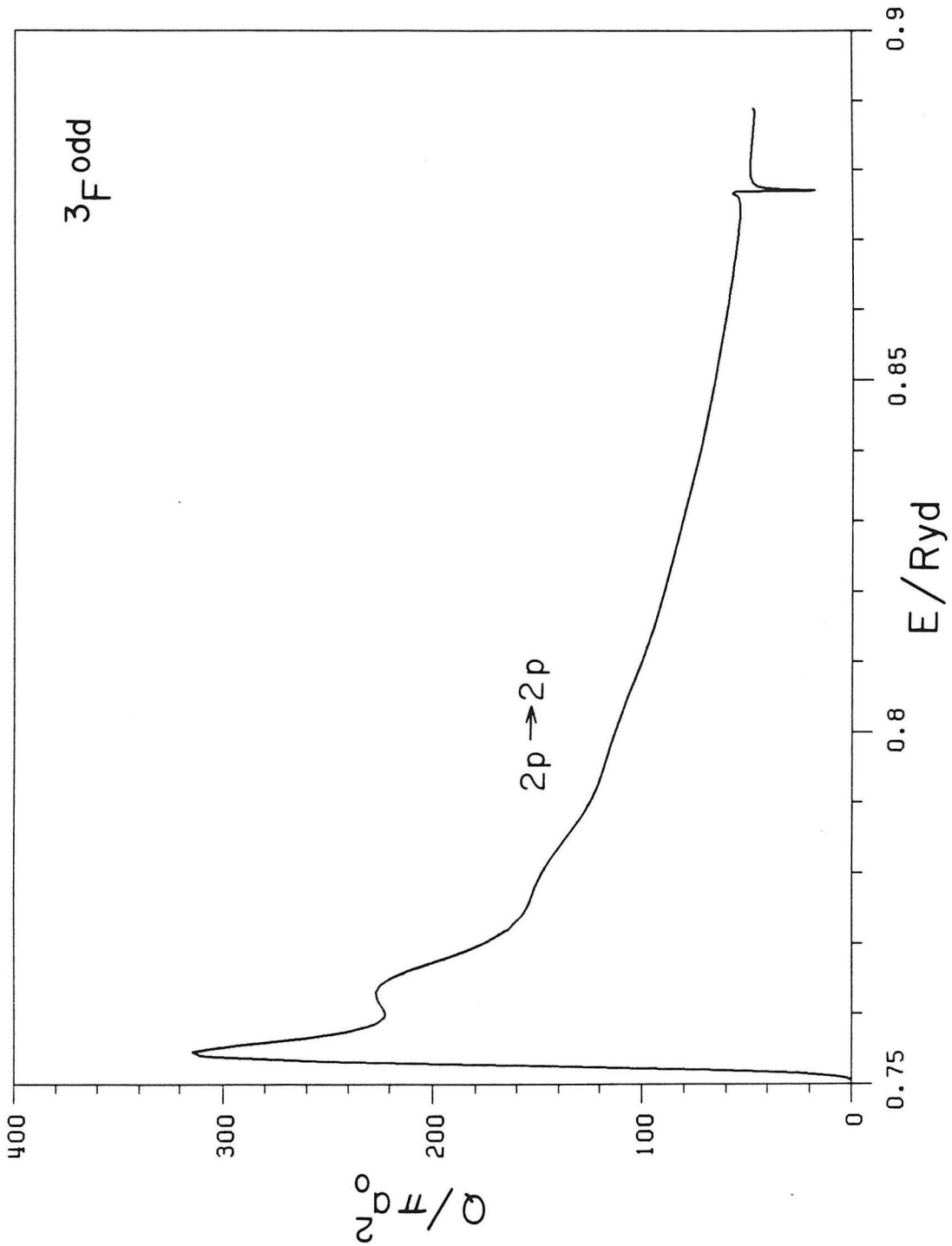
$^3F^{odd}$
$2p \rightarrow 2p$
$Q/\pi a_o^2$
E/Ryd
0
100
200
300
400
0.75
0.8
0.85
0.9

Figure 6.14

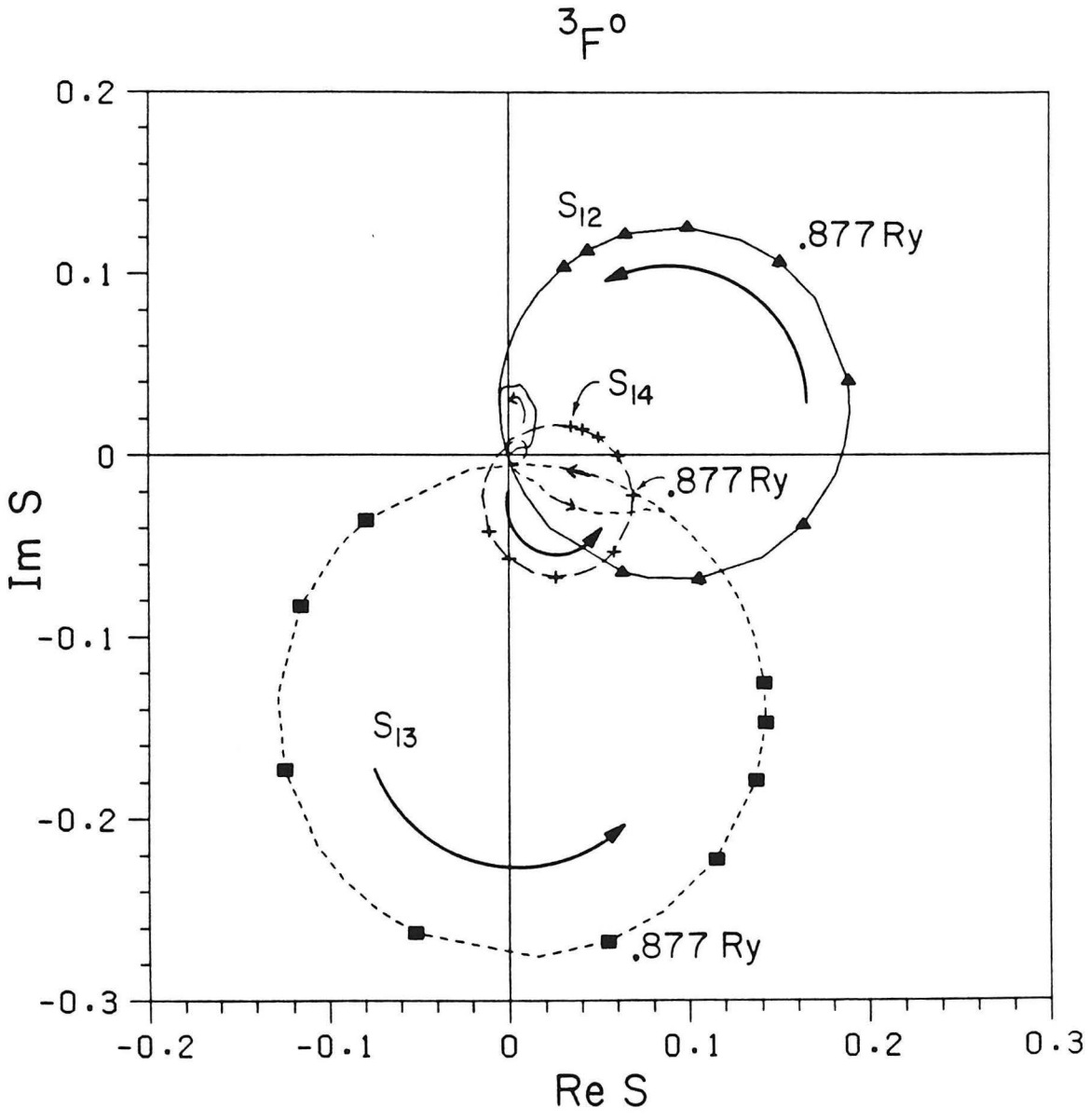
$^3F^o$
0.2
0.1
0
-0.1
-0.2
-0.3
Im S
-0.2
-0.1
0
0.1
0.2
0.3
Re S
S_{12}
.877 Ry
S_{14}
.877 Ry
S_{13}
.877 Ry

Figure 6.15a

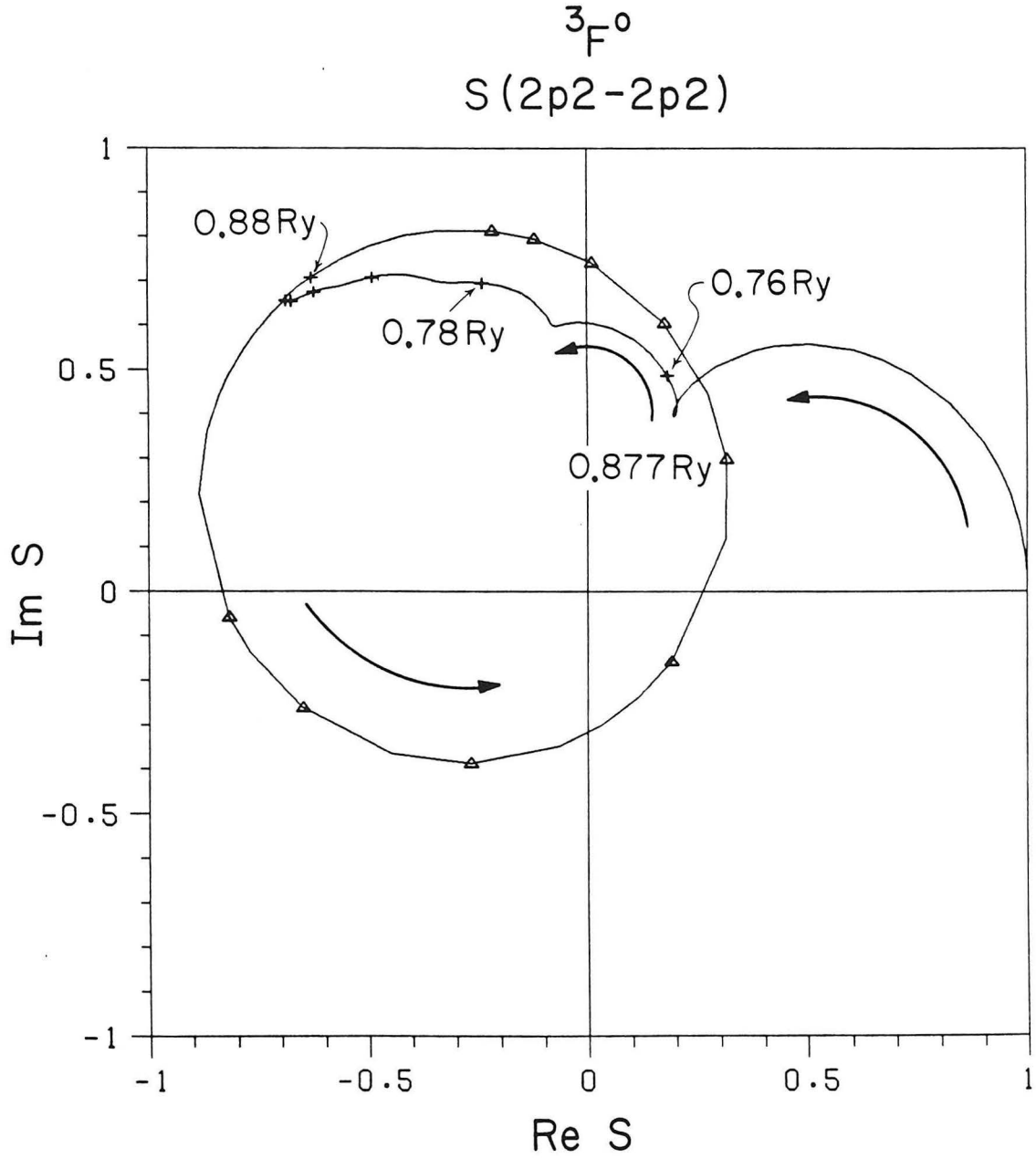
$^3F^o$
S(2p2-2p2)
0.88Ry
0.78Ry
0.76Ry
0.877Ry
Im S
Re S
1
0.5
0
-0.5
-1
-1
-0.5
0
0.5
1

Figure 6.15b

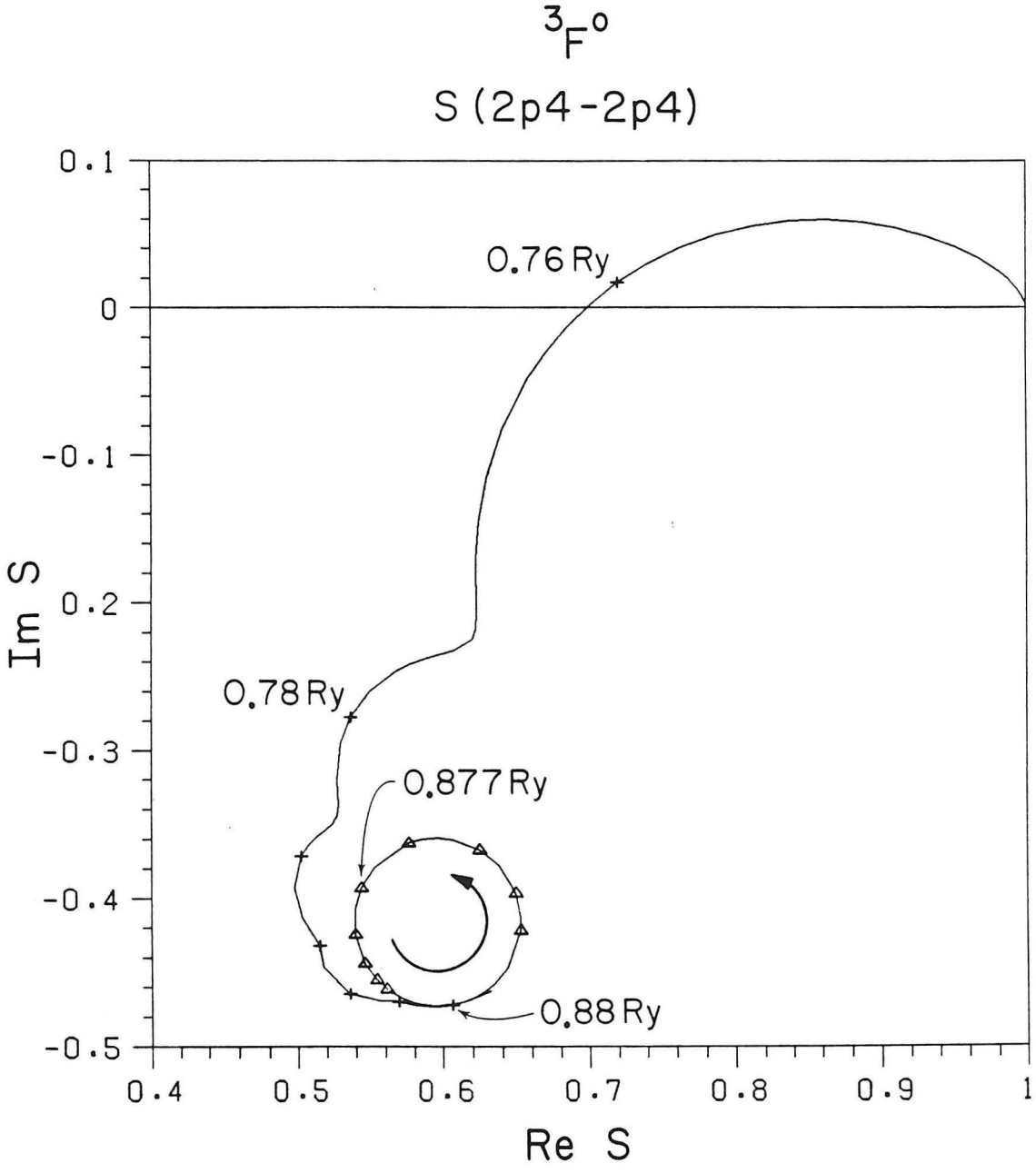
$^3F^o$
S (2p4 - 2p4)
0.1
0
-0.1
-0.2
-0.3
-0.4
-0.5
Im S
0.76 Ry
0.78 Ry
0.877 Ry
0.88 Ry
0.4
0.5
0.6
0.7
0.8
0.9
1
Re S

Figure 6.15c

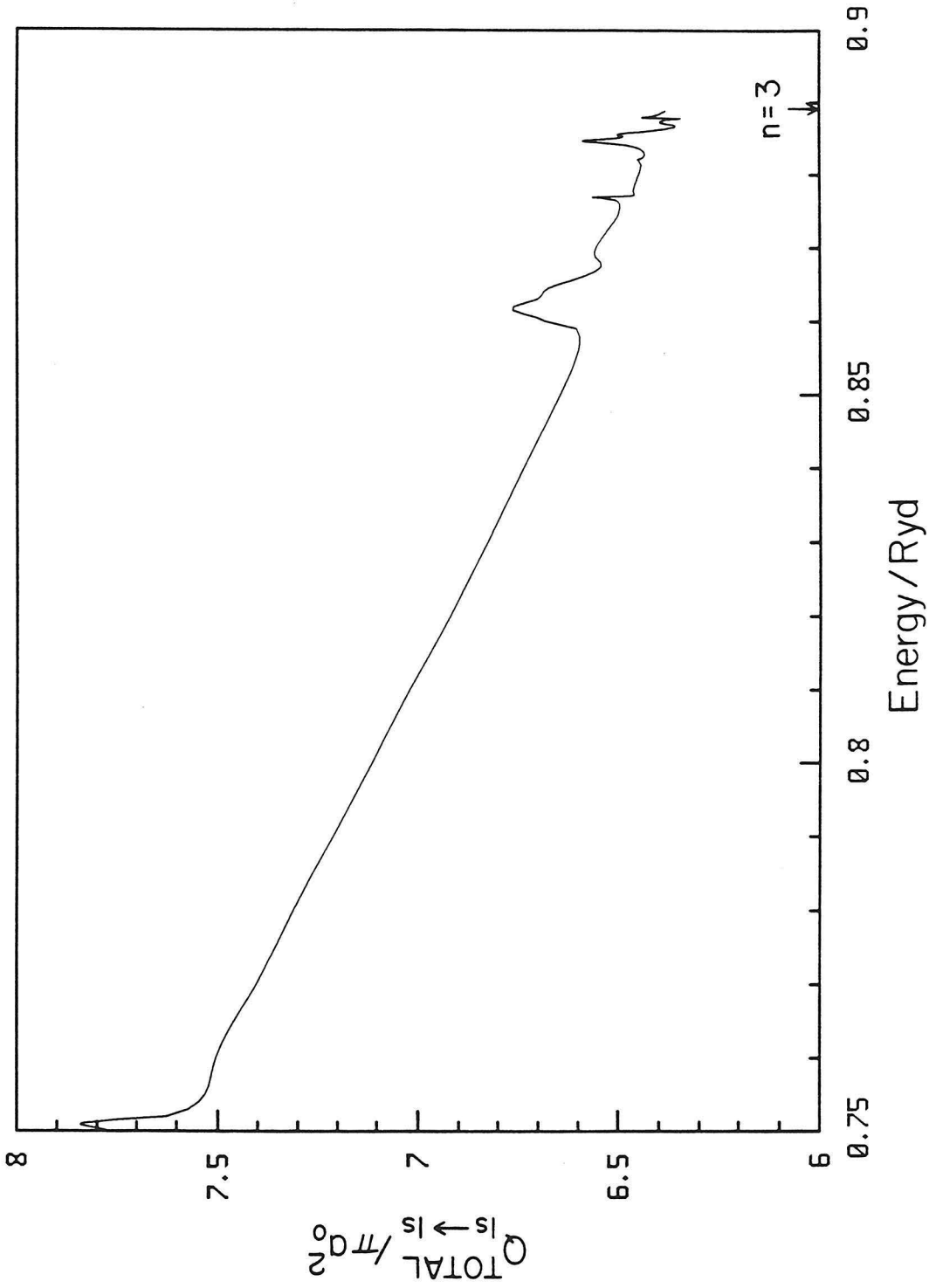
8
7.5
7
6.5
6
0.75
0.8
0.85
0.9
n=3
Energy/Ryd
$Q_{TOTAL}^{1s \rightarrow 1s} / \pi a_o^2$

Figure 6.16

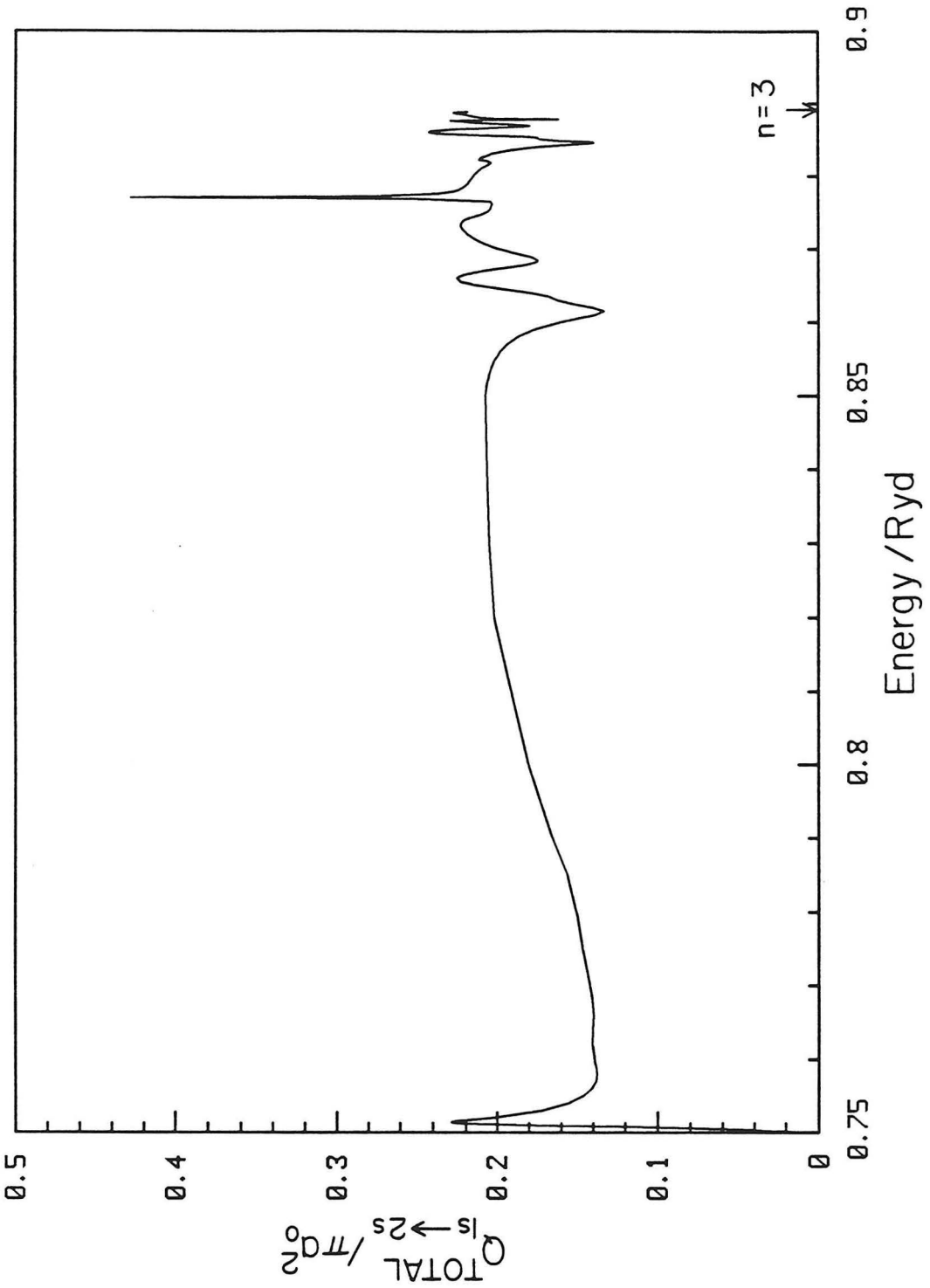
0.5
0.4
0.3
0.2
0.1
0
0.75
0.8
0.85
0.9
n=3
Energy /Ryd
Q_{TOTAL} $_{1s\rightarrow 2s}$ $/\pi a_o^2$

Figure 6.17a

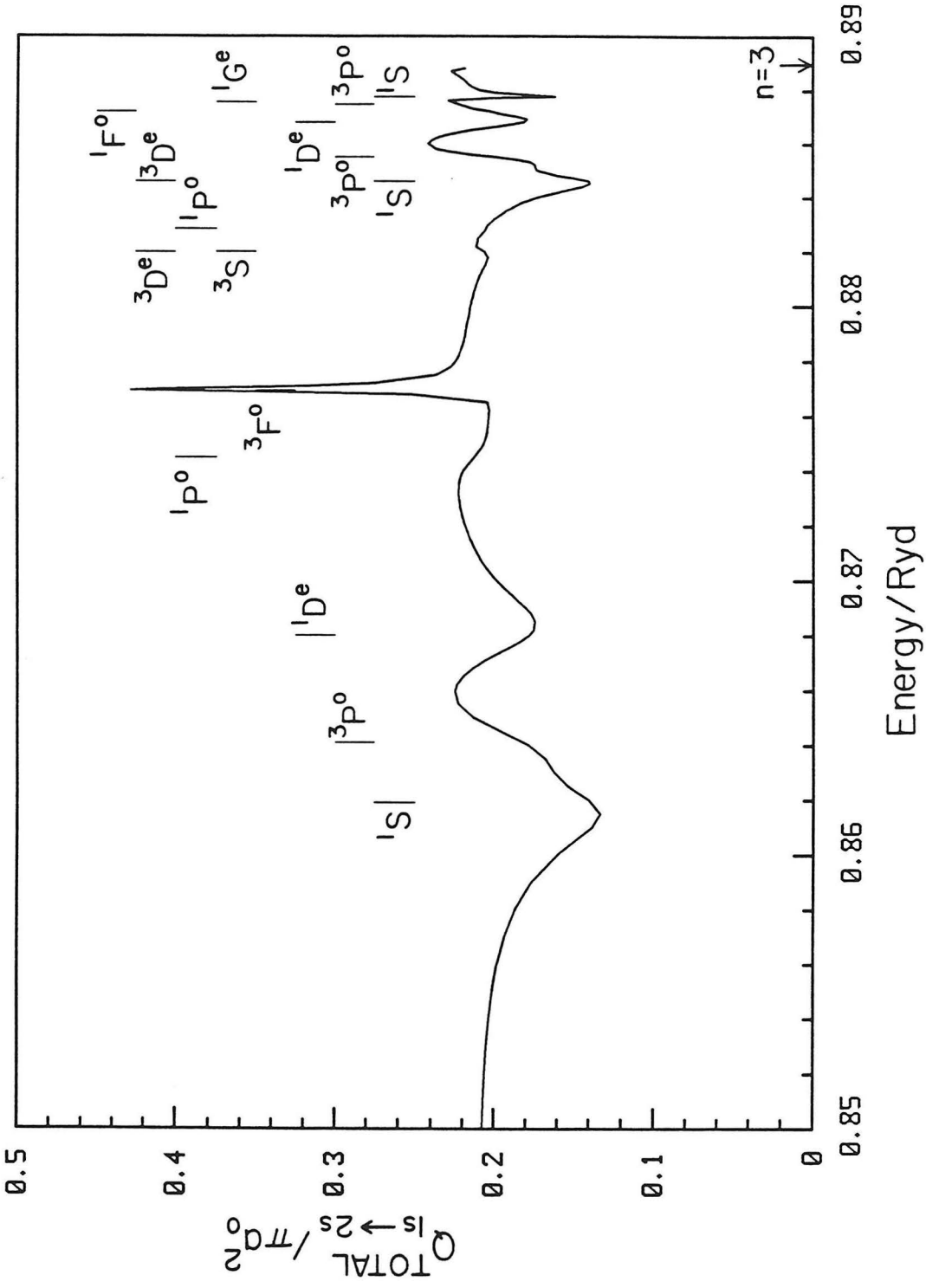
0.5
0.4
0.3
0.2
0.1
0
0.85
0.86
0.87
0.88
0.89
Energy/Ryd
n=3
^1S
$^3P^o$
$^1D^e$
$^1P^o$
$^3F^o$
$^1P^o$
^3S
$^3D^e$
$^1P^o$
$^3D^e$
$^1F^o$
^1S
$^3P^o$
$^1D^e$
$^3P^o$
$^1G^e$
$Q_{TOTAL}/\pi a_o^2$
$1s \rightarrow 2s$

Figure 6.17b

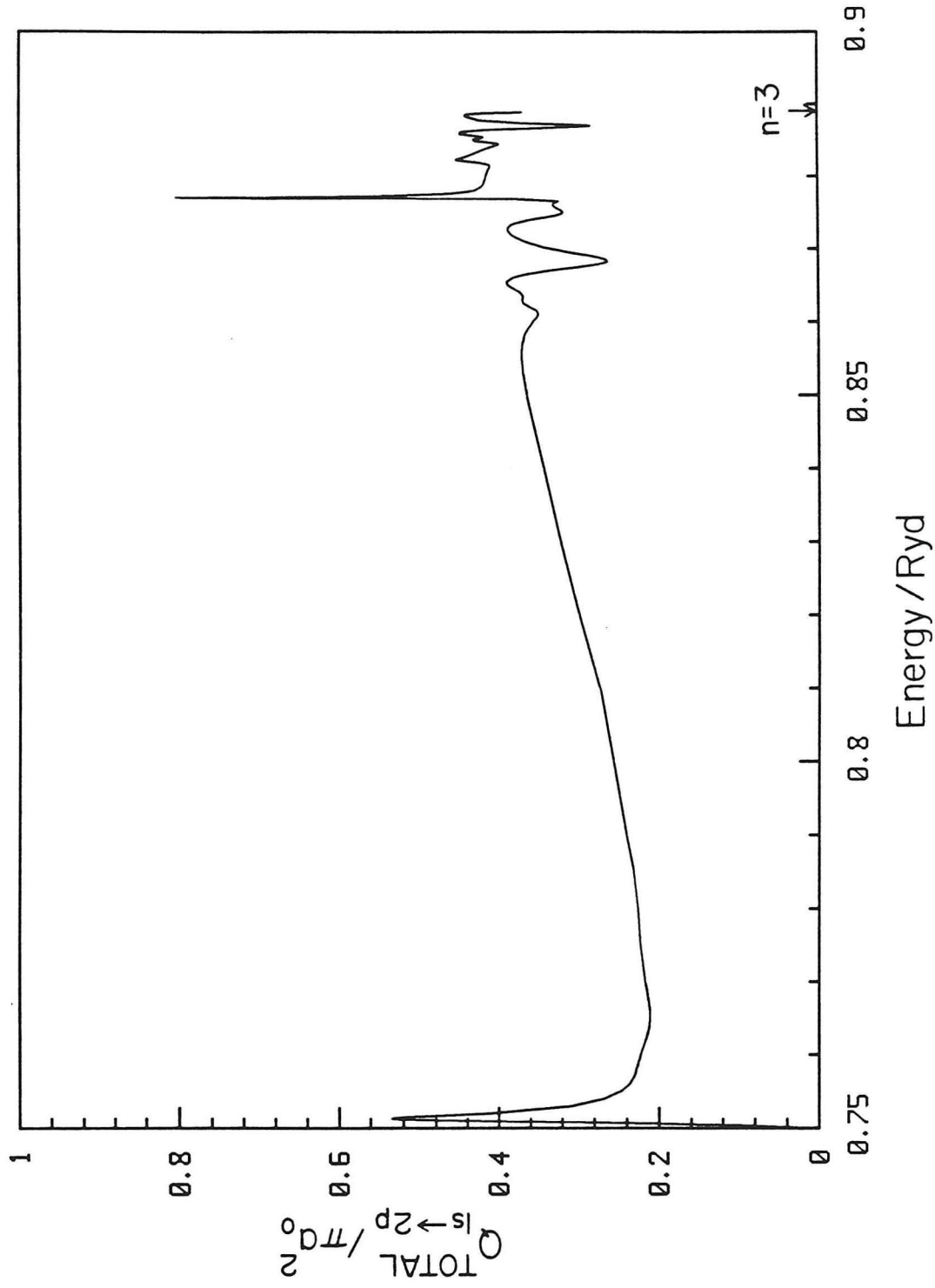
n=3
0.75
0.8
0.85
0.9
Energy / Ryd
0
0.2
0.4
0.6
0.8
1
Q_{TOTAL} / πa_o^2
$Q_{1s \rightarrow 2p}$ / πa_o^2

Figure 6.17c

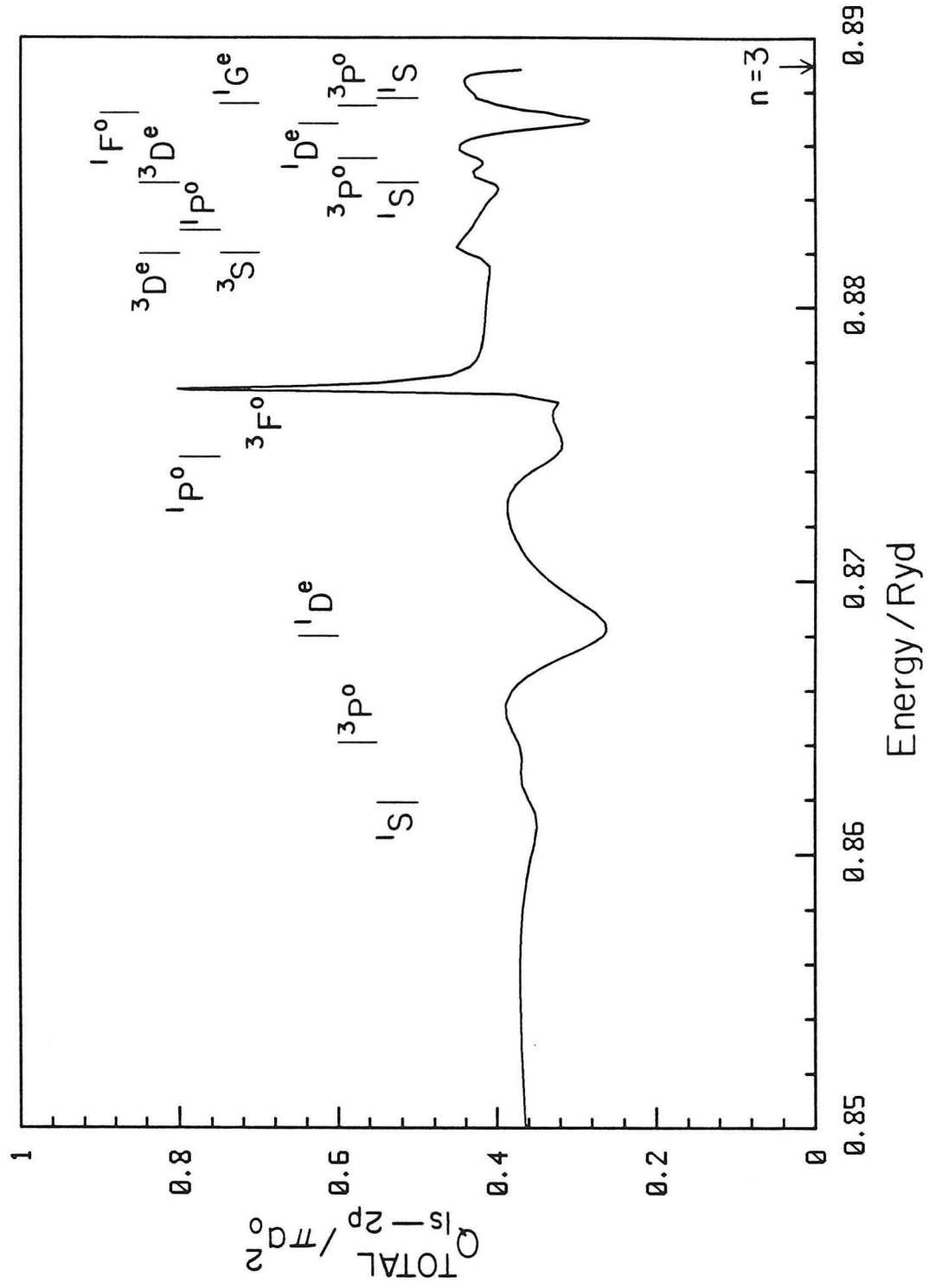
$^1F^o$
$^3D^e$
$^3D^e$
$^1P^o$
$^1G^e$
^3S
$^1D^e$
$^3P^o$
^1S
$^3P^o$
^1S
n=3
$^1P^o$
$^3F^o$
$^1D^e$
$^3P^o$
^1S
1
0.8
0.6
0.4
0.2
0
0.85
0.86
0.87
0.88
0.89
Energy / Ryd
Q_{TOTAL} / πa_o^2
Q_{1s-2p} / πa_o^2

Figure 6.17d

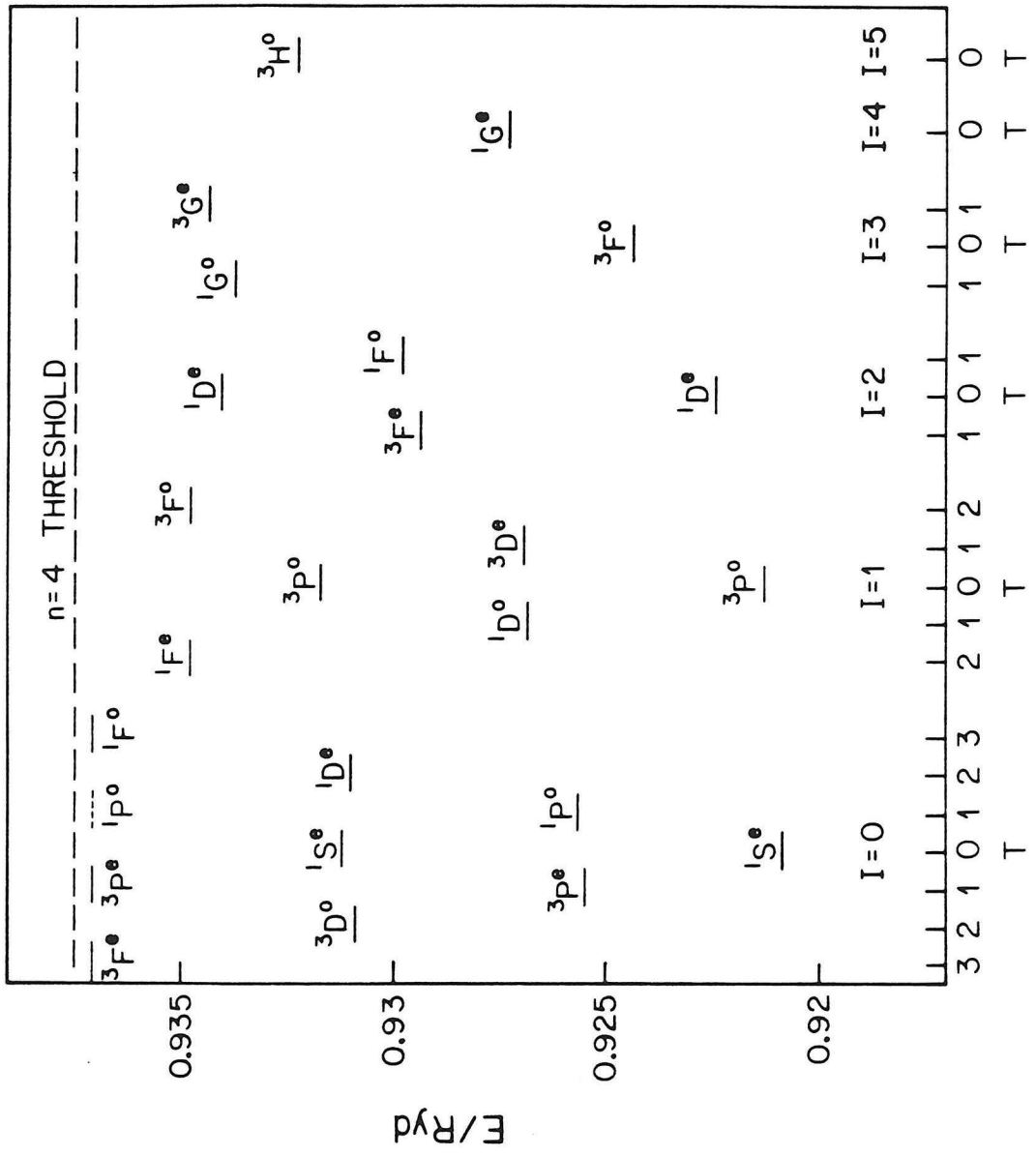
n=4 THRESHOLD
E/Ryd
0.935
0.93
0.925
0.92
I=0
I=1
I=2
I=3
I=4
I=5
T
3 2 1 0 1 2 3
2 1 0 1 2
1 0 1
1 0 1
0 0

Figure 6.18a

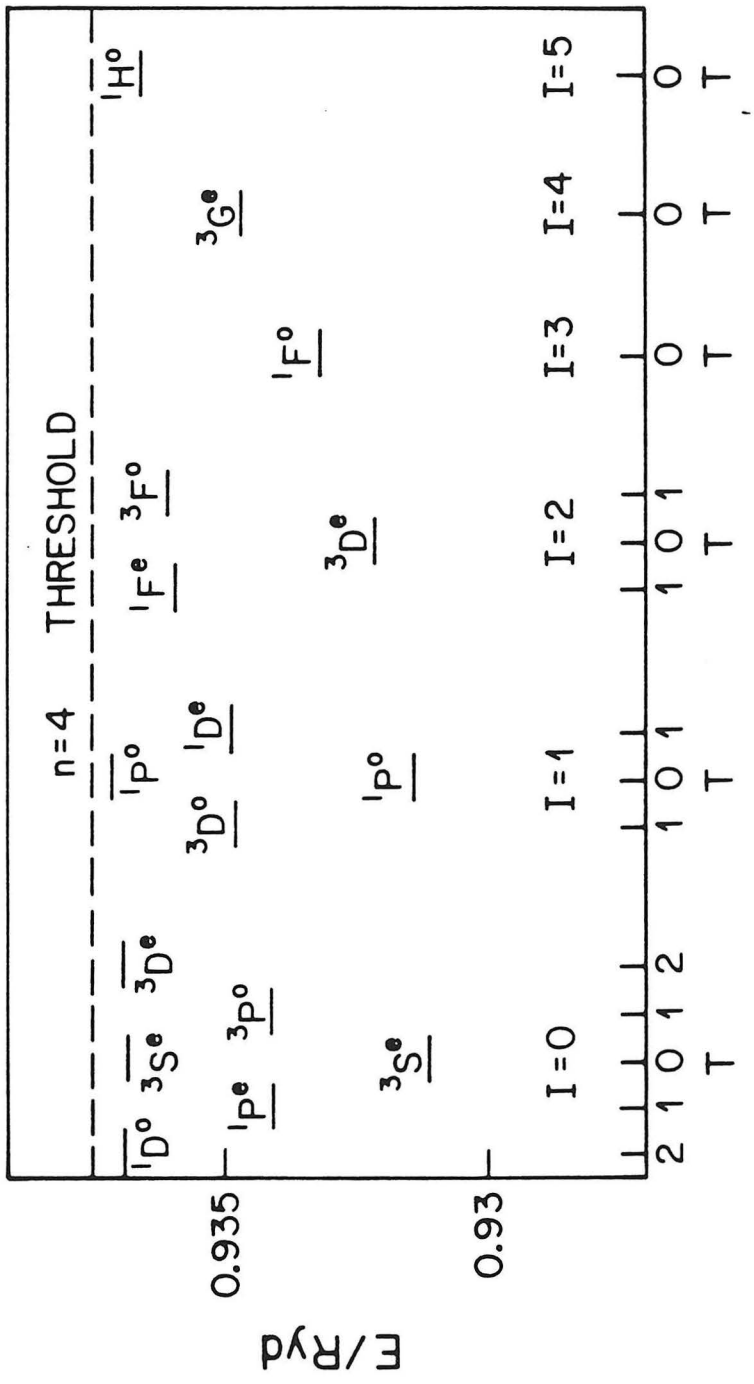
E/Ryd
0.935
0.93
n=4 THRESHOLD
$^1H^o$
$^3G^e$
$^1F^o$
$^1F^e$ $^3F^o$
$^3D^e$
$^1P^o$
$^3D^o$ $^1D^e$
$^1D^o$ $^3S^e$ $^3D^e$
$^1P^e$ $^3P^o$
$^3S^e$
I=0 I=1 I=2 I=3 I=4 I=5
2 1 0 1 2 1 0 1 1 0 1 0 0
T T T T T T

Figure 6.18b

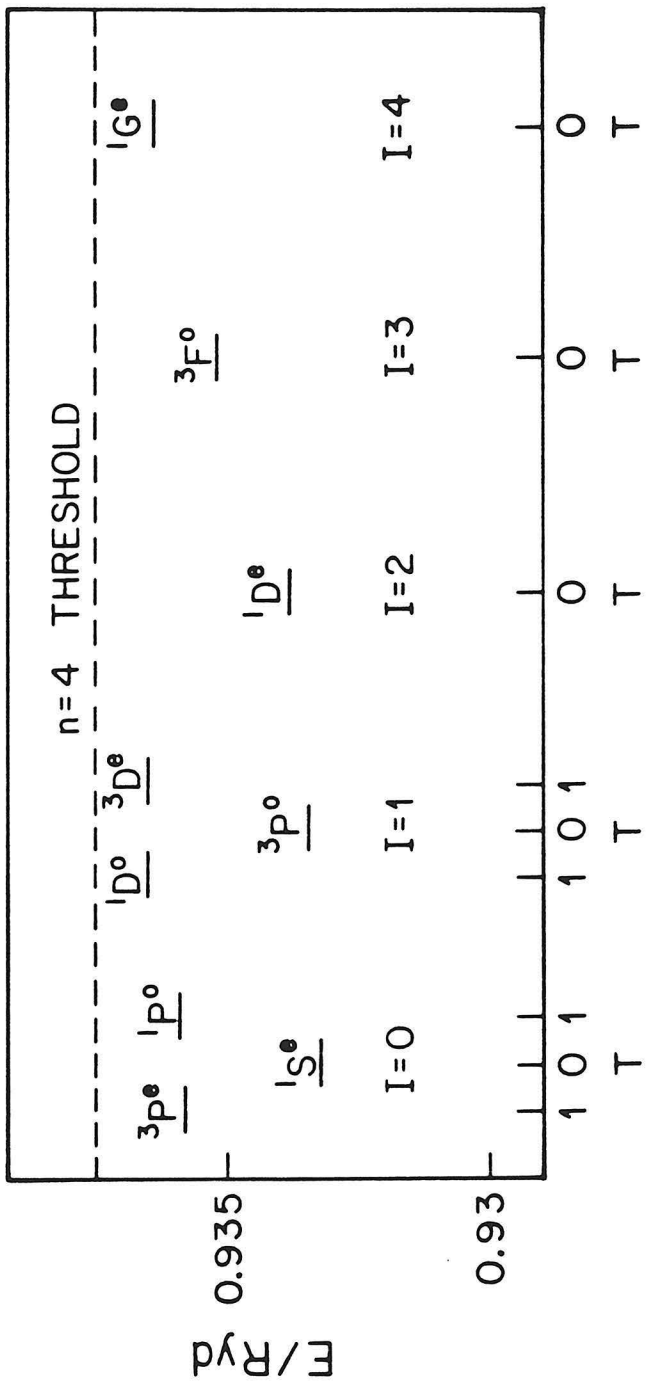
E/Ryd
0.935
0.93
n=4 THRESHOLD
$^3P^e$ $^1P^o$ $^1D^o$ $^3D^e$ $^1G^e$
$^3F^o$
$^1S^e$ $^3P^o$ $^1D^e$
I=0 I=1 I=2 I=3 I=4
1 0 1 1 0 1 0 0
T T T T T

Figure 6.18c

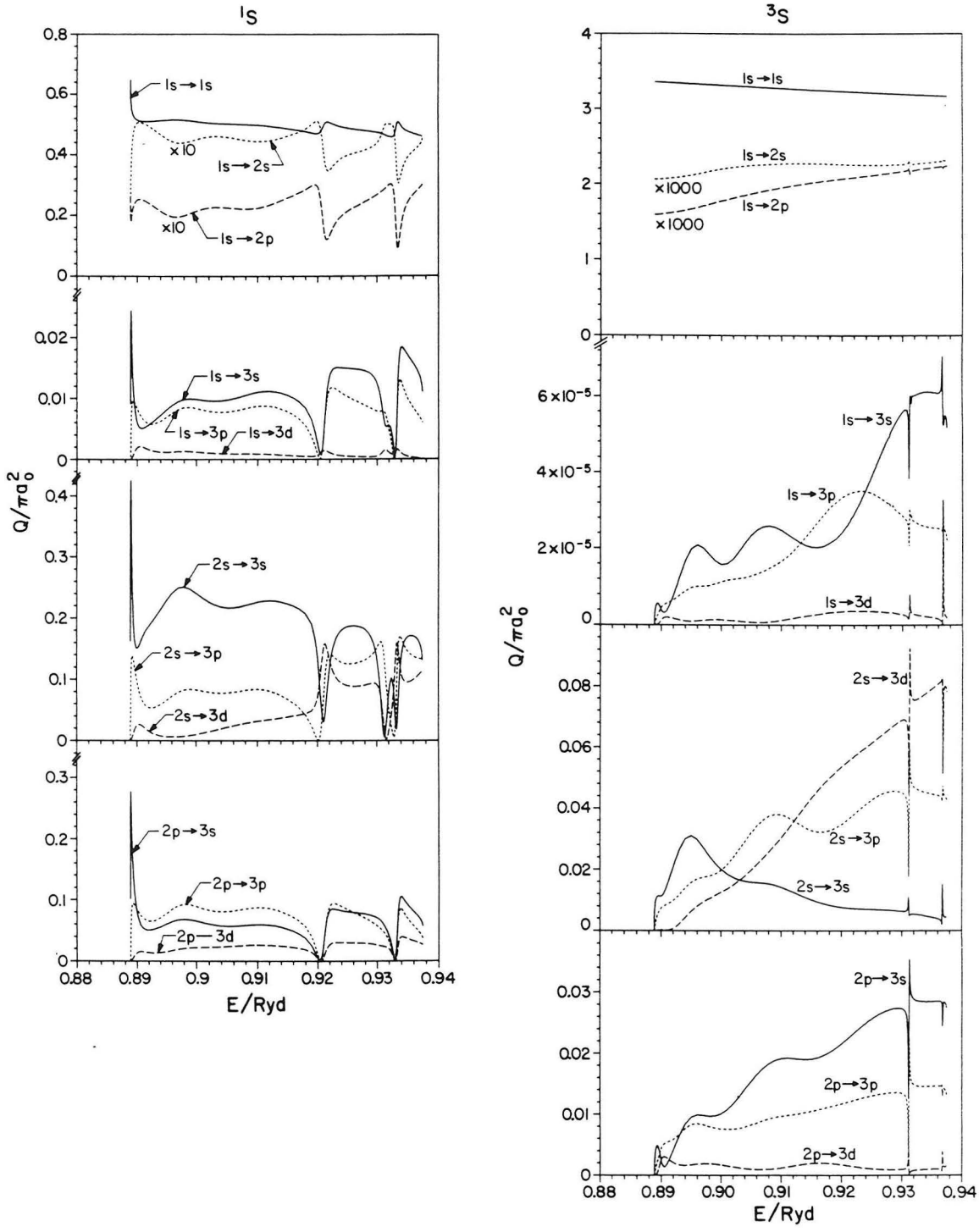
^1S
^3S
$Q/\pi a_0^2$
E/Ryd
1s→1s
×10
1s→2s
×10
1s→2p
1s→3s
1s→3p
1s→3d
2s→3s
2s→3p
2s→3d
2p→3s
2p→3p
2p→3d
×1000
×1000
0.88
0.89
0.9
0.91
0.92
0.93
0.94

Figure 6.19

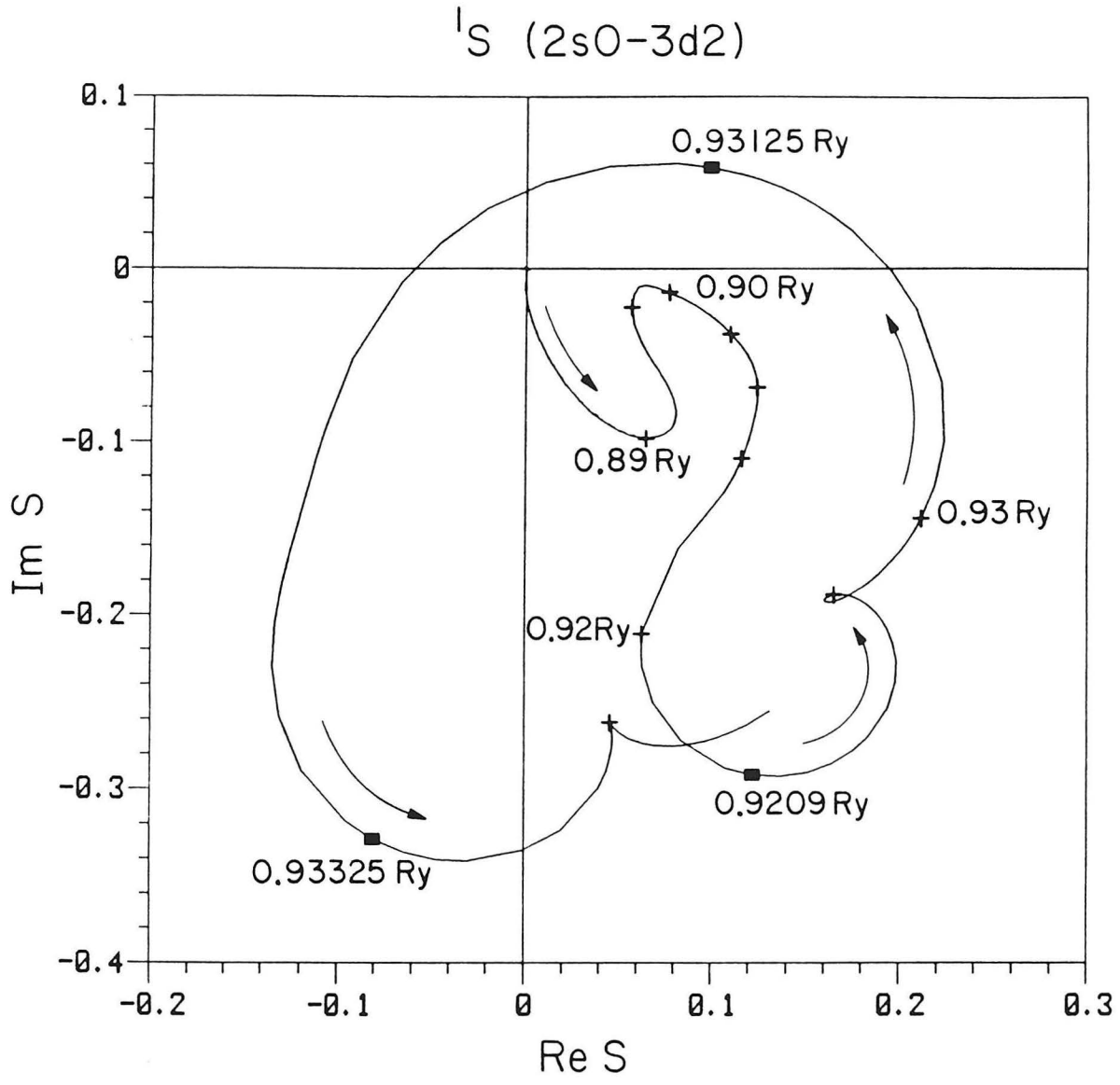
^1S (2s0-3d2)
0.93125 Ry
0.90 Ry
0.89 Ry
0.93 Ry
0.92Ry
0.9209 Ry
0.93325 Ry
Im S
Re S
0.1
0
-0.1
-0.2
-0.3
-0.4
-0.2
-0.1
0
0.1
0.2
0.3

Figure 6.20

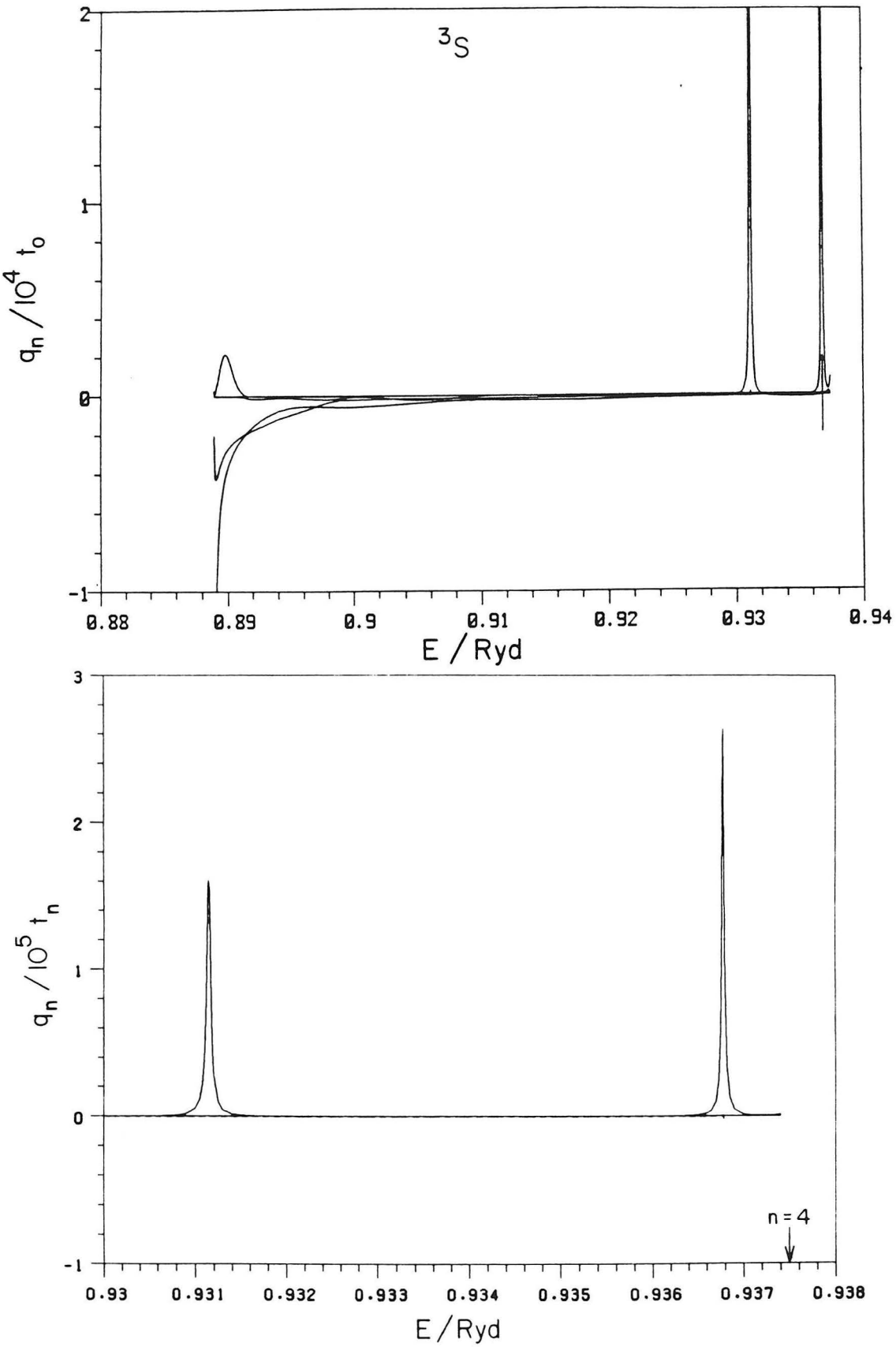
^3S
$q_n / 10^4 t_o$
2
1
0
-1
0.88
0.89
0.9
0.91
0.92
0.93
0.94
E / Ryd
$q_n / 10^5 t_n$
3
2
1
0
-1
n = 4
0.93
0.931
0.932
0.933
0.934
0.935
0.936
0.937
0.938
E / Ryd

Figure 6.21

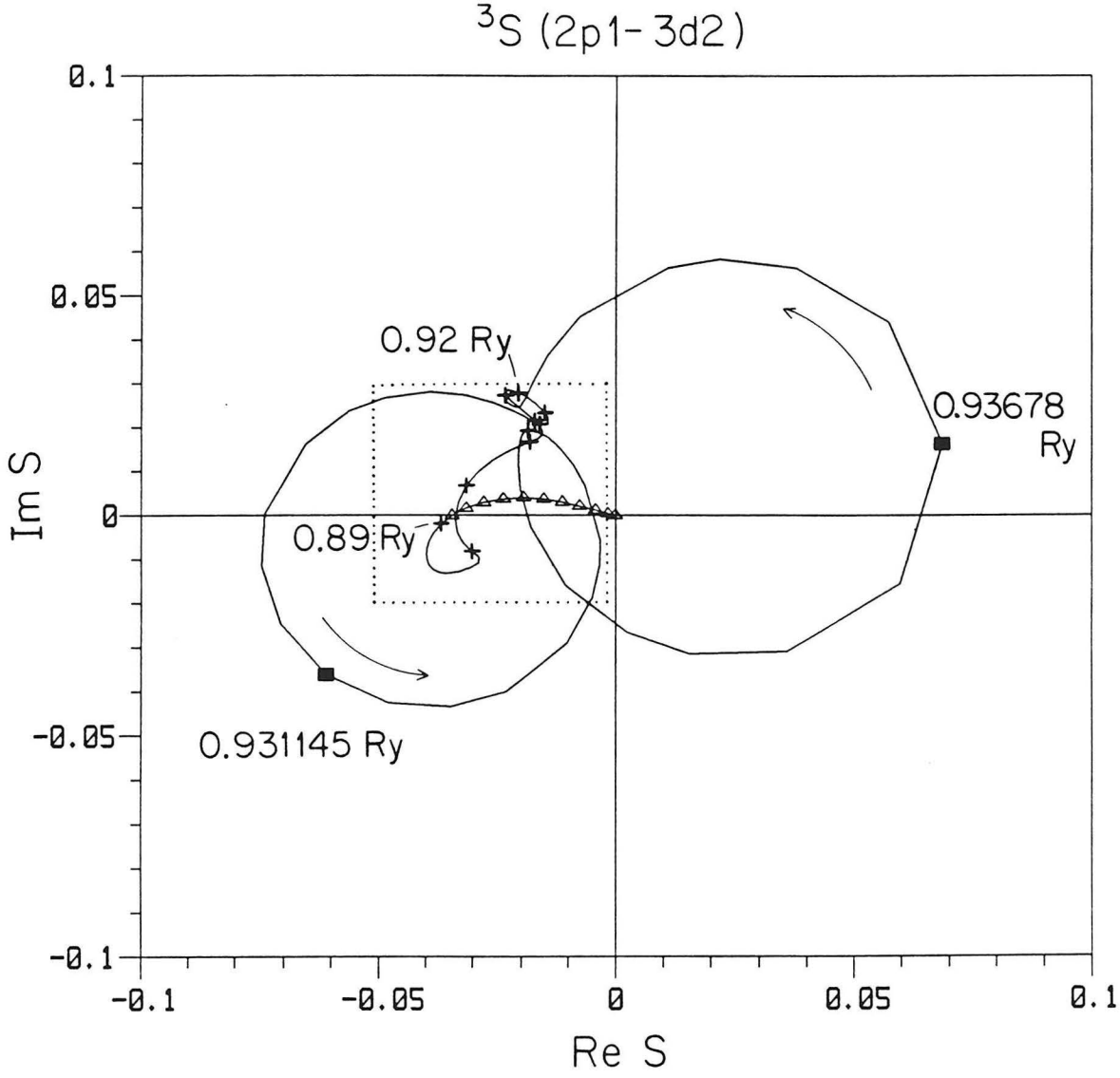
^{3}S (2p1- 3d2)
0.1
0.05
0
-0.05
-0.1
Im S
-0.1
-0.05
0
0.05
0.1
Re S
0.92 Ry
0.89 Ry
0.93678
Ry
0.931145 Ry

Figure 6.22a

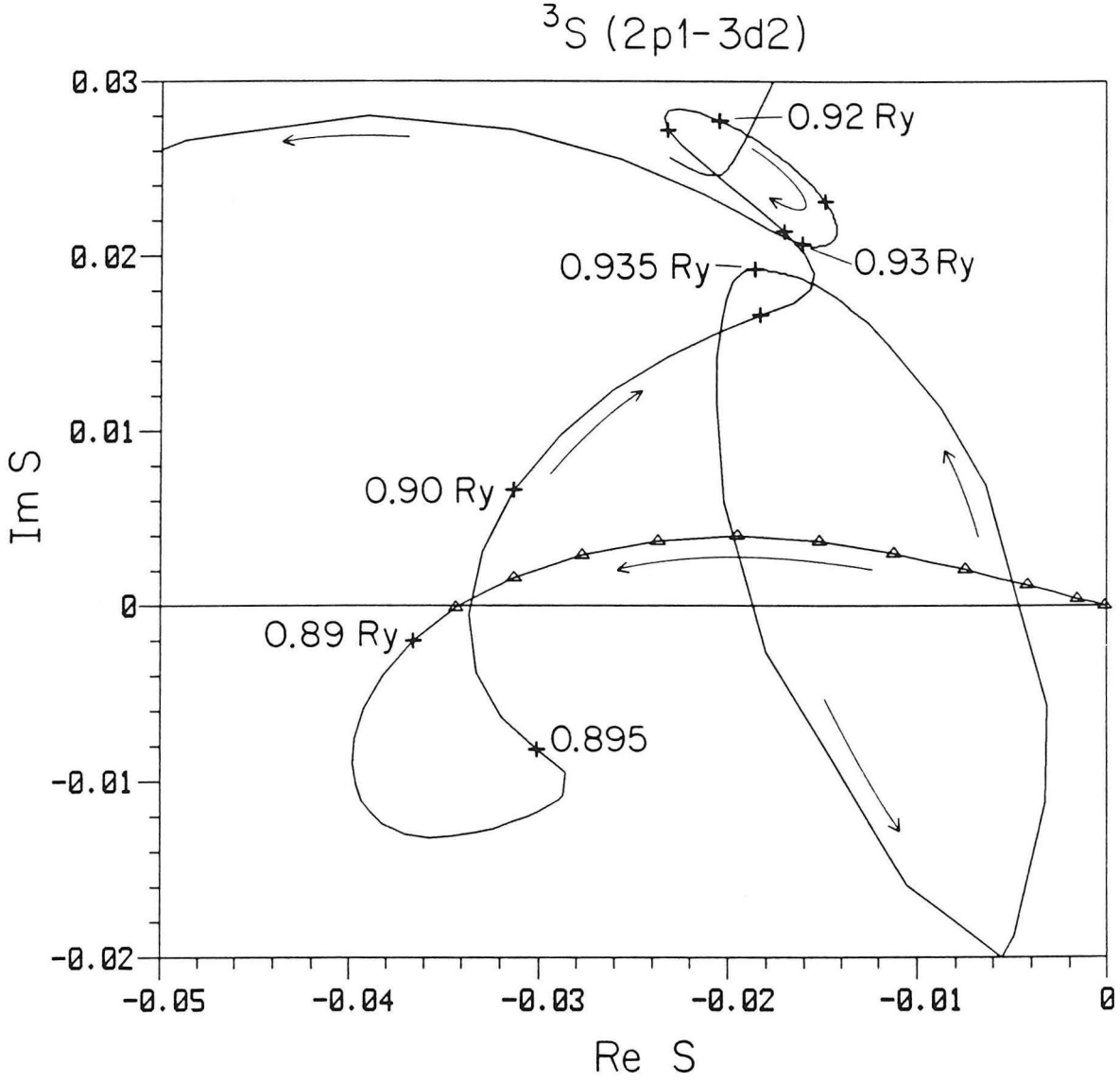
^{3}S (2p1-3d2)
0.92 Ry
0.935 Ry
0.93 Ry
0.90 Ry
0.89 Ry
0.895
0.03
0.02
0.01
0
-0.01
-0.02
-0.05
-0.04
-0.03
-0.02
-0.01
0
Im S
Re S

Figure 6.22b

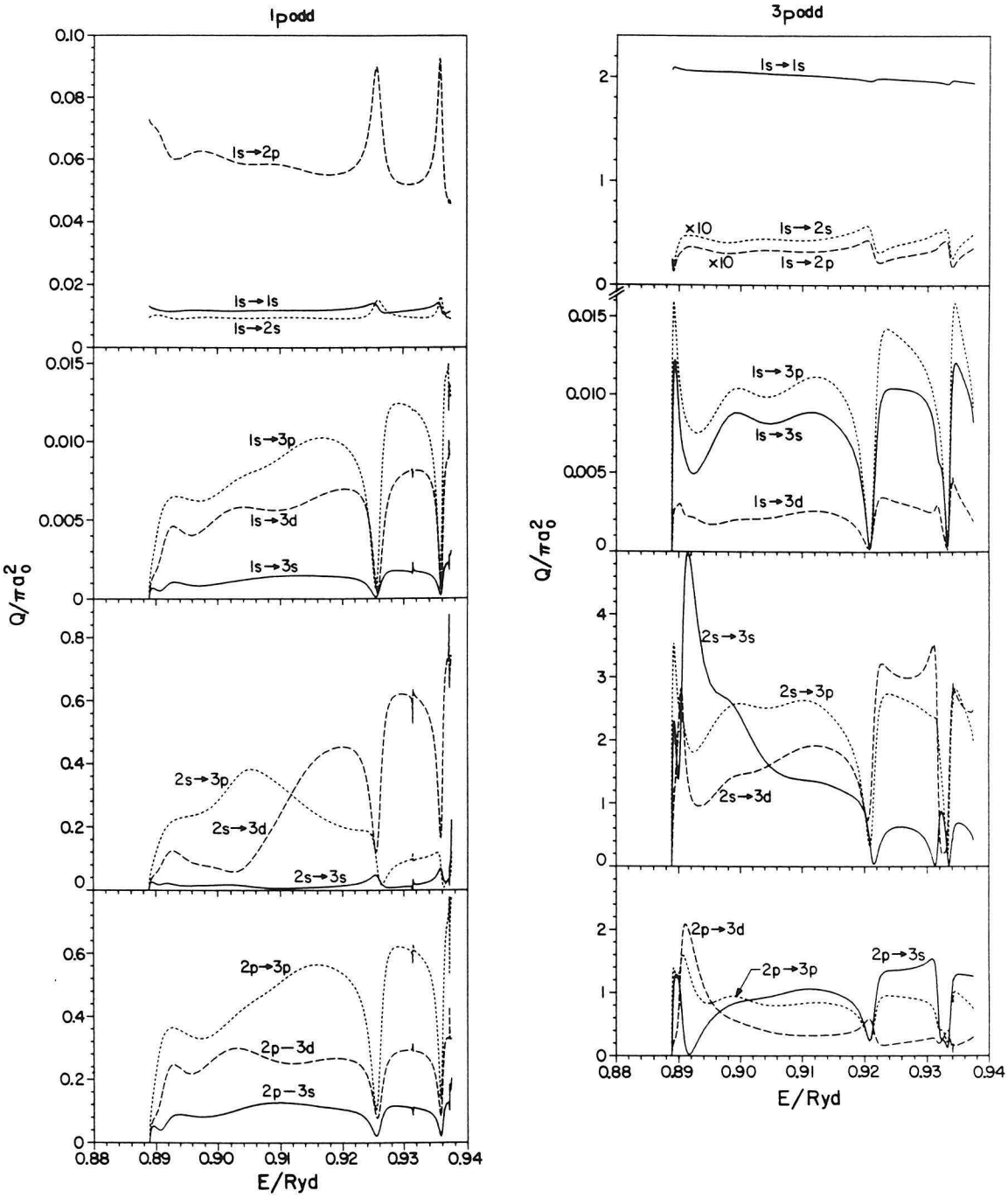
1podd
3podd
1s→1s
1s→2p
1s→2s
×10
1s→3p
1s→3s
1s→3d
2s→3p
2s→3d
2s→3s
2p→3p
2p→3d
2p→3s
Q/πa₀²
E/Ryd

Figure 6.23

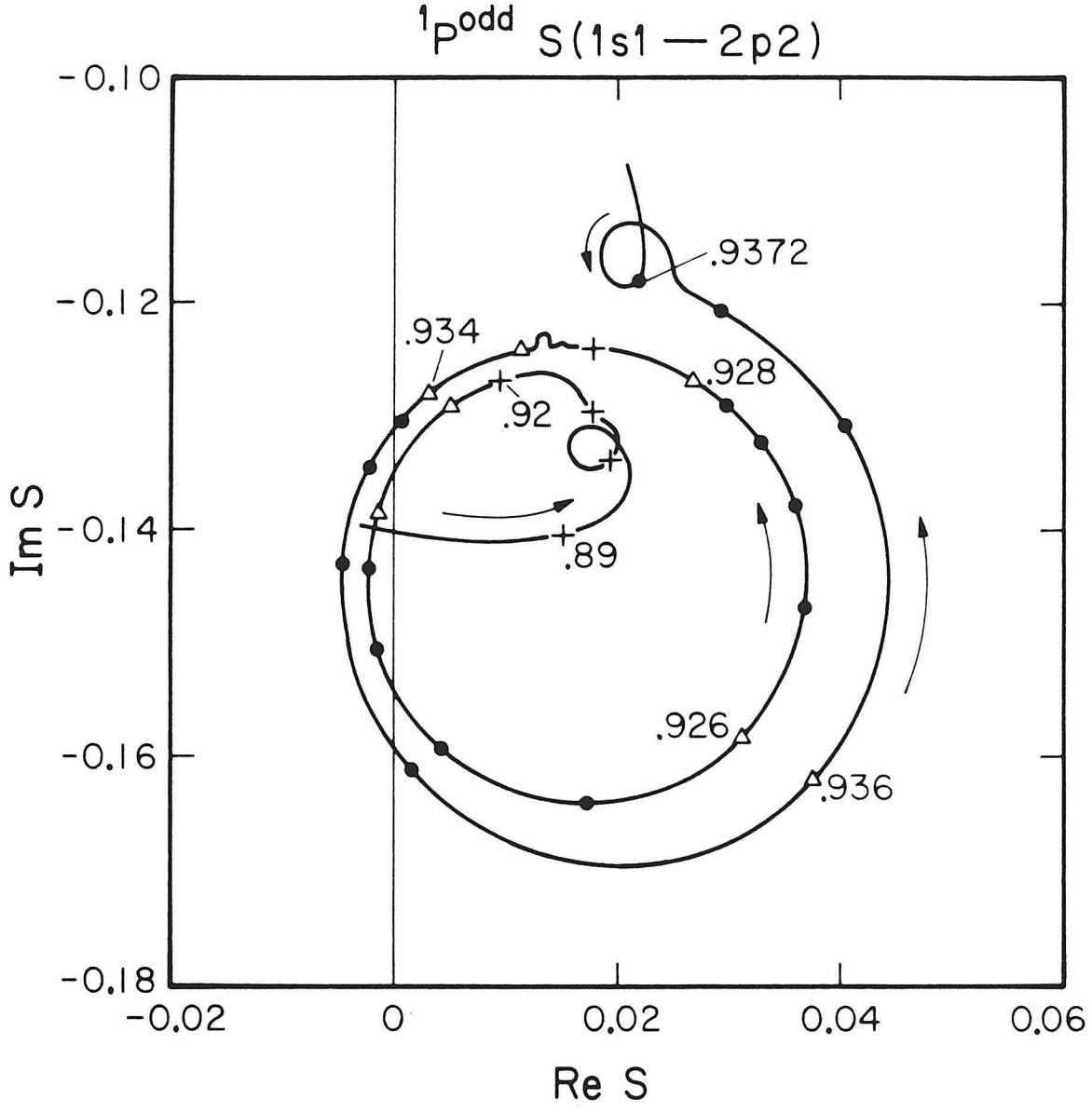
$^1P^{odd}$ S(1s1 — 2p2)
-0.10
-0.12
-0.14
-0.16
-0.18
Im S
-0.02
0
0.02
0.04
0.06
Re S
.9372
.934
.928
.92
.89
.926
.936

Figure 6.24

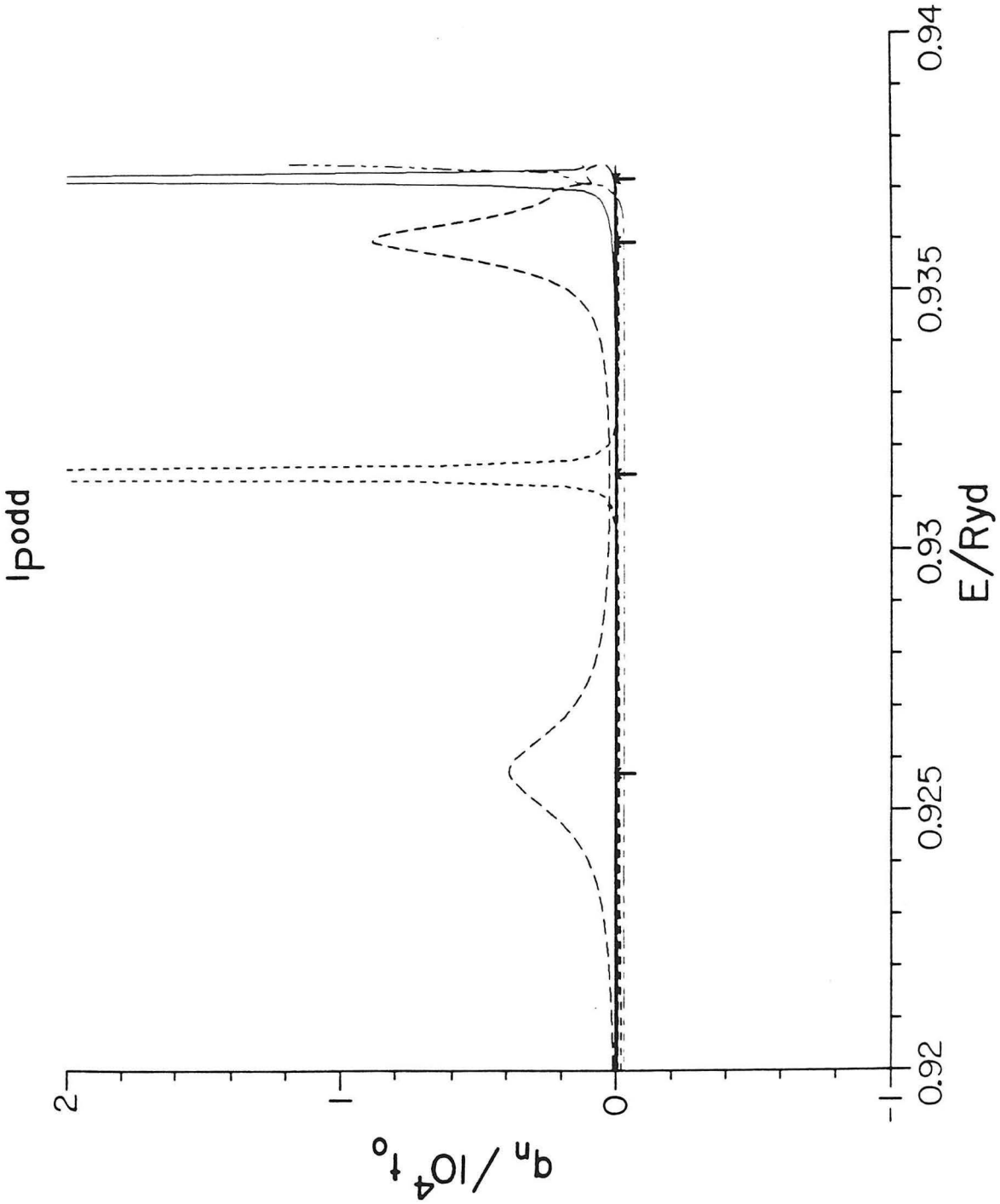

Figure 6.25

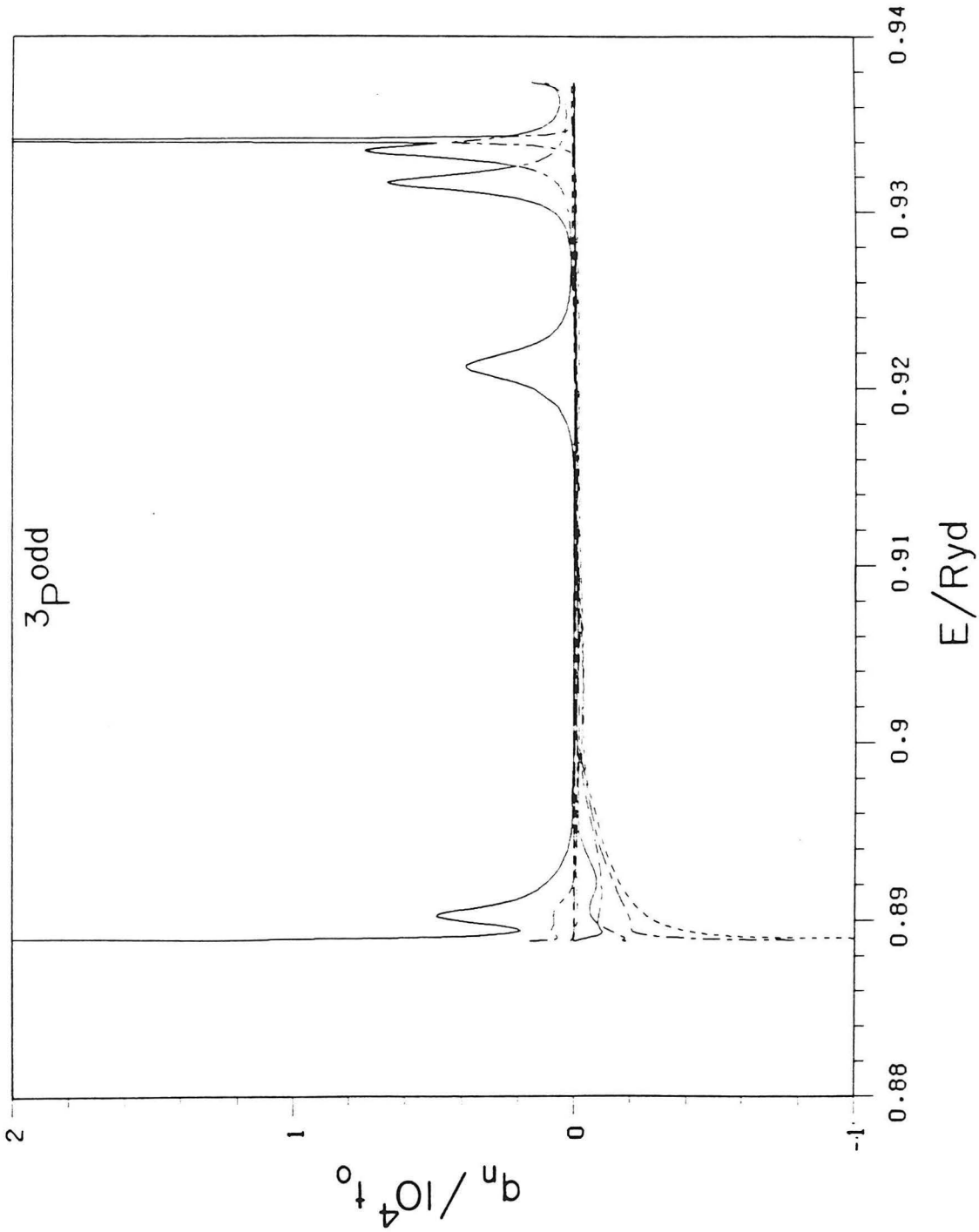

Figure 6.26

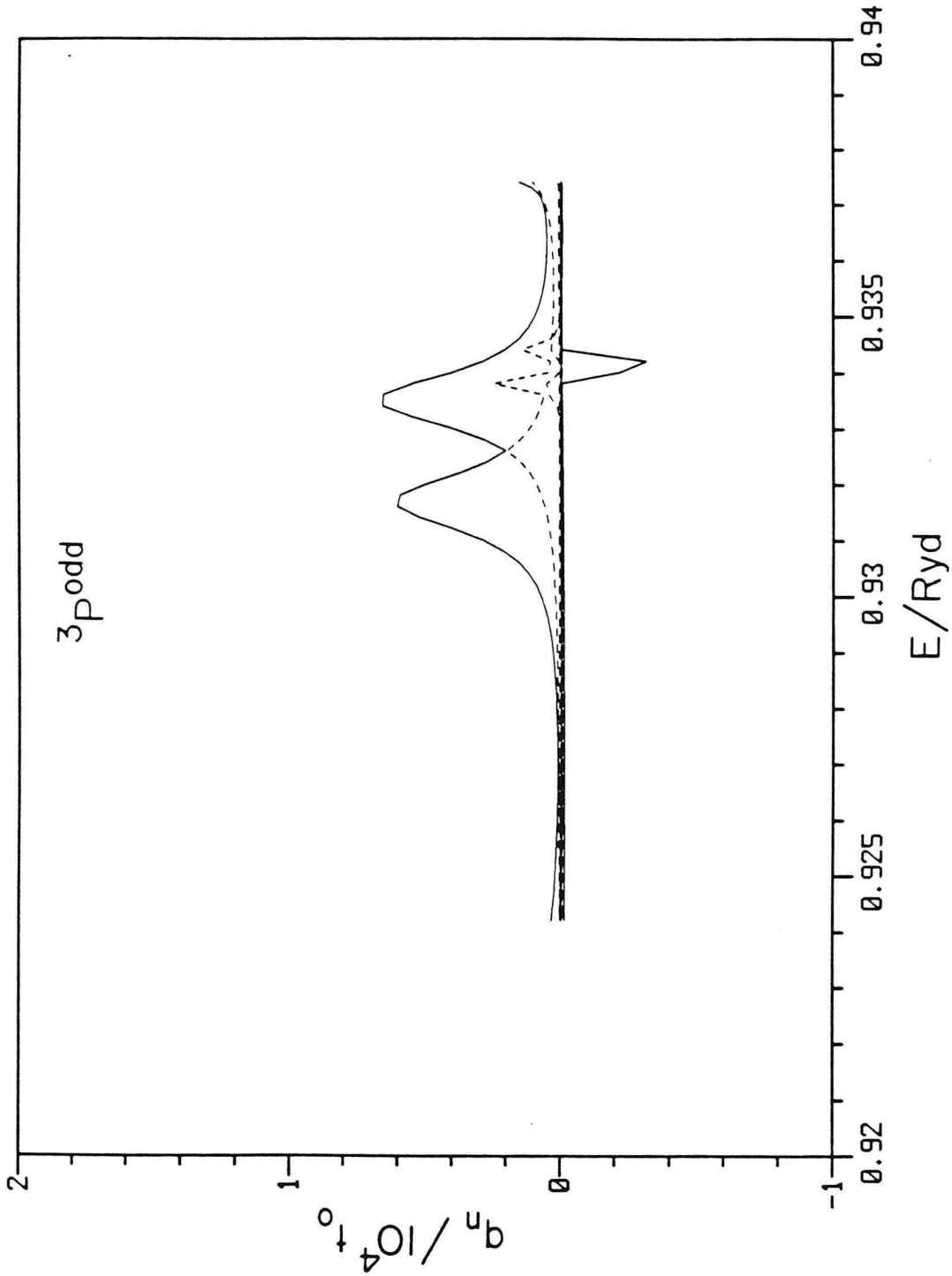

Figure 6.27

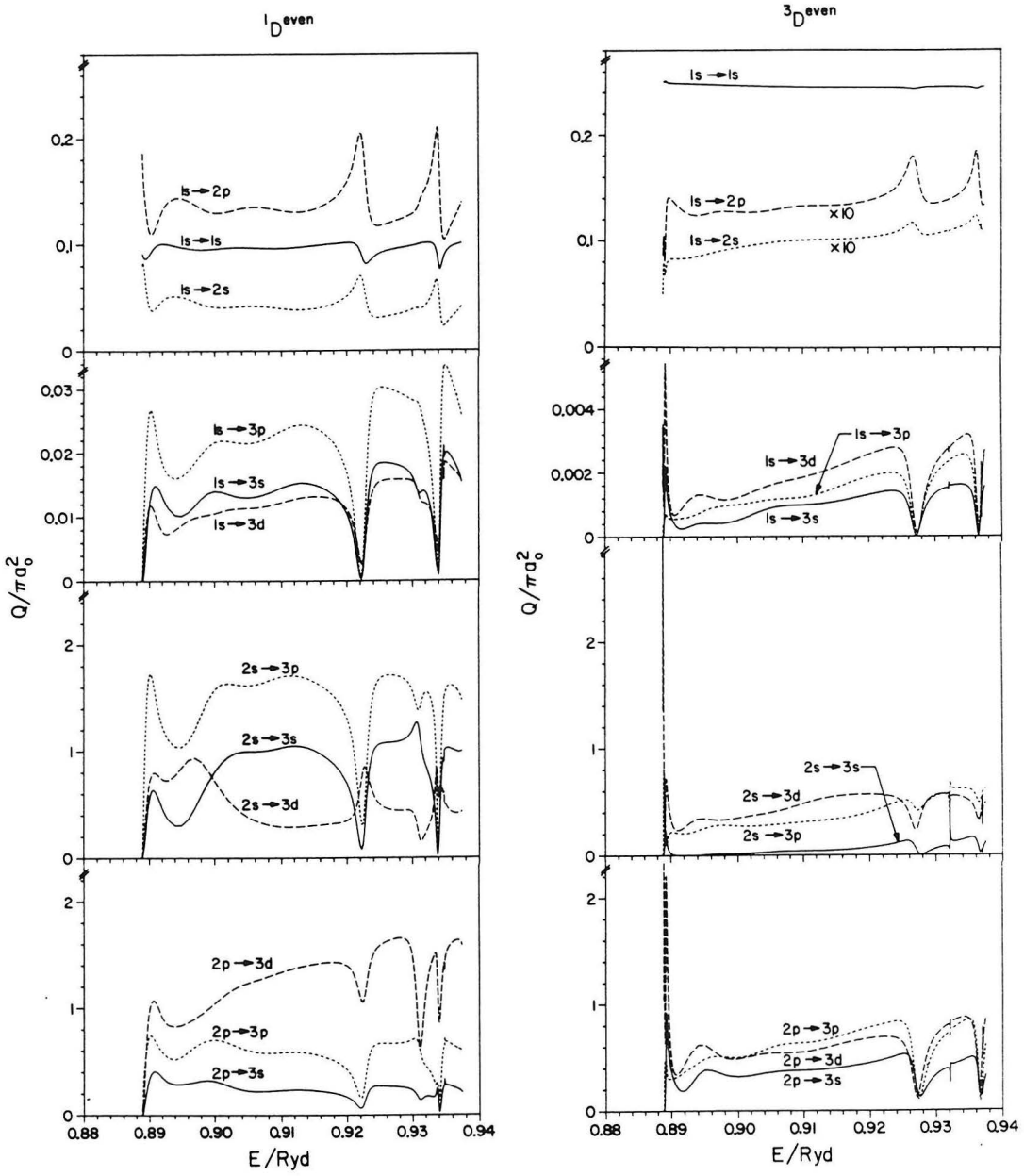
$^1D^{even}$
$^3D^{even}$
1s → 1s
1s → 2p
1s → 2s
1s → 3p
1s → 3s
1s → 3d
2s → 3p
2s → 3s
2s → 3d
2p → 3d
2p → 3p
2p → 3s
×10
×10
$Q/\pi a_0^2$
E/Ryd
0.88
0.89
0.90
0.91
0.92
0.93
0.94

Figure 6.28

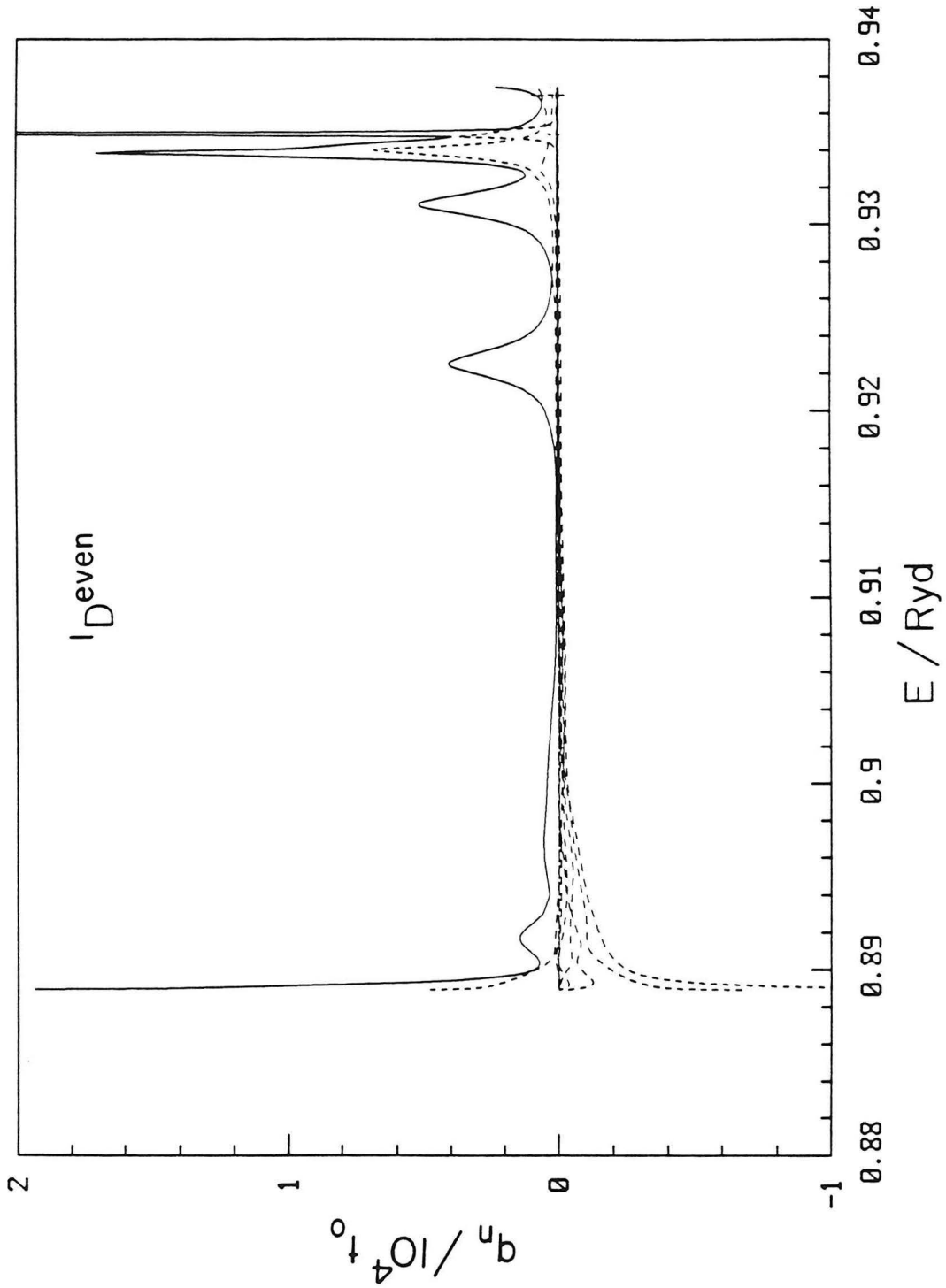

Figure 6.29

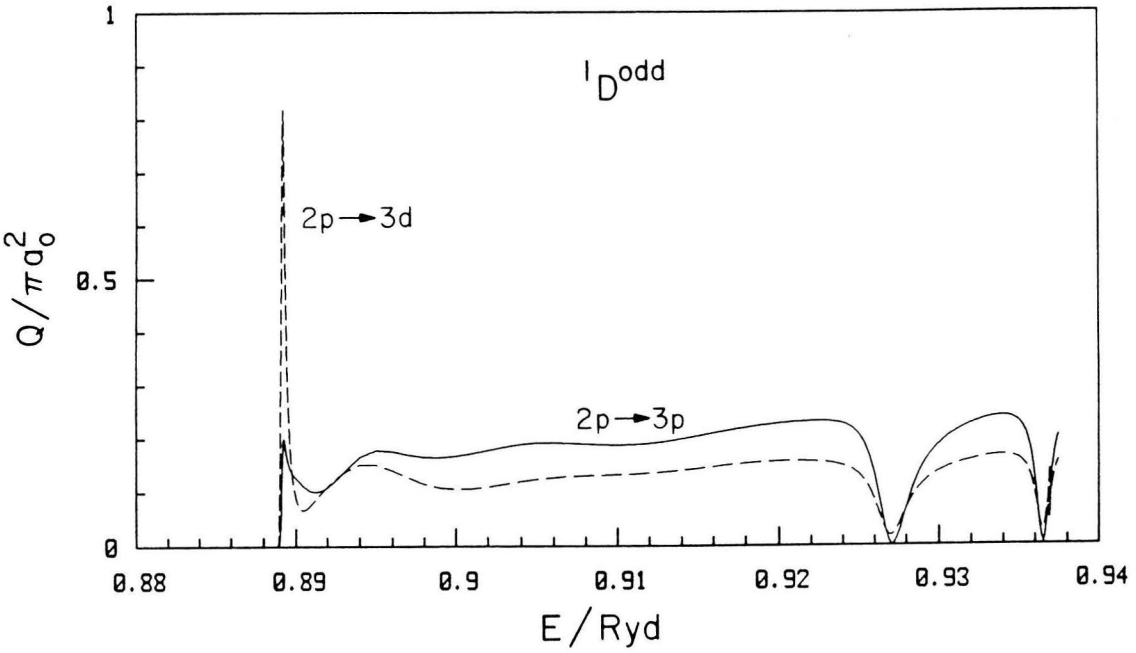
1
0.5
0
$Q/\pi a_o^2$
$^1D^{odd}$
2p→3d
2p→3p
0.88
0.89
0.9
0.91
0.92
0.93
0.94
E/Ryd

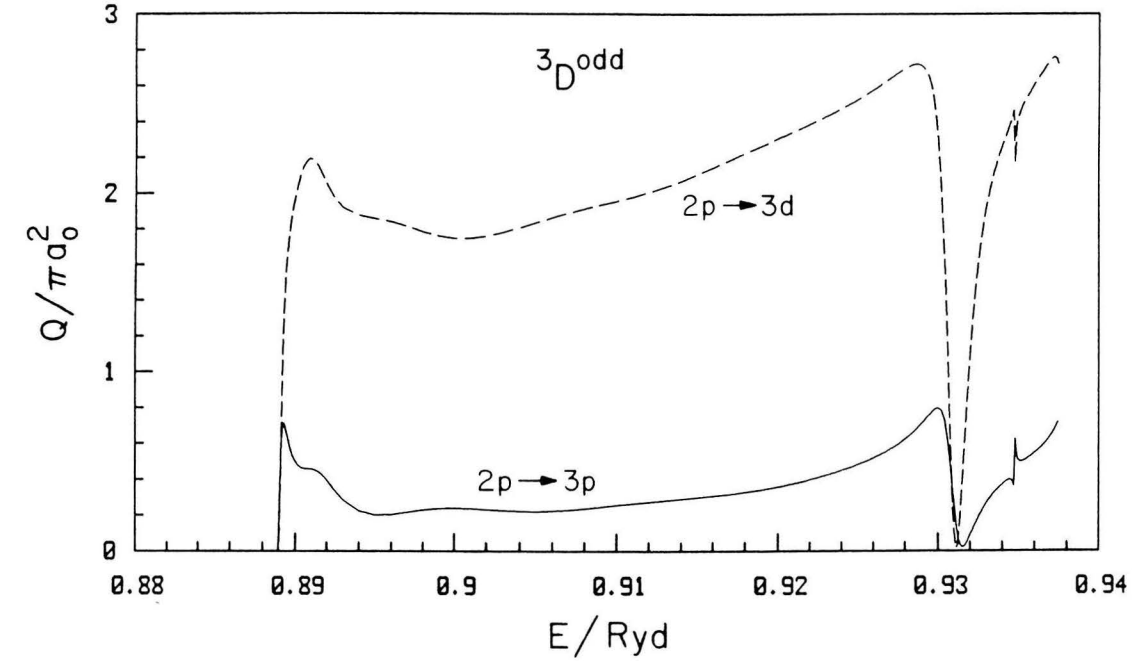
3
2
1
0
$Q/\pi a_o^2$
$^3D^{odd}$
2p→3d
2p→3p
0.88
0.89
0.9
0.91
0.92
0.93
0.94
E/Ryd

Figure 6.30

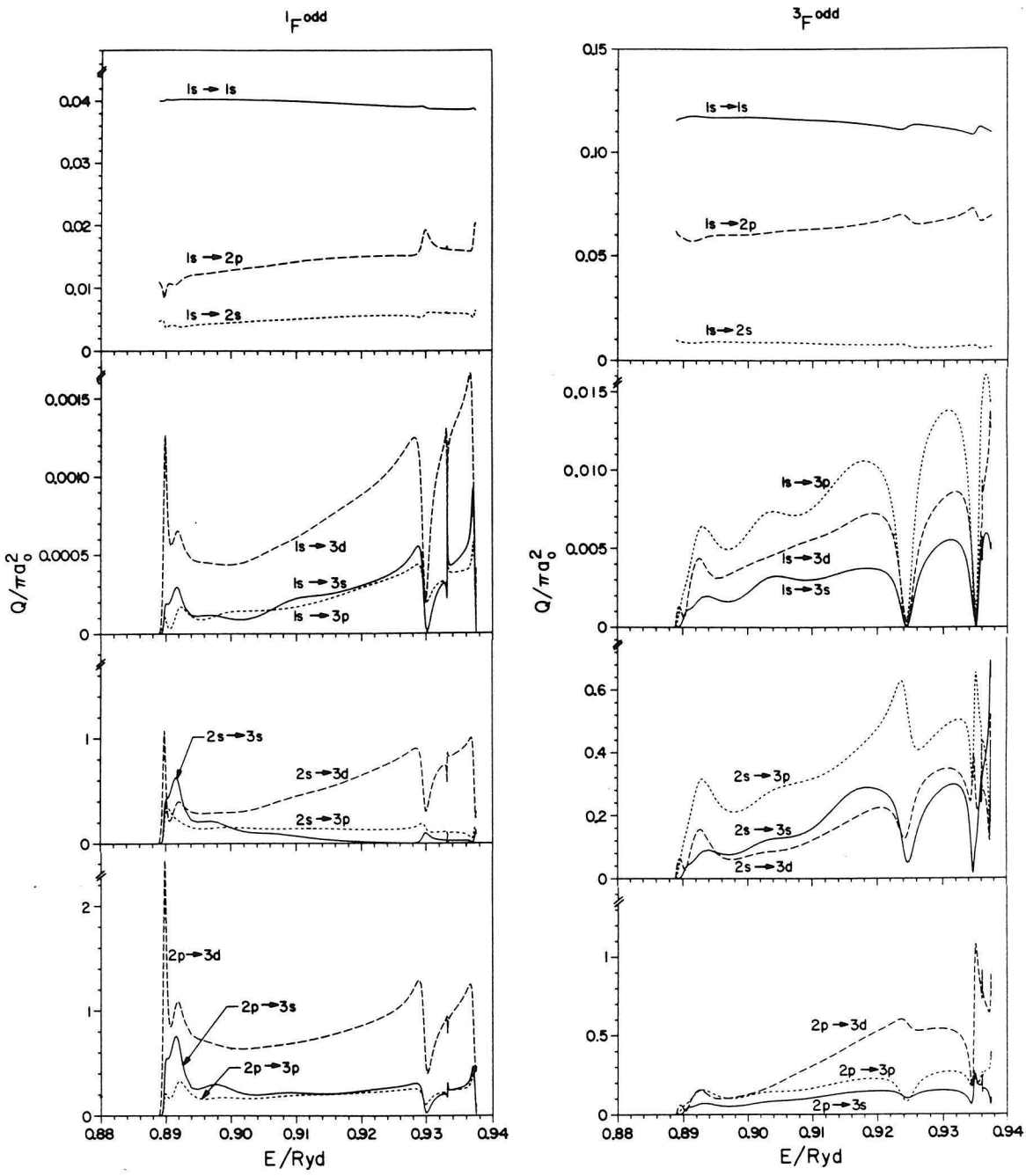
$^1F^{odd}$
$^3F^{odd}$
1s → 1s
1s → 2p
1s → 2s
1s → 3d
1s → 3s
1s → 3p
2s → 3s
2s → 3d
2s → 3p
2p → 3d
2p → 3s
2p → 3p
$Q/\pi a_o^2$
E/Ryd

Figure 6.31

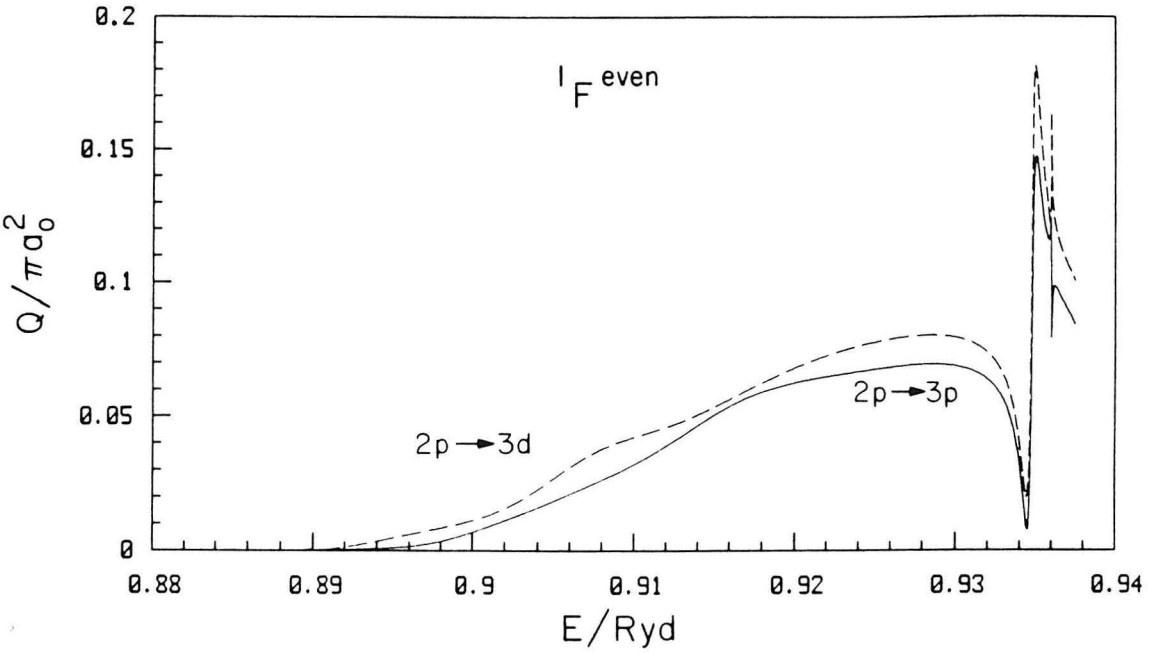
0.2
0.15
0.1
0.05
0
$Q/\pi a_o^2$
$^1F^{even}$
2p→3d
2p→3p
0.88
0.89
0.9
0.91
0.92
0.93
0.94
E/Ryd

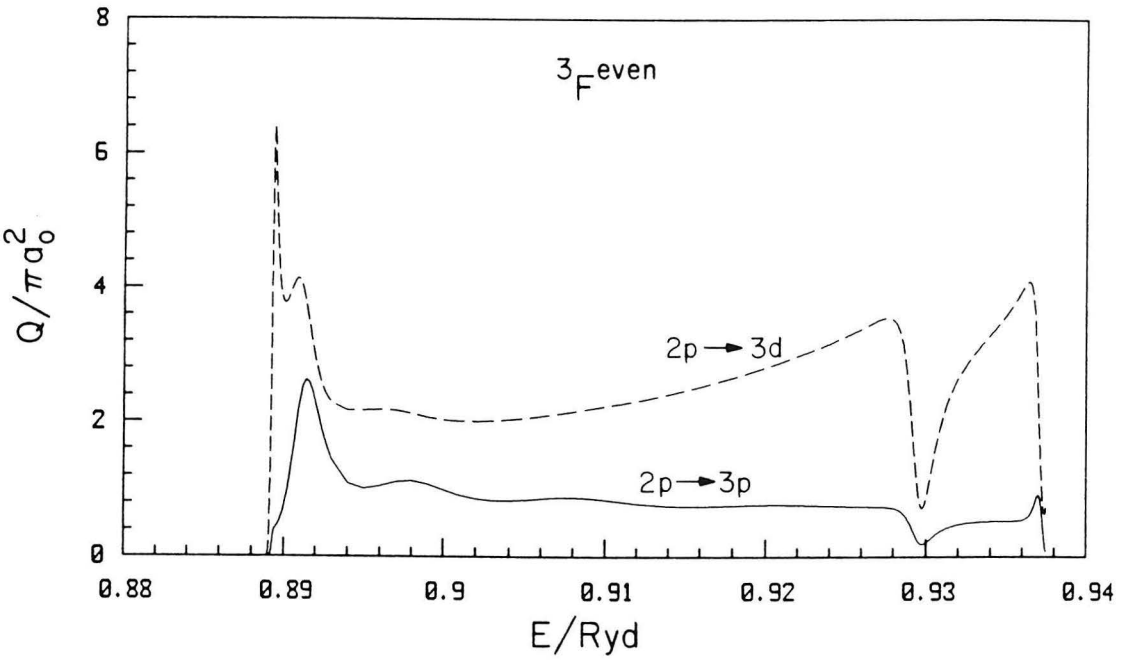
8
6
4
2
0
$Q/\pi a_o^2$
$^3F^{even}$
2p→3d
2p→3p
0.88
0.89
0.9
0.91
0.92
0.93
0.94
E/Ryd

Figure 6.32

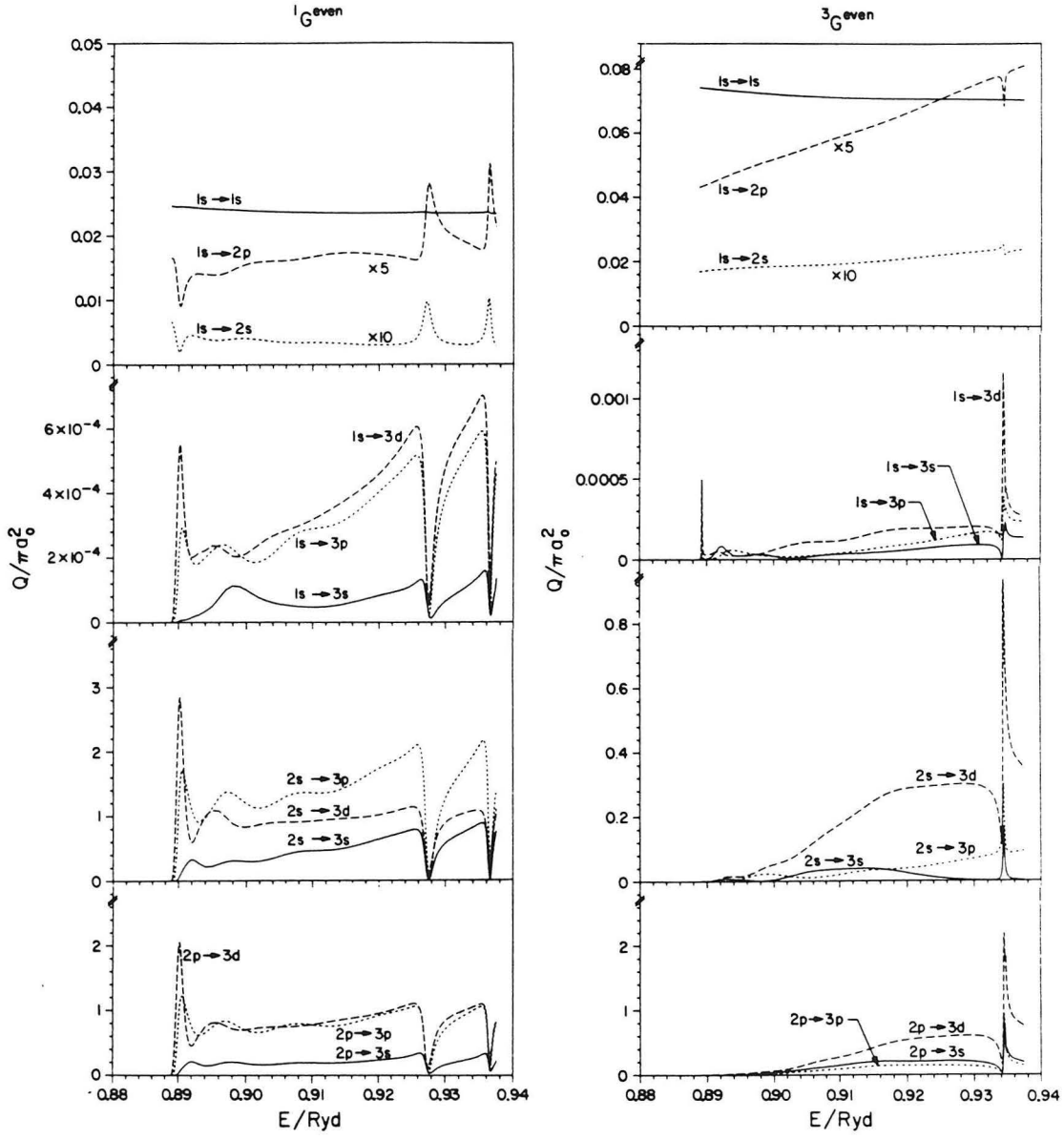
$^1G^{even}$
$^3G^{even}$
$Q/\pi a_o^2$
E/Ryd
1s→1s
1s→2p
1s→2s
1s→3d
1s→3p
1s→3s
2s→3p
2s→3d
2s→3s
2p→3d
2p→3p
2p→3s
×5
×10

Figure 6.33

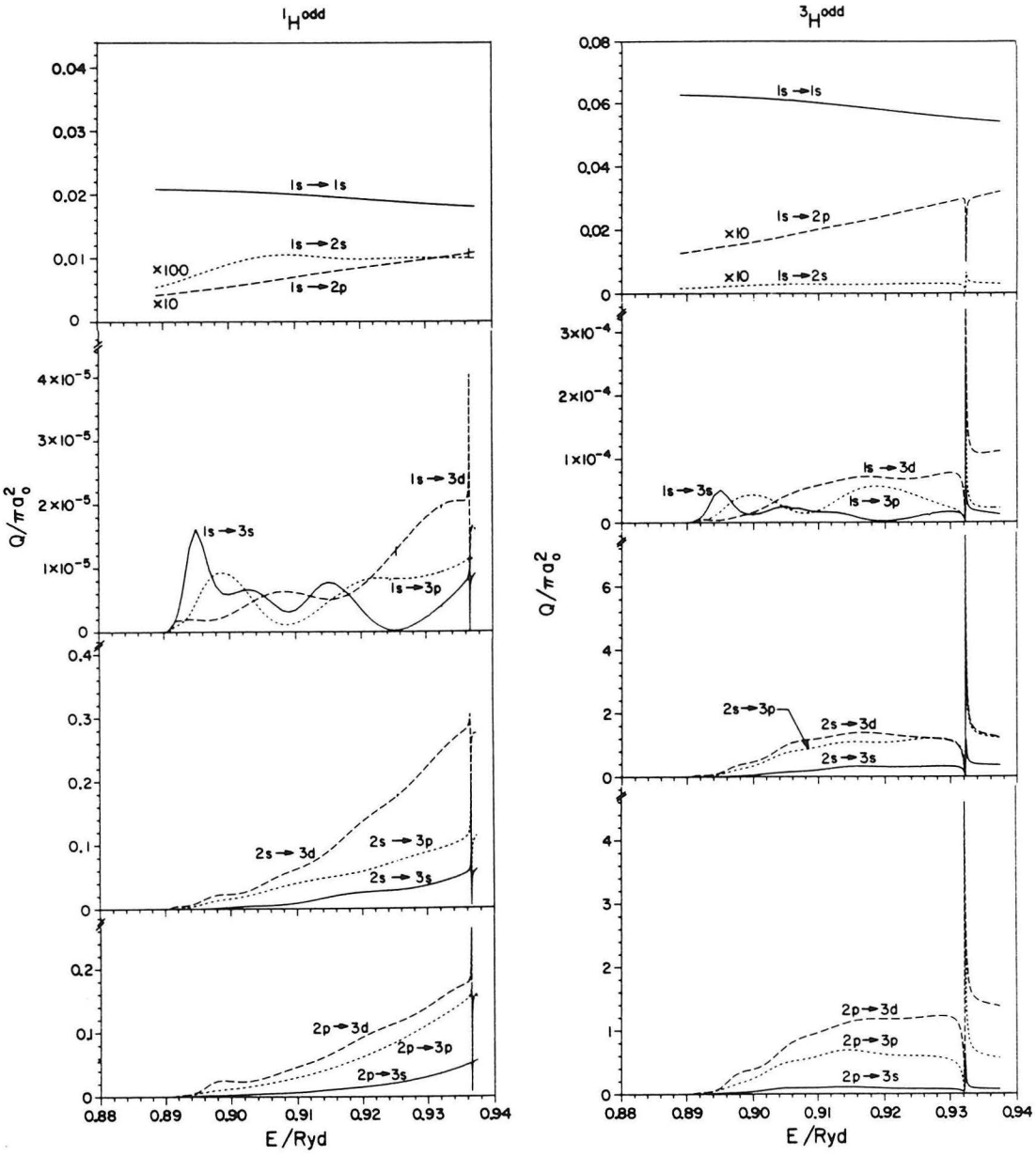
$^1H^{odd}$
$^3H^{odd}$
$Q/\pi a_o^2$
E/Ryd
1s → 1s
1s → 2s
1s → 2p
1s → 3s
1s → 3d
1s → 3p
2s → 3d
2s → 3p
2s → 3s
2p → 3d
2p → 3p
2p → 3s
×100
×10

Figure 6.34

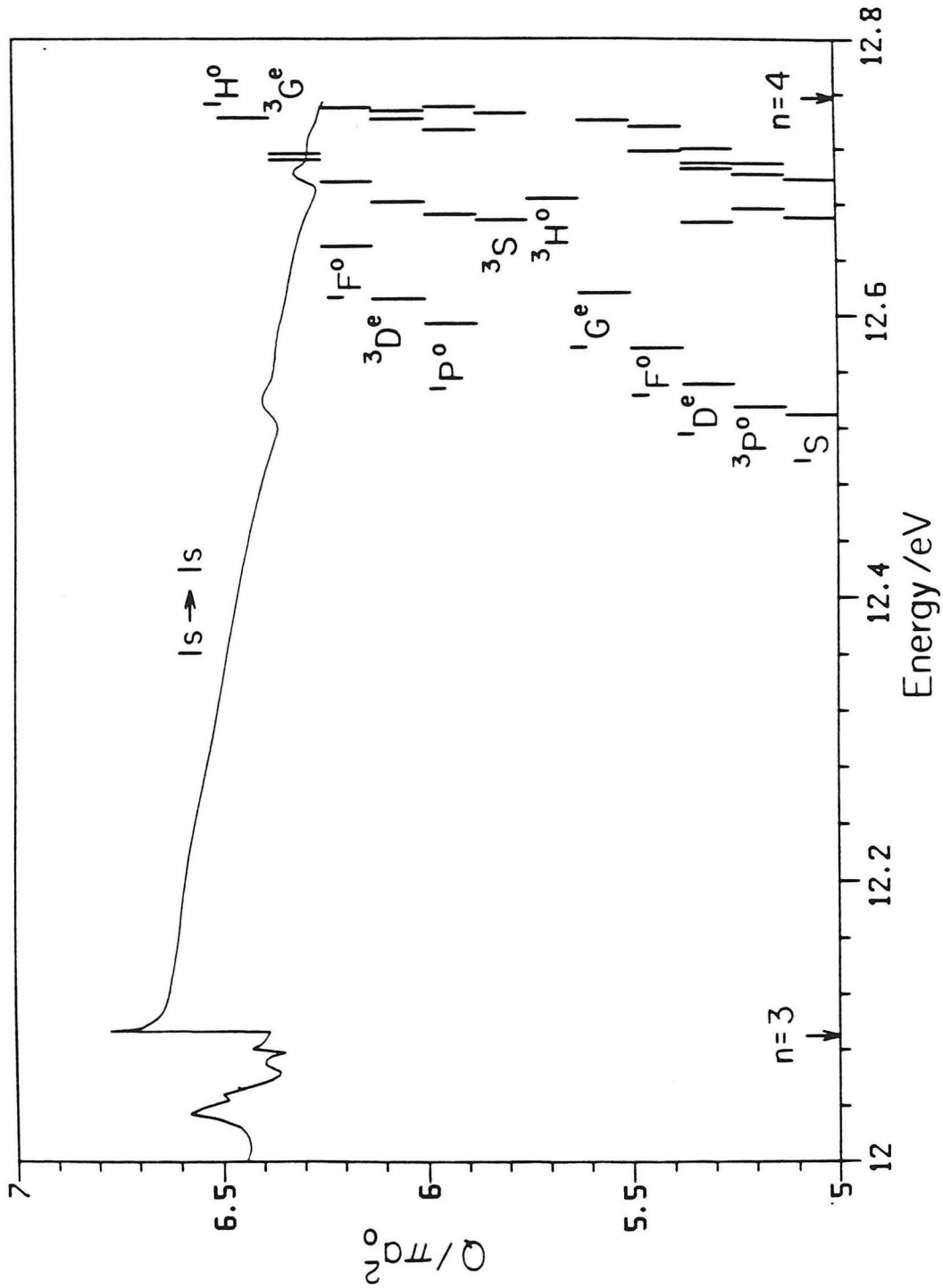
Q/πa₀²
7
6.5
6
5.5
5
12
12.2
12.4
12.6
12.8
Energy/eV
n=3
n=4
1s → 1s
¹H°
³G^e
¹F°
³D^e
¹P°
³S
³H°
¹G^e
¹F°
¹D^e
³P°
¹S

Figure 6.35a

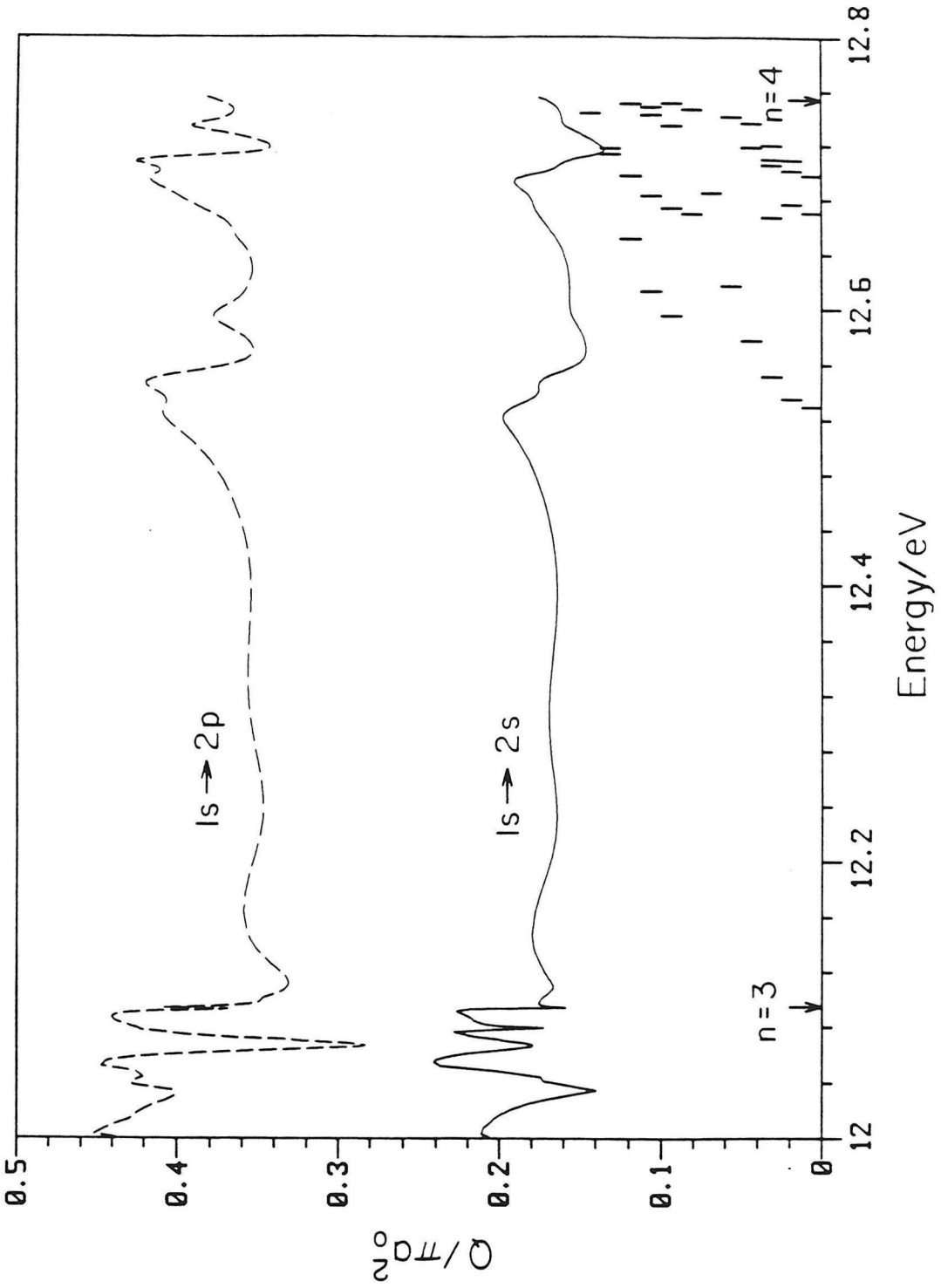
0.5
0.4
0.3
0.2
0.1
0
Q/πa₀²
12
12.2
12.4
12.6
12.8
Energy/eV
1s→2p
1s→2s
n=3
n=4

Figure 6.35b

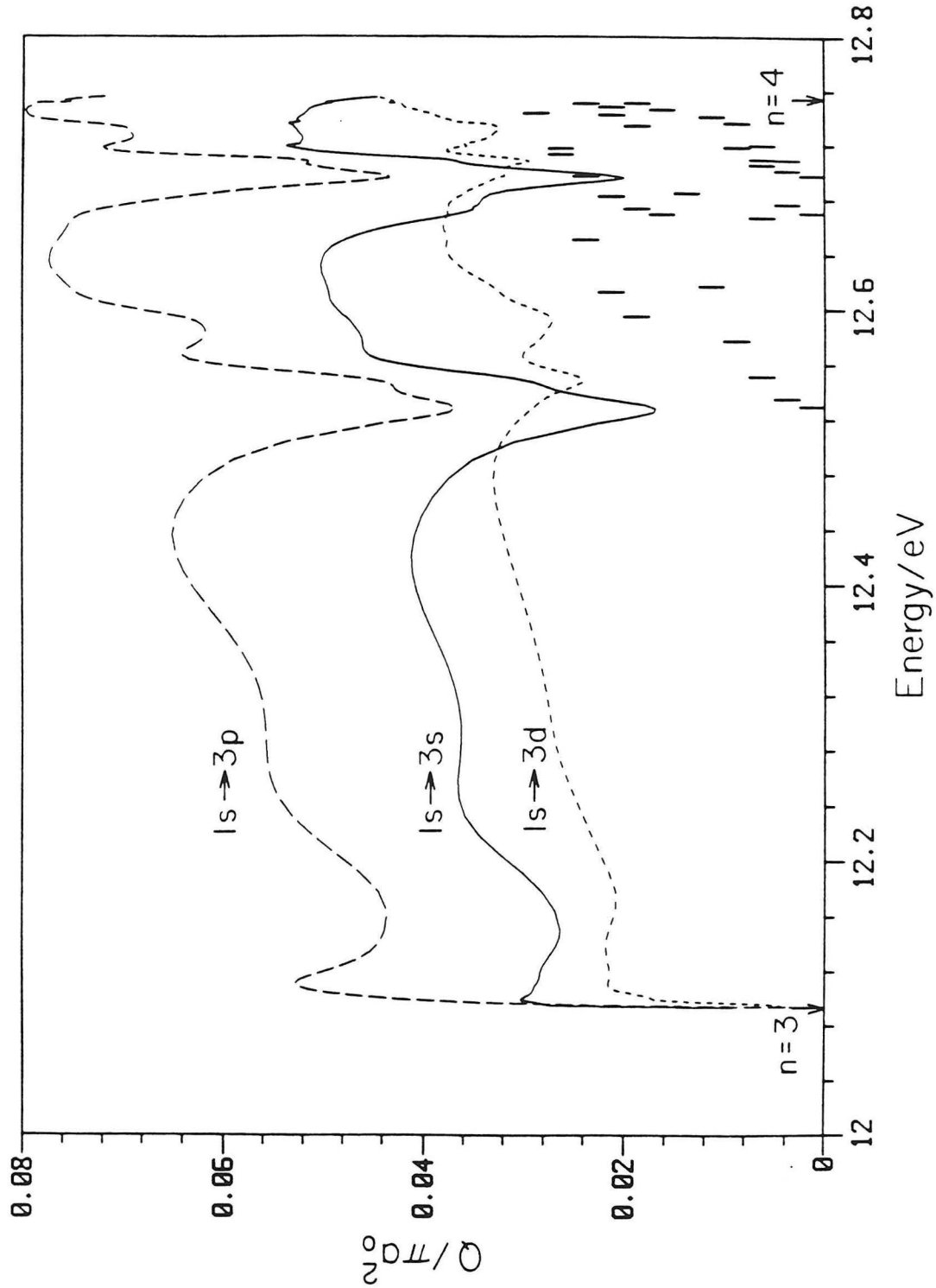
0.08
0.06
0.04
0.02
0
Q/πa₀²
12
12.2
12.4
12.6
12.8
Energy/eV
n=3
n=4
1s→3p
1s→3s
1s→3d

Figure 6.35c

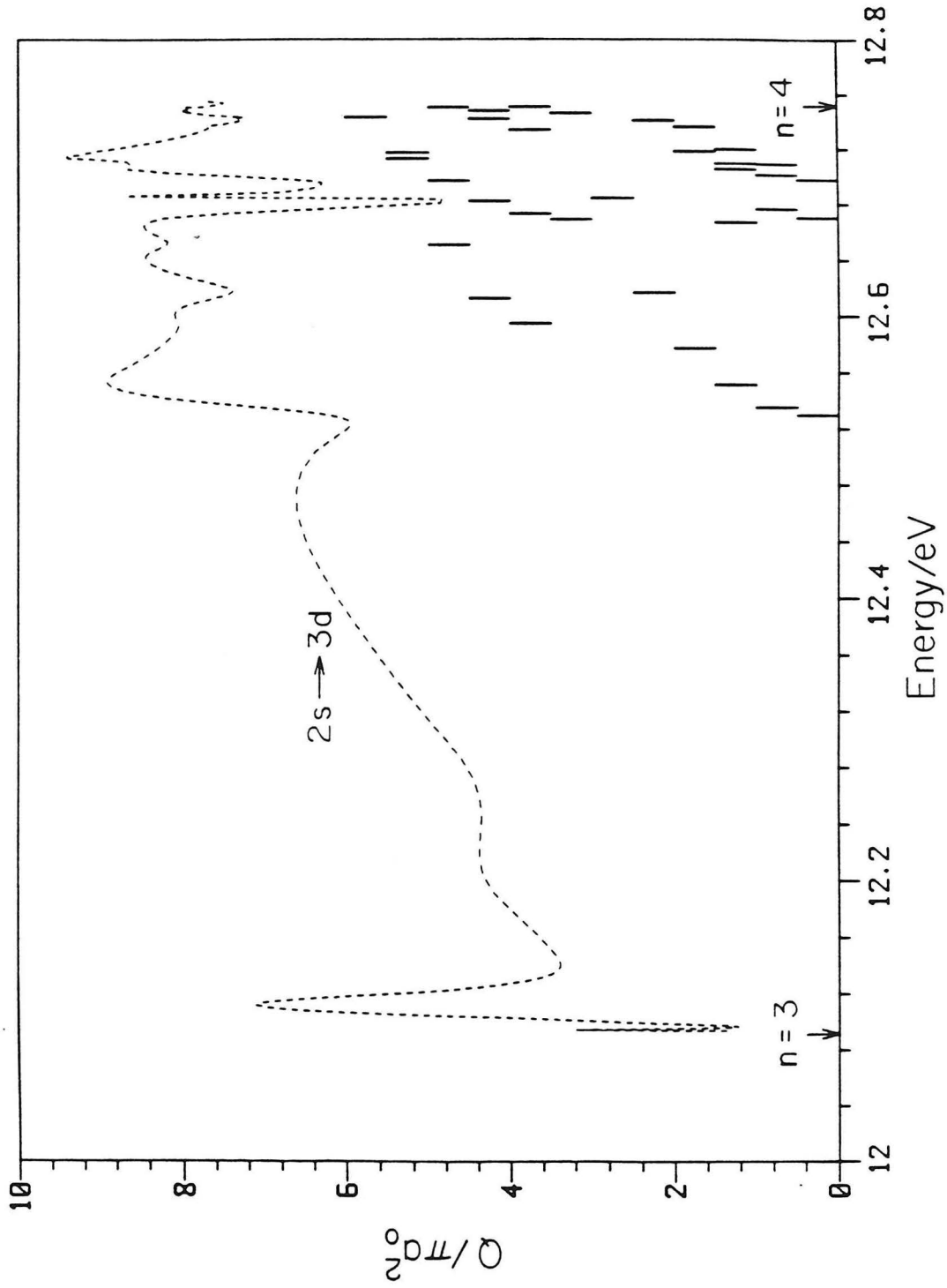

Figure 6.36a

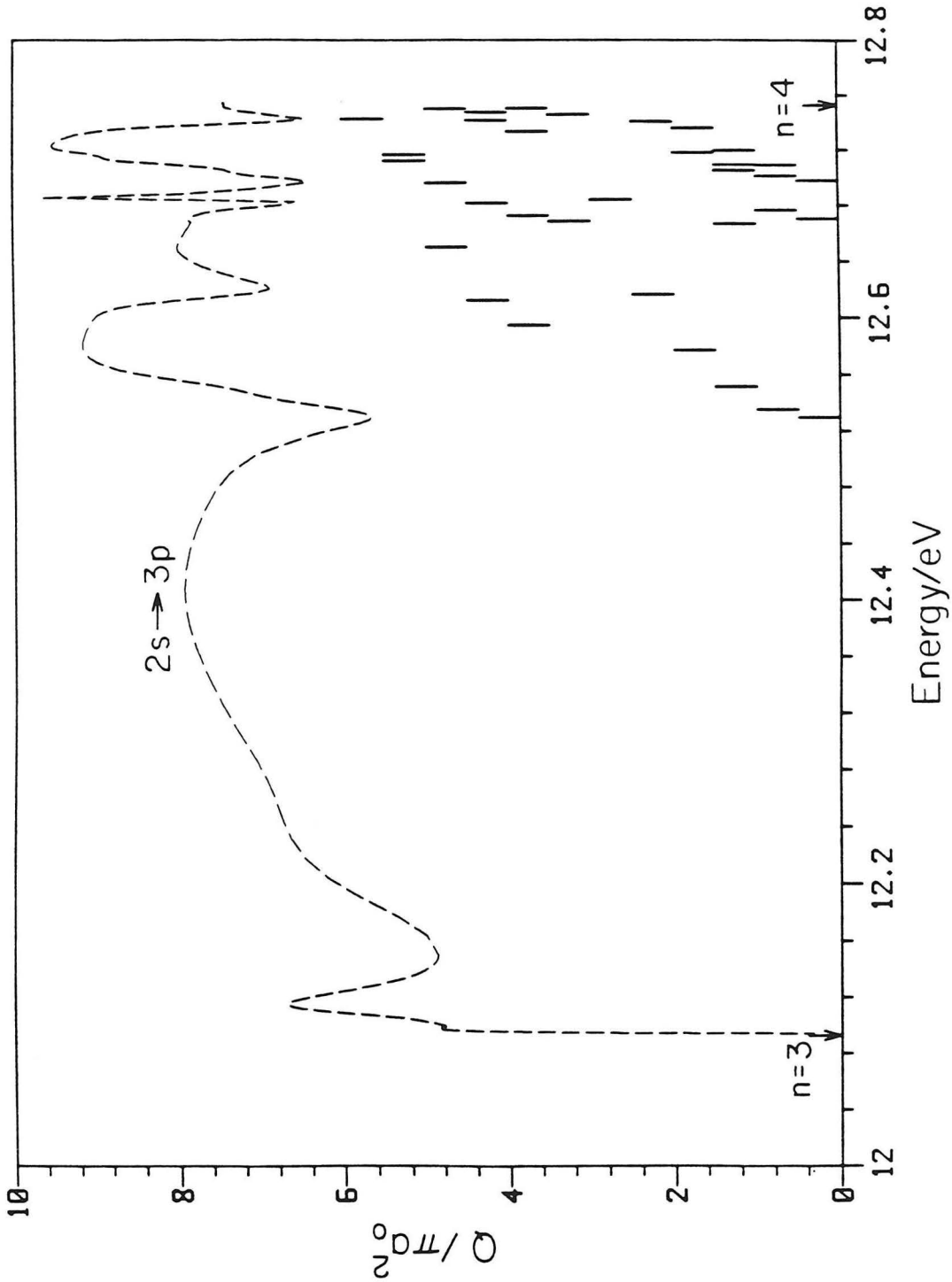

Figure 6.36b

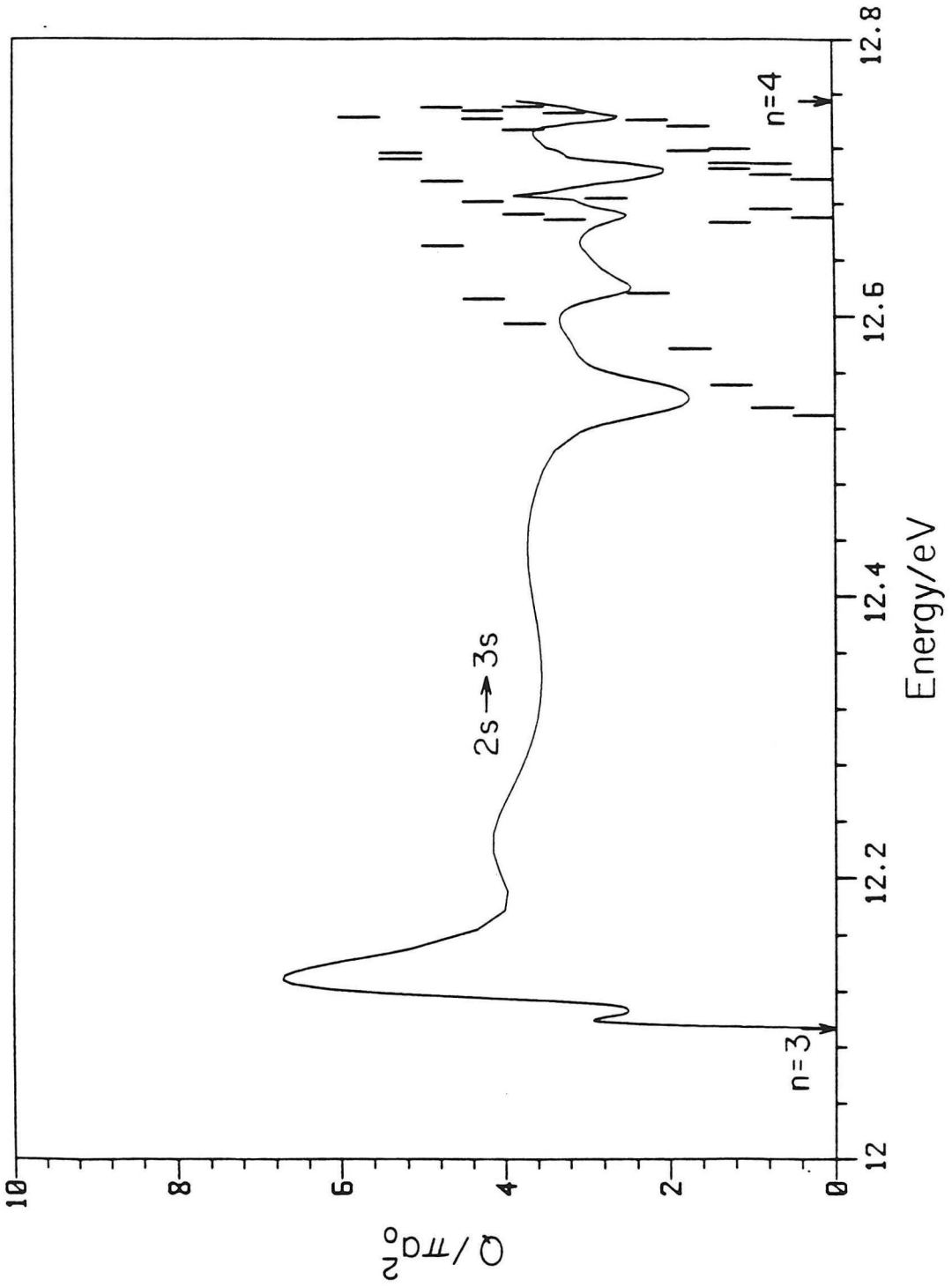

Figure 6.36c

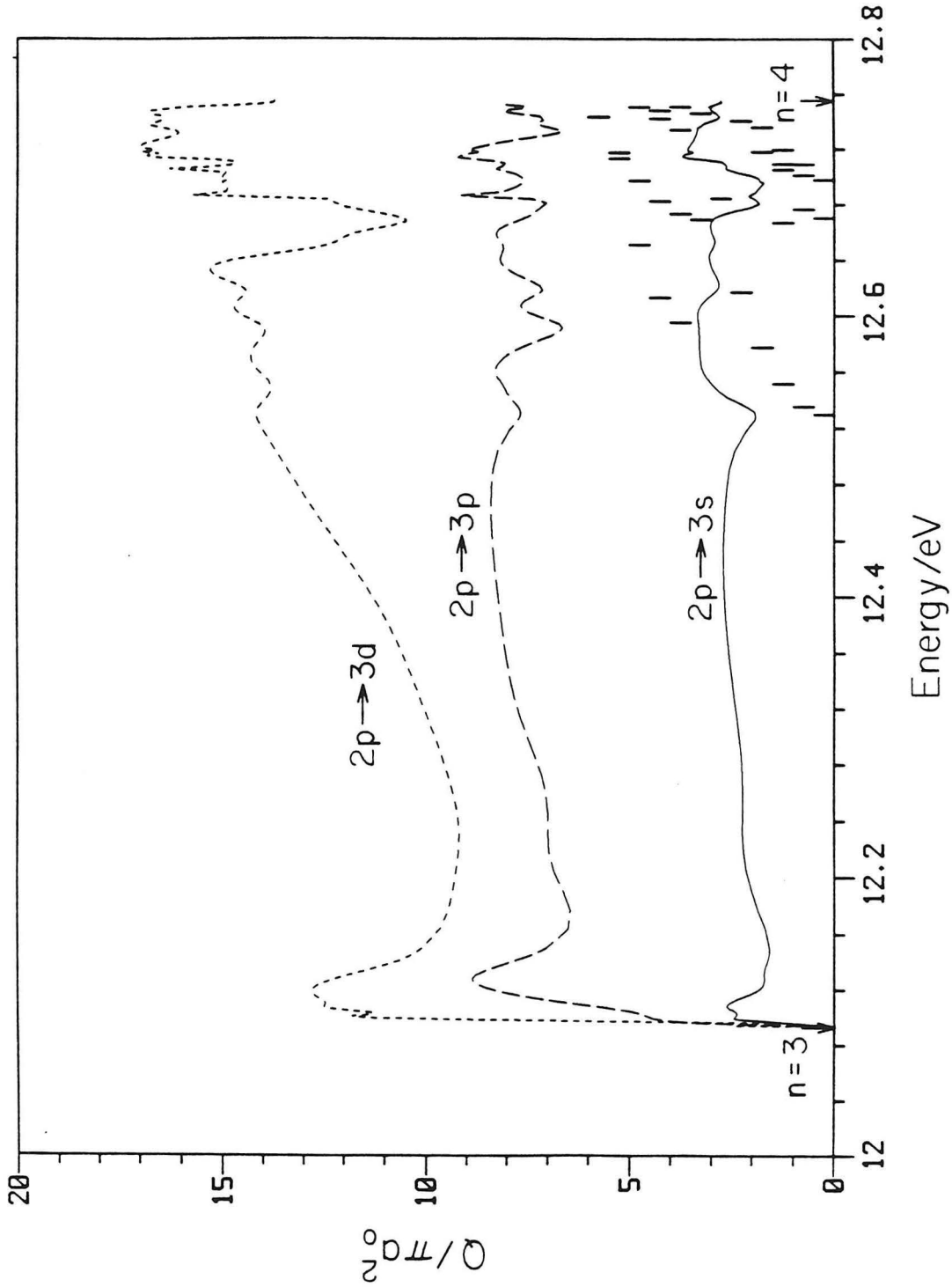
20
15
10
5
0
12
12.2
12.4
12.6
12.8
Energy/eV
$Q/\pi a_0^2$
2p→3d
2p→3p
2p→3s
n=3
n=4

Figure 6.37

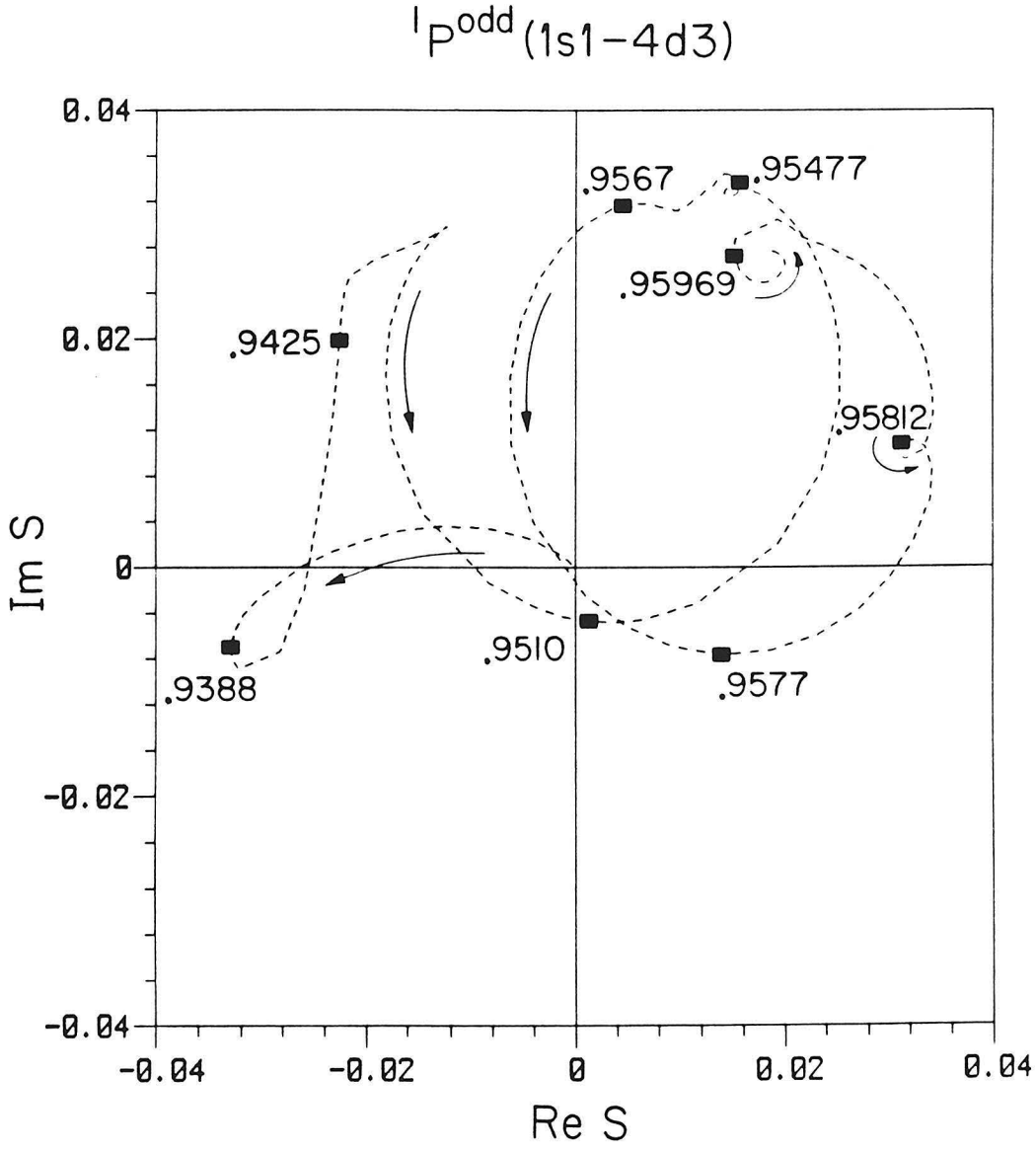
$^1P^{odd}(1s1-4d3)$
0.04
0.02
0
-0.02
-0.04
Im S
-0.04
-0.02
0
0.02
0.04
Re S
.9567
.95477
.95969
.9425
.95812
.9510
.9388
.9577

Figure 6.38

THIS PAGE INTENTIONALLY LEFT BLANK.

THIS PAGE INTENTIONALLY LEFT BLANK.

APPENDIX A

ALTERNATE METHODS OF SOLUTION

In this chapter we will describe an attempt to solve the electron-hydrogen atom scattering problem using two different methods that were tried but subsequently discarded in favor of the formalism described in Chapters 2 and 3. The first method involves a different coordinate system. The second involves a different basis set, but uses the same hyperspherical coordinates as were used in the final calculation.

A.1 Cylindrical Coordinates - Introduction

Consider the cylindrical form of hyperspherical coordinates, which we call z, s, γ, where $z = \rho\cos\omega$, $s = \rho\sin\omega$, and ρ, ω, and γ are the quantities defined in Sections 2.1 and 2.2. These coordinates would seem to be suited to the $e^- + H$ system, because the potential energy function equipotentials approach cylinders far enough away from the origin. In these coordinates the potential function becomes

$$V(s,z,\gamma) = \frac{-e^2}{\sqrt{s^2+z^2}}\left[\sqrt{2}\left(\left[1+\frac{z}{\sqrt{s^2+z^2}}\right]^{-\frac{1}{2}} + \left[1-\frac{z}{\sqrt{s^2+z^2}}\right]^{-\frac{1}{2}}\right) - \left[1-\frac{s\cos\gamma}{\sqrt{s^2+z^2}}\right]^{-\frac{1}{2}}\right] \tag{A.1}$$

In order to better visualize the properties of the system, contour plots of V at constant z, and also at constant γ, were obtained for energies both below and above the ionization potential of hydrogen. The two-dimensional z = *constant*

equipotential curves for $V = 10.5$ ev, for z varying from 0 to 24 bohr, at 2 bohr intervals, were used to construct a three-dimensional wooden model of the surface. A photograph of this model, as well as equipotential curves of the cuts of $V(\rho, \omega, \gamma)$ by different planes were given in Chapter 2. The asymptotic potential curves (large z) are practically circular, that is, independent of γ, the radii of these circles being essentially independent of z. As z becomes large the $V = constant$ surfaces, for potential energies below the ionization potential of the H atom, become as a result cylindrical, that is, independent of z. In this asymptotic region the potential is approximately that of the isolated hydrogen atom and so depends only on the distance r, which in these coordinates is almost proportional to s:

$$\begin{aligned} r^2 &= \frac{1}{2}\sqrt{s^2+z^2}(\sqrt{s^2+z^2}-z) \\ &= \frac{1}{2}\Big(s^2+z^2(1-(1+\frac{s^2}{z^2})^{\frac{1}{2}})\Big) \\ &\approx \frac{1}{2}\Big(s^2+z^2(1-1-\frac{s^2}{2z^2})\Big) \\ &= \frac{s^2}{4} \end{aligned} \tag{A.2}$$

A.2 Hamiltonian in Cylindrical Coordinates

Because the potential function seemed to be naturally represented in cylindrical coordinates, we decided to try to solve the body-fixed Schrödinger equation using them. As mentioned in Section 2.1, either body-fixed or spaced-fixed angles can be used. We decided in these studies to select the former. In this representation, the kinetic energy operator is not diagonal and couples different values of the quantum number Ω.[1] After expanding the wavefunction in Wigner rotation functions of the Euler angles,

$$\Psi^{JM} = \sum_{\Omega=-J}^{J} D^J_{M\Omega}(\phi\theta\psi)\Phi^J_\Omega \tag{A.3}$$

the three-dimensional wavefunction coefficients Φ^J_Ω satisfy the following non-diagonal Schrödinger equation:

$$H^J_{\Omega,\Omega-1}\Phi^J_{\Omega-1} + H^J_{\Omega,\Omega}\Phi^J_\Omega + H^J_{\Omega,\Omega+1}\Phi^J_{\Omega+1} = E\Phi^J_\Omega \tag{A.4}$$

where the diagonal term of the Hamiltonian is given by

$$\begin{aligned} H^J_{\Omega,\Omega} = &-\frac{\hbar^2}{2\mu}\Big(\frac{\partial^2}{\partial R^2}+\frac{\partial^2}{\partial r^2}\Big) - \frac{\hbar^2}{2\mu r^2}\Big[\frac{1}{\sin\gamma}\frac{\partial}{\partial\gamma}\sin\gamma\frac{\partial}{\partial\gamma} - \frac{\omega^2}{\sin^2\gamma}\Big] \\ &-\frac{\hbar^2}{2\mu R^2}\Big[\frac{1}{\sin\gamma}\frac{\partial}{\partial\gamma}\sin\gamma\frac{\partial}{\partial\gamma} - J(J+1) + 2\Omega^2 - \frac{\Omega^2}{\sin^2\gamma}\Big] + V(R,r,\gamma) \end{aligned} \tag{A.5}$$

and the off-diagonal Hamiltonians are given by

$$H^J_{\Omega,\Omega\pm1} = \frac{\hbar^2}{2\mu r^2}\Big[(J\mp\Omega)(J\pm\Omega+1)\Big]^{\frac{1}{2}}\Big[(\Omega\pm1)\cot\gamma \pm \frac{\partial}{\partial\gamma}\Big] \tag{A.6}$$

We make the $(r,R)\rightarrow(s,z)$ coordinate transformation as follows:

$$\begin{aligned} r^2 + R^2 &= s^2 + z^2 = \rho^2 \\ \operatorname{arccot}\Big(\frac{R}{r}\Big) &= \frac{1}{2}\operatorname{arccot}\Big(\frac{z}{s}\Big) \end{aligned} \tag{A.7}$$

The inverse transformation is

$$\begin{aligned} R^2 &= \frac{\rho(\rho+z)}{2} \\ r^2 &= \frac{\rho(\rho-z)}{2} \end{aligned} \tag{A.8}$$

which leads directly to

$$\begin{aligned} R &= \frac{1}{\sqrt{2}}(s^2+z^2)^{\frac{1}{4}}\big(\sqrt{s^2+z^2}+z\big)^{\frac{1}{2}} \\ r &= \frac{1}{\sqrt{2}}(s^2+z^2)^{\frac{1}{4}}\big(\sqrt{s^2+z^2}-z\big)^{\frac{1}{2}} \end{aligned} \tag{A.9}$$

A.2.1 Differentials and derivatives

The various partial derivatives and differentials are given below. They are obtained by differentiating ($A.9$) to obtain the following expressions for ds and dz:

$$\begin{aligned} ds &= \frac{(sr/2 + zR)\,dr + (sr/2 - zR)\,dR}{\frac{1}{2}(s^2 + z^2)} \\ dz &= \frac{(zr/2 - sR)\,dr + (zR/2 + sr)\,dR}{\frac{1}{2}(s^2 + z^2)} \end{aligned} \tag{A.10}$$

The partial derivatives are easily seen to be

$$\begin{aligned} \left(\frac{\partial s}{\partial r}\right) &= \frac{(sr + 2zR)}{(s^2 + z^2)} \\ \left(\frac{\partial s}{\partial R}\right) &= \frac{(sR - 2zr)}{(s^2 + z^2)} \\ \left(\frac{\partial z}{\partial r}\right) &= \frac{(zr - 2sR)}{(s^2 + z^2)} \\ \left(\frac{\partial z}{\partial R}\right) &= \frac{(zR + 2sr)}{(s^2 + z^2)} \end{aligned} \tag{A.11}$$

In terms of s and z these expressions become

$$\begin{aligned} \left(\frac{\partial s}{\partial r}\right) &= \frac{s(s^2 + z^2)^{\frac{1}{4}}(\sqrt{s^2 + z^2} - z)^{\frac{1}{2}} + 2z(s^2 + z^2)^{\frac{1}{4}}(\sqrt{s^2 + z^2} + z)^{\frac{1}{2}}}{\sqrt{2}(s^2 + z^2)} \\ \left(\frac{\partial s}{\partial R}\right) &= \frac{s(s^2 + z^2)^{\frac{1}{4}}(\sqrt{s^2 + z^2} + z)^{\frac{1}{2}} - 2z(s^2 + z^2)^{\frac{1}{4}}(\sqrt{s^2 + z^2} - z)^{\frac{1}{2}}}{\sqrt{2}(s^2 + z^2)} \\ \left(\frac{\partial z}{\partial r}\right) &= \frac{z(s^2 + z^2)^{\frac{1}{4}}(\sqrt{s^2 + z^2} - z)^{\frac{1}{2}} - 2s(s^2 + z^2)\frac{1}{4}(\sqrt{s^2 + z^2} + z)^{\frac{1}{2}}}{\sqrt{2}(s^2 + z^2)} \\ \left(\frac{\partial z}{\partial R}\right) &= \frac{z(s^2 + z^2)^{\frac{1}{4}}(\sqrt{s^2 + z^2} + z)^{\frac{1}{2}} + 2s(s^2 + z^2)^{\frac{1}{4}}(\sqrt{s^2 + z^2} - z)^{\frac{1}{2}}}{\sqrt{2}(s^2 + z^2)} \end{aligned} \tag{A.12}$$

From the above equations one obtains the differential operators using the chain rule.

$$\begin{aligned} \left(\frac{\partial}{\partial r}\right) = &\frac{s(\sqrt{s^2 + z^2} - z)^{1/2} + 2z(\sqrt{s^2 + z^2} + z)^{1/2}}{\sqrt{2}\,(s^2 + z^2)^{3/4}}\left(\frac{\partial}{\partial s}\right) \\ &+ \frac{z(\sqrt{s^2 + z^2} - z)^{1/2} - 2s(\sqrt{s^2 + z^2} + z)^{1/2}}{\sqrt{2}\,(s^2 + z^2)^{3/4}}\left(\frac{\partial}{\partial z}\right) \end{aligned} \tag{A.13}$$

$$\left(\frac{\partial}{\partial R}\right) = \frac{s(\sqrt{s^2+z^2}+z)^{1/2} - 2z(\sqrt{s^2+z^2}-z)^{1/2}}{\sqrt{2}\,(s^2+z^2)^{3/4}}\left(\frac{\partial}{\partial s}\right) + \frac{z(\sqrt{s^2+z^2}+z)^{1/2} + 2s(\sqrt{s^2+z^2}-z)^{1/2}}{\sqrt{2}\,(s^2+z^2)^{3/4}}\left(\frac{\partial}{\partial z}\right) \tag{A.14}$$

After simplification this leads to

$$\left(\frac{\partial}{\partial R}\right) = \frac{(\rho-z)^{3/2}}{\sqrt{2}\,\rho^{3/2}}\left(\frac{\partial}{\partial s}\right) + \frac{(2\rho-z)(\rho+z)^{1/2}}{\sqrt{2}\,\rho^{3/2}}\left(\frac{\partial}{\partial z}\right) \tag{A.15}$$

$$\left(\frac{\partial}{\partial r}\right) = \frac{(\rho+z)^{3/2}}{\sqrt{2}\,\rho^{3/2}}\left(\frac{\partial}{\partial s}\right) - \frac{(4\rho^3-3z^2\rho-z^3)^{1/2}}{\sqrt{2}\,\rho^{3/2}}\left(\frac{\partial}{\partial z}\right) \tag{A.16}$$

Likewise we obtain second derivatives:

$$\left(\frac{\partial^2}{\partial R^2}\right) = \frac{(\rho-z)^3}{2\rho^3}\left(\frac{\partial^2}{\partial s^2}\right) + \frac{(4\rho^3-3\rho z^2+z^3)}{2\rho^3}\left(\frac{\partial^2}{\partial z^2}\right) - \frac{3s(\rho-z)}{2\rho^3}\left(\frac{\partial}{\partial s}\right) + \frac{(2\rho-z)(\rho-z)s}{\rho^3}\left(\frac{\partial^2}{\partial s\partial z}\right) - \frac{3z(\rho-z)}{2\rho^3}\left(\frac{\partial}{\partial z}\right) \tag{A.17}$$

$$\left(\frac{\partial^2}{\partial r^2}\right) = \frac{(\rho+z)^{3/2}}{2\rho^3}\left(\frac{\partial^2}{\partial s^2}\right) + \frac{(2\rho+z)^2(\rho-z)}{2\rho^3}\left(\frac{\partial^2}{\partial z^2}\right) - \frac{3s(\rho+z)}{2\rho^3}\left(\frac{\partial}{\partial s}\right) - \frac{(2\rho+z)(\rho+z)s}{\rho^3}\left(\frac{\partial^2}{\partial s\partial z}\right) - \frac{3z(\rho+z)}{2\rho^3}\left(\frac{\partial}{\partial z}\right) \tag{A.18}$$

A.3 The Schrödinger Equation in Cylindrical Coordinates

The derivatives in r and R appear only in the diagonal piece of the Hamiltonian, $H^J_{\Omega,\Omega}$, and therefore the off-diagonal terms $H^J_{\Omega,\Omega\pm1}$ are unaffected by the $(r,R) \rightarrow (s,z)$ coordinate transformation. The expression for $H^J_{\Omega,\Omega}$ becomes

$$H^J_{\Omega,\Omega} = \left\{\left(\frac{s^2+4z^2}{s^2+z^2}\right)\left(\frac{\partial^2}{\partial s^2}\right) - \left(\frac{3s}{s^2+z^2}\right)\left(\frac{\partial}{\partial s}\right) - \left(\frac{6sz}{s^2+z^2}\right)\left(\frac{\partial^2}{\partial s\partial z}\right) + \left(\frac{4s^2+z^2}{s^2+z^2}\right)\left(\frac{\partial^2}{\partial z^2}\right) - \left(\frac{3z}{s^2+z^2}\right)\left(\frac{\partial}{\partial z}\right)\right\} - [2\Omega^2 - J(J+1)] + V(s,z,\gamma) \tag{A.19}$$

A major disadvandtage of this expression is the appearance of the mixed derivative operator $\partial^2/\partial s\partial z$.

The proposed method of solving equation $(A.4)$ is to expand $\Phi^J_\Omega(s,z,\gamma)$ in surface eigenfunctions for constant z. Because the potential at large z is practically independent of z and γ, one would expect that hydrogen atom wavefunctions would do very well in describing that region, and that few basis functions would be needed in the expansion. However, we recognized that many basis functions would be needed for small z, in order to take into account the spike in the equipotential surfaces, at the origin.

The surface functions would be eigenfunctions of a well-chosen surface Hamiltonian, $H^{\rm ref}(s,\gamma;z)$. This Hamiltonian would have no derivatives with respect to z, and should be as close as possible to $H^J_{\Omega,\Omega}(s,z,\gamma)$. For example, let us choose the following reference potential:

$$\begin{aligned} H^{\rm ref}(s,\gamma;\bar{z}) = &-\frac{s^2+4\bar{z}^2}{s^2+\bar{z}^2}\left(\frac{\partial^2}{\partial s^2}\right)+\frac{3s}{s^2+\bar{z}^2}\left(\frac{\partial}{\partial s}\right) \\ &-\frac{1}{2}\left[\frac{1}{R^2(\bar{z})}+\frac{1}{r^2(\bar{z})}\right]\frac{1}{\sin\gamma}\left(\frac{\partial}{\partial\gamma}\right)\sin\gamma\left(\frac{\partial}{\partial\gamma}\right)+V(s,\gamma;\bar{z}) \end{aligned} \tag{A.20}$$

which simplifies to

$$\begin{aligned} H^{\rm ref}(s,\gamma;\bar{z}) = &-\frac{s^2+4\bar{z}^2}{s^2+\bar{z}^2}\left(\frac{\partial^2}{\partial s^2}\right)+\frac{3s}{s^2+\bar{z}^2}\left(\frac{\partial}{\partial s}\right) \\ &-\frac{2}{s^2}\frac{1}{\sin\gamma}\left(\frac{\partial}{\partial\gamma}\right)\sin\gamma\left(\frac{\partial}{\partial\gamma}\right)+V(s,\gamma;\bar{z}) \end{aligned} \tag{A.21}$$

However one cannot simply delete the z derivative terms from $H^J_{\Omega,\Omega}$ as we did with derivatives in ρ to obtain the hyperspherical surface Hamiltonian. Consider the $J=0$ case, in which $\Omega=0$. The operator obtained by "freezing" z at a constant value $\bar{z}$ is not a Hermitian operator and therefore has complex eigenvalues. We consider this unacceptable. All of the reference operators we considered were either non-Hermitian, or not very close to the full Hamiltonian.

But let us say that a suitable reference Hamiltonian which is Hermitian has been

found, with eigenfunctions $\phi(s,\gamma;z)$ to be determined, and that $\Phi_{\Omega=0}^{J=0}$ is expanded in ϕ_{nl} thus:

$$\Phi_0^0(s,z,\gamma) = \sum_{nl} g_{nl}(z)\phi_{nl}(s,\gamma;\bar{z}) \tag{A.22}$$

$$H^{\text{ref}}\phi_{nl}(s,\gamma;\bar{z}) = \epsilon_{nl}(z)\phi_{nl} \tag{A.23}$$

The surface functions are then expanded in Legendre polynomials in $\cos\gamma$; this expansion is replaced in the reference equation (A.23). By using the orthogonality of Legendre polynomials, a system of coupled differential equations in the variable s is obtained. After solving these equations one substitutes these ϕ_{nl} into (A.22) which is then replaced into (A.4) with $J = \Omega = 0$. Writing $H_{0,0}^0$ as H simply, we get

$$H = H^{\text{ref}} + H' \tag{A.24}$$

and therefore

$$H\Phi = \sum_{nl} g_{nl}(z)\epsilon_{nl}(\bar{z})\phi_{nl}(s,\gamma;\bar{z}) + \sum_{nl} H'[g_{nl}(z)\phi_{nl}(s,\gamma;\bar{z})] \tag{A.25}$$

H' necessarily containes the mixed partial derivative, $\partial^2/\partial s\partial z$. No function manipulations can be done that will remove it. Also, H' contains the term

$$\left(\frac{4s^2+z^2}{s^2+z^2}\right)\left(\frac{\partial^2}{\partial z^2}\right) \tag{A.26}$$

This means that the differential equation for $g_{nl}(z)$ inevitably has the form:

$$\mathbf{A}(z)\mathbf{g}''(z) + \mathbf{B}(z)\mathbf{g}'(z) + \mathbf{C}(z)\mathbf{g}(z) = \mathbf{0} \tag{A.27}$$

where the matrices $\mathbf{A}(z)$, $\mathbf{B}(z)$, and $\mathbf{C}(z)$ are all functions of z, which by left multiplication by $\mathbf{A}^{-1}$, can be put in the form

$$\mathbf{g}''(z) + \mathbf{D}(z)\mathbf{g}'(z) + \mathbf{F}(z)\mathbf{g}(z) = \mathbf{0} \tag{A.28}$$

Current algorithms for the numerical solution of such an equation are not nearly as efficient as those for the case in which $\mathbf{D} = \mathbf{0}$, i. e., for which the first derivative term is absent. As a result, we decided not to pursue this approach.

The key to why these were not good coordinates may be that too much attention was paid to the potential energy term, and not enough to the kinetic energy one. Although the potential energy seems naturally suited to cylindrical coordinates, the kinetic energy operator expressed in these coordinates is very complicated, and it should be obvious, with hindsight, that the motion is not be quasi-separable.

A.4 Jacobi Polynomial Expansion

In this section we consider an alternate selection of basis functions for expansion of the surface functions. Instead of finding the one-dimensional solutions to the surface function equation that results by keeping only the diagonal elements of the potential matrix (Eq. 2.34), we consider the case in which there is no coupling at all, i. e., for which we take $V = 0$. We will go back to the expansion of the five-dimensional surface functions to start this derivation. Unlike considerations of Section 2.4.2, we will not force symmetry into the basis functions from the beginning. Instead we will use a unitary transformation of the basis functions after the rest of the analysis has been done.

The five-dimensional surface functions $\Phi^{JMS\Pi}$ are expanded in the functions $X^{JM}_{l_2 l_1 \eta}$,

$$\Phi^{JMS\Pi}_i = \sum_{l_2 l_1 p} c^{JS\Pi i}_{l_2 l_1 \eta}(\bar{\rho})\, X^{JM}_{l_2 l_1 \eta}(\omega, 4 \text{ angles}; \rho) \tag{A.29}$$

These functions $X^{JM}_{l_2 l_1 \eta}$ are chosen so as to satisfy the following differential equation:

$$\begin{aligned}\left\{4\left(\frac{\partial^2}{\partial\omega^2} + 2\cot\omega\frac{\partial}{\partial\omega}\right) + \frac{1}{\cos^2\frac{\omega}{2}}\left(\frac{1}{\sin\theta_2}\frac{\partial}{\partial\theta_2}\sin\theta_2\frac{\partial}{\partial\theta_2} + \frac{1}{\sin^2\theta_2}\frac{\partial^2}{\partial\varphi_2^2}\right)\right. \\ \left. + \frac{1}{\sin^2\frac{\omega}{2}}\left(\frac{1}{\sin\theta_1}\frac{\partial}{\partial\theta_1}\sin\theta_1\frac{\partial}{\partial\theta_1} + \frac{1}{\sin^2\theta_1}\frac{\partial^2}{\partial\varphi_1^2}\right)\right\} X^{JM}_{l_2 l_1 \eta} \\ = e_\eta \quad X^{JM}_{l_2 l_1 \eta}(\omega, \theta_1, \varphi_1, \theta_2, \varphi_2)\end{aligned} \tag{A.30}$$

The boundary conditions are that $X^{JM}_{l_2 l_1 \eta}$ be bound, single valued, continuous, and have continuous first derivatives. This equation is separable by the factorization

$$X^{JM}_{l_2 l_1 \eta}(\omega, \theta_1, \varphi_1, \theta_2, \varphi_2) = \mathcal{Y}^{JM}_{l_2 l_1}(\theta_1, \varphi_1, \theta_2, \varphi_2)\; y^{l_2 l_1}_{\eta}(\omega) \qquad (A.31)$$

where

$$\mathcal{Y}^{JM}_{l_2 l_1}(\theta_1, \varphi_1, \theta_2, \varphi_2) = \sum_{m_1 m_2} C(l_1 l_2 J; m_1 m_2 M) Y_{l_2 m_2}(\hat{\mathbf{R}}) Y_{l_1 m_1}(\hat{\mathbf{r}}) \qquad (A.32)$$

The equation which results for $y^{l_2 l_1}_{\eta}$ is

$$\left[4\left(\frac{d^2}{d\omega^2} + 2\cot\omega\frac{d}{d\omega}\right) - \frac{l_1(l_1+1)}{\sin^2\frac{\omega}{2}} - \frac{l_2(l_2+1)}{\cos^2\frac{\omega}{2}}\right] y^{l_2 l_1}_{\eta}(\omega) = e_\eta y^{l_2 l_1}_{\eta} \qquad (A.33)$$

The solutions of $(A.33)$ which are bound, are continuous, and have a continuous first derivative can be obtained analytically and result in

$$e_\eta = -\eta(\eta+4) \qquad (A.34)$$

where

$$\eta = 2L + l_1 + l_2$$

and L is a non-negative integer.[2] Therefore the one-dimensional basis functions $y^{l_2 l_1}_{\eta}$ are degenerate in l_1 and l_2. They are also independent of the total angular momentum quantum numbers, J and M. The functions that satisfy the above equation are modified Jacobi polynomials, of the family of hypergeometric functions.[3]

$$y^{l_2 l_1}_{\eta} = N \sin^{l_1}\frac{\omega}{2}\cos^{l_2}\frac{\omega}{2}\; {}_2F_1[-L, \frac{1}{2}(\eta + l_1 + l_2 + 4); l_1 + \tfrac{3}{2}; \sin^2\frac{\omega}{2}) \qquad (A.35)$$

or, in terms of Jacobi polynomials $P^{(\alpha,\beta)}_m(x)$,[3]

$$y^{l_2 l_1}_{\eta} = N' \sin^{l_1}\frac{\omega}{2}\cos^{l_2}\frac{\omega}{2}\; P^{(l_1+\frac{1}{2}, l_2+\frac{1}{2})}_L(\cos\omega) \qquad (A.36)$$

where N and N' are constants chosen to make $y_\eta^{l_2 l_1}$ square normalized with the volume element $\sin^2\omega\, d\omega$.

$$N = \left[\frac{(\eta+2)(L+l_1+l_2+1)!\;\Gamma(L+l_1+\frac{3}{2})}{4\,L!\,\left[\Gamma(l_1+\frac{3}{2})\right]^2\,\Gamma(L+l_2+\frac{3}{2})}\right]^{1/2} \tag{A.37}$$

$$N' = \left[\frac{(\eta+2)(L+l_1+l_2+1)!\;L!}{4\,\Gamma(L+l_1+\frac{3}{2})\;\Gamma(L+l_2+\frac{3}{2})}\right]^{1/2} \tag{A.38}$$

We use the $X^{JM}_{l_2 l_1 \eta}$ defined by (A.30) through (A.37) in (A.29) and replace this expansion in Eq. 2.27. Multiplying both sides of the resulting equation by ${X^{JM}_{l_2' l_1' \eta'}}^*$, integrating over the five angles and interchanging the primed and unprimed indices gives the following set of coupled equations for the $c^{Ji}_{l_2 l_1 \eta}(\bar\rho)$:

$$\sum_{l_2' l_1' \eta'} \langle X^{JM}_{l_2' l_1' \eta'} | V | X^{JM}_{l_2 l_1 \eta} \rangle c^{JS\Pi i}_{l_2' l_1' \eta'}(\bar\rho) = \left[\varepsilon_i^{JS\Pi}(\bar\rho) - \frac{\hbar^2}{2\mu\rho^2}\eta(\eta+4)\right] c^{JS\Pi i}_{l_2 l_1 \eta}(\bar\rho) \tag{A.39}$$

To find $\mathbf{c}^{JS\Pi}$ and $\varepsilon_i^{JS\Pi}(\rho)$ we must obtain find the eigenvectors and eigenvalues of the matrix

$$\overline{\mathbf{V}}^{J\Pi}{}^{l_2' l_1' \eta'}_{l_2 l_1 \eta} = \frac{\hbar^2}{2\mu}\frac{1}{\bar\rho^2}\eta(\eta+4)\delta^{l_2' l_1' \eta'}_{l_2 l_1 \eta} + \langle X^{JM}_{l_2' l_1' \eta'} | V | X^{JM}_{l_2 l_1 \eta} \rangle \tag{A.40}$$

The $\bar\rho$-dependence of $\overline{\mathbf{V}}^{J\Pi}$ can be written out explicitly. According to Eq. 2.19, we can express the potential function as

$$V(\rho,\omega,\gamma) = \frac{1}{\rho} C(\omega,\gamma) \tag{A.41}$$

This permits us to write $\overline{\mathbf{V}}^{J\Pi}$ as

$$\overline{\mathbf{V}}^{J\Pi}(\bar\rho) = \frac{\hbar^2}{2\mu}\frac{1}{\bar\rho^2}\,\mathbf{n} + \frac{1}{\bar\rho}\,\mathbf{C}^{J\Pi} \tag{A.42}$$

where

$$[\mathbf{n}]^{l_2' l_1' \eta'}_{l_2 l_1 \eta} = \eta(\eta+4)\delta^{l_2' l_1' \eta'}_{l_2 l_1 \eta} \tag{A.43}$$

which is degenerate in l_1 and l_2, and

$$[\mathbf{C}^{J\Pi}]^{l_2' l_1' \eta'}_{l_2 l_1 \eta} = \langle X^{JM}_{l_2' l_1' \eta'} | C(\omega,\gamma) | X^{JM}_{l_2 l_1 \eta} \rangle \tag{A.44}$$

The first step in obtaining the surface functions is the calculation of $\mathbf{C}^{J\Pi}$. This is done by a method analogous to the one used in Section 2.5 to obtain the matrix defined by Eq. 2.32. The basis functions are converted into functions of body-fixed coordinates, and the repulsion term of the potential is expanded in Legendre functions. We treat the attractive and repulsive terms separately, for convenience. Since γ doesn't enter into the attraction terms, the attraction matrix elements are diagonal in l_1 and l_2:

$$[\mathbf{C}^{J\Pi}_a]^{l_2' l_1' p'}_{l_2 l_1 p} = \int y^{l_2 l_1}_{\eta'} \left(\frac{1}{\cos\frac{\omega}{2}} + \frac{1}{\sin\frac{\omega}{2}} \right) y^{l_2 l_1}_{\eta} \sin^2\omega \, d\omega \; \delta^{l_2' l_1'}_{l_2 l_1} \tag{A.45}$$

Another simplifying feature of the attraction integrals is that they depend on the total angular momentum quantum number, J, only indirectly, in that l_1, l_2, and J must satisfy a triangular relationship. Using the properties of the $y^{l_2 l_1}_{\eta}(\omega)$ functions,[3] a recursion scheme, with several stages, was developed to calculate the attraction integrals.

The repulsion elements were calculated directly from the series expansion form of the functions $y^{l_2 l_1}_{\eta}(\omega)$, which is[3]

$$\begin{aligned} y^{l_2 l_1}_{\eta}(\omega) = & \left[\frac{(\eta+2)\; L!\; \Gamma(l_1+L+\frac{3}{2})}{4\,(l_1+l_2+L+1)!\,\Gamma(l_2+L+\frac{3}{2})} \right]^{1/2} \\ & \times \sum_{m=0}^{L} \frac{(-1)^m (m+l_1+l_2+L+1)!}{(L-m)!\,m!\,\Gamma(m+l_1+\frac{3}{2})} \cos^{l_2}\frac{\omega}{2} \sin^{l_1+2m}\frac{\omega}{2} \end{aligned} \tag{A.46}$$

where $L = \frac{1}{2}(\eta - l_1 - l_2)$, and is a non-negative integer. All the matrix element integrals take the form

$$\int_0^{\pi/4} \cos^p \alpha \sin^q \alpha \, d\alpha \qquad (A.47)$$

where p is a positive or negative odd integer, and q is an even positive integer. These matrix elements were calculated by recursion. Macek,[4] Lin,[5] and Klar[6] derived formulae for these matrix elements by slightly different methods.

Although a completely general program was developed at first, so many simplifications were indicated for the case of $J = 0$ that this case was treated separately. First of all, symmetry with respect to $\omega = \pi/2$ is determined by the value of η for S states: even states have $\eta = 0, 4, 8, \ldots$, while the odd states have $\eta = 2, 6, \ldots$. The transformation between body-fixed and spaced-fixed coordinates is trivial. There are other simplifications due to the $l_1 = l_2$ restriction; the symmetry properties have been discussed in Chapter 2 with respect to the counterpart basis functions which were obtained numerically.

Once assured that the potential matrix elements were being calculated properly, we tried to find out how large the basis $X^{JM}_{l_2 l_1 \eta}$ needed to be for the surface function expansion ($A.29$) to converge. The size of a basis is determined by $\eta_{\max}$, the largest allowed value of the index η; all values of l_2 allowed for each η were included.

The surface functions were obtained for various basis sizes at ρ=1.0 bohr, 4.0 bohr, 7.0 bohr, and 10.0 bohr. Table A–1 lists the ^{1}S eigenvalues obtained with several basis sets. Table A–2 lists the eigenvalues for ^{3}S. As ρ increases, the convergence gets slower. We expect the two lowest eigenvalues (one for ^{1}S and one for ^{3}S) to converge to -0.5 hartree as ρ approaches infinity. From the table we see that, even at 10 bohr, the electrons are interacting. Using the largest basis the lowest eigenvalue for $\rho = 10$ bohr is $\varepsilon_1^{^1\mathrm{S}} = -0.514$ hartrees, and still is not converged. Neither is the lowest eigenvalue for $\rho = 7.0$ bohr converged ($\varepsilon_1^{^1\mathrm{S}} = -0.546$); at

$\rho = 4.0$ the lowest eigenvalue seems headed for -0.6985 hartrees; at $\rho = 1.0$ the lowest eigenvalue has converged to -2.3091 hartrees.

Looking at the matrix elements and the eigenvector coefficients, it became apparent that only the basis functions with $l_2 = 0$ were having a significant effect on the lowest $(1s)$ eigenvalue. This is because the contribution of the attraction to the potential matrix elements is much larger than that of the repulsion, and only exists if $l_2 = l_2'$. The most important basis functions in the lowest eigenvectors are $X^{J=0,M=0}_{l_2 l_1 \eta=(000)}$, and X^{00}_{002}, for the lowest ^{1}S and ^{3}S vectors, respectively. The coefficient of each these functions is larger than 0.99, so only those functions that have large matrix elements with X^{00}_{000} or X^{00}_{002} have any effect on the lowest eigenvalue. The selection of basis functions was modified such that only $l_2 = 0$ and $l_2 = 1$ functions were included, for η larger than a certain cut-off (which was chosen as 22). This feature enabled us to achieve the same convergence with respect to $\eta_{\max}$, but without making the total number of basis functions get out of hand. The largest calculation done so far used $\eta_{\max} = 48$. This corresponds to 169 ^{1}S basis functions, or 55 using the $l_2 \leq 1$ criterion, and 156 ^{3}S functions, truncated to 49.

Early research with hyperspherical coordinates has depended on these hyperspherical harmonics for expansion of the surface functions.[7] The potential curves obtained by this method have been used to study the properties of bound states of H^-, Feshbach resonances, and shape resonances.[8] Previous work has always employed the adiabatic, or some other, approximation such that coupling between the channels (i. e., surface functions) was not included in the calculation. Klar and Klar[9] reports using values of η up to 58, and not getting convergence. Our own studies used up to 84 basis functions and still found inadequate convergence. We also found it difficult to obtain the matrix elements by this method.

We have plotted a few of the Jacobi polynomial basis functions in Figures A.1

and A.2. The counterpart numerical functions $t_p^{Jl_2l_1}(\omega;\rho)$ are plotted on the same scale. In the first figure $\rho = 1$ bohr, and the Jacobi functions are almost indistinguishable from the numerical functions, which shows that the Jacobi functions are useful as basis functions for small values of ρ. In the second figure $\rho = 10$ bohr. The Jacobi functions are independent of ρ, of course, and so haven't changed, as compared with the previous figure. The numerical functions, on the other hand, have started to shift to the ends of the range, $\omega = 0$ and $\omega = \pi$, from the center region, $\omega = \frac{\pi}{2}$. The basis functions which adapt to the potential are more appropriate to use.

Table A–2: Eigenvalues of ^{3}S for $\rho = 4.$, $\rho = 7.$, and $\rho = 10.$ bohr for different size Jacobi polynomial bases.[a,b]

n_{max}	N^a	$e_1(4.)$	$e_1(7.)$	$e_2(7.)$	$e_1(10.)$	$e_2(10.)$	$e_3(10.)$
22	36	−.57347	−.51553	−.05299	−.47871	−.12729	−.07996
26	49	−.57553	–	–	−.48998	−.12907	−.08223
30	64	−.57679	−.53467	−.05569	−.49788	−.13028	−.08363
36	[43]	−.57761	−.53730	−.05609	−.50352	−.13115	−.08456
40	[45]	−.57816	−.53914	−.05635	−.50763	−.13175	−.08518
44	[47]	−.57854	−.54046	−.05653	−.51067	−.13220	−.08561
48	[49]	−.57882	−.54144	−.05667	−.51302	−.13254	−.08593

[a]Number of basis functions. The numbers in square brackets indicate that the basis set was truncated to include only $l_2 \leq 1$ states.

[b]The $\rho = 1$ bohr results have been omitted because at $\rho = 1.$ bohr the lowest state is still very high in energy.

Table A–1: Eigenvalues (in hartree) of ^{1}S symmetry at different values of ρ(bohr).[a]

η_{max}	N^a	$e_1(1.)$	$e_1(4.)$	$e_2(4.)$	$e_1(7.)$	$e_2(7.)$	$e_3(7.)$	$e_1(10.)$	$e_2(10.)$	$e_3(10.)$	$e_4(10.)$
14	20	−2.3072	–	–	–	–	–	–	–	–	–
22	42	−2.3086	−.6940	−.1082	−.5261	−.2231	−.1260	−.4715	−.1933	−.1297	−.02513
26	56	−2.3088	−.6956	−.1090	–	–	–	−.4850	−.1947	−.1302	−.02538
30	72	−2.3089	−.6966	−.1095	−.5376	−.2261	−.1270	−.4944	−.1957	−.1305	−.02553
36	[49]	−2.3090	−.6976	−.1100	−.5427	−.2273	−.1273	−.5058	−.1968	−.1309	−.02565
40	[51]	−2.3090	−.6978	−.1101	−.5442	−.2277	−.1274	−.5094	−.1971	−.1310	−.02570
44	[53]	−2.3091	−.6980	−.1102	−.5453	−.2279	−.1275	−.5120	−.1973	−.1311	−.02573
48	[55]	−2.3091	−.6982	−.1103	−.5461	−.2281	−.1275	−.5142	−.1975	−.1312	−.02575

[a]Number of basis functions. The numbers in square brackets indicate that the basis set was truncated to include only $l_2 \leq 1$ states.

A.5 References

1. R. T. Pack, *J. Chem. Phys.*, **60**, 633 (1974).
2. For the ^{1}S partial wave, η is a multiple of 4; for ^{3}S, it is a multiple of four, plus 2; odd values of η are permissible for odd parity states.
3. Handbook of Mathematical Functions, edited by M. Abramowitz and I. A. Stegun (National Bureau of Standards, Washington, D. C., 1964).
4. J. H. Macek, *J. Phys. B*, **1**, 831 (1968).
5. C. D. Lin, *Phys. Rev. A*, **10**, 1986 (1974).
6. H. Klar, *J. Phys. B*, **7**, L436 (1974).
7. U. Fano and C. D. Lin, in Atomic Physics, Vol. 4, ed. G. zu Putlitz (Plenum, New York, 1975), p. 47.
8. C. D. Lin, *Phys. Rev. A*, **14**, 30 (1976).
9. H. Klar and M. Klar, *Phys. Rev. A*, **17**, 1007 (1978); *J. Phys. B*, **13**, 1057, (1980).

A.6 Figures and Captions

FIG. A.1: Comparison of Jacobi polynomials (solid line) y_η^{00}, $\eta = 0$, 4, and 8, from bottom, to numerically determined ^{1}S 1-dimensional basis functions (dashed line): t_{1+}^{000}, t_{2+}^{000}, and t_{3+}^{000}, from bottom, at $\rho = 1.0$ bohr.

FIG. A.2: Comparison of Jacobi polynomials to numerically determined basis functions as in Figure A.1, but for $\rho = 10.0$ bohr.

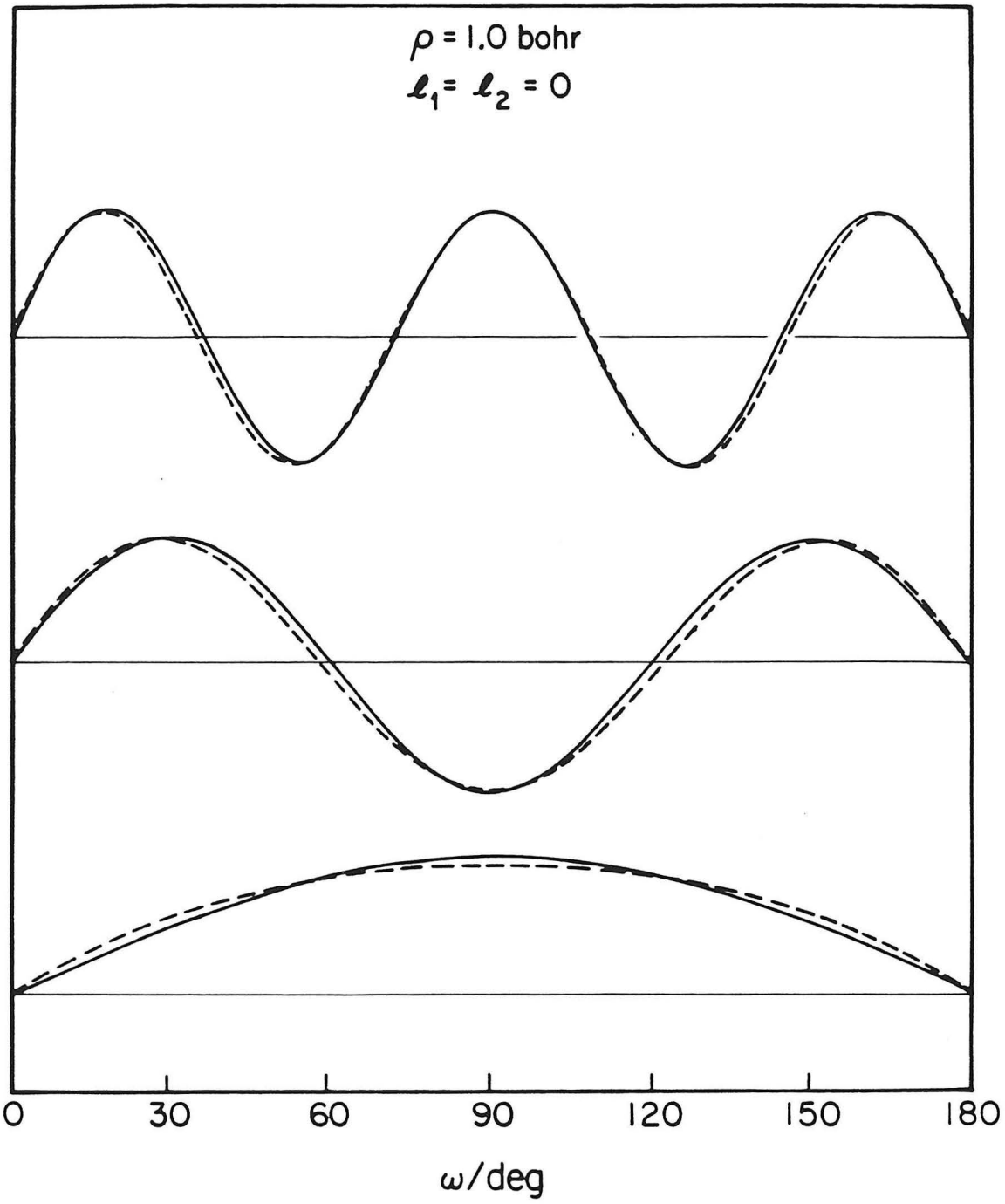

Figure A.1

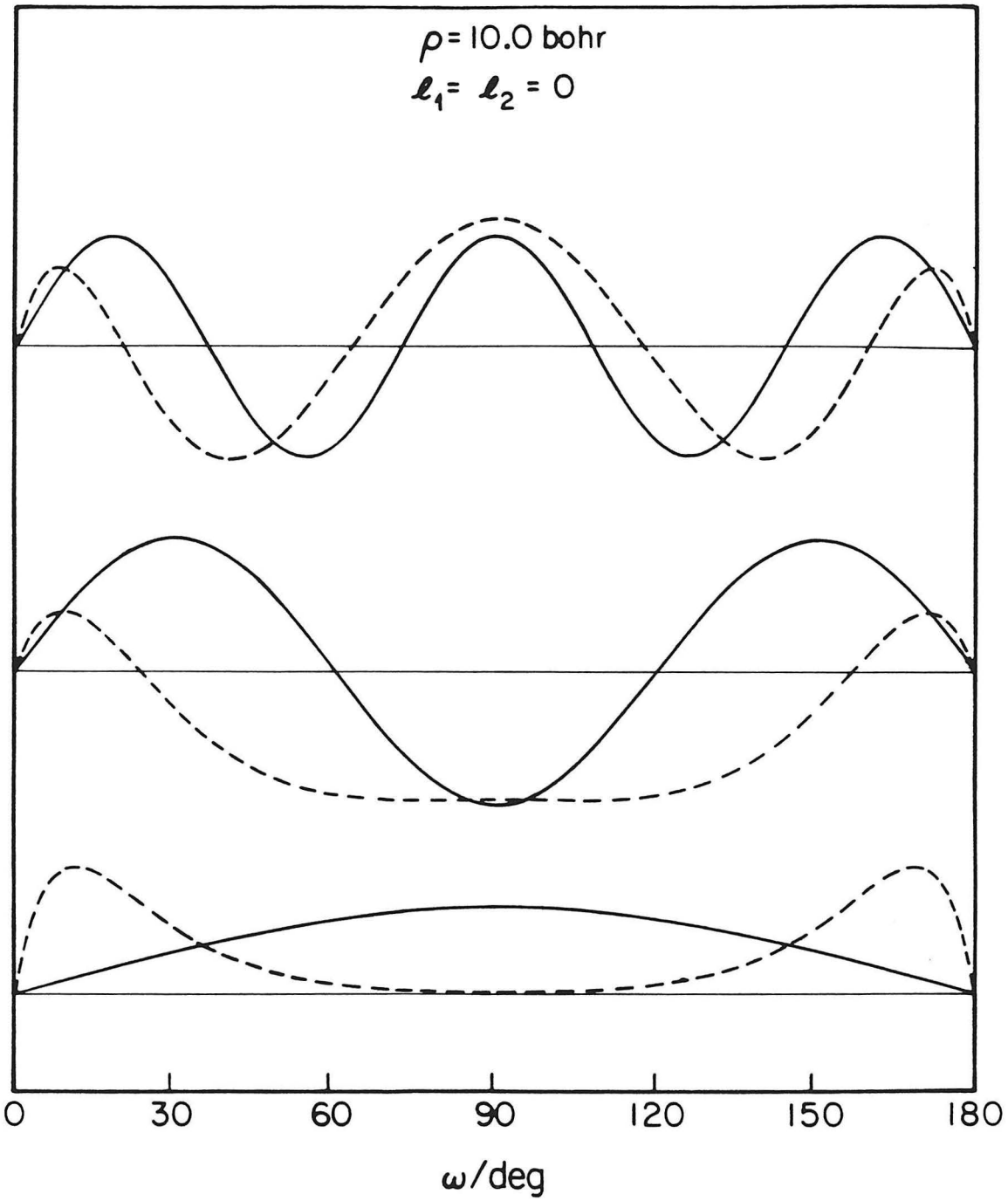

Figure A.2